BRAVO

Big Bend
Regional
Aerosol &
Visibility
Observational

Study Results







CIRA

Colorado State University

ISSN 0737-5352-65

Big Bend Regional Aerosol and Visibility Observational (BRAVO) Study Results:

Air Quality Data and Source Attribution Analyses Results from the National Park Service / Cooperative Institute for Research in the Atmosphere

2004

Bret A. Schichtel
National Park Service

Kristi A. Gebhart
National Park Service

Michael G. Barna
Cooperative Institute for Research in the Atmosphere
Colorado State University

William C. Malm
National Park Service

Derek E. Day
Cooperative Institute for Research in the Atmosphere
Colorado State University

Sonia Kreidenweis
Department of Atmospheric Science
Colorado State University

Jeffrey Collett, Jr.
Department of Atmospheric Science
Colorado State University

Contributor
Mark C. Green
Desert Research Institute

Acknowledgments

BRAVO was a collaborative project involving many participating organizations and individuals. All analyses were conducted within an open forum with developments and ideas continually shared among participants. The analyses and results presented herein were considerably enhanced by the careful thought and deliberations of these participants throughout the process.

The list of organizations that participated in the BRAVO study includes

- **Sponsors:** U.S. Environmental Protection Agency, National Park Service, and the Texas Council on Environmental Quality;
- **Contributors:** EPRI, and the National Oceanic and Atmospheric Administration - Air Resources Laboratory;
- **Research Institutions and Universities:** University of California - Davis, Desert Research Institute and the Cooperative Institute for Atmospheric Science and Terrestrial Applications at the University of Nevada, Cooperative Institute for Research in the Atmosphere (CIRA) at Colorado State University, the Pennsylvania State University, Carolina Environmental Program at the University of North Carolina, and Brookhaven National Laboratory;
- **Consulting Firms:** Atmospheric and Environmental Research, Inc. (AER), Air Resource Specialists, Inc., and Aerosol Dynamics; and
- **Stakeholders:** the Environmental Defense, the Sierra Club, American Electric Power, TXU, and Reliant Energy.

Within these organizations we would like to especially acknowledge Eladio Knipping from EPRI for his many good suggestions and providing us with the CMAQ-MADRID modeling results which were extensively used in the reconciliation process, James W. Yarbrough from the U.S. EPA Region VI and Marc L. Pitchford from National Oceanic and Atmospheric Administration for their due diligence in maintaining the BRAVO process and directing its progress to a successful conclusion, Ivar Tombach of Camarillo, California, for his numerous insightful comments and suggestions, Christian Seigneur and Betty Pun of AER for their early work on the CMAQ-Madrid model and Betty's review of trajectory mass balance techniques, John Vimont and Mark Scruggs of the National Park Service Air Resources Division for their reviews of early drafts of the report, and several individuals from Colorado State University including Hari Iyer from the statistics department for discussions on uncertainties and comparisons of measured to modeled data, Doug Fox of CIRA for his helpful comments concerning REMSAD modeling, Jeff Lemke of CIRA for his work on graphics and color schemes, and Helene Bennett of CIRA for her technical editing expertise.

We wish to thank John King, Superintendent of Big Bend National Park, park pilot Nick Herring, and the park resource management team for their cooperation, local insight, interest, questions, photographs, discussions, and overviews of the park, its heritage, resources, and visitors.

Finally, we would like to thank Philip K. Hopke, Richard L. Poirot, and Alexander V. Polissar for their careful review of the draft manuscript and many good suggestions for improving the report.

Disclaimer

The assumptions, findings, conclusions, judgments, and views presented herein are those of the authors and should not be interpreted as necessarily representing the National Park Service policies. The results, findings, and conclusions expressed in this paper are solely those of the authors and are not necessarily endorsed by the management, sponsors, or collaborators of the BRAVO Study.

TABLE OF CONTENTS

The appendices are numbered by the chapter in which they are first mentioned.

*Available only on cd.

List of Figures

List of Tables

Big Bend Regional Aerosol and Visibility Observational (BRAVO) Study Results: Air Quality Data and Source Attribution Analyses Results from the National Park Service / Cooperative Institute for Research in the Atmosphere

BRAVO Background and Summary of Findings Fact Sheet

The scenic beauty of Big Bend National Park is often spoiled by haze, obscuring its many vistas. In addition, Big Bend is one of the few monitored national parks in which haze has been increasing since the late 1980s. In 1999, the National Park Service (NPS) and the U.S. Environmental Protection Agency (EPA) carried out the Big Bend Regional Aerosol and Visibility Observational (BRAVO) study. Other participating agencies were the Texas Commission on Environmental Quality (TCEQ) and the Electric Power Research Institute (EPRI). The primary objectives of BRAVO were to determine the composition and optical properties of the haze and to quantify the contribution of major sulfur dioxide sources and source regions within Mexico and the United States to the haze. The BRAVO study involved a four-month intensive monitoring period from July through October 1999, followed by a four-year data analysis and modeling effort examining the BRAVO data and past data collected at Big Bend NP. Following is a summary of the key findings from research conducted by the National Park Service and its partners.

What is Causing Big Bend's Haze?

Haze is caused by scattering and absorption of light by suspended fine particles in the air. The composition of the particles varies depending on their human and natural sources, such as sulfate from the transformation of sulfur dioxide emitted from coal-fired power plants, dust from the suspension of soil particles, and carbonaceous material from forest fires. It has been found from monitoring of Big Bend's haze that:

- On average, the haze in Big Bend NP peaks in the spring (April–June) and summer/fall (August–October) months with the lowest haze conditions during the winter months.
- Sulfate is the single largest contributor to particulate haze at Big Bend NP, accounting for about half of the haze on the average and on the haziest days.
- Big Bend is one of the few monitored national parks where both sulfates and haze are increasing.
- Local and international transport of dust and smoke also contribute to haze, particularly in the springtime months.

What are the Common Airmass Transport Pathways to Big Bend NP?

The pollutants responsible for haze generally remain in the air for 3 to 7 days. Over this time period they can be carried up to several thousand kilometers by the winds. Therefore haze is a regional issue with source regions over 1000 km away contributing to Big Bend's haze. A source region's potential to contribute to Big Bend's haze increases as the frequency of airmasses traversing the source region prior to reaching Big Bend increases. To identify the source regions most likely to contribute to Big Bend's haze, the common airmass transport routes to Big Bend were examined throughout the year.

- Throughout the year airmasses en route to Big Bend frequently reside over Mexico, in particular northern Mexico.
- Airflow from eastern Texas and the eastern U.S. is most frequent during late summer and fall months during the period with the greatest contribution to haze by particulate sulfate compounds.
- Airflow from the western U.S. to Big Bend is greatest in the winter months when haze levels at the park are lowest.
- The highest sulfate haze periods during BRAVO were associated with low-speed and low-level transport from the eastern U.S., eastern Texas, and northeastern Mexico.
- The lowest sulfate haze periods during BRAVO were associated with higher-speed transport from the Gulf of Mexico along the Mexican/Texas border to Big Bend, from the north, and from the western U.S.

Where Does the Sulfate Haze Come From?

Sulfate particles are primarily due to sulfur dioxide emissions into the atmosphere where they are chemically transformed (oxidized) to sulfate particles during their transport. The primary sulfur dioxide sources are coal- and oil-fired power plants, metal smelters, refineries, and other industrial processes. Sulfate particles are also hygroscopic, meaning that as moisture in the air increases, sulfate particles will grow larger and scatter more light than when dry. A number of sulfate source attribution techniques were applied during BRAVO and it was found that:

- On average, during the BRAVO period U.S. sources were responsible for about 55% of Big Bend's particulate sulfate, with the eastern U.S. responsible for about 30% and eastern Texas contributing about 17%.
- Mexican sources, including the Carbón power plant, were responsible for about 38% of Big Bend's particulate sulfate.
- At 20%, the Carbón power plant in Mexico is the single largest point source contributor to Big Bend's sulfate haze during the BRAVO study period.
- At any given time during the BRAVO study, over half of the sulfate haze can come from eastern U.S., eastern Texas, or Mexican sources.
- On the clear days Mexico and the western U.S. were the largest contributors during the BRAVO study.

How Can Visibility be Improved at Big Bend National Park?

- Control SO_2 emissions from the Carbón power plants. This will decrease the average sulfate concentrations and thus decrease light scattering on average and on many days throughout the year.
- Significantly reduce SO_2 emission in both eastern Texas and the eastern U.S. This will eliminate or reduce the highest concentrations of sulfate that occur episodically.
- Enhance the clearest days by making small reductions in SO_2 emissions in northern Mexico and the western U.S.

Big Bend Regional Aerosol and Visibility Observational (BRAVO) Study Results: Air Quality Data and Source Attribution Analyses Results from the National Park Service / Cooperative Institute for Research in the Atmosphere

Executive Summary

Big Bend National Park is located in southwestern Texas along the Mexican-Texas border (Figure 1). During the 1990s, the haze at Big Bend and other sites in West Texas and southern New Mexico increased, further obscuring Big Bend's and regions scenic beauty. In response to the increased haze, the Big Bend Regional Aerosol and Visibility Observational (BRAVO) study was conducted. This was an intensive monitoring study sampling aerosol physical, chemical and optical properties, as well atmospheric dispersion using synthetic tracers from July–October 1999. The monitoring was followed by a multi-year assessment of the causes of haze in Big Bend National Park, Texas, with the primary purpose to identify the source regions and source types responsible for the haze at Big Bend. Secondary research objectives of the study were to learn more about the chemical, physical, and optical properties of aerosols responsible for haze. BRAVO study participants include the National Park Service (NPS), the U.S. Environmental Protection Agency (EPA), the Texas Commission on Environmental Quality (TCEQ), and the Electric Power Research Institute (EPRI), among others.

In support of BRAVO, the NPS and Cooperative Institute for Research in the Atmosphere (CIRA) at CSU analyzed the measured aerosol data to better understand the chemical, physical, and optical properties of Big Bend's haze, and conducted a number of complementary qualitative and quantitative haze source apportionment analyses. All source apportionment techniques went through extensive validation and evaluation tests and only those techniques which passed these tests were applied to Big Bend's haze. In addition to the analysis of the BRAVO study data, long-term Big Bend air quality and meteorological data were analyzed to determine the representativeness of the BRAVO time period to other seasons and years.

This Executive Summary summarizes the key findings from the analyses and their implications concerning Big Bend's haze with a focus on the apportionment of particulate sulfate and its contribution to Big Bend's haze. The body of this technical report provides detailed descriptions of the methods, evaluation and validation procedures and results from the multiple analyses employed by the NPS/CIRA group and the reconciliation between all source attribution techniques.

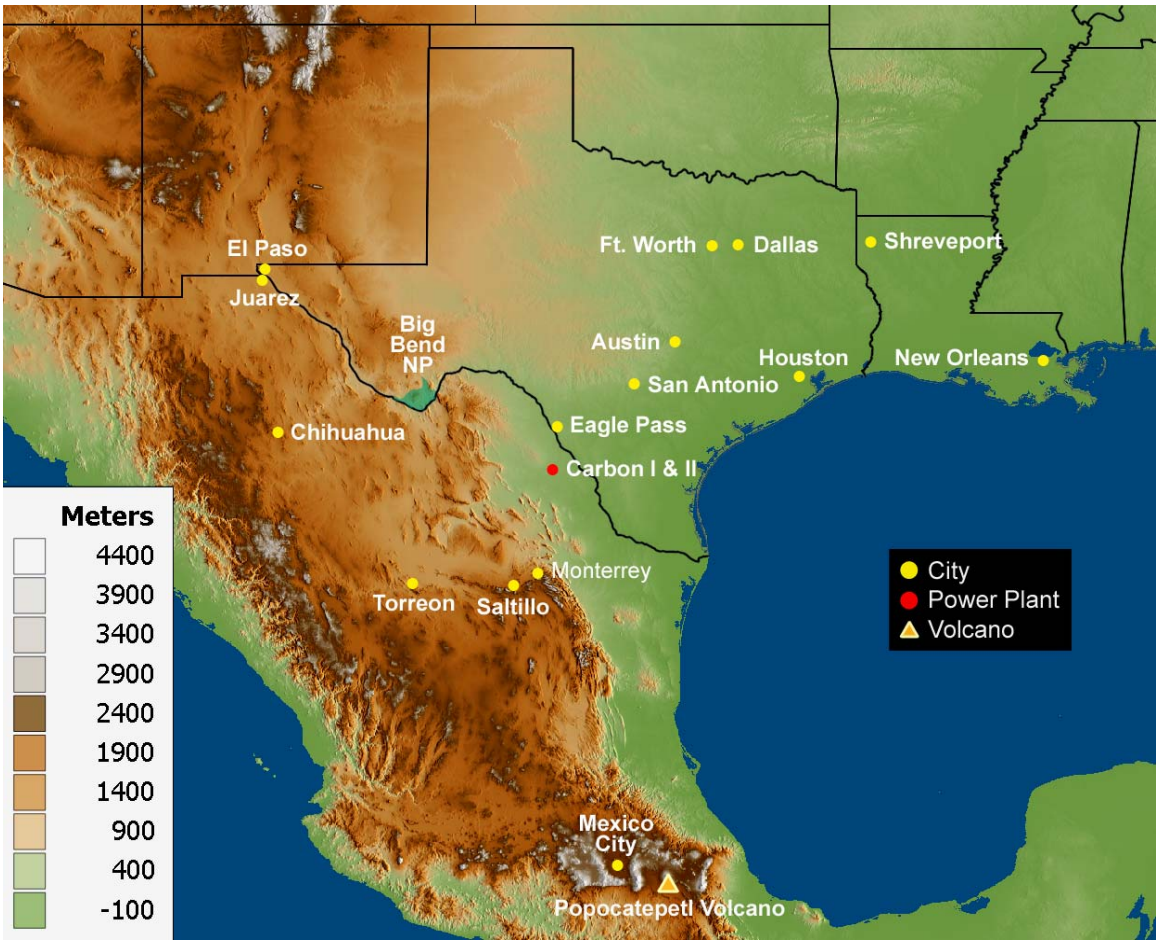

Figure 1. A terrain map of Texas and Mexico as well as some major cites and points of interest to the BRAVO study.

Characterization of Big Bend's Haze

Haze is caused by scattering and absorption of light by suspended fine liquid or solid particles in ambient air, known collectively as atmospheric aerosol. The sum of the light scattering and absorption is known as the light extinction and can be thought of as the fraction of light lost per unit of distance. The units of light extinction are inverse distance, e.g., 1/(million meters) or Mm^{-1}. Higher light extinction levels correspond to hazier conditions.

Detailed particle size and chemical composition measurements made at Big Bend during the BRAVO study were used to develop advanced estimates for each day's contributions to light extinction by the major aerosol components. These compare well to direct optical measurements of light scattering and light extinction. Figure 2 shows the daily particulate light extinction (sum of light scattering and absorption) contributions by the major aerosol components. As shown, there is a distinct difference in the particulate extinction budget in the first and second half of the BRAVO study. From July 1–August 15, the light extinction is primarily due to ammoniated sulfates (35%), organics (20%), and coarse mass (30%). In the second half of the study, post-August 15, the ammoniated sulfates account for 50% of the particulate extinction while organics and coarse mass each account for about 20%. On the haziest $1/5^{th}$ of the days, sulfate compounds accounted for about 55% of the particulate b_{ext} and organics 15%.

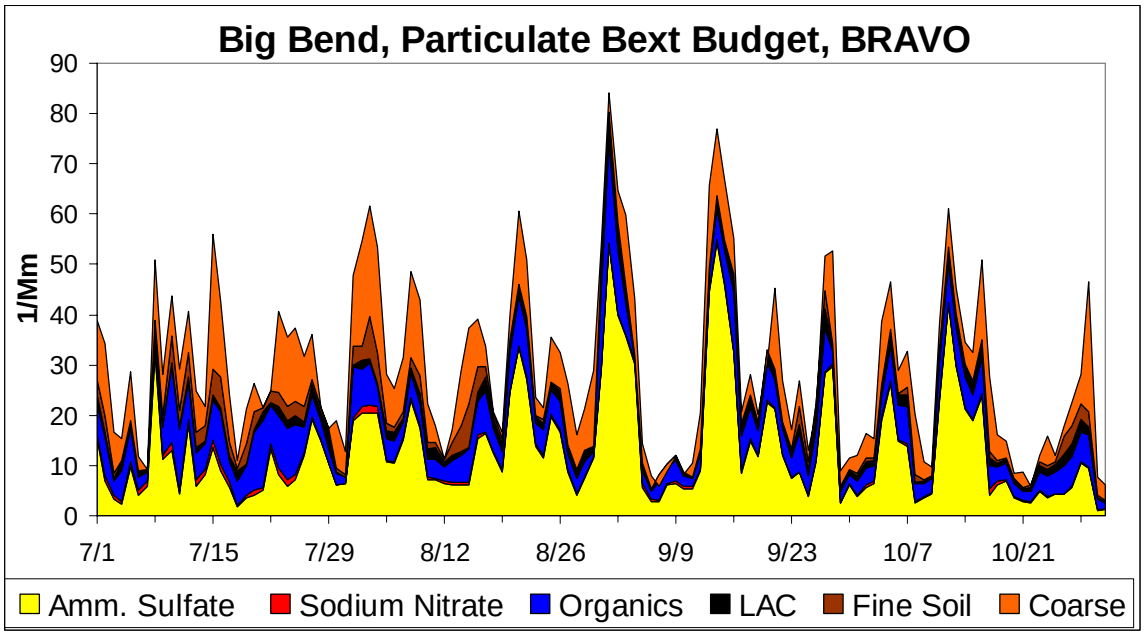

Figure 2. Big Bend's particulate light extinction budget during BRAVO.

The BRAVO period can be put into a larger climatological context by examining Big Bend's extinction budget over a long time period. Figure 3 shows the five-year (1998 through 2002) light extinction budget from measurements made every three days at Big Bend National Park in the IMPROVE monitoring network. In general, there are two periods of high haze at Big Bend National Park – one in spring when particulate sulfate and carbonaceous compounds contribute in similar amounts to haze and another in late-summer/fall when particulate sulfate compounds are the largest contributors to haze. Similar to the BRAVO period, the particulate sulfate compounds usually contribute more to haze than any other individual aerosol component. Carbonaceous particulate matter – organic compounds and light absorbing carbon (LAC) – generally constitute the second largest individual aerosol component contributing to haze at Big Bend NP and on some days are the single largest contributor to haze. Information from other studies shows that during late spring episodes, concentrations of carbonaceous compounds are increased due to biomass burning in Mexico and Central America. Dust, represented by a combination of fine soil and coarse mass, contributes as much to haze as particulate sulfate compounds during the months of March and April.

On average, sulfate compounds contribute more to light extinction on the haziest days (53%) than for average days (48%). The contribution of carbonaceous (i.e., organic and light absorbing carbon) compounds to light extinction remained the about the same at 23% on average and the haziest days. The coarse mass is also a major contributor to the particulate light extinction accounting for about 17% of the particulate light extinction on average and 15% on the haziest days. Since the sulfates accounted for more than half of the particulate extinction on the highest haze days, the lower contribution of organics and the fact that they have a potentially large contribution from smoke and other natural sources lead us to concentrate on understanding the source attribution of sulfate.

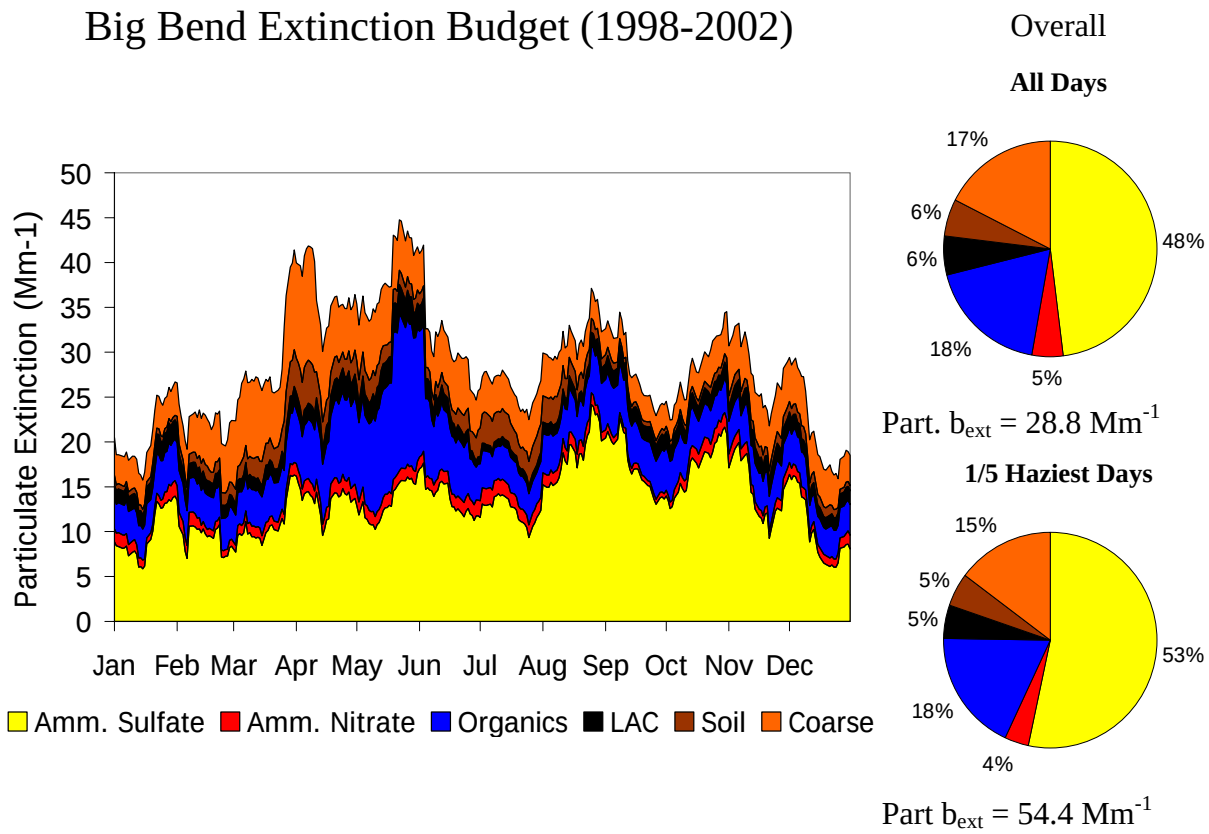

Figure 3. Big Bend National Park five-year light extinction budget. All days with that fall on the same day of the year were averaged together, then the data were smoothed using a 15-day moving average.

Apportionment of Big Bend's Sulfate Haze

Ambient particulate sulfate compounds result from direct emissions of sulfate (primary sulfate) or are produced by chemical transformation (oxidation) of SO_2 emissions in the atmosphere (secondary sulfate). Secondary sulfates constitute most of the particulate sulfate compounds measured at ambient monitoring sites, such as Big Bend National Park. The extent of the oxidation of SO_2 to secondary sulfate depends on the oxidative capacity of the atmosphere, which is influenced in large part by nitrogen oxides (NO_x) and volatile organic carbon emissions. Oxidation of SO_2 to sulfate can be slow, often requiring one to two days to convert about half of the SO_2 to particulate sulfate compounds. However, this extent of transformation can occur much more rapidly, from a few hours to several minutes, in the presence of mists, fogs, and clouds. Meanwhile, atmospheric dispersion and deposition processes are reducing the ambient SO_2 and sulfate concentrations during transport from emission sources to distant monitoring locations. Consequently, it is typically challenging to establish causal relationships between measured ambient particulate sulfate concentrations and SO_2 emissions sources.

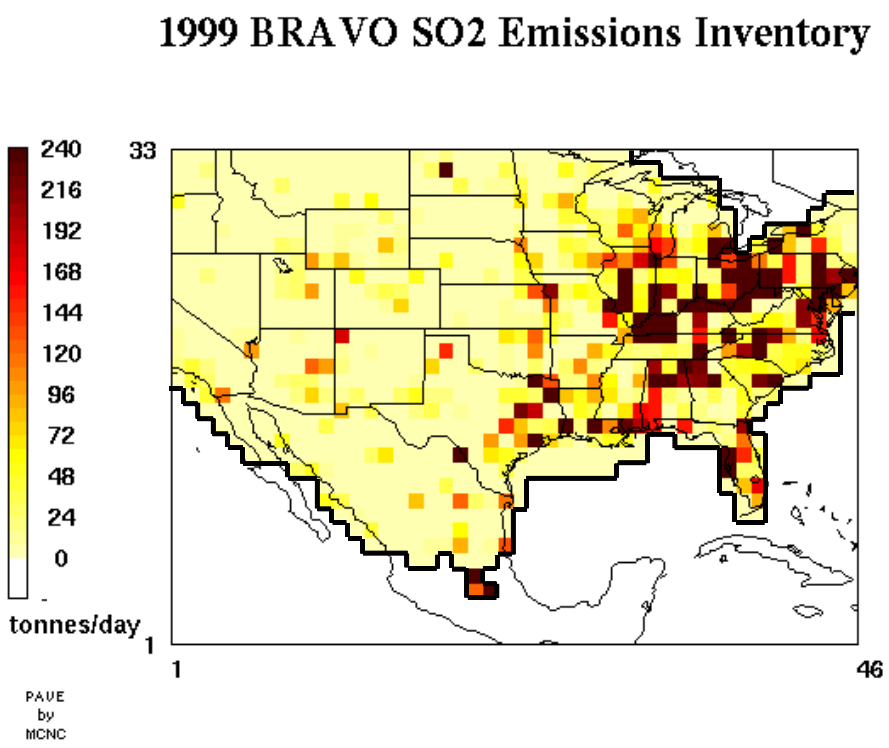

Figure 4. (Left) SO_2 emissions based on the 1999 BRAVO emissions inventory used in the REMSAD and CMAQ-MADRID modeling. No emissions were included beyond the black outline shown in the figure. Mexico City and Popocatepetl volcano emissions are located in the three most southern emission grid cells.

Figure 4 presents the SO_2 emission inventory used in the BRAVO study. As noted on the map the BRAVO study emission inventory did not include sources in southern Mexico (except for Mexico City and the Popocatepetl volcano), Cuba, or other Caribbean islands. Effects of sources outside of the modeling domain, beyond the frames of Figure 4, were accounted for in BRAVO study modeling by use of four-month average boundary conditions obtained from global model simulations. The largest SO_2 emissions are in the eastern U.S. where about 14 million tonnes /year are emitted. In Texas approximately 1 million tonnes of SO_2 are emitted each year, almost all in eastern Texas, and the western U.S. emissions are about 1.7 million tonnes /year. In Mexico, SO_2 emissions are estimated to be about 2.5 million tonnes /year with 1.5 million tonnes/year from the Popocatepetl volcano. There are a few high emitting locations in northern Mexico, including the Carbón I & II coal-fired power plants located about 200 km east-southeast of Big Bend and at urban and industrial areas near Monterrey in northeastern Mexico.

U.S. SO_2 emission inventories have been in development for over 30 years and in the 1990s continuous emission monitors were placed into the largest SO_2 point sources. Therefore the U.S. SO_2 emission inventory is considered to be of a high quality. However, less information was available about the Mexican SO_2 emissions and significant uncertainties in the inventory remain. For example, a recently produced emission inventory for Mexico differs from the BRAVO emissions inventory for SO_2 emissions, with emissions by as much as a factor of two larger in some regions. In addition, uncertainties in Carbón SO_2 emissions exist and emissions of 154,000 and 245,000 tonnes/year were used.

The Popocatepetl volcano in central Mexico near Mexico City has been active for a number of years including during the BRAVO study period and is the largest single SO_2 emissions source in North America. Limited modeling of the flow of its emissions indicated that it likely had little effect on Big Bend haze during the BRAVO study period. The effects of emissions from southern Mexico, Cuba, and other areas outside of the BRAVO study emissions inventory are also thought to be small at Big Bend.

Spatial Patterns of Aerosol Components

Examination of the spatial and temporal patterns in several fine particulate species, including sulfate, measured during BRAVO suggests that there are unique sources for different aerosol types and that transport patterns are seasonal with more transport from Mexico to southern Texas during the summer than during the fall and conversely more transport from the eastern U.S. during the fall than during the summer. These findings are consistent with the back trajectory analyses. Sulfate concentrations at Big Bend were highest during four episodes, September 1 and 2, 14 and 15, October 12, and August 22. The four episodes were characterized by different trace element concentrations and different spatial patterns in sulfate indicating differing contributions from different source types for each episode. Sulfate concentrations measured within a few hundred km are generally highly correlated in time, but measurements in southwestern Texas were not highly correlated with measurements in northeast Texas, and different regions of the state also had different seasonal patterns in sulfate concentrations indicating they are influenced by different sources. Highest sulfate concentrations measured during BRAVO were in northeast Texas during the summer while highest concentrations at Big Bend were during the fall. Spatial patterns in sulfate concentrations show influence from the Carbón I & II power plants, especially north and west of the plants, though the contribution is not quantifiable by these analyses.

Spatial and temporal patterns in the iron concentrations and the abrupt drop in Al/Ca ratios from summer to fall are evidence of Saharan dust episodes during the summer.

The trace element most associated with sulfur at Big Bend is selenium which is usually associated with coal combustion. Selenium concentrations were highest in northeast Texas with evidence of selenium sources within the state, at the Carbón I & II plants, and possibly entering Texas from the east.

Airmass Transport to Big Bend during BRAVO Days with High and Low Particulate Sulfate Concentrations

All other things being the same, a source region's potential to contribute to haze at Big Bend increases for time periods when air parcels frequently pass over and spend more time over the source region prior to transport to Big Bend. These airmass transport characteristics can be estimated from trajectories, where a trajectory gives the estimated location of air parcels every hour prior to their being transported to Big Bend. Residence time analysis is used to aggregate the number of air parcels that resided over an area for selected periods of time at Big Bend (e.g., a month) or selected receptor site conditions (e.g., haziest days at Big Bend). This is related to the aggregate of time all trajectories resided over a given area. While the residence time is dependent on airmass transport frequency from a given region to Big Bend and the time it spends over the region, it has been shown that the difference in the residence time from one region to another is primarily dependent on different transport frequencies.

On days with the 20% highest particulate sulfur concentrations during the BRAVO study, air parcels were most likely to have previously resided over northern Mexico, Texas, and the eastern U.S. (Figure 5a). These tended to be low level and low speed air parcels which are conducive to the accumulation of pollutants from sources. In contrast, on days with the 20% lowest particulate sulfate concentrations, air parcels were most often previously over northern Mexico and the Gulf of Mexico as well as over the western U.S. and infrequently over eastern Texas or the eastern U.S. (Figure 5b). The transport over Mexico tended to be low level but high speed which is not conducive to the accumulation of emissions into the air parcels.

The examination of transport pathways during individual particulate sulfate episodes showed that there were three common pathways associated with elevated sulfate at Big Bend, from eastern Texas, the southeastern U.S., and northeastern Mexico (Figure 6). The largest concentrations occurred when transport over several of these regions occurred. For example, the September 1 episode had transport over all three regions and had the highest concentrations during the BRAVO study. Elevated sulfate was also associated with prior transport over the Midwest (Missouri, Kentucky, and Tennessee), though this was infrequent and airmasses tended to be elevated and had higher speeds relative to the other three regions.

These results show that the transport from eastern Texas and the southeastern U.S. is associated with elevated sulfate concentrations at Big Bend and is not associated with low sulfate concentrations. These results, combined with the fact that eastern Texas and the Southeast have high sulfur dioxide emissions, support the notion that these areas contribute to the sulfate concentrations and haze at Big Bend. Northeastern Mexico appears to be a common transport pathway during both high and low sulfate days. However, the time airmasses spend over northern Mexico prior to reaching Big Bend is greater on the high sulfate days than the low sulfate days. The increased time allows for potentially greater accumulation of SO_2 emissions and time for transformation to sulfate.

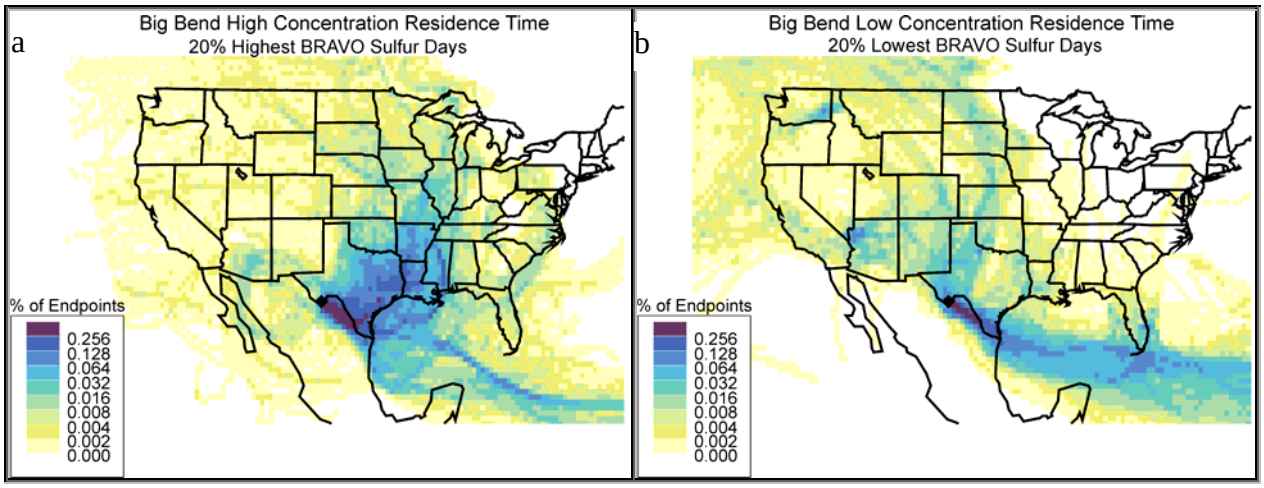

Figure 5. Fraction of time that air parcels spent during ten-day trajectories for periods with the a) 20% highest concentrations of particulate sulfate compounds and b) for the periods with the 20% lowest concentrations of particulate sulfate during the BRAVO study period July through October 1999.

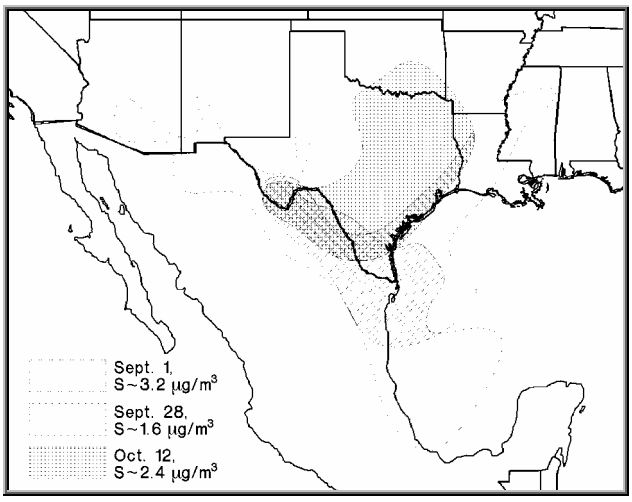

Figure 6. Airmass transport patterns to Big Bend, TX, during three sulfate episodes. Each isopleth shows the most likely pathway the airmass traversed prior to impacting Big Bend.

Quantitative Source Apportionment of Big Bend's Sulfate Haze

NPS/CIRA employed numerous methods to identify the source types (e.g., power plants) or source regions (e.g., Texas, the eastern U.S., the western U.S., and Mexico) that contribute to the particulate sulfate compounds that influence Big Bend haze and to estimate the magnitude of their contributions. The techniques fall into three categories, receptor-oriented modeling, source-oriented modeling and hybrid modeling combining features from both source and receptor modeling.

Airmass History Based Receptor Models: Several airmass history based receptor analysis methods were used for source attribution. These methods developed statistical relationships between the Big Bend particulate sulfate concentrations and airflow prior to reaching Big Bend. Variations of the trajectory methods included the use of two methods of estimating wind over North America (EDAS from the National Weather Service and MM5 applied specifically for the BRAVO study) and the use of back-trajectories from Big Bend employed in Trajectory Mass Balance (TrMB), and forward transport and dispersion from all potential source regions used in Forward Mass Balance Regression (FMBR).

Extensive testing of TrMB and FMBR applied to both sets of wind information showed adequate overall performance when used to attribute artificial tracer released as part of the BRAVO study. Additional evaluations showed that these airmass history regression models were accurate within their stated precision when applied to synthetic sulfate concentration with known attribution results. Only the combination of airmass history model and meteorological data inputs that passed these evaluations was used for attribution of measured sulfate.

An inherent characteristic of these techniques is the estimation of the average relationship between air transport from an area and that area's contribution to sulfate. Therefore, these techniques were used only for estimating average attributions. These techniques are subjected to increased uncertainties due to collinearity of transport from multiple source regions. For example, transport from the eastern U.S. typically traversed Texas in route to Big Bend. In addition, other issues can bias the results. For example, it was found that FMBR tended to enhance attributions to nearby source regions and reduced attribution from more distant source regions.

Regional Air Quality Source Oriented Models: The REMSAD regional air quality model was used to estimate the effects of transport, dispersion, chemical transformation, and deposition on emissions, and thereby to predict particulate sulfate concentrations throughout the modeling domain, including at Big Bend. The difference in predicted concentrations between air quality model prediction with all emissions (base case) and those with emissions for a specific source or source region set to zero (emissions sensitivity case) is interpreted as the particulate sulfate attributed to the specific source or source region. The CMAQ-MADRID air quality model was also operated by EPRI and Atmospheric and Environmental Research (AER).

Eulerian air quality models are limited by the soundness of emissions and meteorological data, as well as the accuracy of transformation, deposition, dispersion, and other numerical algorithms. Biases and uncertainties identified in any of these processes can adversely affect their source attribution estimates. The Eulerian models were tested against the BRAVO tracer data to evaluate their capability of simulating dispersion in Texas where it was found that they could reproduce the tracer concentrations within the inherent uncertainty of the tracer data. Also, the simulated sulfate and SO_2 concentrations and sulfate apportionments were extensively compared to measured data. It was found that both models tended to underestimate particulate sulfate compound concentrations in the first half of the BRAVO study period when sources in Mexico were determined to have the largest contribution. Both models also tended to overestimate particulate sulfate concentrations when flow was from the eastern U.S.

Hybrid Modeling - Synthesis Inversion Analysis of Air Quality Models: Concerns about possible systematic biases that could be the result of Mexico's SO_2 emissions and/or transformation chemistry biases resulted in the development of a hybrid modeling approach. This approach entailed the development of statistical relationships between the daily source attribution results from REMSAD and CMAQ-MADRID and the measured particulate sulfate concentrations in and around Big Bend.

The synthesis inversion technique was unable to resolve distant source regions with small source contributions. To minimize problems caused by this behavior, attribution results for these sources were held close to their originally modeled values. Thus, any sulfate that may have been improperly attributed to small distant sources by the Eulerian models runs was most likely attributed to source regions near Big Bend in the synthesized method. The technique also systematically underestimated the measured sulfate data. It is not known if this underestimation impacts one source region more than another.

It was determined that Synthesized CMAQ-MADRID combined with the attribution of Carbón power plants from Synthesized REMSAD provided the best available estimates of the source attribution for particulate sulfate at Big Bend during the BRAVO study period, henceforth referred to as the BRAVO Estimate.

Figure 7 shows the study period-averaged attribution results for nine methods as well as the BRAVO Estimate results. CMAQ-MADRID and Synthesized CMAQ-MADRID attribution did not include the Carbón power plants. TAGIT was a source attribution technique employed by the Desert Research Institute (DRI) to attribute Carbón power plants' contribution to Big Bend's sulfate.

As shown in Figure 7, during the BRAVO study period U.S. sources contributed to about 55% (BRAVO Estimate) of the particulate sulfate at Big Bend, with a range among methods of 44% to 67%. The Mexico sources contributed about 38% of Big Bend's particulate sulfate, with

a range among methods of 23% to 55%. The eastern U.S. was the largest U.S. contributor at ~30%, followed by Texas at ~17% and the western U.S. at ~9%, with ranges among the methods of 16% to 42%, 16% to 30%, and 0% to 14%, respectively. The Carbón power plants in Mexico contributed to about 20% of the particulate sulfate at Big Bend, more than any other single SO_2 emissions facility, with a range among the methods of 14% to 26%.

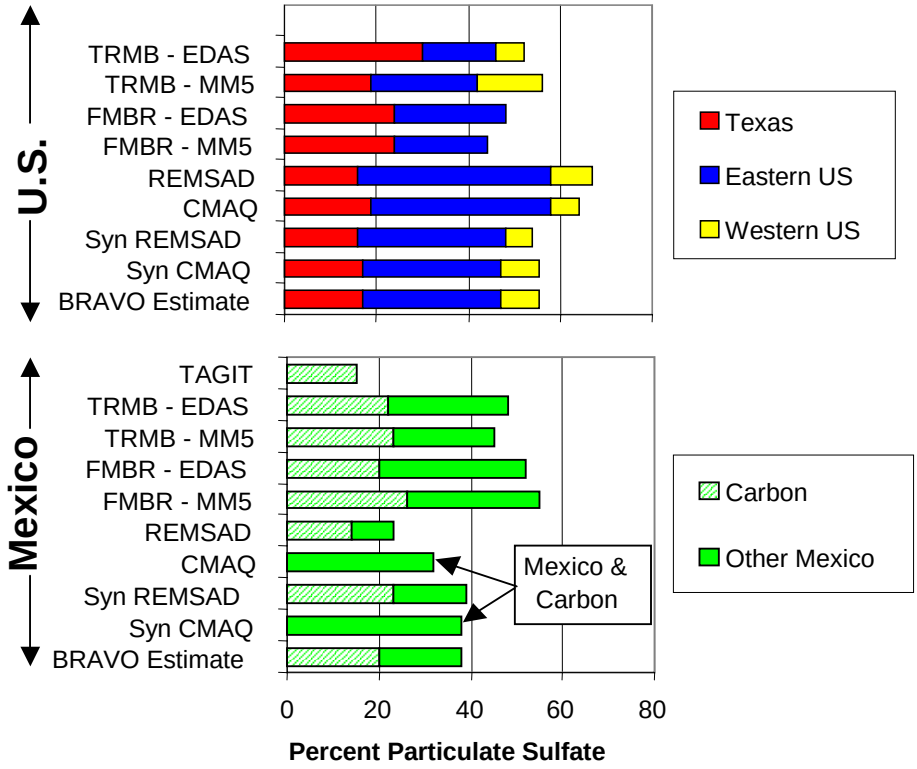

Figure 7. Estimates by several data analysis and modeling methods of the study-period averaged percent contributions to particulate sulfate at Big Bend by U.S. and Mexico sources. TAGIT only attributed the Carbón power plants, while CMAQ and Synthesized CMAQ attribution did not distinguish Carbón from Mexico.

Figure 8 presents a smoothed daily attribution using the BRAVO Estimate method. The top plot in Figure 8 shows attribution in absolute concentrations for direct comparison to the measured particulate sulfate concentrations, while the bottom plot shows the percent fraction of the predicted amount by each source region. As shown, each source region's contribution to Big Bend particulate sulfate had unique characteristics over the BRAVO study period. Sources in Mexico were the largest contributors to sulfate in July and August, contributing from 0.5 to 1.5 $\mu g/m^3$ every day. During the largest peak in late July, sources in Mexico contributed to about 2 $\mu g/m^3$, constituting about 90% of the modeled particulate sulfate. In September and October contributions by sources in Mexico decreased to roughly less than 1 $\mu g/m^3$. Sources in Texas contributed very little to sulfate concentrations in July, with three episodes in the middle months of the study period having peak values from about 0.8 to 1.5 $\mu g/m^3$. During two episodes in October, sources in Texas had peak contributions of about 1.2 to 2.8 $\mu g/m^3$ of particulate sulfate and constituted to over 60% of the largest peak in October. Sources in the eastern U.S. contributed to sulfate concentrations mostly in the middle two months of the study period with

several peak contributions exceeding 1 µg/m^3. The largest of these contributions is greater than 5 µg/m^3 and constitutes about 80% of the largest peak particulate sulfate measured during the BRAVO study period.

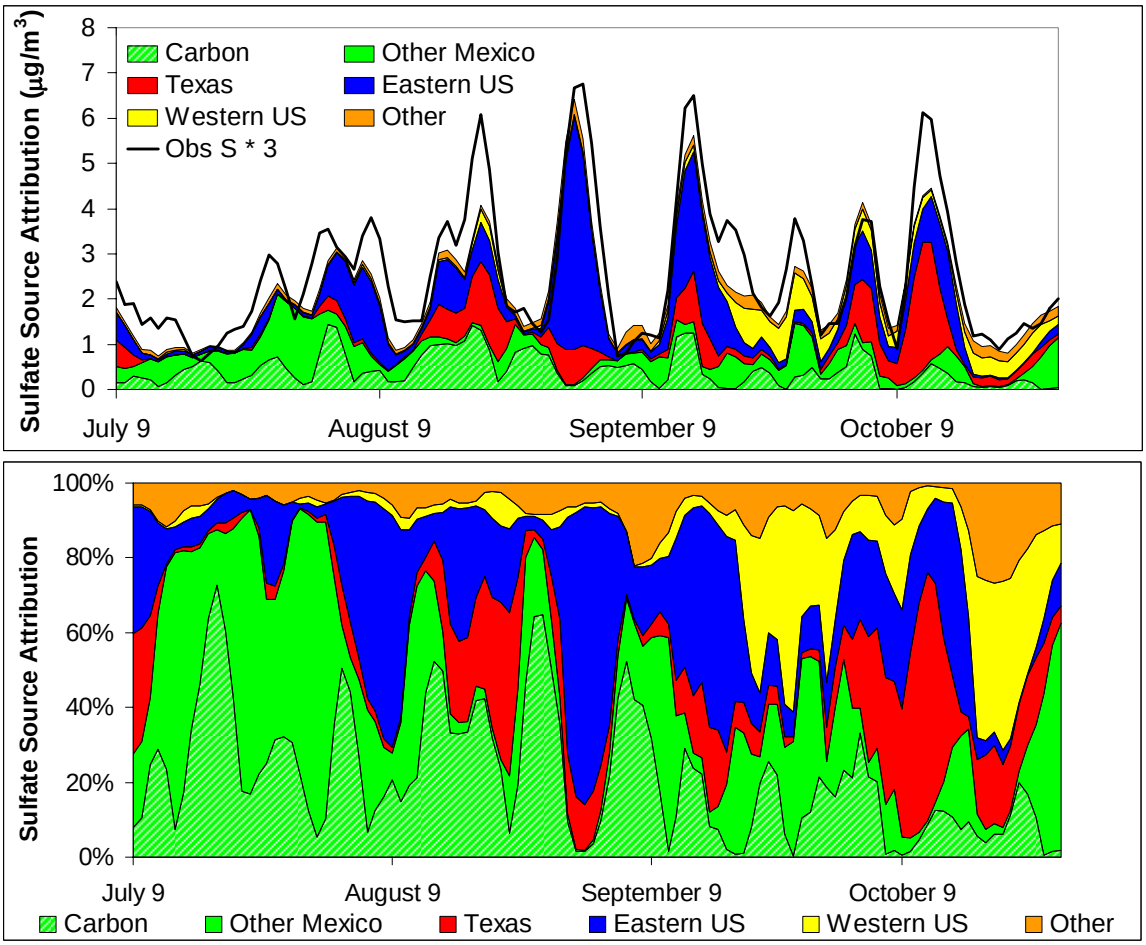

Figure 8. Smoothed daily estimates by source regions to particulate sulfate concentration (top plot) and fraction of total predicted particulate sulfate (bottom plot) at Big Bend during the study period.

The Contribution of Sulfur Source Regions to Particulate Haze Levels at Big Bend National Park during the BRAVO Study Period

Both the fraction of light extinction associated with particulate sulfate (see Figure 2) and the fraction of particulate sulfate attributed to each source region (see Figure 8) varied considerably throughout the BRAVO study period. This information was combined to show variation in the absolute and percent fractional contribution by sulfur source regions to Big Bend light extinction (shown in the top and bottom plots of Figure 9, respectively). Pie diagrams are shown in Figure 10 to illustrate the differences in particulate sulfate contributions by various source regions to light extinction for the study period 20% haziest days compared to the study period 20% least hazy days. The numbers of 20% haziest days during each month of the BRAVO study from July through October are 1, 8, 10, and 4, respectively, while the numbers per month for the 20 least hazy days were 3, 1, 10, and 9, respectively.

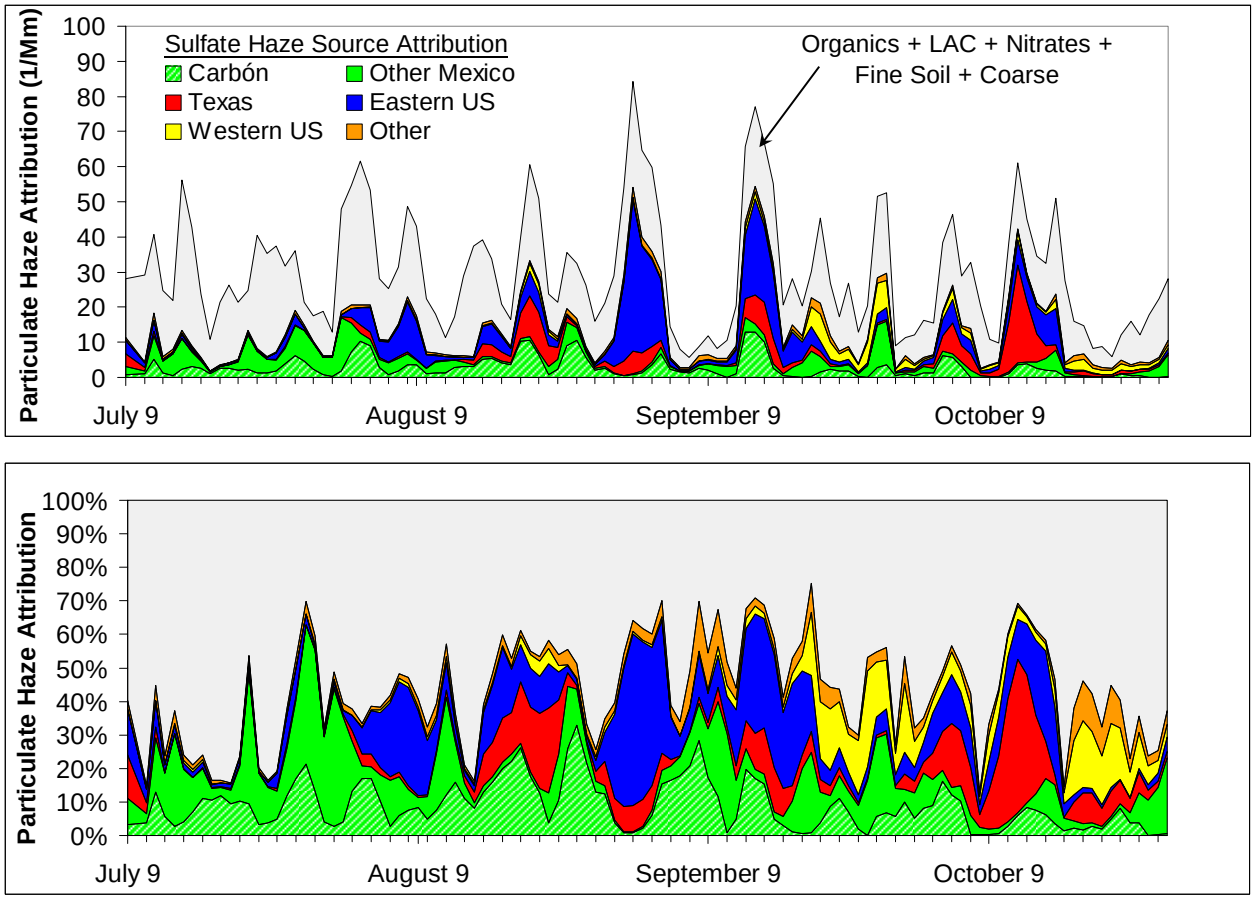

Figure 9. Estimated contributions to particulate haze by various particulate sulfate source regions. The top plot shows the absolute haze contributions by the various particulate sulfate sources as well as the total particulate haze level (black line). The bottom plot shows the fractional contribution to haze by the various sources.

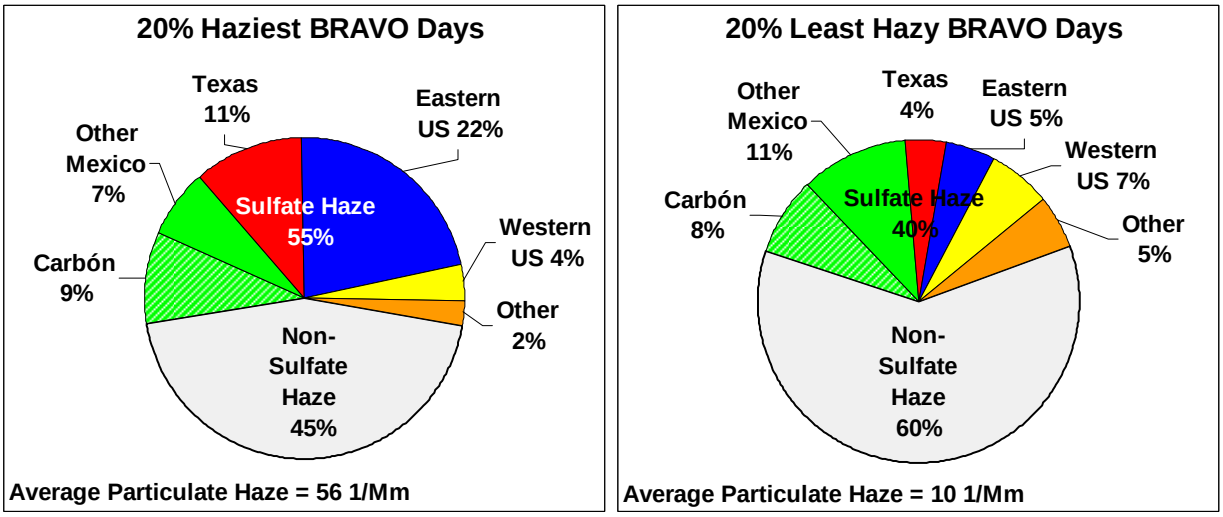

Figure 10. Estimated contributions by particulate sulfate source regions to Big Bend particulate haze levels for the 20% haziest days and the 20% least hazy days of the BRAVO study period.

The SO_2 sources in Mexico generally contributed a moderate 5 Mm^{-1} to 15 Mm^{-1} of the light extinction on most days during the study period, but during some of the minor haze episodes in July and August their relative contributions were 40% to 60% of the average particulate light extinction. SO_2 sources in Texas contributed to less than 5 Mm^{-1} on most days during the study period, but during one of the few periods of higher contribution these sources contributed to nearly 30 Mm^{-1}, corresponding to about 50% of the particulate light extinction on the haziest day in October. SO_2 sources in the eastern U.S. also contributed to less than 5 Mm^{-1} on most days during the study period, but during the two haziest episodes of the study period these sources contributed to about 50 Mm^{-1} and about 30 Mm^{-1} respectively, corresponding to about 50% and 30% of the light extinction.

The sulfate contribution to particulate light extinction is higher on the haziest days compared to the least hazy days (55% compared to 40%). This increase in the sulfate contribution on the haziest days compared to the least hazy days is driven by increased relative contributions from the eastern U.S. and Texas. The relative contribution of sulfate on the haziest days from Texas increased by about a factor of 3 (4% to 11%), and from the eastern U.S. it increased by about a factor of 4 (5% to 22%) compared to the least hazy days. In contrast, the relative contributions for the Carbón I & II power plants remained about the same at 8% to 9% and the contribution of other sources in Mexico decreased from 11% on the least hazy days to 7% on the haziest days. The relative contribution of sulfate sources in the western U.S. to Big Bend's sulfate haze also decreased from 7% on the least hazy days to 4% on the haziest days. These results are consistent with the observation that the Texas and eastern U.S. sources had their largest sulfate contributions during the highest sulfate episodes.

The non-sulfate haze is primarily due to dust (fine soil and coarse particles) and carbonaceous (organic and carbon) compounds. Compared to the least hazy days, the haziest days have a higher relative contribution to light extinction by dust (25% compared to 19%) and a lower relative contribution by carbonaceous particles (19% compared to 39%).

Application of the Source Attribution Results to Other Months and Years

In order to assess the applicability of haze attribution results for the BRAVO study to other years or other times of year, it is necessary to compare the four-month study period with the same months in other years and with other months of the year. Emissions and meteorology are the two most important factors that influence haze levels. Between 1999 and the present the annual emissions responsible for particulate sulfate concentrations in North America have not appreciably changed (U.S. emissions have decreased about 15%, but less is known about emission trends in Mexico). Seasonal variations in SO_2 emissions and in the SO_2 to particulate sulfate oxidation rate make extrapolations of the BRAVO study results to other months of the year prone to additional uncertainty. One of the most influential meteorological processes affecting the haze at Big Bend is the airflow patterns that determine which potential source regions are upwind of Big Bend. In spite of the uncertainties inherent in such a simple approach, comparisons of the meteorological flow patterns from the residence time analysis were used alone in an attempt to assess the applicability of BRAVO study results to other years and times of year.

Residence time plots convey information about both the frequency of transport over potential source regions and its duration over the regions. However, it was shown that the residence time transport patterns are primarily driven by the variations in transport frequency

over regions as opposed to duration variations. Consequently, a change that doubles the residence time over a source region for a specific month can be thought of as doubling the probability of influence of that source region during that month. In this example the monthly averaged contribution would likely double because the numbers of impacting periods would about double, but the amount of the peak impact is not expected to change much.

During the BRAVO study period airflow to Big Bend was mostly similar to the airflow conditions during the five-year period. However, in September 1999 there was typically less flow over the eastern U.S. than for the five-year average, implying that the BRAVO results may underestimate the average haze contributions by that region's sources. In addition, during October 1999 there was typically more flow over Texas and less flow over Mexico, implying that the average October BRAVO haze contributions may be overestimated for Texas and underestimated for Mexico compared to the five-year average. While the estimated average contributions by these source regions may change, the peak contributions are likely not affected by the atypical frequency of flow.

Comparing the airflow patterns for the BRAVO study period to that of the other months of the year (Figure 11) it is evident that SO_2 sources in Mexico are likely to contribute less from November through March. This is because airflow across Mexico is less in general and is over lower emission density regions of Mexico to the west of Big Bend. SO_2 sources in Mexico are likely to be contributing to the particulate sulfate portion of the Big Bend haze during the months of April through June comparable to their contributions for the BRAVO study months of July and August. Sources in Texas are likely to contribute little to the particulate sulfate portion of the Big Bend haze for the months from November through June since the airflow is not frequently over the high emissions regions of east Texas, similar to July 1999. Eastern U.S. sources are unlikely to contribute to Big Bend haze during the months from November through March since airflow to Big Bend is rarely over that region during those months. During the months from April to June, the eastern U.S. sources may contribute a modest amount to sulfate haze, comparable to that estimated for July and early August.

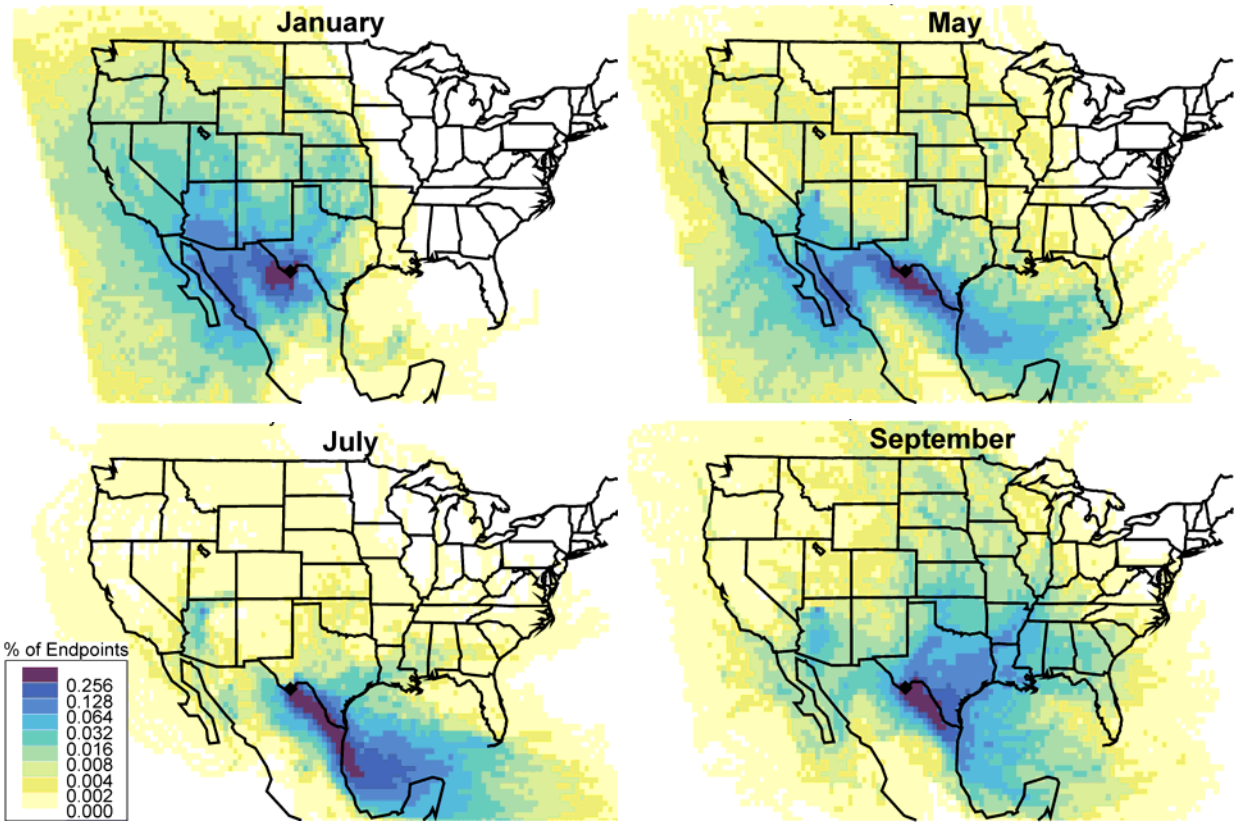

Figure 11. Examples of geographic distribution of the fraction of time that air parcels spend during the five days prior to arriving at Big Bend National Park for the months of January, May, July, and September based upon a five-year analysis period (1998 to 2002).

Implications

There is no single answer to the question of what sources are responsible for the haze at Big Bend National Park; sources in both the U.S. and Mexico are responsible. Mexican SO_2 emissions contribute to the sulfate haze most frequently, but to generate the haziest events that occur in the late summer and fall, contributions from Texas and the eastern U.S. must occur. The greatest individual contribution to haze is the Carbón I & II power plant in northern Mexico. Substantial changes of that facility's emissions would likely result in small but noticeable changes in haze levels on many days, but it would not make much difference to the worst haze episodes during late summer and early fall. To substantially affect all of the haze episodes during the late summer and fall where U.S. contributions are large at Big Bend will require SO_2 emission changes in both Texas and the eastern U.S. Because of the high frequency of air transported to Big Bend from the southeast along a corridor on both sides of the Rio Grande River, emission changes there have a potential to affect haze levels at Big Bend especially during June through September when transport from this region is most frequent.

The clearest days at Big Bend also had low sulfate concentrations. The visual scene on a clear day is more sensitive to small changes in haze than a hazy or moderately hazy day. On these clear days, the Carbón I & II power plants and other sources in northeast Mexico were the largest contributors to Big Bend's sulfate. Reduction in emissions from Carbón would likely result in creating more clear days. On the other hand, growth along this border region will likely further reduce the number of clear days.

Big Bend Regional Aerosol and Visibility Observational (BRAVO) Study Results: Air Quality Data and Source Attribution Analyses Results from the National Park Service / Cooperative Institute for Research in the Atmosphere

Abstract

Big Bend National Park is located in southwestern Texas along the Mexican-Texas border. During the 1990s, the haze at Big Bend increased, further obscuring Big Bend's scenic beauty. In response to the increased haze, the Big Bend Regional Aerosol and Visibility Observational (BRAVO) study was conducted. This was an intensive monitoring study sampling aerosol physical, chemical and optical properties from July–October 1999. The monitoring was followed by a multi-year assessment of the causes of haze in Big Bend National Park, Texas, with the primary purpose to identify the source regions and source types responsible for the haze at Big Bend. Secondary research objectives of the study were to learn more about the chemical, physical, and optical properties of aerosols responsible for haze. In addition to analyzing the BRAVO data, analyses of long-term Big Bend air quality and meteorological data were conducted to examine the representativeness of the BRAVO time period to other seasons and years. BRAVO study participants include the National Park Service (NPS), the U.S. Environmental Protection Agency (EPA), the Texas Commission on Environmental Quality (TCEQ), and the Electric Power Research Institute (EPRI), among others. This technical report describes the methods and results from the multiple analyses employed by the NPS/CIRA (Cooperative Institute for Research in the Atmosphere) group for assessing the composition and optical properties of the haze and source regions responsible for the sulfate haze.

It was found that sulfate compounds are the largest contributor to particulate haze at Big Bend, accounting for about 45% on average and 55% on the haziest days. Dust and carbonaceous compounds comprise the majority of the remaining particulate haze annually. Dust or smoke from local and international sources (Mexico and beyond) is the largest contributor on some of the haziest days, particularly during the spring and early summer. Sulfate haze source attribution results showed that SO_2 emissions from sources in the U.S. and Mexico contributed to about 26% and 18%, respectively, of the particulate haze during the four-month BRAVO study period. The split among U.S. source regions was Texas – 8%, the eastern U.S. – 15%, and the western U.S. – 4%. The two Carbón power plants, located 200 km southeast of Big Bend in Mexico, contributed about 9% of the particulate haze, making them the single largest contributing SO_2 emissions facility. On the haziest 20% of the days during the BRAVO study, SO_2 emissions from sources in the U.S. and Mexico contributed to about 35% and 17%, respectively, of the particulate haze. The split among U.S. source regions was Texas – 11%, the eastern U.S. – 20%, and the western U.S. – 4%. In Mexico, Carbón was responsible for 9%. Throughout the year transport is often from the western U.S. and Mexico on the least hazy days when the appearance of scenic vistas are especially sensitive to small increases in particulate concentrations.

The implication of these results is that first, there is no simple answer to the question of what sources are responsible for the haze at Big Bend National Park; sources in both the U.S. and Mexico are responsible. Mexican SO_2 emissions contribute to the sulfate haze more frequently, but to generate the haziest events that occur in the late summer and fall, contributions

from Texas and the eastern U.S. must occur. Substantial changes to the Carbón I & II power plants' emissions would likely result in small but noticeable changes in haze levels on many days. SO_2 emission changes in both Texas and the eastern U.S. would be required to substantially affect all of the haze episodes during the late summer and fall. Because of the high frequency of air transported to Big Bend from the southeast along a corridor on both sides of the Rio Grande River, emission changes there have a potential to affect haze levels at Big Bend especially during June through September when transport from this region is most frequent. On the clearest days at Big Bend, the Carbón I & II power plants and other sources in northeast Mexico were the largest contributors to Big Bend's sulfate. Reduction in emissions from Carbón would likely result in creating more clear days. On the other hand, growth along this border region will likely further reduce the number of clear days.

1) Introduction

The Big Bend Regional Aerosol and Visibility Observational (BRAVO) study was a multi-year assessment of the causes of haze in the Big Bend National Park, Texas (BBNP). Big Bend is located in southwestern Texas along the Mexican-Texas border. During the 1990s, the haze at Big Bend and other sites in West Texas and southern New Mexico had increased, further obscuring Big Bend's scenic beauty [*Malm et al.*, 2000b; *Malm et al.*, 2001a]. The BRAVO study was performed in response to the increased haze and the construction of the Carbón facilities, two coal-fired power plants in Mexico, approximately 125 miles southeast of the park. Past studies at Big Bend indicated that emissions from both the United States and Mexico contributed to the haze, but the impact due to individual source regions was unknown. A description of the planning process for BRAVO can be found in *Green et al.* [2000]. BRAVO study participants include the National Park Service (NPS), the U.S. Environmental Protection Agency (EPA), Colorado State University (CSU), the Texas Commission on Environmental Quality (TCEQ), and the Electric Power Research Institute (EPRI), among others.

The primary objective of the BRAVO study was to identify the source regions and source types responsible for haze at BBNP. This includes qualitative understanding of the long range transboundary transport of haze from regional sources in the U.S. and Mexico to Big Bend, and the quantitative contribution of specific U.S. and Mexican source regions and source types responsible for Big Bend's haze. Sources and source regions of particular interest were the Mexican Carbón I & II power plants, industrial source areas along the Texas gulf coast and in Monterrey and Tula, Mexico, coal-fired power plants and refineries in Texas and large SO_2 source regions in the southeastern and midwestern U.S. The BRAVO study also had a number of research objectives including the characterization of inorganic and organic aerosol components, developing and testing relationships between measured aerosol composition, concentration, and physical properties and light scattering, and measuring the hygroscopic properties of the aerosol components.

The focus of this report is to provide a detailed description of the modeling and analytical methods that were conducted by the NPS and CSU in support of BRAVO. These include "receptor-oriented" and "source-oriented" models, along with an approach labeled "synthesis inversion analysis" which represents an innovative hybrid technique that can be useful in identifying biases in the source-oriented model. These complementary approaches have resulted in a greatly improved understanding of the pollution sources that contribute to haze in BBNP. In addition, the chemical composition and optical properties of the aerosol responsible for the haze are examined. Several findings of the BRAVO study have already been published [*Brown et al.*, 2002; *Hand et al.*, 2002; *Chow et al.*, 2003; *Malm et al.*, 2003].

1.1 Big Bend National Park Setting

In a remote area of southwestern Texas, where the Rio Grande makes a sweeping turn along the U.S.-Mexico border, lies an area known as the "Big Bend Country." Within this expanse sits BBNP, a 324,247 hectare (1,252 square miles) reserve established as a national park in 1944 and designated as a Biosphere Reserve in 1976 (Figure 1-1). Big Bend is a land of contrasts. The Rio Grande has created deep canyons with sheer walls, and portions of the Rio Grande are designated as a Wild and Scenic River. The majority of the park consists of Chihuahuan desert, with the Chisos Mountains providing an alpine ecosystem in the midst of the desert. It is a region of large biological diversity containing more than 1,000 species of plants,

including 65 cactus species, and 434 bird, 78 mammal, 71 reptile and amphibian, and 35 fish species [*Big Bend Natural History Assoc.*, 1990]. Endangered species include the peregrine falcon, black-capped vireo, Mexican long-nose bat, Big Bend gambusia (a fish), and three threatened cacti [*Big Bend Natural History Assoc.*, 1990]. Because of its contrasting landscapes, however, Big Bend is also known and appreciated for the beauty of its scenic vistas located in both countries.

Although early travelers called the land "el despoblado" – the unpopulated land – there is a rich history associated with the land extending back in time to ca. 8500–6500 B.C. The area is remote and sparsely populated, with approximately 13,000 people occupying an area about the size of the State of Maryland (12,407 square miles). In the 1930s many people who loved the Big Bend country saw that this land of contrast, beauty, and solitude was worth preserving for future generations—an effort that resulted in the establishment of Big Bend Ranch State Park and BBNP.

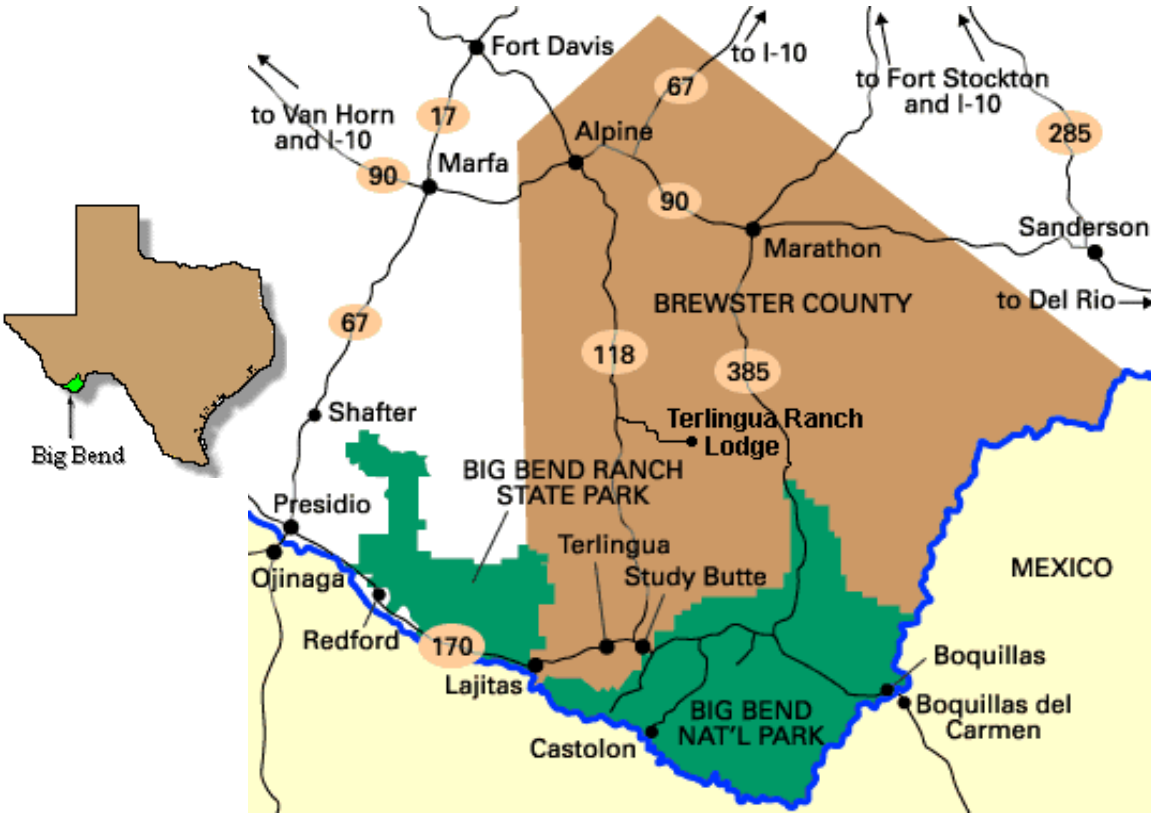

Figure 1-1. Location map of Big Bend National Park in southwestern Texas.

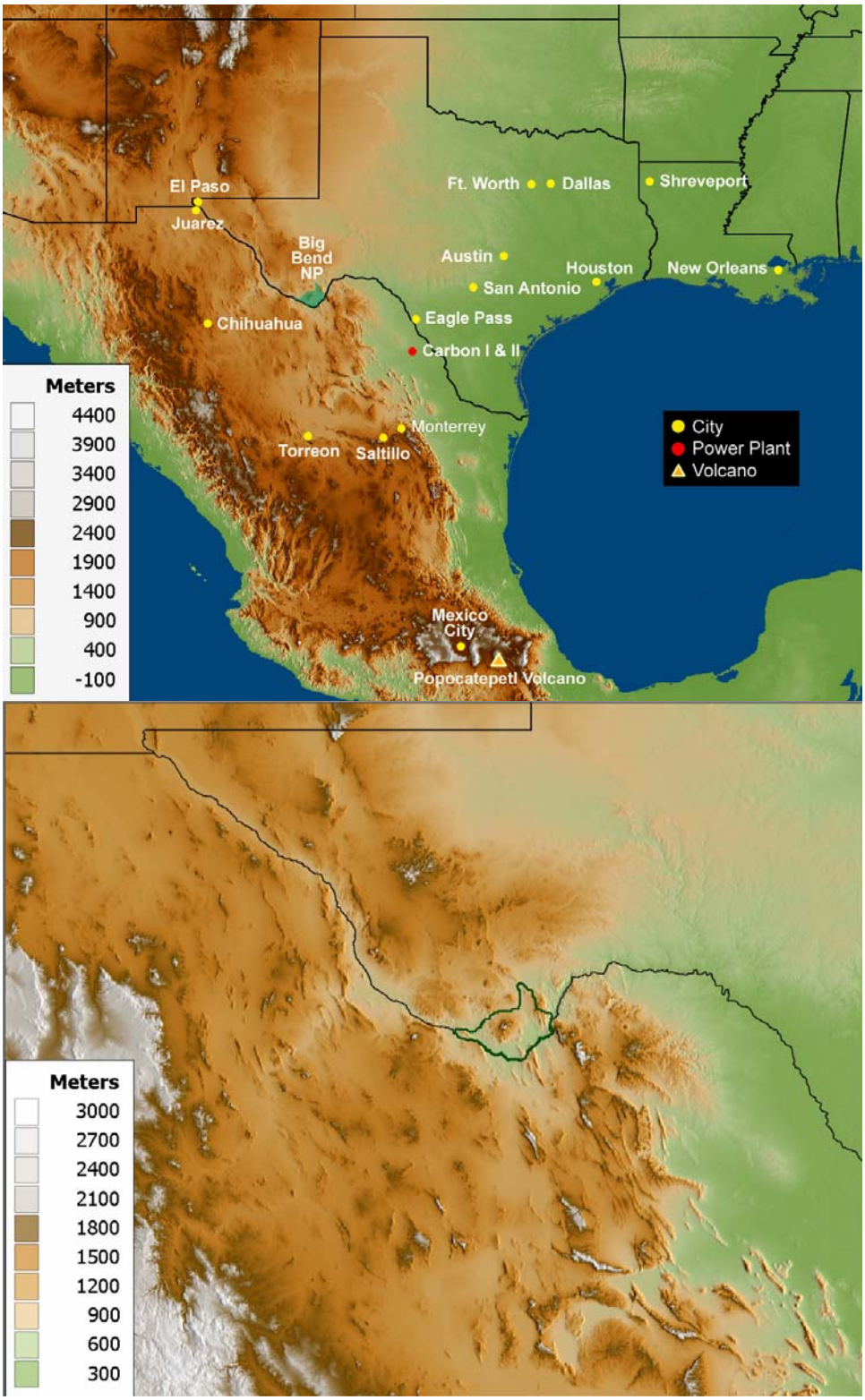

Figure 1-2. Texas and Mexico (above) and the terrain surrounding Big Bend National Park in western Texas and northern Mexico (below).

Big Bend National Park and most of Mexico and west Texas is characterized by complex mountainous terrain (Figure 1-2) which influences both regional and meso-scale transport of

pollutants to the Big Bend region. The Sierra Madre mountain range, located 100–300 km east of Mexico's Gulf Coast, abruptly rises 1 to 2 km above the surface. This is near the top of the boundary layer and hence this mountain range provides an effective barrier to flow from the Gulf of Mexico, channeling airflow from the southeast or northwest toward west Texas. Near Big Bend NP, the Rio Grande cuts a large valley into the mountain ranges. This valley could channel northwesterly flow along the Sierra Madre mountain range to the Big Bend region. Understanding these complex flow patterns is an important component of the BRAVO study.

1.2 Preliminary Study

As a result of concerns over visual air quality at BBNP, a preliminary regional visibility study (1996 Scoping Study) was conducted in Texas and northern Mexico in September and October 1996 [*Gebhart et al.*, 2001]. The primary objective of the preliminary study was to obtain information that would allow for the identification of possible source regions in both countries and source types responsible for visibility degradation at BBNP. The study was conducted at 19 monitoring stations from September 9 through October 13, 1996 (Figure 1-3). The sites sampled $PM_{2.5}$ (particulate matter with a diameter less than 2.5 μm) at all sites and PM_{10} (particulate matter with a diameter less than 10 μm) at Big Bend and Guadalupe Mountains national parks. The $PM_{2.5}$ filters were analyzed for chemical composition.

The preliminary study found that fine particulate sulfate plays a large role in visibility impairment at Big Bend National Park, and that sulfur sources in both the U.S. and Mexico are likely to be contributing to sulfate measured at BBNP. The preliminary study work group made the recommendation that a more extensive field study should be conducted to quantify the impacts from specific sources to visibility impairment at Big Bend National Park; the BRAVO study is the more detailed study recommended in the report of the preliminary study. The United States and Mexico did not reach an agreement on the design of the study, and hence Mexico did not participate in BRAVO.

Figure 1-3. Map showing monitoring sites for preliminary visibility study.

1.3 Big Bend's Seasonal Haze Composition and Long-Term Trends

Haze is caused by scattering and absorption of light by the suspension of fine liquid or solid particles in ambient air, known collectively as atmospheric aerosol. The sum of the light scattering and absorption is known as the light extinction and can be thought of as the fraction of light lost per unit of distance. The units of light extinction are inverse distance (e.g., 1/(million meters) or Mm^{-1}). Higher light extinction levels correspond to hazier conditions.

Estimates of the contributions to light extinction by the major aerosol components can be made from the measured concentrations of those species. Light scattered by particle-free air, known as Rayleigh scattering, is assumed to be a constant value. Though Rayleigh scattering places a limit on our abilities to see distant scenic features clearly, many do not considered it a haze component since it is a natural and fixed consequence of the earth's atmosphere. Particulate haze refers to the non-Rayleigh portion of the light extinction that is the result of both man-made and naturally occurring particles in the atmosphere. Knowledge of the contributions to the total light extinction (including Rayleigh scattering) is useful for judging the perceptibility of changed conditions, while knowing the contributions to particulate haze is a better way to assess the varying components of haze levels. Figure 1-4 shows the five-year composite (1998 through 2002) of the light extinction (sum of light scattering and absorption) from measurements made every three days at Big Bend National Park.

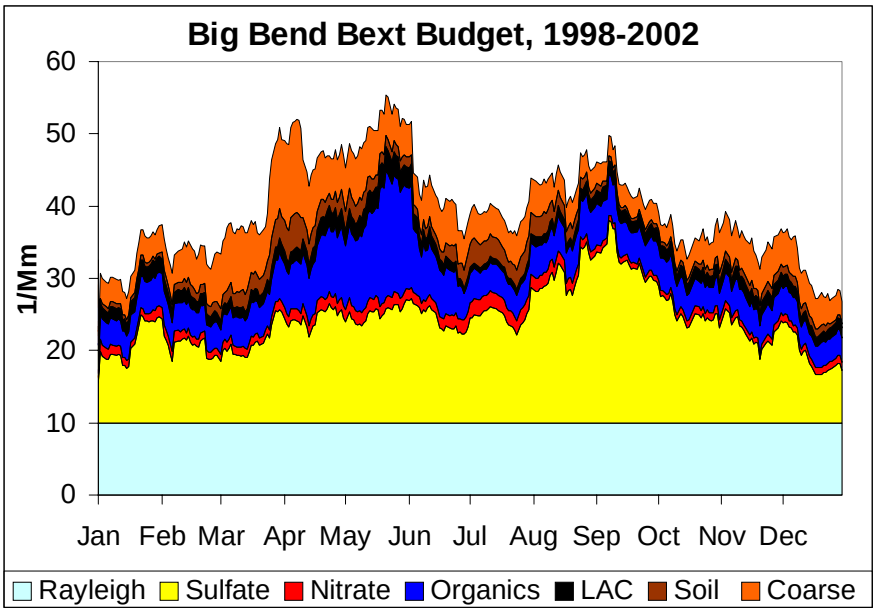

Figure 1-4. Big Bend five-year composite contributions to haze by components. This figure was generated from IMPROVE aerosol data collected at Big Bend NP from 1998–2002.

In general, there are two periods of high haze at Big Bend National Park: one in the spring, when particulate sulfate and carbonaceous compounds contribute similar amounts to haze, and another in the late-summer/fall when particulate sulfate compounds are the largest contributors to haze. Particulate sulfate compounds generally contribute more to haze than any other individual aerosol component. Carbonaceous particulate matter – organic compounds and light absorbing carbon (LAC) – generally constitute the second largest individual aerosol component contributing to haze at Big Bend NP. Information from other studies shows that during late spring episodes, concentrations of carbonaceous compounds are increased due to biomass burning in Mexico and Central America. Dust – a combination of fine soil and coarse mass – can also contribute significantly to haze during March and April.

Figure 1-5 presents Big Bend's trends in the reconstructed particulate light extinction values from 1990–2002. These trends were generated from the IMPROVE fine aerosol data measured at Big Bend NP. As shown, the haze during the worst 20% of the haze days has increased from about 40 Mm^{-1} in 1992 to ~55 Mm^{-1} in 2000, or at a rate of ~17 Mm^{-1} per 10 years during the 1990s as determined by the Theil regression analysis. The haze during the best 20% haze days has not significantly changed during this time period.

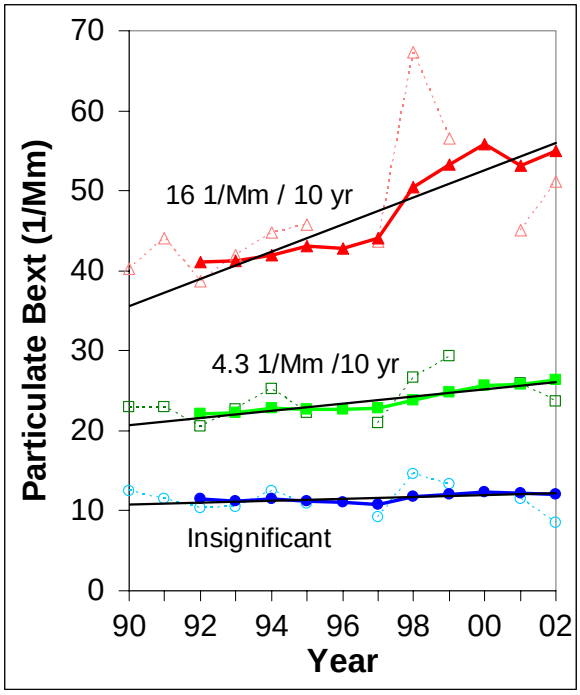

Figure 1-5. Trends in Big Bends reconstructed particulate light extinction for the worst 20% of the haze days (top trend), the middle 20% of the haze days (middle trend) and best 20% of the haze days (bottom trend). The open symbols are annual values and the closed symbols are a 5-year moving average. The Theil regression line and slope are plotted for the 5-year moving average values. The worst and middle 20% trend lines are significant at a p-value below 0.01.

1.4 SO_2 Emissions Sources and Trends

As shown in Figure 1-4, particulate sulfate is typically the largest contributor to haze within the park, and is formed in the atmosphere through the oxidation of sulfur dioxide. Sulfur dioxide is a gas that is generally emitted from combustion sources such as coal-fired power plants. Figure 1-6 is a map of the region that shows BBNP and the locations of SO_2 source areas of importance in Mexico and in Texas (other states in the region have much lower SO_2 emissions).

Major SO_2 sources in Texas include oil refineries, coal-fired power plants, and carbon black producers. The majority of the Texas refineries are located along the eastern shore of Texas on the Gulf of Mexico. Historically, coal-fired power plants were built along the lignite belt which runs from the northeast corner of Texas southwest toward the Carbón I & II facilities in Mexico. Carbon black manufacturers are distributed along the east coast of Texas and near the oil fields in the Texas panhandle. In Mexico, major SO_2 emissions are largely due to fuel oil refining and combustion and coal combustion. The Carbón I & II power plants are the largest coal combustion facilities in Mexico. Major refineries and industrial centers are located in Tampico on the east coast, Manzanillo on the west coast, Tula-Vito-Apasco north of Mexico City, and Toluca-Lerma south of Mexico City.

The 1999 SO_2 U.S. emission rates per state are presented in Figure 1-7. The largest SO_2 emissions in the U.S. are in the eastern U.S. states from the industrial Midwest. Most of these emissions are due to coal fired power plants along the Ohio River Valley. In Texas the SO_2

emissions are about 1.1 million tons SO_2/year, most of which occurs in eastern Texas. The surrounding states of Texas emit another million tons of SO_2 per year.

Figure 1-6. Site map of Mexican cities and Texas counties with SO_2 emissions greater than 5000 tons SO_2/yr. The location of Big Bend National Park is also shown.

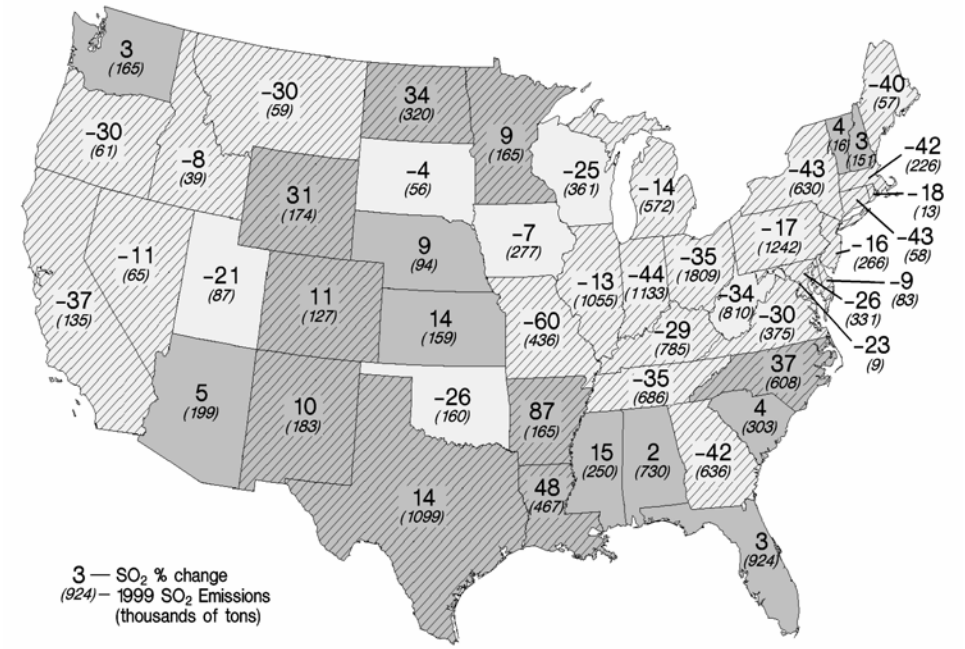

Figure 1-7. The percent change in the SO_2 emissions for each state in the conterminous United States from 1990–1999. The light gray states have decreasing trends while the dark gray states have increasing trends. States with hatch marks have trends that are significant with a two sided P value below 0.1. The percent changes were calculated by dividing the change in emissions over the twelve year period by the 1990 emissions estimated from the trend line. The 1999 SO_2 emission rates for each state are in parentheses. The emission rates are from the National Emission Trend database [U.S. Environmental Protection Agency, 2001].

Figure 1-7 also presents the trends in the SO_2 emissions during the 1990s [*Malm et al.*, 2002]. Most eastern U.S. states from Tennessee and to the north had significantly decreasing trends in emissions, typically on the order of 30% and up to 60% in Missouri (Figure 1-7). In the southeastern U.S. the SO_2 emission trends are flat. The SO_2 emission rates in Texas and its bordering states to the east and west all had significantly increasing trends.

The trends in the 80th percentile of measured sulfate concentrations are compared to these emission trends in Figure 1-8 as time series for northeastern, southeastern, south-middle, and western United States regions. See *Malm et al.* [2002] for details on how this comparison was performed. In each plot, the SO_4^{2-} and SO_2 emission scales have a factor of three change between the low and high values. Therefore, equal slopes in the SO_4^{2-} and SO_2 trends lines represent equal percent changes. As shown, each region has a unique time series pattern and the SO_4^{2-} and SO_2 emission trends closely track each. In the western United States from Arizona to Washington, both SO_2 emissions and SO_4^{2-} steadily declined about 15% throughout the 1990s. In the south-middle United States, encompassing Texas, New Mexico, and Colorado, three of the seven monitoring sites had increasing 80th percentile SO_4^{2-} trends with a statistically significant trend of 32% at Big Bend, Texas. These increasing SO_4^{2-} concentrations are reflected in average SO_4^{2-} time series (Figure 1-8), with a steady increase in SO_4^{2-} of ~15% from 1991 to 1999. The SO_2 emission over this region also had a similar 15% increase. In selecting the south-middle aggregation region, Kansas and Oklahoma were excluded, because these states do not have any monitoring sites in them.

The northeastern United States, from Illinois to Maine, had the largest SO_2 emission rates and declines in emissions during the 1990s (Figure 1-7). As shown in Figure 1-8, the northeastern SO_2 emissions decline is primarily due to a nearly 20% drop between 1994 and 1995. The ambient sulfate concentrations closely follow the SO_2 trend with a similar ~7% decline from 1990 to 1995, the same ~20% drop between 1994 and 1995, and the leveling off afterwards. The sharp 1994 to 1995 decline in SO_4^{2-} and SO_2 was the largest absolute and relative year to year change in all four regions. In the southeastern United States, the SO_4^{2-} and SO_2 emissions did not change appreciatively over the time period, but both regions had a decreasing trend in the early 1990s followed by an increasing trend since 1995–1996.

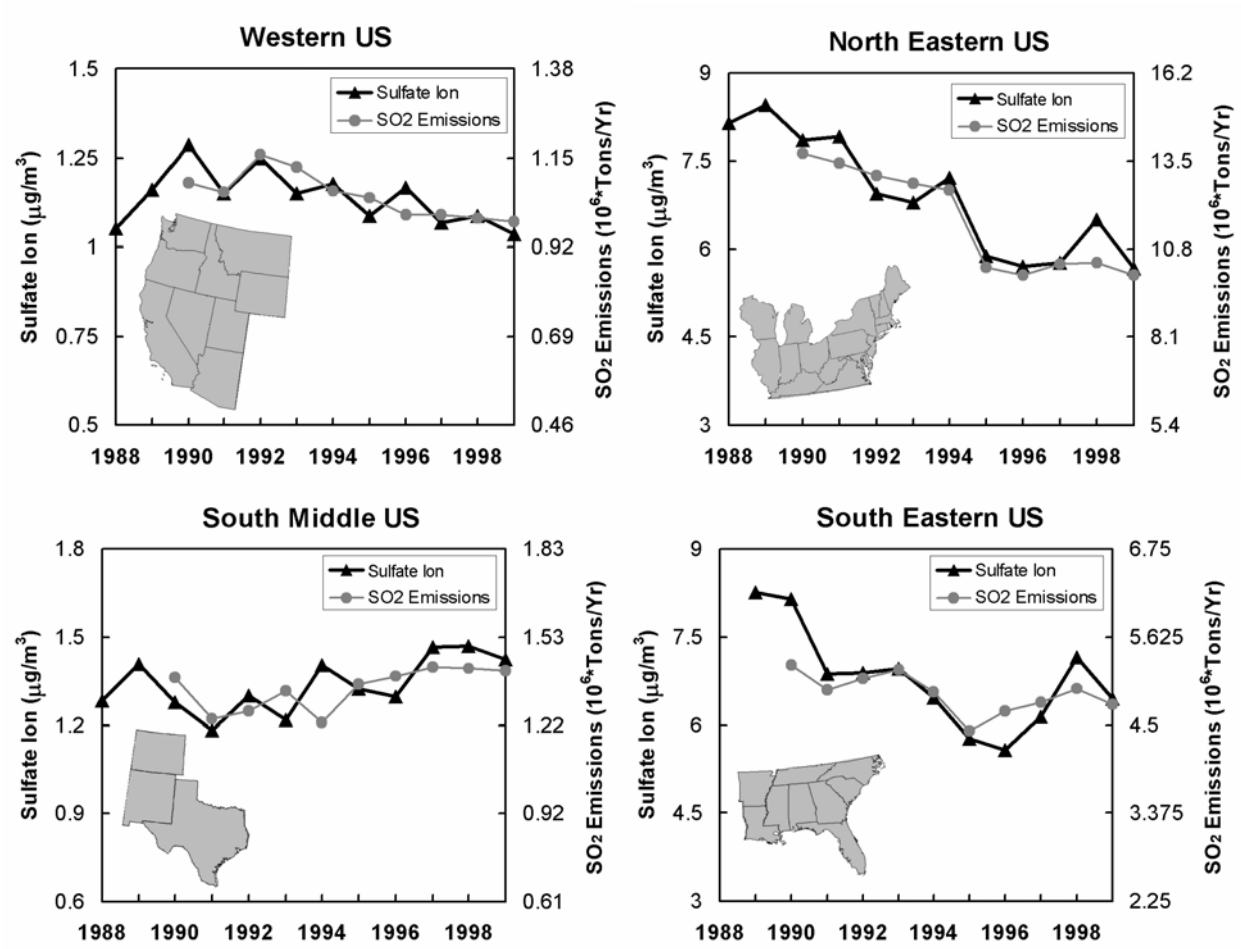

Figure 1-8. Comparison of the ambient sulfate 80th percentile and NET SO_2 emissions aggregated over northeastern, southeastern, south middle and western United States regions. In each plot the SO_4^{2-} and SO_2 emission scales have a factor of 3 change between the low and high values [Malm et al., 2002].

1.5 SO_2 Airmass Transport to Big Bend NP

For a source of sulfur dioxide emissions to contribute to Big Bend's haze, the sulfur dioxide must be transported from the source to Big Bend and the sulfur dioxide converted to particulate sulfate. The rate of conversion of sulfur dioxide to particulate sulfate depends on several factors, and conversion rates can be a few days to as little as a few minutes. For example, the presence of clouds can dramatically accelerate sulfate conversion rates through aqueous-phase chemical reactions. Gas-phase reactions also convert sulfur dioxide to particulate sulfate, although oxidation rates are considerably slower as compared to the aqueous-phase reactions.

All other things being the same, a source region's potential to contribute to haze at Big Bend increases for periods when air parcels frequently pass over and spend more time over the source region prior to transport to Big Bend. Trajectory analysis during a five-year period (1998–2002) shows that transport patterns vary considerably throughout the year, as shown in Figure 1-9. Upwind regions during the months of November through March are primarily to the west of Big Bend; this period generally corresponds to lowest haze levels measured in the park.

In April and May the air flow is frequently from regions to the southeast and west, while June and July are characterized by airflow from regions to the southeast. August through October is the only time of the year with appreciable air flow from regions to the east and northeast, as well as the more common flow from regions to the southeast. This is the period when the highest concentrations of sulfate are measured, and hence is of particular interest. In addition to the general transport patterns described above, it should be noted that throughout the year airmasses en route to Big Bend frequently reside over northern Mexico.

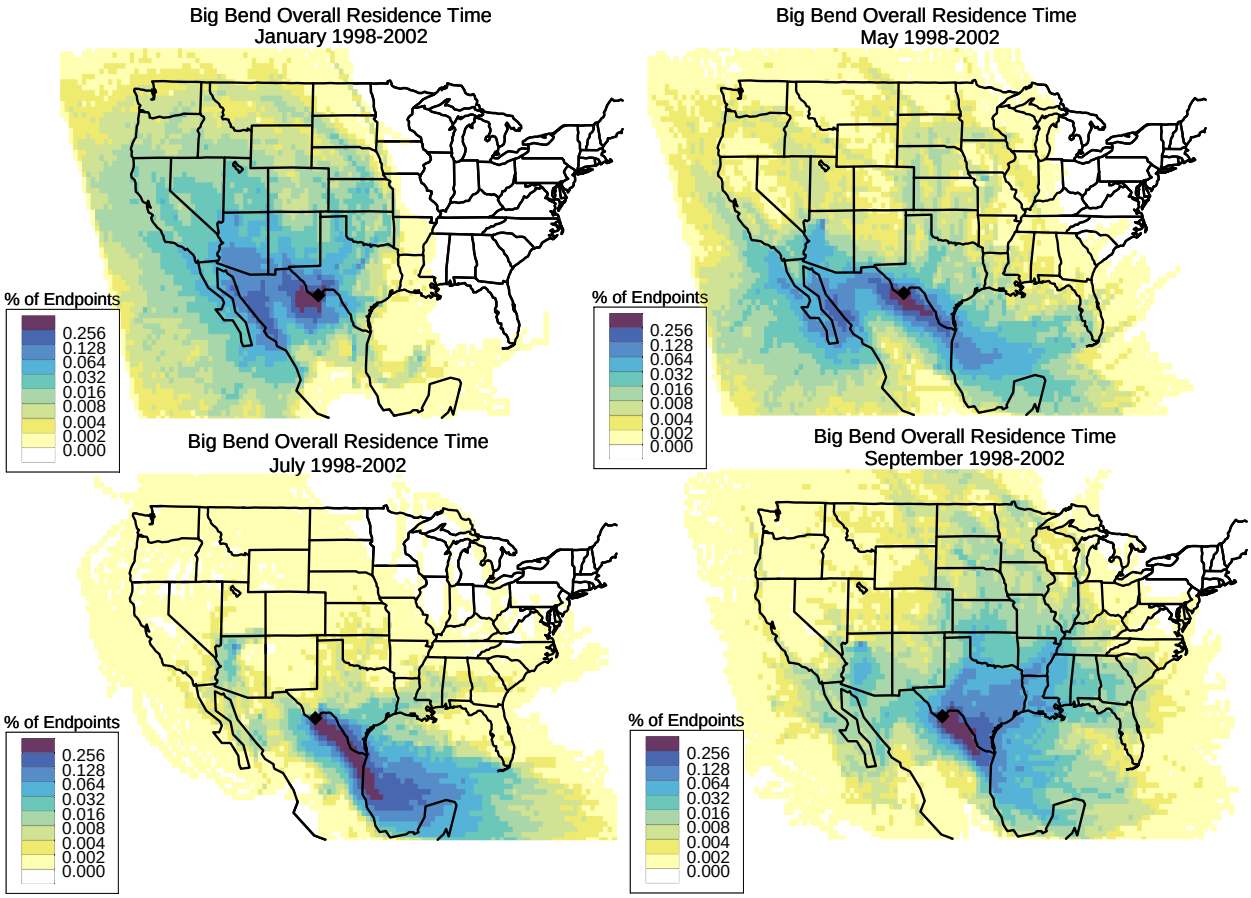

Figure 1-9. Examples of geographic distribution of the fraction of time that air parcels spend during the five days prior to arriving at Big Bend National Park for the months of January, May, July, and September based upon a five-year analysis period (1998 to 2002).

1.6 Techniques for Determining Sulfate Attributions

Sulfates are the single largest contributor to Big Bend's haze, and account for about half of the particulate haze on average (Figure 1-4). As discussed above, sulfate particles are formed through the oxidation of sulfur dioxide, and the largest emitters of this pollutant are anthropogenic sources such as coal-fired power plants.

This report provides a detailed description of the composition and optical properties of haze in the Big Bend region, and also describes the numerous analytical and modeling techniques that were conducted by the NPS and CSU to determine which sources (e.g., Texas, Mexico, the eastern U.S.) were contributing particulate sulfate to BBNP during the BRAVO study period. These techniques include: 1) air quality data analysis 2) airmass history based

receptor models, 3) a regional air quality model, and 4) a synthesis inversion analysis of the regional air quality model.

Several airmass history based receptor analysis methods were used for source attribution. These methods developed statistical relationships between the Big Bend particulate sulfate concentrations and airflow prior to reaching Big Bend to estimate the average source attribution over the study period. Variations of the trajectory methods included the use of two methods of estimating wind over North America (EDAS from the National Weather Service and MM5 applied specifically for the BRAVO study) and the use of back trajectories from Big Bend employed in Tracer Mass Balance (TrMB) [*Gebhart et al.*, 1988; *Iyer et al.*, 1987] and forward transport and dispersion from all potential source regions used in Forward Mass Balance Regression (FMBR) [*Schichtel*, 1996]. Testing of the TrMB and FMBR methods involved reproducing measured tracer concentrations and simulated sulfate concentrations from a deterministic model using both sets of wind information. Trajectories that passed these evaluations were used for attribution of measured sulfate.

The REMSAD regional air quality model [*SAI*, 2001; *Seigneur et al.*, 1999] was also used to predict sulfate attributions from individual source regions and represents a "source-oriented" approach which differs from the "receptor-oriented" techniques described above. REMSAD simulates the physical and chemical processes which control pollutant concentrations in the atmosphere, including transport, dispersion, chemical transformation, wet and dry deposition, and emissions of pollutants and pollutant-precursors from anthropogenic and biogenic sources. Air quality models such as REMSAD depend on the quality of the emissions and meteorological data that are used in the simulation, as well as the accuracy of the advection, transformation, deposition, dispersion, and other numerical algorithms that constitute the model. Biases and uncertainties identified in any of these processes can adversely affect their source attribution estimates.

Finally, a "synthesis inversion analysis" was conducted, which develops a statistical relationship between the daily source attribution results from the REMSAD air quality model and the measured particulate sulfate concentrations in and around Big Bend [*Enting*, 2000; *Enting*, 2002]. This technique is very useful for identifying biases in the original REMSAD model predictions, and can serve as a bridge to help reconcile results from the receptor-oriented techniques and the source-oriented model.

2) Ambient Monitoring Data, Air Quality Models and Source Apportionment Methods

2.1 Air Quality, Emissions, and Meteorological Data and Processing

The BRAVO data analyses examined and integrated aerosol, optical, tracer, emission, and meteorological data sets from a number of different sources. This section describes all of the data sets used in the data analyses as well as specialized data processing that was performed.

2.1.1 Air Quality Monitoring During BRAVO

In order to accomplish the goals of the BRAVO study, an extensive air quality monitoring network was deployed from July–October 1999 by several cooperating agencies including the National Park Service (NPS), the U.S. Environmental Protection Agency (EPA), the Texas Commission on Environmental Quality (TCEQ), and the utility sector. This network collected speciated fine (<2.5 μm, $PM_{2.5}$) aerosol and SO_2 gaseous data throughout Texas. Unique perfluorocarbon tracers were also released from four industrial/urban sites within Texas and monitored throughout Texas. In addition, aircraft measurements of high time resolution of light scattering, sulfur dioxide, nitrogen oxides, sulfate, and meteorological parameters were taken over eastern Texas and the Texas Gulf Coast.

An intensive monitoring site was deployed at the K-Bar Ranch, a site within Big Bend National Park (Figure 2-1). At this site aerosol and gaseous species were measured including: speciated PM_{10} (<10 μm) and $PM_{2.5}$ (<2.5 μm) aerosol, aerosol size distributions, size-resolved aerosol data, gaseous nitric acid, ammonia and hydroperoxides, perfluorocarbon tracer concentrations, as well as aerosol scattering, absorption, total extinction and hygroscopic properties.

In this report, data from the study-wide fine aerosol and tracer networks and some additional sulfate concentrations collected at K-Bar are used. These data are more fully described below. More detailed information on the intensive aerosol and gaseous monitoring at K-Bar can be found in *Green et al.* [2000], *Hand et al.* [2002], *Malm et al.* [2003], and *Lee et al.* [2004].

2.1.1.1 Aerosol and SO_2 Monitoring Network

The monitoring network for collecting speciated $PM_{2.5}$ aerosol and SO_2 gaseous data included 37 sites, all located in Texas except Wichita Mountains in Oklahoma (Figure 2-1, Table 2-1). The locations of the monitoring sites were chosen to satisfy several purposes: general gradient sites in Texas (about 100 km apart), border gradient sites at the Texas/Mexico border, Texas/other U.S. states border sites, coastal gradient sites, Big Bend area gradient sites, Class I areas, and sites predominantly downwind of tracer release locations. The purpose of each site is listed in Table 2-1. Thirty-seven sites collected 24-hour integrated samples. Six sites collected 6-hour samples in Big Bend National Park and to its north (Figure 2-2). At the K-Bar monitoring site, located in the center of Big Bend National Park, collocated samplers were collecting 24-, 12-, and 6-hour integrated samples. It should be noted that 19 of the 37 sites did not begin monitoring until July 22 or 23. Also, initially the Big Bend monitor was located outside of K-Bar, but was moved to the K-Bar location on July 22.

All sites collected aerosols using the Interagency Monitoring of Protected Visual Environments (IMPROVE) sampling system [*Malm et al.*, 1994] to collect the $PM_{2.5}$ samples. These samples were analyzed for mass and elemental composition. In addition, fine particulate

ions and carbon as well as SO_2 were measured at some of these sites. Figure 2-1 and Table 2-2 summarize the type of measurements and the parameters for which the filters were analyzed at each monitoring site.

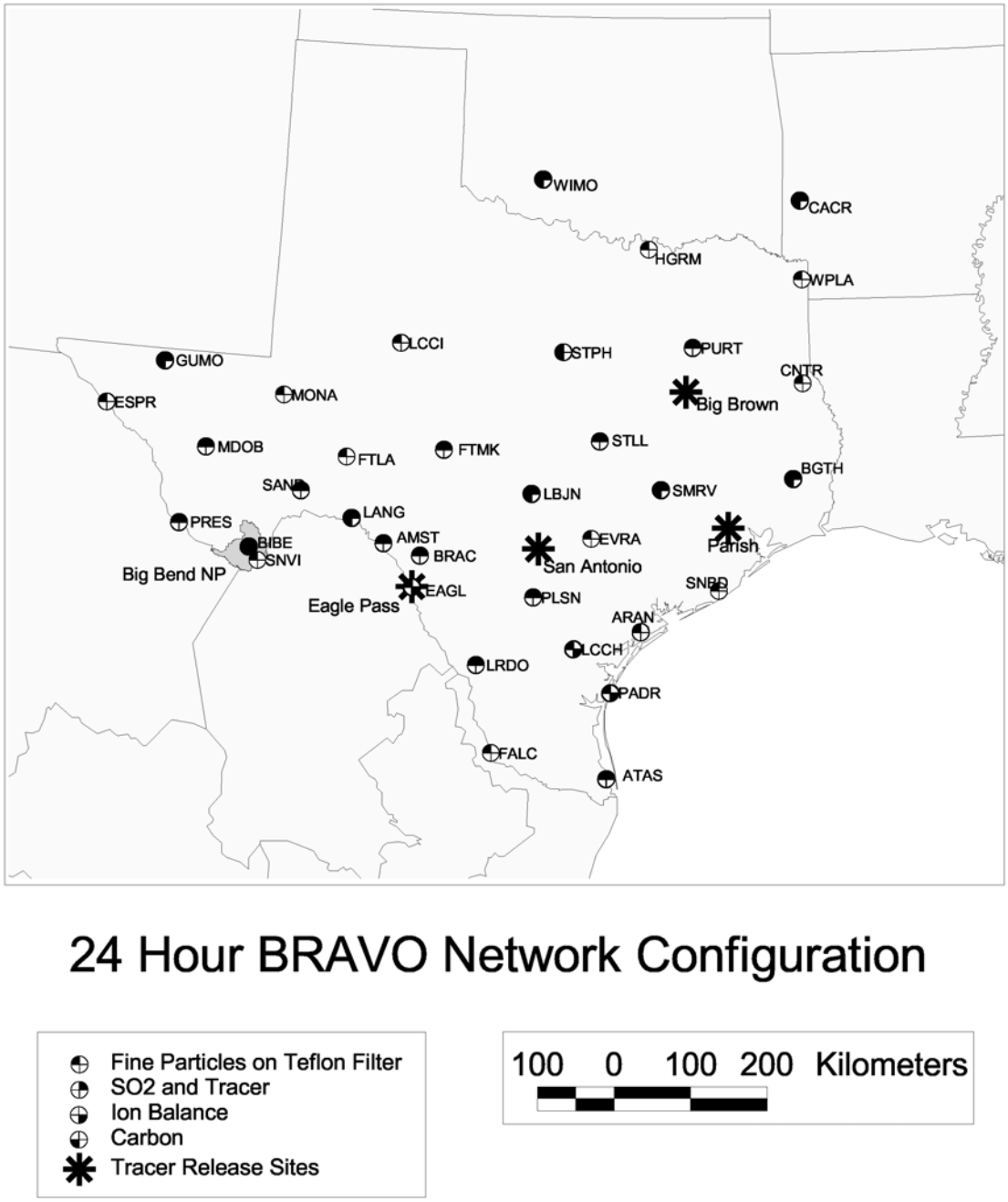

Figure 2-1. 24-hour network of gas and aerosol sampling locations.

Table 2-1. Aerosol and tracer monitoring site abbreviations, names, latitude, longitude, elevation, and purpose.

Site	Name	Latitude	Longitude	Elevation (m)	Purpose
AMST	Amistad	29.47	-101.02	351	Downwind of Carbón/Eagle Pass
ARAN	Aransas	28.32	-96.83	0	Coastal gradient
BIBE	Big Bend (K-Bar)	29.30	-103.18	1052	Receptor/Big Bend area gradient
BGTH	Big Thicket	30.48	-94.35	38	Texas/Louisiana border/gradient
BRAC	Brackettville	29.32	-100.42	335	Downwind of Carbón/Eagle Pass
CNTR	Center	31.83	-94.17	24	Texas/Louisiana border/gradient
EPS	Eagle Pass	28.87	-100.52	274	Mexico border/near Carbón
ESPR	Esperanza	31.17	-105.72	1067	Mexico border gradient
EVRA	Everton Ranch	29.63	-97.65	244	Gradient
FALC	Falcon Dam	26.55	-99.17	61	Border gradient
FTLA	Fort Lancaster	30.67	-101.70	762	Gradient
FTMK	Fort McKavett	30.83	-100.10	671	Gradient
FTST	Ft Stockton	30.92	-102.90	983	Big Bend area gradient
GUMO	Guadalupe Mtns	31.83	-104.82	1659	Class I area
HGRM	Hagerman	33.73	-96.75	244	Texas/Oklahoma border
ATAS	Laguna Atascosa	26.22	-97.35	4	Coastal and Mexico border gradient
LCCI	Lake Colorado City	32.32	-100.90	640	Gradient
LCCH	Lake Corpus Christi	28.07	-97.90	91	Inland ion balance
LANG	Langtry	29.80	-101.55	396	Mexico border/downwind of Carbón
LRDO	Laredo	27.80	-99.45	148	Mexico border gradient
LBJN	LBJ	30.25	-98.63	518	Gradient/downwind of San Antonio
MARA	Marathon	30.20	-103.23	1280	Big Bend area gradient
MDOB	McDonald Observatory	30.67	-104.02	2043	Gradient
MONA	Monahans Sandhills	31.48	-102.80	831	Big Bend area gradient
PADR	North Padre Island	27.45	-97.30	0	Coastal/ion balance
PRSG	Persimmon Gap	29.67	-102.18	915	Big Bend area gradient
PLSN	Pleasanton	28.78	-98.57	122	Gradient
PRES	Presidio	29.57	-104.35	838	Mexico border gradient
PURT	Purtis Creek	32.35	-98.00	187	Gradient/downwind of Big Brown
SNBD	San Bernard	29.90	-95.58	0	Coastal gradient
SNVI	San Vicente	29.12	-103.03	549	Big Bend area gradient
SAND	Sanderson	30.18	-103.22	610	Gradient/downwind of Carbón
SMRV	Somerville Lake	30.33	-96.52	84	Gradient
STPH	Stephenville	32.27	-98.17	274	Gradient
STLL	Stillhouse Lake	31.02	-97.53	213	Gradient
WIMO	Wichita Mtns	34.70	-98.58	488	Class I area
WPLA	Wright Patman Lake	33.30	-94.15	9	Texas/Arkansas/Louisiana border

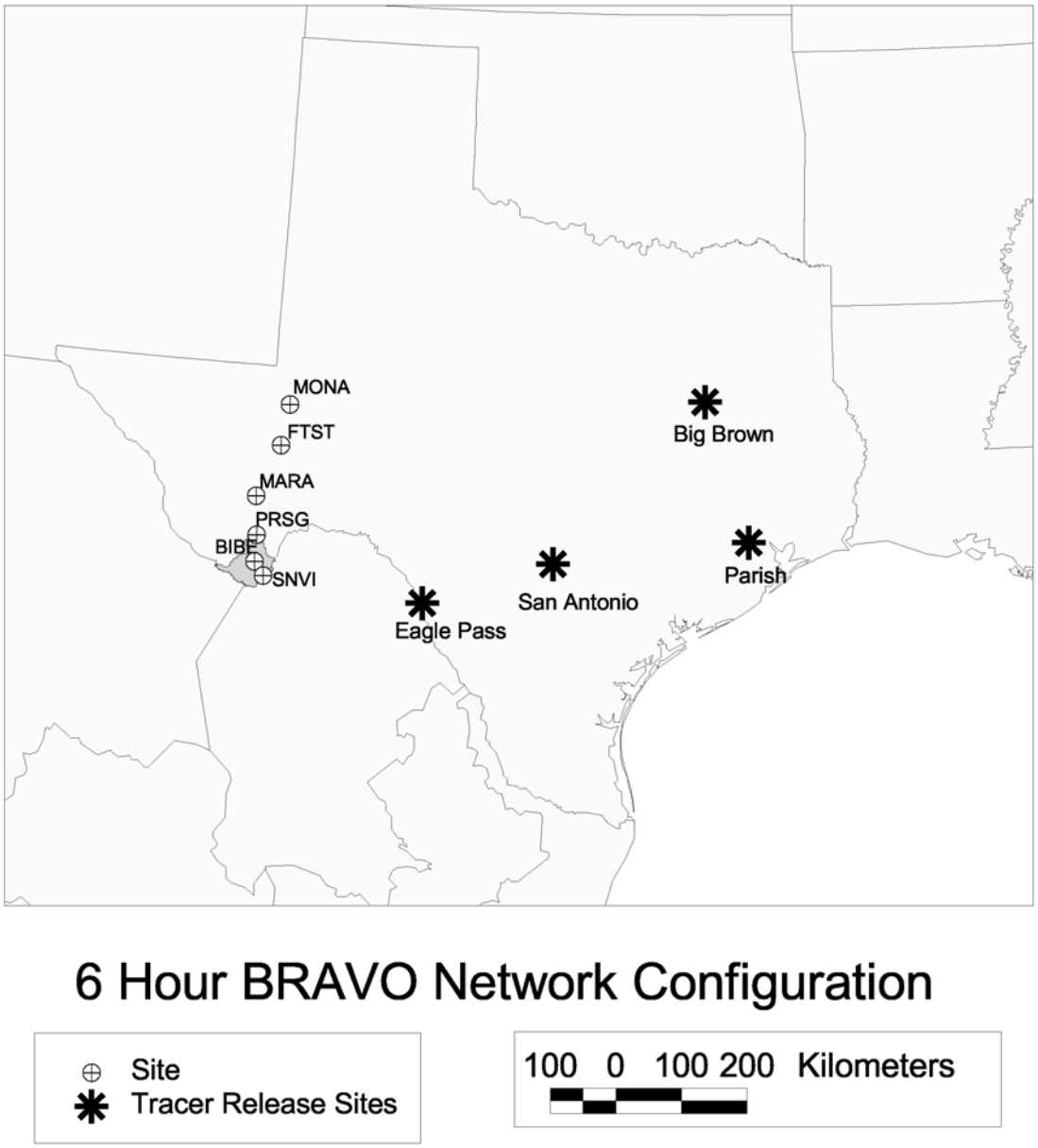

Figure 2-2. 6-hour network of gas and aerosol sampling locations.

Table 2-2. Number of measurement sites by measurement type.

Measurement Type	Number of Sites
24-hour $PM_{2.5}$ elements (H, Na-Pb, mass, b_{abs}) (Teflon filter)	37
24-hour SO_2 and tracer	18
24-hour $PM_{2.5}$ carbon (quartz filter)	7
24-hour $PM_{2.5}$ ions (nylon filter)	4
6-hour $PM_{2.5}$ elements, SO_2, tracer	6
24-hour PM_{10} elements, ions, carbon	1 site at K-Bar
12-hour $PM_{2.5}$ elements, ions, carbon	1 site at K-Bar
Collocated 24-hour $PM_{2.5}$ elements, ions, carbon, SO_2, tracer	1 site at K-Bar
Collocated 24-hour PM_{10} elements, ions, carbon	1 site at K-Bar
Collocated 6-hour $PM_{2.5}$ elements, SO_2, tracer	1 site at K-Bar

The IMPROVE monitoring system used to collect the samples was designed for the IMPROVE network and has been operated extensively in the network and during field studies since 1988 [*Malm et al.,* 1994]. The IMPROVE sampler can employ up to four independent modules, three for monitoring fine particles and the fourth module to collect particles less than 10 μm. Each module incorporates a separate inlet array, filter pack, and pump assembly; however, all modules are controlled by one timing mechanism. It is convenient to consider a particular module, its associated filter, and the parameters measured from the filter as a channel of measurement (e.g., channel A).

Channels A, B, and C were each equipped with a 2.5 μm cyclone inlet. Channel A, which utilizes a Teflon filter, was analyzed for fine mass ($PM_{2.5}$) gravimetrically, nearly all elements with atomic mass number >11 (Na) and <82 (Pb) by proton induced x-ray emission (PIXE) and/or by x-ray florescence (XRF), elemental hydrogen by proton elastic scattering analysis (PESA), and light absorption.

Channel B utilized a single Nylasorb filter as a collection substrate. A denuder, coated with a mixture of Na_2CO_3 and reagent grade glycerol, before the nylon filter removes nitric acid vapors. The material collected on the filter was extracted ultrasonically in an aqueous solution that was subsequently analyzed by ion chromatography for the anions sulfate, nitrate, nitrite, and chloride. Sodium, ammonium, potassium, magnesium, and calcium ion concentration were also measured using extracts from these filters.

Channel C utilized tandem quartz fiber filters for the collection of fine particles and the estimation of an organic carbon artifact from a secondary filter. The positive organic artifact is the results of adsorption of organic gases on the quartz filter. These filters were analyzed by thermal optical reflectance (TOR) for elemental and organic carbon [*Chow et al.,* 1993].

Additional channel A, B, and C samplers were run with PM_{10} rather than $PM_{2.5}$ inlets so that coarse particle species mass concentrations could be estimated by differencing PM_{10} and $PM_{2.5}$ concentrations. The 24-hour filter samples were collected each day starting at 08:00 Central Daylight Time. Exposed cassettes from channels A, B and C were stored in sealed plastic bags and shipped for storage and analysis.

In order to assure high quality data, experiments were designed such that observables could be estimated or modeled in a number of different ways. Mass was gravimetrically determined for both D_{aero} <10 and 2.5 μm, which can be compared to reconstructed mass based on the summation of measured aerosol species. Dry and ambient scattering coefficients were measured, which in turn can be compared to modeled scattering coefficients that are based on aerosol species mass and size measurements.

2.1.1.2 Tracer Data

As part of the BRAVO study, four perfluorocarbon tracers were released from four locations in Texas and monitored at 24 sites throughout Texas. Each tracer monitoring site was collocated with a PM2.5 module A aerosol monitor. The objectives of the tracer component of the study were to tag source areas with the potential for transport of aerosols and gases resulting in significant visibility impairment at Big Bend National Park, evaluate the dispersion (transport and diffusion) capabilities of Eulerian and Lagrangian models deployed for understanding the causes of haze during BRAVO, and to evaluate the receptor-oriented source attribution techniques. In this report the tracer data were only used to evaluate the transport and dispersion

mechanisms in the airmass history and air quality models and the receptor source attribution techniques.

The four tracer release points are Eagle Pass, the Big Brown coal-fired power plant, San Antonio, and the Parish coal-fired power plant in Houston (Figure 2-2). The Eagle Pass release point is about 250 km southeast of Big Bend National Park. The releases at Eagle Pass were made from the top of a 107 m (350 feet) tower to simulate the releases from the Carbón I & II coal-fired power plant stacks located 30 km to the south. At Eagle Pass, ocPDCH was continuously released during the four-month study. In addition, during the first two months of the study PDCB was released on alternate days and PTCH was released during the daytime. The timing tracers were designed to allow estimation of the transport times from Eagle Pass to Big Bend National Park. Big Brown is located at the northern end of the Lignite Belt near Fairfield, TX, and operated by Texas Utilities. The tracer was introduced into the exhaust duct just before the point where the duct enters the stack. The iPPCH tracer was continually released from the Big Brown stack throughout the four-month study.

The two timing tracers, PDCB and PTCH, released from Eagle Pass during the first half of the study, were moved to San Antonio (PDCB) and to the Parish Power Plant in Houston, TX, (PTCH) and were continuously released from these sites from September 17, 1999, to the end of October. The San Antonio release system was located at an air quality monitoring station run by the utility company, City Public Service. The site was inside the beltway and was chosen to represent the San Antonio area source. The release in the Houston area was made from the Parish Power Plant operated by Reliant Energy, located about 64 km southwest of Houston. Tracer was introduced into the stack of Boiler 7 through a sampling port at the 100 ft. level.

Tables 2-3 and 2-4 present the design tracer release rates and schedule for tracer release from the four sites. However, as shown in Figures 2-3 to 2-6 the tracer release rates fluctuated from day to day. At times the fluctuations were significant; for example, the Big Brown tracer was not released from 8/15–17 and 10/8–16. Therefore, the tracer release rates need to be considered when interpreting the tracer concentrations.

Table 2-3. Tracer release schedule first phase of study.

Location	**Eagle Pass**	**Eagle Pass**	**Eagle Pass**	**Big Brown (NE Texas)**
Tracer	Perfluoro-1,2-dimethylcyclo hexane	1,1,2,2,3,4-hexafluoro-3,4-bis(trifluoromethyl) cyclobutane	Perfluoro-1,3,5-trimethylcyclo hexane	perfluoro-isopropylcyclohexane
Tracer Abbrev	**ocPDCH**	**PDCB**	**PTCH**	**iPPCH**
Release period	7/5/99-11/1/99	7/5/99-9/13/99	7/5/99-9/13/99	7/9/99-11/1/99
Design Release Rate (kg/hr)	0.155 (2.6 g/min)	0.525 (8.75 g/min) alternate days (8am-8am) CDT	0.184 (3 g/min) 8am – 8pm CDT only	0.092 (1.5 g/min)

Table 2-4. Tracer release schedule for the second half of the study.

Location	**Eagle Pass**	**San Antonio**	**Parish (Houston)**	**Big Brown (NE Texas)**
Tracer	Perfluoro-1,2-dimethylcyclo hexane	1,1,2,2,3,4-hexafluoro-3,4-bis(trifluoromethyl) cyclobutane	Perfluoro-1,3,5-trimethylcyclo hexane	perfluoro-isopropylcyclohexane
Tracer Abbrev	**ocPDCH**	**PDCB**	**PTCH**	**iPPCH**
Release period	7/5/99-11/1/99	9/17/99-11/1/99	9/17/99-10/25/99	7/9/99-11/1/99
Design Release Rate (kg/hr)	0.155 (2.6 g/min)	0.442 (7.4 g/min)	0.115 (1.9 g/min)	0.092 (1.5 g/min)

The tracer concentrations were monitored at 24 of the 37 aerosol receptor sites (Figure 2-1, Table 2-1). Most of the tracer, aerosol, and SO_2 sampling sites collected 24-hour averaged data; however, six 6-hour tracer sites were located along an approximately 300 km long arc running north-northeast from the Rio Grande River in Big Bend National Park (Figure 2-2). The K-Bar monitoring site also had a collocated 1-hour sampler. The 6-hour monitors had a 4 times larger flow rate than the 24-hour samplers. Therefore, both the 6- and 24-hour samples had equal sample volumes for analysis. More details of the tracer release including the reasons for each of the deviations from the optimum release rates can be found in *Watson et al*. [2000].

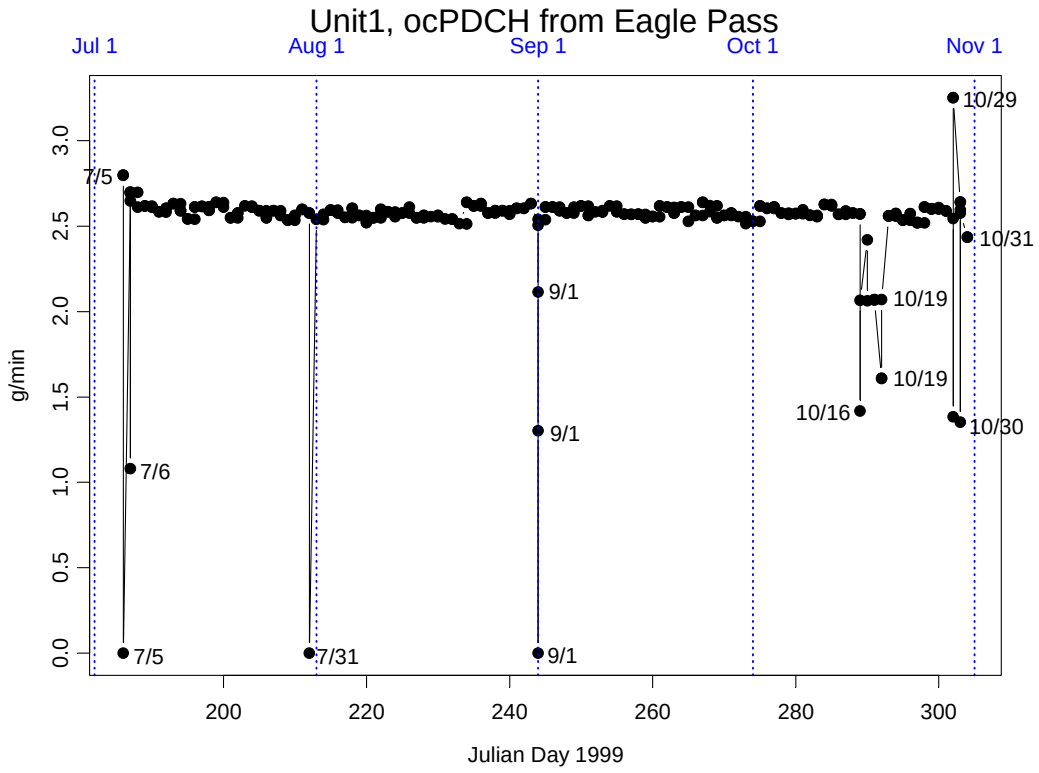

Figure 2-3. Release rates of ocPDCH from Eagle Pass (g/min) during the BRAVO study.

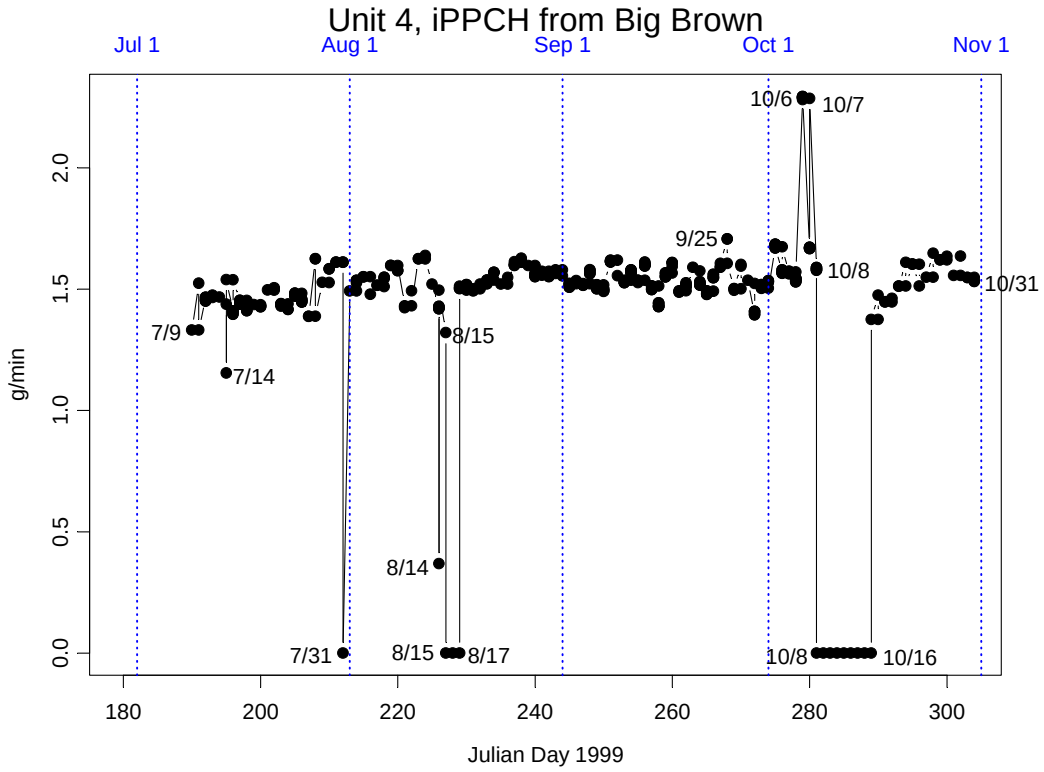

Figure 2-4. Release rates of iPPCH from Big Brown (g/min) during the BRAVO study.

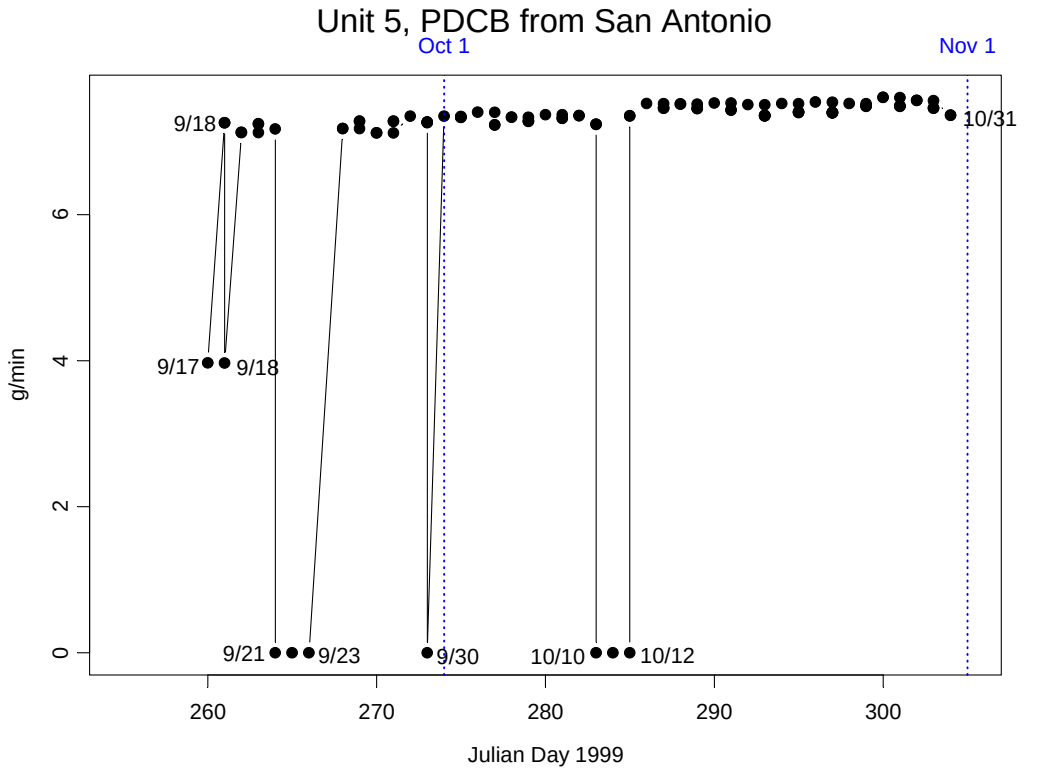

Figure 2-5. Release rates of PDCB from San Antonio (g/min) during the second half of the study.

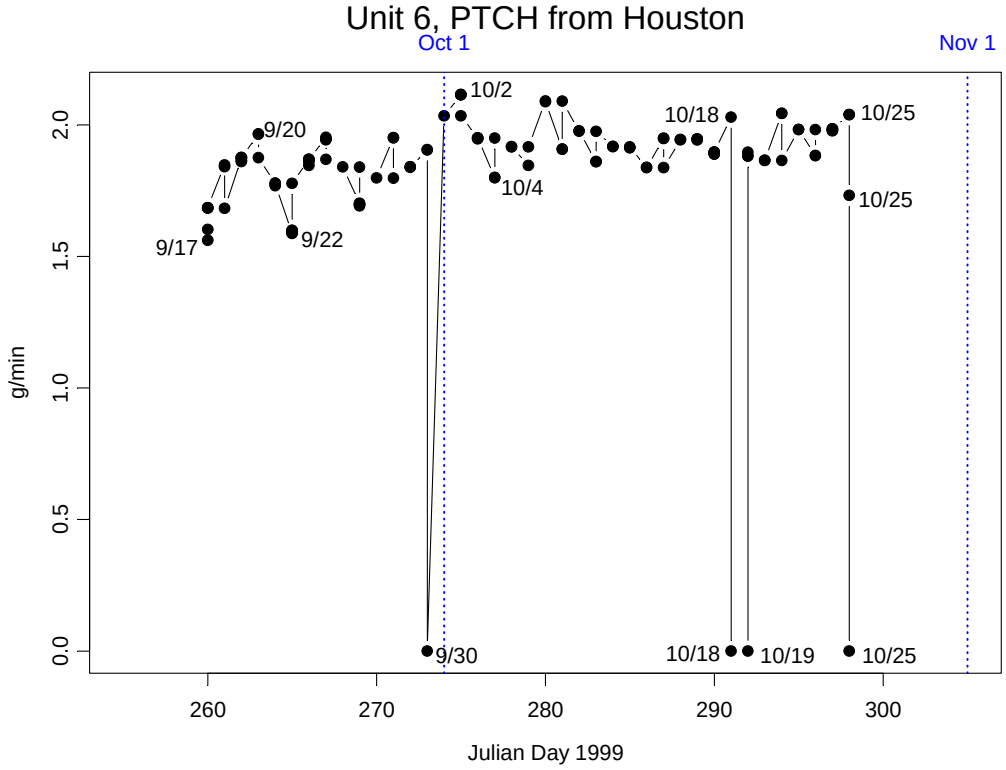

Figure 2-6. Release rates of PTCH from Houston (g/min) during the second half of the study.

2.1.1.3 University Research Glassware (URG) Cyclone/Annular Denuder/Filter Pack Sampling System

Colorado State University (CSU) sampled aerosol composition by collecting 24-hour integrated filter samples using a URG denuder/filter-pack [*Lee and Collett*, 2002; *Lee et al.* 2004] assembly with a $PM_{2.5}$ inlet. Samples were run from 08:00 (CDT)–08:00 (CDT). The filters were analyzed for major ions by Ion Chromatography (IC) using analytical equipment located on site. CSU samplers were located at K-Bar throughout the BRAVO study period (July 1–Oct. 31, 1999).

Two parallel sampling trains were used to facilitate a rapid change between samples. Air was drawn through the sample train at a nominal value of 10 lpm (actual volumetric flow) in order to provide the desired 2.5 μm aerodynamic diameter size cut in the URG cyclone. Flow was provided by a vacuum pump and controlled by a mass flow controller. A dry gas meter was installed in-line between the filter pack and mass flow controller in order to provide an integrated measure of total sample flow. The sample flow read by the dry gas meter was corrected to ambient conditions by correcting for the pressure drop through the denuders and filters. An inline pressure measurement was used to make this correction. The URG samplers were mounted on the top of the scaffolding with the pumps located on the ground below.

Ambient air was drawn through a cyclone (D_{50} = 2.5 μm) and along etched glass denuder walls (air passes through two denuders in series), which were coated with chemicals that absorb the gaseous species of interest. NaCl (0.1%) coated the first denuder for collection of HNO_3 and the second denuder was coated with 0.5 g citric acid in 50 mL of methanol to collect ambient NH_3. Pre-filter collection of NH_3 helps preserve acidic aerosol samples [*Perrino et al.*, 1990].

The remaining air stream was then filtered through 47 mm diameter Teflon, nylon, and coated glass fiber filters in series. The Teflon filter (Gelman Teflo, 2.0 μm pore size) was used to collect particulate matter.

The nylon membrane filter (Gelman Nylasorb) and citric acid impregnated glass fiber filter were used to capture nitric acid and ammonia, respectively, which may be volatilized from particulate matter on the Teflon filter.

The primary $PM_{2.5}$ ionic species, Cl^-, SO_4^{2-}, NO_3^-, Na^+, NH_4^+, K^+, Mg^{2+}, and Ca^{2+}, and gas phase concentrations of HNO_3 and NH_3 were measured. Also, $PM_{2.5}$ aerosol acidity was measured on-site for all study days.

2.1.1.4 Integrating Nephelometers

The details of ambient nephelometer measurements were covered in *Malm et al.* [1994], *Molenar* [1997], *Malm and Day* [2000], and *Day et al.* [2000] and will only be briefly reviewed here. Five Optec NGN-2 integrating nephelometers, in various configurations, were operated during the study. One nephelometer was fitted with an Anderson PM_{10} inlet, while two Optec nephelometers were operated at reduced flow rates (113 l min^{-1}) and were fitted with a Bendix-240 cyclone inlet with a 2.5 μm cutpoint. Two nephelometers utilized the open-air configuration and were operated using standard IMPROVE protocols [*Air Resource Specialists*, 1995]. Thermistors were placed inside the inlet, where sample air was assumed to be at ambient temperature, and at the sample exit, where sample air temperature should have reflected any heating of the aerosol. Monitoring the difference in sample temperature between the inlet and the outlet of each nephelometer allowed determination of whether heating of the sample had occurred and if there was a subsequent change in sample RH. Generally, the degree to which the sample was heated was less than 0.5°C. The accuracy of the nephelometer measurements in this configuration and the degree of heating were discussed in some detail by *Day et al.* [2000].

A sixth and seventh nephelometer (Radiance Research M903 integrating nephelometers) were configured to measure dry and controlled humidity (D_{aero} <2.5 μm) scattering. In the controlled humidity configuration, prior to measurements by the nephelometer, air was drawn through a temperature-controlled humidity conditioner consisting of Perma Pure Nafion dryers, while temperature was controlled by placing the dryers in a constant temperature water bath. Because temperature changes in the sampling plumbing can cause unwanted and unknown RH changes, temperatures were monitored throughout the system.

2.1.1.5 Transmissometer

Transmissometers are calibrated to measure the irradiance, at 550 nm, of a light source after the light has traveled over a finite atmospheric path. The transmittance of the path is calculated by dividing the measured irradiance at the end of the path by the calibrated initial intensity of the light source. The average extinction of the path is calculated using Bouger's law from the transmittance and length of the path. The measurement is ambient in that air samples are not passed through an enclosed chamber.

Transmissometers used in this study are the OPTEC, Inc., LPV-2 instruments, which have been in use since 1986. Their use in remote locations such as national parks is discussed by *Molenar et al.* [1989] while their use in urban settings is presented by *Dietrich et al.* [1989]. Careful operation of the transmissometer (daily cleaning of optics and pre and post calibrations) should result in extinction measurements with an accuracy of about 10% *Molenar et al.* [1989].

The transmissometer used in this study was located near the particle samplers but on the rim of the canyon. Therefore, the separation between the transmissometer and all other instruments was about 1.5 km.

2.1.1.6 Aethalometer

The aethalometer collects aerosol continuously on a quartz fiber filter tape, while measuring the optical transmittance through the filter [*Hansen et al.*, 1982; *Hansen et al.*, 1984]. The rate of decrease of optical transmittance as a function of the rate of increase of filter loading has been found to be proportional to the amount of absorbing carbon loading. The aethalometer can be operated at a flow rate of 5-10 l min^{-1} and is purported to have an accuracy of about 10%. Its sample air was extracted from a sampling plenum that was also fitted with a 2.5 μm cyclone inlet.

2.1.2 BRAVO Emission's Inventory

The BRAVO emissions inventory consists of hourly, gridded emissions of CO, NH_3, NO_x, PM_{10}, $PM_{2.5}$, SO_2, and various VOCs for the U.S. and Mexico [*Kuhns et al*., 2001]. Several different sources were used to determine emissions within the Regional Modeling System for Aerosols and Deposition (REMSAD) model domain, including EPA's National Emission Inventory (NEI) database [*U.S. Environmental Protection Agency*, 2003b], emission factors for Mexican point and area sources from the National Institute of Ecology of Mexico, and biogenic VOC emissions from the Biogenic Emissions Inventory System (BEIS) [*Geron et al*., 1994]. Emissions were processed with the Sparse Matrix Operator Kernel Emissions (SMOKE) model [*MCNC*, 2002].

The concentration of sulfate aerosol is largely determined by regional emissions of SO_2 (Figure 2-7). Large SO_2 sources are prevalent in the eastern U.S. (e.g., power plants along the Ohio River Valley) and eastern Texas. There are also several large SO_2 point sources in northern Mexico within 250 km of Big Bend National Park. The SO_2 sources in Texas include coal-fired power plants, oil refineries, and carbon black producers. Several coal-fired power plants are sited in and near a lignite belt which runs from northeast Texas towards the Mexican state of Coahuila. The principal SO_2 emitters in Mexico consist of coal-fired power plants and fuel oil refining and combustion operations. The Carbón I & II power plants, located near the U.S./Mexico border and 210 km southeast of Big Bend National Park, are the largest coal-combustion facilities in Mexico [*Green et al*., 1999]. SO_2 emissions for the largest point sources in the U.S. were estimated using continuous emissions monitoring (CEM) data, with attendant stack parameter data. These data were generally not available for Mexican point sources, and hence their emissions are estimated using plant through-put calculations [*Kuhns et al*., 2001]. In addition to these anthropogenic SO_2 sources, the Popocatepetl volcano, located 100 km southeast of Mexico City, intermittently releases large amounts of SO_2.

SO_2 emission in southern Mexico, Central America, Cuba, and shipping lanes were not included in the inventory. Contributions from these source areas are expected to be small.

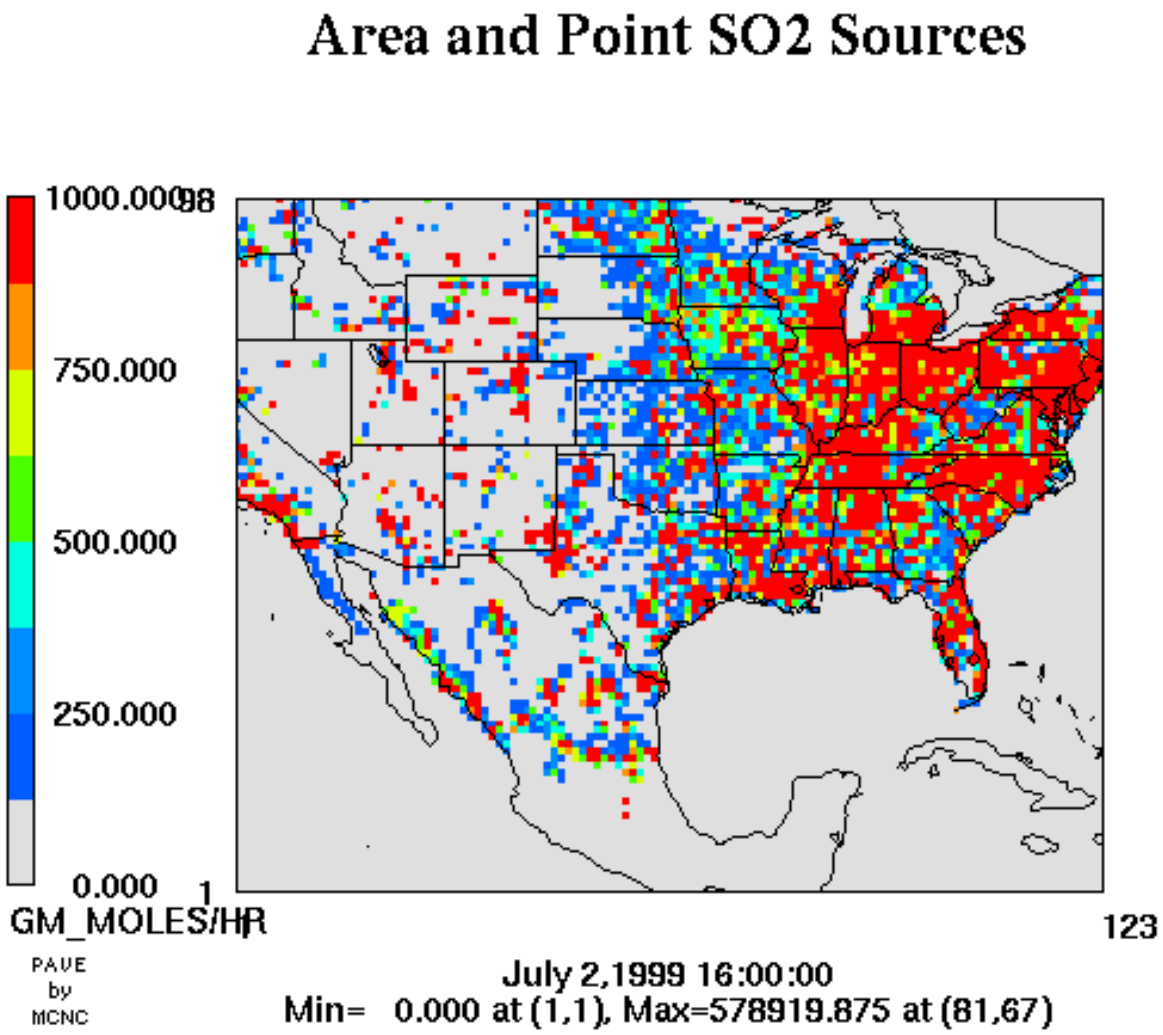

Figure 2-7. Example SO_2 emissions (moles hour^{-1}) from point and area sources within the REMSAD model domain.

Regional-scale SO_2 emission rates for the base emissions scenario are shown in Figure 2-8. SO_2 sources are defined as either elevated point sources (e.g., coal-fired power generation) or area sources (e.g., diesel combustion from mobile sources). Point sources constitute the bulk of the inventory at 73%. Aggregating all of the sources within the REMSAD domain yields a total annual SO_2 emission rate of approximately 19 Tg/yr. Of this, 14 Tg/yr of SO_2 is contributed by the eastern U.S., followed by Mexico at 2.5 Tg/yr, the western U.S. at 1.8 Tg/yr, and Texas at 1.0 Tg/yr.

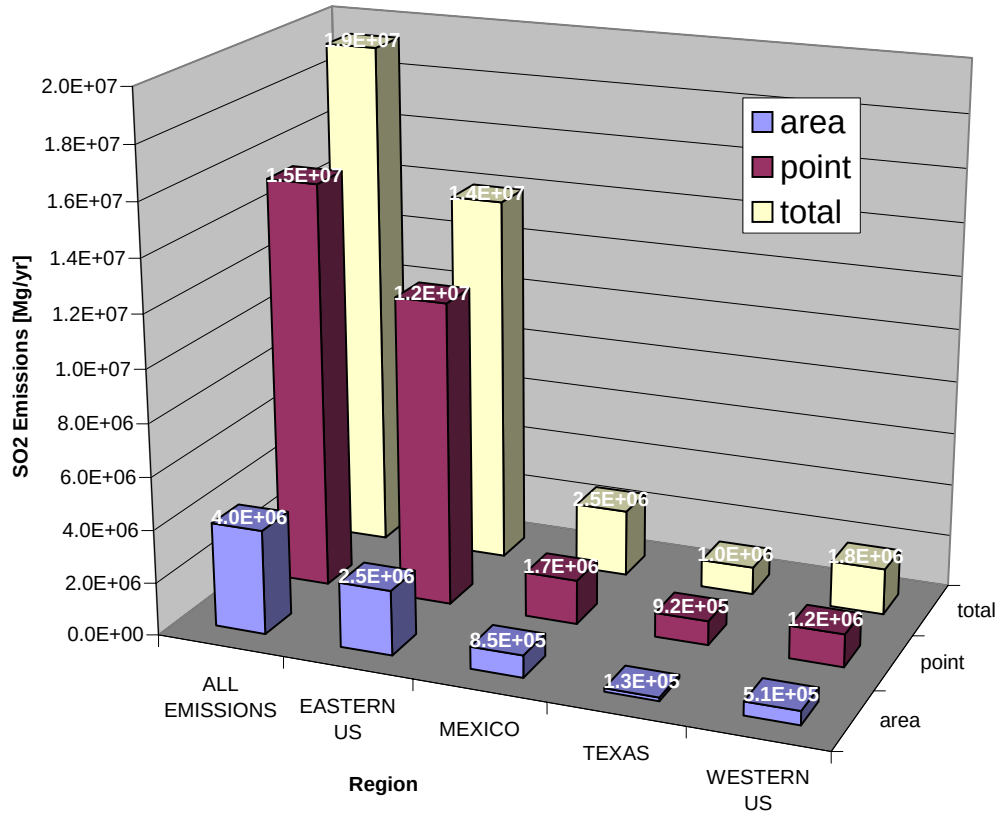

Figure 2-8. SO_2 emissions (Mg/yr) for each source region.

2.1.3 Meteorological Data

2.1.3.1 MM5

The MM5 model was applied for the BRAVO study period to provide custom metrological data fields for use in the air quality modeling. The MM5 model was run in non-hydrostatic mode using a continental-scale 36 km domain with nested 12 km and 4 km domains. MM5 employed observational nudging by incorporating the available surface and upper air measured wind data from the National Weather Service and data from the four BRAVO radar wind profilers. Only the 36 km wind fields were used in the following analyses. See *Seaman and Stauffer* [2003] for details of the MM5 modeling for BRAVO.

2.1.3.2 EDAS

The National Weather Service's National Centers for Environmental Prediction (NCEP) maintain operational meteorological models for weather forecasting. One modeling system is the ETA Data Assimilation System (EDAS) which generates initial conditions for the ETA forecast model [*Black,* 1994; *Parrish et al.,* 1996]. The EDAS meteorological fields are generated using a three-dimensional variational objective data assimilation analysis scheme. This is essentially a sophisticated data interpolation scheme that uses the ETA forecast model to optimally merge and spatially interpolate measured meteorological fields. In 1999, EDAS incorporated 34 different data types from 26 data sets [*Zapotocny et al.,* 2000; *Zapotocny et al.,* 2002] including land and marine surface observations, upper air data from the rawinsonde and wind profiler networks, Aircraft Communications Addressing and Reporting System (ACARS), and meteorological fields derived from satellite data.

NCEP operates EDAS on a 32 km grid on a terrain following vertical coordinate system with 45 levels, and generates meteorological fields every 3 hours. These data are interpolated to a 40 km Lambert Conformal grid and isobaric levels. The National Oceanic and Atmospheric Administration's (NOAA) Air Resource Laboratory (ARL) has direct access to the EDAS data stream and saves out a subset of the EDAS data suitable for input into dispersion models. These data are available from ARL's READY website [*READY,* 2003]. The ARL archive contains the EDAS data interpolated to a 40 km Lambert Conformal grid with every other grid point saved out on 22 isobaric surfaces. The grid in ARL's EDAS archive is presented in Figure 2-9.

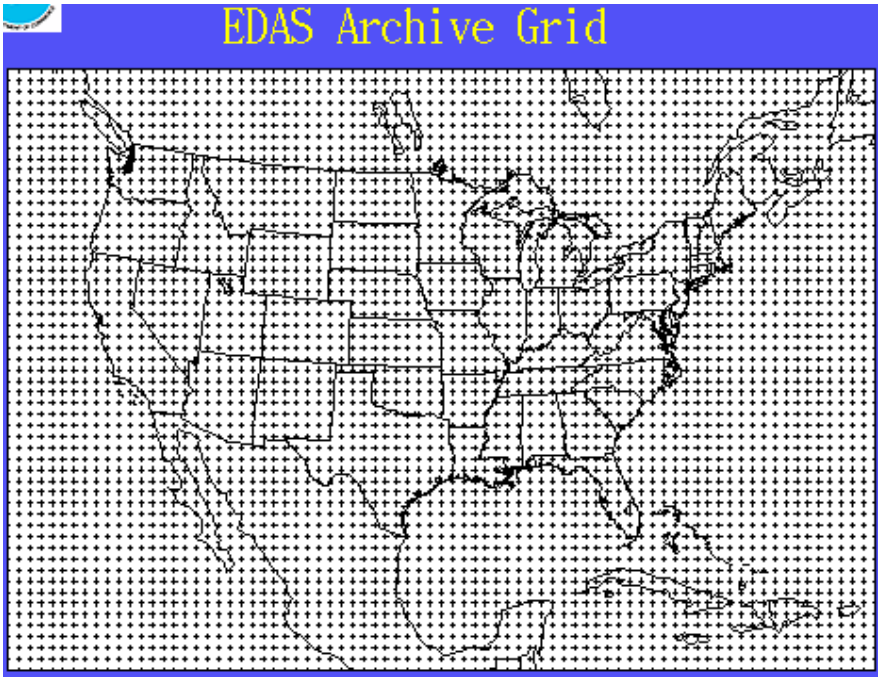

Figure 2-9. The spatial domain and horizontal grid used in ARL's EDAS Archive.

2.1.3.3 FNL

The Global Data Assimilation System (GDAS), [*Kanamitsu*, 1989; *Derber et al*., 1991; *Parrish and Derber,* 1992] is another of the operation systems that NCEP runs to generate inputs into the meteorological forecast models. GDAS uses a Spectral Statistical Interpolation (SSI) scheme coupled with the spectral Medium Range Forecast model (MRF) forecast model [*Sela*, 1980]. The SSI scheme is closely related to the three dimensional variational analysis system used in the EDAS system [*Parrish and Derber,* 1992] and it incorporates similar data to EDAS. However, GDAS is the final run in the series of NCEP operational model runs and includes late arriving data that can not be incorporated into EDAS [*Petersen and Stackpole*, 1989].

NCEP runs GDAS four times a day at 00, 06, 12, and 18 UTC. Model output is for the SSI analysis time and a 6-hour forecast. NCEP's post-processing of the GDAS converts the data from spectral coefficient form to 1 degree latitude-longitude (360 by 181) grids and from the 42 sigma level vertical coordinate system to isobaric levels. NOAA's ARL takes these fields and converts them to polar stereographic grids with ~180 km resolution (Figure 2-10) and saves out 13 of the pressure levels [*Stunder*, 1997]. Some fields such as precipitation and surface fluxes are only available at the forecast time so ARL merges the GDAS and forecast runs to create a complete archive. Since GDAS is the last operational model run, it is known as the Final Run at

NCEP, and ARL calls this archive FNL. The data used in the report were downloaded from ARL's READY website [*READY* 2003].

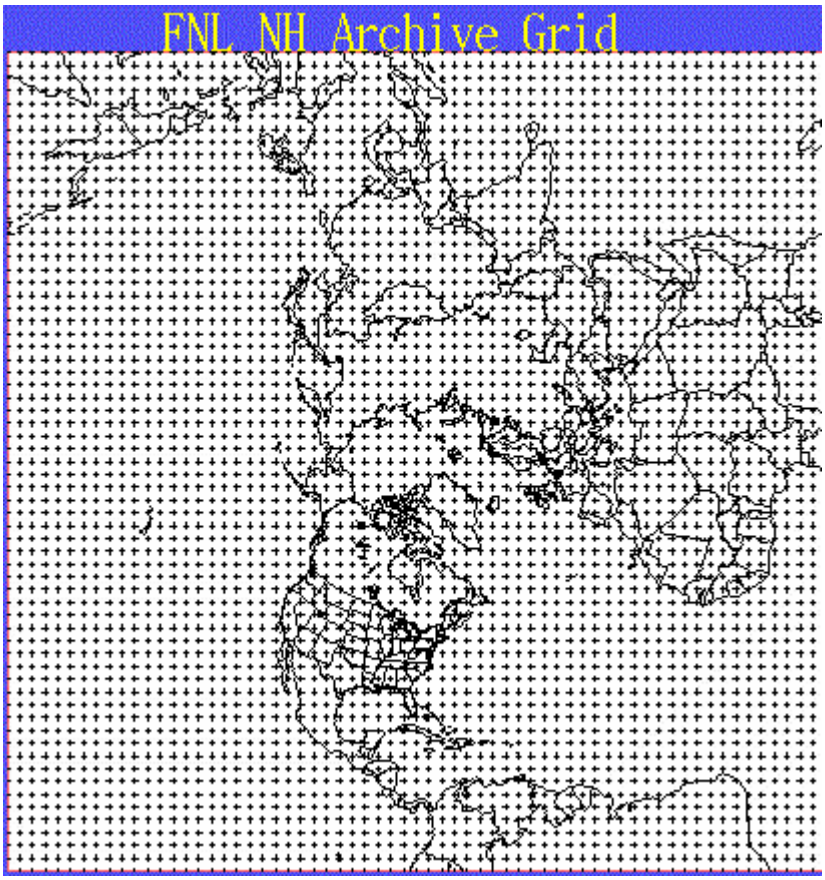

Figure 2-10. The spatial domain and horizontal grid used in ARL's FNL Archive.

2.1.3.4 Rawinsonde Data

The usual upper air data used as input to the Atmospheric Transport and Dispersion (ATAD) model are data from the FSL/NCDC Radiosonde Data Archive. These data are available on compact disk for 1946–1997 from the National Climatic Data Center (NCDC). For later years, including the BRAVO time period, the data can be obtained from a web site maintained by the Forecast Systems Laboratory (FSL), a division of NOAA at http://raob.fsl.noaa.gov/. Data include station information, height, pressure, wind speed, wind direction, temperature, and dew point temperature.

The real-time data archive consists of all observations transmitted via the North American Global Telecommunications Service (GTS), primarily from North and Central American civilian and some military rawinsonde sites. Since late 1998, the archive has been upgraded to include all international observations transmitted via GTS. All of the raw data goes through quality control analyses including extensive gross error and hydrostatic consistency checks. At most rawinsonde sites, weather balloons are launched twice daily at 0 and 12 Greenwich Mean Time (GMT). There are generally 1–3 launch sites per state. Figure 2-11 below shows the locations and number of observations at each site during BRAVO.

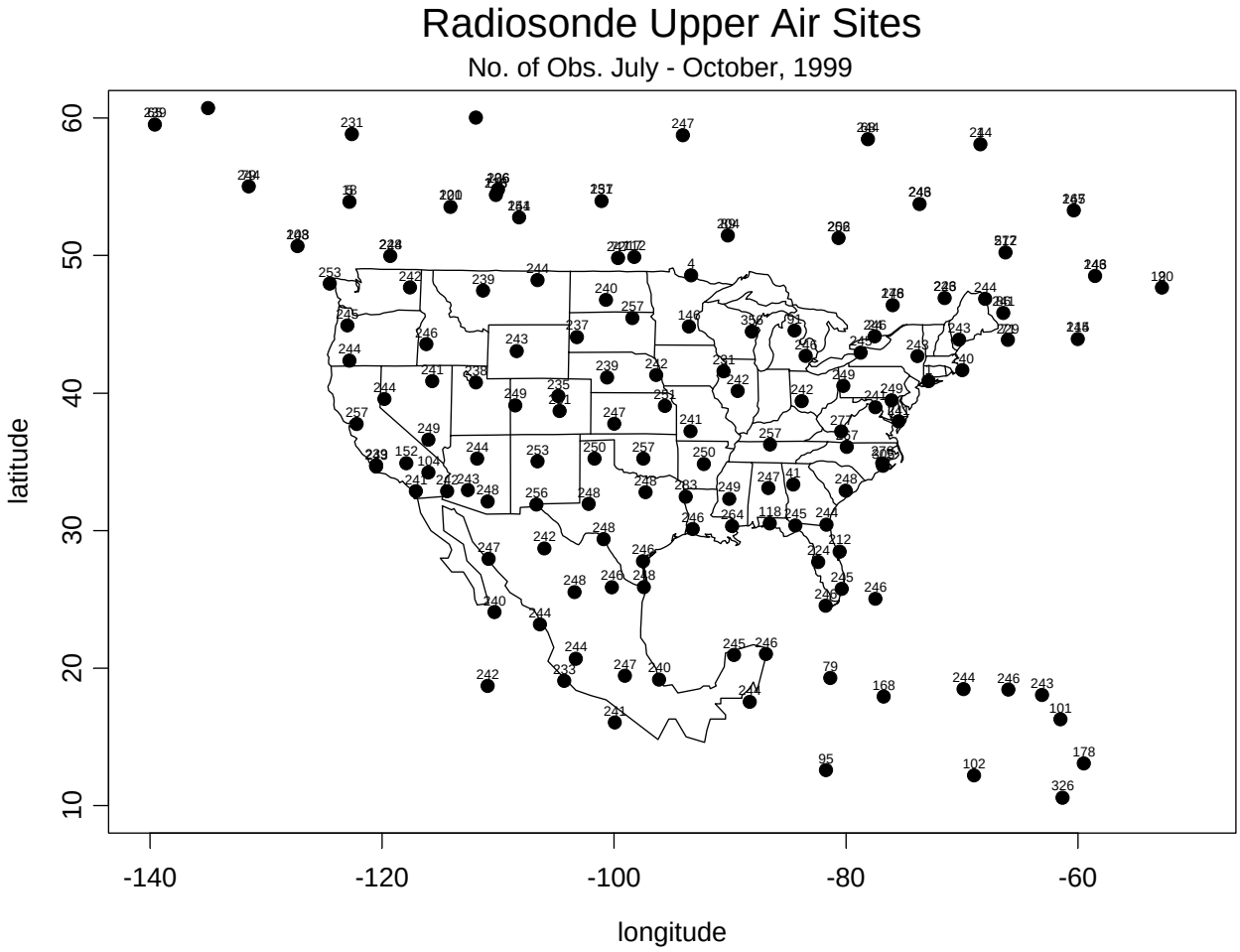

Figure 2-11. Radiosonde upper air sites.

2.1.3.5 BRAVO Wind Profilers

The Bravo study deployed four radar wind profilers in eastern and southern Texas (Figure 2-12). These wind profilers collected wind speed and direction as a function of height, and the data was generally reported every hour. Radar wind profilers equipped with a radio acoustic sounding system (RASS) also obtained vertical profiles of virtual temperature, although usually only to 500–1500 m.

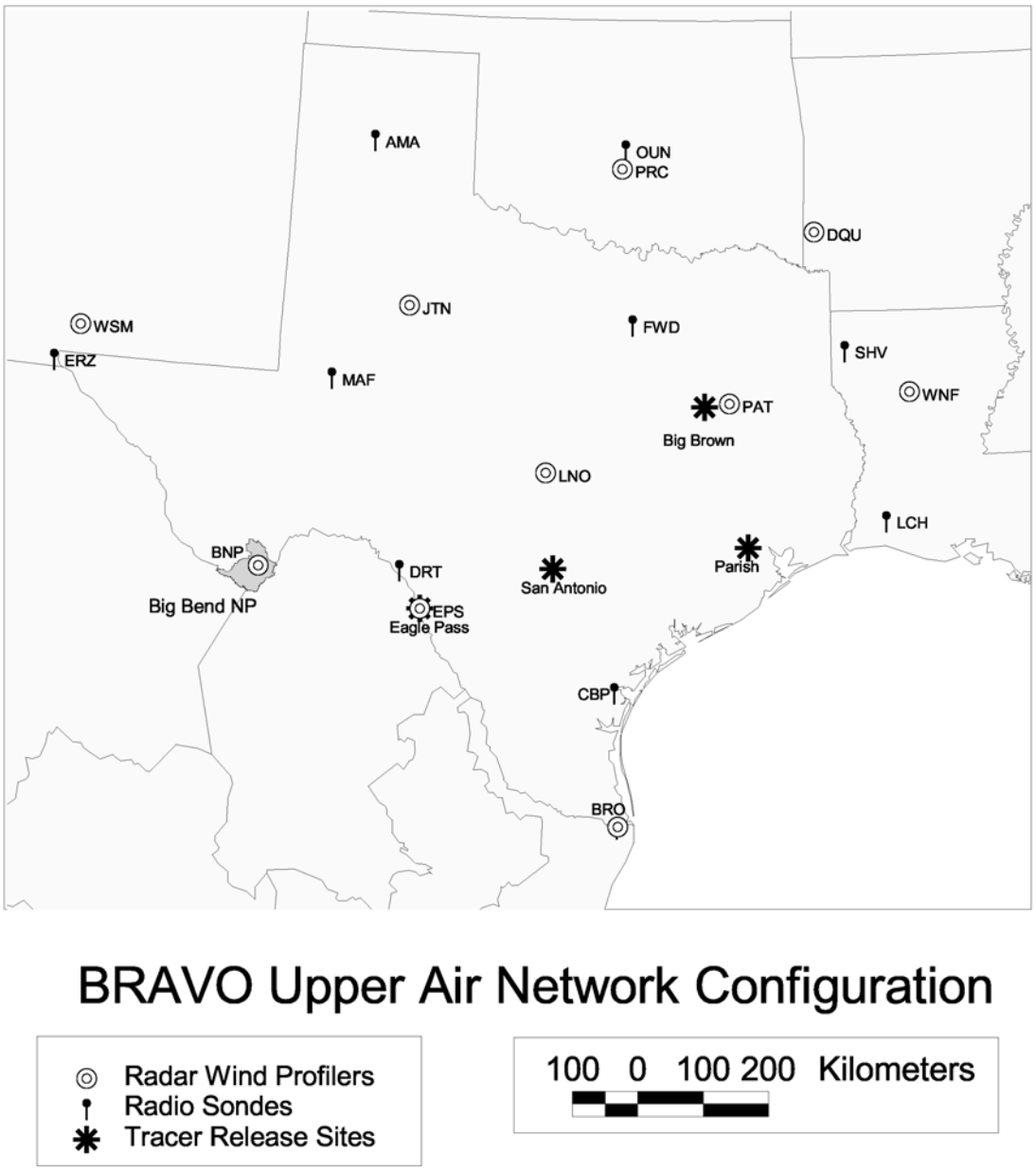

Figure 2-12. BRAVO wind profiles and other upper air meteorological sites.

Wind profiler data were collected in two modes. The 60 m mode gives better vertical resolution but less height coverage while the 100 m mode can extend to higher heights. Generally, the 60 m mode data are used for the lowest 700 mb, with the 100 m data used above that level. See Appendix 2A for a sampling of some of these data presented in graphical form.

2.1.3.6 Surface Meteorological Data

NOAA's Environmental Technology Laboratory (ETL) collected 10-minute and 60-minute averaged data from standard 10 m meteorological towers at the same four sites as the wind profilers from July 1 to October 31, 1999. Data collected included surface pressure, 2 m temperature and relative humidity, wind speed, wind direction, down-welling solar radiation, net

radiation, mixing ratio, precipitation, and peak gusts. Appendix 2B contains some of these data summarized graphically.

2.1.3.7 Relative Humidity Sensors

Three Rotronics mp 100f combination relative humidity/temperature sensors were housed in PVC holders and aspirated by a fan. The reported accuracy of the relative humidity sensor is ±2%. The flow rate through the holder was approximately 120 l min^{-1}. The sensors were approximately six feet above ground level, six feet from each other, and mounted near the inlets of the nephelometers.

2.2 Transport and Air Quality Models

The BRAVO study source attribution analyses, conducted by the NPS/CIRA group, used the Regional Modeling System for Aerosols and Deposition (REMSAD) air quality model, a prognostic Eulerian grid model capable of simulating some of the atmospheric chemical and physical processes. Also, the three transport models: Air Resource Laboratory Atmospheric Transport and Dispersion (ATAD); HYbrid Single-Particle Lagrangian Integrated Trajectory (HYSPLIT) and the CAPITA Monte Carlo model, were used to calculate back trajectories and source plume dispersion estimates.

This section describes each model. The REMSAD model is evaluated against tracer data in chapter 5 and sulfur simulation and source attribution results are presented in chapter 6. Back trajectory estimates from all three models driven by MM5, EDAS/FNL, and measured RAOB data are presented in chapter 4. The CAPITA Monte Carlo source plume dispersion simulation is evaluated against the tracer data in chapter 5. Back trajectory analyses based on the residence time analysis using the CAPITA Monte Carlo model are presented in section 8.1.3. The CAPITA Monte Carlo model was also used to simulate the dispersion of a source's plume which was then used in the FMBR source apportionment technique. This source apportionment technique is described in section 2.3.2.2, evaluated in section 7.1.2 and 7.2.2 and the sulfate source apportionment results presented in section 8.2.3. All three transport models were used in the TrMB source apportionment technique described in section 2.3.2.1, evaluated in section 7.1.1 and 7.2.1 and source apportionment results are presented in section 8.2.2.

2.2.1 REMSAD

REMSAD, the Regional Modeling System for Aerosols and Deposition, is a prognostic, Eulerian-grid air quality model designed to simulate the formation and long-range transport of aerosols and their precursors [*SAI*, 2001; *Seigneur et al.,* 1999]. REMSAD has been optimized to be computationally efficient, allowing the simulation of long time periods (e.g., monthly or yearly) over large model domains (e.g., continental-scale). This is achieved in part through the highly simplified treatment of organic species in the chemistry mechanism. REMSAD is based on the numerical solution of the atmospheric diffusion equation (see, for example, *Seinfeld and Pandis*, 1998), which expresses the physical and chemical processes that affect atmospheric pollutants and their precursors, including advection, diffusion, wet and dry deposition, and chemical transformation.

The REMSAD model domain covers most of the contiguous U.S. and northern Mexico, and is approximately centered on Texas. A geodetic (latitude/longitude) horizontal coordinate system is used, with a model grid resolution of approximately 36 km. The domain extends to 74^{o} W and 120^{o} W at the eastern and western boundaries, respectively, and to 49^{o} N and 16^{o} N for

the northern and southern boundaries, respectively. The vertical dimension is defined in terrain-following sigma-pressure coordinates. Thirteen vertical layers are used, with thinner layers specified near the surface and thicker layers aloft. The top of the model domain is set to 50 mb.

The REMSAD chemistry mechanism treats gas and aqueous phase and aerosol equilibrium processes. Gas phase chemistry is calculated with the Micro Carbon Bond IV mechanism (μCB-IV), which is based on a reduced formulation of the widely-used Carbon Bond IV mechanism [*SAI*, 2002]. The μCB-IV contains a simplified treatment of organic compounds, with only "VOC" (most anthropogenic organics), "CARB" (carbonyls), and "ISOP" (biogenic organics) represented. The inorganic and radical chemistry portions of μCB-IV are identical to CB-IV. Aqueous chemistry, which is particularly important to SO_4 formation, treats the reactions of dissolved SO_2 with H_2O_2, O_3, and atomic oxygen catalyzed by iron and manganese. The MARS-A thermodynamics module is used to calculate the equilibrium between nitrate, SO_4, and ammonia [*Kim et al*., 1993].

SO_2 and SO_4 boundary concentrations were created using results from the Global Ozone Chemistry Aerosol Radiation Transport (GOCART) global climate model [*Chin et al.,* 2000]. GOCART data were not available for 1999; instead, GOCART results for 2000 were used to construct a four month average boundary concentration field for REMSAD, with the presumption that the GOCART predictions between 1999 and 2000 were similar on a seasonal basis.

Wind fields, temperature fields, and other meteorological data for BRAVO were simulated by MM5 [*Grell et al.,* 1994]. MM5 simulations were provided by the Department of Meteorology at the Pennsylvania State University. MM5 is a non-hydrostatic, prognostic, regional-scale meteorological model. Physical parameterizations used for the BRAVO study include the *Kain-Fritsch* [1990] deep-convection parameterization, the *Dudhia* [1989] resolved-scale precipitation model, the *Shafran et al.* [2000] 1.5-order turbulence closure scheme, the *Zhang-Anthes* [1982] surface-flux model, and the *Dudhia* [1989] two-stream broad-band atmospheric radiation scheme. Four dimensional data assimilation (FDDA) [*Stauffer and Seaman*, 1994], using both analysis nudging and observational nudging, was employed. Recent studies have shown the importance of using FDDA when simulating the meteorology of air pollution events [*Seaman*, 2000; *Barna and Lamb*, 2000]. Meteorological observations available for FDDA included surface and upper-air measurements from the National Weather Service and several radar wind profilers located in Texas.

The REMSAD dispersion mechanism is evaluated against the tracer data in chapter 5. Results of the REMSAD modeling and source attribution estimates are presented and discussed in chapter 6.

2.2.2 ATAD

The Air Resource Laboratory Atmospheric Transport and Disperson (ATAD) model [*Heffter*, 1980] is a Lagrangian parcel model with a single variable depth transport layer. The base of the transport layer is generally 300 m above the ground. For most time periods, the top of the transport layer is the lowest level within a critical inversion at which the potential temperature is 2K above that at the inversion base. A critical inversion is defined as an inversion with a potential temperature lapse rate of at least 5K/km. When no critical inversion exists, the transport layer top is assumed to be 3000 m above the ground. For trajectories that begin at night, the initial transport layer depth is approximated by 2 σ_z, where σ_z is the standard deviation of the

vertical dispersion of a Gaussian plume for stable conditions. This is used only until the first daytime period of the trajectory.

Average winds within the transport layer are interpolated spatially (inverse of squared distance weighting) and temporally from all available radiosonde data within 250 km. If there are no stations within 250 km, data from stations within 600 km are used. The trajectory is terminated if there are no upper air data within 600 km. Complex terrain is not explicitly considered in the model, although the transport layer is always at least 300 m above the terrain near each radiosonde station. A back trajectory is started from the receptor every 6 hours. An air parcel position, or "endpoint", is determined for every 3 hours backward in time for a maximum of 120 hours (5 days).

2.2.3 HYSPLIT

The HYbrid Single-Particle Lagrangian Integrated Trajectory (HYSPLIT) model [*Draxler and Hess*, 1998] was developed by the NOAA Air Resources Laboratory. It can compute a range of outputs from simple air parcel trajectories (advection of a single particle) to dispersion and deposition simulations. For BRAVO, the model was used in simple back trajectory mode. Version 4.7 is now available, but HYSPLIT modeling for BRAVO was done initially using version 4.4 and later re-done using version 4.5. The described changes (see the READY HYSPLIT web site at http://www.arl.noaa.gov/ready/hysplit4.html) between versions 4.5 and 4.7 are not expected to result in major changes for the BRAVO output. Trajectories calculated from versions 4.4 and 4.5 were identical for most BRAVO time periods, though there were a few days with differences ranging from subtle to dramatic.

In its trajectory mode, HYSPLIT can do computations forward or backward in time. Default vertical motion, which was employed for BRAVO, is calculated using the input omega field. Other options include isosigma, isobaric, isentropic, and isopycnic. The model can be run with multiple nested input data grids, though this was not done for BRAVO. Required input is a gridded meteorological data set on a polar, Lambert, or Mercator map projection with data at regular intervals. Back trajectory positions or “endpoints” are calculated hourly. For BRAVO, trajectories were calculated for up to 10 days backwards in time.

The advection of a particle or puff is computed from the average of the three-dimensional velocity vectors at the initial position and at the first guess of the next position. Velocity vectors are linearly interpolated in both space and time. Trajectories terminate if they exit the model top (specified as 10 km AGL for BRAVO), but advection continues along the surface if they intersect the ground. The integration time step can vary during the simulation and is computed such that it is less than 0.75 of the meteorological grid spacing. A simple integration method [*Kreyszig*, 1968; *Pettersen*, 1940] is employed. Higher order integration schemes were found to add no precision because data observations are linearly interpolated from the grid to the integration point [*Draxler*, 1998].

2.2.4 CAPITA Monte Carlo Model

The Monte Carlo model is a particle dispersion model capable of simulating regional scale transport, transformation, and dry and wet removal of aerosols [*Schichtel and Husar,* 1997]. In this study, only the atmospheric transport module was used.

The simulation of the regional scale transport and diffusion in the Monte Carlo model is conducted by moving inertialess particles in the Eulerian frame according to the equation

$$\mathbf{x}(t+dt) = \mathbf{x}(t) + [\bar{\mathbf{u}}(\mathbf{x},t) + \mathbf{u}'(\mathbf{x},t)]dt \quad (2\text{-}1)$$

where **x** (=x,y,z) represents the particle position vector, and $\bar{\mathbf{u}}$ ***(=***$\bar{u},\bar{v},\bar{w}$***)*** and **u**' (=u',v',w'), represent the time-averaged and fluctuating components of the flow field, respectively. The basic meteorological information required for this consists of the mean wind field $\bar{u},\bar{v},\bar{w}$ to advect the particles and the fluctuating components u',v',w' to diffuse the particles at all times over the whole model domain.

2.2.4.1 Advection

The advection of the particles is accomplished by multiplying the mean three dimensional wind vectors at the particle's location in space and time by the time step Δt. The mean wind vector is obtained from meteorological models, such as those described in section 2.1.3. These gridded wind fields are interpolated to the particle's position by using bilinear interpolation in the horizontal and linear interpolation in the vertical and time. The model uses a Δt on the order of 20 minutes. This is a large time step so the acceleration of the particle due to curvatures and changes in wind speed needs to be taken into account. This is done by using the iterative Petterssen integration scheme [*Petterssen*, 1940; *Stohl*, 1998], which is equivalent to assuming constant acceleration within the time interval to account for changes in the wind vector from t_n to t_{n+1}. Perfect reflection is assumed at the surface but if a particle reaches the grid edge or top of the model domain, it is terminated.

2.2.4.2 Vertical Diffusion

The random components of the velocity field occur at a resolution smaller than the meteorological model grids used to generate wind fields. Therefore, these components are derived using simplified models of the atmospheric turbulence driven by the available meteorological variables. The vertical and horizontal fluctuating components of the wind fields are modeled separately since the vertical diffusion is primarily dependent on the convective and mechanical mixing process in the atmosphere and horizontal diffusion primarily depends on the divergence of the horizontal wind fields.

In the case of vertical diffusion, during the day the intense convective mixing within the mixed layer causes the turnover time of a large eddy to be about 15 minutes. Therefore, within this time period, the eddy's position is independent of its previous location. In the Monte Carlo model this mixing is simulated by evenly distributing the particles between the surface and the mixing height. The vertical mixing is only applied to particles below the mixing height. Particles enter or leave the mixing layer as the mixing height grows or contracts due to vertical motion from subsiding and rising airmasses. A graphical illustration of the implementation of the above processes is presented by the three trajectories in Figure 2-13. The intense vertical mixing within the mixing layer is indicated by the crossing of the trajectory lines. The stable layers, during nocturnal hours, are illustrated in the lines of near constant height for each quantum. In Texas, the summertime mixing height varies diurnally from 10s of meters at night to 1–2 km during a sunny afternoon. In the nocturnal mixing layer, the assumption of a well-mixed layer is an over-simplification. However, these layers are low, generally less than 200 m, and the error of the particles' vertical position in relation to the meteorological models vertical resolution is not significant. This simple vertical diffusion mechanism has been incorporated into several dispersion models [*Patterson et al.*, 1981; *Anfossi et al.*, 1995; *Saltbones et al.*, 1998].

This vertical diffusion mechanism is rather simple, but it does capture the essential features of the interaction between mixing layer and free troposphere. That is, within the mixing layer, the intense daytime mixing evenly distributes material from the surface to the top of the mixed layer, followed by the collapse of the mixed layer in the evening, allowing wind veer and sheer in the lower layers of the atmosphere to spread the pollutants. It has been shown that this simple dispersion mechanism produces similar regional scale transport estimates as the more complex vertical dispersion mechanism for simulating a passive tracer in the atmosphere [*Desiato et al.,* 1998].

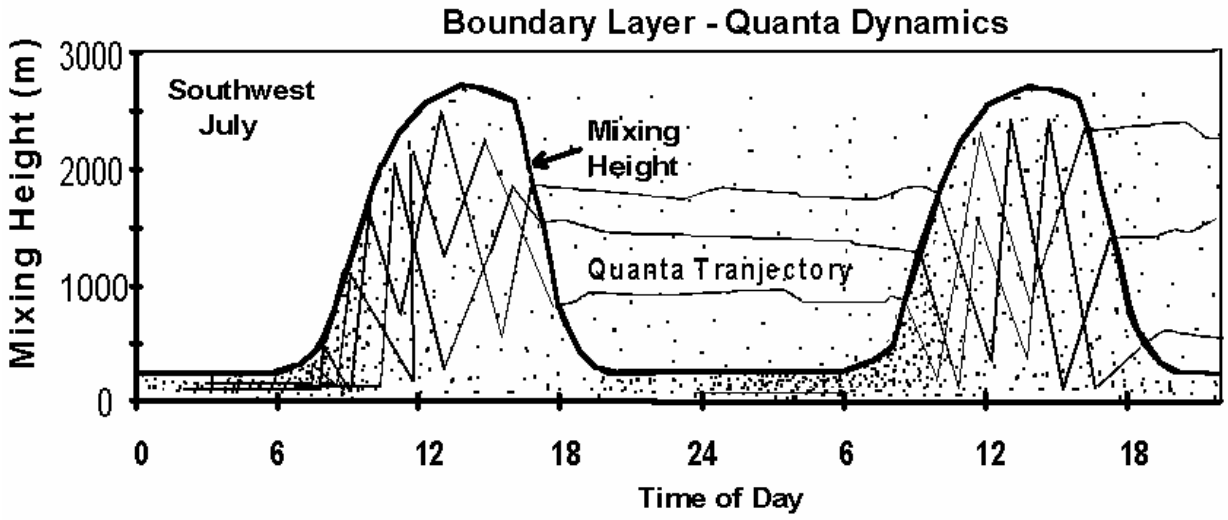

Figure 2-13. The dynamics of the planetary boundary layer and of pollutants being emitting into this layer as simulated by the CAPITA Monte Carlo model.

2.2.4.3 Horizontal Diffusion

A common approach for the calculation of the horizontal diffusion is based upon the Prandtl mixing length model. This allows for the parameterization of the diffusion by an effective eddy diffusion coefficient K. The diffusion process is implemented as a random walk displacement of radius $\sqrt{2K\Delta t}$ for each time step in the model. The position from 0 to $\sqrt{2K\Delta t}$ is chosen from a Gaussian distribution with a mean of 0 and unit standard deviation. The value of the diffusion coefficient is a geographical function of the time of day and season. Values of K ranging between 10^2 m^2/s in stable conditions and 10^6 m^2/s during intense convective activity have been used in the past [*Munn and Bolin* 1971; *Patterson et al*., 1981; *Gifford*, 1982]. Also, *Desiato et al.* [1998] tuned a dispersion model to tracer data and found a best fit constant K of $2.5\ 10^4$ m^2/s, while *Ishikawa* [1995] found a best fit K of $3.3*10^4 – 1.0*10^4$ m^2/s in dispersion simulations of Chernobyl dispersion data.

It is recognized that using an eddy diffusion coefficient to represent horizontal diffusion is a crude approximation. However, it has been shown that horizontal diffusion has a small effect on multi-day regional scale dispersion [*Schichtel and Husar*, 1996; *Uliaz*, 1994].

2.2.4.4 Meteorological Data Processing

The EDAS, FNL, and MM5 36 km wind fields were used to drive the CAPITA Monte Carlo model. The model requires these input data to have terrain following vertical coordinate

systems and an estimate of the mixing height. The MM5 meteorological was on a terrain following coordinate system and had an estimate of the mixing height, so no transformations were necessary. However, the vertical velocity was relative to a flat earth and this was transformed to be relative to the vertical coordinate system.

The EDAS and FNL data were on a constant pressure coordinate system. These data were reprocessed, transforming the constant pressure levels to 20 terrain following Cartesian coordinates from 10 to 10000 m. During this process, the 10 m surface level winds and the 2 m temperature and RH surface variables were incorporated into the first model upper layer. In addition, the vertical velocity was converted from mbar/sec to m/sec.

Neither meteorological data set had an estimate of the mixing height, so this was derived from available metrological parameters using a method based upon a bulk Richardson number approach [*Holtslag et al.*, 1995; *Vogelezang and Holtslag,* 1996]. The mixing height was defined as the height where the bulk Richardson number reaches a critical value of $Ri_c = 0.25$. To account for turbulence due to surface friction in a near neutral or stable mixing layer, the bulk Richardson number was modified to

$$Ri_{bk} = \frac{g\left(\Theta_{vk} - \Theta_{v1}\right)\left(z_k - z_1\right)}{\Theta_{v1}\left[\left(u_k - u_1\right)^2 + \left(v_k - v_1\right)^2 + 100u_*^2\right]} \tag{2-2}$$

where g is gravity, z_1, z_k are the heights of the lowest model level and of the model level k, u and v are the horizontal wind field components, Θ_v is the virtual potential temperature, and u_* is the friction velocity.

The term $100u_*^2$ accounts for turbulence due to friction [*Vogelezang and Holtslag*, 1996]. This equation holds for only neutral and stable conditions. However, it can be extended to convective situations by replacing Θ_{v1} with

$$\Theta'_{v1} = \Theta_{v1} + 8.5\frac{H_{vs}}{w_*} \tag{2-3}$$

where w_* is the convective velocity scale and H_{vs} is the virtual surface heat flux, defined as $H_{vs} = \left(w'\Theta'_v\right)_s$. The second term on the right represents the excess temperature of rising thermals, which is a measure of the strength of the convective mixing [*Vogelezang and Holtslag*, 1996].

This parameterization of the mixing layer depth has been validated against measured data [*Holtslag et al.*, 1995; *Vogelezang and Holtslag,* 1996; *Sorensen,* 1998] where the optimum critical values were found to be between 0.15–0.35. The robustness of this technique has led it to be widely used in dispersion models [*Brandt et al.*, 1998; *Saltbones et al.*, 1998; *Sorensen*, 1998; *Stohl*, 1998].

2.3 Source Apportionment Methods

This section describes the source apportionment techniques applied during BRAVO to assess the contribution of U.S. and Mexican sources on the sulfate concentrations at Big Bend National Park. The methods discussed have been divided into qualitative and quantitative source attribution methods, where the qualitative analyses include trajectory and air quality data

analysis techniques. The quantitative techniques include receptor and source oriented modeling as well as hybrid techniques.

2.3.1 Qualitative

2.3.1.1 Space/Time Pattern Analysis (EOF)

Empirical Orthogonal Functions (EOF) analysis is essentially a spatial factor analysis or principal component analysis. Details can be found in many standard texts. [e.g., *Lawson and Hanson*, 1974, *Green* 1976]. There are several variations of these types of analyses, but all involve decomposing a single matrix into two orthogonal matrices. Here, a matrix of centered concentrations (site means subtracted from each concentration) of a single species is decomposed into two matrices as follows:

$$Z = A \bullet P \tag{2-4}$$

where Z has rows corresponding to observation times and columns to monitoring sites. A is a time by factor orthonormal matrix of dimensionless time weights and P is a factor by site orthogonal matrix of spatial patterns. The values of P are weighted deviations from the mean concentration at each site and have units of concentration. Each row of P can be visualized as a map. The P matrix is calculated by multiplying the eigenvectors of Z^TZ by a matrix which contains the square roots of the eigenvalues of Z^TZ on the diagonal. The A matrix can be found by inverting P. Each column of *A* is visualized as a timeline that shows the relative weight of the factor for each observation time. Optionally, rather than Z^TZ, there are other matrices that could similarly be decomposed. These include the raw data cross product matrix, the correlation matrix, and the covariance matrix. An advantage of using Z^TZ is that the results are easily physically interpretable.

The resulting factors or EOFs are orthogonal, statistically simple, and each explains a decreasing amount of the total variance. Typically, only a few spatial patterns, often only 2-6, are required to explain 80–90% of the covariance in the data. Other physical information is then used to qualitatively interpret the meaning of each of these factors. This is an exploratory data analysis technique. Usually an attempt is made to associate each spatial pattern with meteorological conditions and candidate source areas. For example, strong spatial gradients in one portion of the monitoring domain are indicative of a source in that area or transport from that direction [*Henry et al*., 1991]. Spatial patterns for different chemical species are often quite different and can be used to help determine regionally different trace element ratios. The time weights show when each pattern dominated and can then be used to help evaluate the reasonableness of wind fields and back trajectories. Occasionally an EOF is generated that contains a high value at a single site with a high time factor for only a single day. These are often useful for quickly spotting outliers in the data. Outliers can be due to real events such as fires or due to measurement problems.

EOFs as calculated above are not a unique solution to the decomposition of the data. There are many methods of orthogonal and oblique rotation, of which Varimax [*Kaiser*, 1958; *Richman*, 1986] is probably the best known. Varimax rotation forces each site to load as strongly as possible onto a single factor and has frequently been used in the past in similar field studies. [*Gebhart and Malm*, 1997; *Malm and Gebhart,* 1996, 1997; *Gebhart et al.*, 2000]. However, for the BRAVO study neither Varimax nor Quartimax [*Richman*, 1986] rotations added any information or interpretability to the analysis. The usual result is that after rotation the spatial patterns are essentially the same as before rotation, though the order, time weights, and variance

explained by each were shuffled a bit. Therefore, for simplicity, only the unrotated EOFs are reported here.

EOF analysis requires a time by site matrix of concentrations of a single aerosol species. No missing values are allowed and concentrations below minimum detectable limit are set to 0. All 6-hour data were averaged to 24-hour concentrations and then missing value were eliminated or estimated. First, time periods and then sites with more than 25% of data missing were eliminated. This reduced the analysis period of June 29–October 31 to July 26–October 30, with August 5 and 6 also being removed. Three sites, Padre Island, Guadalupe Mountains, and Wichita Mountains, were also removed, resulting in a matrix of 95 days by 34 sites. Next, all observations immediately preceded and followed by valid data at the same site were approximated by linear interpolation in time. Remaining missing data were filled by inverse distance-weighted spatial interpolation. For the sulfur matrix, only 0.8% of the data were filled by time interpolation and 2.8% by spatial interpolation. Similar fractions of the data matrices for other species were estimated in the same way. Due to the removal of most of July, results of EOF analyses are not expected to be directly comparable to other analyses of BRAVO data that include that time period. EOF analyses were completed for all measured species with adequate data. Results are discussed in section 8.1.1.

2.3.1.2 Factor Analysis

In general, factor analysis is used to attempt to explain the correlations between observed variables in terms of underlying factors which are not directly observable. For BRAVO, in addition to the spatial factor analysis or EOF discussed above, another factor analysis was used to explore the correlations between different measured fine particulate species at a single receptor site (K-Bar). The resulting factors, or groups of species that are correlated, were interpreted as different source types. For example, a factor for which organic carbon, fine mass, and potassium all loaded highly together would be qualitatively interpreted as a smoke factor. Factor analysis, like EOF and principal component analyses, is a method of reducing a large number of observed variables into a few linear combinations of those variables that can explain the data as well or nearly as well as the larger number of individual variables. Furthermore, we would like each factor to have some physical meaning. In this case, each factor represents a source type and each daily factor score represents the relative contribution of that factor type to the measured fine particulate concentrations on that day. Factor analysis is calculated identically to EOF analysis as shown in equation 2-4, except that the initial concentration matrix, Z, is a species by time matrix at one site, rather than a site by time matrix of one species at multiple sites. In this case, the two resulting decomposed matrices, A and P, are a species by factor matrix of loadings, representing the compositions of the derived source types, and a factor by time matrix of factor scores, representing the daily contributions of each source type. Details and results of the factor analysis are discussed in section 8.1.2.

2.3.1.3 Ensemble Airmass History Analyses

An airmass history identifies the 2-D or 3-D pathway an airmass took enroute to the receptor, a trajectory, and other meteorological parameters along this transport pathway. The implication is that sources, or lack of sources, along the pathway and near the receptor are responsible for the receptor's air quality. These are power techniques that potentially link source regions to the receptor concentrations. However, individual airmass histories can have large

errors [*Stohl*, 1998; *Rolph and Draxler*, 1990; *Kahl and Samson*, 1986]. In fact, different model assumptions or wind fields can generate airmass trajectories that are 180 degreesout of phase. The large uncertainty in individual trajectories can be reduced through ensemble airmass history techniques which aggregate large numbers of airmass histories together. These ensemble airmass techniques then identify the typical airmass transport pathways.

This section describes the residence time analysis, one class of ensemble airmass history analysis techniques. These methods are used in chapter 5 to help evaluate the various airmass history model and meteorological drives, and chapter 6 to evaluate the airmass transport to Big Bend National Park during the BRAVO study.

2.3.1.3.1 Residence Time

The residence time analysis [*Ashbaugh*, 1983; *Poirot & Wishinski*, 1986] aggregates airmass histories together by first overlaying a grid over a spatial domain, then counting the number of hours each airmass resided within each grid cell. Usually, the number of hours an airmass resided in a grid cell is approximated by the number of trajectory segment endpoints that fall in the grid cell. These grid cell residence times are then normalized by the total number of hours resulting in a probability field identifying the most likely regions in which an airmass will reside en route to the receptor. The most likely transport directions to a receptor are then along the ridges of the probability fields.

The overall residence time (ORT) for each grid cell is then defined as

$$ORT_{i,j} = \frac{1}{N}\sum_{t=1}^{T} n_{i,j,t} \tag{2-5}$$

where n is the number of back trajectory segment endpoints in the grid cell at longitude i and latitude j before the trajectory arrived at the receptor during measurement period t. N is the total number of endpoints for all time periods and T is the total number of time periods. A trajectory segment endpoint is the position of the airmass at a specific time prior to impacting the receptor. Airmass histories are typically calculated every hour or several times per day, depending on the model. If a grid is used which does not have a uniform area, then the residence time probability field is normalized by each grid cell's area, creating a residence time probability density function (PDF).

High (HRT) and low (LRT) concentration residence times are similar, except only trajectories that arrived at the receptor when the concentration was greater than or less than, respectively, a selected value are considered. The cutoffs for high and low concentrations are arbitrary, but are often the highest and lowest 10–20% of the measurements. HRT and LRT are calculated by

$$HRT_{i,j} = \frac{1}{H}\sum_{t=1}^{T} h_{i,j,t} \tag{2-6}$$

$$LRT_{i,j} = \frac{1}{L}\sum_{t=1}^{T} l_{i,j,t} \tag{2-7}$$

where H and L are the total number of trajectory endpoints arriving during high and low concentration time periods and h and l are the number of trajectory segment endpoints in each grid cell for these times.

If a grid with unequal grid cell areas is used, then the residence time analysis can be biased. For example, as grid cell increases in size, more trajectories are likely to traverse it and its residence time will increase. Normalizing the residence time probabilities by the grid cell removes this potential bias. The units of the residence time analysis are then inverse area. This creates a residence time PDF since if the area-normalized residence time analysis is integrated over all space it will equal one.

2.3.1.3.1.1 Decomposition of the Residence Time Analysis

The residence time probability is the result of the frequency of airmass transport over a grid cell and the length of time the airmasses spent over the grid cell. The residence time PDF was decomposed into two components, a transport directional frequency, the fraction of trajectories that passed over a grid cell, and the accumulation potential, the average time an airmass resided over the grid cells normalized by the grid cell length.

$$RT_{i,j}\,PDF = \frac{D_{i,j} * AP_{i,j}}{\tau} \tag{2-8}$$

$$D_{i,j} = \frac{1}{L} * \frac{1}{Tr} \sum_{t=1}^{T} tr_{i,j,t} \tag{2-9}$$

$$AP_{i,j} = \frac{1}{L} * \frac{1}{Tr} \sum_{t=1}^{T} \left(n_{i,j,t} * \Delta\tau \right) \tag{2-10}$$

where $D_{i,j}$ [1/m] is the normalized transport direction frequency for grid cell i,j, $AP_{i,j}$ [s/m] is the accumulation potential for grid cell i.j, τ [hr] is trajectory length, $\Delta\tau$ [hr] is the trajectory segment endpoint length, $tr_{i,j,t}$ are the number of trajectories in the airmass during time period t that traverses grid cell i,j, Tr = total number of trajectories for all time periods T, and L [m]= length scale; note L^2 is the area of the grid cell

The accumulation potential can be thought of as an inverse of a characteristic transport speed and is related to the inverse of the speed the airmasses are transported over a grid cell and the number of times it traverses the grid cell due to recirculation or flow reversals. This is a better index for determining the exposure of an airmass to a source region's emission than the measured wind speed. For example, fast recirculating winds would spend more time over a source region than slower but directionally persistent winds. Therefore the recirculating airmass would be exposed to a region's emissions for a longer period of time, increasing the potential for pollutants to accumulate.

The residence time analysis used three-dimensional airmass histories. To characterize the heights of the airmass histories, the height of all trajectory segment endpoints within a grid cell were average together. While the average trajectory segment endpoint height gives some indication of an airmass characteristic height, it is independent of the residence time analysis. In the future, it should be possible to create a three-dimensional residence time PDF taking into account the trajectory segment endpoint heights. In this case, the residence time decomposition

would contain a component accounting for the vertical distribution of the trajectory segment endpoints.

2.3.1.3.1.2 Source Contribution Function (Distance Weighted Residence Time)

The overall source contribution function (OSC) is the overall residence time (ORT) normalized by an equal probability surface (EPS). The EPS is defined as being an idealized ORT which would exist if all airmasses arrived at the receptor following a straight trajectory with constant speed with equal probability from all directions. Residence time fields always have a peak at the receptor because all back trajectories originate there. The source contribution function is the residence time with this central tendency removed. It is always proportional to the residence time multiplied by the distance of the grid cell from the receptor. For relative comparisons between grid cells, the proportionality constant is irrelevant, and in many applications it has been set to $1/r_{max}$, where r_{max} is the maximum distance from the receptor to any trajectory. However, the proportionality constant can be derived with a smaller radius if desired.

OSC is defined as

$$OSC_{i,j} = \frac{ORT_{i,j}}{EPS_{i,j}} \tag{2-11}$$

where ORT is the overall residence time and EPS is calculated by

$$EPS_{i,j} = \frac{1}{r_{i,j}} \frac{A_{i,j}}{2\pi R_{norm}} \tag{2-12}$$

where $r_{i,j}$ is the distance from the receptor to the center of the grid cell. The inverse distance factor results from the fact that all trajectories originate at the receptor. Thus a grid cell near the receptor is more likely to have an endpoint in it than a grid cell far away. $A_{i,j}$ is the area of the grid cell. In a grid system based on degrees of latitude and longitude, each grid cell does not have the same area, with cells to the north being smaller than those to the south. Grid cell area in square km for a 1 degree by 1 degree grid cell is calculated by

$$\begin{aligned} A_{i,j} &= \Delta X \ \Delta Y \\ &= (1\,^{\circ}Lat)^2 \, (111.1\ Km/^{\circ}Lat)^2 \, Cos(Lat). \end{aligned} \tag{2-13}$$

R_{norm} is the "normalization radius" or radius of the area in which the EPS integrates to 1, so $(2\ \pi\ R_{norm})$ is the total area in which the EPS is defined and is somewhat arbitrary. Because the EPS is zero beyond R_{norm}, OSC is undefined when $r_{i,j}$ is greater than R_{norm}. As an example, R_{norm} here is calculated such that the ratio of R_{norm} to the total number of endpoints is equal to the ratio of radius to endpoints in the central 9 grid cells. Thus R_{norm} is calculated by solving

$$\frac{R_{norm}}{N} = \frac{R_{cent}}{N_{cent}}$$

where (2-14)

$$N_{cent} = \sum_{i=iorg-1}^{iorg+1} \sum_{j=jorg-1}^{jorg+1} n_{i,j}$$

and iorg and jorg are the i and j coordinates of the grid cell containing the receptor (the origin). R_{cent} is calculated by solving for it in the following relationship.

$$\pi R_{cent}^2 = \sum_{i=iorg-1}^{iorg+1} \sum_{j=jorg-1}^{jorg+1} A_{i,j} \quad (2\text{-}15)$$

The functional equations for the overall high concentration and low concentration source contribution functions are then

$$OSC_{i,j} = \frac{2\pi R_{norm} r_{i,j}}{N A_{i,j}} \sum_{t=1}^{T} n_{i,j,t}$$

$$HSC_{i,j} = \frac{2\pi R_{norm} r_{i,j}}{H A_{i,j}} \sum_{t=1}^{T} h_{i,j,t} \quad (2\text{-}16)$$

$$LSC_{i,j} = \frac{2\pi R_{norm} r_{i,j}}{L A_{i,j}} \sum_{t=1}^{T} l_{i,j,t}$$

H and L are similar to N except they are the total number of back trajectory endpoints associated with high and low concentrations, respectively.

The source contribution function provides a formal means of limiting the extent that is considered in the analysis of the distance an airmass will travel. However, if this cut-off is ignored then the source contribution function is proportional to multiplying the residence time probability by the distance between the receptor and grid cell. In practice, equation 2-16 is reduced to the residence time multiplied by the distance to the grid cell

$$\begin{aligned} OSC_{i,j} &= r_{i,j} ORT_{i,j} \\ HSC_{i,j} &= r_{i,j} HRT_{i,j} \\ LSC_{i,j} &= r_{i,j} LRT_{i,j} \end{aligned} \quad (2\text{-}17)$$

Using a distance-weighted residence time probability to remove the central tendency in the residence time PDF was first put forth by *Poirot and Wishinski* [1986].

2.3.1.3.1.3 Conditional Probability

Conditional probability is the probability that if an airmass passed through a grid cell, it arrived at the receptor when the concentration satisfied a given condition. The selected condition is usually the measurement of a high or low concentration. The high concentration and low concentration conditional probabilities are calculated by

$$HCP_{i,j} = \frac{HRT_{i,j}}{ORT_{i,j}} * \frac{H}{N} = \sum_{t=1}^{T} h_{i,j,t} \; / \; \sum_{t=1}^{T} n_{i,j,t}$$
$$LCP_{i,j} = \frac{LRT_{i,j}}{ORT_{i,j}} * \frac{L}{N} = \sum_{t=1}^{T} l_{i,j,t} \; / \; \sum_{t=1}^{T} n_{i,j,t} \qquad (2\text{-}18)$$

where all variables are as defined in the residence time equations.

Grid cells which have few total endpoints may not have statistically significant conditional probabilities and are usually not reported. An extreme example is a grid cell with only one endpoint. The only possible values for the conditional probability are then 0 or 1. Such grid cells are usually at the edges of the domain.

2.3.1.3.1.4 Incremental Probability

The incremental probability identifies regions that are more or less likely to be traversed when the receptor concentrations satisfied a given condition compared to an average day [*Poirot et al.*, 1999; *Poirot et al.*, 2001]. For example, the high and low incremental probabilities are the difference between the high or low residence time probability and the overall residence time probability:

$$HIP_{i,j} = HRT_{i,j} - ORT_{i,j}$$
$$LIP_{i,j} = LRT_{i,j} - ORT_{i,j} \qquad (2\text{-}19)$$

The high incremental probability (HIP) field differs from the high condition probability (HCP) field because the HIP metric is determined by subtraction (the extent to which the high day probability is greater than the average day), while the HCP metric is determined by division (the fraction of total trajectory segment endpoints passing over a cell that results in high concentration days). Thus, the HCP indicates the potential for a location to contribute if that area is upwind of the receptor, while the HIP reflects the most probable upwind locations if the receptor concentration is high.

2.3.1.4 Trajectory Max

The trajectory max technique is a first order source apportionment technique meant to give an extreme upper bound on the possible contribution of a source region to a receptor's air quality. This is an airmass history technique where it is assumed that if an airmass traversed a source region, then the receptor concentration is solely due to emissions from that source region. Therefore the receptor site would have a 100% potential contribution, while a distant source region that an airmass never traversed would have a 0% contribution.

$$SC_{i,j} = \frac{\sum_{t=1}^{T} C_t \delta_{i,j,t}}{\sum_{t=1}^{T} C_t} \times 100 \qquad (2\text{-}20)$$

$$tr_{i,j,t} > 0, \delta_{i,j,t} = 1$$
$$tr_{i,j,t} = 0, \delta_{i,j,t} = 0$$

where $SC_{i,j}$ is the maximum percent source contribution of source region i,j to the receptor, C_t is the receptor concentration at time period t, and $tr_{i,j,t}$ are the number of trajectories in the airmass during time period t that traverses source region cell i,j.

The residence time analyses are used to evaluate the difference wind fields and airmass history models in chapter 4. Results of the trajectory residence time and related analyses are discussed in section 8.1.3, while results from the trajectory max analysis is presented in section 8.1.4.

2.3.2 Quantitative

2.3.2.1 Trajectory Mass Balance (TrMB)

The Trajectory Mass Balance (TrMB) model [*Pitchford and Pitchford*, 1985; *Iyer et al.*, 1987; *Gebhart et al*., 1988; *Malm et al*., 1989; *Gebhart and Malm*, 1989, 1994; *Malm*, 1992; *Gebhart et al*., 1993] is a special case of the general mass balance equation [*Iyer et al*., 1987; *Malm et al*., 1989) in which measured concentrations at a receptor are assumed to be linearly related to the frequency of airmass transport from a source area to the receptor by the following relationship:

$$C_{it} = \sum_{j=1}^{J} Q_{ijt} T_{ijt} N_{jt} E_{ijt} \qquad (2\text{-}21)$$

The subscripts i,j, and t refer to chemical species, source area, and time, respectively. C is the measured concentration, Q is the emission rate, T is a transformation and deposition factor to account for deposition, diffusion, and chemical conversion, N is the number of back trajectory endpoints and E is an entrainment factor to account for disassociation between the back trajectories and the transport of pollutants. An endpoint is defined as the calculated position of an air parcel that eventually will arrive at the receptor. Endpoints are calculated hourly for 5 days back in time. In this application the only variables used explicitly are C, the concentrations measured at Big Bend and N, the number of back trajectory endpoints in each source area for each day. The remaining term, QTE, called the "transfer coefficients" are estimated by Ordinary Least Squares (OLS) regression for each source such that equation 2-21 simplifies to equation 2-22 where

$$C_t = \bar{a}_0 + \sum_{j=1}^{J} \bar{a}_j N_{jt} + error_t \qquad (2\text{-}22)$$

The subscript i has been dropped for simplicity since we are now dealing with a single measured species. The species concentrations at the receptor per endpoint in the source region are a=QTE and are the regression coefficients with units of concentration per endpoint. These are estimates of the average relationship between airmass residence time in the source area and

measured concentration at the receptor. The intercept was fixed at 0, forcing all identified source areas to account for the measured concentrations. Although emissions and precipitation data are available for BRAVO, they have not been included in the modeling. Note that whenever a quantity is replaced by its average, the error increases.

The error, as shown in equation 2-23, is due to the deviations of the unknown terms from the mean plus measurement error:

$$error_t = \sum_{j=1}^{J} (a_{jt} - \overline{a_j}) N_{jt} + measurement\ error \qquad (2\text{-}23)$$

Source areas are chosen based on several criteria. First, areas are chosen based on interest in the attributions from the area, e.g., separating the influence of sources in Mexico from sources in Texas. Second, sources near the receptor can be smaller than sources farther away due to the inherent error in trajectory endpoint locations as the time from the receptor increases. Third, model performance is better if the source areas have significant emissions of the pollutant of interest and if all or most trajectories passing through the source region would be expected to have similar exposure to emissions, dispersion, and transformation en route to the receptor. Finally, to avoid collinearities between source regions, the timing and number of trajectories passing through each region should be reasonably independent from other regions. It is often difficult to choose areas that simultaneously satisfy all criteria.

Collinearities between source areas are investigated using the Variance Inflation Factor (VIF) [*Belsley et al.*, 1980] where

$$VIF_i = \frac{1}{1 - R_i^2} \qquad (2\text{-}24)$$

R^2 is the multiple correlation coefficient of the endpoints in one source area regressed on the endpoints in the remaining source areas. A high value indicates that the endpoints in a single source region could be nearly explained by a linear combination of the endpoints in the remaining source regions. A VIF greater than 10 is considered strong collinearity. Another indication of collinearities between source areas is the correlation matrix of the endpoints, although correlations can only reveal collinearities between pairs of source areas, e.g., source 1 with source 2, and not cases where two or more source areas could be linearly combined to predict another. A further indication of collinearities is large standard errors for the regression coefficients.

A test of the TrMB method using tracer data is discussed in section 7.1.1, a test of TrMB using simulated sulfate is in section 7.2.1, and TrMB results for measured sulfate at Big Bend National Park are shown in section 8.2.2.

2.3.2.2 Forward Mass Balance Regression (FMBR)

The TrMB technique presented in the previous section is based upon a special case of the general mass balance equation for back trajectories. A similar relationship can be derived using the forward Lagrangian framework (forward airmass histories) such that for a single ambient species [*Lamb et al.*, 1971; *Iyer et al.*, 1987; *Schichtel*, 1996].

$$c_{ik} = \frac{1}{\Delta X_i} \sum_j \sum_\tau T_{i,k|j,k-\tau} K_{i,k|j,k-\tau} E_{j,k-\tau} \quad (2\text{-}25)$$

where c_{ik} is concentration at receptor j and time k, [g/m^3], $E_{j,k-\tau}$ is mass emitted from source j at time k-τ, [g], $T_{i,k|j,k-\tau}$ is transit probability, [ ], $K_{i,k|j,k-\tau}$ is kinetic probability [ ], ΔX_i is the averaging volume at the receptor I, $k - \tau$ is source release time, and τ is age of the source mass at the receptor.

The transit probability describes the dispersion of pollutants emitted into an airmass over time. Specifically, the transit probability is the likelihood of airmass at source j and time k-τ being transported to a receptor i at time k where τ is the time it takes the airmass to be transported from the source j to receptor i, or the age of the airmass. The kinetic probability accounts for the transformation and removal of pollutants during the transport from the source i to the receptor j during the time τ. The kinetic probability has a different interpretation for primary and secondary species. For primary species it is the probability that the mass is not removed during transport from the source to the receptor. For secondary species it is the probability that the primary emissions were transformed to the secondary species and not removed during transport from the source to the receptor.

This equation relates the receptor concentrations c_{ik} to the emissions $E_{j,k-\tau}$ via the transfer coefficient $Tr_{i,k|j,k-\tau} = T_{i,k|j,k-\tau} K_{i,k|j,k-\tau}$ and is also known as the source receptor relationship (SRR). The transfer coefficient is equivalent to the relative contribution of a source to a receptor.

If Tr and E are known, then equation 2-25 can be used to estimate the concentrations C_{ik}. However, if C_{ik} are known and one or more of the factors on the right hand side of equation 2-25 are unknown, then the relationship can be inverted to find these unknown factors. In this application, the concentrations are known and the transit probabilities are estimated from the CAPITA Monte Carlo model. Therefore the kinetic probabilities and emission are unknown. These two terms can be combined into a single source/sink term $(KE)_{i,k|j,k-\tau} = K_{i,k|j,k-\tau} E_{j,k-\tau}$, and equation 2-25 is then inverted to solve for this source/sink term.

The number of elements in the source/sink term is equal to the number observations multiplied by the number of source/time pairs, while the vector of concentration values only has the number of observations. Therefore this is a highly under-determined system and the number of unknowns must be reduced. In this application, this is accomplished by integrating the SRR over the source release time and averaging the source/sink term over the receptor times and sites. Therefore the SRR became

$$c_{ik} = \sum_j T_{i,k|j} (KE)_j + error_{ik} \quad (2\text{-}26)$$

where the term $(KE)_j$ is the source/sink term for each source j and the error term accounts for measurement and averaging errors in the source/sink term. The number of unknown terms is then equal to the number of sources j which can be made smaller than the number of observation giving us an over determined system. The source/sink term is then obtained by inverting equation 2-26, i.e., $(KE) = (T)^{-1} c$. The contribution of individual sources to the receptor concentration can then be estimated from $c_{ikj} = T_{i,k|j} (KE)_j$.

Aggregating the source/sink term over all receptors and times is equivalent to assuming that each source's emission rate and kinetic probability are constant over time and receptors. This may be an adequate assumption for emission rates, but the transformation and removal process driving K will vary dramatically in space and time. For example, K would be about 0 for a heavy rain event, while under dry conditions K could be near 1, i.e. no removed mass. Therefore caution needs to be applied when grouping receptor sites to estimate (KE) and the results are only applicable to the average across all receptors and times used in the analysis.

Equation 2-26 is inverted using linear least squares techniques. However, the source receptor relationship is an ill-conditioned system [*Newsam and Enting*, 1988; *Schichtel*, 1996] causing its inversion by least squares to amplify the errors in the system. This results in an unstable solution with large positive and negative values. To dampen these instabilities information needs to be added to the system. This was done using two approaches. The first approach used singular value decomposition (SVD) [*Jackson* 1972; *Press et al*., 1988; *Schichtel*, 1996]. SVD is equivalent to zeroth-order linear regularization which finds a solution by balancing the model agreement (minimization of the square of the residuals) and the magnitude of the solution vector. In this case, the added information is the magnitude of the solution vector, because as magnitude of the solution vector decreases the solution stability increases. A key to the SVD solution is selecting the appropriate balance or trade off between the model agreement and the solution stability. This was done by selecting the solution that equally maximized the model agreement and solution stability. If the solution was still unstable as evidenced by large positive and negative values, then the weight to the solution stability was increased.

In the zeroth order solution, the more weight given to the solution's stability, the lower the effective resolution of the solution space. This is similar to *a priori* grouping the source regions prior to the inversion. If the source regions are sufficiently grouped together, it is possible to use ordinary least squares techniques to obtain stable solutions. Therefore the second means of adding information to the system was by aggregating the source regions together. The aggregated source/sink regions are defined and discussed in section 2.3.2.6.

The basic idea of the Forward Mass Balance Regression is to determine the average source contribution from pre-defined source regions and measured receptor data, in this case particulate sulfate. FMBR does this by essentially comparing the receptor concentration levels and to the relative inert contribution, i.e. the transit probability, from all modeled source regions impacting the receptor. A source region that repeatedly has a large inert contribution when the concentrations are low will have a low source/sink term. That is, it has low emissions and/or the emitted mass is usually removed before impacting the receptor, or in the case of a secondary species such as sulfate, the primary species was not transformed to the secondary species. On the other hand if a source has a large inert contribution and the concentrations are repeatedly high, then it will have a high source/sink term. Due to the fact that multiple sources impact the receptor at any given time, a regression technique is used to decompose the receptor mass to the source regions, thus deriving multiple average source/sink terms.

The decomposition of the receptor mass among source regions relies on airmasses traversing each source region but following different transport direction to the receptor at different times. Therefore a different number and source regions will be impacting the receptor at different times. Any two source regions with highly correlated relative inert contributions cannot be reliably separated from each other. Therefore one of the key aspects of this technique

is to properly group the source regions so that they have varied source/sink terms and non collinear transit probabilities. The selection of source regions is presented in section 2.3.2.5

The FMBR technique is validated against tracer data in section 7.1.2. It is validated against simulated sulfate concentrations in section 7.2.2, and FMBR results for measured sulfate at Big Bend National are presented in section 8.2.3.

2.3.2.3 Synthesis Inversion – Merging Air Quality Model Source Apportionment Results and Receptor Data

The previous sections defined the source receptor relationship from the backward and forward Lagrangian framework and used these formulations to estimate source contributions to receptor sites by merging measured concentrations and airmass transport calculation. A similar technique can also be applied to Eulerian models. This section outlines a general inverse modeling technique based on the Eulerian model framework. Then it is shown how this can be used in conjunction with the REMSAD and CMAQ-MADRID source attribution results to develop an alternative source attribution of Big Bend's sulfate. CMAQ-MADRID is also an Eulerian grid model similarly employed as REMSAD by the Atmospheric and Environmental Research (AER) and EPRI work groups [*Electric Power Research Institute*, 2004].

2.3.2.3.1 Synthesis Inversion of the Source Receptor Relationship

The conservation of mass equation governing the concentration of trace species in the atmosphere can be written as

$$\frac{\partial}{\partial t} m(\ ,t) = q(\ ,t) + \mathrm{T}[m(\ ,t),t] + \mathrm{K}[m(\ ,t),t] \qquad (2\text{-}27)$$

where m(**r**,t) [g/m^3] is the concentration of the trace species at location **r** and time t, q(**r**,t) [g/m^3/s] is the local source emission rate, $\mathrm{T}[\mathrm{m}(\mathbf{r},\mathrm{t}),\mathrm{t}]$ [g/m^3/s] is a transport operator, and $\mathrm{K}[\mathrm{m}(\mathbf{r},\mathrm{t}),\mathrm{t}]$ [g/m^3/s] is a kinetic operator describing the physical/chemical removal and transformation processes.

Equation 2-27 expresses the rate of change of the concentration at a point **r** and time t as the sum of the local sources, the contribution due to trace-gas transport from other locations, plus net loss and gains due to removal, and chemical transformation processes at **r** and time t. The transport processes account for both advection and turbulent diffusion.

Enting [2000, 2002] showed that if the kinetic and transport operators are linearly dependent on the concentrations, then equation 2-27 is a linear differential equation that linearly relates the concentration field m(**r** ,t) to the sources q(**r** ,t). Therefore given a specified set of linear boundary conditions, equation 2-27 can be solved using the Green function method

$$m(\ ,t) = m_o(\ ,t) + \int_{r'}\int_{t_o}^{t} G(\ ,t,\ \ ,t')q(\ ,t')dt'd^3r' \qquad (2\text{-}28)$$

where m_o(**r**, t) [g/m^3] is the concentration that would result in the absence of emissions from the initial model simulation time t_o and G(**r**,t, **r**',t') [1/m^3] is the Green function. Mathematically, G is a mapping from the space-time distribution of the sources q(**r** ,t) onto the space-time distribution of the concentrations m(**r** ,t). Physically, G is the response of the concentration field due to a change in the source field and is equivalent to the continuous transfer coefficient in equation 2-25.

For inverse modeling purposes it is often useful to work with a discrete form of equation 2-28. This can be done by decomposing the source term into a set of processes and distributions such that

$$q(\ ,t)=\sum_j s_j\sigma_j(\ ,t) \tag{2-29}$$

where s_j is a set of unknown scale factors and $\sigma_j(\mathbf{r},t)$ is a set of known source distributions. Therefore, by integrating over the source space (**r'**) and time t'

$$m(\ ,t)=\sum_j s_j G_j(\ ,t) \tag{2-30}$$

where

$$G_j(\ ,t)=\int_{r'}\int_{t'} G(\ ,t,\ \ ,t')\sigma_j(\ \ ,t')dt'd^3r' \tag{2-31}$$

the concentrations m_o are assumed constant and incorporated into equation 2-29 as a pseudo-source. It is common to normalize the source distributions:

$$\int_{r'}\int_{t'}\sigma_j(\ \ ,t')dt'd^3r'=1 \tag{2-32}$$

Therefore the scale factors s_j have a direct interpretation as average source strengths. Finally, discretisation of equation 2-30 in the receptor space (**r**) and time t can be done by averaging over an appropriate area and time such that

$$c_i=\sum_j G_{ij}s_j+\varepsilon_i=m_i+\varepsilon_i \tag{2-33}$$

where c_i are the observed concentration values, m_i are the modeled concentration values, ε_i are the errors in c_i, s_j are the source strengths, and G_{ij} is the discretisation of G(**r**,t, **r**',t'), estimated through the integration of the air quality model via equation 2-31.

In the development of 2-33, the Green function method required a linear differential equation with respect to the concentrations m(**r**,t). However, from a practical stand point, the discretised G_{ij} is calculated by integrating the air quality model with the appropriate boundary conditions and source distributions $\sigma_j(\mathbf{r},t)$ and the model can contain nonlinearities. The development of source receptor relationship for inversion techniques in this way is known as synthesis inversion, since the discretisation of sources involved synthesizing the results as a linear combination of pre-specified source patterns [*Enting*, 2002].

2.3.2.3.1.1 Application to REMSAD and CMAQ-MADRID Source Attribution Results

The REMSAD model simulated the sulfate concentrations in most of North America and estimated the contribution of sulfate from ten major source regions and the model boundary conditions to Big Bend National Park and the other 36 BRAVO monitoring sites. The CMAQ-MADRID model was similarly employed to simulate the contribution from 4 major source regions and the boundary conditions. In both cases, $\sigma_j(\mathbf{r},t)$ are the actual source emission rates for each source region used in REMSAD and CMAQ-MADRID. The discrete Green function is

then equal to the contribution of the modeled source region q to the monitoring site p for the 24-hour average time period k. By letting the source/time pair q and k equal index j and the receptor/time pair p and k equal index i, the REMSAD or CMAQ-MDRIS source attribution results can be represented by equation 2-33, where G_{ij} is the daily contribution from each source region to each daily sulfate concentration at one or more BRAVO monitoring sites and s_j is the source attribution scaling coefficient. If $s_j = 1$, then $\Sigma_j G_{ij}$ is approximately equal to the predicted sulfate for the model observation $_i$ (m_i). It does not exactly equal the predicted concentrations due to non-linearities in the air quality models' chemistry modules, though the non-linearities were found to be small.

In this application, c_i are the measured sulfate concentrations and equation 2-33 is solved for s_j using Bayesian least squares regression. In the manner that equation 2-33 was developed, s_j represents biases in the source emission rates. However, s_j compensates for errors in the source attribution results which are due to errors in the emissions, transport, chemical transformation, and removal of sulfur. Therefore s_j represents the biases in the source attribution results and will be referred to as the source attribution scaling coefficient. If the model source attributions are unbiased, then the regression coefficients (s_j) will be equal to 1.

In section 7.2.3 the synthesis inversion approach is tested against synthetic sulfate data and source attribution estimates from the REMSAD model. In section 8.2.1 the results from the Synthesized REMSAD and CMAQ-MADRID are presented.

2.3.2.4 REMSAD Emission Sensitivity Simulations

Results from the base emissions simulation were used to assess REMSAD's skill in predicting sulfate concentrations within the domain, and in particular at Big Bend NP. Once this base simulation was established, it was compared to simulations in which regional sulfur emissions were modified. The change in predicted sulfate arising from these emission sensitivity simulations defined a source region's contribution at Big Bend NP. Four source regions were evaluated for their contribution to predicted sulfate at Big Bend NP: Mexico, Texas, the eastern U.S., and the western U.S. (Figure 2-14). Sulfur dioxide and primary sulfate emissions from the source regions of interest were modified by either 1) removing these emissions from the source region ("emissions out" scenario), or 2) retaining these emissions, but removing sulfur dioxide and primary sulfate emissions from the rest of the domain ("emissions in" scenario). Examples of the modified emission inventories are shown in Figure 2-15. These two approaches for treating emissions were designed to elucidate the potential nonlinear behavior in the chemical conversion of SO_2 to SO_4 due to the availability of oxidants (e.g., hydroxyl, hydrogen peroxide). For example, in the "emissions out" simulation for Texas (Figure 2-15a), more SO_2 is present within the model domain as compared to the "emissions in" simulation (Figure 2-15b). This additional SO_2 could have the effect of reducing the predicted oxidizing capacity of the atmosphere, as oxidants would be consumed by reacting with the available SO_2 outside of the source region of interest. In contrast, more oxidants will be available in the "emissions in" simulation, as they will not have reacted with SO_2 from areas outside of the source region of interest. The difference between these two emission scenarios should indicate the model's sensitivity to predicted oxidant concentrations, and whether the conversion of SO_2 to SO_4 is "oxidant limited". In addition to the four large regions discussed here, several smaller source regions were also evaluated in an effort to refine the source contributions to sulfate at Big Bend NP.

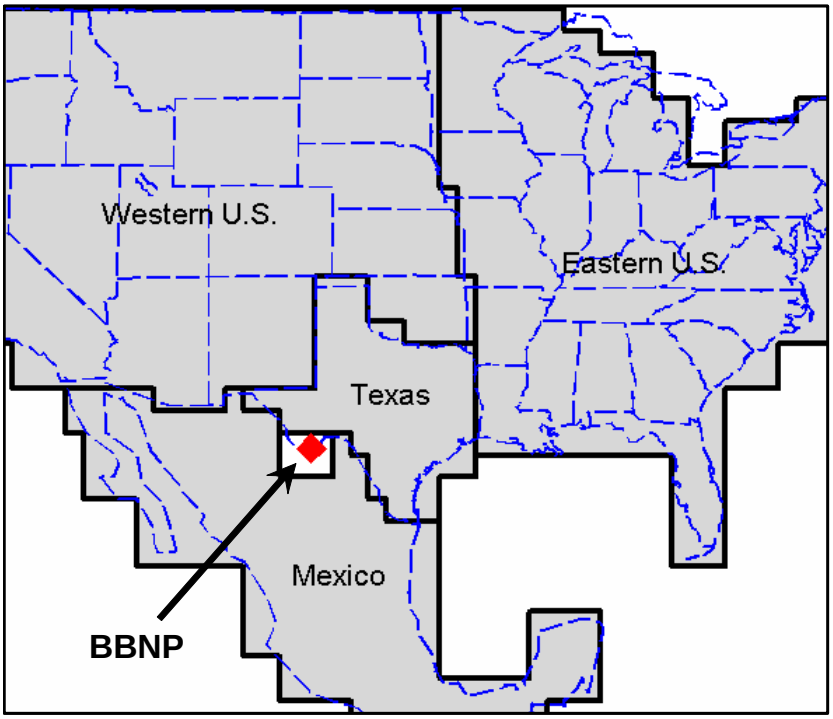

Figure 2-14. The four source regions evaluated for their impact on SO_4 predicted at BBNP: Mexico, Texas, the eastern U.S., and the western U.S. SO_2 emissions in the region immediately surrounding BBNP are near zero and not included in the emissions processing.

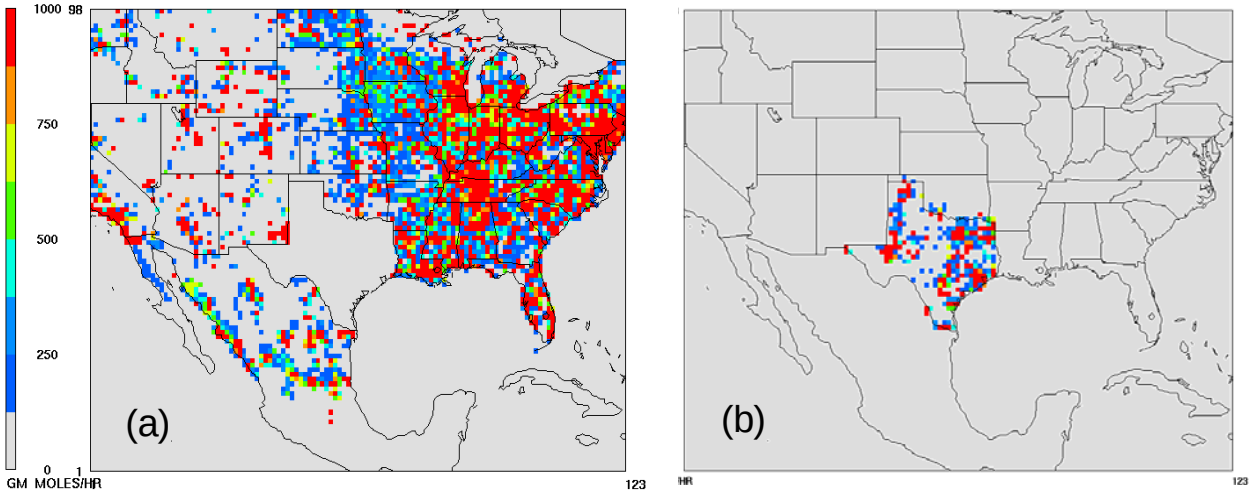

Figure 2-15. Example SO_2 emissions (moles/hr) for (a) the Texas "emissions out" scenario and (b) the Texas "emissions in" scenario.

2.3.2.5 BRAVO Source Areas

BRAVO source areas used for sulfate source attribution were chosen by group consensus in order to facilitate comparison of the results from different models.

Factors considered in the choice of source areas were:

1. Division of areas based on political or scientific desire to know the contributions from those areas to concentrations at Big Bend. For example, there was interest in knowing the relative contributions of sources in Mexico vs. sources in the United States to sulfate at Big Bend. There was also interest in estimating the contribution of the Carbón I & II electric generating stations and in knowing how much of the U.S. contribution was from Texas vs. how much was from outside Texas.
2. For the receptor models that utilize forward or backward trajectories, collinearities between source areas had to be minimized. Using those techniques, it's not possible to separate the contributions from two areas if airmasses always or almost always pass over both areas before arriving at the receptor.
3. Limitations of the modeling domain. For example, although Africa is a suspected source of dust during the summer, the modeling domain did not extend that far from Big Bend due to the geographic limits of the gridded wind fields.
4. For trajectory-based models, source areas should generally be larger as the distance from the receptor increases. This is to allow for increased uncertainty in trajectory locations and increased dispersion as the distance and travel time between source and receptor increase. Dispersion is explicitly calculated by some models, but not by others.
5. For trajectory-based regression models, the source areas should be small enough so that a single coefficient is sufficient to explain the mean relationship between source area and receptor no matter which portion of the source area the trajectories go through.
6. The regression techniques rely on the contribution from the source regions being larger than the errors in the model and observations. Therefore, each source region needed large SO_2 emission rates.

Sources chosen for sulfate source attribution after consideration of these factors are shown in Figure 2-16, with the names given in Table 2-5. Each of the 27 smaller source areas was also assigned to one of four large regions: Texas, Mexico, the eastern U.S., or the western U.S. These are also shown in Table 2-5.

Similar criteria were used to choose the four source areas representing the perfluorocarbon tracer release sites for Trajectory Mass Balance receptor modeling which are shown in Figure 2-17.

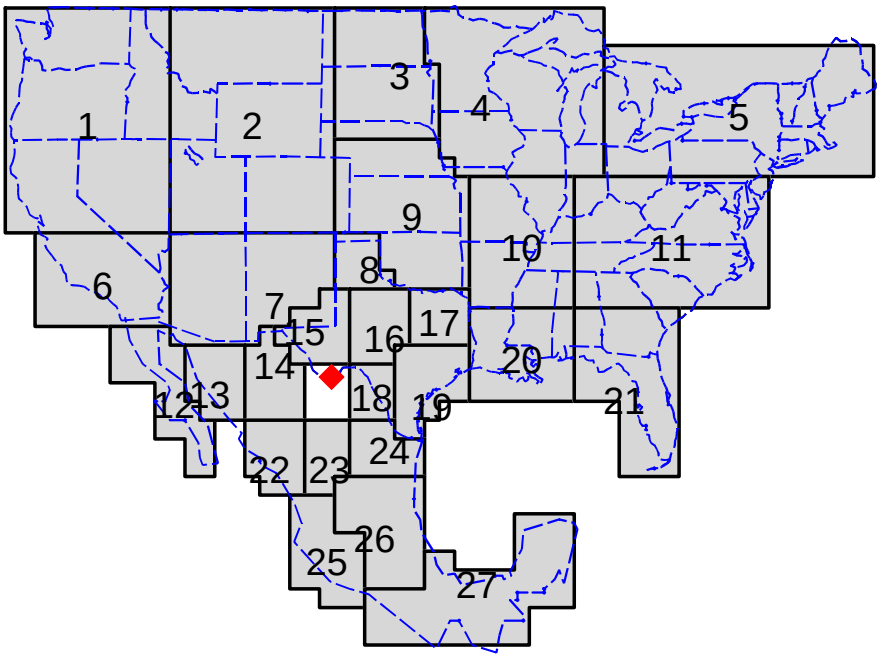

Figure 2-16. Consensus source areas used for source attribution of sulfate at Big Bend.

Table 2-5. Sulfate source area names.

Source Number	Individual Source Name	Large Source Name
1	Pacific Northwest	Western U.S.
2	Northern Rockies	Western U.S.
3	Dakotas	Western U.S.
4	North Central States	Eastern U.S.
5	Northeast	Eastern U.S.
6	Southern California	Western U.S.
7	AZ/NM	Western U.S.
8	Texas Panhandle	Texas
9	Central Plains	Western U.S.
10	MO/IL/AR	Eastern U.S.
11	East Central States	Eastern U.S.
12	Baja California	Mexico
13	Northwest Mexico	Mexico
14	North Central Mexico	Mexico
15	West Texas	Texas
16	North Central Texas	Texas
17	Northeast Texas	Texas
18	Carbón I & II	Mexico
19	Southeast Texas	Texas
20	LA/MS	Eastern U.S.
21	FL/GA	Eastern U.S.
22	West Central Mexico	Mexico
23	Central Mexico	Mexico
24	Monterrey Region, MX	Mexico
25	SW Coast of Mexico	Mexico
26	Mexico City & Volcano	Mexico
27	S. Mexico/ Yucatan	Mexico

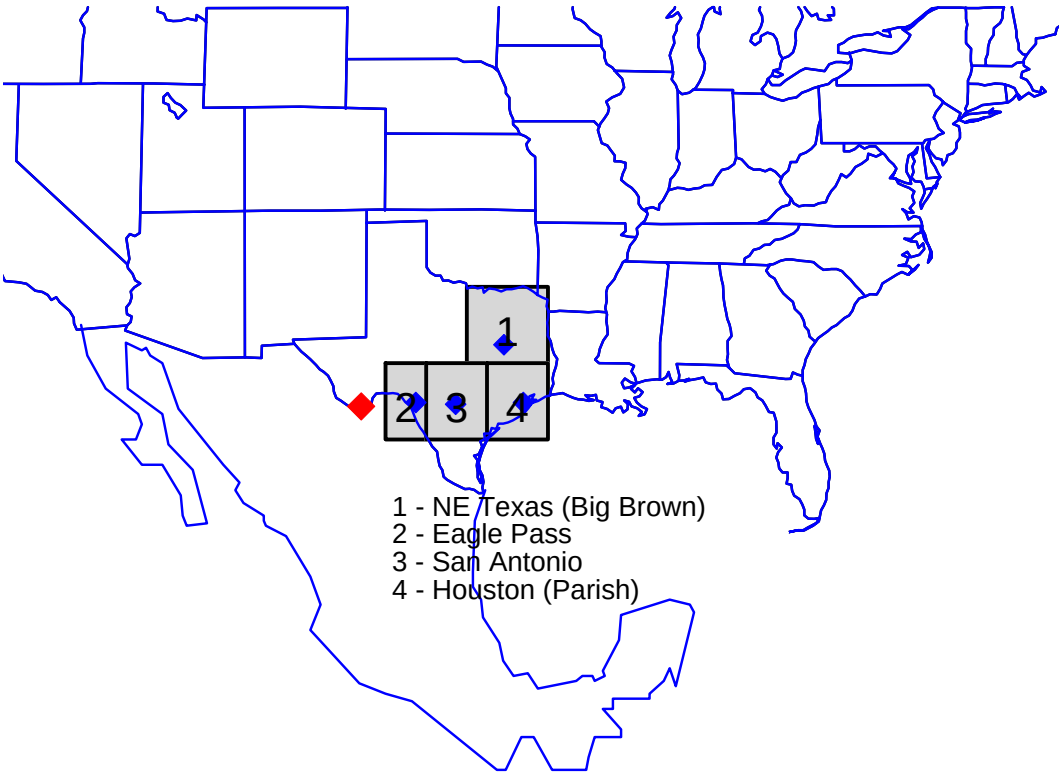

Figure 2-17. Source areas used for TrMB modeling of tracers.

The Forward Mass Balance Regression (FMBR) technique used a modified version of the source regions in Figures 2-16 and 2-17. This was necessary, because in the FMBR analysis forward airmass transport was simulated from 100 x 100 km areas throughout a domain smaller than depicted in Figure 2-16. The source areas could not transect one of the 100 x 100 km areas, so the source areas in Figure 2-16 were shifted up to 50 km. In addition, correlations of transport between some of the source areas were above 0.7, indicating a high degree of collinearity. These source areas were merged and adjusted until no correlation coefficient was above 0.7. This process reduced the 27 source regions to only 17 which are presented in Figure 2-18. Figure 2-19 presents the modified source areas representing the perfluorocarbon tracer release sites used in the FMBR modeling of the tracer data.

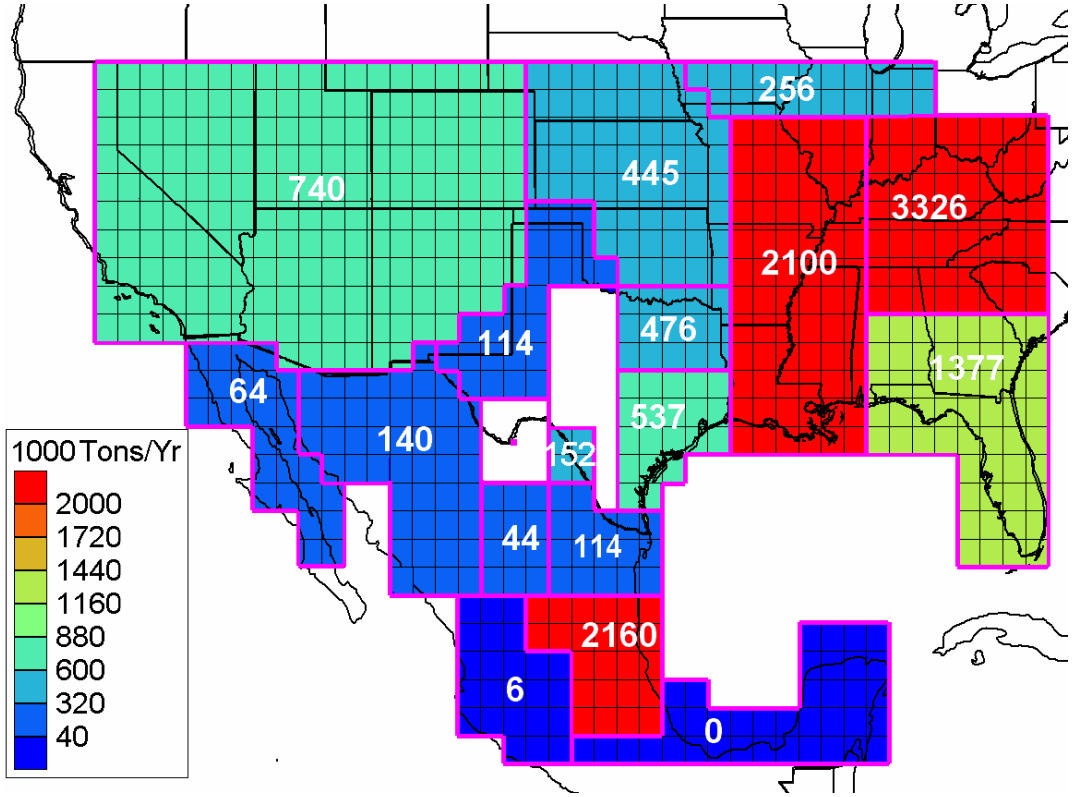

Figure 2-18. Modified consensus source areas used in the FMBR source attribution of sulfate at Big Bend. The grid represents the 100 x 100 km areas that forward airmass transport was simulated from. The values and colors of each source region are the SO_2 emission rates in 1000 tons/year from the BRAVO and National Emission Trend inventories.

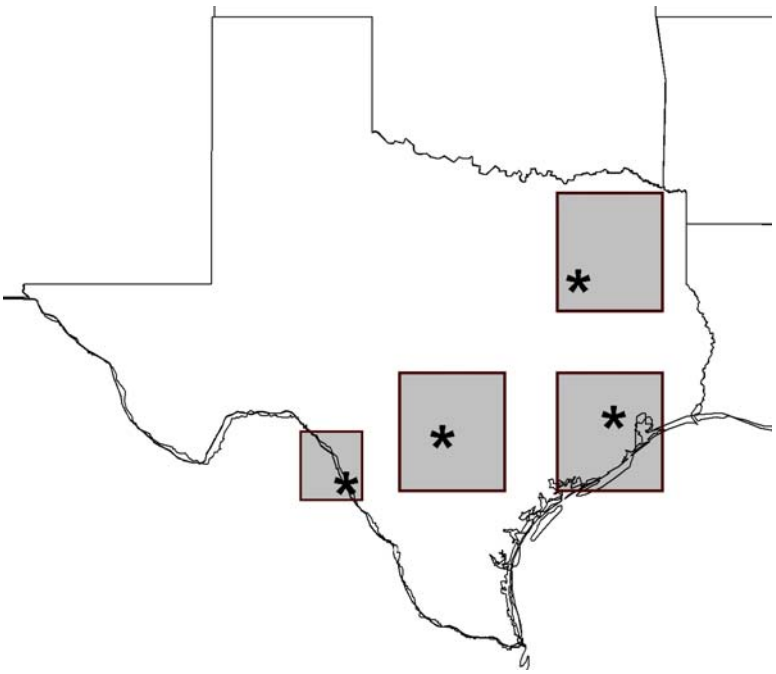

Figure 2-19. Source areas used for FMBR modeling of tracers.

3) Big Bend's Aerosol and Extinction Budgets during BRAVO

3.1 Introduction

The primary goal of the BRAVO study was to apportion the major aerosol species to their emission sources, with the secondary goals of understanding the physio/chemical/optical properties of aerosols at Big Bend and surrounding areas. To achieve the secondary goals, a number of detailed measurements of the particulate chemical composition, size distribution, hygroscopicity, and the particles' optical properties were made (see chapter 2). These measurements were sufficient to perform chemical and optical closure calculations on the measured aerosol. This chapter reports on the findings from these measurements.

Past studies have achieved closure between fine mass estimated from measured species and gravimetric mass and estimated or modeled fine particle scattering and measured scattering. However, coarse particle scattering plus absorption, as determined using open air nephelometery and filter based absorption measurements, is underestimated in routine monitoring systems by factors of as much as two [*Malm et al.*, 2000b]. To address this issue, special attention was given to measuring large particle (>1.0 μm) physio-chemical characteristics. Detailed chemical composition was measured in the fine (0.0–2.5 μm) and coarse (2.5–10.0 μm) modes (IMPROVE sampling system), as well as in eight size ranges using the MOUDI and DRUM impactors. Inorganic ions, elements, and organic and elemental carbon were measured with the IMPROVE system, inorganic ions with the MOUDI impactor, and soil related elements with a DRUM sampler. Optical measurements were made with ambient integrating nephelometers with one fitted with a cyclone (admitting particles with diameters <2.5 μm), another with PM_{10} inlet, and a third in the "open air" configuration. Fine particle absorption estimates were made with an aethalometer and from measurements of elemental carbon. The hygroscopic properties of ambient particles were examined using a humidograph with the ability to measure scattering as a function of humidity over ranges of about 15–95%. *Day et al.* [2000] described the instrument design in some detail and therefore its operation will only be summarized here.

Experiments were designed such that observables could be estimated or modeled in a number of different ways. Mass was gravimetrically determined for both D_{aero} <10 and 2.5 μm, which can be compared to reconstructed mass based on measured aerosol species. Dry and ambient scattering coefficients were measured, which in turn can be compared to modeled scattering coefficients that are based on aerosol species mass and size measurements. Humidograph measurements of scattering coefficients as functions of relative humidity can be compared to modeled scattering coefficients that include thermodynamic model predictions of inorganic aerosol hygroscopic growth.

Previous studies of aerosol hygroscopicity have been made using tandem differential mobility analyzers (TDMA) and have been summarized in *Cocker et al.* [2001]. Most studies used humidification ranges of 80–90%. A number of these studies reported two growth modes: a less hygroscopic mode with growth factors of 1.0–1.4 and more hygroscopic mode with growth factors as high as 1.8. In chamber studies, *Virkkula et al.* [1999] reported a growth factor of about 1.1 for a no-seed secondary organic case and a growth factor starting at 1.5 for an ammonium sulfate seed, but dropping to 1.1 near the end of the experiment. The affinity of organic compounds for water, particularly those organic species found in the ambient atmosphere, is not as well characterized, despite the fact these species often account for a significant amount of the total fine mass in continental aerosols [*Malm et al.,* 1994]. As reviewed

by *Saxena and Hildemann* [1996], organic particulate matter contains hundreds of compounds, spanning a range of carbon numbers, functional groups, and solubility in polar and non-polar solvents.

Measurement of particle scattering as a function of relative humidity was pioneered by *Covert et al.* [1979] and *Waggoner et al.* [1983]. They made limited measurements at a number of locations including Tyson, Missouri, Point Reyes, California, Shenandoah National Park, and Houston, Texas. *Malm and Day* [2001] reported on measurements of the relative humidity enhancement factor which is defined to be the ratio of the scattering coefficient at some relative humidity divided by the scattering coefficient at some minimum relative humidity ($f(RH)=b_{scat}(RH)/b_{scat}(RH_{min})$). Measurements were carried out at Great Smoky Mountains and Grand Canyon national parks. The f(RH) function was smoothly increasing as a function of increasing relative humidity for both data sets. However, for the most part, the f(RH) at Great Smoky Mountains began to increase at relative humidities just above 20%, while at Grand Canyon increases did not take place until approximately 40–45%, and in some cases not until 60%. At Grand Canyon, the f(RH) was more varied than at Great Smoky Mountains. For instance, in the range of 80–85% relative humidity the f(RH) values varied between 1.53 and 2.75 at Great Smoky Mountains, while at Grand Canyon the range was from near 1 to 4.0. In general, as the contributions of organics and soil dust to mass concentration increase, the increase of f(RH) with humidity decreases. Growth factors and ambient light-scattering efficiencies have previously been observed to be rather smooth functions of relative humidity [*Sloane,* 1986; *Malm et al.,* 2000a]. Measurements of f(RH) at coastal sites in Tasmania and Portugal showed qualitatively similar results in which pollution-dominated aerosols showed smoothly varying f(RH), though marine-dominated aerosols showed strongly deliquescent and more hygroscopic f(RH) [*Carrico et al*., 1998; 2000]. *Rood et al.* [1989] showed evidence for the existence of metastable aerosol in the ambient atmosphere. Differences in measurements of f(RH) between the deliquescence and crystallization branches were ~10% on average for polluted aerosols and ~20% on average for marine aerosols, though as much as 50% for individual RH scans [*Carrico et al.*, 2000].

A variety of scattering models were used in an attempt to reproduce measured f(RH) curves. At Great Smoky Mountains, both internally and externally mixed aerosol models were used assuming the measured sulfate ion was fully neutralized, assuming variable degrees of neutralization corresponding to the measured ammonium ion concentrations, and with and without accounting for sampling-period-to-sampling-period shifts in size distribution [*Malm et al.,* 2000a]. The model sensitivity to using the deliquescence and crystallization branches, as well as a curve smoothed between the deliquescence and crystallization points of D/D_o curves as a function of relative humidity for inorganic salts, was also explored. Scattering coefficient predictions as a function of relative humidity were most sensitive to the assumptions regarding sulfate ammoniation and the smoothed D/D_o growth curves. Changes in f(RH) as a function of assumptions concerning mixing were less than 10% on the average.

For the analysis of the data from Grand Canyon [*Malm and Day,* 2001], only the externally-mixed model was used; sulfate was assumed to be in the form of ammonium sulfate, and a smoothed f(RH) curve was used based on size distribution measurements made in previous studies. At Grand Canyon the assumptions of constant mass scattering efficiencies, complete sulfate ammoniation, and a constant f(RH) yielded, on the average, very reasonable results. However, on some days parts of the measured and predicted f(RH) curves varied by as much as

±20%. An ordinary least squares (OLS) regression between measured and predicted f(RH) values yielded a R^2= 0.82 with a slope of 1.02 ±0.006 when the intercept term was forced through zero. The implication is that, on the average, predicted f(RH) values were about 2% greater than measured. The results of both the Grand Canyon and Great Smoky Mountains studies suggested that organic aerosols were weakly hygroscopic or non-hygroscopic.

In this chapter, the chemical and optical properties of Big Bend's haze is examined and the influence particle size distribution, the degree of sulfate ammoniation, and chemical composition have on aerosol scattering dry and ambient scattering and as a function of relative humidity is further explored. Two equilibrium models, ISORROPIA [*Nenes et al.,* 1998] and the Aerosol Inorganics Model (AIM), [*Clegg et al.,* 1992, 1998b] are used to estimate inorganic aerosol growth.

3.2 Determination of Aerosol Types

The fine aerosol species at most continental sites can be classified into five major types: sulfates, nitrates, organics, light-absorbing carbon, and soil. Other fine species such as non-soil potassium, sea salt, and other trace elements are less important from a visibility standpoint. Details of standard methods for apportionment of measured mass to the various aerosol species are described in some detail in *Malm et al.* [1994]

An average ambient particulate organic compound was assumed to have a constant fraction of carbon by weight. Organic carbon mass concentration (OMC) was assumed to be [OMC] = 1.4[OC]. The factor of 1.4 corrects the organic carbon mass for other elements associated with an assumed average organic molecular composition [*White and Roberts,* 1977]. However, *Turpin and Lim* [2001] suggest that this factor could be as high as 2.1. The effect of varying this factor over a range of 1.4–2.1 is not considered here. Elemental carbon (EC) was also obtained.

Soil mass concentration (SOIL) was estimated by summing the elements predominantly associated with soil, plus oxygen for the common compounds (Al_2O_3, SiO_2, CaO, K_2O, FeO, Fe_2O_3, TiO_2), and applying a correction for other compounds such as MgO, Na_2O, water, and carbonate.

Aerosol species distributions were measured using an eight-stage MOUDI sampler and, on 41 of the 125 sampling days, the substrates were analyzed for the inorganic species. The 41 samples analyzed represented a variety of chemical and transport regimes. For the analyzed samples, the nitrate and sodium ions were found in the coarse mass fraction (1.0–10.0 μm), while the sulfate and ammonium ions were found, as expected, in the 0.1–1.0 μm, or fine size, range.

Because the majority of nitrate and sodium mass concentrations were in the coarse mode and the molar ratio of sodium to nitrate was about one, it will be assumed that nitrate was in the form of $NaNO_3$ and, furthermore, that sulfate was in the form of ammoniated sulfate. Ammoniated sulfate is calculated from the available ammonium and sulfate ion mass. The presence of Ca^{2+} in the coarse mode suggests that $Ca(NO_3)_2$ may also be present, although we did not consider this species in our analyses. It is noteworthy to point out that the IMPROVE and URG samplers used for measurements of the fine mode employed a cyclone inlet with a cutpoint aerodynamic diameter of 2.5 μm, which was typically near the middle of the coarse mode nitrate and sodium distributions. Concurrent number size distributions reported by *Hand*

et al. [2002] showed that, in general, the fine and coarse modes of the derived volume size distributions were also separated at about 1.0 μm aerodynamic diameter.

3.3 Summary of Optical Measurements

Table 3-1 summarizes the optical measurement in the form of mean, standard deviation, minimum, and maximum. The number of valid data points is also given. The extinction measurements, b_{ext}, were made with a transmissometer, while $b_{sp,open}$, $b_{sp,10\mu m}$ $b_{sp,2.5\mu m}$, and $b_{sp,dry}$ refer to scattering measurements made with an open air nephelometer, a nephelometer fitted with a PM_{10} inlet, a nephelometer fitted with a 2.5 μm inlet, and a nephelometer designed to operate with an inlet that dried the aerosol, respectively. The absorption measurements referred to in this table were estimated from light absorbing carbon measurements in the fine and coarse (PM_{10}–$PM_{2.5}$) mode. Note that $b_{sp,open}$, and $b_{sp,pm10}$, measurements of scattering by all particles and particles less than 10.0 μm, are within measurement uncertainty, the same implying few particles larger than 10.0 μm.

Table 3-1. Statistical summary of optical characteristics of fine and coarse particle absorption and scattering.

Variable (Mm^{-1})	Mean	Std Dev	Minimum	Maximum	*Valid*
b_{ext}	29.25	19.66	3.58	71.96	*54*
$b_{abs,2.5\mu m}$	1.32	0.62	0.36	2.51	*54*
$b_{abs,coarse}$	0.87	1.05	-1.26	3.05	*54*
$b_{sp,open}$	24.16	16.20	6.66	63.54	*54*
$b_{sp,pm10}$	25.11	17.25	6.12	65.71	*54*
$b_{sp,2.5,ambient}$	21.88	15.91	4.49	61.87	*54*
$b_{sp,2.5,dry}$	17.74	13.47	2.91	53.76	*54*
b_{ext}-$b_{sp,open}$	5.09	5.09	-3.94	16.16	*54*
$b_{sp,open}$-$b_{sp,2.5,ambient}$	2.29	1.22	0.65	8.07	*54*
$b_{sp,2.5,ambient}$-$b_{sp,2.5,dry}$	*4.14*	*3.46*	*0.58*	*17.87*	*54*

Figure 3-1 is a temporal plot of b_{ext}, ambient $b_{sp,2.5\mu m}$, and $b_{sp,coarse}$($b_{sp,open}$- $b_{sp,2.5\mu m}$). The difference between b_{ext} and $b_{sp,2.5\mu m}$ is coarse particle scattering and absorption. b_{abs} is not shown because its magnitude is about the same as $b_{sp,coarse}$ and nearly falls on top of the coarse scattering trace. From Figure 3-1, it is obvious that fine particle scattering is the largest single component of extinction and, therefore, fine particle scattering and extinction track each other very closely.

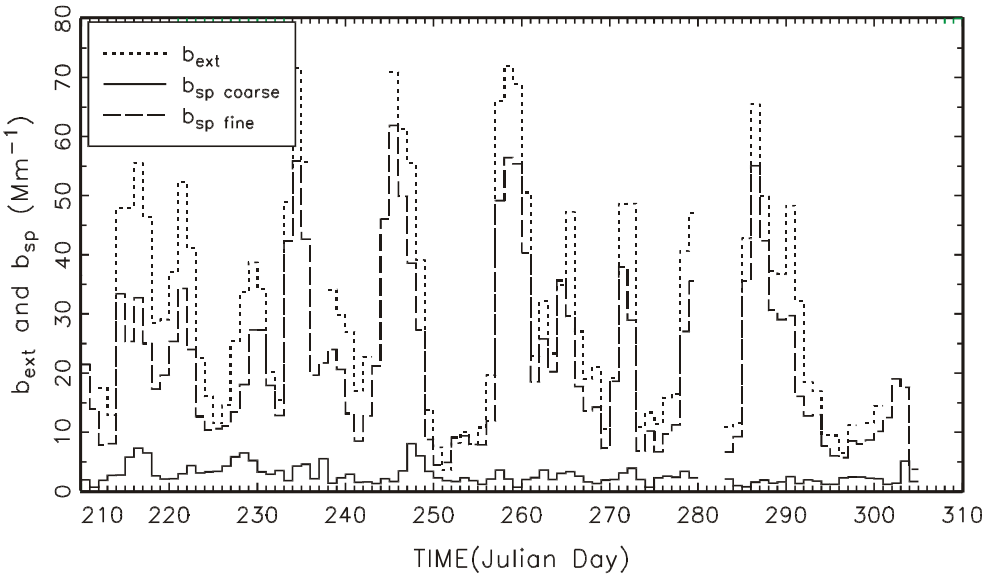

Figure 3-1. Temporal plot of b_{ext}, ambient $b_{sp,\ 2.5\mu m,}$ and $b_{sp,coarse}$.

Referencing Table 3-1, b_{ext} exceeds $b_{scat,2.5\mu m}$ by about 7.4 Mm^{-1} or 25% of aerosol extinction. Summing $b_{sp,2.5\mu m}$, $b_{sp,coarse}$, and coarse and fine absorption yields 26.38 Mm^{-1} which is 2.87 Mm^{-1}, or 10%, short of measured extinction. Coarse particle scattering is estimated to be 2.29 Mm^{-1}. Coarse particle scattering is underestimated by about a factor of one third to a half because of forward angle truncation errors and doubling coarse particle scattering would about make up for the underestimated or missing extinction [*Molenar*, 1997]. Finally, referring to Table 3-1, fine particle scattering due to water associated with hygroscopic particles ($b_{sp,2.5,ambient}$-$b_{sp,2.5,dry}$) is 4.14 Mm^{-1} or about 14% of total extinction while the total fine particle scattering fraction of extinction is 74%. Absorption, fine plus coarse, makes up another 8%. Figure 3-2 is a pie chart summarizing the fraction each of the scattering/absorption components contributes to total extinction.

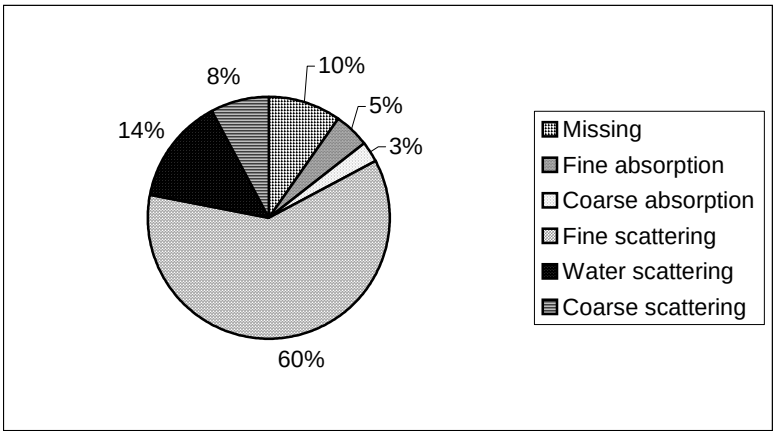

Figure 3-2. Summary of the percent scattering associated with fine and coarse particle scattering/absorption.

The degree to which absorption and/or coarse particle scattering are over- or underestimated can be explored using regression analysis. Assuming that $b_{sp,open}$-$b_{sp,2.5\mu m}$ is proportional to coarse particle scattering and b_{ext}-$b_{sp,2.5\mu m}$ is coarse particle scattering plus absorption of both coarse and fine particles, one can write the following equation:

$$(b_{ext} - b_{sp,2.5\mu m})_i = a_o + a_1(b_{sp,open} - b_{sp,2.5\mu m})_i + a_2(b_{abs,2.5\mu m} + b_{sp,course})_i \quad (3\text{-}1)$$

where i = the i^{th} sampling period and the a_o, a_1, and a_2 = constants. This series of equations can be solved using ordinary least square (OLS) regression analysis.

For purposes of the regression analysis, short temporal variability in the data was minimized by averaging to 24 hours requiring that the 24-hour data had at least 15 hours of non-missing values. The regression coefficient, a_1=2.06±0.42, is highly significant with standard error for the coefficient being about 20% while the standard error associated with total absorption, a_2=1.01±0.38, is 38%. The overall R^2 is low at only 0.23. The coefficient associated with coarse particle scattering as determined by the nephelometers ($b_{sp,open}$-$b_{sp,2.5\mu m}$) suggests that coarse particle scattering is underestimated by about a factor of two. On the other hand, the coefficient associated total absorption implies that absorption as estimated from measured fine and coarse elemental carbon is about right. Therefore this analysis suggests that the missing extinction is likely associated with an underestimate of coarse particle scattering, and fine and coarse particle extinction are, within statistical uncertainty, about right. Coarse particle absorption is 38% of total absorption.

3.4 Summary of Aerosol Species

Fine and coarse mass species concentrations are summarized in Tables 3-2 and 3-3. Measured fine mass is about 8% greater than reconstructed fine mass with ammoniated sulfate contributing 50% of the mass and organics and soil contributing 21% and 23%, respectively. The mass difference between fully neutralized or ammoniated sulfate is about 8% with ammoniated sulfate having less mass. MOUDI mass size distribution data suggested that nitrate found in the fine mode was associated with the fine tail of coarse particle sodium nitrate.

On the other hand, reconstructed coarse mass is 16% greater than gravimetric mass. Coarse mass has usually been interpreted as crustal material; however, referring to Table 3-3, 31% of reconstructed coarse mass was carbon based material while soil or crustal material made up 53% of reconstructed coarse mass. Nitrates were interpreted as sodium nitrate because MOUDI mass size distribution measurements showed very little ammonium in the coarse mode and very little sodium in the fine mode. Coarse nitrate contributed 8% of the coarse mass.

Table 3-2. Statistical summary of fine mass species concentrations. The parenthetical values are the fraction that each respective species contributes to reconstructed fine mass.

FINE MASS CONCENTRATIONS					
Variable (μg/m^3)	**Mean**	**Std Dev**	**Minimum**	**Maximum**	**Valid**
Fine Mass	6.85	4.33	0.04	19.22	116
Reconstructed FM	6.31	3.42	1.05	16.89	114
Ammoniated SO4	3.15 (0.50)	2.19	0.41	10.66	123
Sulfate Ion	2.48	1.79	0.30	8.57	123
$NaNO_3$	0.23 (0.04)	0.14	0.02	0.93	123
Nitrate Ion	0.17	0.10	0.02	0.68	123
OMC	1.34 (0.21)	0.78	0.13	5.10	116
LAC	0.15 (0.02)	0.10	0.00	0.52	116
SOIL	1.45 (0.23)	1.74	0.03	8.63	116

Table 3-3. Statistical summary of coarse mass concentrations.

COARSE MASS CONCENTRATIONS					
Variable (μg/m^3)	**Mean**	**Std Dev**	**Minimum**	**Maximum**	**Valid**
Coarse Mass	4.69	4.31	0.00	29.01	72
Reconstructed CM	5.42	4.54	0.00	32.02	72
Sulfate Ion	0.36	0.52	0.00	2.76	72
Ammoniated Sulfate	0.45 (0.08)	0.68	0.00	3.59	72
Nitrate Ion	0.30	0.26	0.00	1.32	72
$NaNO_3$	0.41 (0.08)	0.35	0.00	1.81	72
OMC	1.58 (0.29)	1.13	0.00	7.14	72
SOIL	2.90 (0.53)	3.27	0.00	23.66	72
LAC	0.09 (0.02)	0.09	0.00	0.31	72

3.5 Comparison between Measured and Modeled Dry Fine Mass Scattering Coefficients

Because little difference, on the order of 10% or less, [*Ouimette and Flagan,* 1982; *Sloane,* 1986; *Malm and Kreidenweis,* 1997; *Malm et al.,* 2000b] has been found between scattering predicted by internally and externally mixed aerosol models, the following externally mixed model was used to estimate reconstructed particle scattering:

$$b_{scat} = (e_{sf})f_s(RH)[Ammoniated\ SO_4] + (e_{nf})f_n(RH)[NaNO_3] + (e_{ocmf})f_{ocm}(RH)[OMC] + (e_{soilf})[SOIL]. \quad (3\text{-}2)$$

The brackets indicate the species concentration, while e_{sf}, e_{nf}, e_{ocmf}, and e_{soilf} refer to the fine or $PM_{2.5}$ dry mass scattering efficiencies of ammoniated sulfate, sodium nitrate, organic carbon, and soil mass concentrations, respectively, and the f(RH) term is the scattering enhancement term associated with particle growth as a function of relative humidity as obtained from the thermodynamic and Mie scattering models.

Average dry mass scattering efficiencies, e_{sf}, geometric mass mean diameters, d_g, and standard deviations, σ_g, of ammoniated sulfate were calculated using MOUDI data, corrected to physical diameter. These calculations are summarized in Table 3-4 and Figure 3-3. Figure 3-3 shows the relationship between these variables for the 41 MOUDI sample days. Some interesting relationships are readily apparent. As might be expected, as σ_g increased, e_{sf} decreased (Figure 3-3a). More interesting, at low mass levels (<2 μg/m^3) σ_g varied between about 1.4 and 2.5; however, at higher mass levels the variability in σ_g decreased (mass size distribution narrowed) and approached 1.4 at the highest mass loadings (Figure 3-3b). This narrowing of σ_g as mass levels increased was reflected in the relationship between mass and mass scattering efficiencies. Generally, as mass increased so did mass scattering efficiency (Figure 3-3c). Also, distributions with large mass mean diameters (>0.44 μm) had mass scattering efficiencies that varied from 2.5–4.0 m^2/g and σ_gs that varied between 1.4 and 2.5, while those size distributions with mass mean diameters less than about 0.28 μm had efficiencies of about 2.5m^2/g and σ_g of about 1.6 (Figures 3-3d and 3-3e). Furthermore, Figure 3-3f shows that at low mass loadings the mass mean diameter varies from 0.24–0.48 μm, while at higher mass loadings d_g varies less. These relationships were similar to those found by *Hand et al.* [2002] using measured number size distributions; however, those authors assumed that all aerosol species were internally mixed.

Table 3-4. Statistical summary of size and scattering properties of $PM_{2.5}$ ammoniated sulfate mass. The number of data points was 41.

Variable	Mean	Std Dev	Minimum	Maximum
Ammoniated Sulfate Mass ($\mu g/m^3$)	3.65	3.31	0.50	12.04
d_g (μm)	0.38	0.05	0.26	0.47
σ_g	1.88	0.26	1.50	2.42
e_{sf} (m^2/g)	3.15	0.43	2.42	4.06

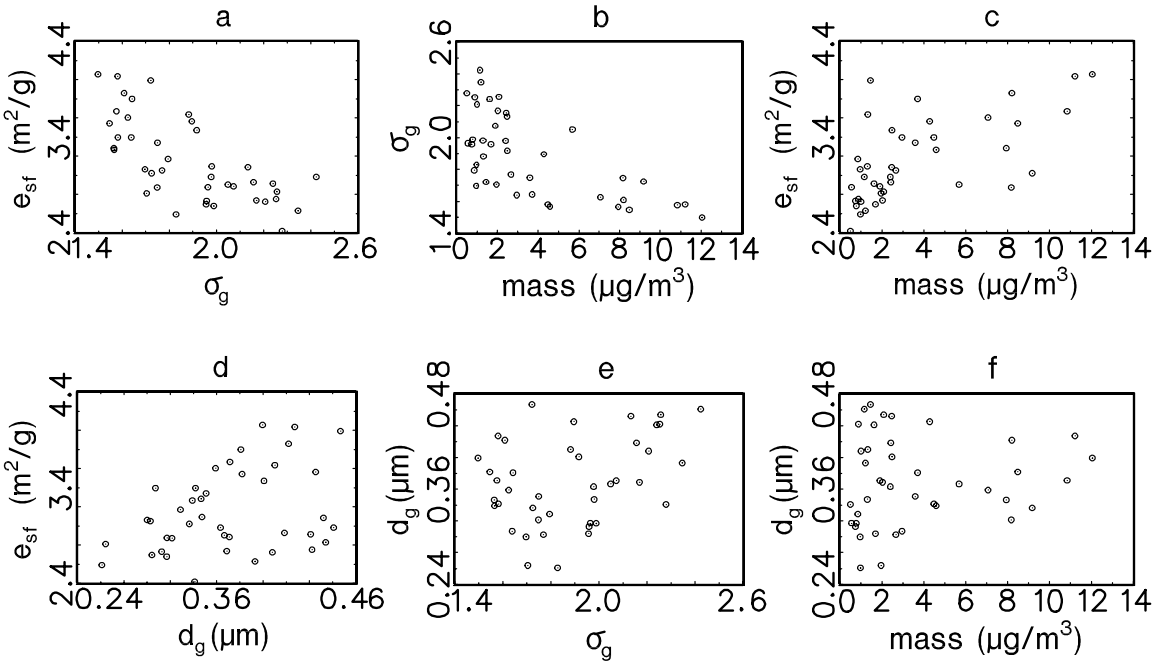

Figure 3-3. Multiple scatter plots of ammoniated sulfate dry mass scattering efficiency (eff_d), geometric mass mean diameter (d_g), geometric standard deviation (σ_g), and ammoniated sulfate mass for the 41 days on which MOUDI size mass size distribution were made.

Because mass size distribution data were only available on 41 out of 104 sampling periods, an effort was made to capture the general relationships presented in Figure 3-3 and apply them to the full dataset. To account for the daily variations in the mass scattering efficiency for ammoniated sulfate, e_{sf} was varied as a function of ammoniated sulfate mass using 2.4+0.42*[ammoniated sulfate] below ammoniated sulfate mass equal to 2.0 $\mu g/m^3$ and 3.2+0.07*[ammoniated sulfate] above 2.0 $\mu g/m^3$. Mass scattering efficiencies assumed for organics and soil were 4.0 and 1.0 m^2/g, respectively [*Trijonis et al.,* 1990; *Malm et al.,* 1994], while that used for sodium nitrate was 1.6 m^2/g. 1.6 m^2/g is an average of the 41 MOUDI samples, assuming that nitrate was in the form of sodium nitrate with its peak in the coarse fraction. The efficiency of the IMPROVE 2.5 µm cyclone inlet was used to apportion only the nitrate in particles smaller than 2.5 µm to $PM_{2.5}$ scattering.

Table 3-5 contains a summary of measured and reconstructed dry scattering coefficients along with the scattering coefficient contribution associated with each species. The difference between average measured and reconstructed dry scattering was 4%. The parenthetical values represent the fraction of scattering associated with each species. A linear regression of measured

scattering as the dependent variable and reconstructed scattering as the independent variable yielded an R^2=0.93 with a slope of 0.96±0.03 and an intercept term of 0.11±0.62. Thus we conclude that the model as given by equation 3-1 reproduced measured dry scattering quite well.

Table 3-5. Statistical summary of reconstructed and measured dry fine mass scattering and the scattering associated with each species assuming a model represented by equation 3-1. The parenthetical values are the fraction of scattering associated with each species. The number of data points was 64.

Scattering (Mm^{-1})	Mean	Std Dev	Minimum	Maximum
Reconstructed	18.45	12.49	3.56	63.17
Measured	17.73	13.30	2.27	53.76
Sulfate	12.31(0.67)	9.77	1.07	42.08
Nitrate	0.26(0.01)	0.12	0.11	0.84
Organics	5.11(0.28)	3.35	0.52	20.41
Soil	0.77(0.04)	0.96	0.06	3.73

3.6 Comparison of Equilibrium Models

To represent atmospheric aerosol water contents as functions of relative humidity, two different thermodynamic models were explored for use in this work: AIM [*Clegg et al.,* 1998b] and ISORROPIA [*Nenes et al.,* 1998]. AIM and ISORROPIA can be run in various configurations that predict the equilibrium state of the system, including partitioning of species between the liquid, solid, and gaseous phases. Here we specified the mass concentrations of aerosol-phase species based on the filter measurements described earlier, and used the models only to compute the equilibrium aerosol water contents over a range of relative humidity (RH) from 20–90%.

The version of AIM used here considers systems composed of sodium-ammonium-chloride-sulfate-nitrate-water at 298.15 K. Equilibrium states are calculated using Gibbs' energy minimization, using a global search to find the minimum. The calculations of activities of water and ions present in the aqueous phase utilize the Pitzer, Simonson, and Clegg equations [*Pitzer and Simonson*, 1986; *Clegg et al.,* 1992]. The model considers 19 possible solid phases and is valid for concentrations to saturation with respect to the solid phases. Thus, it is not generally applicable to supersaturated, metastable solutions, although the user is permitted to run in this mode, which suppresses precipitation of solids. We checked the metastable water contents against the predictions of an alternative version of AIM [*Clegg et al.,* 1998a] that is more applicable to those cases and found the differences in aerosol water content to lead to negligible differences in predicted ratios of wet to dry scattering (f(RH)) for the species considered in this report. The composition dependence of the deliquescence relative humidity is included in the formulations while the efflorescence behavior is not.

ISORROPIA considers the same chemical components as AIM, but only allows nine possible solid phases. The solution scheme differs from that used in AIM in that fifteen equilibrium reactions are solved, using a fast and stable solution algorithm [*Nenes et al.,* 1998] and permitting only certain aerosol and solution compositions depending on the ratios $R_{Na} = [Na^+]/[SO_4^{2-}]$ and $R_{SO4} = \{[Na^+]+[NH_4^+]\}/[SO_4^{2-}]$. These ratios are used to define combinations of sulfate-rich, sulfate-poor, sodium-rich, and sodium-poor domains, along with the appropriate subsets of possible solid and ionic species. This method is called "divided composition domain" [e.g., *Ansari and Pandis*, 1999]. Binary activity coefficients are calculated using the Kusik and Meissner relationships, whereas multicomponent activity coefficients are obtained from

Bromley's formula. The water content of aerosols is computed from the Zdanovskii-Stokes-Robinson (ZSR) relationship.

ISORROPIA differs from earlier equation-based models in that the mutual deliquescence relative humidity (MDRH) of mixtures of salts is considered. The value of the MDRH depends upon the mixture composition, but is always less than the minimum deliquescence humidity of any of the individual salts, so that the presence of an aqueous phase may be predicted by ISORROPIA where simpler models would predict a dry aerosol. It is important to note, however, that ISORROPIA uses data from the phase diagrams of *Potukuchi and Wexler* [1995a, 1995b] to determine the deliquescence RH (DRH); since not all possible compositions are represented, DRH behavior must be approximated from other combinations of species in such cases. The water contents in the MDRH regions are obtained by assuming a RH-weighted mean between the completely dissolved state for the most hygroscopic salt, and the completely dry state of the aerosol. This contrasts with the treatment in AIM, which solves the full minimization problem and thus can predict the gradual dissolution of solids.

ISORROPIA can also be used to compute water contents for the metastable phase. In this mode the formation of solid phases is suppressed, and calculations are made for the aqueous phase assuming the applicability of the necessary thermodynamic data at relative humidities below deliquescence. Since solid formation is not allowed for the metastable calculations, crystallization cannot be explicitly modeled. Instead, efflorescence behavior is approximated by assuming the applicability of crystallization points for ammoniated sulfate salts that are reported in the literature. Then, for calculations below these crystallization RHs, the thermodynamic data are not further extrapolated but instead a fixed, highly concentrated solution composition is assumed, leading to a discontinuity in predicted water contents that approximates the crystallization behavior.

The models were used to estimate D/D_o growth and f(RH) curves for each sampling period. For purposes of comparing these models, log normal aerosol mass size distributions were assumed for both the fine and coarse modes with geometric mass mean diameters of 0.38 and 3.0 μm, respectively, and a geometric standard deviation of 1.9 for both modes. These size parameters were derived from the average for the 41 MOUDI samples, as discussed further in the next section.

f(RH) curves were calculated for ammoniated sulfate assuming all sulfate occurred in the fine mode, while sodium nitrate was assumed to be in the coarse mode with size parameters discussed above. Because the nephelometers and fine particle samplers were operated with 2.5 μm cut points, the average mass size distribution for sodium nitrate (coarse mode) was multiplied by the sampler efficiency curve in an effort to estimate the f(RH) curves only for the fine component of the coarse mode.

Mean, maximum, and minimum differences between the metastable models are listed in Table 3-6. In about one-third of the cases, the metastable AIM f(RH) curve is well below (more than a few percent) that of ISORROPIA above the crystallization point, implying that the AIM model predicts less aerosol water than ISORROPIA. Below the crystallization point as estimated by ISORROPIA, the AIM model predicts some dissolved water and smoothly approaches zero as RH approaches zero. For a few cases the reverse was true. In general, for the metastable models, the maximum difference is always near the crystallization point with differences approaching zero for high RH values.

Table 3-6. Statistical summary of the mean percent difference between f(RH) curves in specific relative humidity ranges that were derived from aerosol growth predicted by the AIM and ISORROPIA models. The number of data points is 66.

	ISORROPIA minus AIM (metastable)		
RH	**Mean**	**Minimum**	**Maximum**
15-20	-0.06	-0.13	0.03
20-25	-0.10	-0.17	0.01
25-30	-0.14	-0.21	-0.01
30-35	-0.17	-0.25	-0.03
35-40	-0.01	-0.06	0.08
40-45	-0.01	-0.06	0.08
45-50	0.00	-0.06	0.07
50-55	0.00	-0.05	0.07
55-60	0.00	-0.04	0.06
60-65	0.01	-0.03	0.05
65-70	0.01	-0.04	0.05
70-75	0.02	-0.04	0.05
75-80	0.02	-0.03	0.05
80-85	0.03	-0.02	0.06
85-90	0.03	-0.01	0.07
90-95	0.00	-0.04	0.06

Generally, the deliquescence points predicted by the two models were the same within a few RH percentage points and, because the AIM model accounted for intermolecular interactions, the AIM model predicted deliquescence points which were less "abrupt" than ISORROPIA. Therefore, as with the metastable branch, the maximum difference between the models occurred at the deliquescence points.

3.7 Comparison of Measured and Theoretical Ambient (Wet) Fine Particle Scattering Coefficients

Table 3-7 summarizes the comparisons of measured and modeled ambient scattering coefficients as well as the contribution of each species to ambient scattering coefficients based on equation 3-1. Twenty-four hour average deliquescence and crystallization f(RH) values were calculated for ammoniated sulfate and sodium nitrate for each of the three equilibrium models described above by averaging hourly f(RH) values. As discussed above, it was assumed that all sulfate and ammonium were in the fine mode while nitrate was in the form of sodium nitrate and had a concentration peak in the coarse mode. The f(RH) of sodium nitrate was based on the fraction of this $NaNO_3$ mass in particles smaller than 2.5 μm. It was assumed that the aerosol composition and size distribution were constant over a 24-hour period, but the water contents varied hourly as a function of relative humidity. f(RH) for organics was assumed to be one, that is, they were assumed to be non-hygroscopic.

Table 3-7. Statistical summary of measured and reconstructed ambient fine mass scattering and scattering associated with each species. Ambient scattering predictions resulting from using different equilibrium model assumptions are also presented. The parenthetical values are the percent scattering associated with that species assuming the AIM metastable equilibrium model. The number of data points was 104.

Variable	Mean	Std Dev	Minimum	Maximum
RH (%)	44.63	11.68	20.92	74.38
Measured Ambient $b_{sp2.5}$ (Mm^{-1})	20.94	13.71	3.62	61.87
SOIL (Mm^{-1})	1.43(6.9)	1.78	0.06	8.63
OCM (Mm^{-1})	5.13(24.7)	3.74	0.60	26.67
Sulfate Ambient (AIM metastable) (Mm^{-1})	13.64(65.6)	10.89	1.77	52.16
Sulfate Dry (Mm^{-1})	9.11	7.49	1.02	40.13
Nitrate Ambient (AIM metastable) (Mm^{-1})	0.60(2.9)	0.38	0.14	1.99
Nitrate Dry (Mm^{-1})	0.34	0.19	0.11	0.99
Theoretical Dry $b_{sp2.5}$ (Mm^{-1})	16.01	10.66	3.24	67.47
Theoretical Ambient $b_{sp2.5}$ (AIM metastable) (Mm^{-1})	20.80	13.74	4.71	79.61
Theoretical Ambient $b_{sp2.5}$ (AIM deliquescence) (Mm^{-1})	18.33	12.58	3.68	74.05
Theoretical Ambient $b_{sp2.5}$ (ISO metastable) (Mm^{-1})	20.49	13.92	4.33	81.00

As pointed out above, ISORROPIA predicted almost no water below the crystallization point for the metastable branch, while under the "no solids" option the AIM model predicted some water below this point. Some examples of the effect that assuming water contents as given by either the crystallization or deliquescence branch had on predicted scattering are presented in Table 3-8. Average modeled dry scattering was 16.01 Mm^{-1} while average ambient scattering using the AIM metastable f(RH) curve and hourly values of relative humidity was 20.80 Mm^{-1}, which is nearly equal (1% difference) to the average measured ambient scattering value of 20.94 Mm^{-1}. Even though the AIM metastable branch ascribed some water to the aerosol below the ISORROPIA crystallization point, the average ambient scattering predicted using the ISORROPIA model was only about 1.5% less than the model using the AIM metastable solution assumptions. Using the AIM deliquescence branch yielded an ambient modeled value of 18.33 Mm^{-1} which was about 12% less than the average theoretical value using AIM metastable branch.

Table 3-8. Statistical summary of the difference between modeled and observed f(RH).

RH	Mean	Std Dev	Minimum	Maximum	N
20-25	1.37	3.33	-2.00	10.25	14
25-30	-0.48	3.03	-7.15	5.51	27
30-35	-0.51	3.42	-4.94	12.85	29
35-40	0.11	4.55	-6.64	18.07	29
40-45	-1.20	4.79	-7.78	16.87	29
45-50	-1.29	4.76	-7.97	15.28	29
50-55	-0.84	4.64	-7.04	15.50	29
55-60	-0.30	5.42	-11.36	18.02	29
60-65	0.44	3.50	-6.30	7.43	28
65-70	1.73	5.39	-10.30	16.08	29
70-75	2.32	6.03	-6.89	18.86	28

75-80	2.89	7.17	-8.19	19.98	27
80-85	3.82	10.00	-10.11	30.64	25
85-90	4.88	14.55	-12.15	43.07	20
90-95	-1.63	15.59	-17.24	36.33	15

Based on this analysis, the model using metastable water content from AIM to compute the f(RH) curves yielded the best overall fit to measured ambient scattering. An OLS estimate, with measured and theoretical ambient scattering and with the AIM metastable f(RH) curves as the dependent and independent variables, respectively, resulted in an R^2 of 0.90 with a slope of 0.99 ± 0.02. Using the ISORROPIA metastable f(RH) curves only marginally degraded the comparison between modeled and measured ambient scattering, while use of the deliquescence f(RH) curves significantly degraded the fit (>10%), implying that, in general, the ambient aerosols had been exposed to relative humidities greater than the deliquescence relative humidity and were on the crystallization branch of the curve. Despite the good agreement between predictions and measurements that was found with this approach, it is also possible that other species, namely organic carbon compounds, were responsible for the retention of water that we attribute to the metastable water associated with inorganic compounds. We explore this possibility further in the following sections.

Assuming the AIM metastable state water content and the external mixture model, sulfates and organics contributed 65.6 and 24.7 % of $PM_{2.5}$ ambient scattering while soil contributed 6.9% and nitrates 2.9%. The difference between theoretical ambient and dry $PM_{2.5}$ scattering was about 4.8 Mm^{-1} or 19%, implying that despite the study average relative humidity of only 44%, 19% of ambient scattering was associated with sulfate and nitrate water absorption. Ambient sulfate scattering was 33% greater than dry scattering while $PM_{2.5}$ nitrate scattering, which was small compared to sulfate scattering, increased by 43%. Also, 19% was close to the scattering difference measured by the ambient and dry $PM_{2.5}$ nephelometers. It should be noted that the calculations presented in Table 3-8 are for 104 sampling days while concurrent ambient and dry nephelometer scattering data were available on only 54 days.

The "best fit" model assumed only inorganic salts were hygroscopic and that their hygroscopicity was described by the AIM metastable f(RH) curve. These assumptions can be further explored by comparing measured f(RH) curves to those theoretically estimated using the model described by equation 3-1 in combination with f(RH) curves associated with various equilibrium models and the assumption concerning the hygroscopicity of carbonaceous material.

3.8 Comparison of Measured and Theoretical Scattering Coefficients as Functions of Relative Humidity

To estimate f(RH) curves, one Radiance Research nephelometer was operated continuously in a dry mode while a second nephelometer was scanned through relative humidities that ranged from about 20% to 90%. The ambient aerosol was first dried from ambient relative humidity, usually about 40%, to relative humidities less than ambient and then humidified to humidities greater than ambient. Figure 3-4 shows a typical relative humidity “scan” (Julian Day 284) with the dotted and solid lines representing the dry and relative humidity dependent nephelometers, respectively, and the inset showing the resultant f(RH) curve. The minute to minute changes in aerosol concentration as represented by the dry scattering were quite variable. In this example, during the first half of the day aerosol scattering was approximately 10 Mm^{-1}, while during the second half aerosol scattering was more variable and on the average

about 30 Mm^{-1}. During the scan the dry scattering varied between 20 and 30 Mm^{-1}. The ambient f(RH) curves were then calculated by dividing the instantaneous variable RH b_{scat} by the instantaneous dry scattering coefficient $b_{scat}(RH)/b_{scat}(RH_{min})$. Not accounting for the short term temporal variability of dry scattering would introduce significant error into the f(RH) determination.

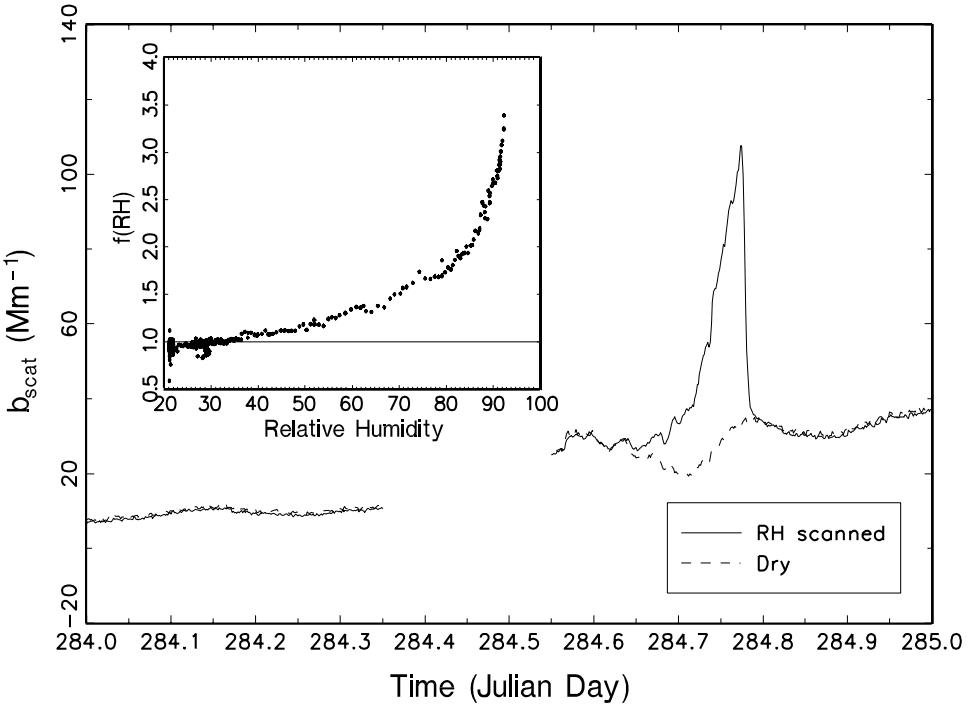

Figure 3-4. An example of dry and relative humidity ramped scattering coefficient for Julian Day 284. The hours showing missing data correspond to a calibration period.

Operating the humidograph in this configuration could have resulted in: 1) observation of crystallization if the ambient aerosol had been exposed to relative humidities above its deliquescence point and the crystallization point was below the ambient relative humidity, 2) observation of deliquescence if the aerosol had not been exposed to humidities above the deliquescence point and the ambient relative humidity was below the deliquescence point, or 3) observation of a continuous f(RH) curve over the entire RH range.

Because aerosol speciation data were collected using filter measurements that aggregated aerosol concentration into 24-hour averages, direct comparison of 24-hour theoretical f(RH) curves based on the use of equation 3-1 to measurements of f(RH) that were made on the time scale of a few hours was problematic. *Hand et al.* [2002] reported dry scattering estimates derived from dry number size distribution measurements which show that fine particle scattering and aerosol concentration track each other (R^2=0.97) on time scales on the order of minutes, suggesting that sulfate and organic mass concentrations, the primary constituents of the fine mode, varied temporally in proportion to dry scattering. Furthermore, *Hand et al*. [2002] reported a high degree of correlation between dry scattering and highly time-resolved sulfate measurements. An OLS regression between the two variables resulted in an R^2=0.86. Therefore, to account for the small time scale variation (<1 hour), the 24-hour average sulfate and organic mass concentrations were temporally scaled to the dry nephelometer data such that the sulfate

and organic scaled data integrated to the 24-hour average concentrations but reflected short-time scale fluctuations.

The dry and relative humidity scanned $PM_{2.5}$ nephelometer measurements were simulated using equation 3-1 with f(RH)=1 for organics and with the temporally adjusted sulfate and organic data on a two minute by two minute basis. Soil and nitrate mass concentrations were not adjusted for short term temporal fluctuations, and the mass scattering efficiencies applied for these species were those determined for that fraction of their masses found in the fine aerosol mode. Theoretical ambient f(RH) curves were then calculated using $b_{scat}(RH)/b_{scat}(RH_{min})$.

Forty-four f(RH) scans were made between Julian Day 238 and 301. The average measured and calculated f(RH) values are summarized in Table 3-8. Figures 3-5, 3-6, 3-7, and 3-8 show four general types of behavior of ambient and theoretical f(RH) curves. The solid line in each figure is a running three point average of two minute data while error bars are plotted every 5^{th} data point. The uncertainty associated with relative humidity is calculated from the uncertainty inherent in the RH sensor (±2%) [*Rotronic Instrument Corp*., 1998] and from the uncertainty in RH caused by a change in temperature inside the nephelometer. The exact RH inside the nephelometer is unknown; however, it is bounded by the RH at the inlet and outlet of the instrument. At low RH this difference is less than 1% (as estimated from a temperature difference of 0.3 ^{o}C), while at 90% RH the difference in RH is on the order of 2%. Therefore the combined uncertainty is on the order of ±3% at high RH values and less at lower humidities. To be conservative, the maximum uncertainty of ± 3% is presented in Figures 3-3 through 3-6. The uncertainty in f(RH) is based on a nephelometer measurement uncertainty of 5% [*Molenar,* 1997].

The dotted and dashed lines correspond to various model calculations. There were five days where there was a clear deliquescence point; one day, Julian Day 275, is shown in Figure 3-5. The model calculations shown in Figure 3-5 were based on the AIM ammoniated sulfate deliquescence growth for an ammonium to sulfate ratio of 1.74. There were two modeled deliquescence points at about 68% and 75% which correspond closely to the measured deliquescence points. On Julian Day 301 the ammonium to sulfate molar ratio was 1.8, and again the modeled and measured deliquescence points match within a few RH percentage points. However, on three other days when the ammonium to sulfate ratio was measured to be near two (fully neutralized), the model-predicted deliquescence points, as expected, were near 80% while the measured deliquescence points were at approximately 65–70% relative humidity. Undoubtedly the hygroscopic salt was not pure ammonium sulfate. On one of the three days MOUDI mass size distribution data were available and did show 1.1 and 0.22 nanomoles m^{-3} of K^+ and Ca^{++} in addition to 43.0 nanomoles m^{-3} of NH_4^+ and 22.2 nanomoles m^{-3} of SO_4^{2-}. However, neither the ISORROPIA nor AIM models incorporate K^+ or Ca^{++} in the equilibrium calculation. The average mean difference relative to the measured f(RH) curve above 80% was 17%.

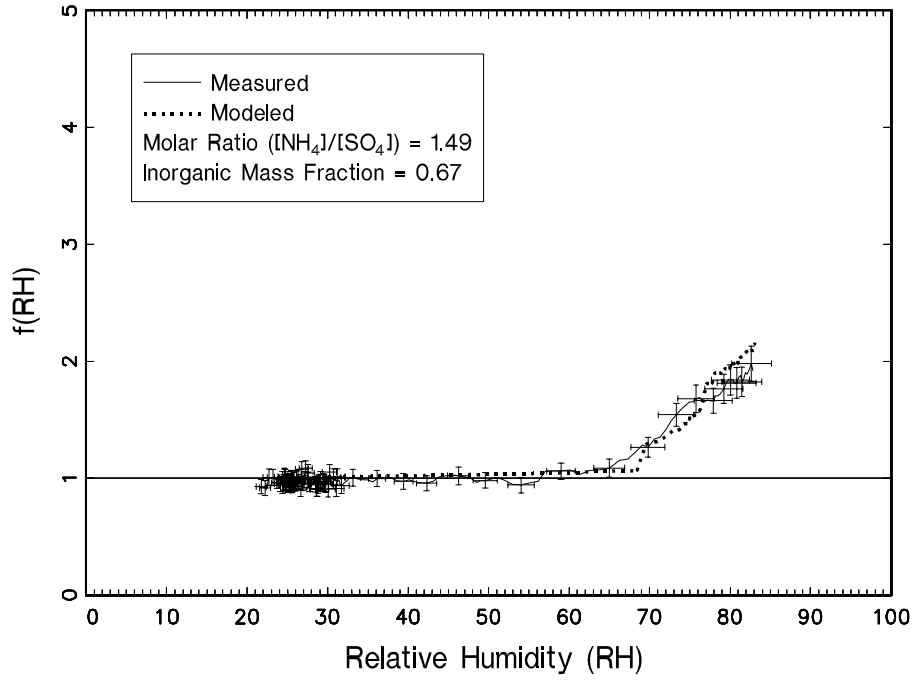

Figure 3-5. An example of measured and modeled f(RH) curves where deliquescence was observed for Julian Day 275. The molar ratio of ammonium to sulfate was 1.49 and the inorganic (SO_4+NH_4+NO_3+Na) fine mass fraction was 0.67.

Figure 3-6 shows one of five days, Julian Day 286, where there are intimations of observed crystallization. Also shown in Figure 3-6 is the modeled f(RH) curve based on the ISORROPIA metastable water absorption curve. There was close agreement between the predicted and measured f(RH) curves, and the measured and modeled crystallization points agreed well. The ISORROPIA model was used because it predicted a crystallization point, whereas the AIM model, exercised in the metastable configuration, did not. On all five days the measured and predicted crystallization points agreed to within a few RH percentage points and the f(RH) curves agreed well above the crystallization points. The average difference for the five days between measured and theoretical f(RH) curves above 35% was less than 1%.

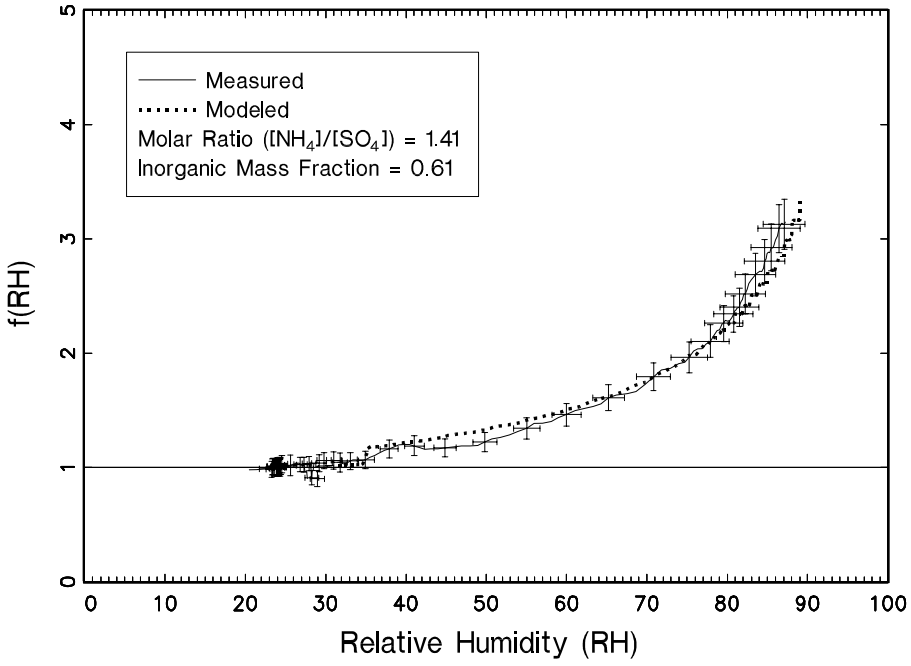

Figure 3-6. An example of measured and modeled f(RH) curves for a day where crystallization was observed. The molar ratio of ammonium to sulfate was 1.41 and the inorganic (SO_4+NH_4+NO_3+Na) fine mass fraction was 0.61.

Figure 3-7, measured on Julian Day 238, represents a third type of f(RH) curve of which there are also five cases. The measured and calculated f(RH) curves agreed well above the deliquescence point; however, below the deliquescence point the measured curve did not fall on either the ascending or descending branch of the growth curve but varied smoothly between the two points and exhibited neither deliquescence nor crystallization. On all five days water uptake began at relative humidities of about 30–35%. Above the deliquescence point (80%) the average difference between observed and modeled f(RH) for all five days was again about 1%.

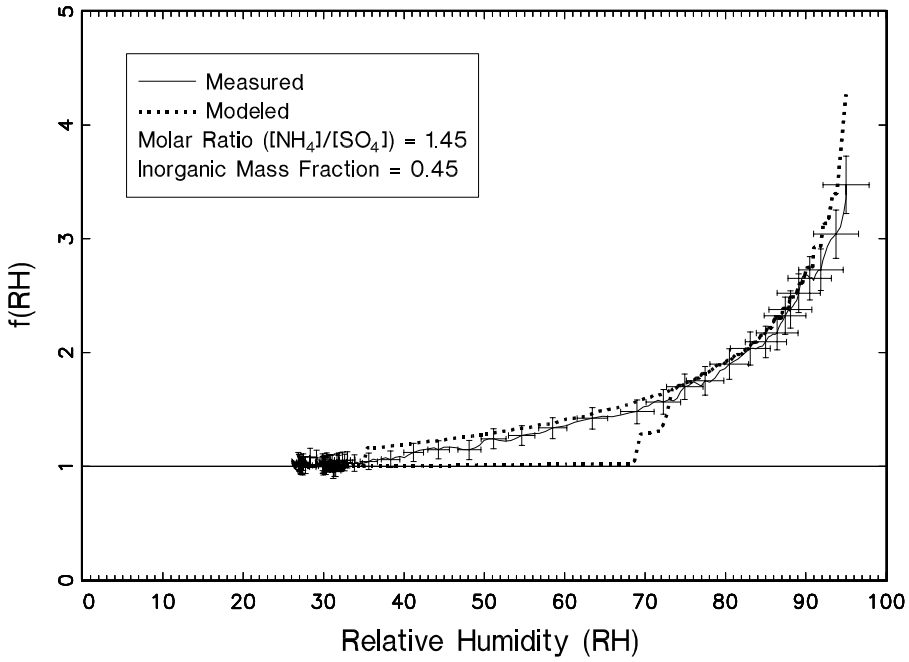

Figure 3-7. An example of a measured f(RH) curve where neither deliquescence or crystallization was observed. The modeled f(RH) curves for both deliquescence and crystallization are shown for reference. The molar ratio of ammonium to sulfate was 1.45 and the inorganic (SO_4+NH_4+NO_3+Na) fine mass fraction was 0.45.

Figure 3-8, measured on Julian Day 242, shows an example of the predominant type of f(RH) pattern of which there were 29. The 29 measured f(RH) curves again were continuous, indicating no crystallization or deliquescence from approximately one to their respective maximum values. The two theoretical f(RH) curves in Figure 3-8 are based on AIM and ISORROPIA derived metastable growth curves. The relative humidity scan for the measured f(RH) curve was initiated at a relative humidity between 26–28%, which was below the crystallization point predicted by ISORROPIA. Therefore the dry scattering coefficient based on the ISORROPIA model at 26% RH did not have any contribution due to water, while the dry scattering estimate based on AIM did. Therefore, when estimating f(RH) using $b_{scat}(RH)/b_{scat}(RH=26\%)$, the AIM based f(RH) curve was a significant fraction lower than the ISORROPIA based f(RH) curve because the AIM based $b_{scat}(RH=26\%)$ was larger than ISORROPIA. The measured and AIM based f(RH) curves were in better agreement than assuming a "dry" aerosol at 26–28%, suggesting that the aerosol was not "dried out" at the beginning of the relative humidity ramp.

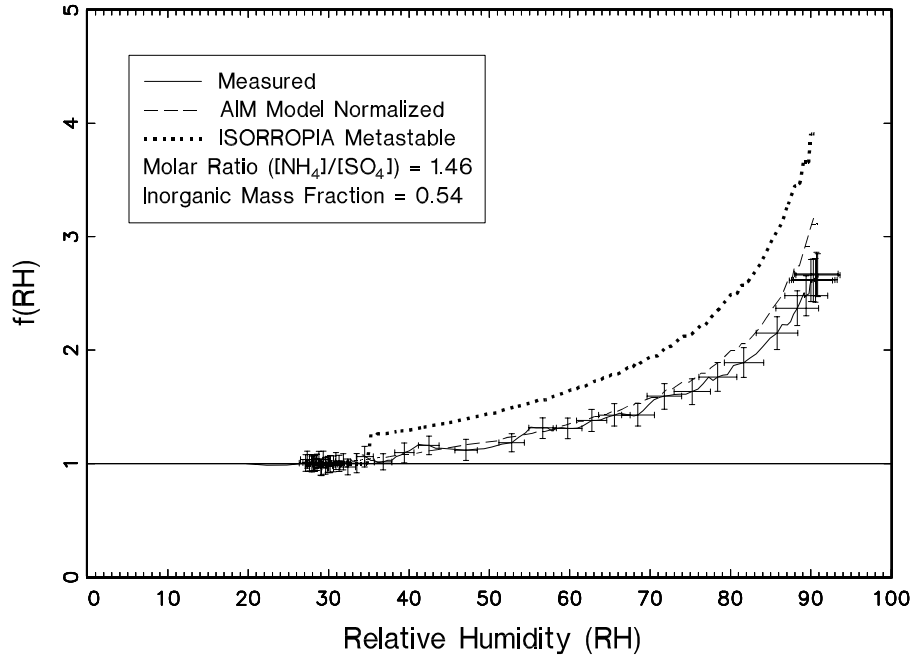

Figure 3-8. An example of measured f(RH) curve showing the over-prediction of modeled f(RH) when it was assumed the aerosol was dry below 30% RH and the modeled f(RH) when it assumed an amount of water absorption predicted by the AIM equilibrium model at 30% RH. The molar ratio of ammonium to sulfate was 1.46 and the inorganic (SO_4+NH_4+NO_3+Na) fine mass fraction was 0.54.

Table 3-8 summarizes percent differences between measured and modeled f(RH) for the 29 days in increments of 5% relative humidity. The mean difference varied from a low of -1.3% to 4.9% at 85–90% relative humidity range. The average difference above 35% relative humidity between measured and predicted f(RH) curves over all 29 days was on the order of 1%. The highest organic mass concentrations of 3.8(0.34), 5.1(0.30), and 3.2(0.27) $\mu g/m^3$ occurred on Julian Days 243, 244, and 245, respectively. The parenthetical values are the fraction of fine mass attributed to organics. The average difference, with f(RH)=1 for carbonaceous material and soil, between measured and modeled f(RH) over relative humidity ranges from 35–95% on those three days was 1.5%.

There were four days where the measured f(RH) curves were 50–60% greater than the theoretical curves at 90% relative humidity. The average difference above 80% relative humidity for the four days was 59%. Two of those days exhibited crystallization in the 35% RH range which was also predicted by the ISORROPIA model, one day showed clear deliquescence at 55% while the model predicted 65%, and one day exhibited continuous growth. All of these days were among those days with the lowest aerosol concentrations. Organics and ammoniated sulfate were less than about 1 $\mu g/m^3$ which corresponds to a dry scattering coefficient of only about 5–8 Mm^{-1}. Therefore the measured f(RH) curve reflected increased measurement uncertainty. Also, at these low concentrations, the positive organic carbon artifact was on the order of the ambient organic concentration which can result in a positive or negative bias of reported organic concentrations, depending on whether the blank correction is too large or too small. Overestimation of organic aerosol (underestimation of organic blank correction) would serve to suppress the theoretical f(RH) curve. Another possibility is that on those four days organics absorbed about as much water as the inorganic species.

3.9 Statistical Estimates of Species Specific f(RH) Curves

The amount of scattering at a specific relative humidity associated with individual species can be estimated statistically using:

$$b_{scat,water}(RH) = a_o + a_1[Ammoniated \quad SO_4] + a_2[OMC] + ... + a_n[Other\ Species] \qquad (3\text{-}3)$$

where $b_{scat,water}(RH)$ is scattering due to water at some RH, $a_1=e_s[f(RH)_s-1]$, $a_2=e_{oc}[f(RH)_{oc}-1]$, and so forth. a_o is interpreted as scattering associated with residual water or it can be set to zero, implying that all water scattering is associated with the aerosol species explicitly included in the equation. e_s and e_{oc} are the average dry mass scattering coefficients associated with sulfates and organics, respectively. $b_{scat,water}(RH)=b_{scat}(RH)-b_{scat,dry}$ is calculated on a 24-hour sampling-period-by-sampling-period basis by estimating $b_{scat}(RH)$ using measured $b_{scat}(RH)/b_{scat,dry}$ ratios and then differencing scattering at that RH and at the minimum RH. Equation 3-3 can then be solved at specific humidities using OLS regressions with or without an intercept (with or without residual water). It is emphasized that the resulting f(RH) curves are, except for the assumed dry mass scattering coefficients, based solely on measured data.

Figure 3-9 is a plot of the f(RH) curves derived from the OLS analysis without an intercept term assuming $e_s=3.2\pm0.4$ m^2/g and $e_{oc}=4.0$ m^2/g. The error bars represent the standard error of the regression coefficients, while the rectangle enclosing each error bar is associated with the standard deviation of the theoretically calculated dry mass scattering efficiencies (±0.4 m^2/g) that are based on measured sulfate size distributions.

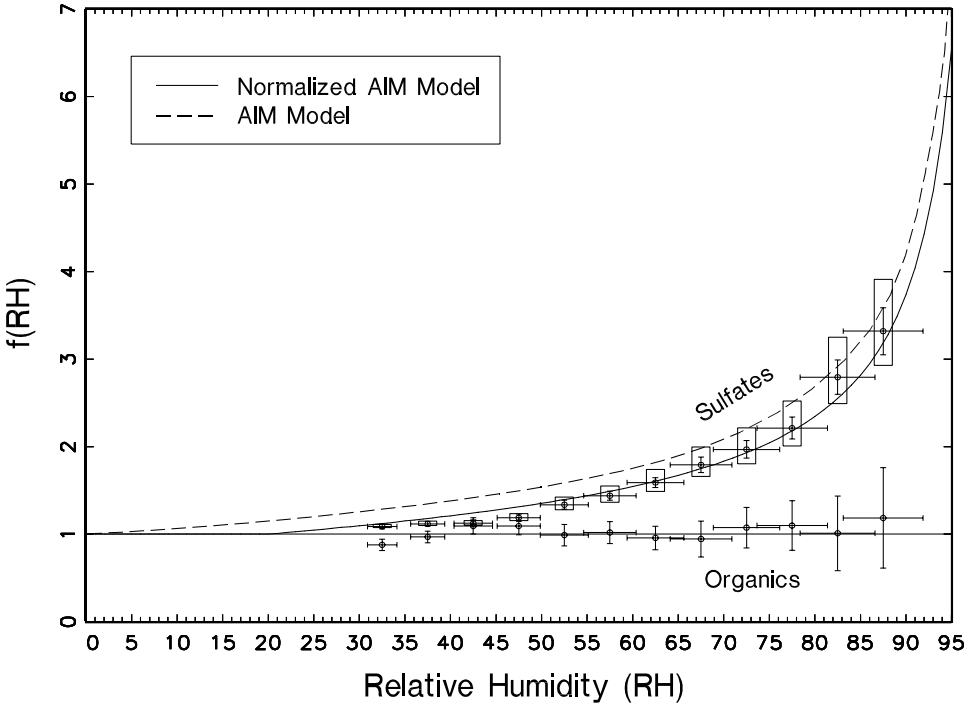

Figure 3-9. The f(RH) values for ammoniated sulfate and organics derived from a statistical model whose only inputs were measured scattering associated with absorbed water and ammoniated sulfate and organic mass concentrations. Also shown for reference are the average f(RH) curves derived from the AIM equilibrium modeled metastable D/D_0 curves without normalization and with normalization to 20% relative humidity.

The sulfate regression coefficient was significant at less than 1% at all humidities greater than 30%, while the regression coefficient associated with any other species was not statistically significant. Moreover, because the intercept term was not statistically different from zero, the results presented in Figure 3-9 were with a_o set equal to zero. The R^2 values varied between a low of 0.14 at RH=30% to above 0.80 for RH values above 50%. Even though the organic regression coefficients were not statistically significant, the implied organic f(RH) curve was included for reference. Notice that the average f(RH) data points shown in Figure 3-9 reflect some water absorption at 32% relative humidity and possible deliquescence at about 45% relative humidity and a second deliquescence point that occurred in the 75–80% range. The dotted line corresponds to the average f(RH) calculated directly from the AIM metastable growth curve while the solid line is the f(RH) normalized to 20%. The f(RH) curve, which is based on the normalized AIM metastable growth curve, approximates the statistically derived growth curve quite well.

These results are consistent with the modeled f(RH) curves where good agreement between modeled and measured f(RH) was achieved by assuming organics did not absorb water and that on most days the aerosol contained some water at relative humidities in the 20–30% range. The water retention at these low relative humidities was consistent with the amount of water predicted by the AIM equilibrium model under conditions where solids were not allowed to form (metastable state). In the statistical model no prior assumptions were made about the hygroscopicity of various aerosol species. The analysis produced an f(RH) function for ammoniated sulfate that was nearly identical to the average f(RH) curve derived from the AIM metastable growth curves that were normalized to 20% relative humidity (f(RH)normalized= f(RH)/f(20%)) and an f(RH)≈1 for organics and soil).

3.10 Summary of Particle Scattering and Absorption Estimates

The following equation is used to estimate reconstructed particle extinction:

$$b_{ext} = (e_{sf})f_s(RH)[Ammoniated\ SO_4] + (e_{nf})f_n(RH)[NaNO_3] + (e_{ocmf})[OMC] + (e_{soilf})[SOIL] \quad (3\text{-}4)$$
$$(e_{sc})f_s(RH)[Ammoniated\ SO_4] + (e_{nc})f_n(RH)[naNO_3] + (e_{ocmc})[OMC] + (e_{soilc})[SOIL] + 10[lacf + lacc].$$

The brackets indicate the species concentration, while e_{sf}, e_{nf}, e_{ocmf}, and e_{soilf} refer to the dry mass scattering efficiencies of ammoniated sulfate, ammonium nitrate, organic mass, and soil mass concentrations, respectively. The second set of these same variables refers to coarse mass efficiencies. $f_s(RH)$ and $f_n(RH)$ refer to the enhancement factors for sulfates and nitrates, respectively. The f(RH) curves for sulfates and nitrates were calculated using AIM derived growth curves while the f(RH) for organics was assumed to be one.

The fine and coarse scattering/absorption values are summarized in Table 3-9. The first and second rows are the average measured and reconstructed total particle extinction. The following four rows are measured and estimated coarse and fine particle scattering while remaining rows are the scattering associated with each fine and coarse species and total absorption (fine + coarse). The parenthetical values are the fraction of total particle extinction associated with the respective species. The estimated or modeled extinction is within 3% of measured while estimated coarse and fine particle scattering are within 12% and 2% of measured coarse and fine particle scattering. Coarse and fine particle scattering contribute 4.4 Mm^{-1} and

22.4 Mm^{-1}, or about 15% and 77%, respectively, to extinction while coarse plus fine particle absorption adds another 2.5 Mm^{-1} or 9%. The fractional contribution of fine plus coarse particle sulfates, nitrates, organics, and crustal material is 58.0%, 2.6%, 24.9%, and 7.3%, respectively. 8.6% of total extinction is linked to absorption with 38% associated with the coarse mode leaving 62% of absorption linked to the fine mode.

Table 3-9. Statistical summary of extinction and the contribution of each species to extinction. The parenthetical values are the fraction that each species contributes to extinction.

Variable (Mm^{-1})	Mean	Std Dev	Minimum	Maximum	Valid
b_{ext}	30.26	20.11	3.58	71.96	60
Reconstructed b_{ext}	29.31	18.58	7.46	83.95	60
$b_{sp,coarse}$	4.99	5.14	-4.78	17.65	60
Reconstructed $b_{sp,coarse}$	4.37 (14.9)	2.74	0.00	16.29	60
$b_{sp,2.5\mu m}$	22.75	16.31	4.49	61.87	60
Reconstructed $b_{sp,2.5\mu m}$	22.41 (76.5)	16.60	5.05	75.20	60
SO_4 $b_{sp,coarse}$	0.69 (2.4)	1.36	0.00	7.33	60
NO_3 $b_{sp,coarse}$	0.38 (1.3)	0.35	0.00	1.98	60
OCM $b_{sp,coarse}$	1.82 (6.2)	1.02	0.00	4.17	60
Soil $b_{sp,coarse}$	1.48 (5.1)	1.13	0.00	5.40	60
SO_4 $b_{sp,2.5\mu m}$	16.29 (55.6)	14.17	2.44	54.51	60
NO_3 $b_{sp,2.5\mu m}$	0.37 (1.3)	0.20	0.12	1.30	60
OCM $b_{sp,2.5\mu m}$	5.11 (17.4)	3.26	0.52	20.41	60
SOIL $b_{sp,2.5\mu m}$	0.64 (2.2)	0.78	0.06	3.62	60
Fine + Coarse b_{abs}	2.52 (8.6)	1.41	0.64	6.51	60

It is interesting to point out that even though crustal material makes 54% of the coarse mass on a scattering basis, it contributes less to extinction than coarse organics because organics have a mass scattering efficiency which is twice that of crustal material.

3.11 Temporal Variation in the Particulate and Light Extinction Budgets

The previous discussion examined the particulate chemical composition and contribution to light extinction averaged over the BRAVO time period. It is also instructive to examine their temporal variability. The daily fine mass species used to generate Table 3-2 are plotted in Figure 3-10. Figure 3-11 presents the daily ambient light extinction budgets during the BRAVO period.

The light extinction budgets require having valid contributions from all of the major fine and coarse aerosol measurements. However, only 60 out of 123 days had all of the necessary data (Table 3-9). The loss of more than half of the days was primarily due to missing coarse particle data. To fill in these missing days, coarse scattering was estimated using several methods. If all extinction, scattering, and absorption measurements were available, then coarse extinction was estimated by: $b_{ext,coarse} = b_{ext} - b_{sp,2.5\mu m} - b_{abs,2.5\ \mu m}$. $b_{abs,2.5\ \mu m}$ was estimated by multiplying the fine light absorbing carbon concentration by an absorption factor of 10 m^2/g. Coarse extinction was estimated this way for 78% (96/123) of the BRAVO study days. When any of these measurements were missing, coarse extinction was reconstructed from the coarse particle measurements by summing the scattering due to coarse sulfates, nitrates, soil, and organic and coarse light absorbing carbon. This method was used for 10% (12/123) of the coarse extinction values. Occasionally, total coarse mass was available, but some of the individual species concentrations, usually carbons or ions, were missing. In those cases, coarse extinction

was estimated by $b_{ext,coarse}$ = 0.6 m^2/g [Coarse mass] * (1.1), where 0.6 m^2/g is the estimated scattering efficiency of coarse mass and 1.1 is a factor to account for the additional light extinction due to coarse absorption. The 1.1 factor is the median of the coarse extinction divided by the coarse scattering for days when those values were available. This method was used for 5% (6/125) of the values. The remaining days were filled in by combining the available light scattering and absorption measurement and aerosol data and ratios of the missing and available components from the previous day.

As shown in Figure 3-10, there is a distinct difference in the chemical composition of the fine mass in the first and second half of the BRAVO study. From July 1–August 15, the fine mass is primarily composed of ammonium sulfate (35%), soil (35%), and organics (20%). In the second half of the study, post-August 15, the fine mass is primarily composed of sulfate (60%) and organics (20%) with soil comprising only 15%. In both time periods of the study, sulfate was the largest contributor to b_{ext}, accounting for 35% of the particulate b_{ext} in the first half of the study and 50% in the second half (Figure 3-11). Organic carbon accounted for 20% and 18%, and coarse mass accounted for about 30% and 20% of the particulate light extinction in the first and second half of the BRAVO study, respectively. On the haziest 1/5th of the days sulfate compounds accounted for about 55% of the particulate b_{ext} and organics about 15%. The lower contribution of organics and the fact that they have a potentially large contribution from smoke and other natural sources [*Collet et al.*, 2001; *Brown et al.*, 2002] lead us to concentrate on understanding the source attribution of sulfate.

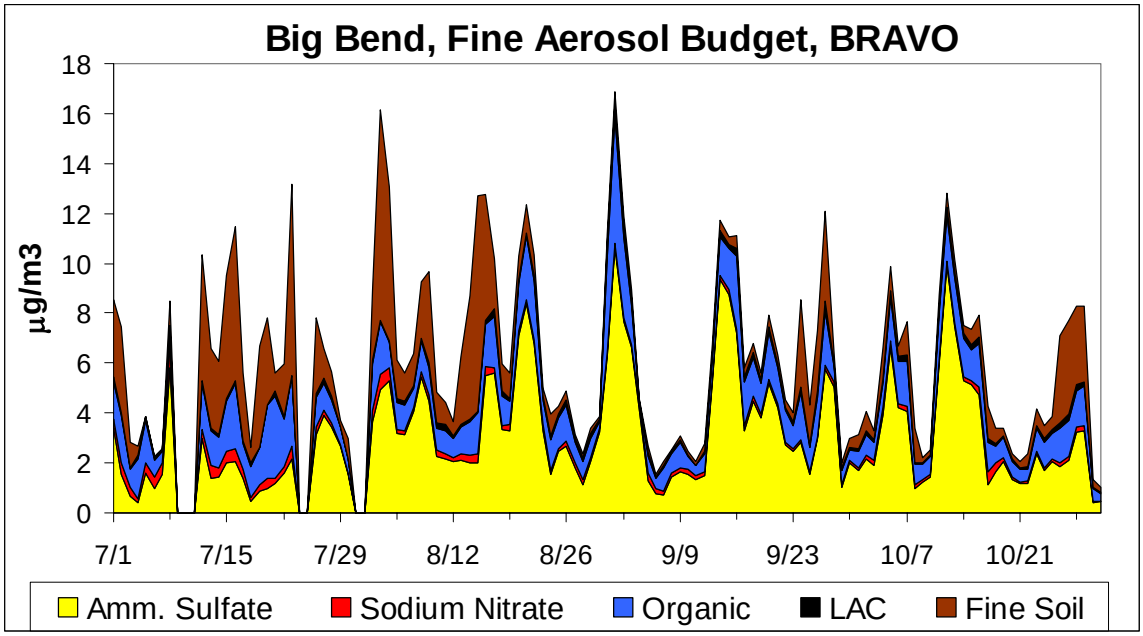

Figure 3-10. Big Bend's daily fine particulate mass budget during the BRAVO study.

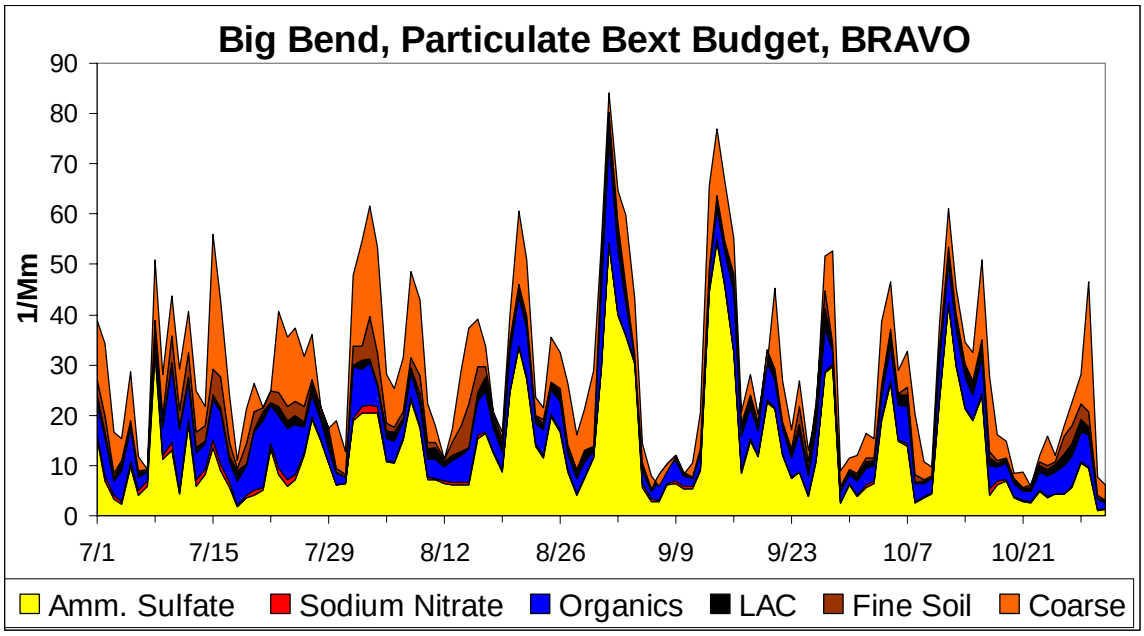

Figure 3-11. Big Bend's particulate light extinction budget during BRAVO.

3.11.1 Big Bend's Average Seasonal Light Extinction Budget

The BRAVO period can be put into a larger climatological context by examining Big Bend's extinction budget over a long time period. Figure 3-12 shows the five-year (1998 through 2002) light extinction budget from measurements made every three days at Big Bend National Park in the IMPROVE monitoring network. The contribution to b_{ext} of each particulate component was calculated based upon the regional haze guidance document [*U.S. Environmental Protection Agency*, 2003a], but the increase in scattering due to particle growth from water, i.e., f(RH), was estimated using the measured relative humidity at Big Bend.

In general, there are two periods of high haze at Big Bend National Park, one in spring when particulate sulfate and carbonaceous compounds contribute in similar amounts to haze, and another in late-summer/fall when particulate sulfate compounds are the largest contributors to haze. Similar to the BRAVO period, the particulate sulfate compounds generally contribute more to haze than any other individual aerosol component. Carbonaceous particulate matter—organic compounds and light absorbing carbon (LAC)—generally constitute the second largest individual aerosol component contributing to haze at Big Bend NP. Information from other studies shows that during late spring episodes, concentrations of carbonaceous compounds are increased due to biomass burning in Mexico and Central America. Dust, represented by a combination of fine soil and coarse mass, contributes as much to haze as particulate sulfate compounds during the months of March and April.

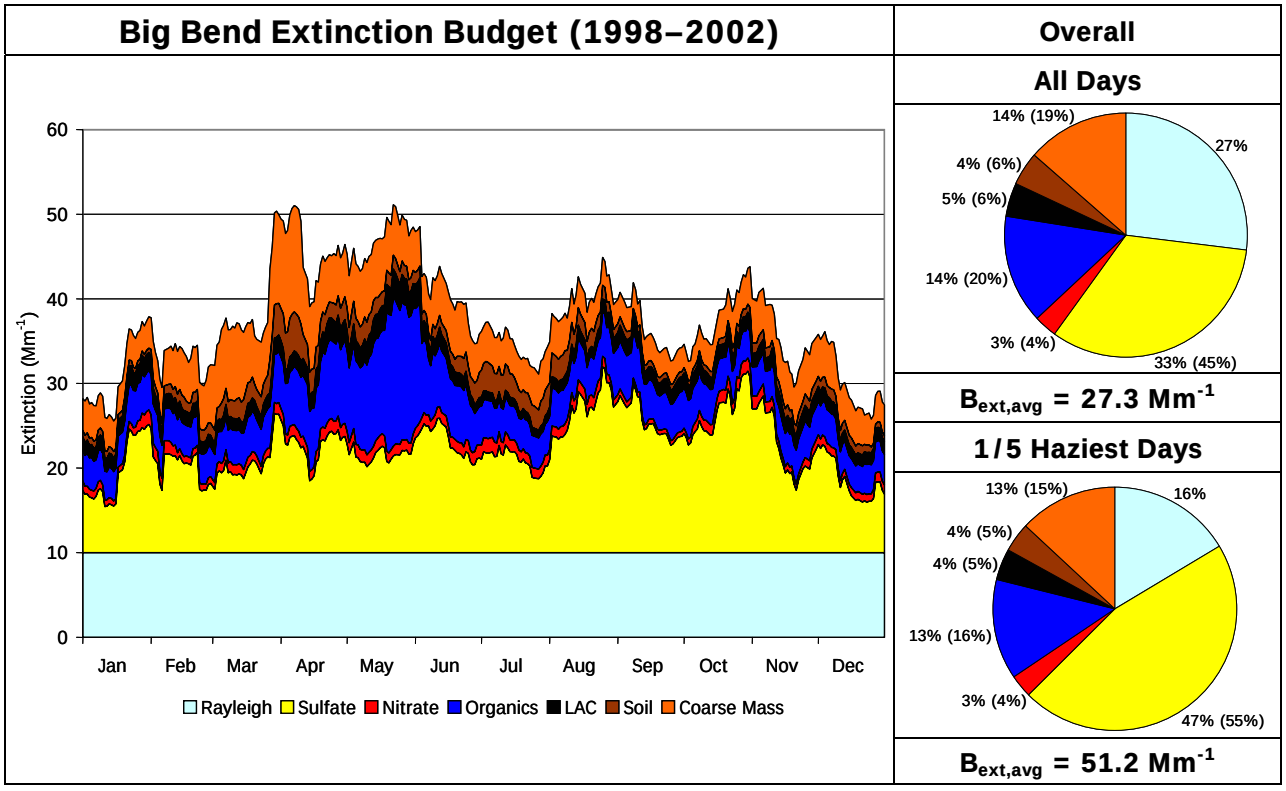

Figure 3-12. Big Bend National Park five-year light extinction budget. All days that fall on the same day of the year were averaged together, then the data were smoothed using a 15-day moving average.

Figure 3-13 contains pie diagrams that show the average estimated contributions to light extinction by the various aerosol components and Rayleigh scattering. Separate pie diagrams display the averages by calendar quarter for all days and the 1/5 haziest days each year for the five-year period from 1998 to 2002. The Rayleigh scattering percent contribution necessarily decreases for the haziest days compared to all days because its absolute contribution is taken to be constant for all days. As shown, more of the annual haziest days are in the second and third calendar quarters (63%) than in the other quarters. Particulate sulfate compounds contribute more to light extinction on the haziest days than for average days during all quarters. Over the entire five-year period the contribution to particulate light extinction increases from 45% on all days to 55% for the 1/5 haziest days (Figure 3-12).

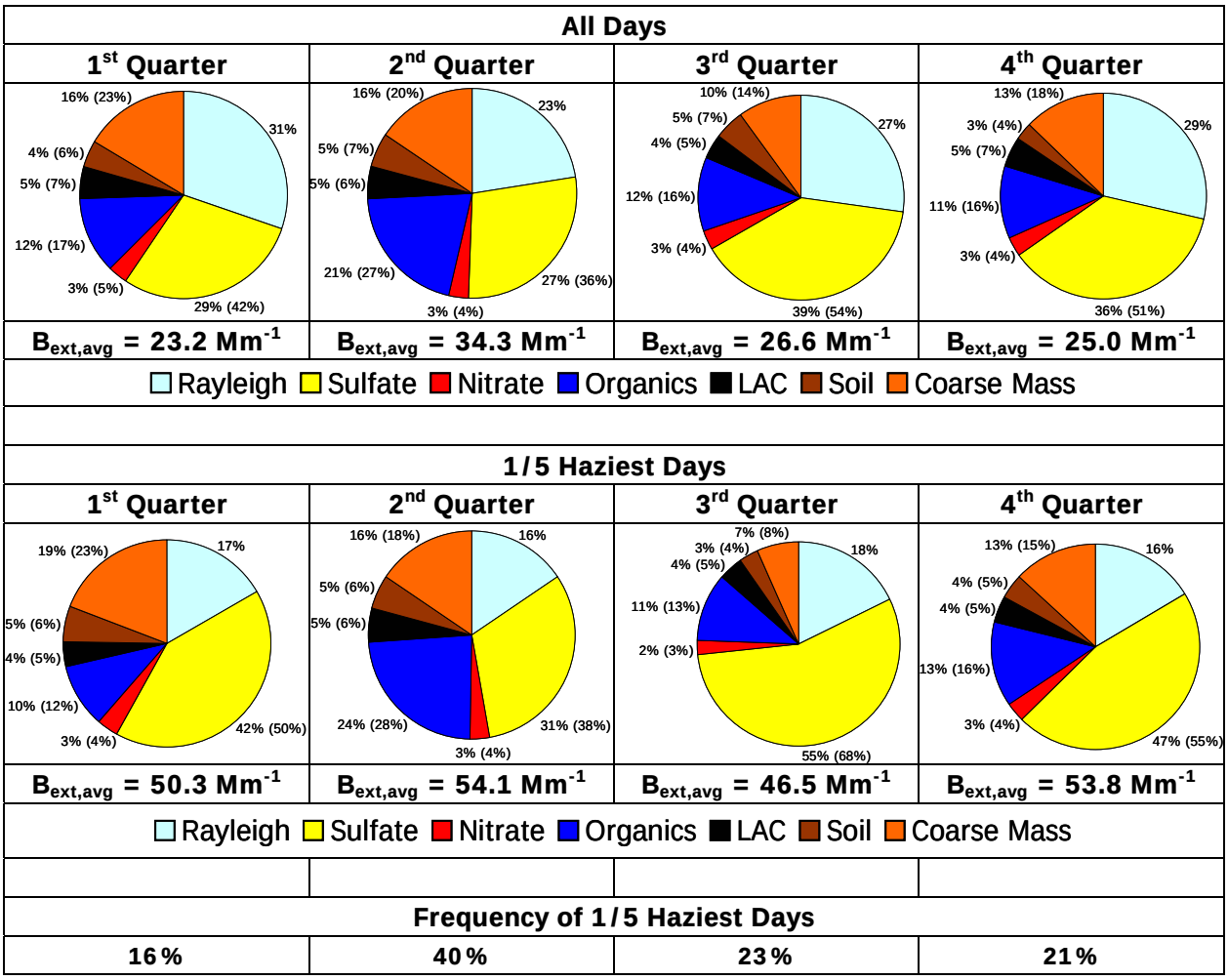

Figure 3-13. Quarterly aerosol contributions to light extinction averaged over five years (1998–2002). Top graphs: all days in each quarter; bottom graphs: annual haziest 1/5 of the days. Percent contributions to particulate haze (the non-Rayleigh light extinction) are shown in parentheses.

The contribution of carbonaceous (i.e., organic and light absorbing carbon) compounds to light extinction decreases from 26% on average to 21% on the haziest days. In the quarter with the greatest number of haziest days (2nd quarter), the contribution to particulate light extinction by carbonaceous compounds is about 34% on average and for the haziest days, which is similar to the contribution by the sulfate compounds at 36–38%.

The coarse mass is also a major contributor to the particulate light extinction accounting for 18–23% on all days and the haziest days during quarters 1 and 2. The contribution of coarse material to light extinction is similar for all days in a quarter and the haziest days, except for quarter 3 where coarse mass accounted for only 8% of the particulate light extinction on the haziest days compared to 14% on average. In the past, the coarse mass was assumed to be composed of primarily soil; however, during BRAVO soil accounted for 53% of the coarse mass, carbonaceous compounds accounted for 31%, and sulfate accounted for 8% (Table 3.3). The coarse carbon material could still be part of the wind blown dust.

4) Airmass History Biases as Functions of Back Trajectory Model and Input Meteorological Data

4.1 Introduction

The goals of the evaluation of wind fields and back trajectory models within BRAVO were to determine, using this very data-rich project, 1) whether there are biases between the various available back trajectory models and available input fields; 2) whether past studies using the older Atmospheric Transport and Diffusion (ATAD) model with the usual raw rawinsonde data as input are valid in the light of new models and new gridded wind fields; 3) to determine the best model and wind fields to use for future routine back trajectory modeling both for Big Bend National Park and for other sites; 4) to determine whether the unavailability of the EDAS gridded wind field during October caused any biases during that month; and, 5) to determine whether any findings of biases in trajectory models and wind fields are valid for Big Bend during summer and fall 1999 only (the BRAVO study period) or whether similar biases exist for other regions of the country and for other seasons and other years in south Texas.

Models to be examined include ATAD, HYSPLIT ver. 4.5, and CAPITA Monte Carlo (CMC). Input meteorological data include North American rawinsonde data, these data plus information from the four BRAVO wind profilers, and three gridded wind fields, EDAS, FNL, and MM5. Details of the input meteorology are discussed in section 2.1.3 and details of the three back trajectory models are given in section 2.2. Table 4-1 briefly summarizes the major differences between the three back trajectory models. Appendix 4a has additional analyses and discussion of the MM5 and EDAS wind fields.

4.2. Evaluations to Determine Whether or Not There Is a Bias during the BRAVO Period

4.2.1 Simple Plotting of Trajectories Generated in Various Ways.

As a first step, we graphically examined the horizontal and vertical locations of back trajectories generated by each model/data set combination four times per day for the duration of the BRAVO study period (July 1–October 31, 1999). All of these trajectory plots are in Appendices 4b, 4c, and 4d. HYSPLIT trajectories were started at 10, 100, 200, 500, 1000, and 2000 m above ground. All trajectories were traced for 5 days backward in time from Big Bend National Park, TX (103.18 deg W, 29.30 deg N). In order to calculate a back trajectory, it is necessary to have meteorological data for a few days preceding and usually a few hours following the start time of the trajectory. Since the start and end dates of the MM5 data were July 1 and October 31, it was not possible to use the MM5 data for the first few days of the study, the last day, or part of the last day depending on the requirements of the back trajectory model. Several general observations resulted. Illustrations of these findings are discussed below.

Table 4-1. Summary of the major differences between the three trajectory models used for BRAVO.

Feature	ATAD	HySPLIT	CAPITA MC
Input Data Type	Designed for raw sounding data. Gridded data or supplemental profiler data can also be used	Gridded meteorological data. BRAVO study used EDAS, FNL, and MM5 36 km	Gridded meteorological data. BRAVO study used EDAS, FNL, and MM5 36 km
Available Input data	1946–present for raw soundings. 1997–present for EDAS and FNL, July–October 1999 for MM5 and BRAVO wind profilers	1997-present for EDAS and FNL July–October 1999 for MM5	1997-present for EDAS and FNL July–October 1999 for MM5
Horizontal Motion	Within the transport layer, average winds calculated from stations within a given radius.	Input horizontal winds	Input horizontal winds
Trajectory Start Height	As run for BRAVO, Depends on transport layer (see vertical motion).	Chosen by user, for BRAVO, 10, 100, 200, 500, 1000, 2000 m above ground.	Below mixing height
Vertical Motion	Trajectory stays in a variable calculated transport layer, approximately 300–3000 km above ground. Fixed vertical layers are also possible	For BRAVO, input vertical winds used to calculate transport. Maximum 10 km height. Other options are available.	Random vertical motion in mixed layer, vertical motion by input data above
Trajectory Start Frequency	Maximum of 4 times per day at 0, 6, 12, and 18 GMT.	Hourly at multiple heights	Unlimited particles per hour (used 20–50 for BRAVO applications)
Frequency of Output	Every 3 hours	Hourly * number of start heights	Hourly * number of particles per start time
Trajectory Length	Maximum 5 days	For BRAVO 5, 7, and 10 days	For BRAVO 5, 7, and 10 days

On some days all trajectories are similar, thus the choice of model, input data, and even starting height is unimportant. This is more likely to occur during the fall than during summer. An example for trajectories started on September 15, hour 18, is shown in Figure 4-1. Although there certainly are subtle differences in trajectory placement depending on start height, data, and model, all trajectories are arriving from east Texas. The CMC trajectories started at this time (shown on the right side) are horizontally similar to those generated by HYSPLIT and ATAD (on the left side), though those generated using MM5 input extend farther into the southern tier states to the east of Texas than do any of the others, including the other two models with the same input wind field. For this start time, the heights of the CMC trajectories generated with EDAS are much lower than those generated with MM5 and seem to be more similar to the heights of the HYSPLIT trajectories.

A common pattern, especially in the summer, is that there is a directional bias between trajectories generated with different input data. ATAD with raw rawinsonde data as input typically has airmasses arriving from the most southerly direction; HYSPLIT and CMC with EDAS input have airmasses arriving from the most easterly; while either HYSPLIT or CMC with FNL input generate trajectories between the extremes. Figure 4-2 (July 19, hour 6) shows an example of the typical type of directional bias that was observed frequently during July and

August. The ATAD trajectory with rawinsonde input (black) is arriving from the most southerly direction. Trajectories generated by HYSPLIT using EDAS (solid colored lines) generally arrive from the most northeasterly directions, while those generated by HYSPLIT with FNL (dotted colored lines) or MM5 (dashed colored lines) fall between the extremes. Note that ATAD trajectories generated with a gridded wind field (brown lines) are more similar to HYSPLIT trajectories than ATAD trajectories generated with raw sounding data. The CMC trajectories, shown in the right panel, also show a tendency for those generated using EDAS input to be more northeasterly than those generated with MM5 input for this start time.

An example of a day when choice of model and wind field made a large difference in the resultant back trajectories is shown in Figure 4-3 (September 20, hour 18). ATAD with rawinsonde data (black line) indicates airmasses arrived from deep within Mexico after possibly crossing the Gulf of Mexico. However, note trajectories generated with HYSPLIT and started at 200 m. The EDAS input (solid blue) creates a trajectory from the north, FNL input (dotted blue) creates a trajectory arriving from across the Gulf of Mexico, and MM5 input (dashed blue) generates a trajectory arriving from the west. The CMC trajectories, shown on the right, arrive mostly from the east with MM5 input, but mostly from the west with EDAS input. The differences are related to the height of the particles, with higher level airmasses arriving from the west. In this case, the CMC trajectories generated using EDAS input are higher than those generated with MM5 input. This is the reverse of the example shown in Figure 4-1.

For HYSPLIT, which requires specification of a start height, height differences between trajectories started at the same height, but generated with EDAS vs. FNL can be as large as several thousand meters after 5 days. In the example, shown in Figure 4-4 (July 24, hour 12), this is particularly evident in the trajectories started at 1000 m (green lines) and 2000 m (orange lines).

Directional differences between trajectories generated by HYSPLIT using EDAS vs. FNL can occasionally be as much as 180 degrees and, as expected, are largest when trajectory height differences are large. Again, in the example shown in Figure 4-5 (July 18, hour 6), this is particularly evident in the trajectories started at 1000 m (green lines) and 2000 m (orange lines). The CMC trajectories started at this same time are similar to the HYSPLIT trajectories started at the lower start heights. On this day, while the CMC heights are similar for both EDAS and MM5 inputs, the EDAS trajectories arrive from a more northeasterly direction.

For HYSPLIT, directional differences between input wind fields can exist even when the trajectory heights are similar. For example, see the HYSPLIT trajectories started at 500 m (cyan lines) in the example shown in Figure 4-6 (August 6, hour 18). This day also illustrates the occasional differences between outputs from the CMC model vs. HYSPLIT. Notice that except for the trajectory started at 2000 m and using EDAS input (dashed orange), all the HYSPLIT and ATAD trajectories arrive from the southeast. However, roughly half of the CMC trajectories, including those generated with both EDAS and MM5 input, arrive from a much more northeasterly direction.

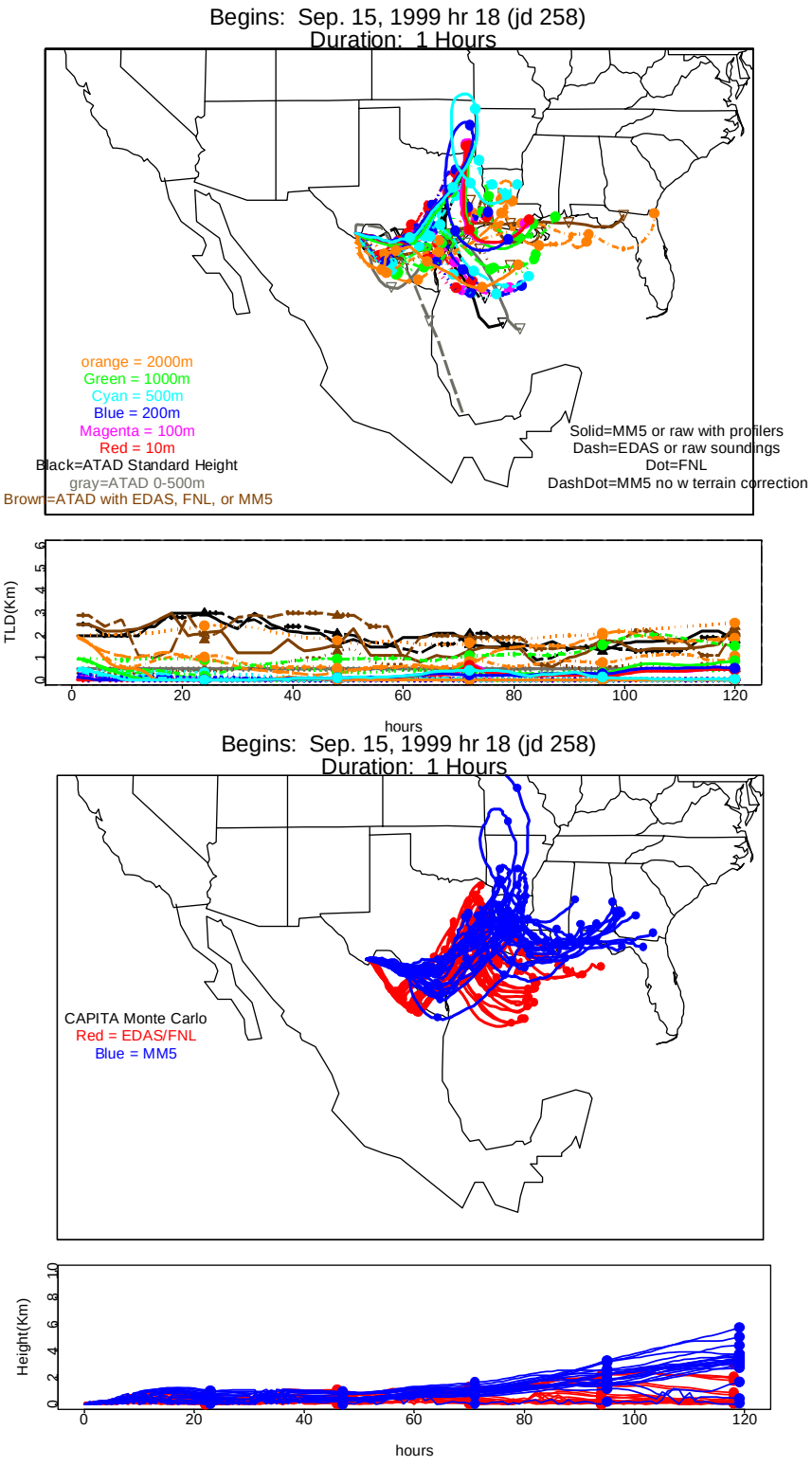

Figure 4-1. Five-day back trajectories generated by all model/input combinations beginning on 9/15/1999, 18:00 CDT. Top are HYSPLIT and ATAD outputs, bottom is CMC.

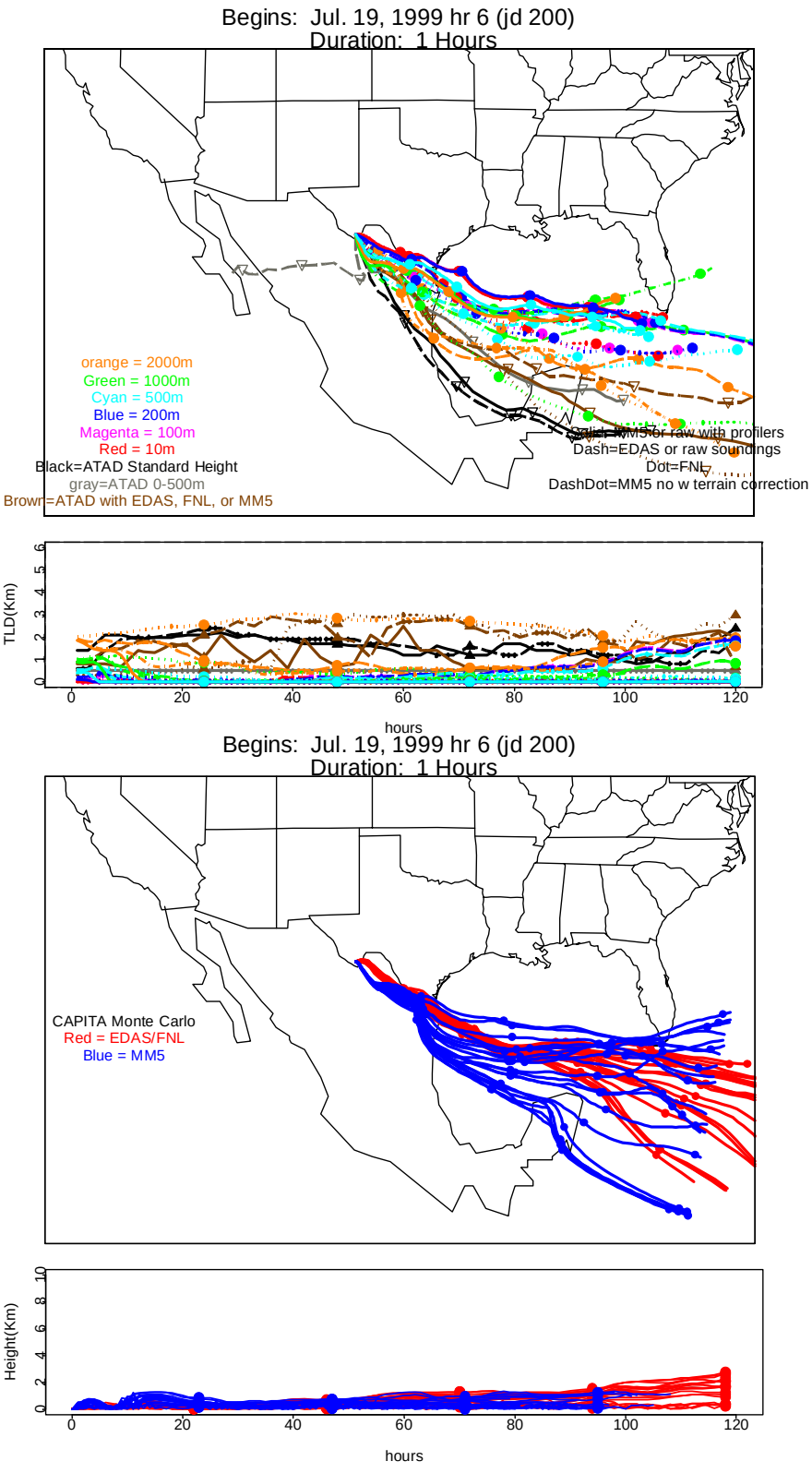

Figure 4-2. Five-day back trajectories generated by all model/input combinations beginning on 7/19/1999, 6:00 CDT. Top are HYSPLIT and ATAD outputs, bottom is CMC.

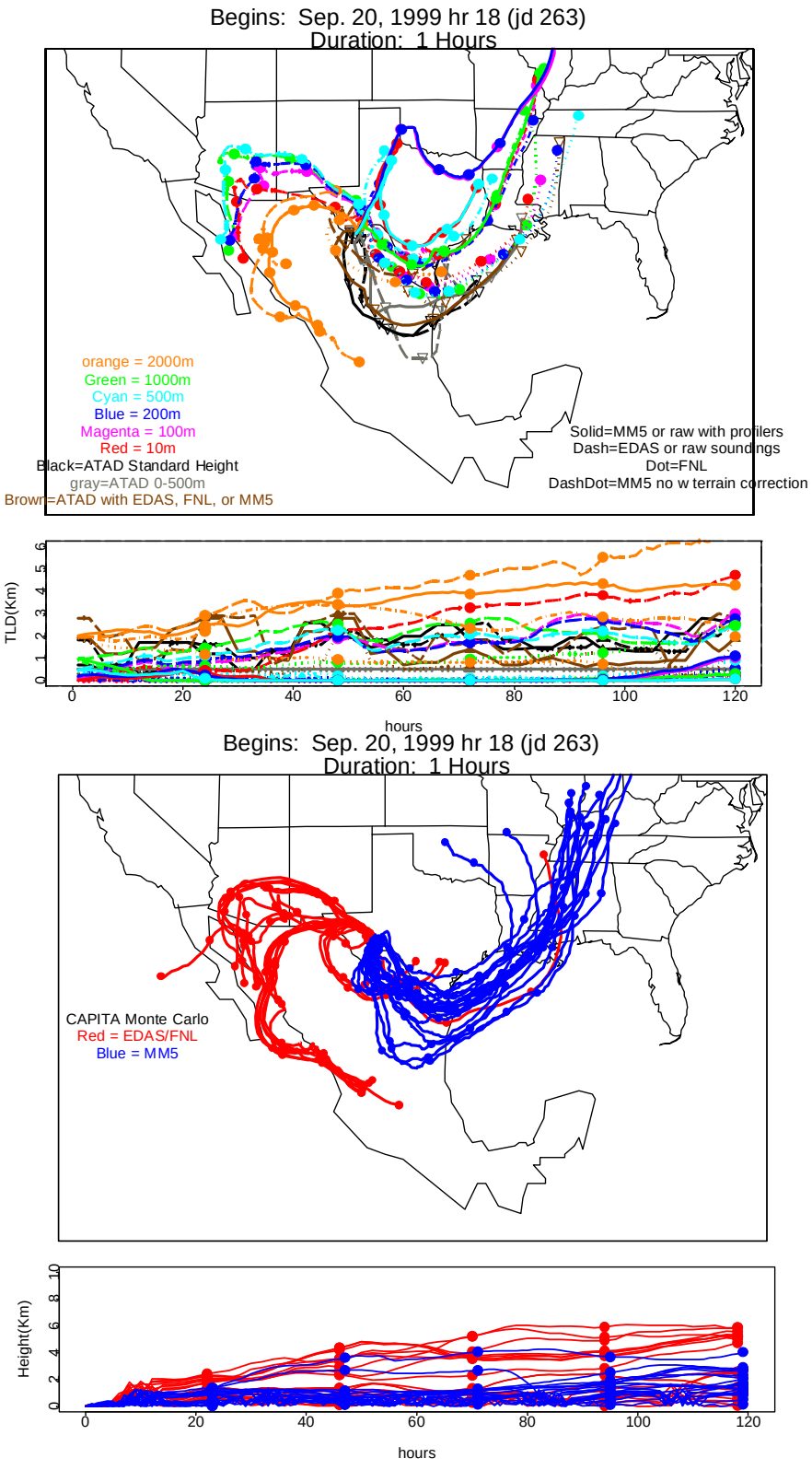

Figure 4-3. Five-day back trajectories generated by all model/input combinations beginning on 9/20/1999, 18:00 CDT. Top are HYSPLIT and ATAD output, bottom is CMC.

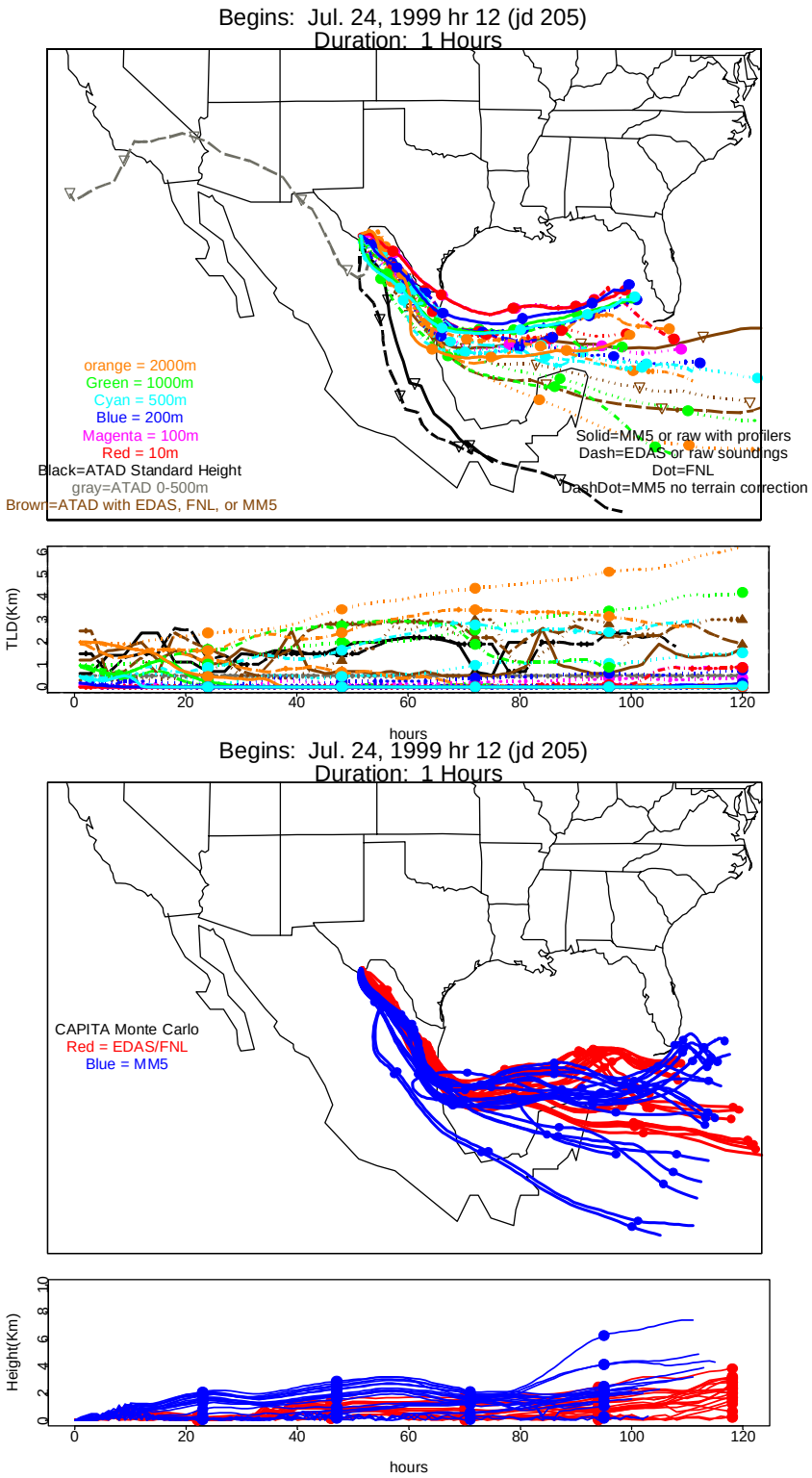

Figure 4-4. Five-day back trajectories generated by all model/input combinations beginning on 7/24/1999, 12:00 CDT. Top are HYSPLIT and ATAD output, bottom is CMC.

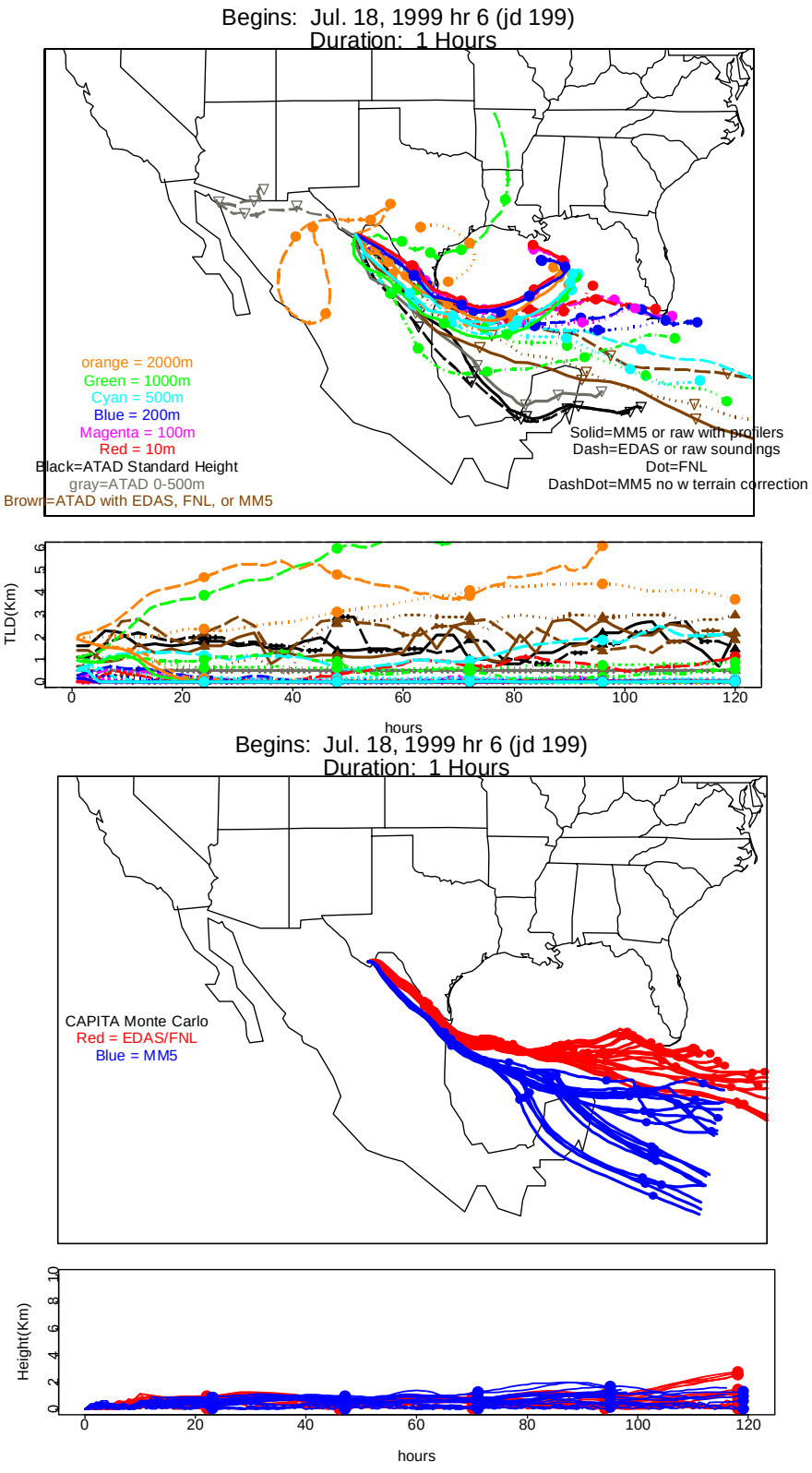

Figure 4-5. Five-day back trajectories generated by all model/input combinations beginning on 7/18/1999, 6:00 CDT. Top are HYSPLIT and ATAD output, bottom is CMC.

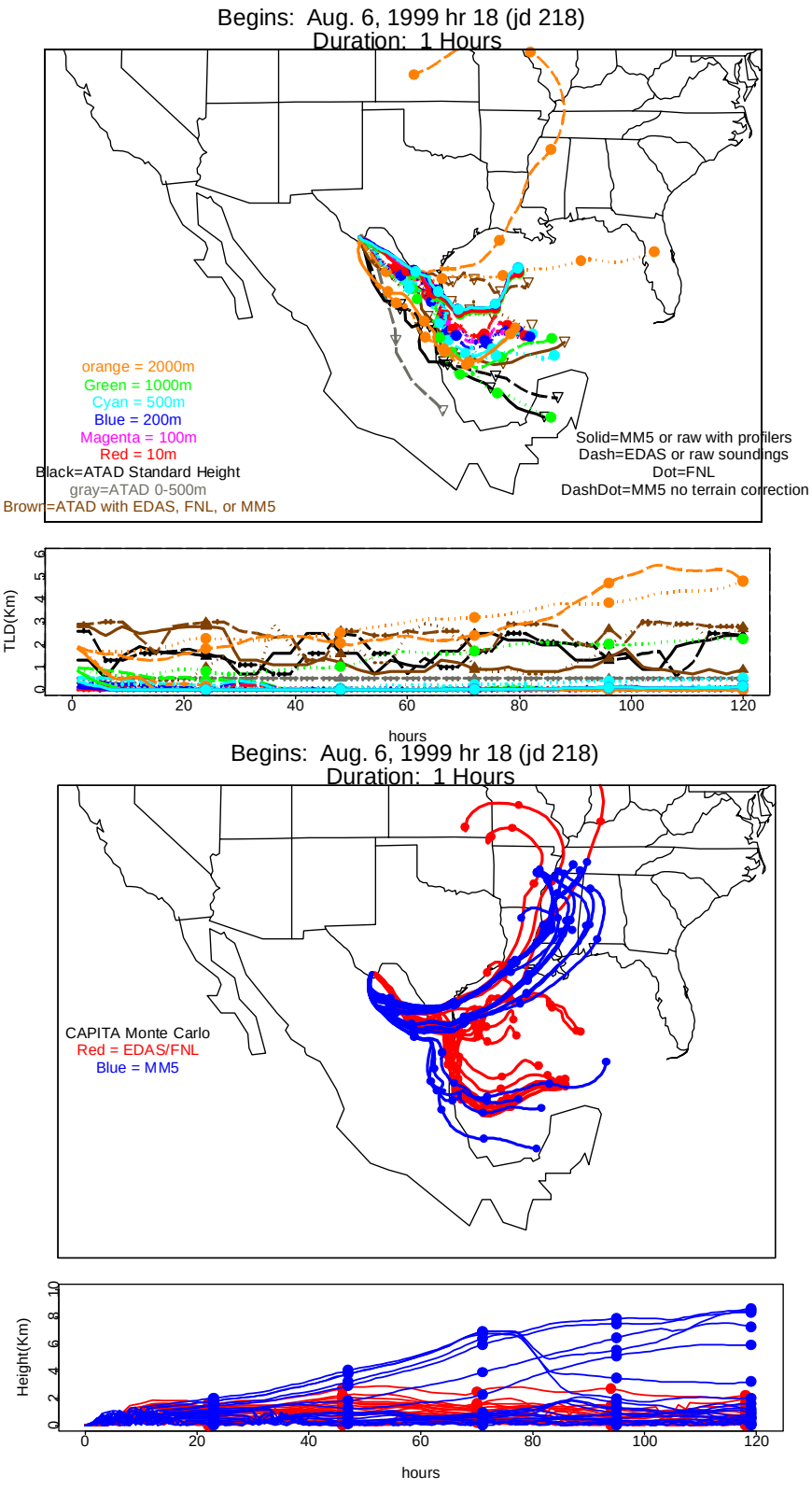

Figure 4-6. Five-day back trajectories generated by all model/input combinations beginning on 8/6/1999, 18:00 CDT. Top are HYSPLIT and ATAD output, bottom is CMC.

Trajectories generated with either HYSPLIT or CMC can reach heights as high as 10 km, clearly above the mixed layer that is likely to be carrying most air pollutants. An advantage of CMC over HYSPLIT is that the height of the mixed layer is known and available as output. Both CMC and ATAD provide estimates of transport integrated throughout the mixing layer. Due to its different design, ATAD does not generate trajectories above its "transport layer" which has a maximum of about 3 km above ground.

From these simple graphical analyses, it is apparent that there can be significant episodic differences between the modeled back trajectories depending on the model and input data used to generate the trajectories. These observations are examined in a more systematic manner in the following sections.

4.2.2 Calculation of BRAVO Overall Residence Times and the Differences between Them

Overall residence times (ORT) were calculated for Big Bend for July–October, for July–September, for each of the four months individually, and for each of seven high sulfur episodes using 5-day and 10-day back trajectories generated with each model/data set. Evaluating periods without October in some cases allowed a comparison between results using EDAS vs. FNL inputs. Briefly, ORT is a count of the number of back trajectory endpoints or particles in each grid cell and shows the predominant direction(s) from which airmasses arrived as predicted by the model. The methodology is described in detail in section 2.3.1.3. While the graphical analysis described in the previous section made it apparent that there were occasional differences between the model/input combinations, ORT allows a more systematic evaluation of the average differences between the modeled back trajectories. Specifically, we would like to 1) examine the consequences of using ATAD with raw sounding data in previous studies, 2) examine the consequences of using FNL rather than EDAS data during October, 3) determine a reasonable start height or heights for HYSPLIT, and 4) determine whether there are systematic differences between the results when using a single model but different input meteorology or when using a fixed input data set in different models.

4.2.2.1 ATAD Model with Rawinsonde Data Compared to Other Combinations; Implications for Previous Studies

ORTs for July–October 1999 all generated with ATAD, but using four different input data sets, rawinsonde data only, rawinsonde data plus data from the four BRAVO wind profilers, MM5 36 km gridded wind field, and the EDAS/FNL gridded wind field, are shown in Figure 4-7. Moving from a) through d), ATAD predicts that airmasses arrive predominantly from progressively less southerly and more easterly directions. Use of the raw rawinsonde data in ATAD (Figure 4-7a) results in the most southerly predominant wind direction. The addition of even a small quantity of additional data, such as adding data from the four BRAVO wind profilers (Figure 4-7b), causes ATAD to predict a slightly more easterly average transport direction. ATAD with MM5 input (Figure 4-7c) yields yet a more easterly mean inflow direction, while ATAD with EDAS/FNL input (Figure 4-7d) is the most easterly of the four sets.

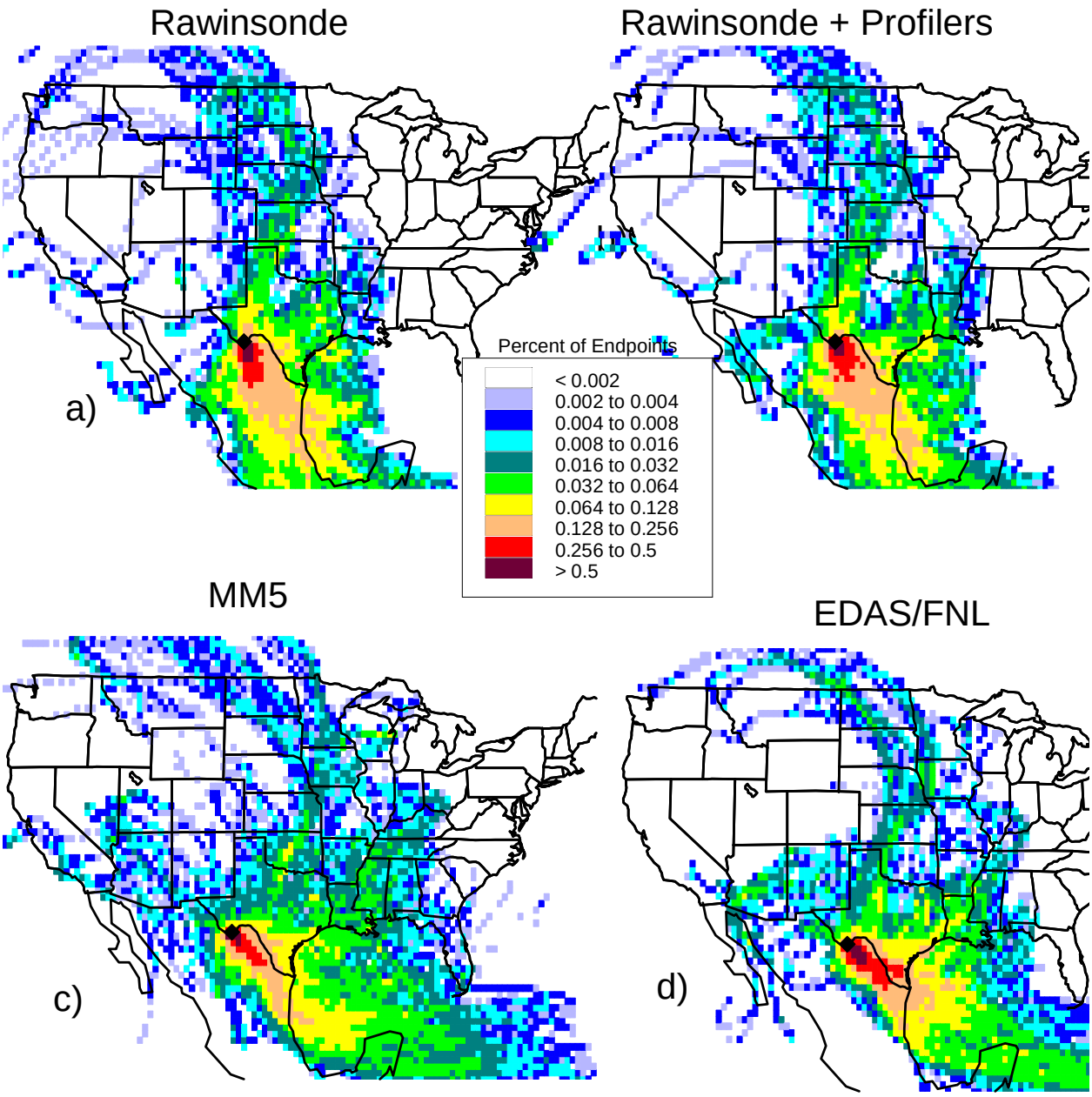

Figure 4-7. Overall Residence Times all generated with ATAD for July–October 1999, grid size ½ deg lat by ½ deg lon. a) using NOAA rawinsonde data b) using rawinsonde data plus data from four BRAVO wind profilers c) using MM5 36 km gridded meteorology d) using EDAS when available and FNL for October.

Big Bend is a particularly challenging receptor site to model using only rawinsonde data due to its proximity to both complex terrain and to data-sparse areas. In Mexico there are fewer balloon launch sites than in the U.S. and often there are data for these sites only once per day rather twice per day as is usual in the U.S. Also there are no rawinsonde data over the Gulf of Mexico. If the reason for the southerly bias in ATAD when the rawinsonde data are used alone as input is due to the sparseness of the input data, then trajectories generated by this combination of model/input data should not be used for further source attribution at Big Bend. This

conclusion does not necessarily extend to other receptor sites located in areas with less complex terrain and more rawinsonde data. Also, it's unclear from this limited analysis whether a similar problem exists during other seasons when the predominant wind directions in the region are different and more likely to arrive from areas in the U.S. where there are more data than in Mexico and over the Gulf of Mexico.

Another issue is whether ATAD trajectories are similar to or different from trajectories from the other two trajectory models when identical data sets are used as input. Figure 4-8 shows the four-month average ORT generated by ATAD, CAPITA MC, and HYSPLIT, all using MM5 data as input. Figure 4-9 is the same except all three models are using the EDAS/FNL combination input. For HYSPLIT, results shown are for an aggregation of start heights including 100, 200, 500, and 1000 m AGL.

For both MM5 and EDAS/FNL input, results from ATAD and CMC appear the most similar while the predominant wind direction calculated by HYSPLIT using the same input data is less southerly and more along the Texas-Mexico border. An obvious difference is in the smoothness of the contours. ATAD has orders of magnitude fewer endpoints, generating only 40 during a single 5-day trajectory compared to 120 by HYSPLIT and a variable number by CMC depending on how many particles were released per hour and how often the particle position was saved. While ATAD can have only 4 incoming pathways per day, HYSPLIT can have 24 per start height (four heights in this case) and CMC has 480 for this case of 20 particles per hour. The total number of endpoints used for July–October ORT statistics was approximately 20,000 for ATAD, 1.3-1.4 x 10^6 for HYSPLIT depending on the input data, 1.7 x 10^6 for CMC with EDAS/FNL, and 3.1 x 10^6 for CMC with MM5 input.

As we already know from examining the individual start times in the previous section, the height of the back trajectory can have a large influence on the horizontal placement of the trajectory; in general, the higher the mean height, the faster the mean speed of the trajectory. This has implications for source attribution because higher wind speeds will tend to implicate more distant sources at the expense of closer sources, with lower speeds preferentially implicating nearer source areas. Table 4-2 shows the mean endpoint heights and wind speeds for all model and input data combinations used for BRAVO. When EDAS/FNL data are used as input, HYSPLIT generated trajectories were higher on average than when MM5 data were used at the same start height. However, ATAD and CMC generated trajectories with higher mean heights when MM5 data were used as input. Also, there is a large difference in mean heights between HYSPLIT and the other two models. This is a function of the start heights chosen for HYSPLIT. A HYSPLIT start height of 1000 m most closely matches the mean heights generated by ATAD and CMC which do more averaging within the mixed layer. For HYSPLIT with start heights of 500 m and greater, the mean trajectory height is approximately equal to the start height. For lower start heights, the mean trajectory height was never lower than 200 m, no matter what the start height.

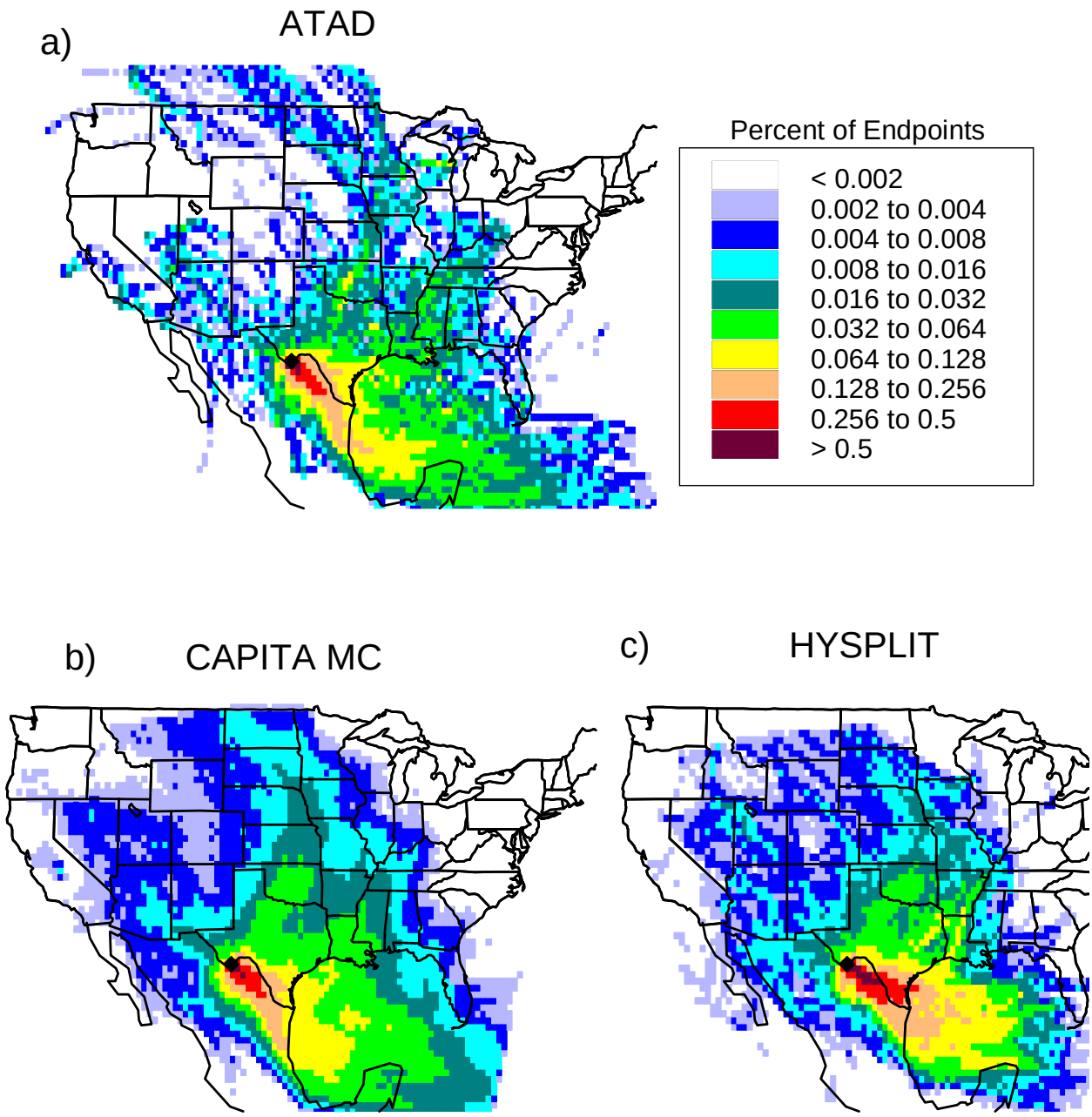

Figure 4-8. Overall Residence Times for July–October 1999, grid size ½ deg lat by ½ deg lon. all with 36 km MM5 input a) ATAD b) CAPITA MC c) HYSPLIT started at 100, 200, 500, 1000 m AGL.

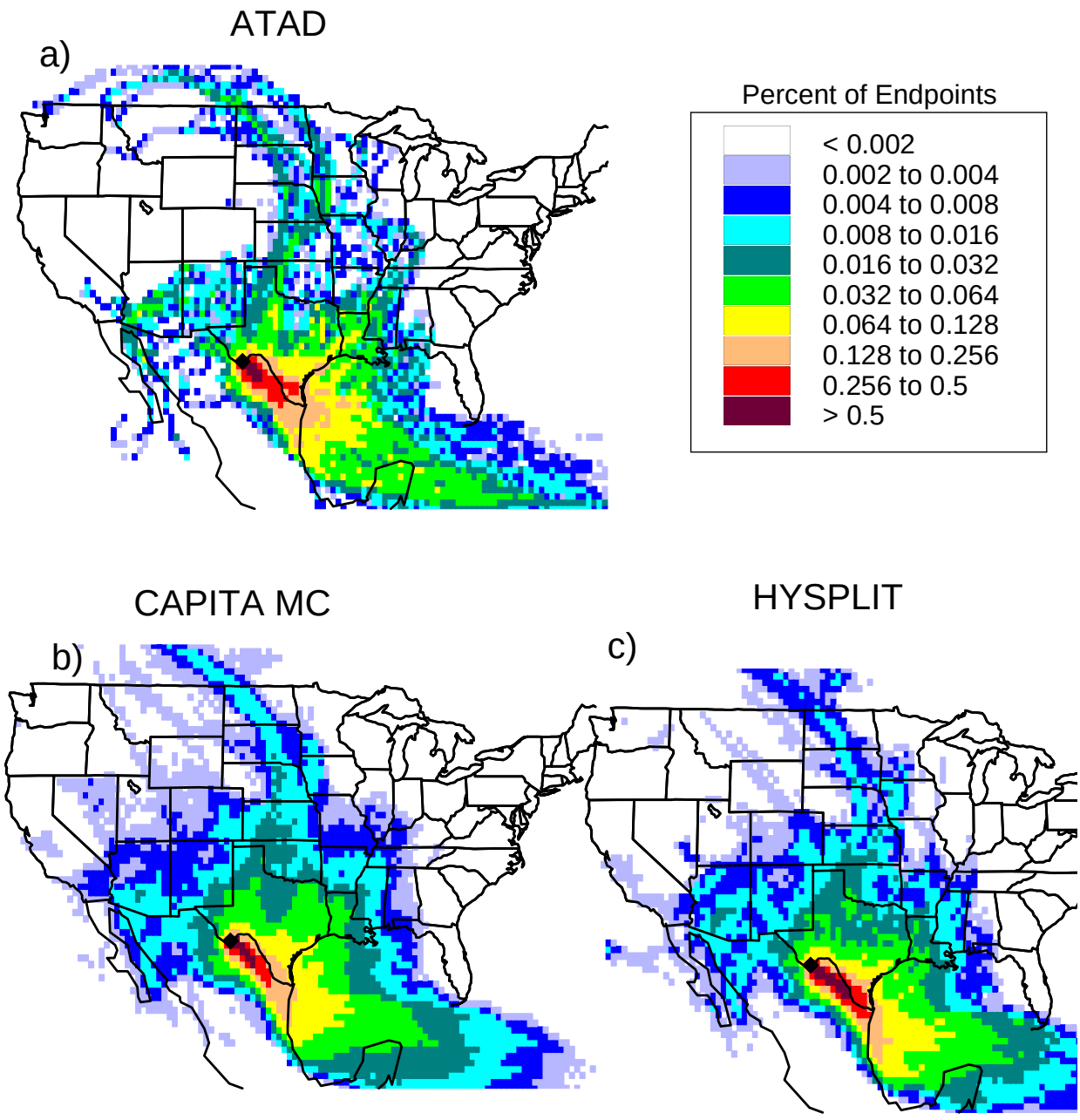

Figure 4-9. Overall Residence Times for July–October 1999, grid size ½ deg lat by ½ deg lon. All with EDAS/FNL input a) ATAD b) CAPITA MC c) HYSPLIT started at 100, 200, 500, and 1000 m AGL.

Table 4-2. Mean endpoint heights and wind speeds for 5-day back trajectories for July–October 1999 generated by all the model and input data combinations including all the start heights for HYSPLIT. A HYSPLIT start height of 100–1000 refers to an average of the results from 100, 200, 500, and 1000 m start heights.

Model	Input Data	Start Height (m AGL)	Mean Endpoint Height (m AGL)	Mean Wind Speed (m/sec)
ATAD	Rawinsonde	NA	1721	5.3
	Rawinsonde + BRAVO profilers	NA	1726	5.4
	EDAS/FNL	NA	1718	6.2
	FNL	NA	1181	5.9
	MM5	NA	1255	6.9
HYSPLIT ver. 4.5	EDAS/FNL	10	238	4.6
		100	364	5.0
		200	447	5.3
		500	706	5.8
		1000	1240	6.2
		2000	2617	6.9
		100–1000	686	5.6
	MM5	10	238	5.0
		100	252	5.1
		200	288	5.2
		500	462	5.3
		1000	950	5.4
		2000	2009	5.5
		100–1000	487	5.3
CMC	EDAS/FNL	NA	1156	6.2
	MM5	NA	1164	7.0

Figures 4-10 and 4-11 show typical representations of the heights of the layers of the MM5, EDAS, and FNL meteorological fields calculated using a U.S. Standard Atmosphere to convert pressures to heights. Because sigma height coordinates are used in all of the gridded data, (see section 2.1.3) the actual heights of the layers vary in time and space, but these figures illustrate typical differences between the three sets of data. Figure 4-10 shows all layers and 4-11 shows the lowest 5000 m so that the lower levels can be seen and include dotted red lines to show the HYSPLIT start heights. For BRAVO, HYSPLIT was run with a maximum height of 10,000 m and ATAD does not use data above 3000 m. It is evident from the thickness of the layers as shown in these figures that HYSPLIT trajectories will be least sensitive to start height when FNL data are used and most sensitive when MM5 data are input.

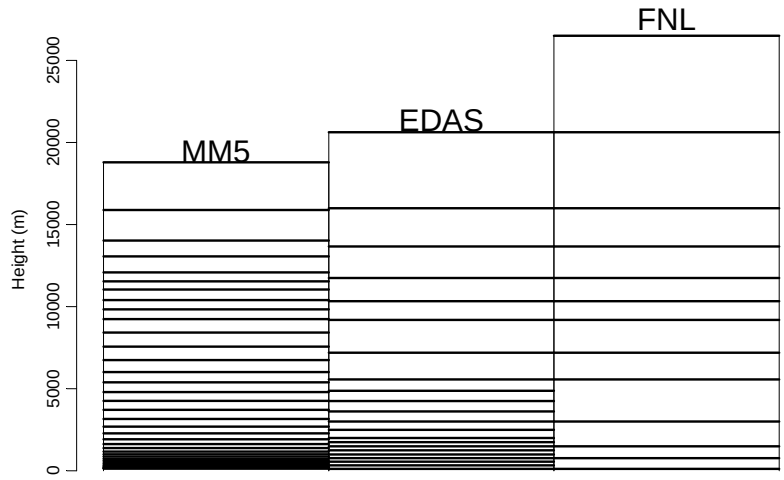

Figure 4-10. Typical heights of all vertical layers for each of the three gridded wind fields. See Figure 4-11 for detail of the lowest layers.

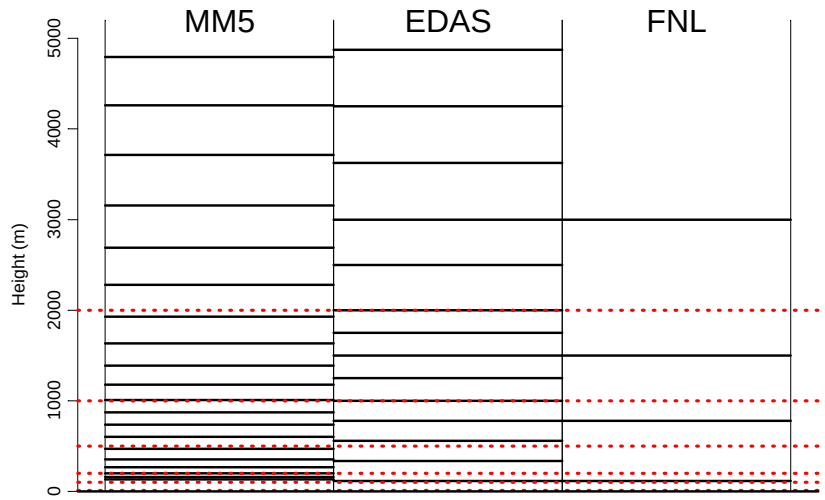

Figure 4-11. Typical heights of the vertical layers for each of the three gridded wind fields for the lowest 5000 m (black solid lines) and five HYSPLIT start heights of 10, 100, 200, 500, 1000, and 2000 m, shown as dotted red lines.

The fastest mean wind speeds are generated with the CMC model, with MM5 input being faster on average than EDAS/FNL input, possibly due to the mean height also being somewhat higher with MM5 input. Fastest mean wind speeds from ATAD are also with MM5 input, followed by EDAS/FNL input.

Figures 4-12 and 4-13 show maps of the differences between pairs of overall residence time output fields. Figure 4-12a shows the differences between ATAD with MM5 and CMC with MM5, while Figure 4-12b shows the differences between ATAD with MM5 and HYSPLIT with MM5. Figure 4-13 is the same except all results are using EDAS/FNL input data rather than MM5. In all cases the warmer colors, yellow through dark red, indicate a positive difference, or areas where the first model of the pair was more likely to place endpoints, while the cooler blue and green colors indicate a negative difference, or areas where the second model was more likely to place endpoints. For MM5 input, both CMC and HYSPLIT are somewhat more likely than ATAD to place endpoints along the Texas-Mexico border, while ATAD is somewhat more likely to place endpoints to the south of this pathway. This is also true for HYSPLIT with EDAS/FNL input. However, CMC with EDAS/FNL input is more likely than ATAD with EDAS/FNL to have endpoints along the border. In all cases, the ATAD model is somewhat less likely than either of the other two models to place endpoints in north and northwest Texas.

4.2.2.2 Consequences of Using FNL Data Rather Than EDAS during October

It is assumed that the EDAS wind field is superior to the FNL field due to its finer horizontal and vertical grid resolution and better resolution in time. One method to determine possible differences caused by use of FNL vs. EDAS data during October 1999 is to examine the differences between the ORTs generated with these two input fields by a single model. ORT difference results can be examined for July–September during BRAVO and also for October during other years. Both EDAS and FNL data are currently available for five Octobers during 1997–1998 and 2000–2002. Figure 4-14 shows these ORT difference fields during July–September 1999 and Figure 4-15 shows the same for the five Octobers for which data are available. CMC was not run with FNL input, so only results from ATAD and HYSPLIT can be compared. In both figures, the areas in the warmer colors, yellow through red-black, are where the given model with EDAS input was more likely to place endpoints while the cooler colors, blue through green, show areas where FNL input resulted in more endpoints.

During the first three months of the BRAVO study, July–September 1999, with both the ATAD and HYSPLIT models EDAS input was more likely to result in endpoints along the Texas-Mexico border, while FNL input resulted in more endpoints following the same general direction, but more likely to be south of the border.

Unfortunately, for ease of interpretation, the differences are not exactly the same for the five Octobers. During the Octobers of 1997–98 and 2000–02, EDAS input with either model was more likely than FNL input to result in endpoints to the southwest of Big Bend. When the HYSPLIT model is used, endpoints were also more likely to arrive from the northwest of Big Bend, especially Arizona. This is also seen to a lesser extent in the July–September 1999 difference fields for both ATAD and HYSPLIT. FNL input in either HYSPLIT or ATAD during these five Octobers, similar to FNL input during July–September 1999, was more likely to result in endpoints arriving from the northeast area of Mexico just south of the border. During the five Octobers it was also more likely for FNL input in either model to result in more endpoints in east Texas and more endpoints in northwest Mexico than predicted using EDAS input.

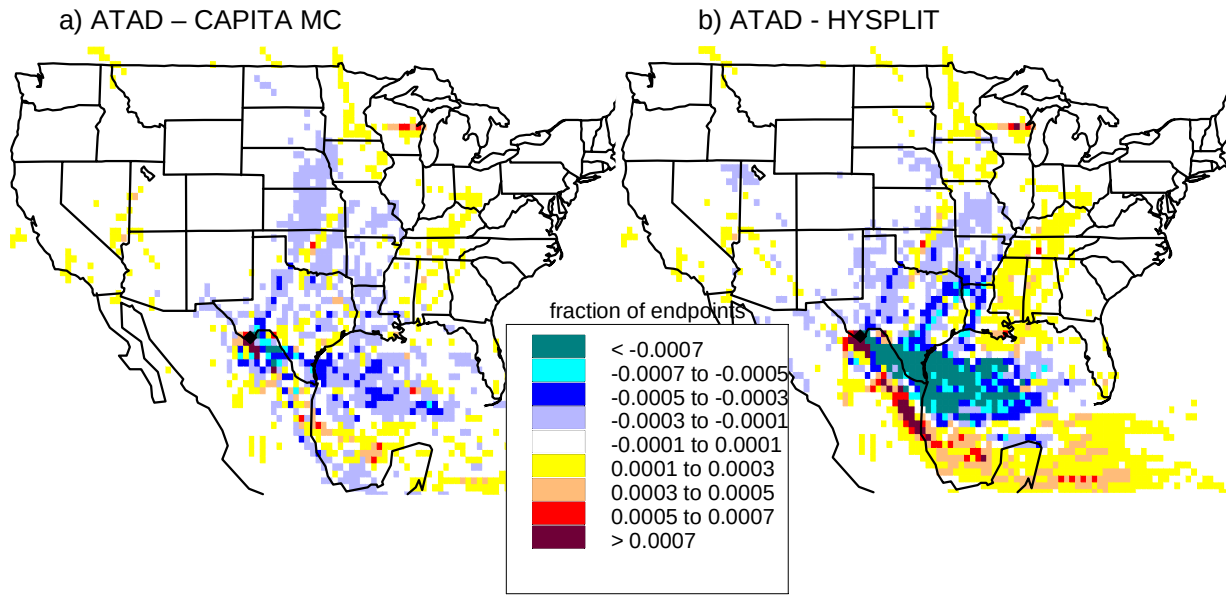

Figure 4-12. Overall Residence Time Differences for July–October 1999, grid size ½ deg lat by ½ deg lon. All with 36 km MM5 input a) ATAD-CAPITAMC b) ATAD-HYSPLIT.

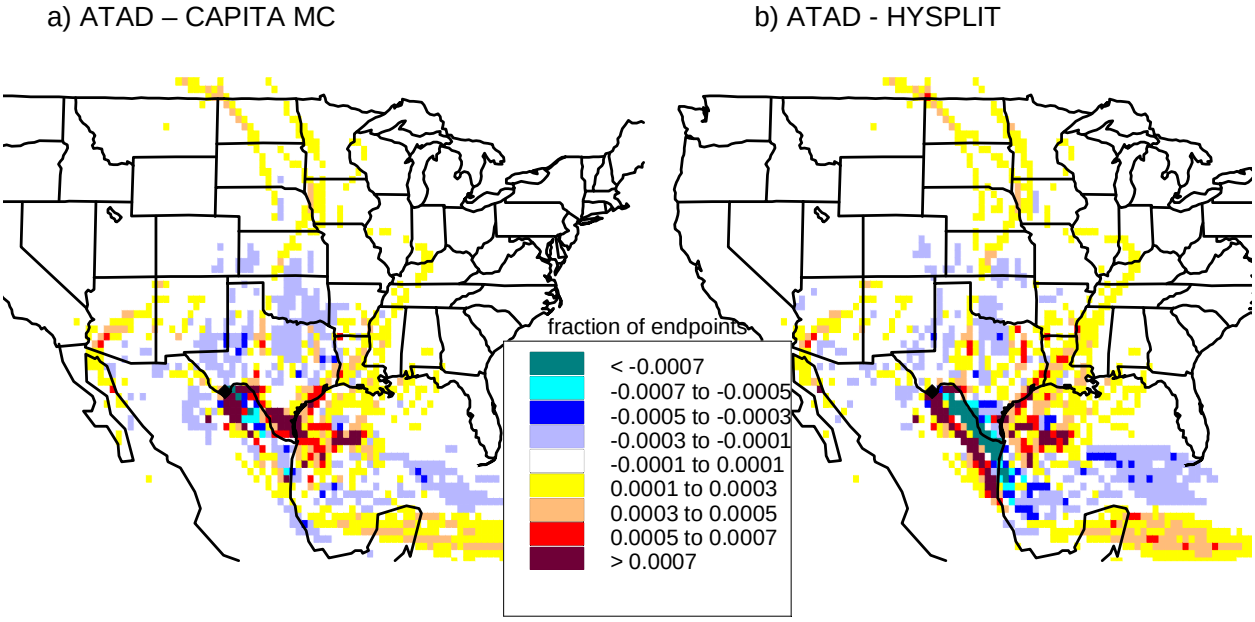

Figure 4-13. Overall Residence Time Differences for July–October 1999, grid size ½ deg lat by ½ deg lon. All with 36 km EDAS/FNL input a) ATAD-CAPITAMC b) ATAD-HYSPLIT.

Table 4-3 shows the mean endpoint heights and mean wind speeds for the combinations tested during the five Octobers. The most obvious difference is that the EDAS trajectories are substantially higher, sometimes twice as high on average, as those generated using FNL data. Like the analyses discussed in the previous section for the BRAVO period, the lower heights associated with FNL result in lower average wind speeds and so preferentially place endpoints

closer to the receptor rather than in more distant source areas. Also, consistent with the previous analyses, is that lower heights are associated with fewer endpoints in the western U.S.

Table 4-3. Mean endpoint heights and wind speeds for 5-day back trajectories for Octobers of 1997–1998 and 2000–2002 generated by all the model and input data combinations including all the start heights for HYSPLIT. A HYSPLIT start height of 100–1000 refers to an average of the results from 100, 200, 500, and 1000 m start heights.

Model	Input Data	Start Height (m AGL)	Mean Endpoint Height (m AGL)	Mean wind speed (m/sec)
ATAD	Rawinsonde	NA	1500	6.0
	EDAS	NA	1598	6.1
	FNL	NA	717	6.0
HYSPLIT	EDAS	100	651	5.6
		200	726	5.8
		500	945	6.3
		1000	1299	7.1
		100–1000	899	6.2
	FNL	100	236	5.2
		200	377	5.8
		500	742	6.9
		1000	1286	7.5
		100–1000	660	6.3

It seems likely that, on average, the meteorology during October 1999 was more similar to the average meteorological conditions during five other Octobers than during July–September of 1999. Transport directions are highly seasonal at Big Bend with airmasses tending to arrive with greater frequency from the south and southeast during spring and summer, from the southeast and northeast during the fall, and from more westerly directions during the winter. If this is true, then the results shown in Figure 4-15 are probably more similar to October 1999 than the results shown in Figure 4-14, though this is speculation and some inter-annual variability is expected.

With these caveats in mind, then it seems probable that the result of using FNL data rather than EDAS for trajectory modeling during October of the BRAVO study is that airmasses arriving from west and southwest Mexico and the southwestern U.S. are underestimated during this month, while airmasses arriving from east Texas and from Mexico just south of the Texas border are overestimated. However, it is impossible to quantify the actual differences during October 1999. Also, since most forward and back trajectory modeling was used for qualitative and quantitative source attribution for the average of the four-month study period and not for October alone, the difference in mean results for July–October 1999 due to the FNL data substitution will be smaller than for only October 1999.

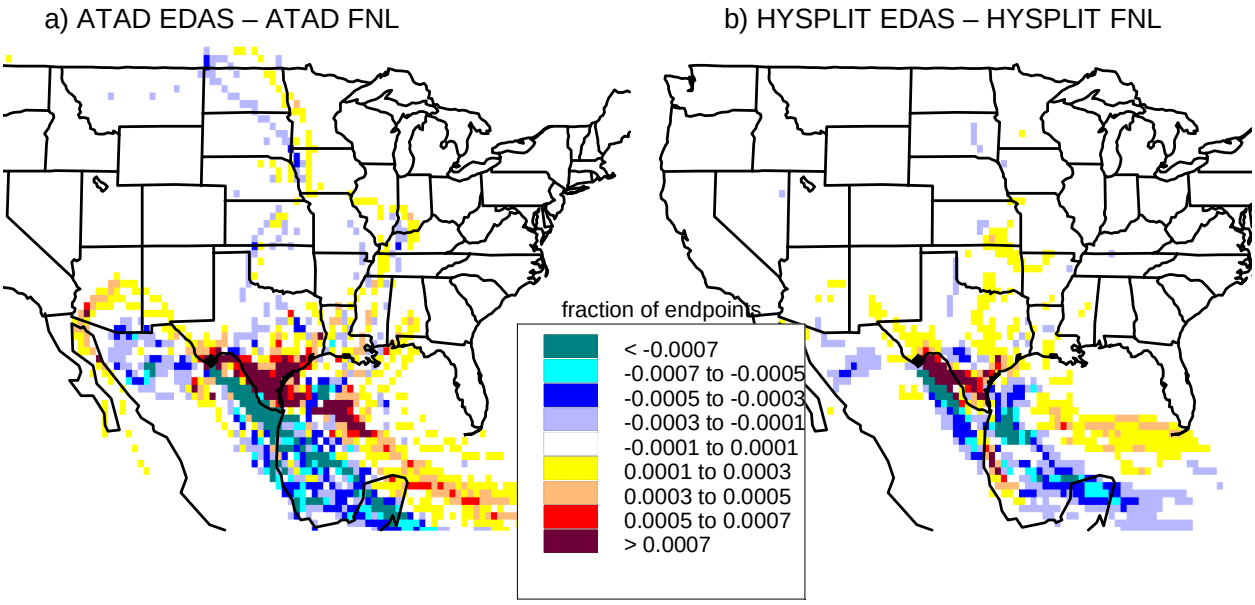

Figure 4-14. Overall Residence Time differences during July–September 1999 a) ATAD/EDAS-ATADFNL, b) HYSPLIT EDAS-HYSPLIT FNL.

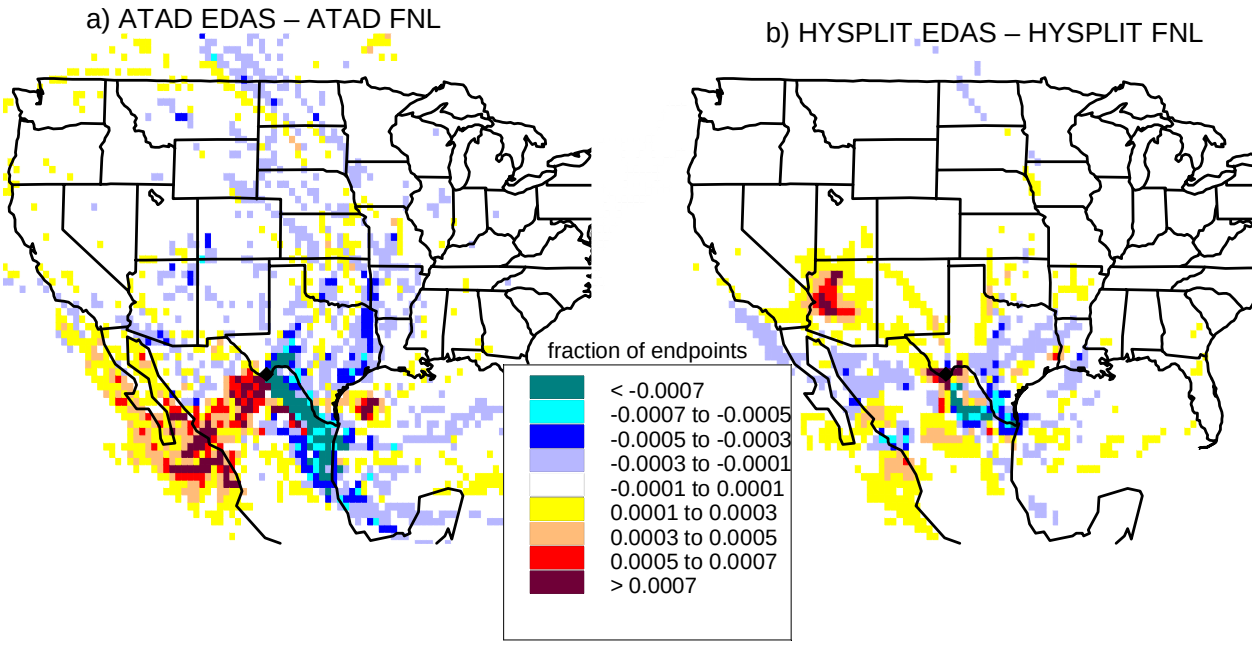

Figure 4-15. Overall Residence Time differences during Octobers 1997, 1998, 2000–2002 a) ATAD/EDAS-ATAD/FNL, b) HYSPLIT EDAS-HYSPLIT FNL.

4.2.2.3 Biases between HYSPLIT and CMC Models

To examine differences in trajectory placement due to the trajectory model rather than the input meteorological data, the differences in ORT for a single input data set with two different models are examined. Figure 4-16a shows the differences between CMC and HYSPLIT when both used EDAS/FNL data as input and Figure 4-16b shows the differences between CMC and

HYSPLIT when both have MM5 data as input. The patterns are similar. With both sets of input data, HYSPLIT is more likely than CMC to place endpoints along the Texas-Mexico border, while CMC is more likely to place them both southeast of this pathway in Mexico and northeast of this pathway in either east Texas (for EDAS/FNL data) or in the eastern U.S. (for MM5 data).

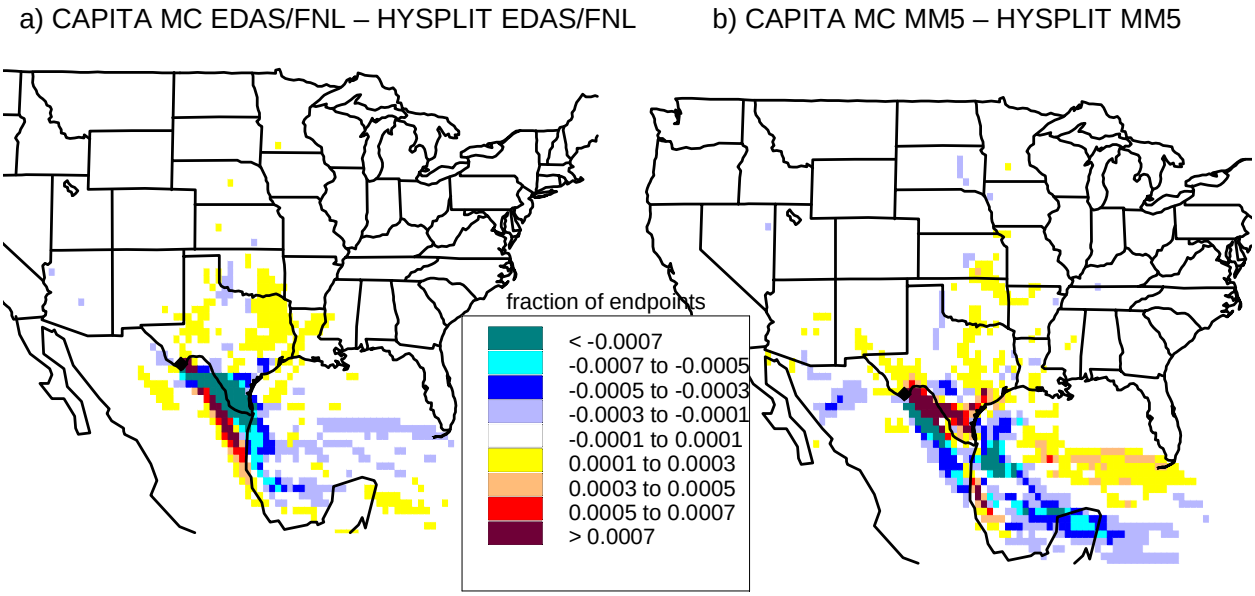

Figure 4-16. Overall Residence Time differences during July–October 1999 a) CMC with EDAS/FNL-HYSPLIT with EDAS/FNL, b) CMC with MM5-HYSPLIT with MM5.

4.2.2.4 Further Evaluation of HYSPLIT Start Heights

An issue when using the HYSPLIT model is the choice of trajectory start-height or heights at the receptor. This is not an issue for either ATAD or CMC. By default, ATAD calculates a transport layer depth and averages the horizontal winds within this transport layer (see section 2.2.2 for details of how the transport layer depth is determined). ATAD can also generate trajectories within fixed layers, but this was not how the model was run for BRAVO. In CMC, particles below the mixed layer are allowed random vertical movements within this layer, so most particles started below the mixing height will tend to follow a similar pathway (see section 2.2.4). However, HYSPLIT, which does less vertical averaging than ATAD and does not use the random vertical movements of CMC, is more sensitive to start height. This is especially true if different start heights fall within different vertical layers of the input meteorological data.

Figures 4-17 and 4-18 show the resultant five-day ORTs for each of several start heights for EDAS/FNL and MM5 inputs, respectively. The start height needs to be low enough to capture the transport of pollutants within the mixed layer, but high enough to avoid the difficulties of measuring and modeling near-surface wind flow. In each figure, the top left corner has a start height of 10 m AGL, top right is 100 m AGL, middle row 200 and 500 m AGL, and bottom row is 1000 and 2000 m AGL. The average ORTs for the four-month study period have subtle differences for subtle changes in start heights. As shown in Table 4-1, as the start heights increase the mean wind speeds increase, thus allowing endpoints to get farther from the receptor. The lowest start heights a have very small fraction of endpoints in the western U.S. and for the EDAS/FNL input, there are very few endpoints in Mexico west and southwest of Big Bend. The

fractions of endpoints in these areas increase as the start heights and, consequently, the average trajectory heights increase. The most different pattern is for the 2000 m start height, which for both HYSPLIT and MM5 results in the most endpoints west of Big Bend both in Mexico and in the U.S.

Because the 2000 m start height is, on average, above the mixed layer where most pollutants are transported, it was not used for source attribution of sulfate. Also, because the trajectories started at 10 m and 100 m were very similar, they were deemed redundant, and the trajectories started at 10 m were also not used for source attribution. The remaining start heights all generate trajectories that are on average within the mixed layer and it was decided to aggregate the endpoints from start heights of 100–1000 m when doing source attribution for sulfate.

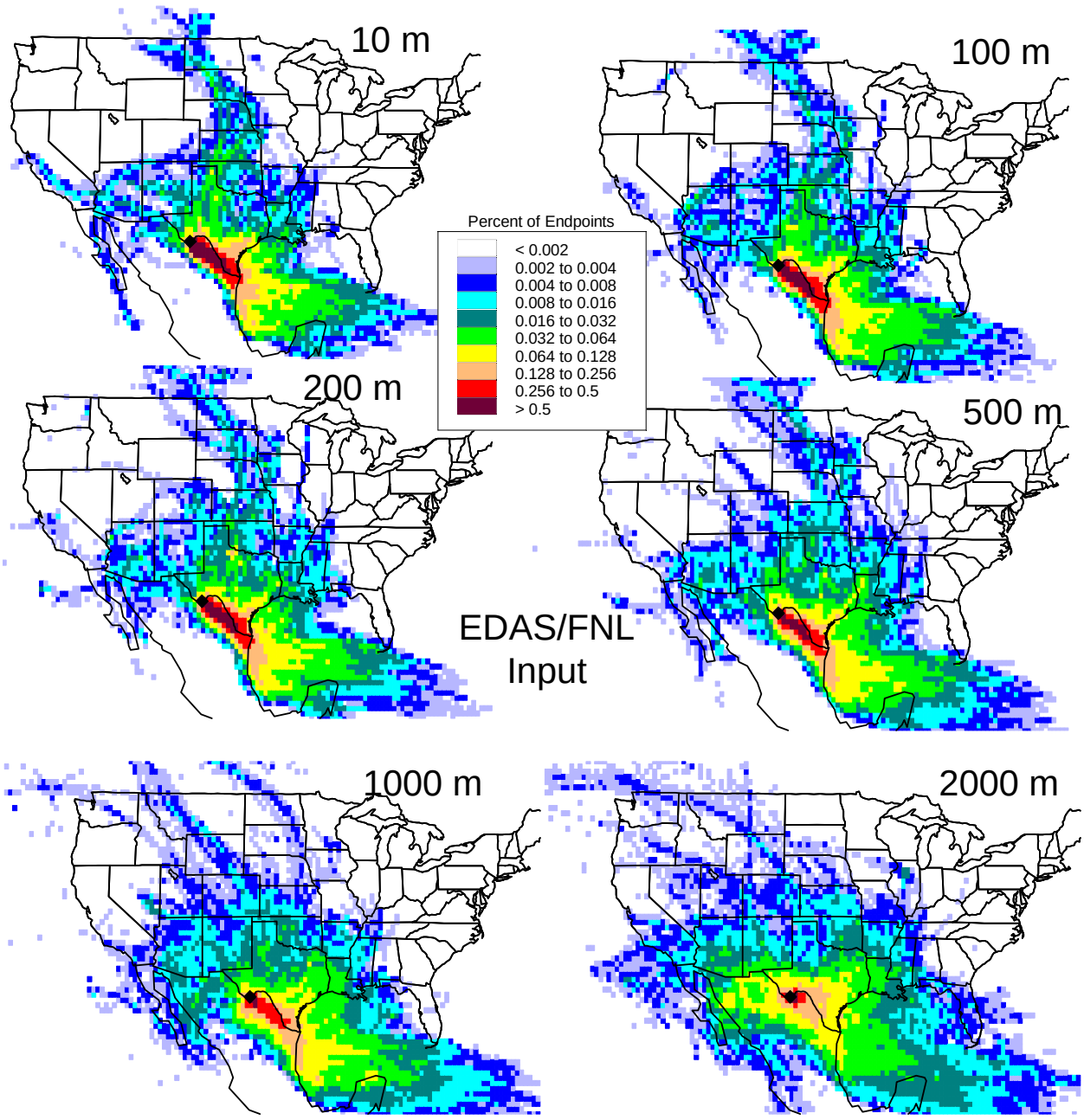

Figure 4-17. Overall Residence Times calculated with HYSPLIT and EDAS/FNL data during July–October 1999 with start heights of 10, 100, 200, 500, 1000, and 2000 m AGL.

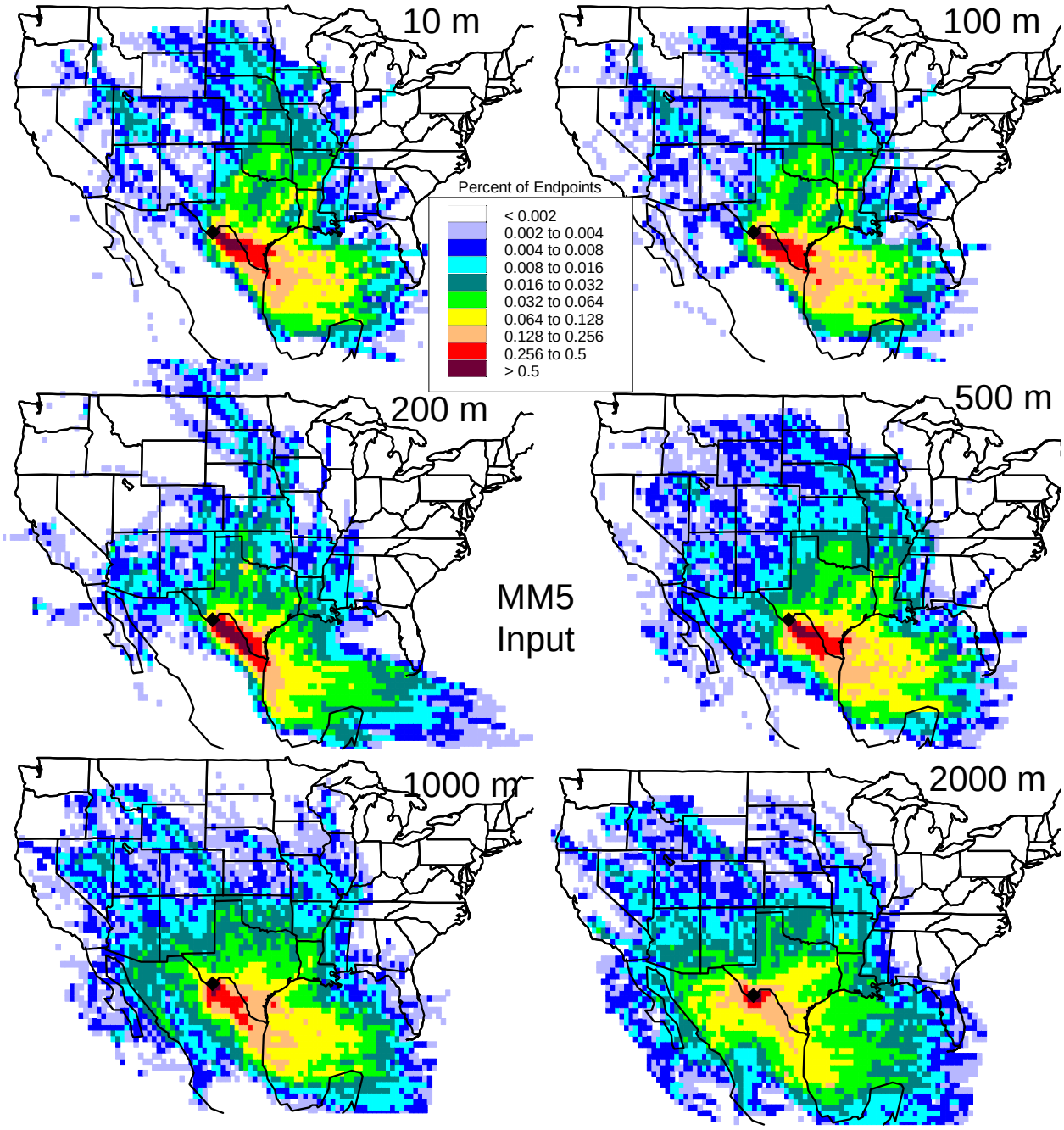

Figure 4-18. Overall Residence Times calculated with HYSPLIT and MM5 data during July–October 1999 with start heights of 10, 100, 200, 500, 1000, and 2000 m AGL.

4.3 Qualitative Evaluations Using Tracer Data

Several analyses can take advantage of the BRAVO tracer data to help determine the accuracy of the various back trajectories. Among the simplest qualitative analyses are those to determine whether the back trajectories correctly indicate a transport pathway between the known tracer-release sites and the receptor, especially for time periods when the tracer concentrations are high. An example is shown in Figure 4-19. Each row of the graph is for the day with the maximum 24-hour average measured tracer concentration for one of the four tracers

at Big Bend (K-Bar). Each column shows the trajectories generated by one of the back trajectory models. The colors indicate the input wind field: blue is MM5, red is EDAS (EDAS/FNL for CMC), green is FNL, black is rawinsonde data only, and brown is the rawinsonde data plus the BRAVO wind profilers. The black dots on each map show the tracer release site for the tracer which had the maximum concentration on that day.

Results are mixed and inconclusive. All models and wind field combinations are able to correctly locate the proper tracer release sites on the days of the highest Eagle Pass (August 22) and San Antonio (October 5) tracer concentrations. None of the combinations does well with the maximum Big Brown tracer (October 23), although CMC and HYSPLIT with MM5 come closest. For the day with the maximum Houston tracer (October 12), CMC with either input and ATAD with all inputs except MM5 correctly pass over the release site, while HYSPLIT with either FNL or MM5 input and for all start heights produces trajectories that are too far north.

A more efficient method of determining which model/wind field is best at locating the correct tracer emission sites is to examine the differences between the high concentration residence time and the overall residence times for each of the tracers. In this case, a high concentration was defined to be a 24-hour tracer concentration at the 80^{th} percentile or higher at Big Bend (K-Bar). Peak (HRT-ORT) differences should occur over the tracer release site or at least along the transport pathway between the tracer release site and the receptor.

As was the case with simply plotting trajectories for individual high tracer days, there was not a single back trajectory model or a single wind field input that uniformly performed better for all four tracers. All combinations did reasonably well at correctly finding the Eagle Pass and San Antonio release sites and, conversely, most combinations were unable to generate peak residence time differences in the vicinity of Big Brown for the iPPCH tracer. The two model/wind field combinations which did best for Big Brown were ATAD with EDAS/FNL and ATAD with MM5 data. For the Houston tracer, any model with EDAS/FNL input did reasonably well and ATAD with MM5 performed moderately well. In general, when model/wind field combinations missed the correct tracer release site, all combinations tended to miss in the same direction. For ocPDCH (Eagle Pass) those combinations that did less well missed the correct location by being too southerly (or too clockwise). For PDCB and PTCH from San Antonio and Houston, respectively, the trajectories tended to either be correct or be too far to the northwest (or too counterclockwise.) These results are illustrated in Figures 4-20 through 4-23.

Other, more quantitative analyses involving back trajectories and tracer concentrations are discussed in section 7.1 and analyses using forward trajectories from the CMC model are discussed in section 5.2.

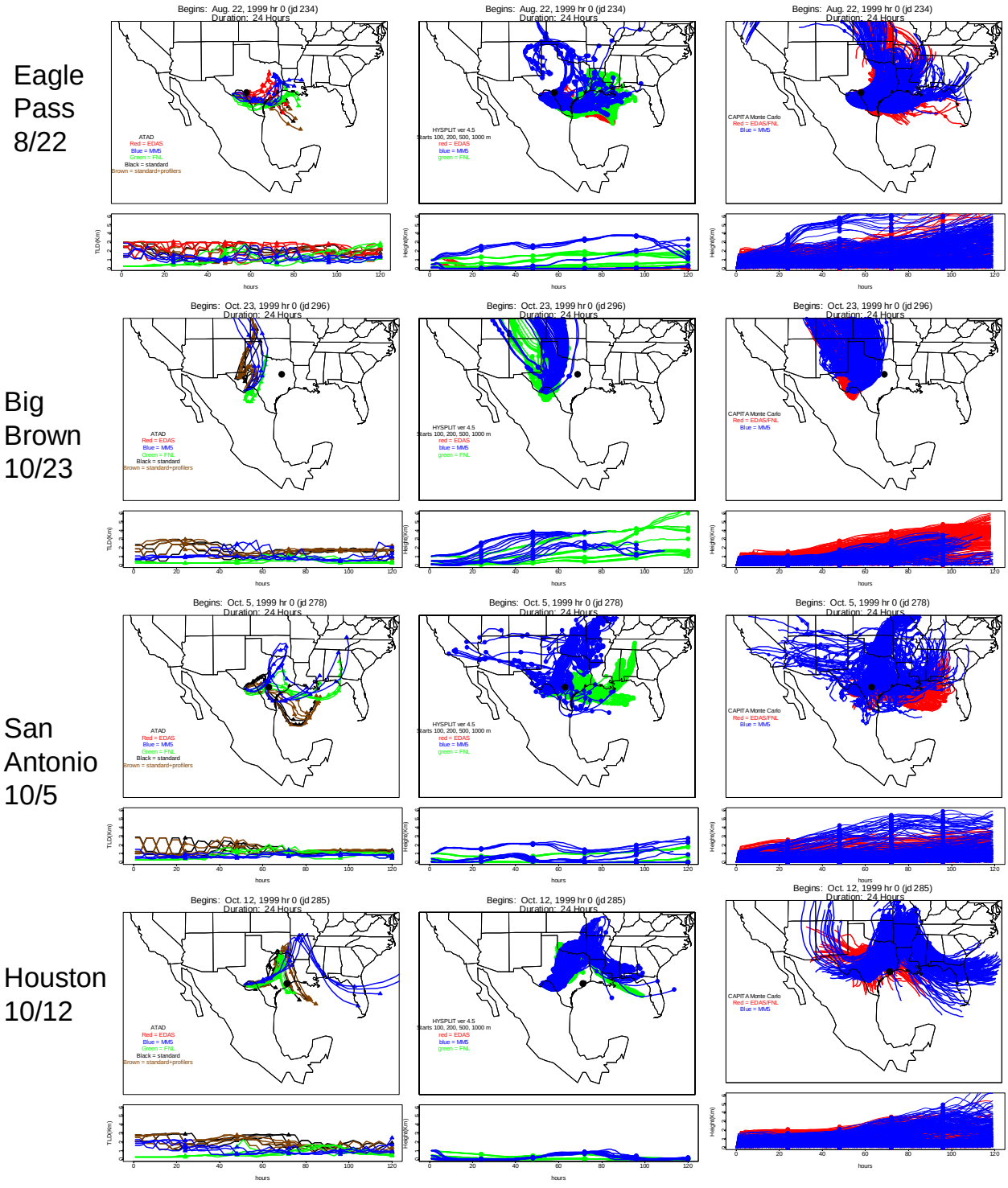

Figure 4-19. Back trajectories generated by all model and wind field combinations for the day of maximum tracer concentration at Big Bend for each tracer. The black dots indicate the tracer release sites for the tracer that had the high concentration on that day.

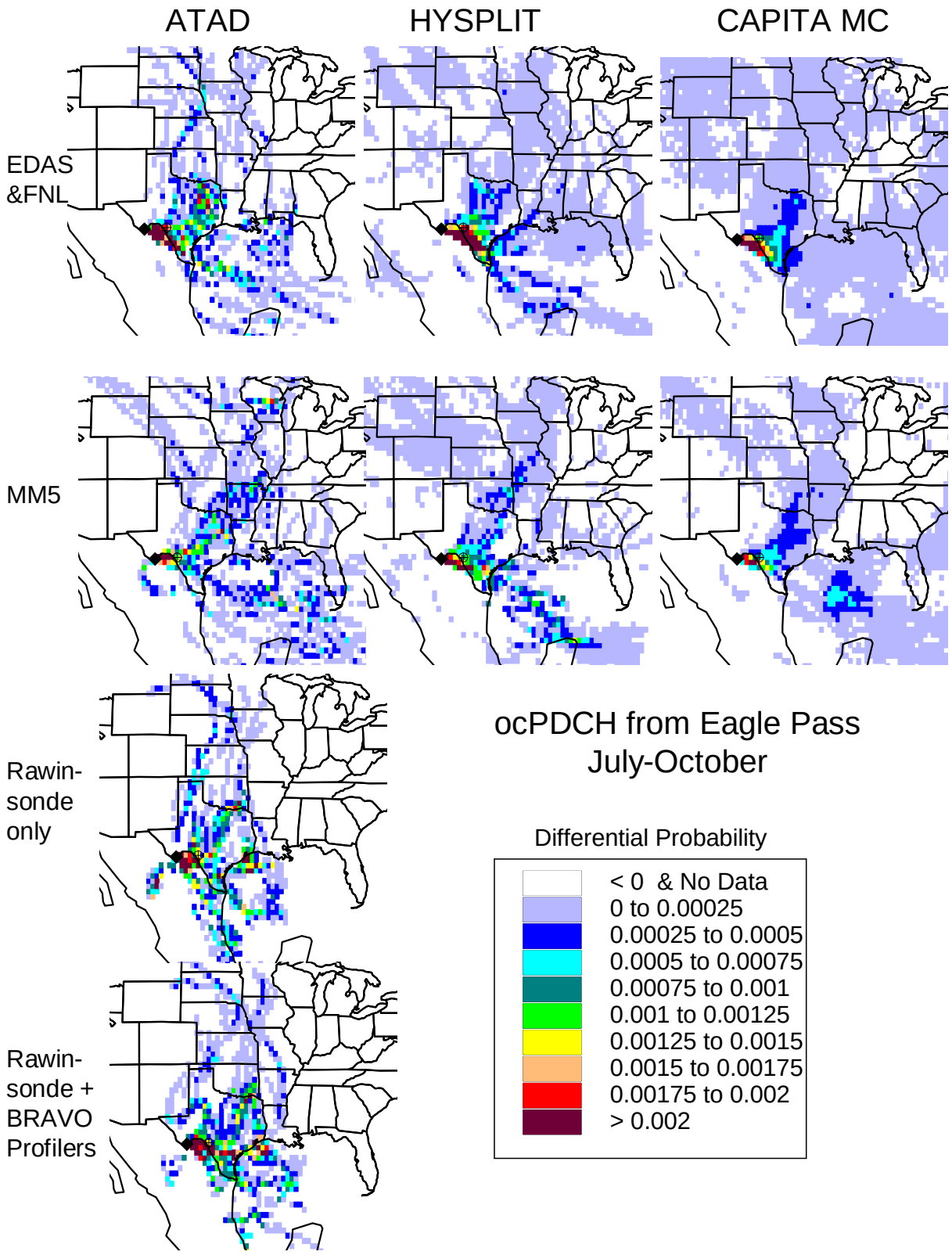

Figure 4-20. Differential Probability (HRT-ORT) for the Eagle Pass Tracer (ocPDCH). A high concentration is defined as 80th percentile or greater.

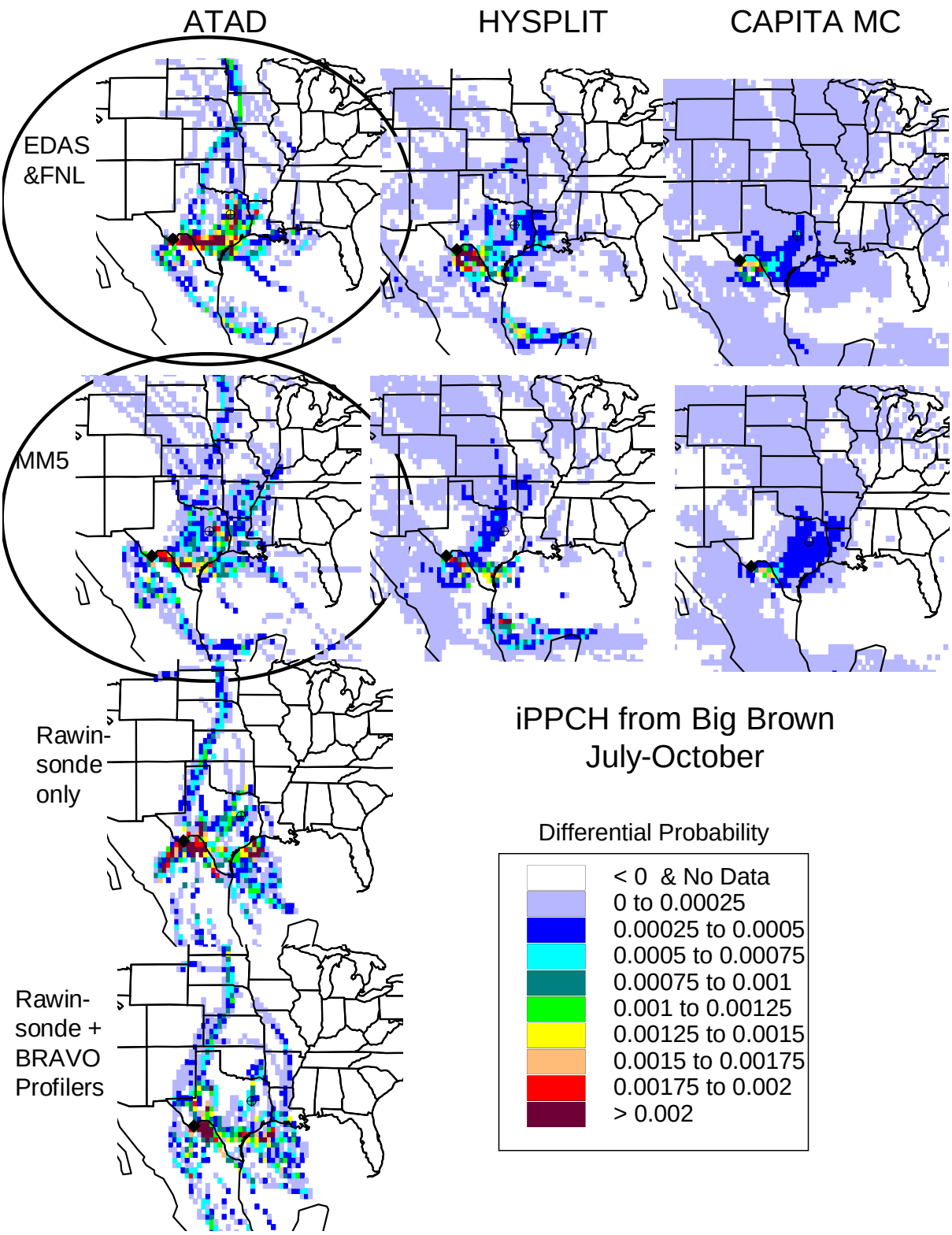

Figure 4-21. Differential Probability (HRT-ORT) for the Big Brown (iPPCH). A high concentration is defined as 80th percentile or greater. The two combinations that were subjectively determined to do the best are circled.

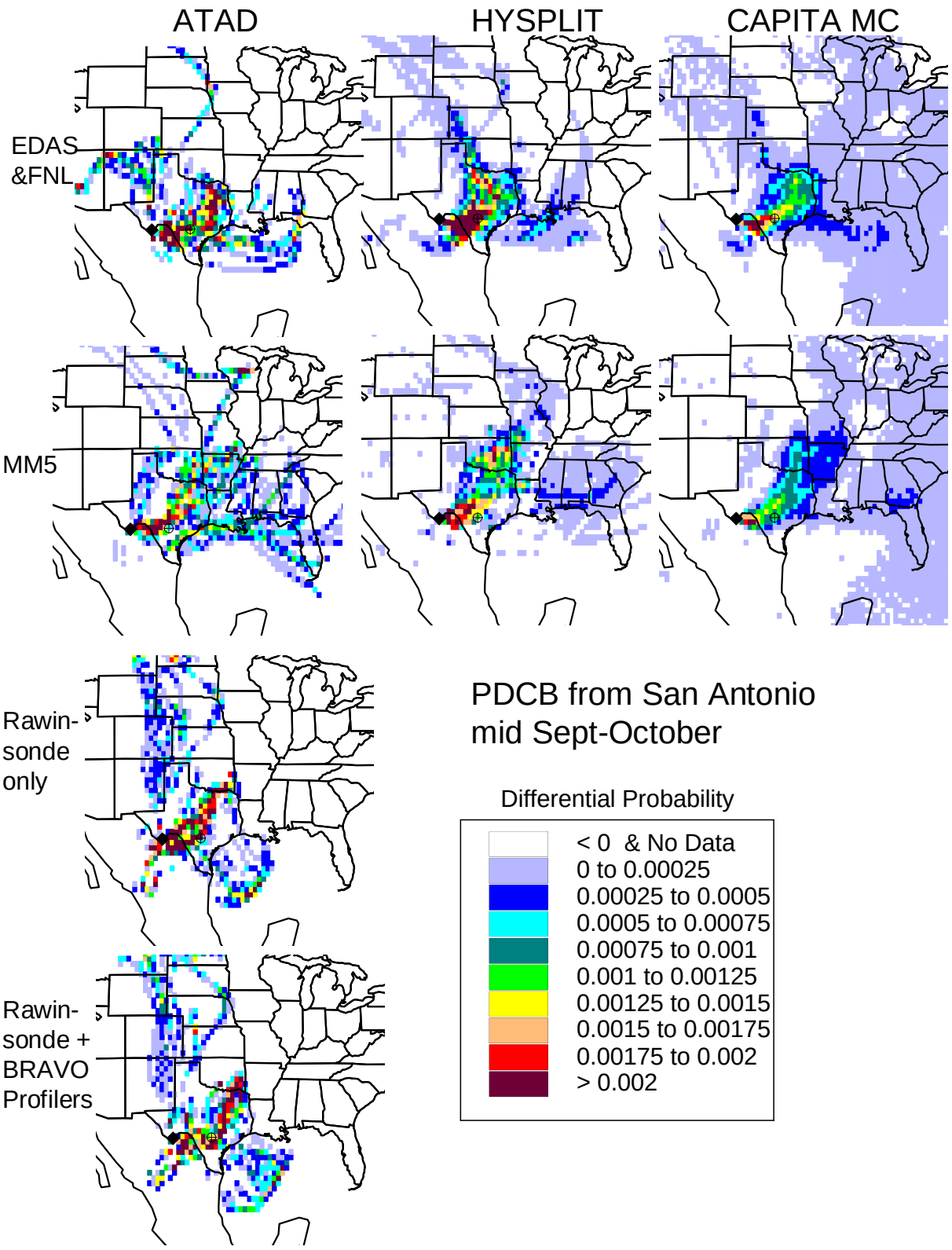

Figure 4-22. Differential Probability (HRT-ORT) for the San Antonio Tracer (PDCB). A high concentration is defined as 80th percentile or greater.

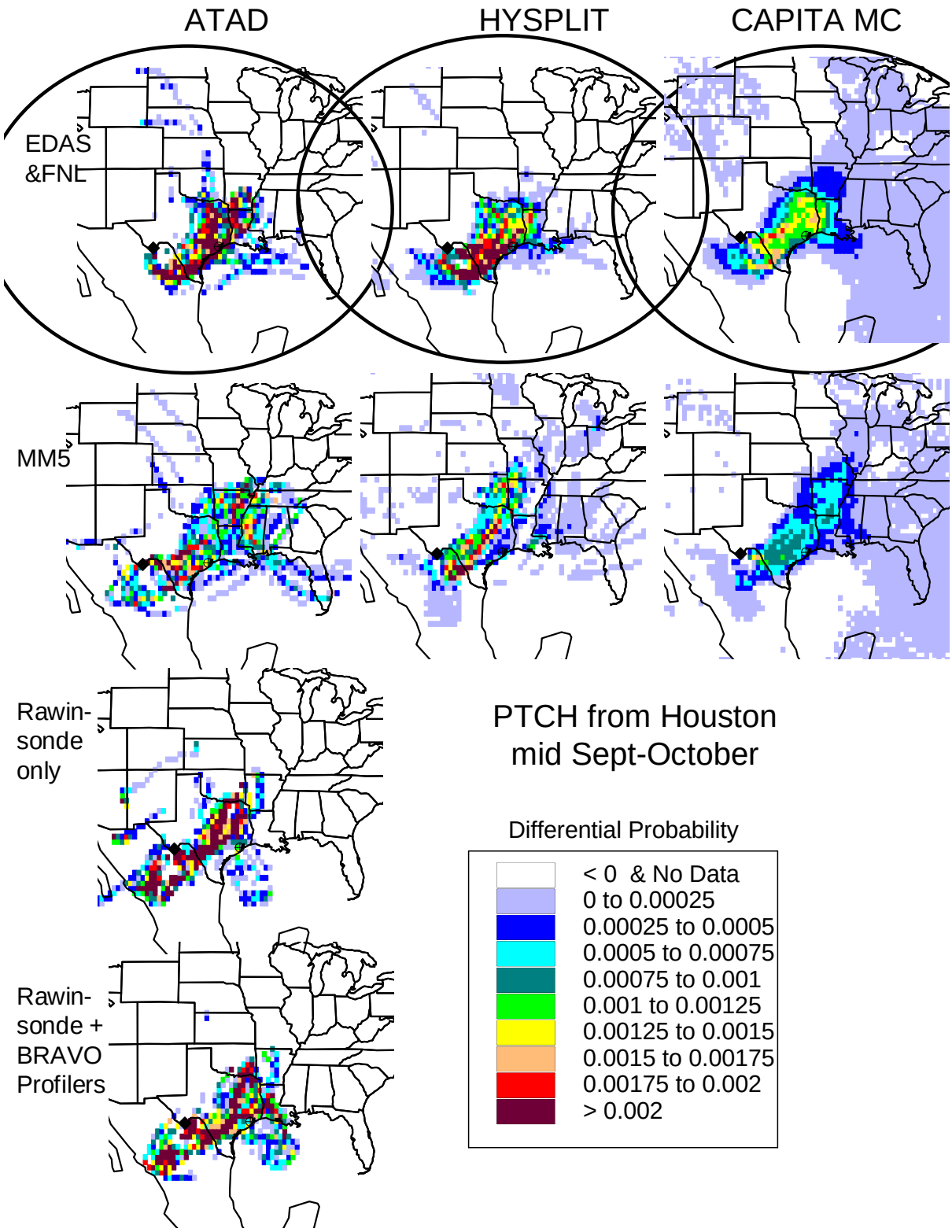

Figure 4-23. Differential Probability (HRT-ORT) for the Houston Tracer (PTCH). A high concentration is defined as 80th percentile or greater. The combinations that were subjectively determined to be doing better than the others are circled.

4.4 Biases at Big Bend during Other Seasons and Other Years

All of the analyses to this point are valid only for Big Bend during July–October 1999. Differences between the models and between the wind fields may be quite different during other years, during other seasons, and at other receptor sites. MM5 data and BRAVO wind profiler data are not readily available for other time periods. However, it is possible to easily examine differences between seasonal overall residence times as generated in previous studies with ATAD and using HYSPLIT with the most readily available wind fields, EDAS and FNL. All of these combinations can be run for six full years, 1997–2002.

Figure 4-24 shows the overall residence times for each season for these years and for each of these three combinations. Seasons are climatological, e.g., winter is December, January, and February.

For the fall season, 1999 is not included in any of the analyses to avoid having the HYSPLIT/EDAS analysis be for different years. For the summer season, the biases discussed for the BRAVO year appear to be consistent throughout the other years. ATAD is the most southerly, EDAS is the most easterly, and FNL falls between. During all other seasons, the major difference between ATAD and the HYSPLIT analyses is that HYSPLIT with either EDAS or FNL input has more trajectories arriving from the west. This indicates that previous analyses based only on ATAD trajectories may have underestimated the transport of airmasses, particularly from northwestern Mexico and Arizona.

Another simple test was to count the number of endpoints in each quadrant (NW, NE, SW, and SE) from the receptor and compare the results of each model/input data combination. Data for 1999 and 2000 were used, except fall included only 2000 to avoid the month of missing EDAS data.

Results for Big Bend are shown in Figure 4-25. ATAD in this figure refers to ATAD run with the typical rawinsonde data. EDAS and FNL refer to HYSPLIT output with these input data started at 1000 m. This is the start height that gives trajectories most similar to ATAD. HYSPLIT results in these analyses were limited to four start times per day and ATAD endpoints were interpolated to 1-hourly positions from the standard 3-hourly output. This gives the same total number of endpoints for each model/input combination. Days without full trajectories were eliminated. All models agree that the predominant wind direction is easterly during the summer (red). However, HYSPLIT/EDAS has nearly 5 times as many endpoints in the NE during the summer than ATAD, which has many more from the SE. This is consistent with all of the analyses for the BRAVO period. Predominant wind direction in the fall (yellow) is southerly with all model/input combinations showing little differences between SE and SW. However, HYSPLIT with either EDAS or FNL input has many more endpoints in the NW quadrant during the fall than does ATAD, which again shows more from the SE. During the winter (blue) and spring (green), ATAD is more likely to have trajectories arriving from the SE as opposed to HYPSLIT/EDAS with more from the SW.

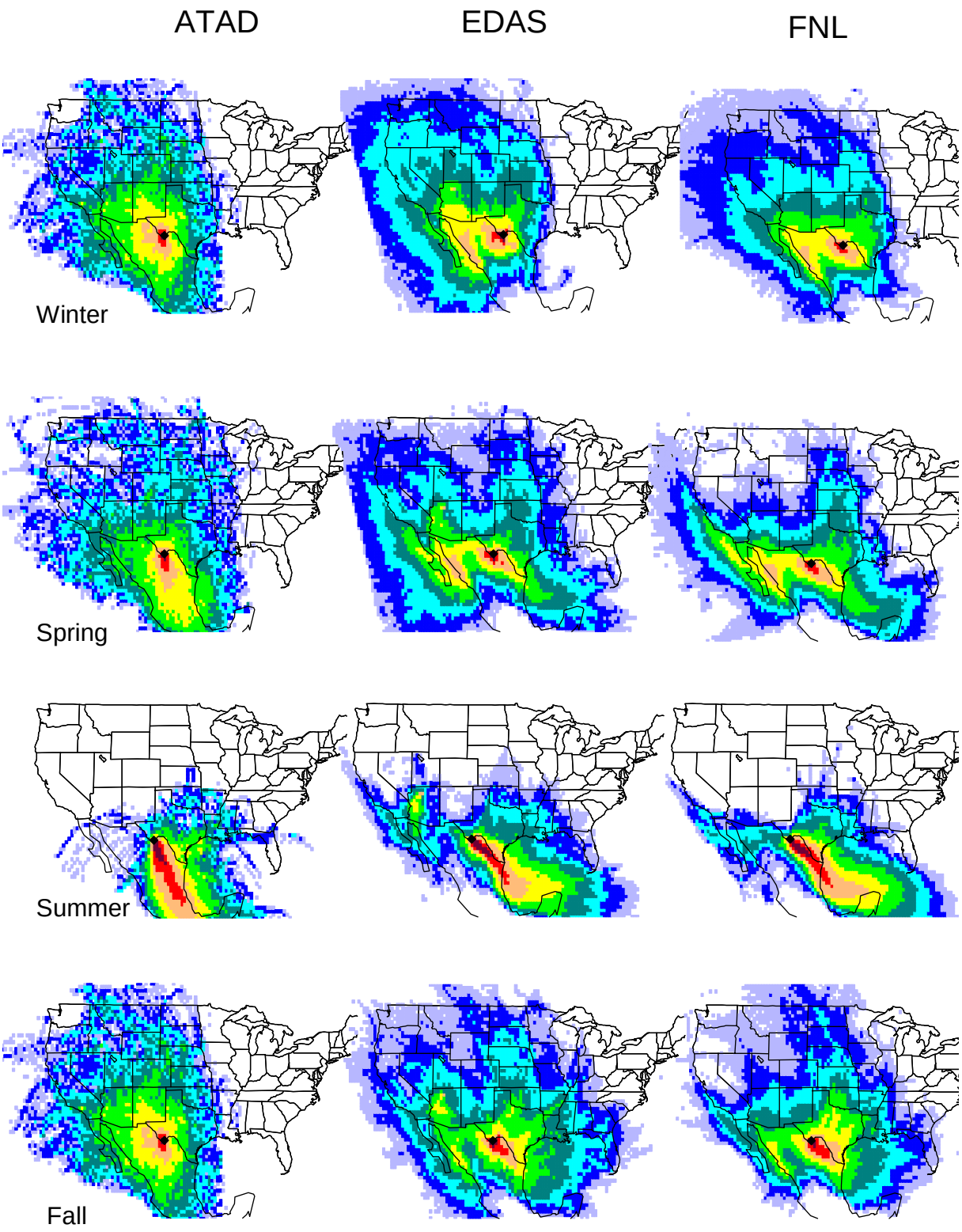

Figure 4-24. Overall Residence Times for 1997–2002 by season, and using ATAD with rawinsonde data, HYSPLIT with EDAS data, and HYSPLIT with FNL data. HYSPLIT results include start heights of 100, 200, 500, and 1000 m. Fall does not include 1999. Colors are the same as in Figure 4-18.

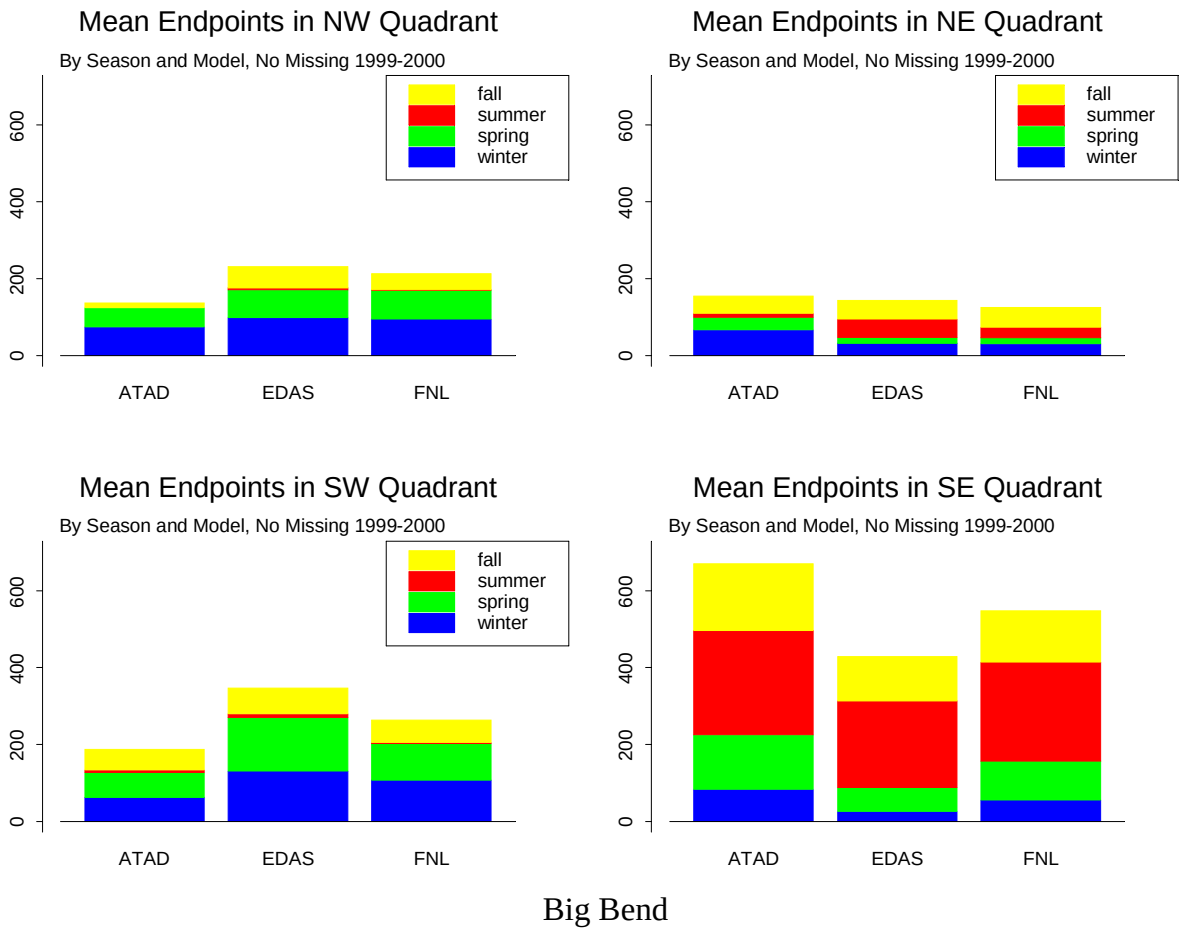

Figure 4-25. Mean number of back trajectory endpoints in each directional quadrant from Big Bend using ATAD with rawinsonde data and HYSPLIT with EDAS and FNL data started at 1000 m. Bar colors indicate seasons.

4.5 Biases in Other Regions during All Seasons

Comparisons between ATAD with rawinsonde input and results from HYSPLIT with both EDAS and FNL input, similar to those discussed in the previous section for Big Bend, were also compiled for Grand Canyon National Park, Arizona, and Great Smoky Mountains, Tennessee. This was to get a qualitative indication of whether similar directional differences in back trajectory output also exist for other parts of the country and whether conclusions drawn from BRAVO can be extrapolated to other sites and seasons.

Differences between model/input sets are smallest at Great Smoky Mountains, Tennessee. The largest differences at that site are in the spring (green bars) when ATAD has more trajectories arriving from the NE than does HYSPLIT/FNL, which has more from the NW. At Grand Canyon, Arizona, differences are small for all seasons for the predominant wind direction (airmasses from the SW). Largest differences are during the winter (blue bars) when ATAD is much more likely to have trajectories arriving from the NE and HYSPLIT/EDAS much more likely to show them arriving from the SE. On an annual average, HYSPLIT/EDAS has more trajectories arriving from the SE than either of the other combinations at both Grand

Canyon and Great Smoky Mountains. Interestingly, this is opposite of the directional bias at Big Bend where HYSPLIT/EDAS has the fewest endpoints arriving from the SE. These are shown in Figures 4-26 and 4-27. Results for these other sites will not be discussed in detail here, but in general, the results are different enough from the results for Big Bend that it seems likely that any biases between models and wind fields in other regions may be different from what was observed at Big Bend during BRAVO.

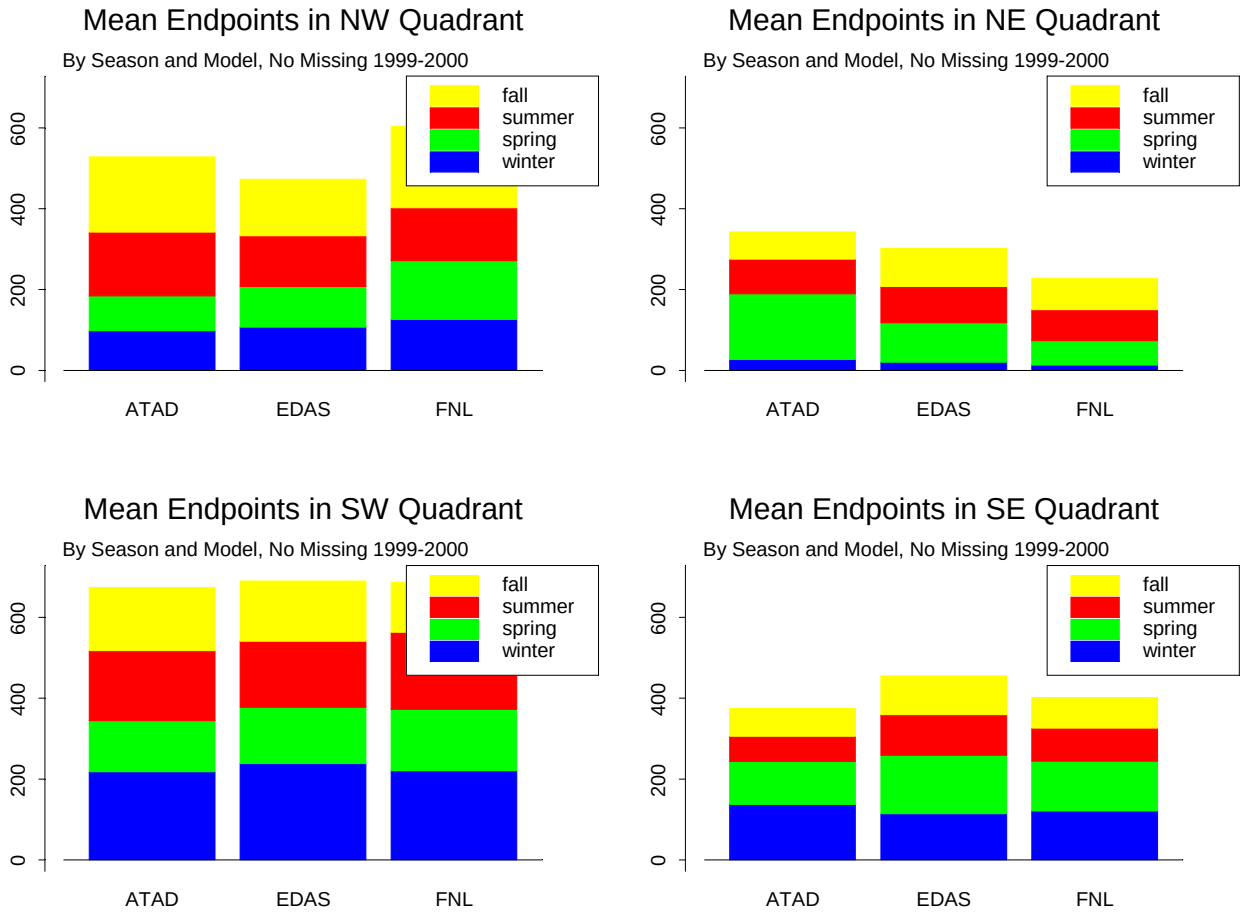

Figure 4-26. Mean number of back trajectory endpoints in each directional quadrant from Great Smoky Mountains National Park using ATAD with rawinsonde data and HYSPLIT with EDAS and FNL data started at 1000 m. Bar colors indicate seasons.

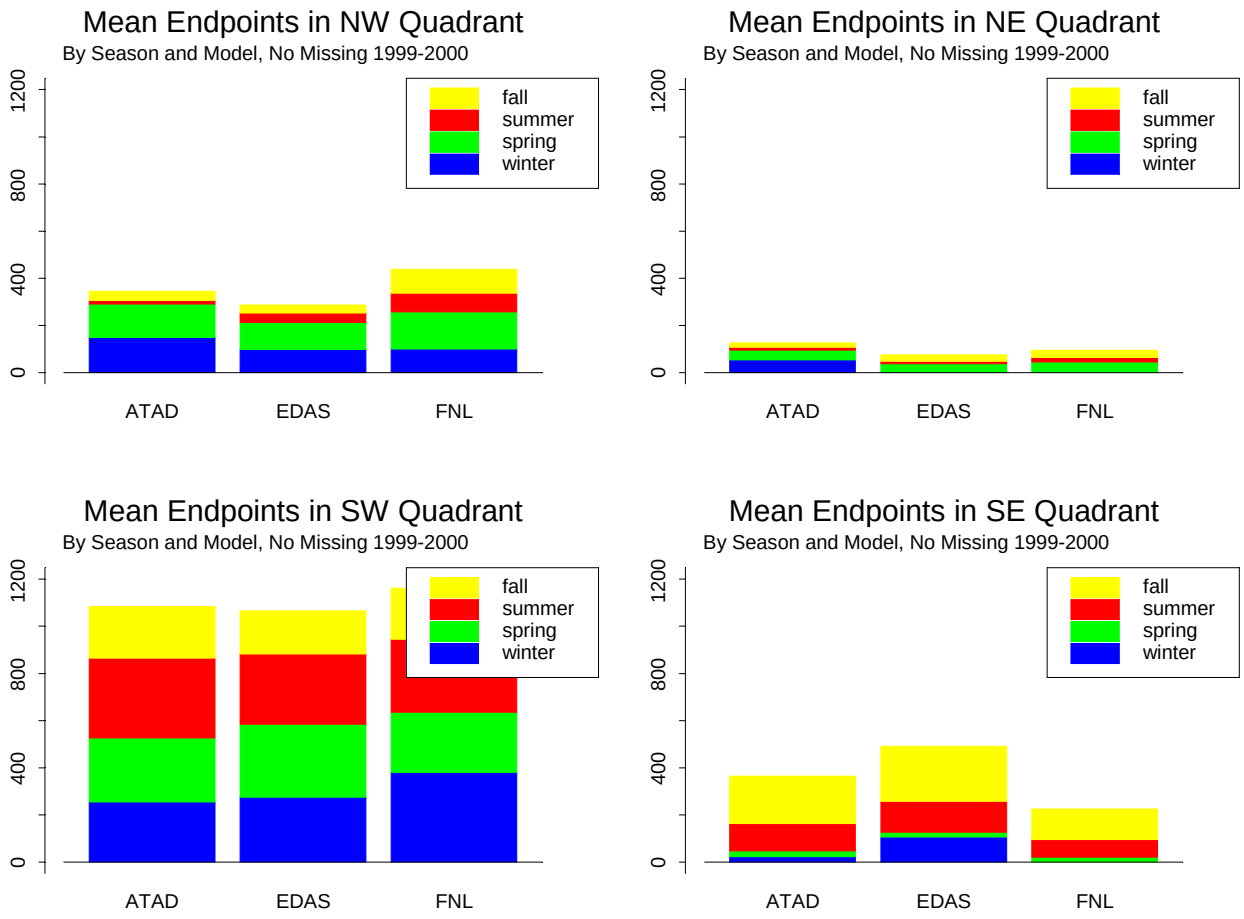

Figure 4-27. Mean number of back trajectory endpoints in each directional quadrant from Grand Canyon National Park using ATAD with rawinsonde data and HYSPLIT with EDAS and FNL data started at 1000 m. Bar colors indicate seasons.

4.6 Conclusions

Big Bend is a particularly challenging receptor site for which to generate back trajectories due to its proximity to both complex terrain and data-sparse areas. Analyses of back trajectories by several methods have shown that there are systematic differences between the results of different back trajectory model/input data combinations at Big Bend National Park during BRAVO.

Much of the difference appears to be due to the input wind field rather than the back trajectory model, although there are also some differences due to model alone. Using rawinsonde data alone (ATAD model only) gives back trajectories arriving from the most southerly direction, EDAS data results in the most easterly trajectories, with those generated using MM5 and FNL data falling between these extremes. These general directional biases are consistent across models and are more pronounced during summer than fall. The BRAVO tracer data clearly indicate that ATAD with rawinsonde data alone results in trajectories that are too southerly, especially during the summer. This is most likely due to the scarcity of rawinsonde data in Mexico and the absence of these data over the Gulf of Mexico. Even supplementing the

rawinsonde data with minimal additional data, e.g., information from the four BRAVO wind profilers, causes the ATAD/rawinsonde trajectories to be more similar to those generated using the gridded wind fields.

There are also some differences between results from different trajectory models even when the same input meteorological data are used. In general ATAD and CMC give results more similar to each other than to HYSPLIT. This is primarily because both ATAD and CMC, though different in mechanism, have the result of averaging the horizontal transport within the mixed layer. The predominant wind direction calculated by HYSPLIT is less southerly and more along the Texas-Mexico border than that calculated by ATAD and CMC using the same input wind fields. This is true for both EDAS/FNL and MM5 input.

HYSPLIT, which uses the gridded wind fields without the averaging of ATAD and without the random vertical movements of CMC, is more sensitive to start location, start height, and placement of individual endpoints. This is because slight changes in position can affect the grid cell for which data are used for the next time step. Slight differences in trajectory height can result in large differences in horizontal placement of trajectories in HYSPLIT during time periods when there is significant directional wind sheer with height, so that moving a trajectory endpoint from one horizontal level to the next drastically changes the wind direction. CMC can also be somewhat sensitive to height if a particle is moved from within the mixed layer to above. Differences caused by occasional bumping of a trajectory from one grid cell and/or horizontal layer to a neighboring one will tend to be minimized if trajectory data are aggregated over longer time periods, several start heights in HYSPLIT, more particles in CMC, and more start times per day. Both HYSPLIT and CMC allow trajectories to get as high as 10 km. Due to its different design, ATAD does not have trajectories above the mixed layer, with a maximum height of 3 km. An advantage of the CMC model over HYSPLIT is easy output of the height of the mixed layer.

Start heights in HYSPLIT affect the mean trajectory height and so the mean trajectory speed. Higher speeds and heights will tend to implicate more distant source areas, while lower speeds and heights give more weight to nearer sources. The lowest start heights result in the fewest endpoints in the western U.S. during BRAVO. Also for EDAS/FNL input, lower start heights have fewer endpoints in Mexico to the west and southwest of Big Bend. The fractions of endpoints in these areas increase as the start heights increase.

During October 1999, one quarter of the BRAVO time period, the EDAS winds were unavailable due to a lab fire. Evaluations of the possible consequences of having to substitute the lower-resolution FNL data during this month were investigated. The differences during October 1999 are not quantifiable, but during five other Octobers, using FNL data rather than EDAS resulted in fewer airmasses arriving from west and southwest Mexico and the southwestern United States, and more airmasses arriving from east Texas and from Mexico just south of the Texas border. During these five Octobers, HYSPLIT trajectories generated using FNL data were on average much lower than those generated with EDAS data and consequently had lower average wind speeds. The consequences of these biases will be smaller for the 4-month average of the BRAVO period than for October alone.

Cursory investigation of trajectory differences for other regions and other seasons indicate that the magnitude of the directional differences between the ATAD (rawinsonde), EDAS and FNL wind fields appears to be both geographically and seasonally dependent. So,

though there are also likely to be biases in other regions, the directions of these biases cannot be inferred from the BRAVO data.

The 36 km MM5 data and the EDAS/FNL data had approximately equal skill at predicting the tracer release locations and both data sets will be used for further back trajectory modeling. The MM5 data have a higher mean wind speed and will therefore be somewhat more likely to attribute concentrations to source areas farther away from Big Bend than will the EDAS/FNL wind fields. Further quantitative testing of the back trajectories against known attributions of both measured tracer concentrations and simulated sulfate concentrations were able to eliminate some combinations of trajectory models and input data. These tests are discussed in detail in chapter 7.

5) Forward Model Simulation of BRAVO Tracer Concentrations

The Regional Modeling System for Aerosols and Deposition (REMSAD) model is a prognostic, Eulerian-grid air quality model designed to simulate the formation and long-range transport of aerosols and their precursors (see section 2.2.1 for a full description). In this study, REMSAD was used to simulate the transport of sulfur from sources to Big Bend and other receptors and assess the source contributions of sulfate to these receptors. The CAPITA Monte Carlo (CMC) model is a particle dispersion model capable of simulating airmass advection and diffusion both forward and backward in time (see section 2.2.4 for a full description). The CMC model was used in both forward and backward airmass history analyses to analyze sulfur transport and estimate sulfur source apportionment.

In order to evaluate the ability of these two models to properly simulate the transport and diffusion processes, the models were used to simulate four conservative tracers that were released during the BRAVO study period. The models were then evaluated for their skill at reproducing the observed tracer time series in the Big Bend region. The REMSAD model was driven by the MM5 meteorological data while the CMC model was driven by both the MM5 and EDAS/FNL fields, and all simulations were run over the entire four month BRAVO period. The MM5 and EDAS/FNL field wind fields each have their advantages, the MM5 data having a higher resolution (36 km vs. 80 km), and the EDAS/FNL data incorporating more measured data in its data assimilation process.

This chapter reports on the comparison of the simulated to observed tracer concentrations to evaluate the ability of these models and wind fields to simulate medium- to long-range transport. The evaluation was conducted over the entire four month period, generating an aggregated model performance over a range of meteorological conditions. Identifying particular meteorological conditions and events that the models performed well and not well was not conducted. The performance of the two models using the MM5 meteorological data are also compared, as well as the difference between the CMC performance using the MM5 and EDAS meteorological drivers.

5.1 Perfluorocarbon Tracer Data and Model Simulation Requirements

The BRAVO tracer network consisted of four unique perfluorocarbon tracers released from or representing urban/electric utilities and measured at 24 monitors throughout West Texas The tracer data are fully described in section 2.1.1.2 and this section summarizes these tracer release and monitoring networks. Figure 5-1 presents both the tracer release sites and the monitoring network. The perfluorocarbon tracer experiment was conducted in two phases. In the first phase (July 5–September 13, 1999), two “timing” tracers were released at Eagle Pass to help characterize transport times from Eagle Pass to Big Bend NP. During the second phase of the study (September 17–November 1), the two timing tracers were moved to sites in eastern Texas in San Antonio and the Parish power plant in Houston where they were continually released. The tracer release sites were 230–750 km from the Big Bend National Park, which allowed for evaluating both near and distant mesoscale transport (100–1000 km). However, Big Bend is impacted from sources throughout North America, and this evaluation was unable to assess the regional scale (1000–5000) transport abilities of these models.

The tracer network included six 6-hour receptor sites, located along an arc extending from Big Bend to about 300 km north-northeast (Figure 5-1). These sites collected data throughout the four month period with high collection efficiencies. The other sites collected data

in July and only part of August and October and generally had lower collection efficiency. Only the 6-hour sites were used in this evaluation study due to their extended sampling period and their good collection efficiency.

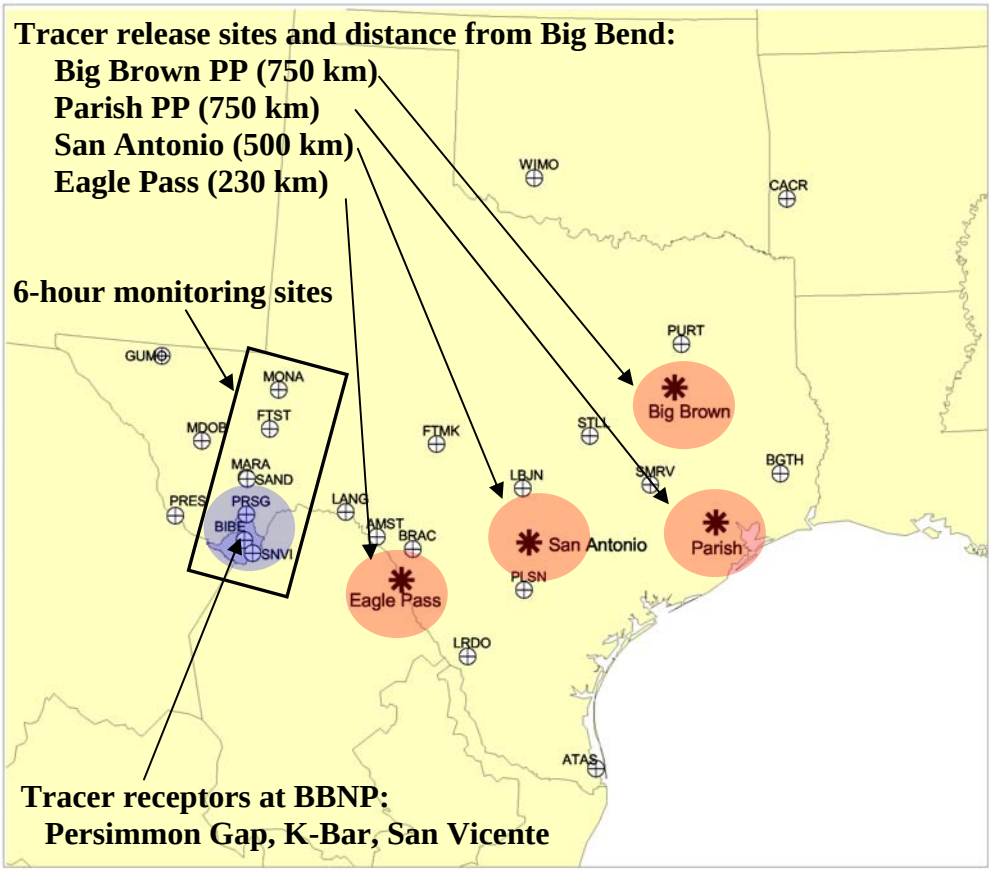

Figure 5-1. The location of the tracer release sites and tracer monitoring network. The distance from the tracer release sites to Big Bend is also noted.

5.1.1 Spatial Variability in the Tracer Concentration Field

The simulation of the BRAVO tracer data requires properly simulating the transport direction and speed from the tracer release sites to the receptor sites as well as the vertical and horizontal spreading of the tracer plume. This requires simulating the microscale processes of molecular and turbulent diffusion and the mesoscale process of advection, both of which are influenced by the topography and meteorology. The tracer concentration fields are sensitive to transport directions, since small errors can be the difference between a tracer impacting or missing a receptor site. In addition, the horizontal and vertical dilution of a plume is critical to properly simulating the concentration for a plume hit.

These processes result in a spatially and temporally heterogeneous concentration field. This is shown in Table 5-1, the correlation of the ocPDCH tracer released from Eagle Pass between the six 6-hour tracer monitoring sites. As shown, the correlation coefficients fall off rapidly with distance. For example, Marathon is about 100 km north of K-Bar Ranch in Big Bend National Park and the r=0.36 between these two sites. Consequently, the K-Bar tracer concentrations can explain only about 13% of the variance in Marathon's concentrations. Table

5-1 also presents the correlation between the sites for the 6-hour concentrations aggregated up to 24-hour concentrations. As shown, the correlations between the monitoring sites do improve somewhat for the nearby sites, e.g., r increased from 0.42 to 0.62 between K-Bar and Persimmon Gap.

Table 5-1. A) The correlation between the measured ocPDCH tracer concentrations at the six 6-hour monitoring sites. B) The same correlation matrix as in A) but the data were aggregated up to 24 hours. The distance between the receptor sites in km are in parentheses.

A) Eagle Pass (ocPDCH) Observed Tracer 6 hr Average Correlation Matrix

	San Vicente	K-Bar	Persimmon	Marathon	Ft Stocton	Monahans
San Vicente	1 (0)	0.76 (25)	0.32 (62)	0.32 (122)	0.34 (200)	0.12 (265)
K-Bar	0.76 (25)	1 (0)	0.42 (41)	0.36 (100)	0.28 (182)	-0.05 (245)
Persimmon	0.32 (62)	0.42 (41)	1 (0)	0.41 (60)	0.44 (140)	0.09 (205)
Marathon	0.32 (122)	0.36 (100)	0.41 (60)	1 (0)	0.53 (85)	0.06 (148)
Ft Stocton	0.34 (200)	0.28 (182)	0.44 (140)	0.53 (85)	1 (0)	0.22 (63)
Monahans	0.12 (265)	-0.05 (245)	0.09 (205)	0.06 (148)	0.22 (63)	1 (0)

B) Eagle Pass (ocPDCH) Observed Tracer 24 hr Average Correlation Matrix

	San Vicente	K-Bar	Persimmon	Marathon	Ft Stocton	Monahans
San Vicente	1 (0)	0.77 (25)	0.53 (62)	0.31 (122)	0.27 (200)	0.13 (265)
K-Bar	0.77 (25)	1 (0)	0.62 (41)	0.42 (100)	0.23 (182)	-0.07 (245)
Persimmon	0.53 (62)	0.62 (41)	1 (0)	0.69 (60)	0.3 (140)	-0.07 (205)
Marathon	0.31 (122)	0.42 (100)	0.69 (60)	1 (0)	0.64 (85)	0.12 (148)
Ft Stocton	0.27 (200)	0.23 (182)	0.3 (140)	0.64 (85)	1 (0)	0.41 (63)
Monahans	0.13 (265)	-0.07 (245)	-0.0 (205)	0.12 (148)	0.41 (63)	1 (0)

The correlation between the fine particulate sulfur and sulfur dioxide for the same six sites are presented in Table 5-2. The correlation between sites for particulate sulfur is greater than 0.8 for all site pairs indicating a spatially uniform concentration field compared to the tracer data. On the other hand, the sulfur dioxide correlations decrease more rapidly with distance than the tracer data. The spatially homogeneous particulate sulfur concentrations are due to it being a long-lived secondary species with characteristic lifetimes often in excess of 5 days, and the concentrations are impacted by emission from sources over a broad region. Sulfur dioxide is a shorter-lived species, with lifetimes on the order of 1–3 days, and the receptors are impacted by more nearby sources resulting in a more heterogeneous concentration field. The large variability in the tracer and sulfur dioxide concentrations make it a challenge to properly simulate their concentrations with regional scale models. However, the scale of variability in particulate sulfur is better matched to these regional models.

Table 5-2. The correlation of the A) 24-hour particulate sulfur concentrations and B) 24-hour sulfur dioxide between the same six monitoring sites as in Table 5-1.

A) Particle Sulfur observed 24 hr Average Correlation Matrix

	San Vicente	K-Bar	Persimmon	Marathon	Ft Stocton	Monahans
San Vicente	1 (0)	0.94 (25)	0.93 (62)	0.88 (122)	0.86 (200)	0.84 (265)
K-Bar	0.94 (25)	1 (0)	0.9 (41)	0.86 (100)	0.83 (182)	0.82 (245)
Persimmon	0.93 (62)	0.9 (41)	1 (0)	0.94 (60)	0.89 (140)	0.87 (205)
Marathon	0.88 (122)	0.86 (100)	0.94 (60)	1 (0)	0.92 (85)	0.89 (148)
Ft Stocton	0.86 (200)	0.83 (182)	0.89 (140)	0.92 (85)	1 (0)	0.89 (63)
Monahans	0.84 (265)	0.82 (245)	0.87 (205)	0.89 (148)	0.89 (63)	1 (0)

B) SO_2 24 hr Observed Average Correlation Matrix

	San Vicente	K-Bar	Persimmon	Marathon	Ft Stocton	Monahans
San Vicente	1 (0)	0.8 (25)	0.2 (62)	0.29 (122)	0.07 (200)	0.06 (265)
K-Bar	0.8 (25)	1 (0)	0.34 (41)	0.17 (100)	0.06 (182)	0 (245)
Persimmon	0.2 (62)	0.34 (41)	1 (0)	0.58 (60)	0.27 (140)	0.11 (205)
Marathon	0.29 (122)	0.17 (100)	0.58 (60)	1 (0)	0.45 (85)	0.1 (148)
Ft Stocton	0.07 (200)	0.06 (182)	0.27 (140)	0.45 (85)	1 (0)	0.11 (63)
Monahans	0.06 (265)	0 (245)	0.11 (205)	0.1 (148)	0.11 (63)	1 (0)

5.1.2 Inherent Uncertainty in the Tracer Simulation

The above section illustrated the high degree of variability in the tracer concentrations at distances as little as 25 and 40 km. The grid size of the REMSAD model is 36 km and in the CMC model it varied between 36 and 180 km depending on the wind field used. These models cannot capture the sub-grid variability in the tracer concentration. In addition, the true model resolution is four times the grid spacing [*Pielke*, 1984; *Grasso*, 2000], and the models cannot reproduce a high degree of spatial variability below this resolution. In the case of REMSAD the true spatial resolution of the 36 km grid is 144 x 144 km^2.

The REMSAD and CMC model resolutions place an upper limit on the skill that the models can achieve when simulating the tracer data. For example, even if the REMSAD simulation of tracer perfectly matched the measured tracer concentrations at K-Bar, there would be errors when compared to San Vicente which is in the same grid cell as K-Bar. In addition to errors due to model resolution, uncertainties in the measured data exist due to errors in the measurements and in the background concentrations subtracted from the measured concentration. The models cannot account for these measurement uncertainties. The total error due to the spatial resolution of the model and errors in the measured data can be viewed as the inherent uncertainty in the model simulation.

In order to assess this inherent uncertainty in the simulated tracer, the tracer time series from K-Bar, San Vicente, and Persimmon Gap were compared to each other. These sites are between 25 and 62 km of each other, which is less than twice the 36 km MM5 grid spacing. Differences between these tracer data measured at these monitoring sites can be viewed as a measure of the sub-grid scale variability and tracer measurement error. The tracer time series were compared by examining ratios in the pair-wise average concentrations, the root mean square (RMS) difference between pairs of data, and the correlation coefficient (Tables 5-3 to 5-5). These metrics are similar to the standard model performance statistics of bias, RMS error, and correlation coefficient which are used to compare the simulated results to the observed values. The Big Brown tracer concentrations were usually below detection limit and negative, leading to poor data quality. The comparisons of the Big Brown data are included Tables 5-3 to 5-5 for completeness, but are not discussed.

As shown in Tables 5-3 to 5-5, the K-Bar and San Vicente monitoring sites had mean tracer concentrations within 15% of each other for all three tracers. However, the average concentration at Persimmon Gap was about a factor of 3 larger than at K-Bar or San Vicente for the Eagle Pass tracer and within a factor of two for the tracers released from the more distant San Antonio and Parish tracers. The RMS difference varies between 100–400% for the Eagle Pass tracer, while for the San Antonio and Parish tracers it varies between 50–200%. The largest differences for all tracers were for Persimmon Gap data compared to the other sites.

These results illustrate the difficulty in simulating the tracer data. Since San Vicente and K-Bar are in the same REMSAD grid cell, even if the model perfectly matched the Eagle Pass tracer at K-Bar it would have a 100% RMS error compared to San Vicente. In order to reduce this inherent uncertainty in the tracer simulation, the observed and modeled tracer data were compared by aggregating the results for the three Big Bend sites, San Vicente, K-Bar and Persimmon Gap, and for the six 6-hour tracer sites extending from San Vicente north 265 km to Monahans Sandhills. The Big Bend sites were aggregated together since the MM5 and EDAS/FNL wind fields could not resolve transport to individual sites 30 km apart. Aggregating the six sites over the 300 km range allowed for the examination of the capabilities of the models to properly simulate the timing of the tracer reaching the receptors, while allowing for small spatial displacements in the tracer plume. This is a less stringent and more appropriate test for the models and their intended use. To obtain as complete a time series as possible, data from only one monitoring site was needed to have a valid average observed tracer concentration. Also, due to the background tracer concentration being subtracted from the measured concentrations, negative concentration values do occur. These negative values represent the error in the data and zeroing them out would lead to biased measured values. Therefore all negative values were left in the comparison.

Table 5-3. Comparison of K-Bar and San Vicente's tracer data.

K-Bar Vs San Vicente's Tracer Data								
		Avg (ppq)		Ratio	RMS Difference			
Tracer and Dates	#	K-Bar	San Vicente	SV/KB	Abs (ppq)	Relative to KB	Relative to SV	r
Eagle Pass (7/1–10/31)	88	0.14	0.12	0.86	0.14	0.97	1.17	0.81
San Antonio (9/17–10/31)	32	0.41	0.37	0.89	0.25	0.44	0.67	0.90
Parish (9/17–10/31)	32	0.060	0.063	1.0	0.05	0.78	0.72	0.77
Big Brown (7/1–10/31)	88	-0.012	-0.001	0.07	0.03	-2.5	-33.3	0.66

Table 5-4. Comparison of K-Bar's and Persimmon Gap's tracer data.

K-Bar Vs Persimmons Gap's Tracer Data								
		Avg (ppq)		Ratio	RMS Difference			
Tracer and Dates	#	K-Bar	Pers. Gap	PG/KB	Abs (ppq)	Relative to KB	Relative to PG	r
Eagle Pass (7/1–10/31)	95	0.15	0.39	2.7	0.47	3.2	1.20	0.47
San Antonio (9/17–10/31)	38	0.59	0.35	0.59	0.45	0.80	1.28	0.88
Parish (9/17–10/31)	95	0.060	0.046	0.77	0.07	1.2	1.50	0.72
Big Brown (7/1–10/31)	38	-0.012	0.006	-0.48	0.05	-3.9	8.0	0.47

Table 5-5. Comparison of San Vicente and Persimmon Gap's tracer data.

San Vicente Vs Persimmon Gap's Tracer Data								
		Avg (ppq)		Ratio	RMS Difference			
Tracer and Dates	#	San Vicente	Pers. Gap	PG/SV	Abs (ppq)	Relative to SV	Relative to PG	r
Eagle Pass (7/1–10/31)	81	0.12	0.37	3.2	0.49	4.2	1.31	0.37
San Antonio (9/17–10/31)	31	0.33	0.18	0.54	0.40	1.2	2.29	0.58
Parish (9/17–10/31)	31	0.059	0.048	0.81	0.05	0.93	1.14	0.74
Big Brown (7/1–10/31)	81	-0.003	0.009	-2.8	0.05	-14.4	5.1	0.40

5.2 CAPITA Monte Carlo Model Simulation of Tracer Data

The CAPITA Monte Carlo model was used to simulate the tracer released from all four locations driven by either the BRAVO 36 km MM5 winds or a combination of the EDAS and FNL meteorological fields. The FNL data were used in October 1999 since the EDAS fields were not available. Section 2.1.3 provides detailed descriptions of the wind fields and data processing needed for input into the CMC model. The model was operated by releasing 100 particles every hour from each tracer release location at a fixed effective release height (Table 5-6). The Eagle Pass and San Antonio tracers were released from towers, so the effective stack height is the actual release point. The Big Brown and Parish tracers were injected into power plant stacks, and their effective release heights were the stack height plus a plume rise calculated from average stack and meteorological parameters. The particles were tracked for five days or until they left the meteorological grid. Each particle was weighted by the actual tracer emission rates divided by the number of particles release each hour. Simulated tracer concentration fields were generated every hour by summing the weights of all particles that fell in a given 36 km grid and below the mixed layer. This mass was normalized by the receptor cell's volume, the grid area times the mixing height, creating concentration fields.

Table 5-6. The tracer effective release heights and design tracer emission rates used in the CMC for each simulated tracer release location.

Release Site	Tracer	Release Rate (kg/day)	Release Schedule	Eff. Release Hgt. (m)	Distance from Big Bend (km)
Eagle Pass	ocPDCH	3.7	Continuous 7/1 – 11/1/99	100	230
San Antonio	PDCB	9.7	Continuous 9/17 – 11/1/99	20	500
Parish (Houston TX)	1PTCH	2.6	Continuous 9/17 – 11/1/99	400	750
Big Brown (Northeast TX)	iPPCH	2	Continuous 7/1 – 11/1/99	400	750

The actual tracer release rates used in the simulation are presented in Figures 2-3 to 2-6. These release rates were similar to the designed release rates reported in Table 5-6, but show some diurnal cycling and periods where no tracer was released. For example, PPCH was not released from the Big Brown power plant from October 8–16. This was unfortunate since this was one of the intensive modeling periods and a period when transport simulations showed transport from northern Texas.

5.2.1 Results of the Monte Carlo Model Tracer Simulation

The results of the simulation are presented in Figures 5-2 and 5-3 and Tables 5-7 and 5-8. As shown in Figure 5-2, the model simulations using the MM5 or the EDAS/FNL meteorological fields were able to reproduce the timing of the major Eagle Pass (ocPDCH) tracer impacts to Big Bend. The duration of the simulated tracer impacts tended to be about the same as measured or shorter. The MM5 simulation was better able to predict the Eagle Pass tracer pattern particularly from August 10 to September 12. Neither simulation was able to reproduce the day to day variability of the observed data with great skill, having correlation coefficients of 0.44 for MM5 and 0.53 for the EDAS/FNL meteorological fields. However, the correlation coefficient in both cases is significant at the 1% level. The EDAS simulation underestimated the Eagle Pass tracer by about a factor of 2 at Big Bend while the MM5 simulation underestimated the average

concentration by only 10%. Both simulations reproduce the measured data's standard deviation. Therefore, the MM5 simulation had a similar distribution as the observed values, while the EDAS simulation is biased low. Both simulations also had similar RMS errors of about 120% or an error greater than a factor of 2 in simulating transport from Eagle Pass to Big Bend.

The Eagle Pass tracer simulation averaged over all six monitoring sites is presented in Figure 5-3 and Table 5-8. Again, both model simulations reproduce the observed tracer pattern. The MM5 simulation properly identifies the time and duration of the Eagle Pass tracer impacts to this region and the correlation coefficient increased from 0.44 to 0.54 compared to the Big Bend simulation. However, the MM5 simulation does not fully capture the observed tracer peaks. This is reflected in the performance statistics (Table 5-8) where the predicted tracer concentrations are underestimated by 30% on average, and the standard deviation of the predicted values is 0.2 ppq compared to 0.29 ppq for the observed data. The RMS error decreased by almost half to 73%, indicating that the model is able to simulate the transport to within ±150 km of the receptor with concentrations within less than a factor of 2 of the observed values.

The performance statistics for the EDAS/FNL winds averaged over all six sites did not show as large an improvement over those for just the Big Bend region. The EDAS/FNL simulation still underestimated the observed values by a factor of two and the correlation coefficient decreased from 0.53 to 0.46. The RMS error did improve from 120% to 95%. Examination of the vertical profiles of the EDAS/FNL simulations showed that, on average, ~50% of the mass was above the mixing layer. Therefore, the underestimation could be due to the particles being mixed too high prior to reaching Big Bend or the vertical velocities are inappropriately carrying mass above the mixed layer.

Tracer was released from San Antonio, Texas, and the Parish power plant in Houston, Texas, from September 17 through October. These tracer release sites are further from Big Bend than Eagle Pass, at ~500 km and 750 km, respectively. Therefore these tracers were a better test of the model's ability to simulate more regional scale transport. The tracer released from San Antonio was measured at Big Bend above the background a number of times in the first half of October. Impacts of the simulated tracer at Big Bend also occurred during this time period (Figure 5-2). The model run using EDAS/FNL had the most skill at reproducing the day to day variability with a correlation coefficient of 0.69 compared to 0.36 using the MM5 winds (Table 5-7). In addition, the EDAS/FNL simulation underestimated the San Antonio tracer at Big Bend by about 13% while the MM5 simulation overestimated the tracer by about 25%. The San Antonio RMS error was 140% using the EDAS/FNL winds, but 240% using the MM5 winds. The large RMS error for the MM5 simulation was due to the overestimation of the concentrations by about a factor of 5 on September 30 and October 24.

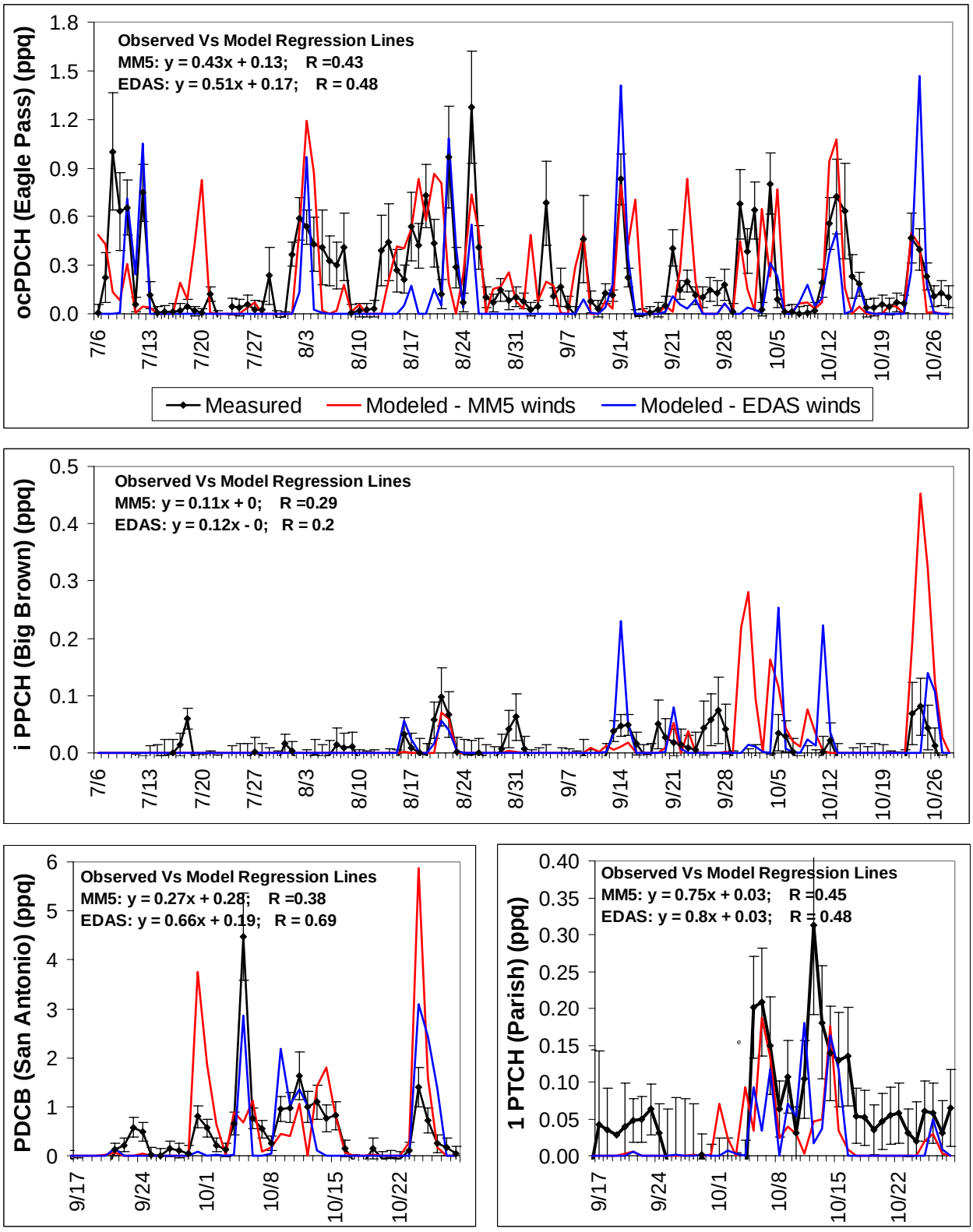

Figure 5-2. Comparison of observed and CMC modeled tracer data at Big Bend, Texas. The observed and modeled tracer data were averaged over the K-Bar, Persimmon Gap, and San Vicente monitoring sites which are in or at the boundary of the park. The measured data include error bars.

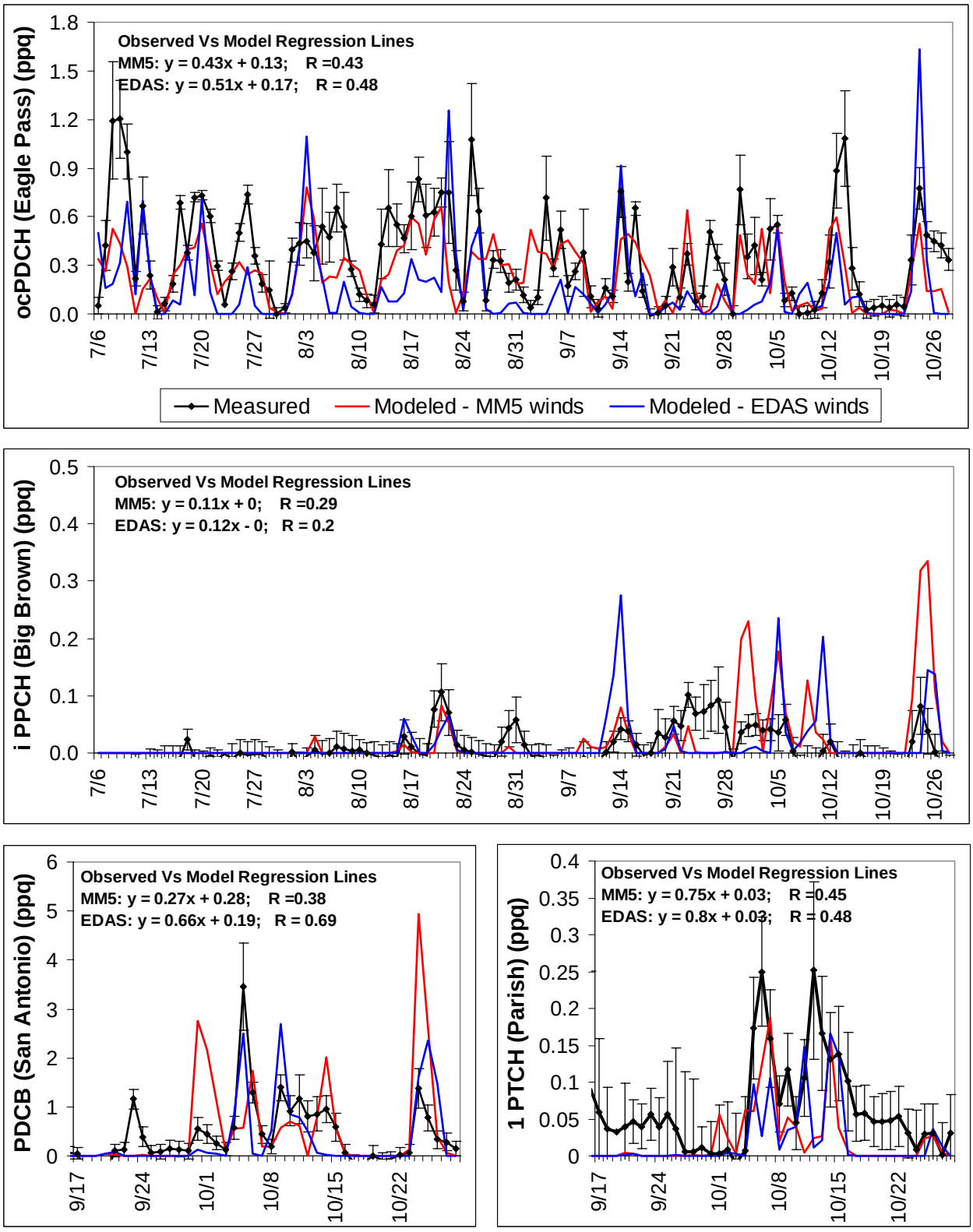

Figure 5-3. Comparison of observed and CMC modeled tracer data in southwest Texas. The observed and modeled tracer data were averaged over the six 6-hour monitoring sites: San Vicente, K-Bar, Persimmon Gap, Marathon, Fort Stockton, and Monahans Sandhills. The measured data include error bars.

Table 5-7. The CMC model performance statistics for the simulation of tracer average over the three Big Bend sites (San Vicente, K-Bar and Persimmon Gap). The modeled and observed statistics used the same days.

	MM5 Wind Fields Average Over Big Bend Sites (K-Bar, Persimmon Gap, San Vicente)											
		Average (ppq)		Bias	Std Dev (ppq)		Coef. of Variation		RMS Error		Correlation Line (ppq)	
	#	Obs	Model	Model/Obs	Obs	Model	Obs	Model	Abs.(ppq)	Relative	r	Intercept	slope
Eagle Pass (ocPDCH)	109	0.24	0.21	0.89	0.28	0.29	1.12	1.4	0.29	1.23	0.44*	0.13	0.43
San Antonio (PDCB)	40	0.46	0.58	1.26	0.79	1.12	1.8	2.0	1.1	2.4	0.36	0.28	0.27
Parish (1PTCH)	40	0.057	0.025	0.44	0.08	0.05	1.4	1.8	0.072	1.26	0.51*	0.03	0.75
Big Brown (iPPCH)	109	0.001	0.021	16.90	0.03	0.07	30.0	3.3	0.07	54.76	0.29*	0.00	0.11

	EDAS Wind Fields Average Over Big Bend Sites (K-Bar, Persimmon Gap, San Vicente)											
		Average(ppq)		Bias	Std Dev (ppq)		Coef. of Variation		RMS Error		Correlation Line (ppq)	
	#	Obs	Model	Model/Obs	Obs	Model	Obs	Model	Abs.(ppq)	Relative	r	Intercept	slope
Eagle Pass (ocPDCH)	109	0.24	0.11	0.47	0.28	0.26	1.12	2.5	0.30	1.22	0.53*	0.17	0.51
San Antonio (PDCB)	40	0.46	0.4	0.87	0.79	0.82	1.8	2.1	0.63	1.4	0.69*	0.19	0.66
Parish (1PTCH)	40	0.057	0.024	0.42	0.08	0.05	1.4	2.0	0.074	1.3	0.49*	0.03	0.80
Big Brown (iPPCH)	109	0.001	0.012	9.77	0.03	0.04	30.0	3.3	0.05	37.20	0.20	0.00	0.12

*Significant at the 1% level.

Table 5-8. The CMC model performance statistics for the simulation of tracer average over the six 6-hour tracer sites: San Vicente, K-Bar, Persimmon Gap, Marathon, Fort Stockton and Monahans Sandhills. The modeled and observed statistics used the same days.

	MM5 Wind Fields Average Over All 6-hour Tracer Sites												
		Average (ppq)		Bias	Std Dev (ppq)		Coef. of Variation		RMS Error		Correlation Line (ppq)		
	#	Obs	Model	Model/Obs	Obs	Model	Obs	Model	Abs.(ppq)	Relative	r	Intercept	slope
Eagle Pass (ocPDCH)	111	0.37	0.26	0.7	0.29	0.19	0.78	0.74	0.27	0.73	0.54*	0.13	0.85
San Antonio (PDCB)	41	0.43	0.56	1.28	0.67	1.01	1.6	1.8	0.94	2.2	0.41*	0.27	0.28
Parish (1PTCH)	41	0.063	0.023	0.37	0.06	0.04	1.0	1.9	0.064	1.05	0.55*	0.04	0.81
Big Brown (iPPCH)	111	0.004	0.021	4.86	0.03	0.06	7.5	2.9	0.06	12.88	0.38*	0.00	0.21

	EDAS Wind Fields Average Over All 6-hour Tracer Sites												
		Average(ppq)		Bias	Std Dev (ppq)		Coef. of Variation		RMS Error		Correlation Line (ppq)		
	#	Obs	Model	Model/Obs	Obs	Model	Obs	Model	Abs.(ppq)	Relative	r	Intercept	slope
Eagle Pass (ocPDCH)	111	0.37	0.17	0.46	0.29	0.26	0.78	1.6	0.34	0.95	0.46*	0.26	0.51
San Antonio (PDCB)	41	0.43	0.36	0.84	0.67	0.71	1.6	2.0	0.55	1.28	0.69*	0.20	0.63
Parish (1PTCH)	41	0.063	0.021	0.33	0.06	0.04	1.0	2.1	0.07	1.1	0.51*	0.04	0.74
Big Brown	111	0.004	0.015	3.45	0.03	0.04	7.5	2.7	0.05	11.88	0.17	0.00	0.12

*Significant at the 1% level.

The tracer released from the Parish site also had the largest impacts at Big Bend in the first half of October. Both EDAS/FNL and MM5 simulations reproduced these impacts and simulated the tracer with about equal skill, underestimating the average concentration by about a factor of 2 and correlation coefficients of ~0.5. The large underestimation was primarily due to the simulations missing the tracer impacts in September and late October when the measured tracer was low. Also, the largest measured tracer concentration on October 12, 1999, was not reproduced in either simulation (Figure 5-2). The RMS error for the Parish tracer simulation was about 130% for both wind fields (Table 5-7).

The simulations compared to the measured tracer concentrations averaged over all 6 sites did not appreciably improve the model comparison statistics for the San Antonio tracer, with the RMS error decreasing by only ~10%. However, the RMS error for the Parish tracer simulations decreased by more than 20% (Tables 5-8 and 5-9) from ~130% to ~110% for both simulations.

The Big Brown power plant is about 750 km from Big Bend located in northeastern Texas. The tracer released from this plant was only occasionally measured above the background concentrations at Big Bend, leading to poor quality tracer data. Both model runs were able to closely reproduce the timing and magnitudes of the August 15–24 Big Brown tracer episode; however, overall, the model simulation did not compare well with the observed concentration. It is not known whether this poor correspondence is due to errors in the measurements or the model simulations.

These modeling performance statistics were also calculated for each monitoring site. In nearly all cases, the simulation compared better to the spatially aggregated tracer concentrations than to the individual sites. This was expected, due to the large spatial heterogeneity in the measured tracer data.

5.3 REMSAD Simulation of Tracer Data

The REMSAD regional air quality model was used to simulate the transport and dispersion of the four inert tracers. The configuration of REMSAD for the tracer simulation was similar to the base emissions simulation, except that 1) the chemistry mechanism was not invoked, since the tracer did not undergo chemical transformation, 2) loss via depositional settling was not considered, since it was assumed that the tracers have very low deposition velocities, and 3) background concentrations were set to zero. Horizontal winds, temperature, and other meteorological fields were simulated by MM5.

Each of the four tracer releases was treated as a point source emission within REMSAD. REMSAD simulates the initial plume rise of an elevated point source. Two of the tracers – PPCH at the Big Brown power plant and 1PTCH at the Parish power plant – were released inside a plant stack and hence were lofted higher into the boundary layer due to buoyant and momentum plume rise. Plume rise can affect the subsequent transport of the tracer, as the transport can depend on the initial elevation of its release.

5.3.1 Results of the REMSAD Tracer Simulation

The performance of the REMSAD tracer simulation was evaluated by comparing the predicted tracer time series at the three Big Bend NP monitors with the observed tracer time series. Results for the Eagle Pass and northeast Texas tracers are shown for the entire four month BRAVO period, while results for the San Antonio and Parish tracers are shown for the last six weeks of the BRAVO period when the tracers were released from these sites. Observed and

predicted tracer time series plots are shown in Figure 5-4, and model performance statistics are shown in Table 5.9.

The Eagle Pass tracer (Figure 5-4) was designed to be a surrogate for the Carbón I/II power plants. Measured concentrations generally range between 0 and 1 ppq during the four month BRAVO period, except for a peak concentration of 1.6 ppq measured on August 25. Episodes of elevated concentration of the Eagle Pass tracer observed at Big Bend NP are generally well replicated by REMSAD, although the average predicted value of 0.5 ppq was about twice the observed value of 0.24 ppq, and from mid-August through September there is a clear tendency for REMSAD to over-predict tracer concentrations. The RMS error is 200% and the correlation coefficient is 0.46. One notable aspect of the Eagle Pass tracer is that the region between the tracer release and Big Bend NP is dominated by complex terrain, and is likely to be more difficult to simulate than the other three tracers.

The northeast Texas tracer (Figure 5-4), released from the Big Brown power plant, was measured in very low concentrations at the Big Bend NP monitors. The average observed tracer concentration during the four month study was only 0.003 ppq; this is nominally above the lower detection limit of the analytical method. The time series and performance statistics for the northeast Texas tracer are presented for completeness, but should be regarded with caution given the difficulties in quantifying the tracer concentration. Both the observed and predicted time series show concentrations ranging between 0 and 0.2 ppq, with REMSAD typically overestimating the peak concentration.

The time series of the predicted and observed San Antonio tracer (Figure 5-4) indicate that REMSAD is generally able to reproduce the timing of the observed tracer peaks; however, the simulated tracer is too low during the two episodes that occur during the first two weeks of October. This is especially true on October 5, when a peak value of 4.5 ppq was observed as compared to a predicted concentration of only about 1.5 ppq. Average observed and predicted concentrations of the San Antonio tracer are 0.46 ppq and 0.51 ppq, respectively. The normalized RMSE is 1.56 and the correlation coefficient is 0.53.

Similar to the San Antonio tracer, the Parish tracer (Figure 5-4) shows elevated concentrations during the first two weeks of October. The simulated tracer concentration is also highest during this period, but peak concentrations are under-predicted. Average observed and predicted concentrations of the Parish tracer are 0.057 ppq and 0.034 ppq, respectively. The normalized RMSE is 1.27 and the correlation coefficient is 0.41.

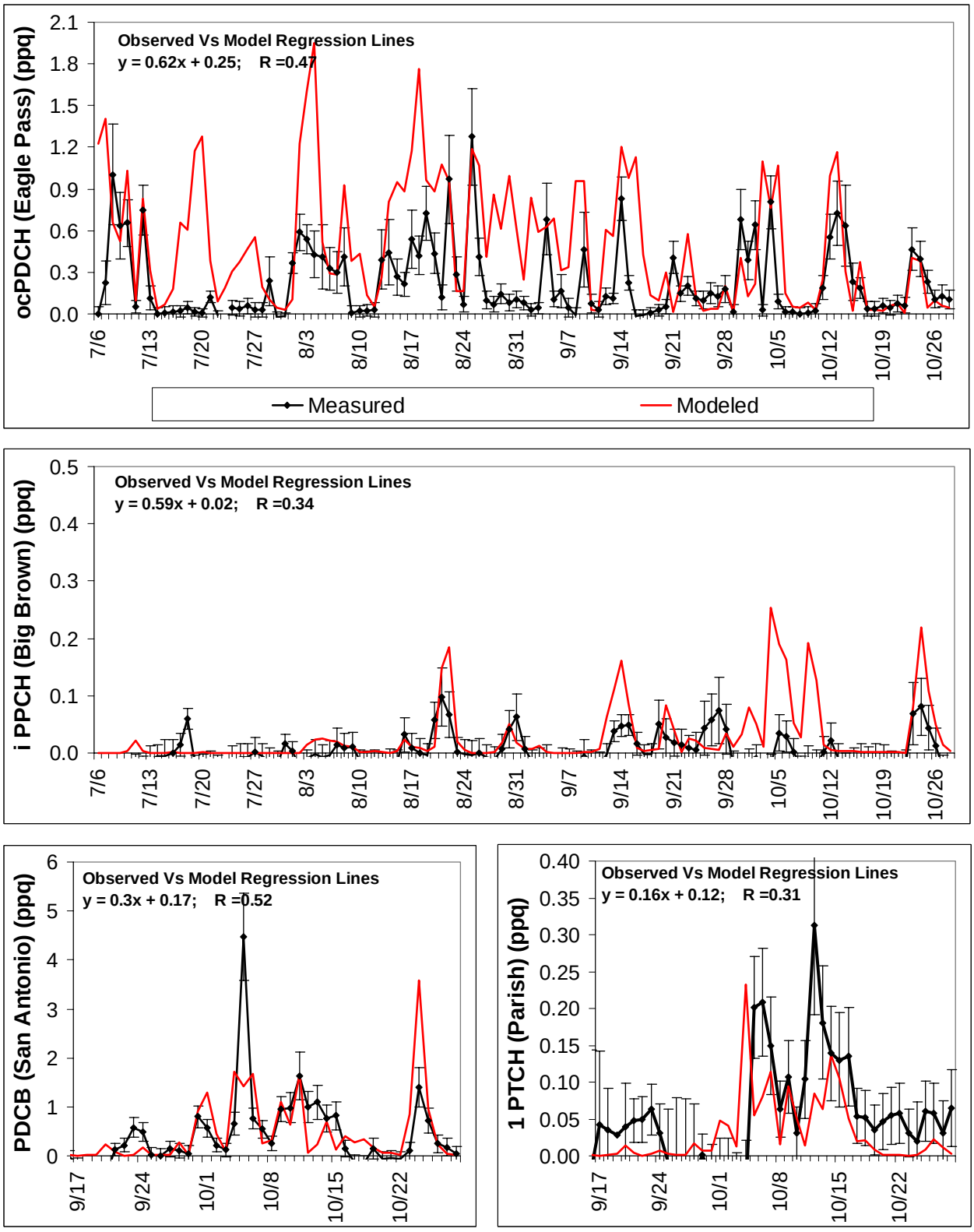

Figure 5-4. Observed and REMSAD predicted tracer mixing ratios for the a) Eagle Pass tracer, b) northeast Texas tracer, c) San Antonio tracer, and d) tracer released from Parish power plant in Houston.

Table 5-9. The REMSAD model performance statistics for the simulation of tracer average over the three Big Bend sites (San Vicente, K-Bar, and Persimmon Gap). The modeled and observed statistics used the same days.

	REMSAD Over Big Bend Sites (K-Bar, Persimmon Gap, San Vicente)												
		Average (ppq)		Bias	Std Dev (ppq)		Coef. of Variation		RMS Error		Correlation Line (ppq)		
	#	Obs	Model	Model/Obs	Obs	Model	Obs	Model	Abs.(ppq)	Relative	r	Intercept	slope
Eagle Pass (ocPDCH)	109	0.24	0.5	2.1	0.27	0.45	1.12	0.89	0.48	2	0.46	0.25	0.62
San Antonio (PDCB)	40	0.46	0.51	1.1	0.83	0.71	1.8	1.4	0.72	1.56	0.53	0.17	0.30
Parish (1PTCH)	40	0.057	0.034	0.6	0.078	0.049	1.37	1.43	0.072	1.27	0.41	0.02	0.16
Big Brown (iPPCH)	109	0.003	0.025	8.43	0.03	0.04	8.61	1.79	0.05	16.38	0.34	0.02	0.59

5.4 Discussion

The primary purpose of this analysis was to evaluate the ability of the CMC and REMSAD models driven by the MM5 wind fields for simulating medium- to long-range transport, and whether or not the CMC model was suitable for airmass history analyses, and, in addition, to determine if there was a difference between the CMC model being driven by the MM5 or EDAS/FNL wind fields and the differences between REMSAD and CMC models driven by the same MM5 winds.

The demand on a model's dispersion for airmass history analysis is lower than for source apportionment. Airmass history analyses rely on only the model properly reproducing the direction and timing or speed of transport from the source to the receptor. The fact that the CMC model reproduced the timing of the tracer impacts to the vicinity of Big Bend supports the use of this model in airmass history analyses. This corroborates the results found in chapter 4 and section 8.1.3.2, where airmass histories, via residence time analysis, were able to identify a transport pathway from the tracer release site to Big Bend when aggregated over the 20 days with highest measured tracer concentrations at Big Bend. The trajectory analysis also showed that on a given day, the airmass history envelope could miss the tracer release site when elevated tracer concentrations were measured at Big Bend. This is also seen in these results where simulated tracer concentrations could be shifted in time compared to the measured tracer at Big Bend. Therefore, errors in the transport could be reduced by averaging over multiple days as was done in the residence time analysis.

Properly simulating dispersion for source apportionment requires not only simulating the transport direction and speed, but also the horizontal and vertical dilution of the plume. The skill of the models to simulate the day to day variability and magnitude of the tracer was assessed via a number of model performance statistics. Depending on the model/wind field combination and the aggregation region the model bias was between 0.33 and 2.1, the RMS error between 73% and 240%, and correlation coefficient between 0.36 and 0.69 (Table 5-10). As previously discussed, there is a limit in the skill of the models, or inherent uncertainty, due to their inability to capture sub-resolution spatial variability and errors in the measured tracer data. Comparing the simulation performance statistics to this inherent uncertainty in the simulation (Table 5-11) it is seen that the Eagle Pass and San Antonio tracers are all within this uncertainty. Therefore the simulations for these two tracers are valid within the model resolution and measured tracer uncertainty.

On the other hand, the simulations systematically underestimated the Parish tracer by a factor of 2 and the correlation coefficients were all below the correlations between the measured sites (Tables 5-10 and 5-11). Therefore these models do underestimate the contribution from the Parish power plant. This underestimation could be due to model error or an underestimation in the PTCH background concentrations subtracted from the measured data. The RMS errors for the Parish tracer simulations are below the largest RMS differences between the three Big Bend receptor sites, indicating the overall error is within the inherent error of the model/data comparison.

The fact that the RMS errors for all three tracers are within the inherent error of this analysis does not conclusively validate the models and meteorological drivers, but does provide an upper bound to its uncertainty. The assessment also addressed only the dispersion component

of the models. Add to this the uncertainty in the emission and physical/chemical processes and the errors in the source attribution results will be larger.

The models are primarily being used to simulate sulfate aerosol which was shown to be spatially homogeneous within the resolution of the models. This spatial homogeneity is primarily due to sulfate being a long-lived aerosol species, on the order of 3–5 days [*Husar and Husar,* 1978] and resulting from many sources distributed over broad and distant regions. The long residence time allows the aerosol to be transported over thousands of kilometers and mixed with other sources. As would be expected, REMSAD has significantly better performance statistics compared to measured sulfate than the tracer data (see chapter 6). However, this improvement is likely due to compensating errors in transport between one source/source region and another and the improved sulfate simulation performance statistics do not translate into improved source attribution results.

Table 5-10. The range of tracer simulation performance statistics over all model wind field pairs and aggregation regions in Tables 5-7 to 5-9.

	Bias	Relative RMS Error (%)	r
Eagle Pass (ocPDCH)	0.46 – 2.1	73 – 200	0.44 – 0.54
San Antonio (PDCB)	0.63 – 1.3	128 – 240	0.36 – 0.69
Parish (1PTCH)	0.33 – 0.6	105 – 130	0.41 – 0.55
All three tracers	0.33 – 2.1	73 – 240	0.36 – 0.69

Table 5-11. The range of comparisons between the measured tracer concentrations from the three Big Bend monitoring sites in Tables 5-3 to 5-5. These statistics are a measure of the inherent uncertainty due to the model resolution and measured tracer data errors.

	Ratio of averages	Relative RMS Difference (%)	r
Eagle Pass (ocPDCH)	0.31 – 3.2	97 – 420	0.37 – 0.81
San Antonio (PDCB)	0.54 – 1.9	44 – 230	0.58 – 0.9
Parish (1PTCH)	0.77 – 1.3	72 – 150	0.72 – 0.77
All three tracers	0.31 – 1.9	44 – 420	0.37 – 0.9

This analysis also provided the opportunity to contrast the differences between Eulerian and Lagrangian dispersion techniques and the two meteorological fields. The influence of the MM5 and EDAS/FNL wind fields on the simulation can be examined by comparing the two CMC modeling results. The MM5 wind field proved superior to the EDAS/FNL winds for the Eagle Pass tracer. This was most evident when the simulations were compared to the average over all six receptor sites. However, the EDAS/FNL simulation was superior to the MM5 simulation for the San Antonio tracer, and both wind fields produced similar results for the Parish tracer released from Houston. The CMC-EDAS simulation of the San Antonio tracer had the highest correlation coefficient of 0.69 in this study. The Eagle Pass site was the closest release site to Big Bend, so it appears that the higher resolution MM5 winds were better able to simulate the more near field transport, but the two wind fields are about equal or the EDAS/FNL superior for more distant mesoscale transport. Overall, these results indicate that the routinely available EDAS wind fields are comparable to the MM5 36 km winds which were generated for the BRAVO study for simulating tracer transport in Texas.

The similarity of the tracer simulation using the two wind fields is a bit surprising. In comparison of the airmass history models and wind fields (chapter 4) and the evaluation of airmass transport to Big Bend (section 8.1.3), the EDAS/FNL wind fields tended to show more transport from northeast Texas than MM5. Unfortunately, the tracer released from the Big Brown power plant in northeast Texas was at such a low rate that the concentrations were often near the background and transport from this region using the tracer was difficult to assess. In addition, no tracer was released from Big Brown from October 8–16. This was a period of transport from northeast Texas and we may have been able to better resolve the question of which wind field properly simulated transport from northeast Texas had these data been available.

The Eulerian REMSAD model and Lagrangian CMC model were both driven by the MM5 wind fields. The simulation of the tracer data by these two dispersion mechanism produced no clear cut differences. The CMC model better simulated the Eagle Pass tracer data with a smaller bias and RMS error. However, the REMSAD simulations had the lowest RMS error and bias for both the San Antonio and Parish tracer simulations (Table 5-12).

Table 5-12. Comparison of the REMSAD and CMC model performance statistics for the simulation of tracer average over the three Big Bend sites (San Vicente, K-Bar, and Persimmon Gap). The modeled and observed statistics used the same days. The bias and RMS relative error are ratios; therefore, they are dimensionless.

	MM5 Wind Fields Average Over Big Bend Sites (K-Bar, Persimmon Gap, San Vicente)						
		Bias (Model/Obs)		RMS Relative Error		Correlation (r)	
	#	CMC	REMSAD	CMC	REMSAD	CMC	REMSAD
Eagle Pass (ocPDCH)	109	0.89	2.1	1.23	2	0.44	0.46
San Antonio (PDCB)	43	1.26	1.1	2.4	1.56	0.36	0.53
Parish (1PTCH)	43	0.44	0.6	1.26	1.27	0.51	0.41
Big Brown (iPPCH)	109	16.90	8.43	54.76	16.38	0.29	0.34

6) REMSAD Sulfur Simulation and Apportionment for BBNP

6.1 Introduction

The REMSAD air quality model was used to predict sulfate concentrations during the BRAVO study period (July–October 1999) and to estimate the sulfate contributions from regional sources that were impacting Big Bend NP during the study. REMSAD is used to estimate the chemical and physical processes that lead to the formation of sulfate particles, including emissions of sulfate precursors (namely sulfur dioxide), subsequent gas-phase and aqueous-phase oxidation of sulfur dioxide to particulate sulfate, transport of sulfate and its precursors via advection and turbulent diffusion, and wet and dry deposition, which constitute the principal loss mechanism for sulfate. REMSAD also simulates the occurrence of clouds, and their impact in rapidly transforming sulfur dioxide to particulate sulfate. An example of predicted sulfur dioxide and sulfate plumes from REMSAD is shown in Figure 6-1. The bulk of sulfur dioxide within the model domain is clearly dominated by sources in the eastern U.S. (Figure 6-1a), and individual point sources are evident in the western U.S. and Mexico. The Popocatepetl volcano, near Mexico City, is the dominant sulfur dioxide source in Mexico and is clearly evident in Figure 6-1a. The subsequent atmospheric oxidation of sulfur dioxide to sulfate particles results in the sulfate plume which is shown in Figure 6-1b. This sulfate plume is affected not only by the concentration of ambient sulfur dioxide but also by the presence of clouds, which are very effective at converting sulfur dioxide to sulfate via aqueous-phase reactions with hydrogen peroxide and ozone, and the presence of hydroxyl radical, which is the primary gas-phase oxidant of sulfur dioxide.

Input data to REMSAD include an emission inventory that defines the hourly emissions of chemical species such as sulfur dioxide, oxides of nitrogen, carbon monoxide, and various volatile organic compounds. Emission rates for these species are defined for each model grid cell. Meteorological data, including wind and temperature fields, precipitation rates, and cloud cover, are provided by the MM5 mesoscale weather model. Details about REMSAD's formulation and configuration for the BRAVO study can be found in section 2.2.1.

Four major sulfur dioxide source regions were considered for their contributions to predicted sulfate at Big Bend NP: 1) Texas, 2) Mexico, 3) the eastern U.S., and 4) the western U.S. (Figure 6-2). In addition to these four major source regions, the sulfate contributions from smaller subregions were also considered. These subregions include, for example, southeastern and northeastern Texas, the Ohio River Valley, and the Carbón I & II power plants located 250 km southeast of Big Bend NP. REMSAD was also used to investigate the impact of sulfur concentrations specified at the model boundary on simulated sulfate concentrations at Big Bend NP.

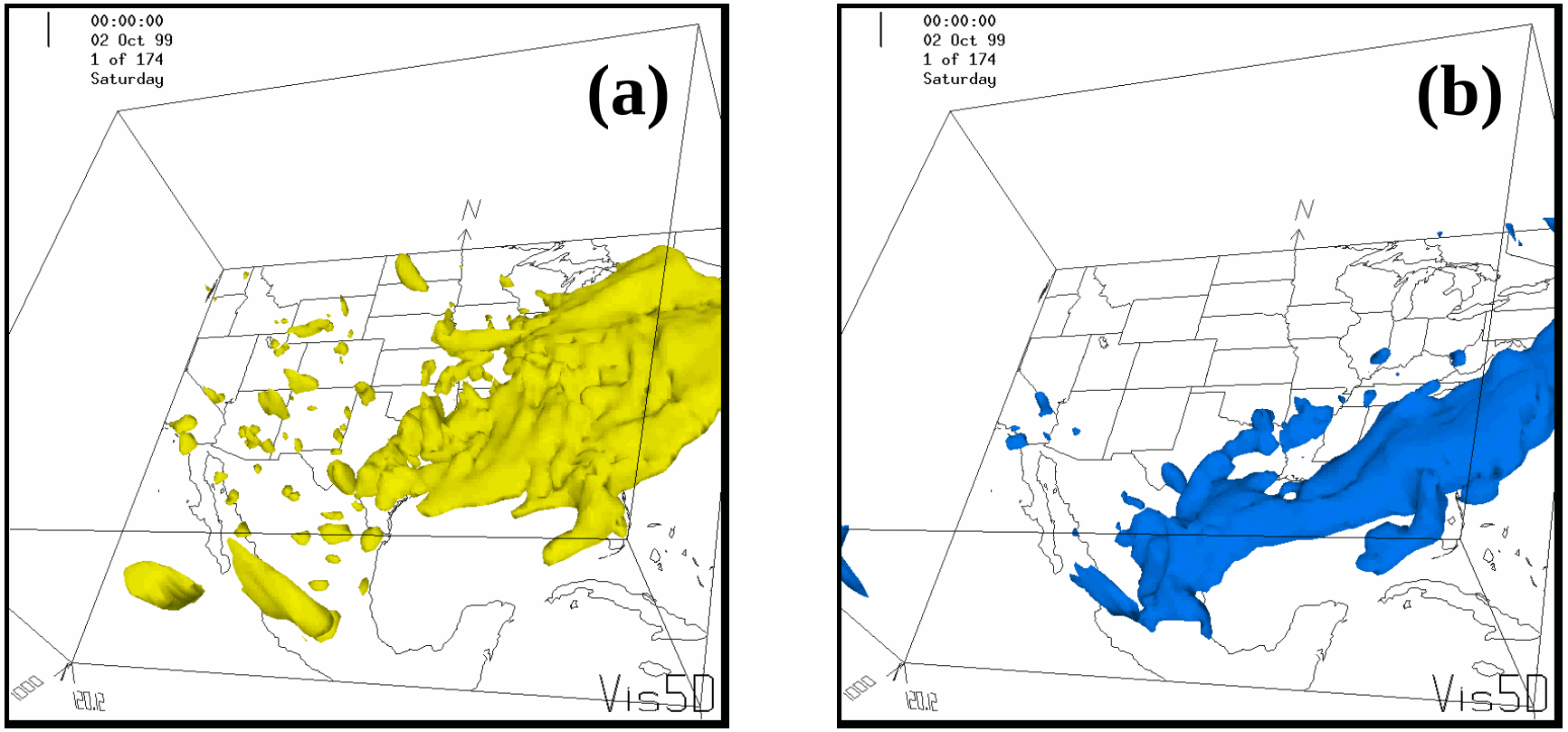

Figure 6-1. Plumes of (a) sulfur dioxide and (b) sulfate defined by 5 µg/m^3 isosurfaces for October 2, 1999.

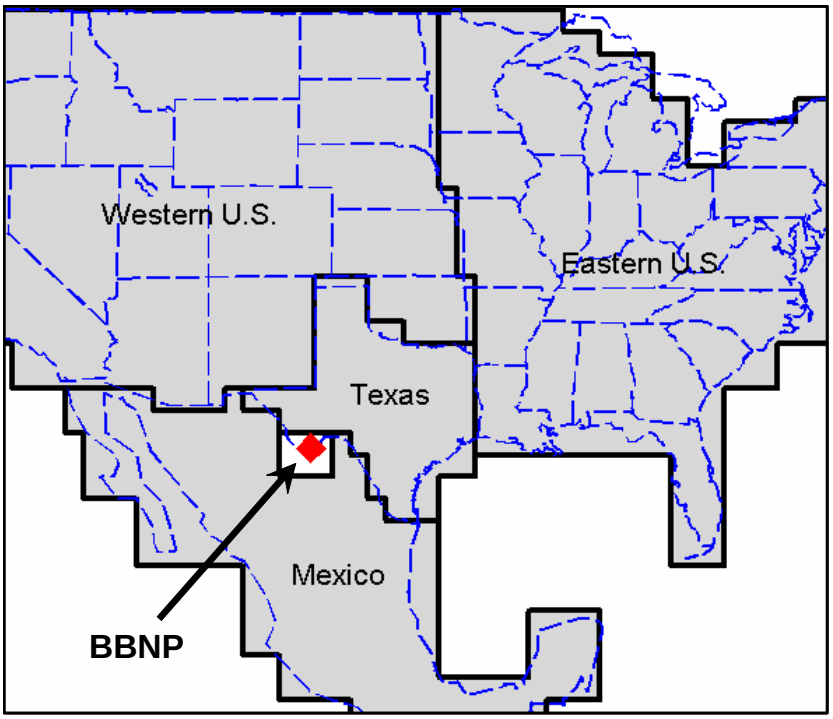

Figure 6-2. The four source regions evaluated for their impact on SO_4 predicted at BBNP: Mexico, Texas, the eastern U.S., and the western U.S.

Prior to applying REMSAD to the "emission sensitivity simulations" described above, the model's ability to predict "real world" sulfate concentrations during the four month BRAVO period was assessed. Therefore a "base simulation" was developed and statistically evaluated to determine the model's skill at predicting sulfate concentrations at Big Bend NP and at other monitoring sites located throughout the model domain. This base simulation specified sulfur dioxide emissions from coal-fired power plants, smelters, petroleum refineries, and other sources at their normal emission rates. Sulfate concentrations predicted by this REMSAD base simulation were compared to the observed concentrations collected at the sulfate monitors deployed throughout Texas during the BRAVO study, as well as the larger network of CASTNET monitors that are located throughout the U.S. This combination of 37 BRAVO monitoring sites and 67 CASTNET monitoring sites (that fall within the REMSAD model domain) provides the large-scale spatial coverage that is necessary to adequately assess model performance and to identify regions of the modeling domain where biases might exist. It is also of interest to examine the statistical evaluation over different time periods, e.g., daily versus monthly, as this can elucidate trends that exist on synoptic or seasonal time scales.

After the REMSAD base simulation has been established, the emissions sensitivity simulations can be performed to determine the impact of emissions from regional and subregional sulfur dioxide sources on predicted sulfate at Big Bend NP. The emission sensitivity simulations are run by repeating the original base simulation, with the one difference being that all sulfur dioxide emissions from the source region of interest are removed. Primary particulate sulfate emissions, which constitute less than a few percent of the total sulfur emissions, are also removed. The impact of sulfur dioxide emissions from a source region on sulfate predicted at a downwind receptor is defined as the difference between the sulfate concentration predicted by the original base simulation and the sulfate concentration from the emission sensitivity

simulation. Several factors can influence whether emissions from a source region will have an appreciable impact on a receptor site (e.g., Big Bend NP), including whether the receptor is frequently downwind of the source region, the magnitude of the emissions from the source region, and the percentage of sulfur dioxide that is oxidized to sulfate en route to the receptor.

An interesting aspect of this work was an investigation of REMSAD's response to two types of emission sensitivity simulations. The sulfate attribution results presented in this chapter were derived from the emission sensitivity simulations described above, where REMSAD was run after sulfur dioxide emissions from a source region were removed. These simulations are termed "emissions out" simulations. There is, however, a complementary approach where sulfur dioxide emissions from a source region can be retained, but sulfur dioxide emissions outside of the source region are removed. These simulations are termed "emissions in" simulations. An important question is whether the sulfate attributions derived from the "emissions out" simulations are equivalent to the "emissions in" simulations. The attributions between the two methods will be equivalent if sulfate concentrations predicted by REMSAD respond in direct proportion to changes in sulfur dioxide emissions. Results from this study show that these two approaches to performing emissions sensitivity simulations, i.e., "emissions out" and "emissions in", are indeed very nearly equivalent, and hence only results from the "emissions out" simulations will be presented. Further details on this topic can be found in section 6.3.

The following sections of this chapter are divided into three major topics: a statistical evaluation of REMSAD's skill in predicting sulfate concentrations during the four month BRAVO study (section 6.2), an investigation of the degree of linearity in REMSAD's sulfate predictions with regard to the "emissions out" and "emissions in" simulations (section 6.3), and the results of the emission sensitivity simulations to determine the attributions from regional and subregional emission sources to sulfate predicted at Big Bend NP (section 6.4).

6.2 Evaluation of REMSAD Base Simulation

As described above, the REMSAD regional air quality model was used to create a base simulation for the July–October 1999 BRAVO period. This base simulation used an emission inventory that was estimated at "real world" levels and was designed to evaluate the model's skill in predicting the formation and transport of particulate sulfate during the BRAVO field study. An example of surface-level sulfate predicted by REMSAD is shown in Figure 6-3, where concentrations range from < 1 $\mu g/m^3$ in remote and maritime areas to well over 15 $\mu g/m^3$ in regions downwind of large sulfur dioxide sources. The patterns evident in Figure 6-3 are a result of several factors, including the emissions of sulfur dioxide in the atmosphere, the presence of clouds which rapidly convert sulfur dioxide to sulfate, wind patterns, and rates of deposition. An interesting aspect of Figure 6-3 is the strong concentration gradients that exist in proximity to Big Bend NP; their potential impact with regard to model evaluation will be considered in the following sections.

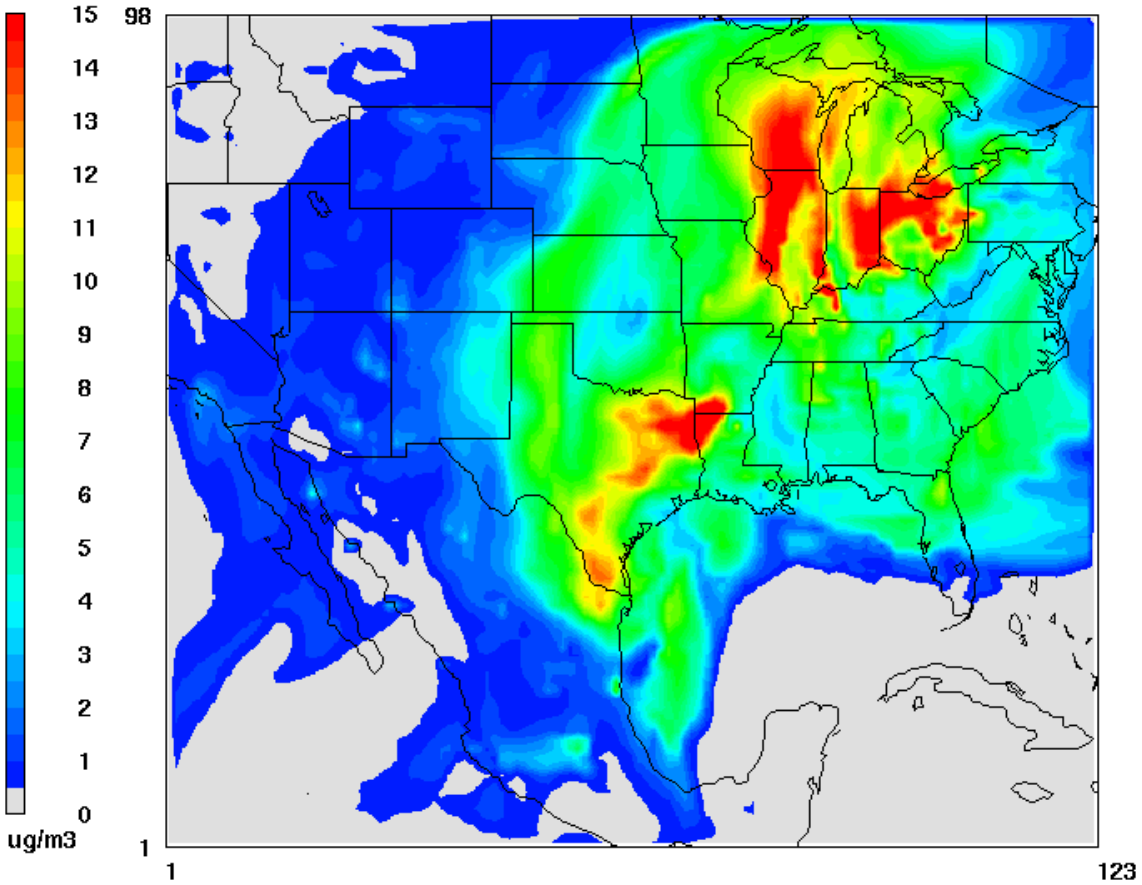

Figure 6-3. Ground-level sulfate concentrations (µg/m^3) predicted by the REMSAD air quality model for 1500 CST, September 1, 1999.

An evaluation of REMSAD's predictive skill was conducted by comparing simulated sulfate concentrations with observed concentrations. Sulfate observations were collected from either the BRAVO or CASTNET monitoring networks. The BRAVO monitoring network measured daily-average sulfate concentrations and consisted of 37 sites that were deployed throughout Texas during the four months of the study. The CASTNET monitoring network has a much broader coverage, with monitoring sites concentrated in the northeastern portion of the U.S. The CASTNET monitoring network collects samples on a weekly average, and 67 of these monitors lie within the REMSAD model domain. The BRAVO and CASTNET monitoring sites are shown in Figures 6-4 and 6-5, respectively.

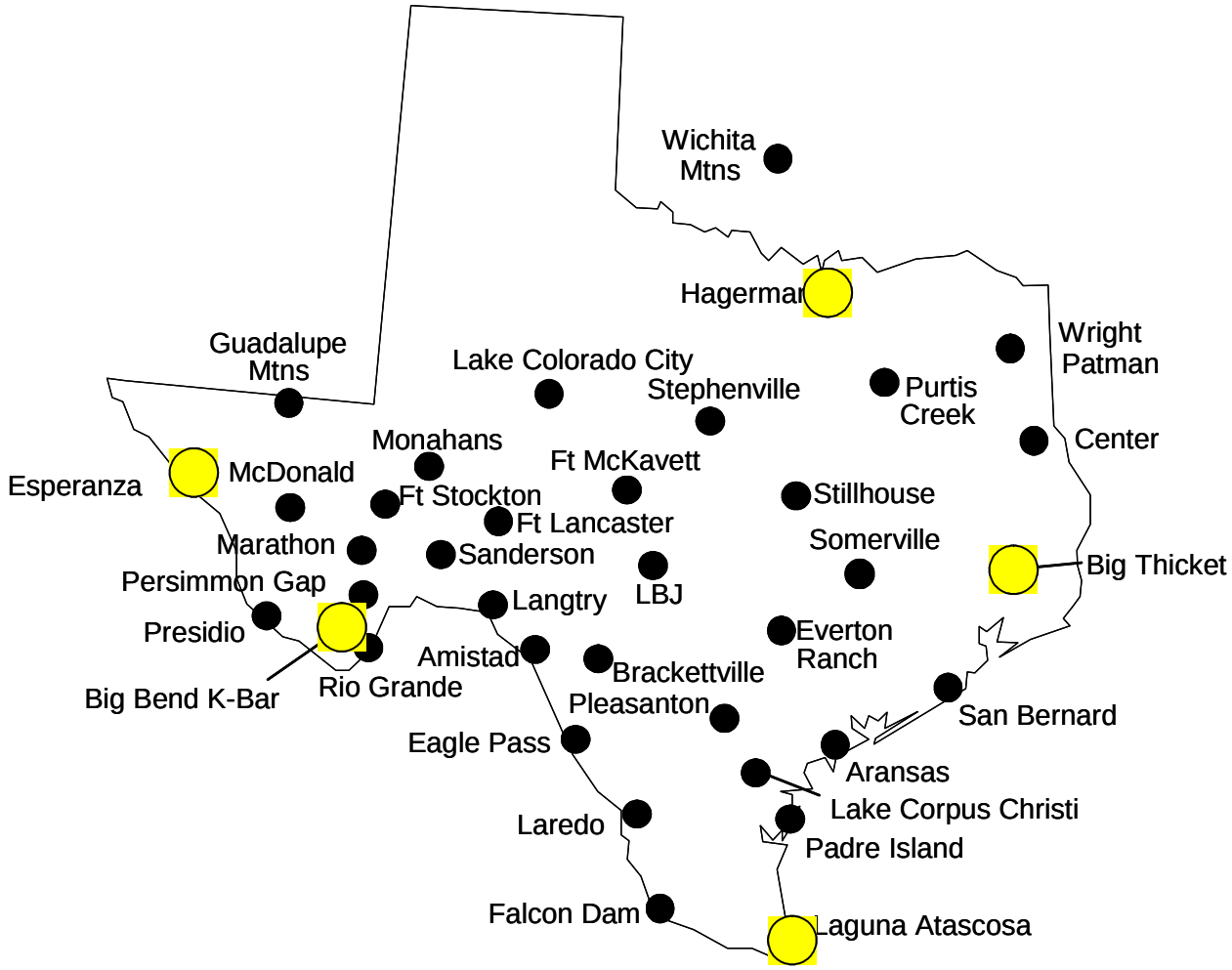

Figure 6-4. The BRAVO monitoring network. Example time series plots and statistics are presented for highlighted monitors.

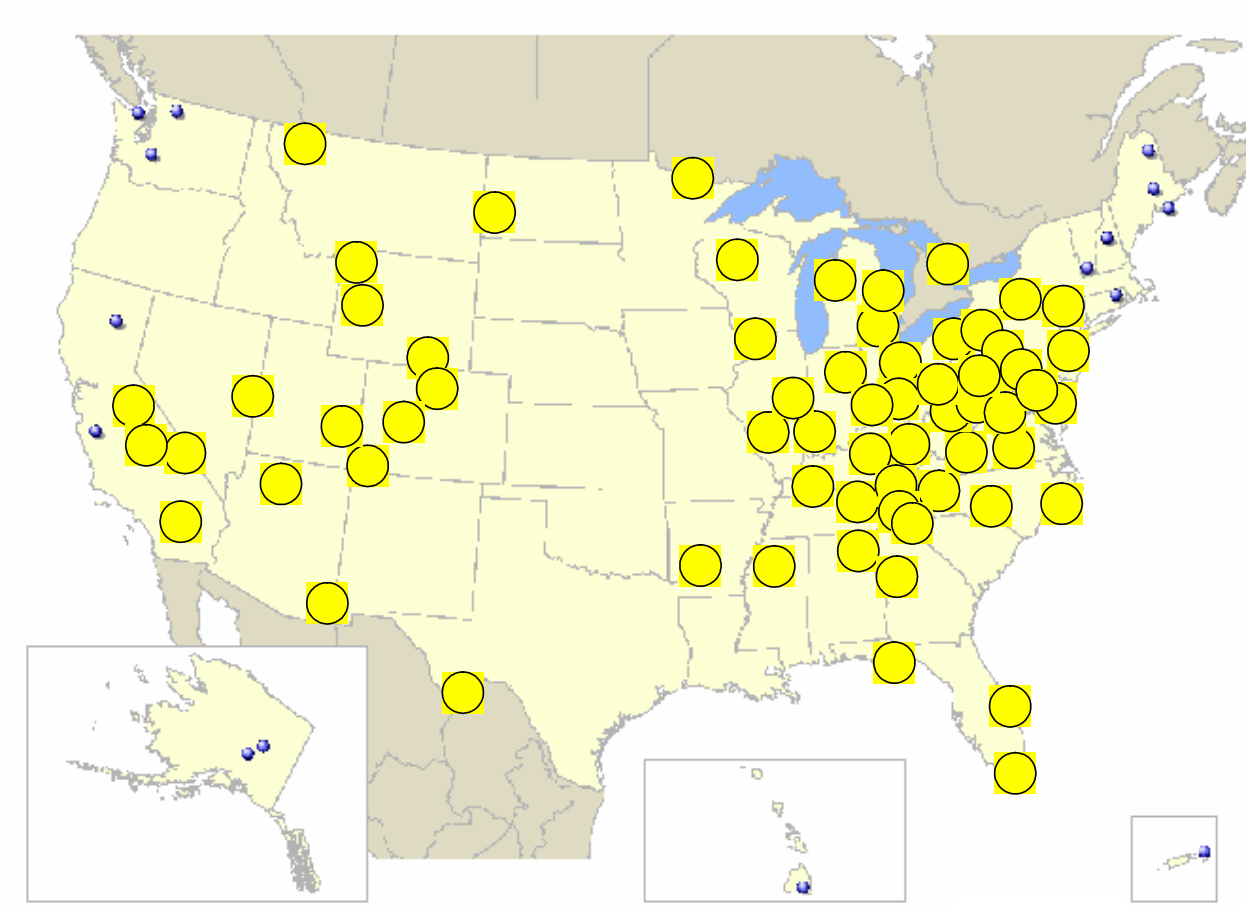

Figure 6-5. The CASTNET monitoring network. Highlighted monitors fall within the REMSAD model domain.

The performance evaluation of the base simulation will be presented in four major components:

1) Time series plots and statistics of predicted versus observed sulfate at Big Bend NP and at four sites that lie north, east, south, and west of Big Bend NP.
2) Scatter plots and statistics of predicted versus observed sulfate for all 37 BRAVO monitors.
3) Scatter plots and statistics of predicted versus observed sulfate for the 67 CASTNET monitors that fall within the model domain.
4) Contour maps showing spatial patterns of model bias and error.

Statistics used to assess model performance include the correlation coefficient (R), normalized bias (Bn), and normalized error (En). The normalized bias is defined as

$$Bn = \frac{1}{N}\sum_i \left(\frac{P_i - O_i}{O_i} \right) \qquad (6\text{-}1)$$

and the normalized error is defined as

$$En = \frac{1}{N}\sum_i \left| \frac{P_i - O_i}{O_i} \right| \quad (6\text{-}2)$$

It should be noted that both Bn and En are susceptible to over-weighting over-predictions as compared to under-predictions (for the normalized difference shown above the under-predictions are bounded by -1 while over-predictions can grow arbitrarily large). To help minimize skewing of Bn and En, observations less than 0.1 $\mu g/m^3$ are not included in the statistical analysis. Observations less than this 0.1 $\mu g/m^3$ threshold represent a very small portion of the measured sulfate values. All observations and predictions are paired in space and time, i.e., there is no temporal or spatial averaging (except for the case of the contour maps of Bn and En in section 6.2.4, where the daily BRAVO network data was converted to a weekly average to match the CASTNET network data). It should be noted that the statistics calculated for the four month average may not necessarily match the average of the monthly statistics, as several of the months contain missing data.

All four of the assessments listed above will be presented on a monthly basis (July, August, September, and October 1999) and on an overall study basis (the four month average of July–October 1999). The purpose of examining model performance on a monthly basis will be to elucidate seasonal trends in the model predictions. Performance on a daily time scale will be apparent through the time series plots presented for the Big Bend NP monitor and the four peripheral monitors of the BRAVO network. Finally, spatial patterns derived by combining both the BRAVO and CASTNET networks will indicate which regions within the model domain are most likely to experience bias.

6.2.1. BRAVO Network: Big Bend NP and Four Peripheral Monitors

Time series plots of the daily predicted and observed sulfate at Big Bend NP and four peripheral sites within the BRAVO monitoring network are shown in Figure 6-6, and model performance statistics are shown in Table 6-1. At the K-Bar monitor in Big Bend NP (Figure 6-6a), observed sulfate concentrations range from < 1 $\mu g/m^3$ to over 9 $\mu g/m^3$, with the periods of peak sulfate levels occurring between mid-August and October. This period corresponds to a transition of wind flow patterns, where transport primarily from Mexico in July and early August yields to transport from eastern Texas and the eastern U.S. during mid-August through October. Although REMSAD frequently predicts the correct timing of sulfate peaks, there is a clear bias to underestimate sulfate concentrations during the first half of the study, with a normalized bias of predicted sulfate of -41% and -43% for July and August, respectively. This negative bias may indicate that Mexican sulfur dioxide emissions are underestimated, as flow from Mexico dominates during this period, or that sulfur dioxide from Mexican sources is not being oxidized rapidly enough en route to Big Bend NP. From the latter half of August until the end of October, sulfate concentrations are higher, with a peak observed sulfate concentration of 9 $\mu g/m^3$ recorded on September 1 at the K-Bar monitor. Again, the timing of the predicted peak concentrations generally appears to be in good agreement with the observations. There are, however, a few notable exceptions, such as the 5 $\mu g/m^3$ peak that was observed September 27–29. This episode is clearly not evident in the predicted time series at any of the three monitors, although concentrations of this magnitude were predicted within 100 km of Big Bend NP, as shown in Figure 6-7. Also, there appears to be a shift in the timing of the mid-October sulfate peak, with the predicted maximum occurring October 9 while the actual maximum was observed October

12. The four-month observed and predicted sulfate concentrations at Big Bend NP were 2.0 $\mu g/m^3$ and 2.5 $\mu g/m^3$, respectively.

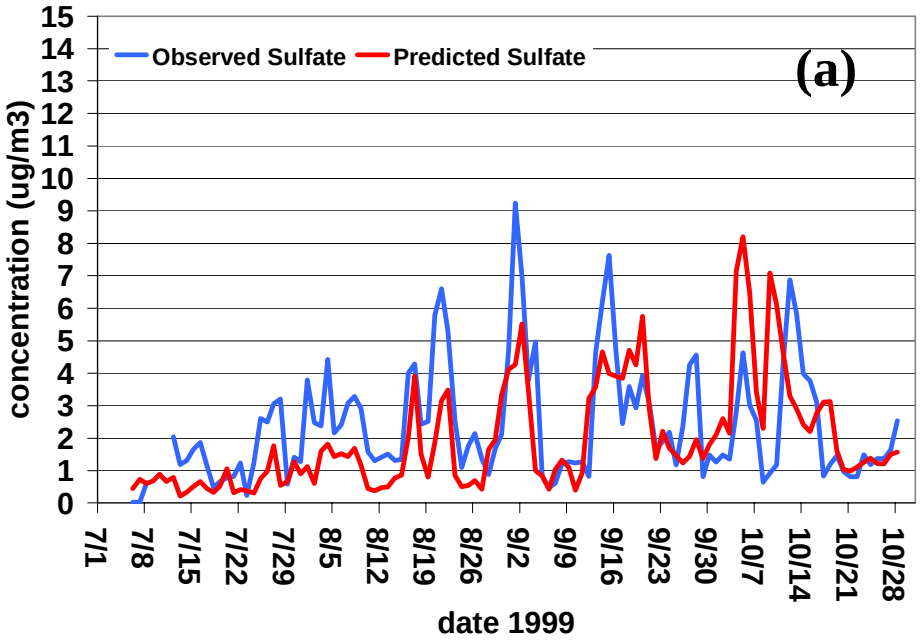

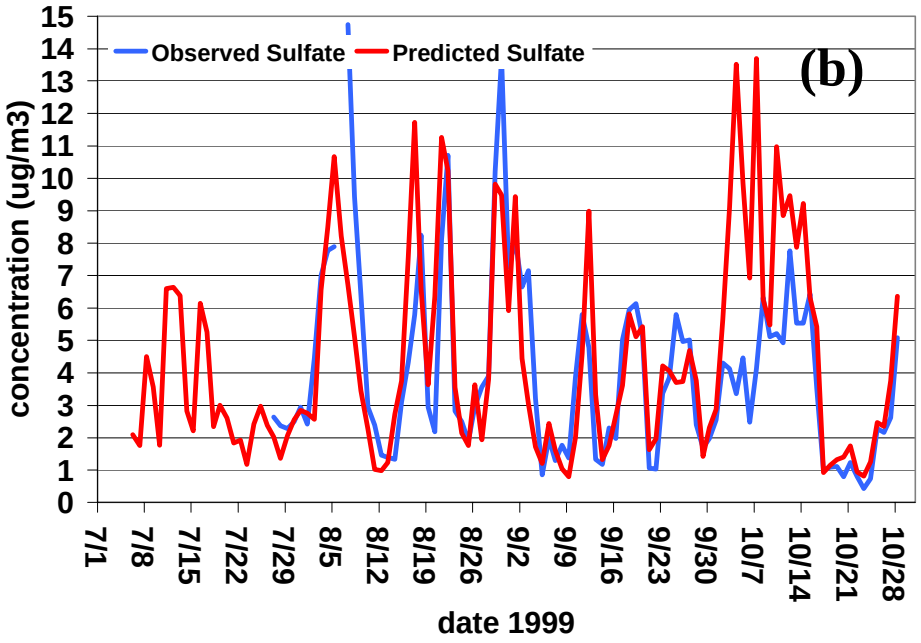

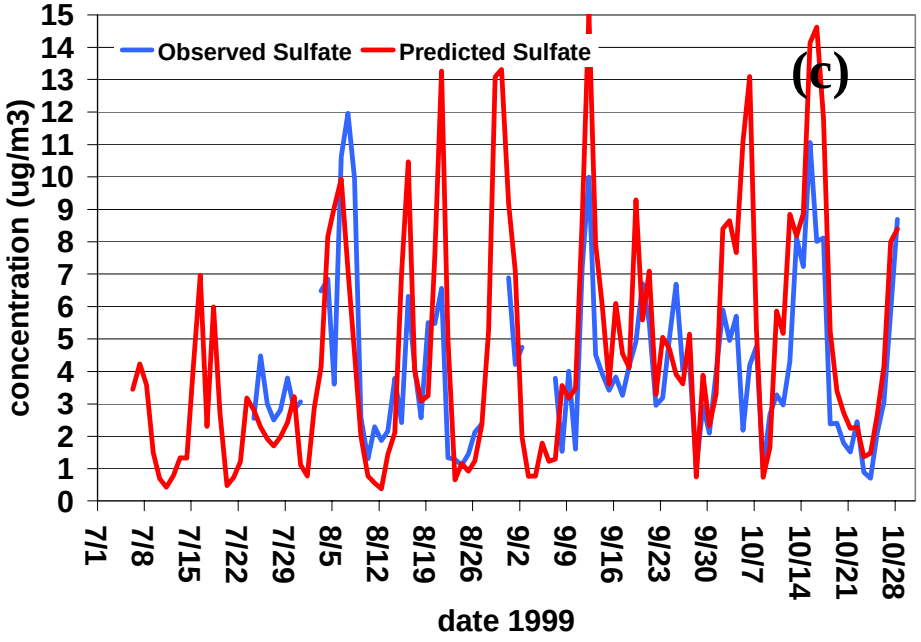
Observed Sulfate
Predicted Sulfate
(c)
concentration (ug/m3)
0
1
2
3
4
5
6
7
8
9
10
11
12
13
14
15
7/1
7/8
7/15
7/22
7/29
8/5
8/12
8/19
8/26
9/2
9/9
9/16
9/23
9/30
10/7
10/14
10/21
10/28
date 1999

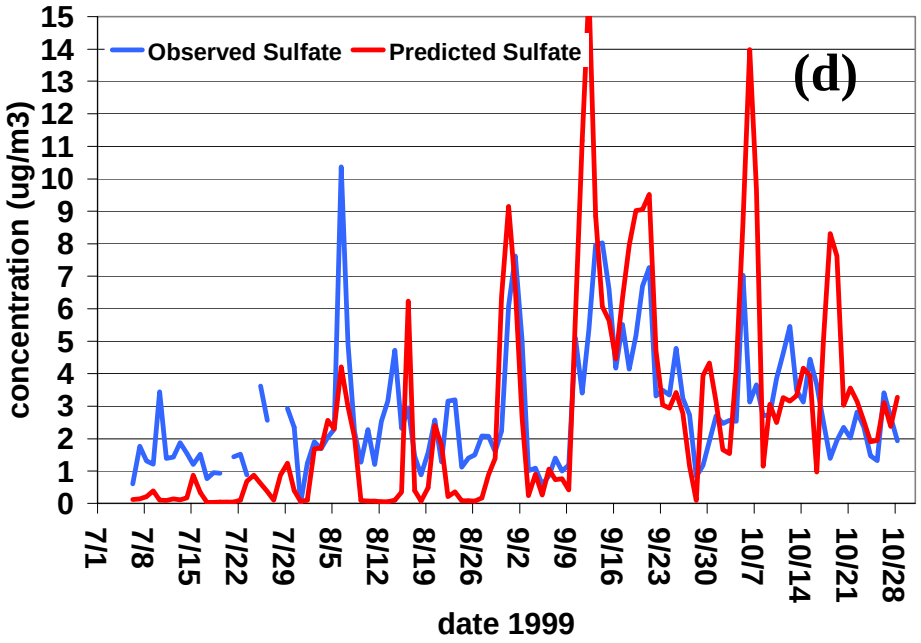
Observed Sulfate
Predicted Sulfate
(d)
concentration (ug/m3)
0
1
2
3
4
5
6
7
8
9
10
11
12
13
14
15
7/1
7/8
7/15
7/22
7/29
8/5
8/12
8/19
8/26
9/2
9/9
9/16
9/23
9/30
10/7
10/14
10/21
10/28
date 1999

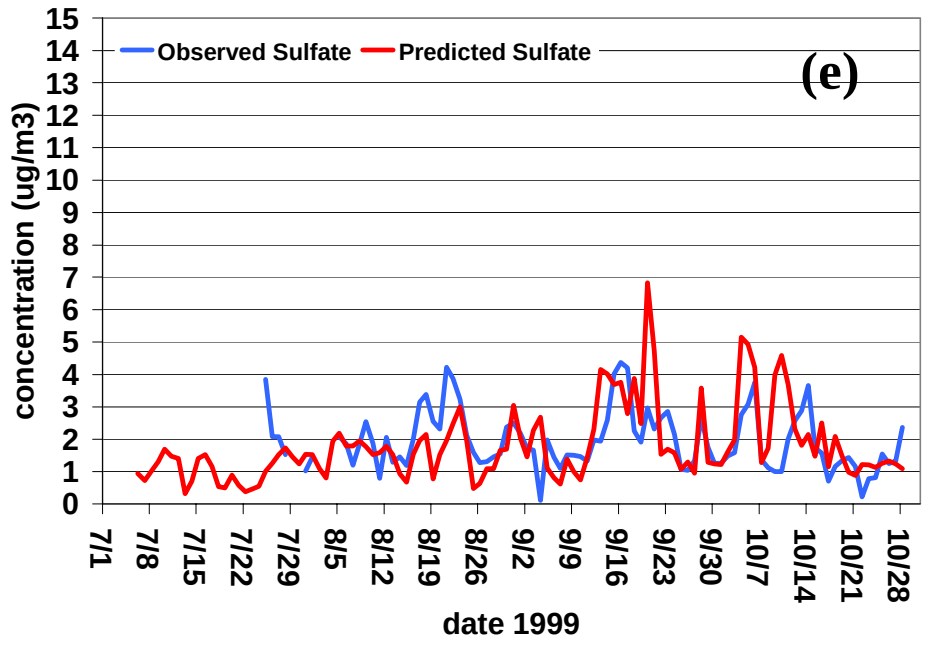

Figure 6-6. Observed and predicted sulfate time series for five monitors within the BRAVO network: (a) K-Bar, (b) Hagerman, (c) Big Thicket, (d) Laguna Atascosa, and (e) Esperanza.

Table 6-1. REMSAD performance statistics for the base simulation calculated at Big Bend NP (K-Bar) and four peripheral sites (Hagerman – northern Texas, Big Thicket – eastern Texas, Laguna Atascosa – southern Texas, Esperanza – western Texas).

	Overall	July 99	August 99	September 99	October 99
K-Bar					
Observed Average (µg/m^3)	2.5	1.3	2.7	3.1	2.3
Predicted Average (µg/m^3)	2.0	0.6	1.5	2.5	3.0
R	0.50	0.46	0.69	0.67	0.32
Normalized Error	62%	51%	53%	43%	98%
Normalized Bias	1%	-41%	-43%	2%	78%
Data Completeness	98%	88%	100%	100%	100%
Hagerman					
Observed Average (µg/m^3)	4.1	2.1	5.5	3.6	3.4
Predicted Average (µg/m^3)	4.6	2.2	5.3	3.4	5.6
R	0.66	0.21	0.71	0.75	0.73
Normalized Error	44%	16%	38%	36%	64%
Normalized Bias	23%	-15%	6%	7%	64%
Data Completeness	84%	23%	97%	100%	100%
Big Thicket					
Observed Average (µg/m^3)	4.2	2.8	4.3	4.2	4.3
Predicted Average (µg/m^3)	5.1	2.3	4.6	5.0	6.4

R	0.70	-0.47	0.65	0.75	0.78
Normalized Error	54%	34%	58%	43%	66%
Normalized Bias	27%	-28%	11%	24%	59%
Data Completeness	79%	35%	84%	87%	100%
Laguna Atascosa					
Observed Average (µg/m^3)	2.9	1.6	2.6	3.8	3.0
Predicted Average (µg/m^3)	2.9	0.3	1.6	4.7	4.1
R	0.60	0.39	0.50	0.70	0.19
Normalized Error	70%	81%	70%	58%	77%
Normalized Bias	-7%	-81%	-43%	18%	52%
Data Completeness	96%	85%	100%	100%	100%
Esperanza					
Observed Average (µg/m^3)	2.0	1.8	2.1	2.0	1.7
Predicted Average (µg/m^3)	2.0	1.3	1.6	2.3	2.1
R	0.43	-0.09	0.58	0.54	0.48
Normalized Error	71%	41%	31%	112%	72%
Normalized Bias	38%	-15%	-15%	81%	54%
Data Completeness	82%	23%	90%	100%	100%

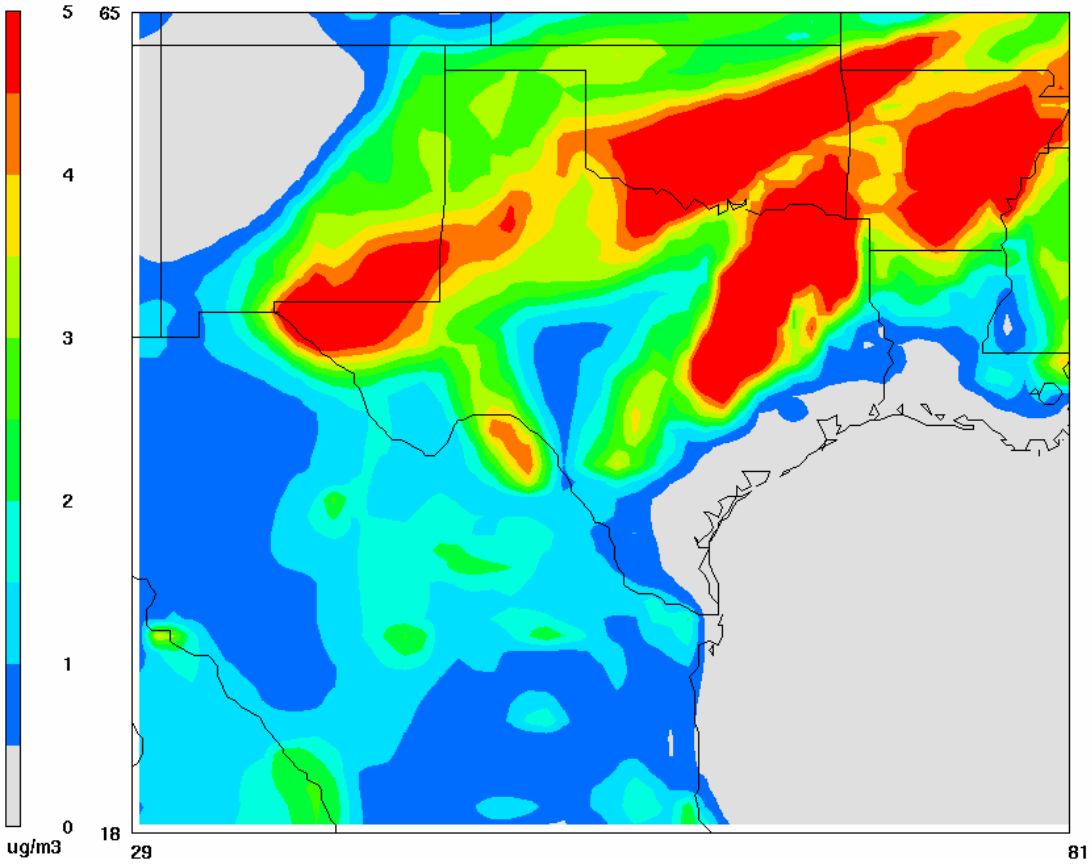

Figure 6-7. Ground-level sulfate concentrations (µg/m^3), September 28, 1999.

Figures 6-6b to 6-6e show time series plots of four sites that represent the periphery of the BRAVO monitoring network. These include the Hagerman monitor in northern Texas, the Big Thicket monitor in eastern Texas, the Laguna Atascosa monitor in southern Texas, and the Esperanza monitor in western Texas. In general, the northern and eastern monitors of Hagerman (Figure 6-6b) and Big Thicket (Figure 6-6c), respectively, show higher sulfate concentrations. Four month average observed and predicted sulfate concentrations at Hagerman are 4.1 $\mu g/m^3$ and 4.6 $\mu g/m^3$, respectively, and 4.2 $\mu g/m^3$ and 5.1 $\mu g/m^3$, respectively, at Big Thicket. Sulfate concentrations are lower at the southern monitor of Laguna Atascosa, with average observed and predicted sulfate concentrations of 2.9 $\mu g/m^3$, and lower still at the western monitor of Esperanza, with average observed and predicted sulfate concentrations of 2.0 $\mu g/m^3$. From Table 6-1 it is apparent for all five monitoring sites that REMSAD has a tendency to under-predict sulfate concentrations during July with normalized biases ranging between -15% and -81%, and over-predict sulfate concentrations during October, with normalized biases ranging between 52% and 78%.

6.2.2. BRAVO Network: Aggregation of 37 BRAVO Monitors

To assess REMSAD's performance over the entire BRAVO monitoring network, the observed and predicted sulfate concentrations were aggregated and evaluated on an overall and monthly basis (Figure 6-8 and Table 6-2). The four month observed and predicted sulfate concentrations were 3.1 $\mu g/m^3$ and 3.3 $\mu g/m^3$, respectively. Other performance measures for this period were R = 0.61, Bn= 19%, and En = 65%. There was a significant under-prediction of sulfate in July (Figure 6-8b), and a significant over-prediction in October (Figure 6-8e); corresponding biases for these two months were -38% and 82%, respectively. Model performance is best during the months of August (R = 0.75, Bn = -25%, En = 49%) and September (R = 0.63, Bn = 30%, En = 61%).

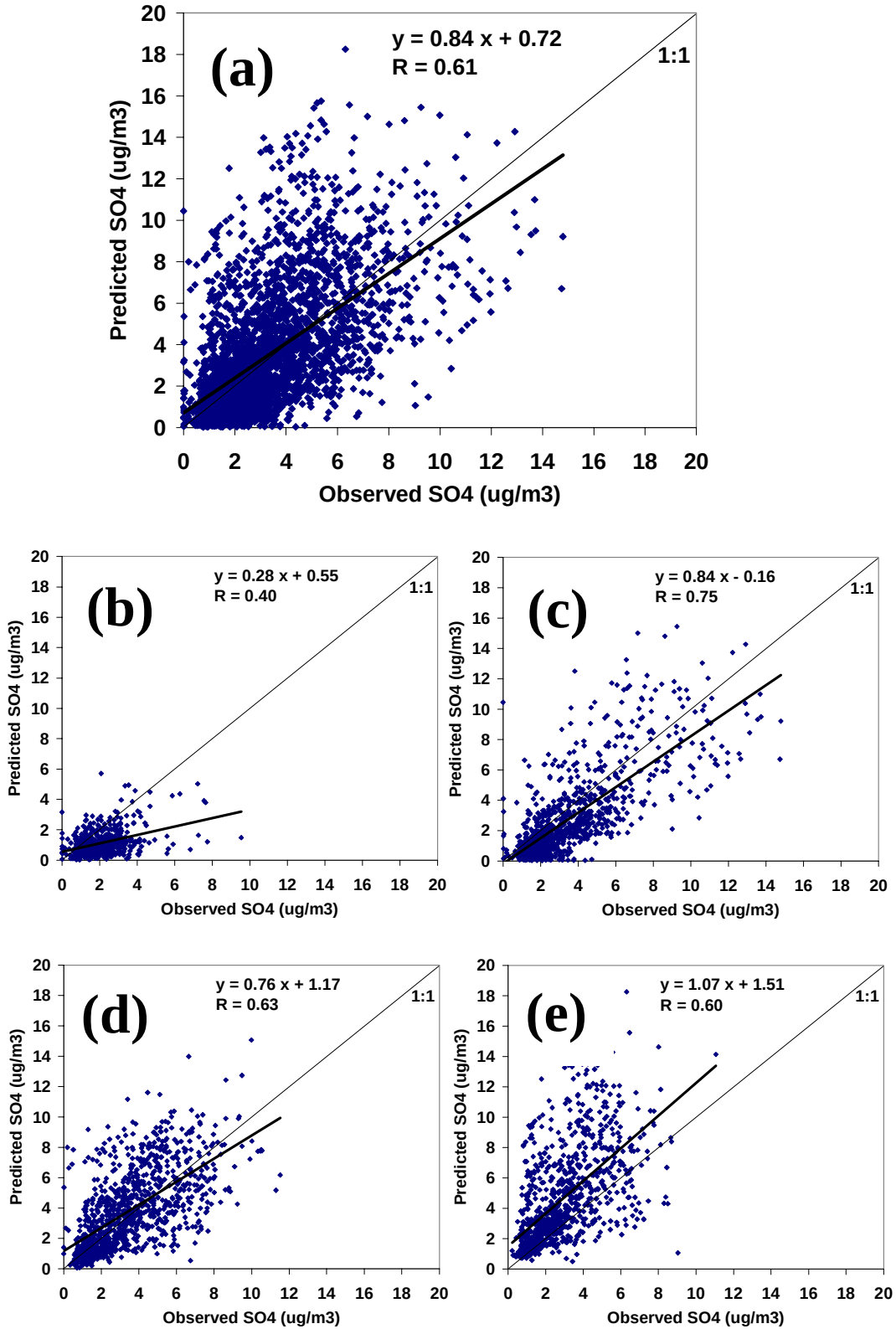

Figure 6-8. Scatter plots of predicted versus observed sulfate concentrations for all 37 BRAVO monitors: (a) July–October, (b) July, (c) August, (d) September, and (e) October. A least-squares linear regression equation and line is also shown.

Table 6-2. REMSAD performance statistics for the base simulation calculated for all 37 BRAVO monitors.

	Overall	July 99	August 99	September 99	October 99
Observed Average (μg/m^3)	3.1	2.1	3.5	3.5	2.8
Predicted Average (μg/m^3)	3.3	1.1	2.8	3.8	4.6
R	0.61	0.40	0.75	0.63	0.60
Normalized Error	62%	51%	53%	43%	98%
Normalized Bias	1%	-41%	-43%	2%	78%
Data Completeness	98%	88%	100%	100%	100%

6.2.3. CASTNET Network: Aggregation of 67 CASTNET Monitors

To investigate REMSAD's performance over a larger scale, the observed and predicted sulfate from the 67 CASTNET monitors that lie within the model domain were aggregated and evaluated on an overall and monthly basis (Figure 6-9 and Table 6-3). Unlike the BRAVO monitoring network, the CASTNET observations are collected weekly instead of daily, and hence the REMSAD predictions were averaged over the same weekly interval as the CASTNET observations. Observed and predicted sulfate concentrations from the CASTNET sites were significantly higher as compared to the BRAVO network due to the large number of CASTNET monitors located within the northeastern U.S. Overall observed and predicted sulfate concentrations were 4.5 μg/m^3 and 5.0 μg/m^3, respectively. REMSAD model performance was significantly better when evaluated against the CASTNET observations as compared to BRAVO observations; this is due at least in part to the longer temporal average of the CASTNET data. Overall performance statistics were R = 0.90, Bn = 21%, and En = 45%. Model performance on a monthly basis was best during the first three months of the study period, with R ranging between 0.88 and 0.92, Bn ranging between 3% and 21%, and En ranging between 36% and 43%. Similar to the previous discussion, significant over-predictions are evident in October, with Bn = 50% and En = 65%.

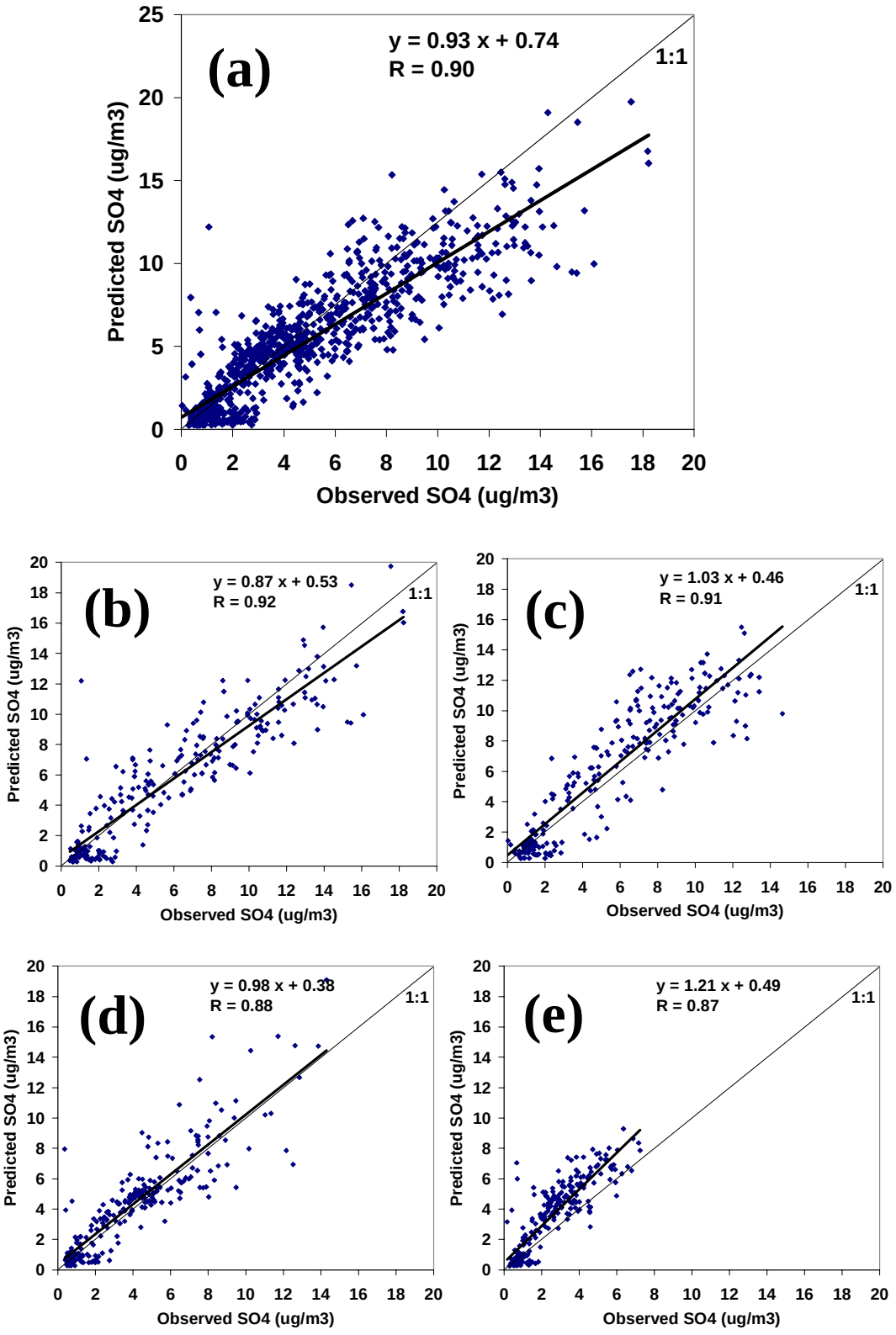

Figure 6-9. Scatter plots of predicted versus observed sulfate concentrations for the 67 CASTNET monitors that lie within the REMSAD model domain: (a) July–October, (b) July, (c) August, (d) September, and (e) October. A least squares linear regression equation and line is also shown.

Table 6-3. REMSAD performance statistics for the base simulation calculated for the 67 CASTNET monitors that fall within the model domain.

	Overall	July 99	August 99	September 99	October 99
Observed Average (µg/m^3)	4.5	5.8	5.6	4.1	2.6
Predicted Average (µg/m^3)	5.0	5.6	6.2	4.5	3.6
R	0.90	0.92	0.91	0.88	0.87
Normalized Error	45%	36%	36%	43%	65%
Normalized Bias	21%	3%	12%	21%	50%
Data Completeness	97%	99%	97%	96%	97%

6.2.4. Spatial Patterns of Model Bias

A final aspect of the model evaluation of the base simulation was to examine how model performance varied spatially across the domain. Contour maps of normalized bias are shown in Figure 6-10. These maps were created by aggregating all of the available sulfate data from the BRAVO and CASTNET monitoring networks, and calculating weekly averages for the BRAVO sulfate concentrations to match the time scale of the CASTNET concentrations. The overall four month average bias is shown in Figure 6-10a. In general, Bn ranges between -25% and 25% for BRAVO monitors in Texas and rises towards the northeast, where Bn can exceed 50%. On a monthly basis, the lowest biases are evident in July. It is particularly interesting to note the gradient of Bn that exists for the Texas monitors during this month, with Bn ranging between -45% and -84% at sites near the Texas/Mexico border. This gradient is also apparent to a lesser extent in August. September and October see a transition towards positive values of Bn, especially in Texas and the Midwest (Figures 6-10d and 6-10e, respectively).

(a)

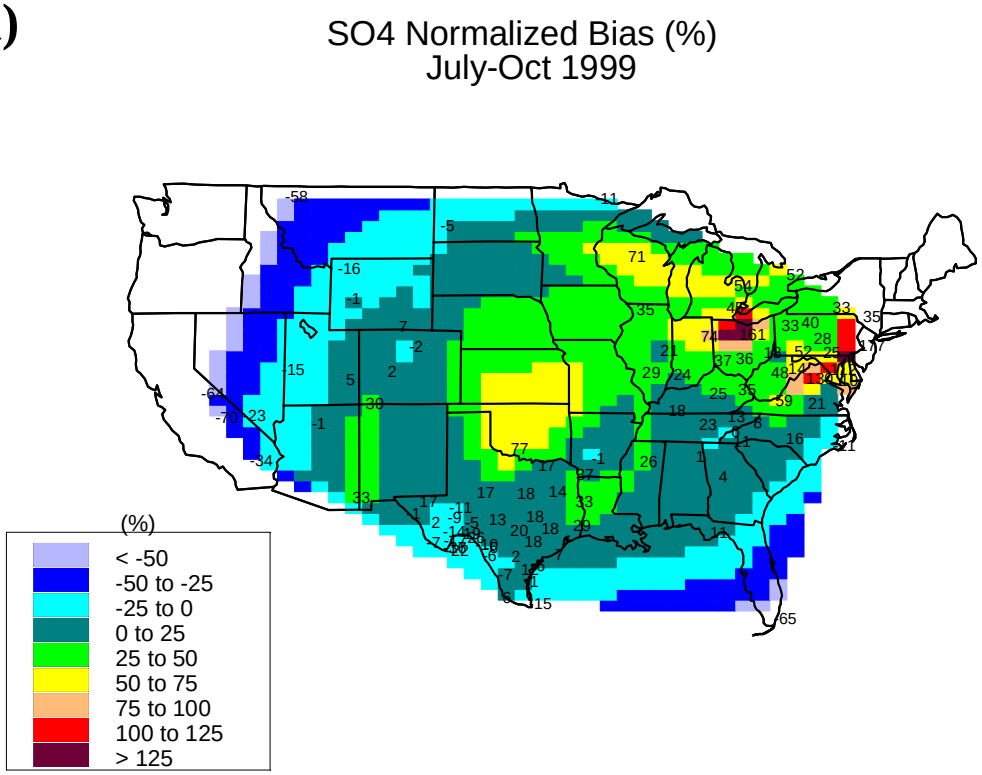

(b)

SO4 Normalized Bias (%)
July 1999

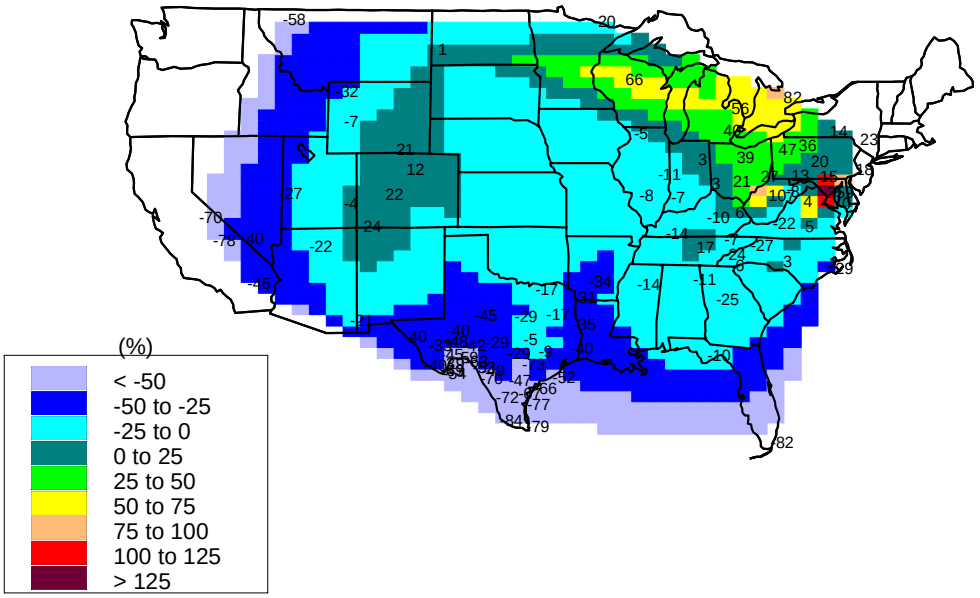

(c)

SO4 Normalized Bias (%)
Aug 1999

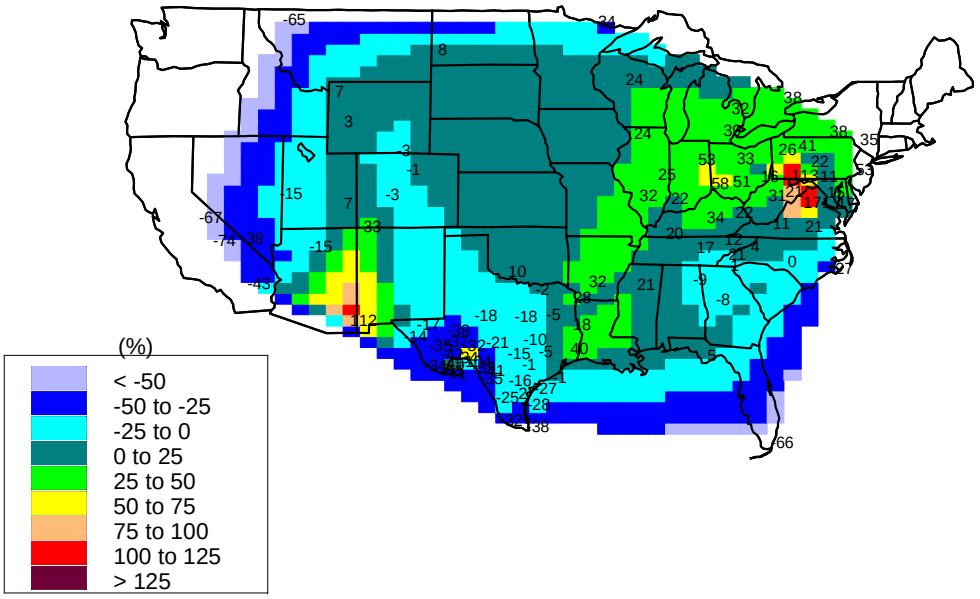

(d)

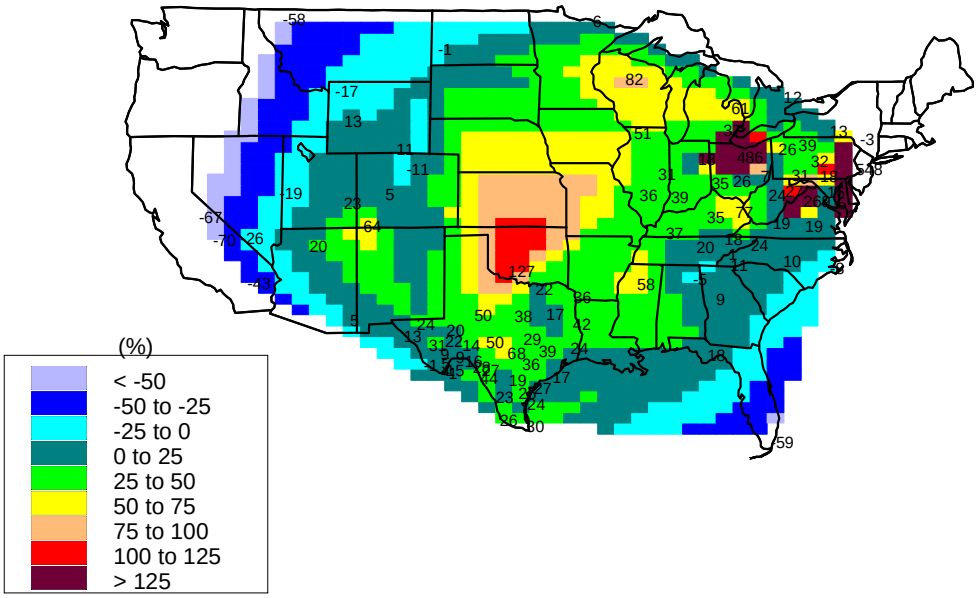

(e)

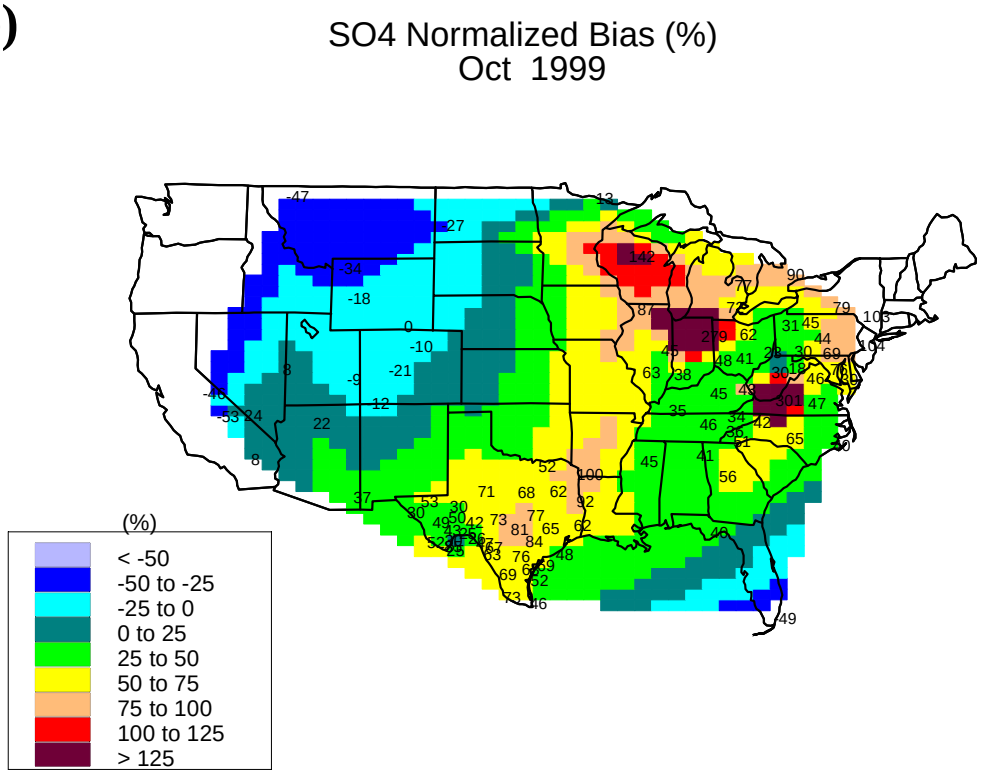

Figure 6-10. Contour maps of interpolated normalized bias: (a) July–October, (b) July, (c) August, (d) September, and (e) October.

6.3 Linearity of Sulfate Predictions

As discussed earlier, the emissions sensitivity simulations were conducted by removing sulfur dioxide (and primary sulfate) emissions from a source region, and comparing the resulting sulfate prediction to the original base simulation. These simulations, where sulfur dioxide was removed from the source region of interest, were termed "emissions out" sensitivity simulations. A complementary set of "emissions in" simulations was also evaluated where sulfur emissions were retained for the source region of interest but removed elsewhere. Examples of the emission inventory modifications that were performed for these two sets of simulations are shown in Figure 6-11. It should be noted that only sulfur dioxide and primary sulfate emissions were modified, and emissions of volatile organic compounds, oxides of nitrogen, carbon monoxide, etc., were left at their base case levels.

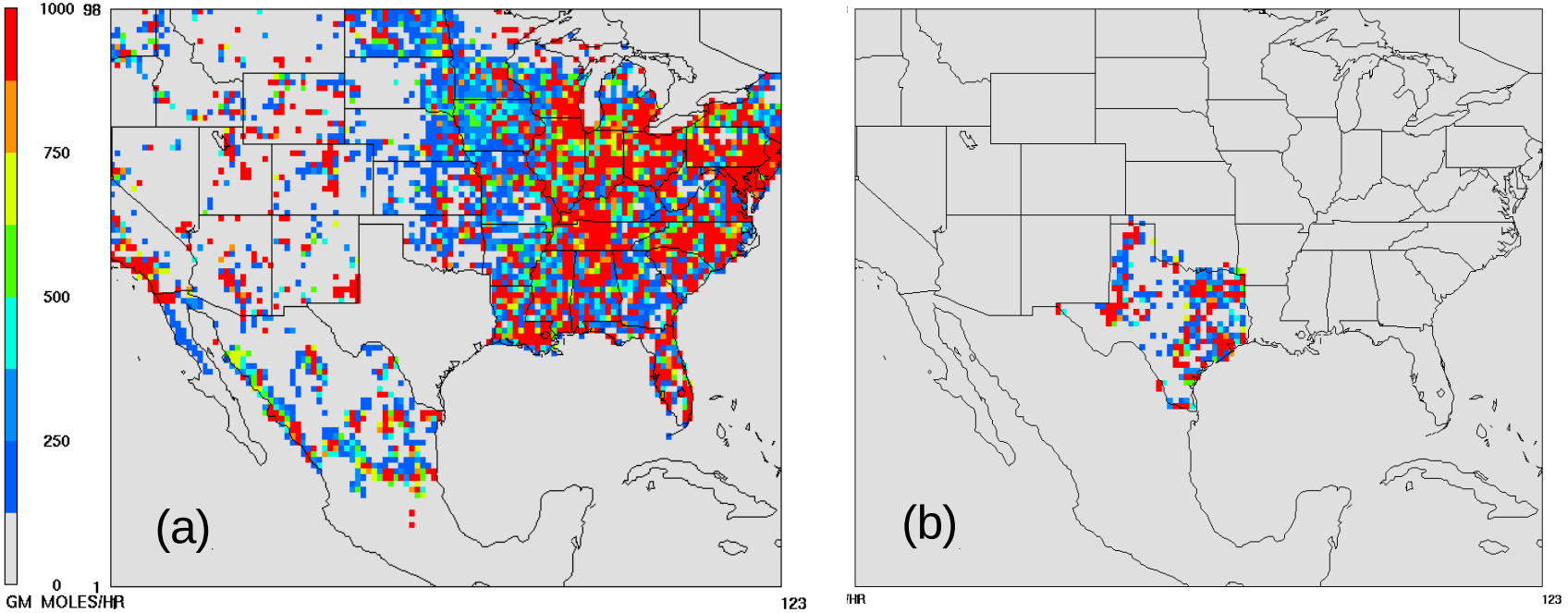

Figure 6-11. Example SO_2 emissions (moles/hr) for (a) the Texas "emissions out" scenario and (b) the Texas "emissions in" scenario.

It is important to investigate the equivalency of these two methods as either one could be regarded as a suitable approach for determining the impact of emissions from a source region on pollutant concentrations at a downwind receptor. Many processes within the model can be assumed to be linear and hence would yield the same results whether the "emissions out" or the "emissions in" inventory was used. These processes include, for example, dry deposition, as deposition fluxes scale in direct proportion to ambient concentrations. It is not obvious, however, that the rate of chemical transformation of sulfur dioxide to sulfate will respond in a linear fashion with regard to the "emissions out" and "emissions in" simulations. This is because the photochemistry that forms the oxidants that convert sulfur dioxide to sulfate is typically nonlinear. This includes the formation of hydroxyl for the gas-phase oxidation of sulfur dioxide and the formation of hydrogen peroxide and ozone for the aqueous-phase oxidation of sulfur dioxide. If there is a deficit in the concentration of available oxidants for converting sulfur dioxide to sulfate, i.e. an "oxidant limited" regime, then sulfate production will be sensitive to a change in the availability and distribution of oxidants. Sulfur dioxide acts as a sink for these oxidants, and the spatial distribution and total mass of sulfur dioxide within the model domain will be different between the "emissions out" and "emissions in" simulations. Oxidant levels should be greater in the "emissions in" scenarios as there is less total sulfur dioxide within the model domain to act as an oxidant sink and hence sulfate production should be enhanced relative to the "emissions out" scenarios.

The degree of linearity between the "emissions out" and "emissions in" sensitivity simulations is presented in Figure 6-12. Sulfate concentrations predicted at the K-Bar monitor for the original base simulation are shown in Figure 6-12a. Figures 6-12b through 6-12f show the difference in predicted sulfate contributions for the "emissions in" and "emissions out" simulations for the four major source regions, as well as the sulfate contribution from the boundary concentrations. For example, the time series shown in Figure 6-12b represents the sulfate contribution from Texas sources for the "emissions out" simulation, subtracted from the sulfate contribution from Texas sources for the "emissions in" simulation. If the predicted contributions are the same for the two sensitivity simulations, the difference will be zero and the model can be considered linear. Figures 6-12b through 6-12e show that this is generally the case, with the difference between the two sets of attributions at zero or very nearly zero for most of the four month simulation. A notable exception is evident, however, during the first half of October. During October 3–7 the maximum difference between the "emissions in" and "emissions out" contribution for both Texas and the eastern U.S. is approximately 0.5 $\mu g/m^3$, indicating an enhancement of sulfate formation for the "emissions in" simulation. A smaller enhancement also occurs during October 9–12, with the "emissions in" simulation yielding sulfate concentrations 0.3 $\mu g/m^3$ higher than the "emissions out" simulation. It is interesting to note that these periods coincide with enhanced transport from the oxidant-rich Houston area, as evidenced by the observed and predicted tracer time series shown in Figure 6-13.

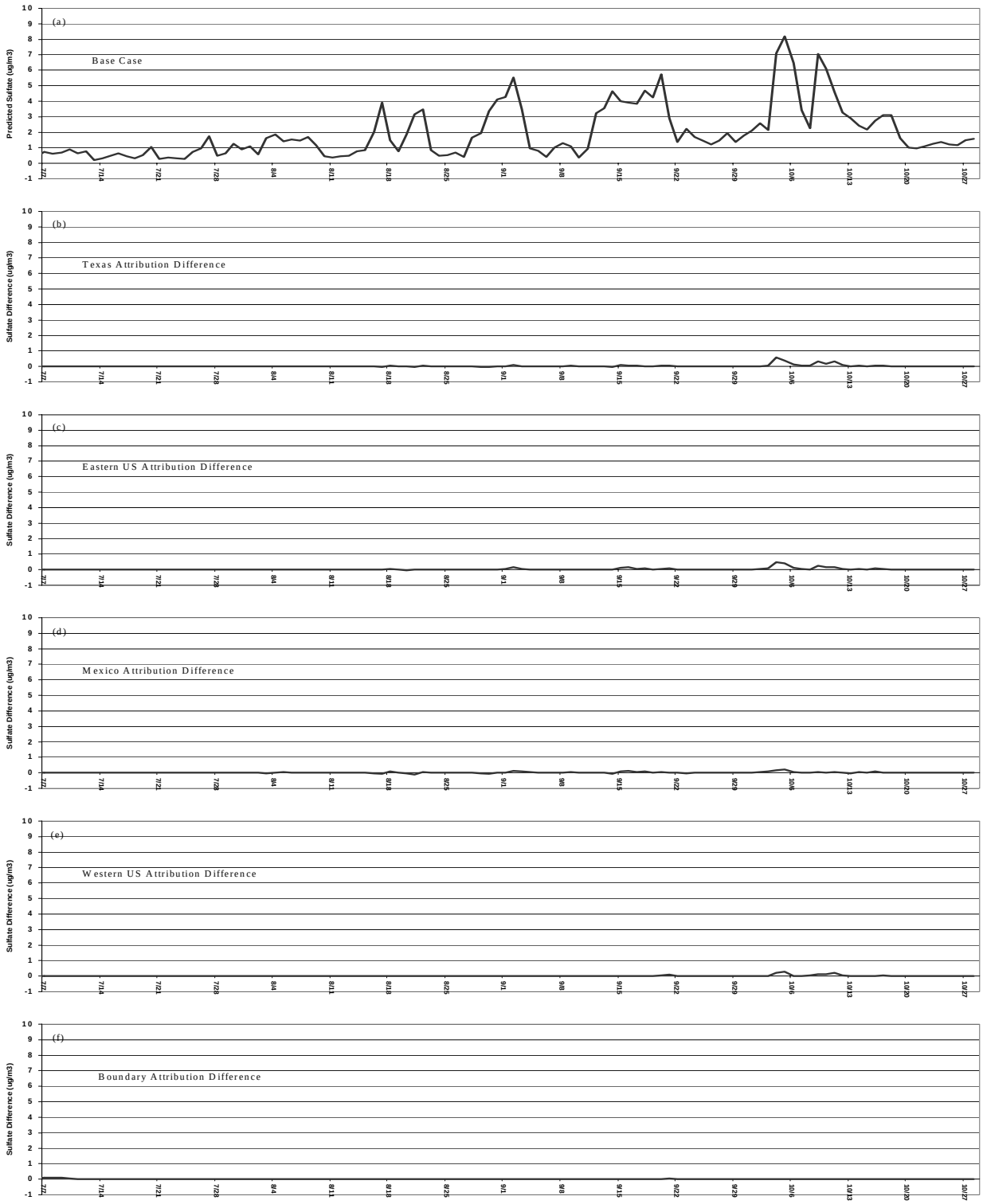

Figure 6-12. Degree of non-linearity between the "emissions out" and the "emissions in" simulations. (a) Predicted sulfate at K-Bar for the base emissions simulation. (b–e) Difference in predicted attributions for each source region (i.e. attribution from the "emissions out" simulation subtracted from the attribution from the "emissions in" simulation) for emission sources in (b) Texas, (c) the eastern U.S., (d) Mexico, (e) the western U.S., and (f) boundary concentrations.

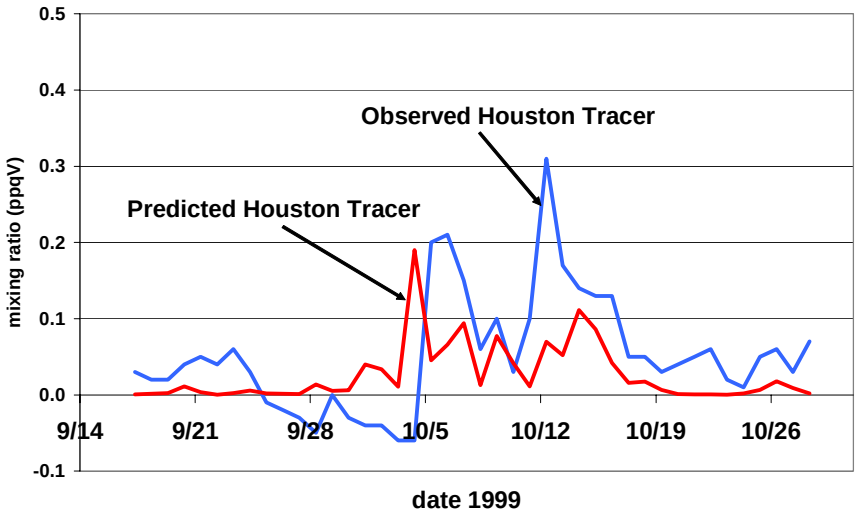

Figure 6-13. Predicted and observed Houston tracer concentrations measured at K-Bar.

From Figure 6-12 it is clear that the predicted attributions arising from the "emissions out" and the "emissions in" sensitivity simulations are very similar, with the "emissions in" simulations resulting in slightly enhanced sulfate production as expected. During the four month BRAVO period, the relative enhancements associated with the "emissions in" simulations were 2.8% for Mexican sources, 7.4% for Texas sources, 3.4% for eastern U.S. sources, 6.7% for western U.S. sources, and 4.2% for the boundary concentrations. This indicates that, in general, REMSAD behaves linearly with regard to the gross emission modifications presented in this chapter, and that attributions arising from the "emissions out" and "emissions in" sensitivity simulations are approximately equivalent. Therefore, to streamline the presentation of the following sulfate attribution section, only one set of attributions – the "emissions out" attributions – will be presented.

6.4 Sulfate Attribution Simulations

To determine the contribution of each of the four major regional source areas (Mexico, Texas, the eastern U.S., the western U.S.) on SO_4 concentrations at Big Bend NP, a series of REMSAD sensitivity simulations were evaluated with respect to the base emissions simulations. Additional emission sensitivity simulations were also conducted for evaluating the impact of several subregions and point sources, including northeastern and southeastern Texas, the Carbón I & II power plants near the Texas-Mexico border, and the Ohio River Valley. The influence of the GOCART-derived boundary concentration was also considered.

Example surface-level sulfate concentrations for the base emissions simulation and the emissions sensitivity simulations are shown in Figure 6-14 for a sulfate episode which occurred in mid-August of the BRAVO field study. The sulfate concentrations shown in Figures 6-14b–f are actually difference maps between the original base emissions simulation and the "emissions out" sensitivity simulation. In this particular example, observed and predicted sulfate concentrations at Big Bend NP were approximately 4 $\mu g/m^3$. During this period a region of elevated sulfate is evident in the base emissions simulation, ranging from 10 $\mu g/m^3$ to over 20 $\mu g/m^3$, and extends from eastern Texas toward Ohio and Pennsylvania (Figure 6-14a). Predicted sulfate concentrations are considerably lower over the western U.S., most of Mexico, and the Gulf of Mexico, with concentrations generally ranging between 0 $\mu g/m^3$ and 2 $\mu g/m^3$.

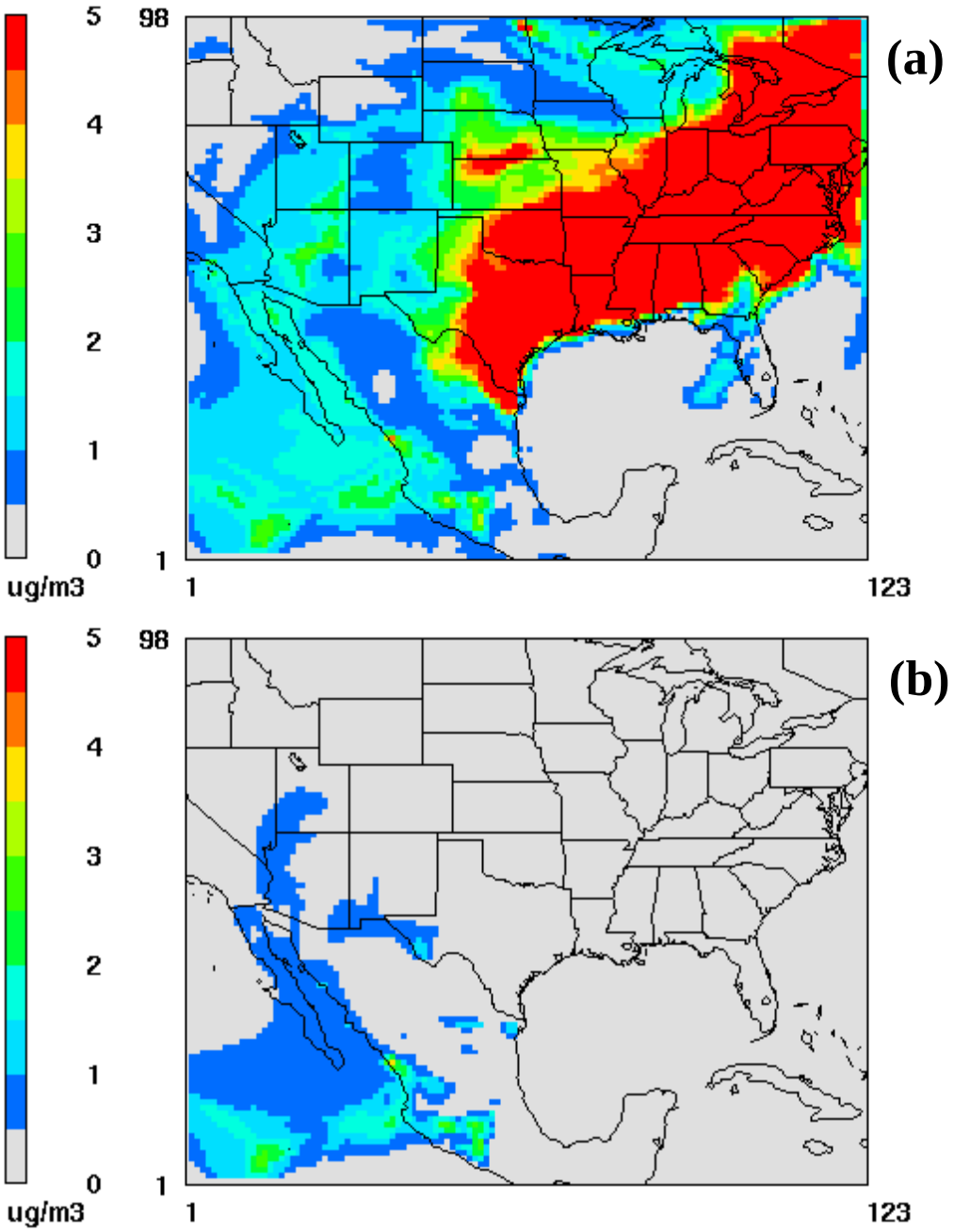
5
4
3
2
1
0
ug/m3
98
1
1
123
(a)
5
4
3
2
1
0
ug/m3
98
1
1
123
(b)

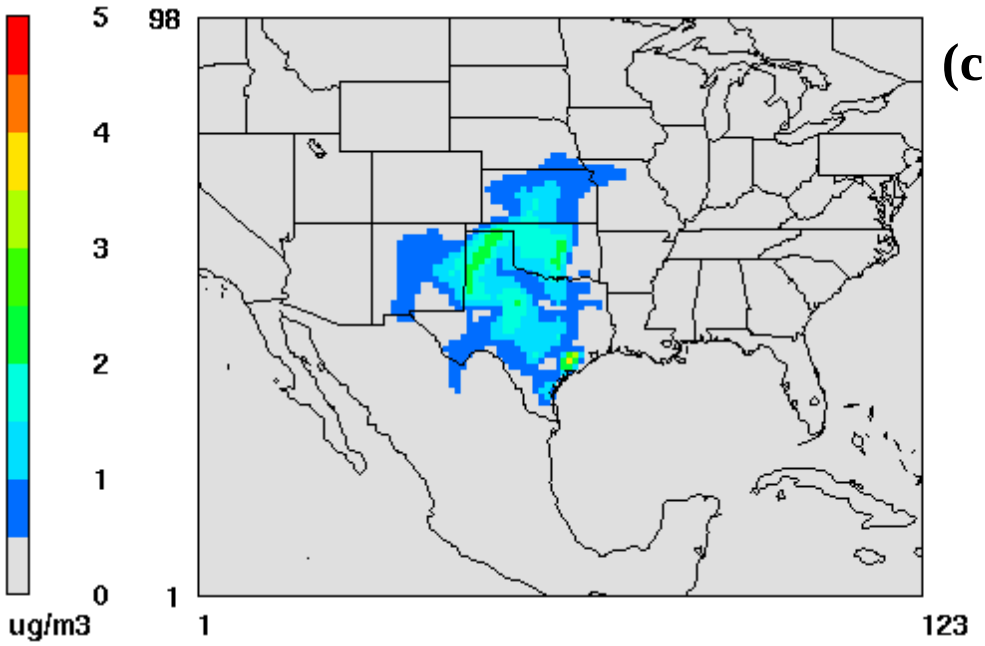

(c)

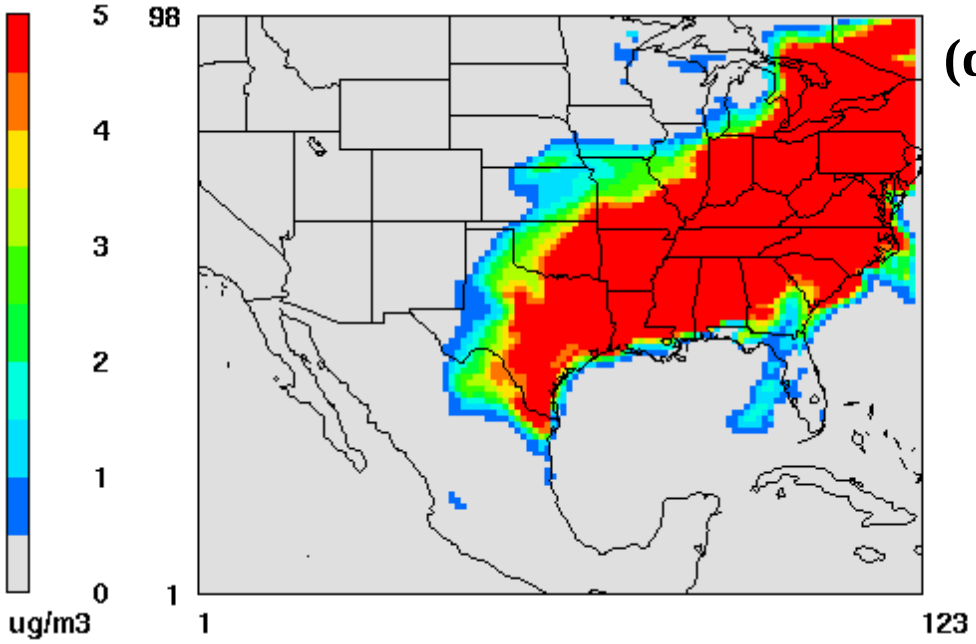

(d)

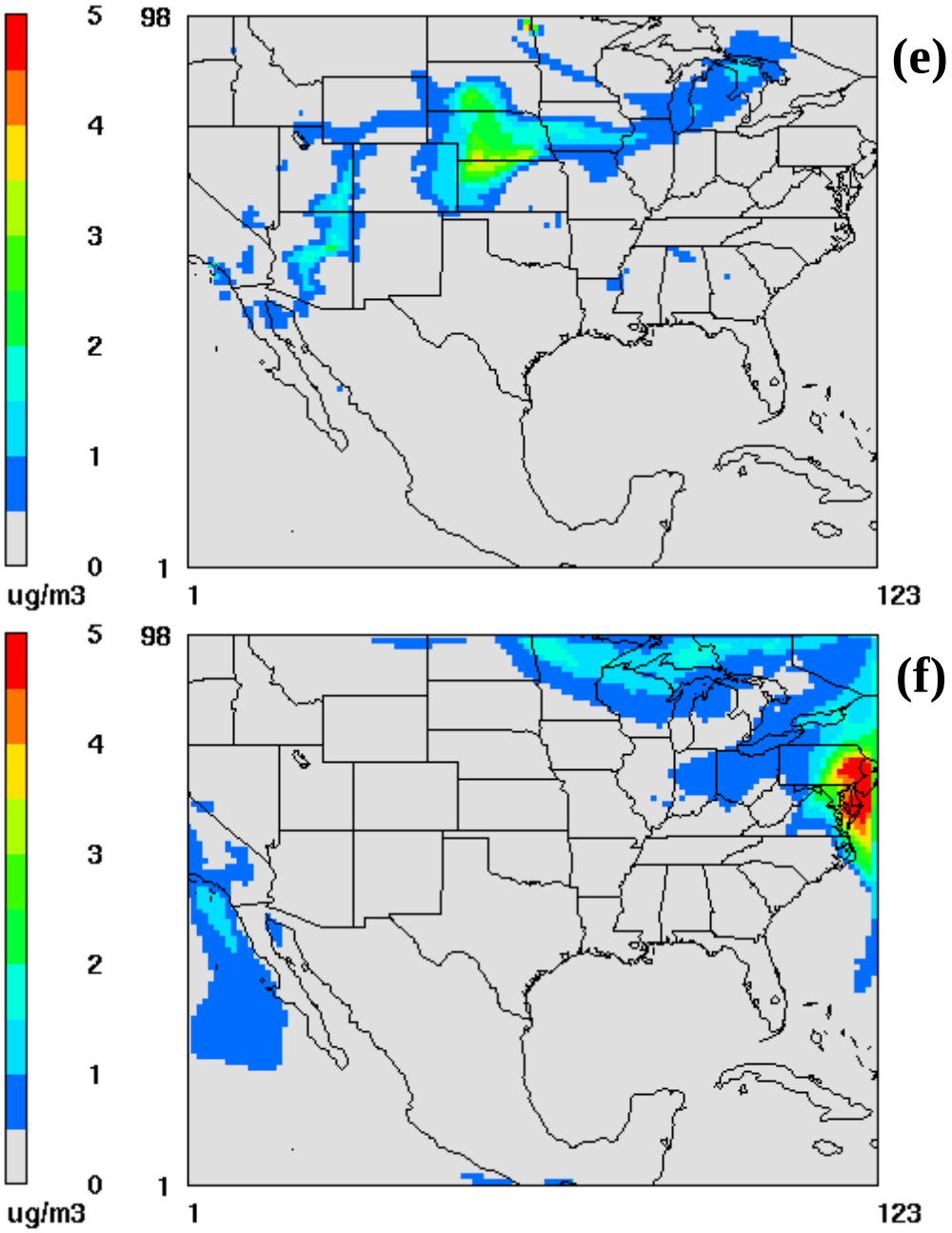

Figure 6-14. Surface sulfate concentrations (μg/m^3) on August 17, 1999, 1500 UTC, for the (a) base emissions simulation and contributions from the five emissions sensitivity simulations: (b) Mexico, (c) Texas, (d) the eastern U.S., (e) the western U.S., and (f) GOCART boundary concentrations.

The aggregation of sulfate contributions shown in the Figures 6-14b–f should approximate the base emissions scenario (Figure 6-14a). The contribution of each regional source (and the contribution of the concentrations specified at the model boundary) to total predicted sulfate levels for this period can be assessed by examining Figures 6-14b–f. For example, the magnitude of predicted sulfate attributed to eastern U.S. sources is clearly evident in Figure 6-14d, with sulfate concentrations exceeding 5 μg/m^3 in the mid- and eastern portions of the model domain. The dominance of eastern U.S. sources should be anticipated, given that approximately 77% of the SO_2 emitted within the REMSAD domain is from the eastern U.S.

Mexican sulfur sources, and in particular the Popocateptl volcano, result in elevated sulfate levels apparent off the western coast of Mexico, and the sulfate plume of the Carbón I & II power plants, in excess of 1.5 $\mu g/m^3$ near Big Bend NP, is evident along the western Texas-Mexico border (Figure 6-14b). Texas sulfur sources, located primarily in eastern Texas, are contributing to sulfate levels ranging from 0.5 $\mu g/m^3$ to 3 $\mu g/m^3$ which extend into western Texas and north into Oklahoma and Kansas (Figure 6-14c). Finally, for this particular period, the influence of western sulfur sources and sulfur concentrations specified at the model boundary is negligible on sulfate predicted at Big Bend NP (Figures 6-14e–f).

A notable aspect of Figures 6-14b–f is the extent to which a source region can influence predicted SO_4 concentrations downwind. For example, during this particular mid-August episode, sulfur emissions from eastern U.S. sources are contributing to sulfate concentrations in excess of 5 $\mu g/m^3$ in eastern Texas and extending into the border region of eastern Mexico (Figure 6-14d). Mexican sources are contributing approximately 1 $\mu g/m^3$ to predicted sulfate concentrations in southwestern Utah and western Arizona (Figure 6-14b), and similar levels are attributed to predicted sulfate in the Great Lakes region from western U.S. sources (Figure 6-14e). The impact of sulfur boundary concentrations specified by GOCART is primarily confined to the domain periphery, although a large contribution is clearly evident in proximity to the northeastern boundary (Figure 6-14f).

6.4.1 Simulated Sulfate Apportionment at Big Bend NP

Predicted source contributions at the K-Bar air quality monitor are shown in Figure 6-15 for each source region and emissions scenario combination for the four month BRAVO period. During July–August 1999 the largest contributor to sulfate at Big Bend NP is the eastern U.S., (42.1%), followed by Mexico (23.4%), Texas (16.1%), the western U.S. (9.1%), and the sulfur boundary concentrations derived from GOCART (6.7%). Figure 6-16 shows the overall and monthly sulfate concentrations predicted at Big Bend NP. As discussed in section 6.2, REMSAD under-predicts sulfate concentrations with respect to the average of the four month BRAVO period by approximately 20% (2.5 $\mu g/m^3$ observed vs. 2.0 $\mu g/m^3$ predicted). Possible explanations for this under-prediction include: 1) an under-estimation of SO_2 emissions for some regions, 2) errors in the simulated transport of SO_2 and SO_4, 3) slow SO_2 conversion rates, or 4) excessive wet or dry SO_4 deposition. The impact of these potential errors will influence the predicted source attributions. This bias, however, does not manifest itself consistently on a monthly basis. For example, predicted sulfate concentrations at Big Bend NP during July and August are approximately half the observed values (Figures 6-16b, c), while under-predictions during September are less acute (Figure 6-16d). Simulated sulfate during October, however, is over-predicted by approximately 25% (Figure 6-16e). This change in bias corresponds to different flow regimes that were evident during the BRAVO study. For example, trajectory analysis indicates that transport to Big Bend NP was predominately from Mexico during July and several periods in August. Transport patterns transitioned during September and October, however, yielding more influence from eastern U.S. and Texas sources during this period.

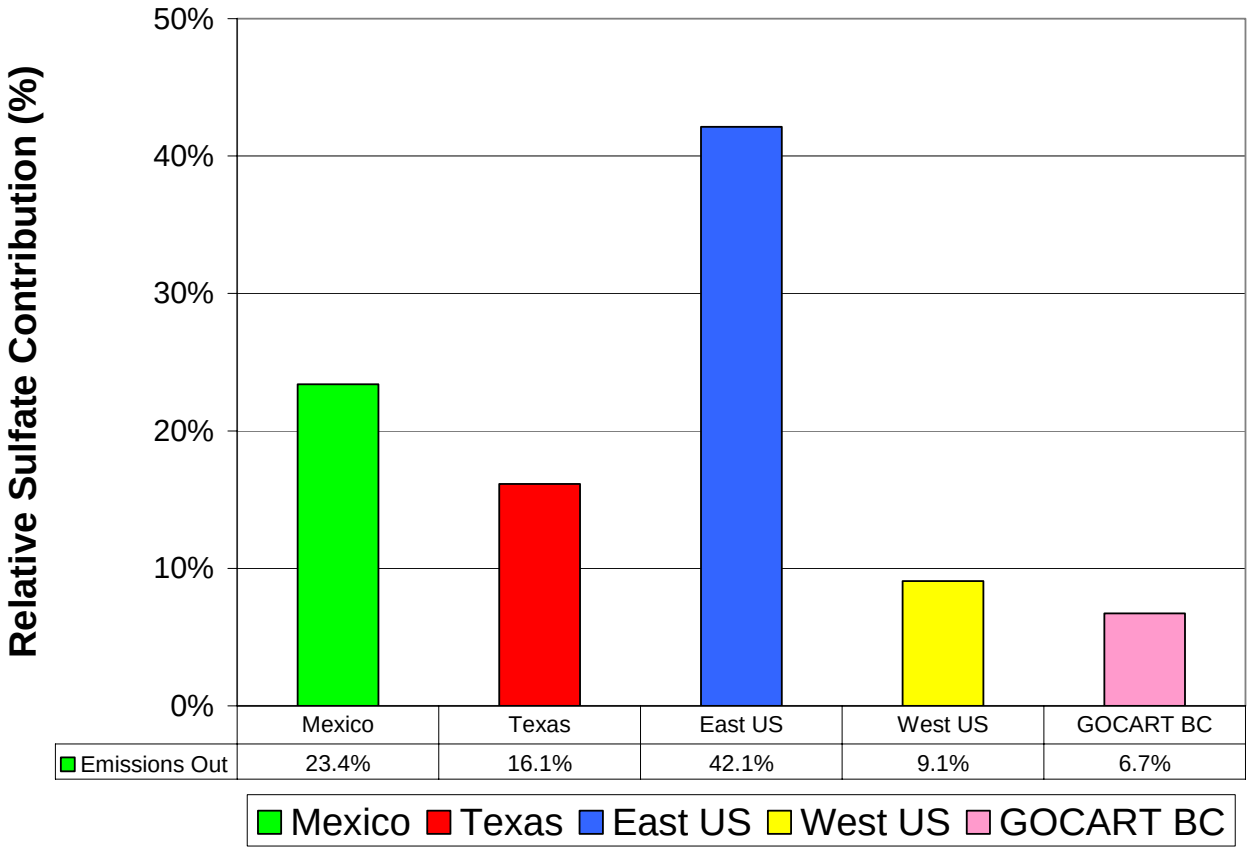

Figure 6-15. Four month average contributions to predicted sulfate at Big Bend NP from the "emissions out" sensitivity simulations for the four regional sources and the boundary concentrations.

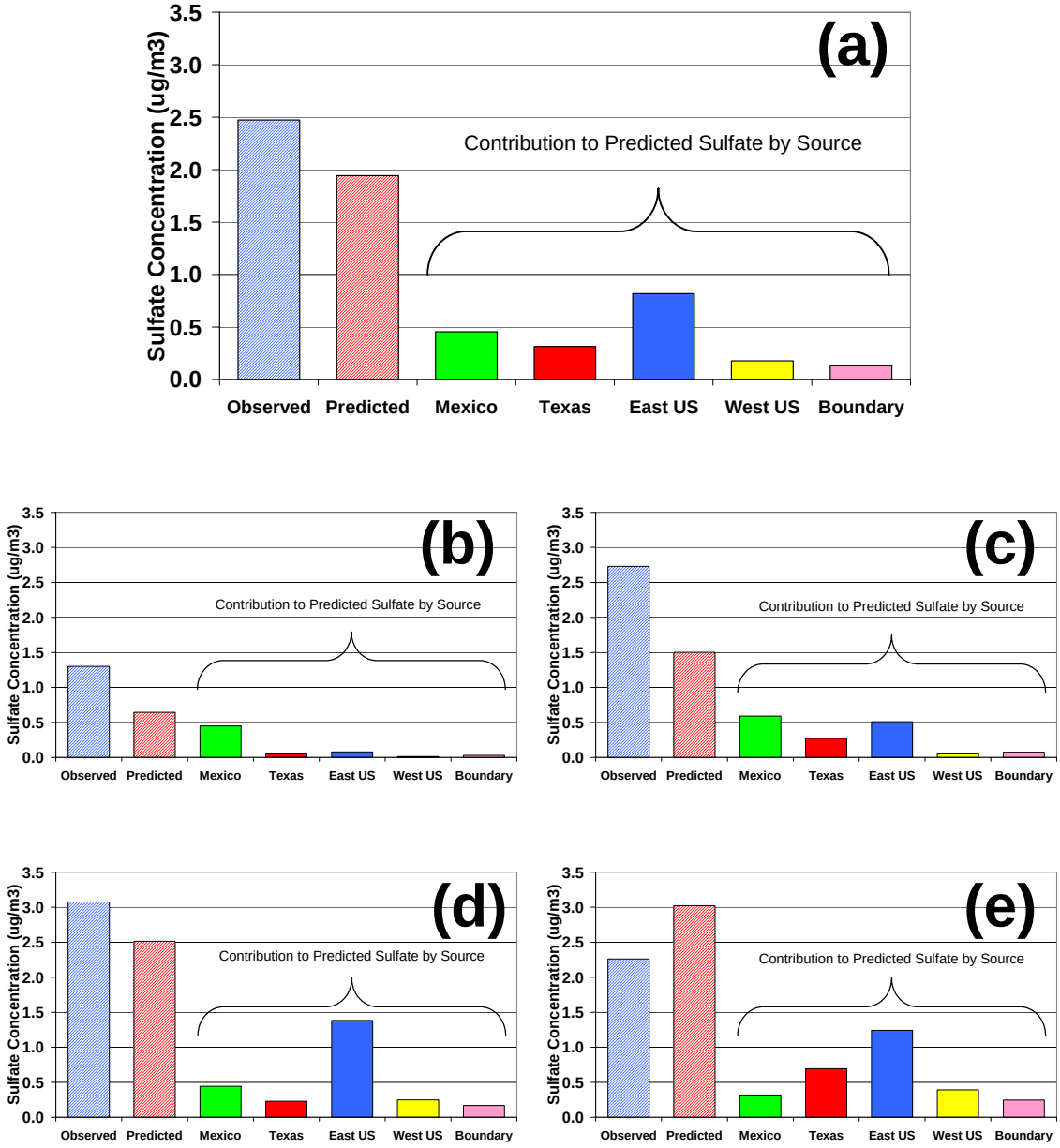

Figure 6-16. Observed sulfate, predicted sulfate, and predicted sulfate by source region at Big Bend NP for the "emissions out" simulations for (a) the entire BRAVO study period (July–October 1999), (b) July 1999, (c) August 1999, (d) September 1999, and (e) October 1999.

Relative sulfate attributions are presented Figures 6-17. Again, the overall relative attribution is significantly different than the monthly attributions, with a transition from a Mexican-dominated influence in the early part of the study (Figures 6-17b,c) to a regime where eastern U.S. sources, and to a lesser extent, Texas sources, are prevalent. For example, Mexican contributions to Big Bend NP sulfate drop from 70% in July (Figure 6-17b) to only 11% in October (Figure 6-17e), while eastern U.S. sources rise from 12% (Figure 6-17b) to 55% in September (Figure 6-17d) and 41% in October (Figure 6-17e).

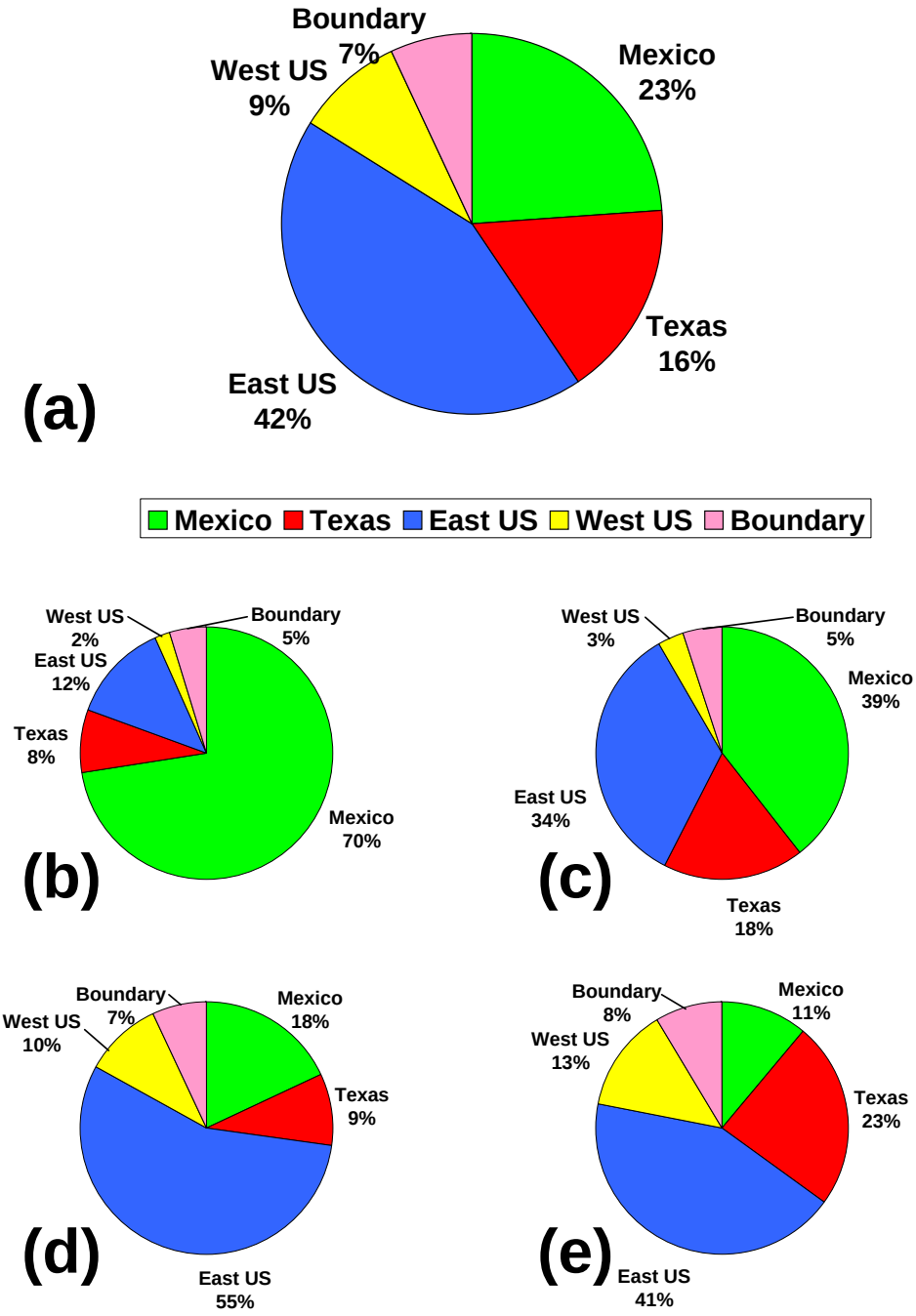

Figure 6-17. Relative contribution of predicted sulfate to Big Bend NP by source region for the "emissions out" simulations for (a) the entire BRAVO study period (July–October 1999), (b) July 1999, (c) August 1999, (d) September 1999, and (e) October 1999.

SO_4 source attributions at the K-Bar monitor can also be examined on a daily basis, as shown in Figures 6-18 and 6-19. Figure 6-18 displays the absolute SO_4 contribution for each source region, and Figure 6-19 illustrates the relative contribution for each source region. During July and the first half of August, transport is predominantly from Mexico. Predicted SO_4 concentrations during this period are lower than observed. Although the absolute contribution

from Mexican sources may be quite small during this period (< 1 μg/m^3), these contributions will have a disproportionate impact on visibility since SO_4 concentrations within Big Bend NP are relatively low during this time. Small incursions of SO_4 from western U.S. sources are evident from July through mid-September.

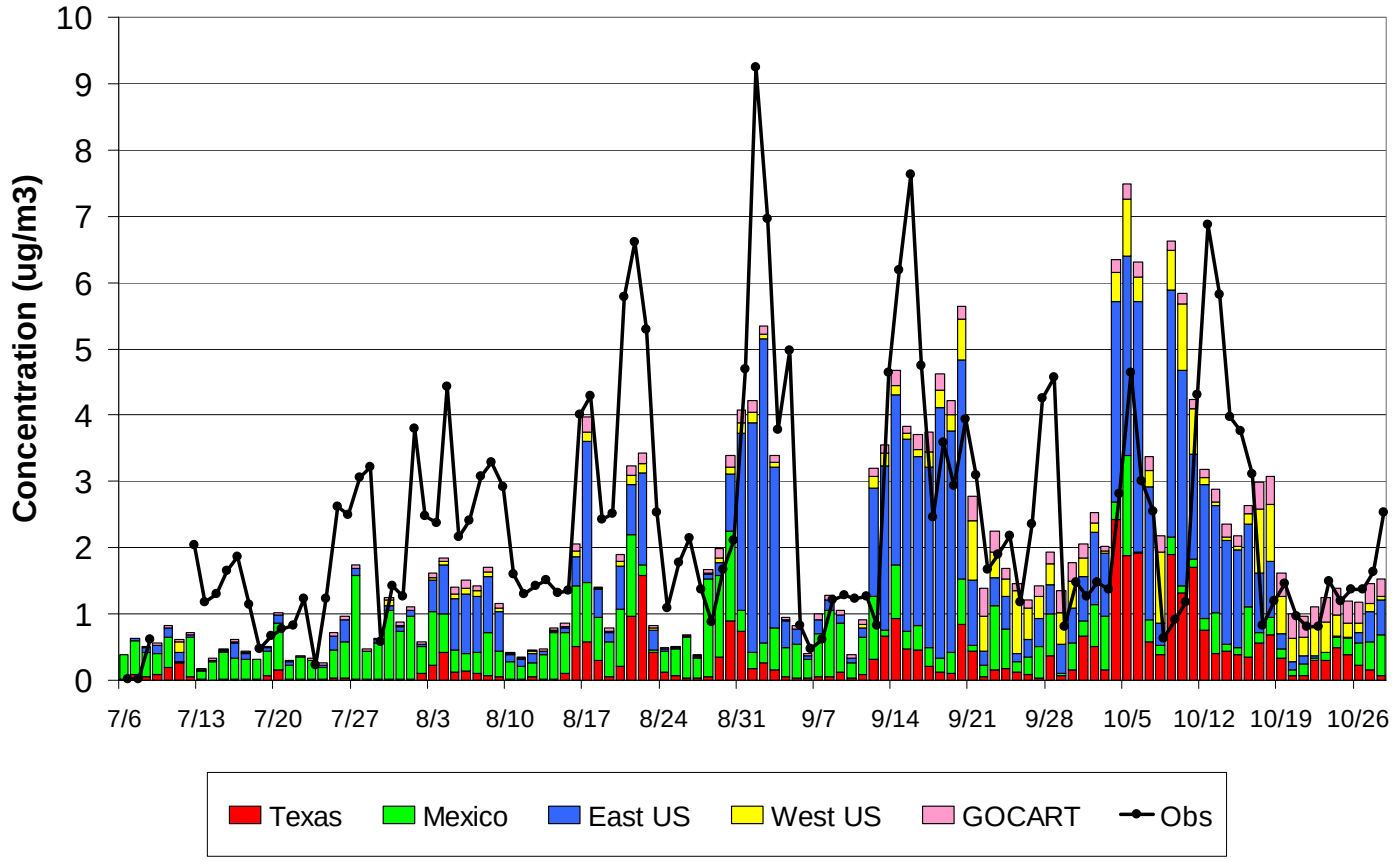

Figure 6-18. Daily absolute attribution of sulfate to Big Bend NP.

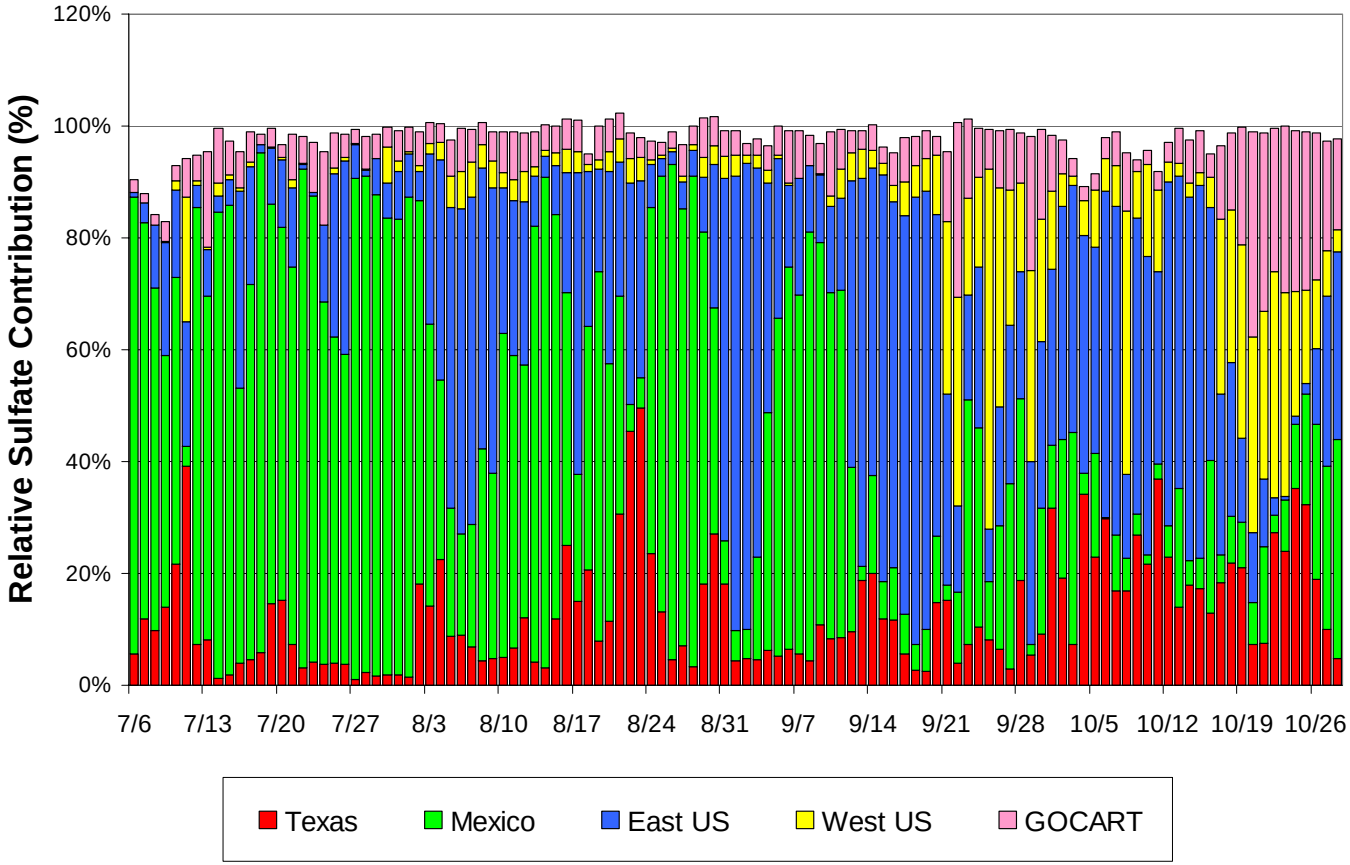

Figure 6-19. Daily relative attribution of sulfate to Big Bend NP.

From mid-August onward the high SO_4 episodes show a major component of eastern U.S. SO_4. This is especially evident in the two September SO_4 episodes, when the relative proportion of eastern U.S. SO_4 can exceed 80%. It is also notable that during these two episodes the predicted SO_4 concentrations are significantly lower than the observed values. Mexican emissions dominate the relatively clean period between these two September episodes. The two October SO_4 episodes also show a major contribution from eastern U.S. sources, but Texas sources, and to a lesser extent Mexican and western U.S. sources, also have a considerable impact. In contrast to the September SO_4 episodes, there is a substantial over-prediction of the October 5 SO_4 peak, and the subsequent peak (observed on October 12) appears to be shifted forward by three days. The intervening periods between the late September and October SO_4 episodes show a more evenly mixed distribution among all four source regions.

In addition to the four major source regions discussed above, sulfate apportionment at Big Bend NP can also be refined to smaller subregions, as shown in Figure 6-20. In proximity to Big Bend NP are the subregions of northeast and southeast Texas, with SO_2 emissions of 506,000 tons/year and 445,000 tons/year, respectively, and the Carbón I & II power plants, with SO_2 emissions of 152,000 ton/year. Also, three subregions within the eastern U.S. are considered: (1) Louisiana and southern Mississippi, with SO_2 emissions of 935,000 tons/year, (2) Missouri, Arkansas, southern Illinois, northern Mississippi, and portions of Indiana, Kentucky and Tennessee, with SO_2 emissions of 2,812,000 tons/year, and (3) an "East Central" region consisting of Virginia, North Carolina, South Carolina, West Virginia, northern Georgia and Alabama, eastern Kentucky and Tennessee, southern Indiana and Ohio, Maryland, Delaware, and southern New Jersey, with emissions of 5,514,000 tons/year. Emission sensitivity simulations were performed for these subregions, and contributions are shown in Table 6-4. Of these subregions, the Carbón I & II power plants have the largest impact at Big Bend NP, contributing approximately 14% of the total sulfate. Northeast and southeast Texas contribute 5% and 9%, respectively, and contributions from the three subregions within the eastern U.S. range between 9% and 13%.

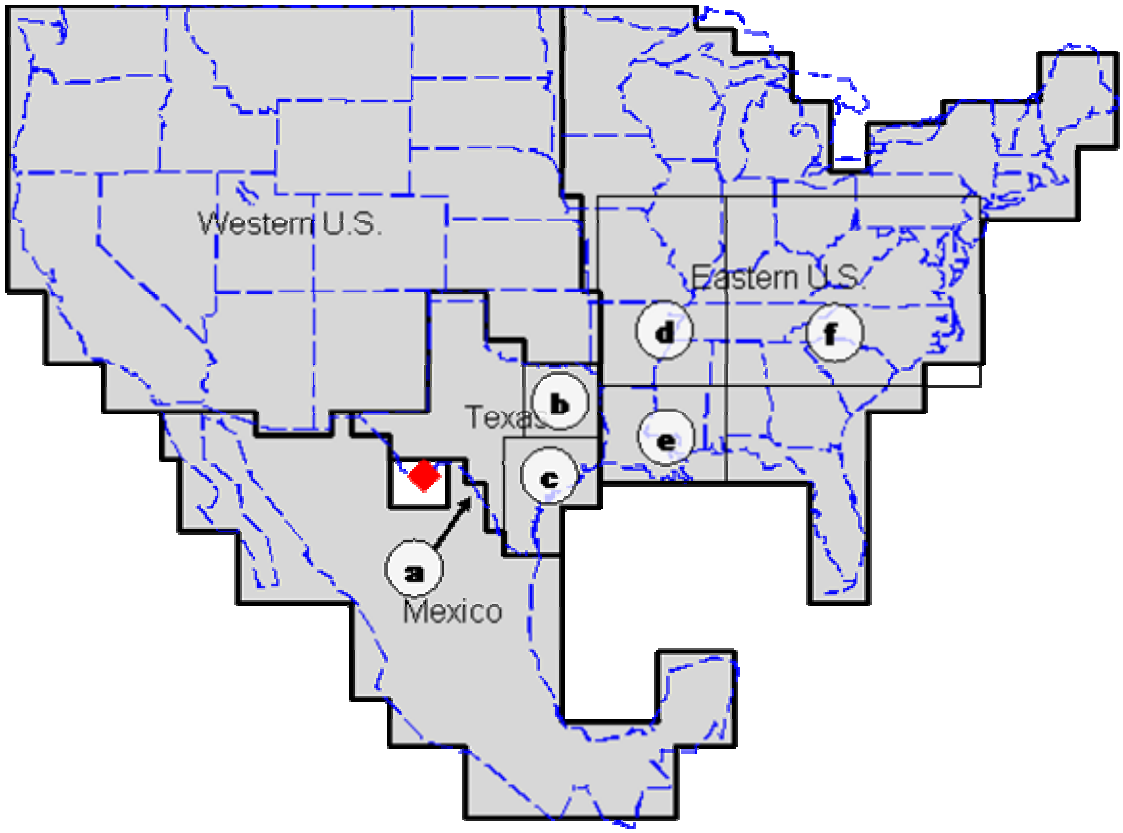

Figure 6-20. Domain map, showing the (a) Carbón I & II power plants and the subregions of (b) northeastern Texas, (c) southeastern Texas, (d) Missouri/Illinois/Arkansas, (e) Louisiana/Mississippi, and (f) "East Central".

Table 6-4. Predicted subregional contributions to Big Bend NP sulfate.

	Regional Contribution	Subregional Contribution
	(%)	(%)
Mexico (all)	**23.4%**	
Carbón I & II		13.7%
Rest of Mexico		9.7%
Texas (all)	**16.1%**	
NE Texas		5.3%
SE Texas		8.6%
Western Texas		2.2%
Eastern U.S. (all)	**42.1%**	
Louisiana/Mississippi		9.0%
"East Central"		13.2%
Missouri/Illinois/Arkansas		12.7%
Rest of Eastern U.S.		7.2%
Western U.S. (all)	**9.1%**	
Boundary Concentrations	**6.7%**	
Total Contribution	**97.5%**	

6.4.2 Simulated Sulfate Apportionment at the BRAVO Monitors

The predicted and observed sulfate concentrations and the contribution of the major source regions to the predicted sulfate were examined for each site by aggregating over each month (Tables 6-5 to 6-8, Figure 6-21) and for each day by aggregating over large regions within Texas (Figure 6-22). As shown in Figures 6-21 and 6-23, during July REMSAD underestimated the sulfate at all of the monitoring sites. This is most severe in southern Texas where the average sulfate was underestimated by more than a factor of 2 over all sites (Figure 6-23b) and a factor of 4 to 5 along the Texas-Mexico Border. Western Texas, around the Big Bend region, was also underestimated by about a factor of 2. During July, Mexico contributed more than half of the predicted sulfate at most sites in west Texas and about 75% of the sulfate at Big Bend. In southern Texas, eastern U.S. and Texas sources contributed equally to the predicted sulfate, while Texas sources were the largest contributor to eastern Texas sulfate.

Table 6-5. The average July source attribution for all BRAVO monitoring sites. All units are in μg/m^3.

Region/Site	Western U.S.	Mexico	Texas	Eastern U.S.	Pred SO_4	Obs SO_4
West Texas						
Amistad	0.00	0.56	0.12	0.16	0.92	2.01
Esperanza	0.15	0.94	0.06	0.19	1.41	2.11
Fort Lancaster	0.00	0.64	0.10	0.20	0.99	2.14
Fort Stockton	0.07	0.63	0.12	0.14	1.05	2.03
Guadalupe Mtns						

K-Bar	0.01	0.47	0.03	0.07	0.63	1.30
Langtry	0.01	0.62	0.17	0.17	1.04	2.86
Marathon	0.05	0.66	0.10	0.13	1.00	1.80
McDonald Obs	0.13	0.85	0.05	0.13	1.20	1.62
Monahans Sandhills	0.08	0.53	0.27	0.18	1.16	2.00
Persimmon Gap	0.04	0.56	0.11	0.10	0.88	1.54
Presidio	0.14	0.83	0.03	0.15	1.22	1.58
Sanderson	0.03	0.66	0.14	0.15	1.04	2.59
San Vicente	0.01	0.45	0.05	0.08	0.65	1.38
Average	0.05	0.65	0.11	0.14	1.01	1.92
South Texas						
Aransas	0.01	0.00	0.09	0.73	0.90	2.20
Brackettville	0.00	0.09	0.19	0.24	0.57	1.42
Eagle Pass	0.00	0.15	0.08	0.18	0.48	1.62
Falcon Dam	0.00	0.21	0.02	0.13	0.41	3.09
Laguna Atascosa	0.00	0.01	0.02	0.20	0.28	1.61
Lake Corpus Christi	0.01	0.01	0.21	0.49	0.78	2.27
Laredo	0.00	0.18	0.03	0.15	0.42	1.68
Padre Island	0.01	0.03	0.06	0.64	0.80	2.61
Pleasanton	0.00	0.03	0.55	0.30	0.97	1.96
San Bernard	0.02	0.01	0.39	0.79	1.27	2.26
Average	0.01	0.15	0.15	0.34	0.71	2.00
East Texas						
Big Thicket	0.02	0.01	1.12	0.95	2.16	3.13
Center	0.03	0.02	1.57	1.13	2.81	3.43
Everton Ranch	0.01	0.01	0.29	0.63	1.00	3.37
Hagerman	0.01	0.02	1.55	0.54	2.17	2.55
LBJ NHS	0.00	0.01	1.23	0.32	1.66	2.48
Purtis Creek	0.02	0.01	1.49	0.60	2.18	2.72
Somerville Lake	0.01	0.01	1.13	0.59	1.86	2.14
Stephenville	0.01	0.01	0.69	0.31	1.06	1.99
Stillhouse Lake	0.01	0.00	1.45	0.53	2.10	2.26
Wright Patman	0.04	0.02	3.03	0.81	3.96	5.35
Average	0.02	0.02	1.17	0.63	1.91	2.81
Other						
Fort McKavett	0.03	0.11	0.63	0.28	1.16	1.70
Lake Colorado City	0.00	0.41	0.32	0.17	0.95	1.97
Wichita Mtns						
Average	0.01	0.06	1.18	0.49	1.82	2.67

Table 6-6. The average August source attribution for all BRAVO monitoring sites. All units are in µg/m^3.

Region/Site	Western U.S.	Mexico	Texas	Eastern U.S.	Pred SO_4	Obs SO_4
West Texas						
Amistad	0.06	0.30	0.54	0.91	1.91	3.25
Esperanza	0.14	0.59	0.36	0.45	1.65	2.09
Fort Lancaster	0.08	0.22	0.65	0.99	2.04	2.81
Fort Stockton	0.07	0.46	0.42	0.66	1.69	2.86
Guadalupe Mtns	0.15	0.46	0.44	0.35	1.52	2.28
K-Bar	0.05	0.59	0.27	0.51	1.50	2.73
Langtry	0.07	0.30	0.54	0.95	1.97	3.58
Marathon	0.06	0.46	0.36	0.60	1.57	2.74
McDonald Obs	0.08	0.51	0.36	0.52	1.56	2.47
Monahans Sandhills	0.08	0.40	0.70	0.82	2.10	3.24
Persimmon Gap	0.06	0.55	0.34	0.57	1.61	3.13
Presidio	0.05	0.61	0.26	0.48	1.48	2.21
Sanderson	0.06	0.42	0.45	0.71	1.73	3.31
San Vicente	0.05	0.55	0.29	0.54	1.51	2.90
Average	0.08	0.46	0.43	0.65	1.70	2.83
South Texas						
Aransas	0.08	0.04	0.40	2.12	2.77	3.60
Brackettville	0.07	0.05	0.64	1.11	1.98	3.52
Eagle Pass	0.06	0.05	0.42	1.04	1.68	2.79
Falcon Dam	0.05	0.20	0.23	0.94	1.49	2.58
Laguna Atascosa	0.06	0.03	0.18	1.22	1.56	2.56
Lake Corpus Christi	0.08	0.05	0.63	1.59	2.46	2.42
Laredo	0.06	0.11	0.37	1.15	1.79	2.50
Padre Island	0.06	0.02	0.10	1.39	1.66	3.51
Pleasanton	0.08	0.07	0.96	1.62	2.84	3.34
San Bernard	0.09	0.04	0.83	2.31	3.41	3.60
Average	0.07	0.14	0.46	1.31	2.07	3.01
East Texas						
Big Thicket	0.12	0.04	0.65	3.59	4.59	4.35
Center	0.16	0.03	0.61	5.09	6.15	5.56
Everton Ranch	0.08	0.05	0.85	1.69	2.79	3.53
Hagerman	0.24	0.04	1.11	3.59	5.26	5.47
LBJ NHS	0.10	0.05	1.26	1.72	3.25	3.88
Purtis Creek	0.20	0.03	1.10	3.49	5.06	5.58
Somerville Lake	0.13	0.04	1.05	2.69	4.07	4.31
Stephenville	0.16	0.05	1.12	2.27	3.77	4.67
Stillhouse Lake	0.14	0.04	1.13	2.55	4.03	4.86
Wright Patman	0.23	0.04	1.01	6.24	7.87	6.19
Average	0.14	0.05	0.93	3.04	4.36	4.58
Other						
Fort McKavett	0.10	0.09	0.98	1.33	2.61	3.20

Lake Colorado City	0.14	0.14	1.06	1.31	2.76	3.35
Wichita Mtns	0.41	0.04	1.01	2.99	4.72	4.55
Average	0.17	0.06	1.05	2.74	4.21	4.51

Table 6-7. The average September source attribution for all BRAVO monitoring sites. All units are in µg/m^3.

Region/Site	**Western U.S.**	**Mexico**	**Texas**	**Eastern U.S.**	**Pred SO_4**	**Obs SO_4**
West Texas						
Amistad	0.21	0.56	0.58	2.42	4.01	3.69
Esperanza	0.40	0.44	0.40	0.86	2.28	2.05
Fort Lancaster	0.28	0.50	0.69	1.87	3.58	3.87
Fort Stockton	0.31	0.52	0.53	1.57	3.15	2.96
Guadalupe Mtns	0.34	0.38	0.45	1.08	2.44	2.27
K-Bar	0.25	0.44	0.23	1.41	2.52	3.08
Langtry	0.23	0.62	0.59	2.20	3.88	4.04
Marathon	0.29	0.53	0.41	1.54	2.97	3.22
McDonald Obs	0.34	0.42	0.41	1.18	2.53	2.29
Monahans Sandhills	0.33	0.49	0.68	1.60	3.32	3.63
Persimmon Gap	0.28	0.53	0.37	1.53	2.91	3.25
Presidio	0.28	0.42	0.25	1.25	2.38	2.84
Sanderson	0.28	0.58	0.53	1.84	3.45	3.27
San Vicente	0.25	0.44	0.23	1.41	2.52	3.09
Average	0.29	0.49	0.45	1.55	3.00	3.11
South Texas						
Aransas	0.12	0.02	0.39	3.93	4.78	4.12
Brackettville	0.18	0.04	0.65	2.74	3.89	3.67
Eagle Pass	0.21	0.06	0.73	3.41	4.70	3.54
Falcon Dam	0.14	0.22	0.35	3.52	4.47	3.69
Laguna Atascosa	0.11	0.02	0.30	3.96	4.65	3.80
Lake Corpus Christi	0.13	0.02	0.49	3.97	4.91	3.78
Laredo	0.16	0.11	0.48	3.60	4.60	3.92
Padre Island	0.15	0.03	0.53	4.53	5.57	4.24
Pleasanton	0.16	0.03	0.92	3.96	5.38	4.38
San Bernard	0.10	0.01	0.67	3.87	4.98	4.61
Average	0.17	0.12	0.52	3.37	4.45	3.83
East Texas						
Big Thicket	0.10	0.01	0.35	4.21	5.04	4.22
Center	0.09	0.01	0.28	3.47	4.20	3.49
Everton Ranch	0.16	0.02	0.80	3.50	4.79	4.00
Hagerman	0.16	0.02	0.91	1.95	3.39	3.57
LBJ NHS	0.19	0.03	1.10	2.76	4.35	3.22
Purtis Creek	0.11	0.01	1.04	2.64	4.14	4.04
Somerville Lake	0.14	0.02	0.76	2.92	4.16	3.52
Stephenville	0.19	0.05	0.85	2.24	3.64	3.38
Stillhouse Lake	0.16	0.02	0.88	2.72	4.09	3.67
Wright Patman	0.09	0.01	0.62	3.09	4.22	3.67

Average	0.14	0.03	0.73	3.06	4.29	3.77
Other						
Fort McKavett	0.24	0.15	0.80	2.09	3.53	3.08
Lake Colorado City	0.40	0.28	0.84	1.68	3.46	3.03
Wichita Mtns	0.38	0.09	0.88	1.67	3.36	2.54
Average	0.20	0.06	0.85	2.53	3.95	3.46

Table 6-8. The average October source attribution for all BRAVO monitoring sites. All units are in µg/m^3.

Region/Site	Western U.S.	Mexico	Texas	Eastern U.S.	Pred SO_4	Obs SO_4
West Texas						
Amistad	0.42	0.46	0.78	2.57	4.60	3.00
Esperanza	0.47	0.25	0.51	0.65	2.13	1.68
Fort Lancaster	0.46	0.39	0.74	2.17	4.11	2.68
Fort Stockton	0.46	0.33	0.71	1.40	3.22	2.14
Guadalupe Mtns	0.54	0.19	0.51	0.64	2.15	1.56
K-Bar	0.39	0.32	0.69	1.32	3.02	2.26
Langtry	0.44	0.45	0.75	2.34	4.35	3.26
Marathon	0.44	0.31	0.69	1.41	3.15	2.22
McDonald Obs	0.44	0.30	0.61	0.91	2.54	1.67
Monahans Sandhills	0.49	0.38	0.84	1.68	3.73	2.78
Persimmon Gap	0.44	0.30	0.70	1.45	3.19	2.50
Presidio	0.42	0.36	0.70	1.12	2.89	1.96
Sanderson	0.46	0.38	0.72	1.90	3.79	2.77
San Vicente	0.37	0.34	0.74	1.43	3.16	2.51
Average	0.45	0.34	0.69	1.50	3.29	2.36
South Texas						
Aransas	0.15	0.03	0.94	4.38	5.80	3.67
Brackettville	0.37	0.14	0.83	2.92	4.63	2.72
Eagle Pass	0.35	0.18	0.83	2.92	4.64	2.86
Falcon Dam	0.20	0.17	0.94	2.86	4.46	2.85
Laguna Atascosa	0.13	0.03	0.71	2.93	4.06	3.02
Lake Corpus Christi	0.17	0.06	1.23	3.74	5.53	3.39
Laredo	0.25	0.20	1.06	3.12	4.96	3.11
Padre Island	0.15	0.03	1.05	3.91	5.45	3.60
Pleasanton	0.24	0.08	1.30	3.70	5.69	3.17
San Bernard	0.12	0.02	0.79	4.75	5.99	4.12
Average	0.24	0.13	0.93	3.18	4.81	3.12
East Texas						
Big Thicket	0.13	0.02	0.32	5.57	6.37	4.30
Center	0.14	0.01	0.28	5.33	6.12	3.04
Everton Ranch	0.24	0.04	1.17	4.20	6.04	3.19
Hagerman	0.38	0.02	0.78	3.99	5.55	3.40
LBJ NHS	0.32	0.04	1.03	3.38	5.14	2.68
Purtis Creek	0.26	0.01	0.99	4.13	5.79	3.52
Somerville Lake	0.22	0.02	1.10	4.49	6.20	3.65

Stephenville	0.37	0.03	0.82	3.41	4.99	2.68
Stillhouse Lake	0.29	0.02	1.15	4.06	5.90	3.23
Wright Patman	0.19	0.01	0.67	4.79	6.04	3.02
Average	0.24	0.03	0.84	4.27	5.74	3.33
Other						
Fort McKavett	0.43	0.11	0.78	2.63	4.29	2.21
Lake Colorado City	0.50	0.27	0.81	2.24	4.20	2.24
Wichita Mtns						
Average	0.31	0.06	0.92	3.78	5.44	3.01

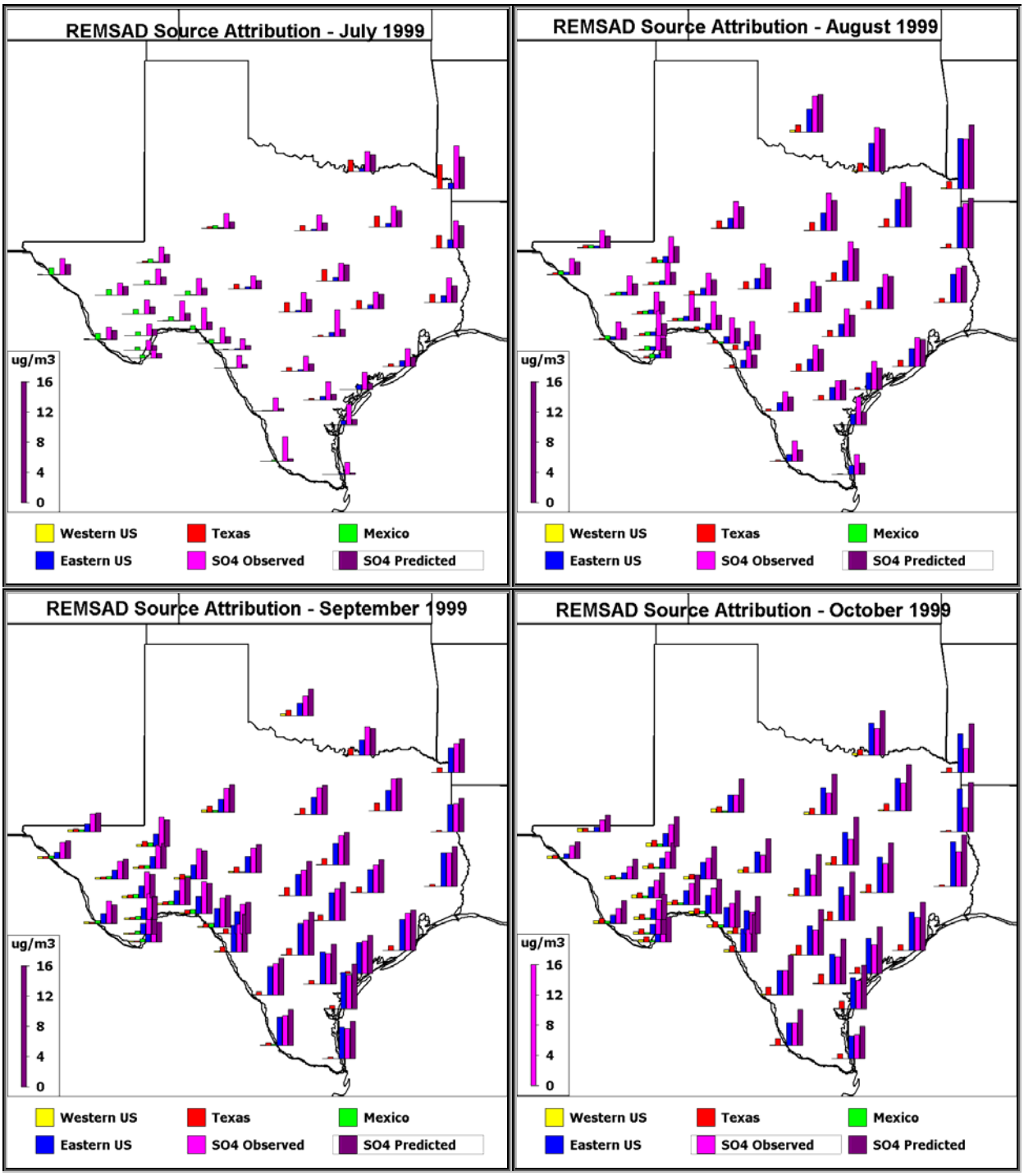

Figure 6-21. The average source attribution to each BRAVO monitoring site for each month during BRAVO. The average observed sulfate and REMSAD predicted sulfate are also included. Only days with a valid measured sulfate concentration were used in each site's averages.

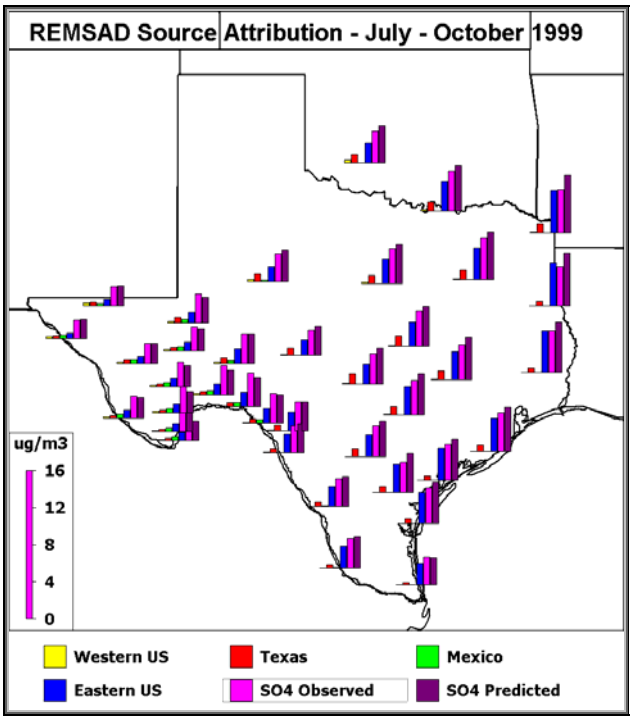

Figure 6-22. The average source attribution to each BRAVO monitoring site over the entire BRAVO period. Only days with a valid measured sulfate concentration were used in each site's averages. The boxes show the west, south, and east Texas aggregation regions used in Figure 23.

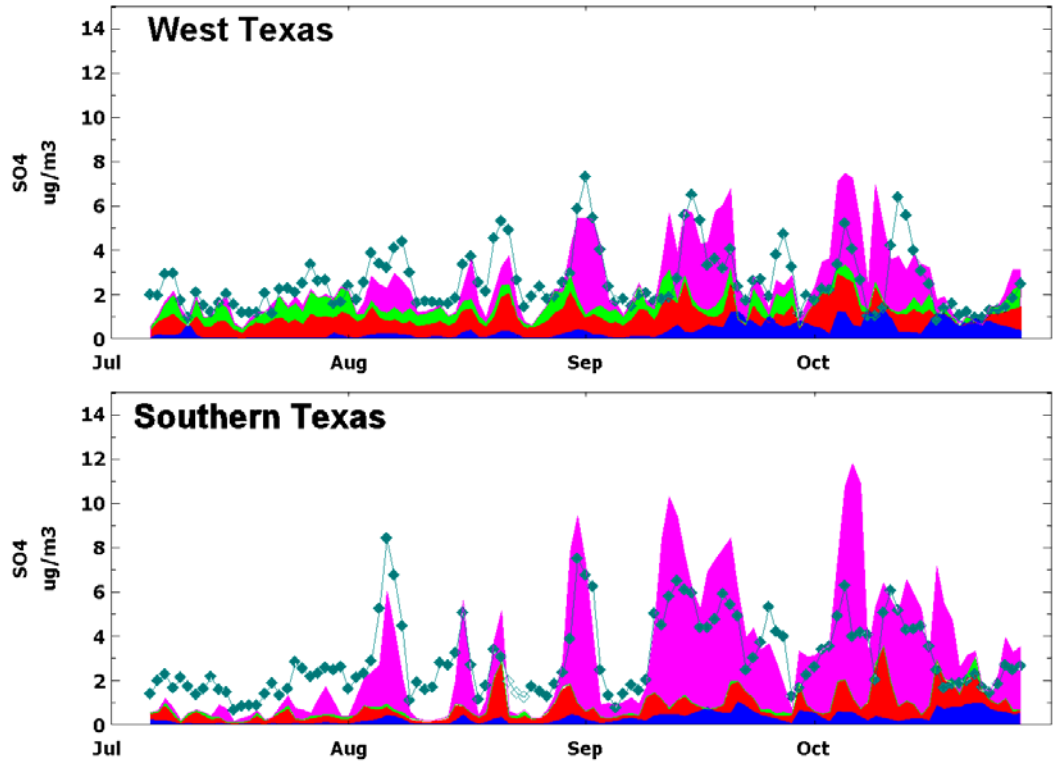

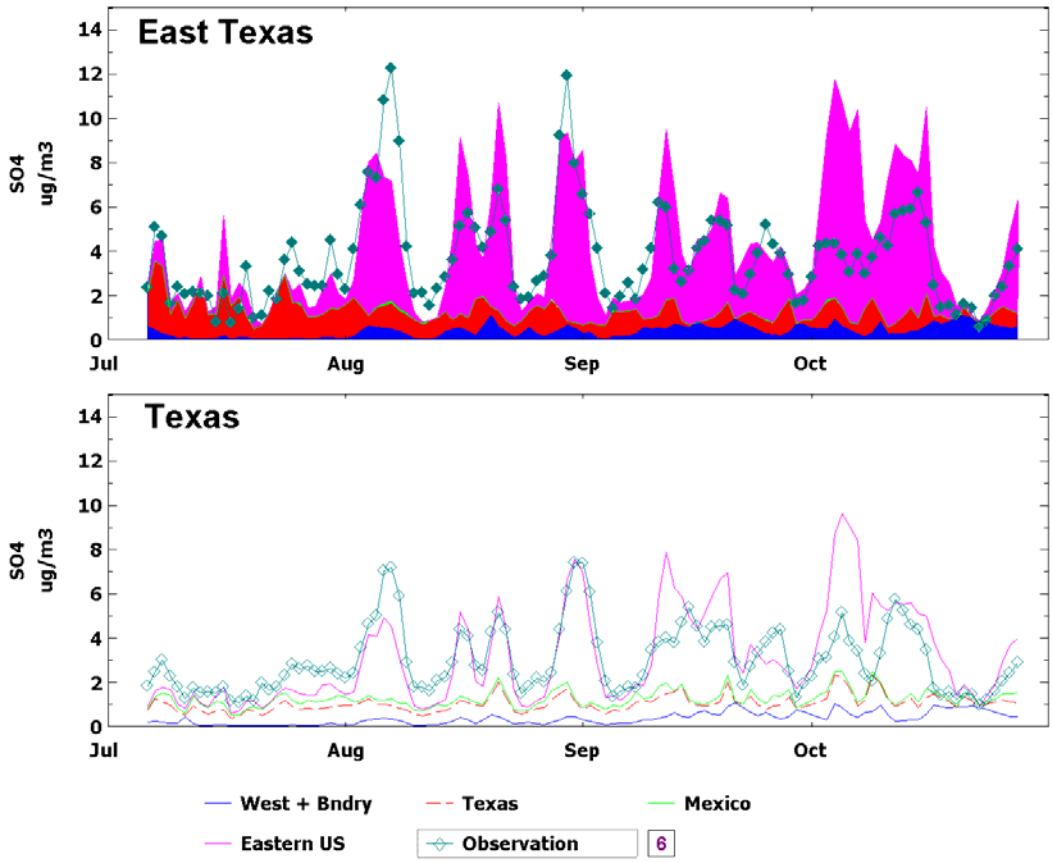

Figure 6-23. The daily source attribution average over all monitoring sites in a) West Texas, b) southern Texas, c) East Texas, and d) all of Texas. The size of the aggregation regions are defined in Figure 22. The sum of the source contribution from the four regions is approximately equal to the predicted sulfate concentrations.

The underestimation of observed sulfate throughout Texas decreased in August, and by September the REMSAD the average predicted and observed sulfate matched well overall and even overestimated the eastern Texas observed sulfate by 10–15% (Figures 6-21c and 6-23). REMSAD also captured the timing and duration of the sulfate episodes averaged over each region. The predicted sulfate in southern and eastern Texas was dominated by eastern U.S. sources. At several of the southern Texas sites the eastern U.S. source contribution was equal to or larger than the observed sulfate. This is a clear indication that the predicted eastern U.S. source attribution was overestimated at these sites. In western Texas, Mexican, Texan, and eastern U.S. sources contributed about equally to the predicted sulfate during August. All three source regions contributed to the western Texas monitoring sites during September, but sources in the eastern U.S. contributed about half of the predicted sulfate.

The results for October are presented in Table 6-8 and Figures 6-21d and 6-23. As shown, REMSAD over-predicts the measured sulfate throughout Texas. In western Texas, all four major source regions contribute to the predicted sulfate with the eastern U.S. contributing about 45%, Texas about 20%, and the western U.S. and Mexico under 15%. In south and east Texas, sources in Texas contributed 15–23% of the predicted sulfate while eastern U.S. sources contributed 65–85%. Compared to the observed sulfate concentrations the eastern U.S. source region contributed between 100–175% of the sulfate. Therefore the eastern U.S. contribution is

overestimated as far west as Eagle Pass and Fort McKavett (Table 6-8) which are only 250–350 km from Big Bend NP. Presumably, eastern U.S. contribution is overestimated in western Texas and Big Bend NP as well.

Figures 6-22 and 6-23d and Table 6-9 present the source contribution to all BRAVO sites averaged over the entire BRAVO time period. Over the four month period there is no systematic bias in the predicted sulfate compared to the observed values. Therefore the underestimation in July is compensated by the overestimation in October.

Table 6-9. The average July–October source attribution for all BRAVO monitoring sites. All units are in μg/m^3.

Region/Site	Western U.S.	Mexico	Texas	Eastern U.S.	Pred SO_4	Obs SO_4
West Texas						
Amistad	0.18	0.47	0.52	1.56	2.91	3.03
Esperanza	0.33	0.45	0.40	0.63	1.99	1.95
Fort Lancaster	0.25	0.39	0.65	1.55	3.05	3.05
Fort Stockton	0.23	0.48	0.45	0.96	2.30	2.52
Guadalupe Mtns	0.36	0.34	0.47	0.71	2.07	2.02
K-Bar	0.18	0.46	0.32	0.87	1.97	2.41
Langtry	0.20	0.50	0.53	1.51	2.95	3.47
Marathon	0.21	0.48	0.40	0.95	2.21	2.53
McDonald Obs	0.27	0.45	0.42	0.80	2.11	2.11
Monahans Sandhills	0.25	0.45	0.63	1.09	2.61	2.95
Persimmon Gap	0.22	0.48	0.40	0.98	2.24	2.71
Presidio	0.24	0.49	0.37	0.90	2.17	2.30
Sanderson	0.21	0.51	0.47	1.18	2.55	3.00
San Vicente	0.17	0.45	0.33	0.89	1.99	2.54
Average	0.23	0.46	0.45	1.04	2.37	2.62
South Texas						
Aransas	0.11	0.03	0.53	3.29	4.19	3.66
Brackettville	0.17	0.08	0.62	1.92	3.00	2.98
Eagle Pass	0.16	0.11	0.53	1.93	2.95	2.73
Falcon Dam	0.12	0.19	0.47	2.29	3.27	3.04
Laguna Atascosa	0.08	0.02	0.31	2.19	2.77	2.82
Lake Corpus Christi	0.12	0.04	0.73	2.88	4.00	3.13
Laredo	0.12	0.15	0.51	2.09	3.05	2.86
Padre Island	0.12	0.03	0.59	3.20	4.18	3.66
Pleasanton	0.12	0.06	0.94	2.32	3.64	3.17
San Bernard	0.09	0.02	0.73	3.35	4.44	3.94
Average	0.13	0.14	0.56	2.28	3.32	3.10
East Texas						
Big Thicket	0.11	0.02	0.50	4.16	5.07	4.18
Center	0.12	0.02	0.49	4.32	5.25	4.00
Everton Ranch	0.15	0.04	0.90	2.89	4.21	3.54
Hagerman	0.24	0.03	0.97	3.02	4.58	4.07
LBJ NHS	0.16	0.03	1.15	2.09	3.65	3.09

Purtis Creek	0.17	0.02	1.08	3.21	4.78	4.28
Somerville Lake	0.14	0.02	0.99	2.92	4.33	3.56
Stephenville	0.23	0.04	0.92	2.55	4.01	3.55
Stillhouse Lake	0.15	0.02	1.14	2.50	4.07	3.56
Wright Patman	0.16	0.02	0.96	4.36	5.85	4.39
Average	0.16	0.04	0.87	3.14	4.46	3.77
Other						
Fort McKavett	0.20	0.12	0.80	1.61	2.93	2.58
Lake Colorado City	0.31	0.25	0.85	1.59	3.23	2.80
Wichita Mtns	0.39	0.07	0.92	2.11	3.81	3.21
Average	0.20	0.06	0.96	2.66	4.16	3.54

7) Receptor Model Evaluation

A test of the accuracy of any source attribution method is to determine how well it can reproduce known attributions. There are at least two known source attributions with which to test receptor models during BRAVO. The first is the attribution of the measured perfluorocarbon tracer concentrations to the four tracer release sites. In that case only transport and dispersion are tested since the tracers are non-reacting and essentially non-depositing. Both MM5 and EDAS/FNL wind fields can be tested using the tracers.

A similar test involving chemistry and deposition in addition to dispersion is to determine how accurately the receptor models can reproduce the sulfate source attributions simulated by the REMSAD model. In this case we know the concentrations and source attributions of the 24-hour average sulfate predicted by REMSAD. For purposes of the test, there is no assertion that the REMSAD-simulated sulfate source attributions are accurate in the real world, only that in the simulated REMSAD world we have known emissions, chemistry, and meteorology and so if we model these using receptor techniques, we would expect to reproduce the simulated source attributions. In this case only the MM5 meteorological data are used since this is what was used by REMSAD and so is therefore the correct wind field for transport of the simulated sulfate. The tests of REMSAD sulfate attribution also allow testing of the receptor models with source areas beyond the state of Texas, whereas the perfluorocarbon tracers were all emitted within the state and therefore cannot be used to test longer range transport. All three back trajectory models, ATAD, HYSPLIT, and CMC, were used in both these tracer and REMSAD sulfur tests. See chapter 5 for another evaluation for the forward transport models using the tracer data.

7.1 Source Apportionment of Tracer Data

7.1.1 Trajectory Mass Balance

To test the accuracy of the Trajectory Mass Balance (TrMB) model, it was exercised using the total perfluorocarbon tracer concentration at Big Bend as the dependent variable and back trajectory endpoints from the four tracer release sites as the independent variables.

7.1.1.1 Tracer Concentrations

The daily total tracer concentrations for attribution testing by TrMB were calculated by summing the 24-hour average concentrations of the four perfluorocarbon tracers for each day during the second half of the study when the four tracers were released from four different sites. The fraction of the total concentration due to each tracer is the fraction arriving from each tracer's corresponding release site. The four tracer release sites and the TrMB source areas used to represent each are shown in section 2.3.2.5.

A problem for use of the tracer concentrations in TrMB is how to handle the many negative concentrations. Negative concentrations result when the mean background is subtracted from the analyzed value. The most severe problem is with iPPCH, the northeast Texas or Big Brown tracer, which has a negative mean concentration at K-Bar and would therefore require a negative regression coefficient in order to reproduce the mean concentration accurately. Four options were explored: 1) leaving negative concentrations as negative, 2) setting all negative concentrations to zero, 3) adding a constant concentration to all days to raise the minimum concentration of each tracer to zero, or 4) removing all days with negative concentrations. Option 4 proved unreasonable since too many days would be removed. All of the remaining options were tried. There were only minimal differences in the results and model performance for these

three options, though in general options 2 and 3 performed slightly better. It was decided to continue using option 2, setting all negative 24-hour concentrations of the individual tracers to zero before summing them to calculate the total tracer concentration for each day and further, to proceed without using iPPCH, because on average, the concentration of this tracer was so low as to be mostly undetectable at K-Bar, and in fact, was zero plus or minus measurement error.

Another option for the total tracer concentration was to use the mean of the measured tracers at K-Bar, Persimmon Gap, and San Vicente. These three sites are all within or near the boundaries of Big Bend National Park. Again, the model results and model performance did not change substantially when data from one or both of the additional sites were averaged with the K-Bar data. For simplicity, the experiment was continued using data from K-Bar only. Figure 7-1 shows the resulting total tracer concentrations at K-Bar for each day with the bar colors showing the contribution of each of the three remaining tracers.

Several different begin and end dates were also tried, and these did affect model results and performance because different dates resulted in different regression coefficients. This is expected due to changes in the mean meteorology and emissions when different time periods are used. The final time period chosen was September 17–October 28. Releases of PDCB and PTCH were halted at Eagle Pass on September 13 and begun at San Antonio and Houston, respectively, on September 17, so this was a reasonable beginning date. Tracer release of PTCH from Houston was stopped on October 25, though emissions for the other three sites continued until November 1. After October 28, release of ocPDCH from Eagle Pass became erratic with much higher releases than average on the 29th and lower than average on the 30th, so an end date of October 28 was chosen. Tracer emissions during the second half of BRAVO are shown in Figures 2-3 through 2-6. A constant release of tracers throughout the study would be ideal for TrMB analysis. This did not occur, with each of the tracers having periods of higher than average, lower than average, and no emissions.

7.1.1.2 Results and Discussion of TrMB Tracer Test

Table 7-1 is a summary of the TrMB model results for total tracer at K-Bar during the second half of the BRAVO study. Several model and data combinations are able to reproduce the known attributions of all three tracers to within the error in the measured concentration and the standard errors of the regression coefficients. These include HYSPLIT with EDAS/FNL input, CAPITA MC with MM5, ATAD with MM5, and ATAD with raw sounding data. In general, the choice of 5-, 7-, or 10-day back trajectories made little difference and the results were usually the same within the standard error of the regression coefficients, no matter what the trajectory length. This is most likely because the tracer release sites are all within 5 days transport of K-Bar.

Worst model performance is by HYSPLIT with MM5 input which dramatically over-predicts Eagle Pass and under-predicts San Antonio. Eagle Pass is approximately 250 km from K-Bar, while San Antonio is almost twice as distant at approximately 400 km. This may be an indication that HYSPLIT with MM5 has too many back trajectory endpoints close to the receptor at the expense of too few farther away. Other problem combinations were ATAD with EDAS/FNL input and CAPITA MC with EDAS/FNL input, which both overestimate tracer arriving from Houston and underestimate San Antonio. Houston is the most distant of the three modeled release sites at approximately 700 km from K-Bar, so these latter combinations are overestimating the most distant source area.

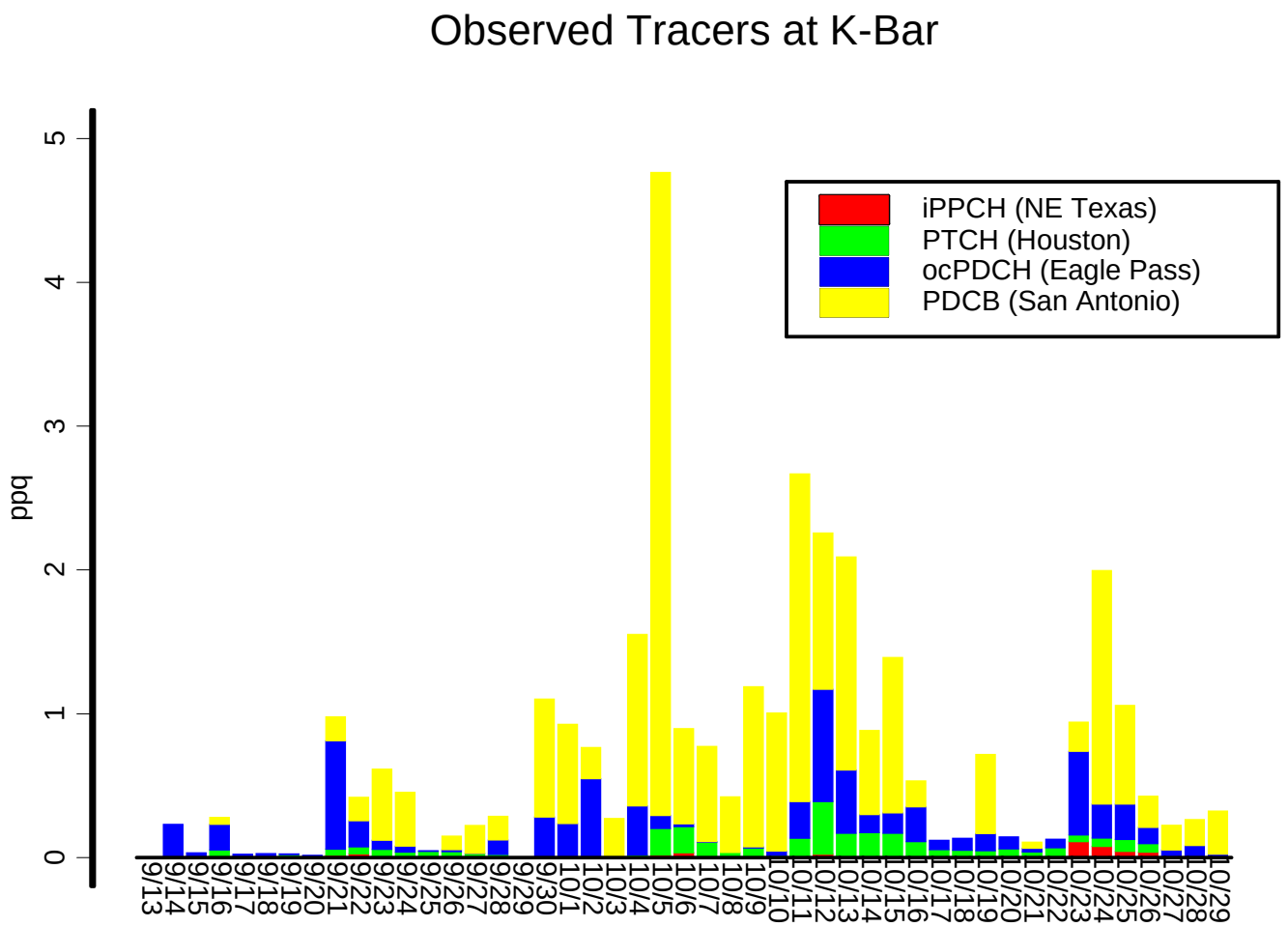

Figure 7-1. Observed perfluorocarbon tracer concentrations (ppq) at K-Bar during the second half of the BRAVO study after negative concentrations were set to zero.

The problems with the under-performing combinations seem to be unrelated to collinearities between the source areas. In all cases the variance inflation factors (VIF) (see section 2.3.2.1) were less than 3 for all sources. A high VIF indicates that the endpoints in a single source region could be nearly explained by a linear combination of the endpoints in other source regions. A VIF greater than 10 is considered strong collinearity. Correlations between source area endpoints were as high as 0.675, but the amount of correlation between source areas was unrelated to how well the model/wind field combination predicted the correct attribution.

The remaining two possibilities for error are either the tracer concentrations or the back trajectory endpoints. Since several trajectory model and wind field combinations were able to reproduce the tracer attributions, we assume that the concentrations are reasonably accurate to within their reported uncertainties, or at least that we do not have errors so large that the mean percentages due to the three release sites are grossly wrong. This leaves the placement of the back trajectory endpoints within Texas as the only possibility for error. Influential days in the regression are October 5, 11–13, and 23–24. However, examination of the relationships between tracer concentrations and endpoints and between the endpoints from different model/wind field combinations did not reveal any obvious problems with the back trajectories on these individual days.

Results of this test then suggest that source attribution results generated by TrMB using back trajectories from the HYSPLIT model with MM5 input wind fields should not be used for source attribution of sulfate. TrMB modeling using back trajectories from either CAPITA MC or ATAD models with EDAS/FNL input are also suspect. The best model/wind field combination for tracer attributions, and thus for accurate back trajectory placement within south Texas, was HYSPLIT with EDAS/FNL input. The remaining combinations of CAPITA MC or ATAD with MM5 input and ATAD with raw sounding input also were able to re-create the known tracer attributions.

Table 7-1. Results of TrMB modeling of three BRAVO tracers at K-Bar for 9/17–10/28 (42 days). The first three rows show the tracer name, the release site, the mean measured concentrations, and the percent of the total measured concentration due to each tracer. Negative concentrations were set to zero before summing. The remaining rows give the TrMB modeled percent attributions for several combinations of back trajectory models and input meteorological data and trajectory lengths. Attributions that are accurate to within the uncertainty of the measurement and standard error of the regression coefficients are shown in bold and a larger font for easy identification.

	ocPDCH Eagle Pass	**PTCH San Antonio**	**PDCB Houston**	**R^2**
Mean Concentration (ppq)	0.155±0.024	0.559±0.081	0.062±0.008	NA
Mean Percent (%)	**20±4**	**72±13**	**8±1**	NA
ATAD Raw 5-day	**35±12**	**65±14**	**0±9**	0.495
ATAD EDAS/FNL 5-day	**16±8**	33±9	51±9	0.708
HYSPLIT EDAS/FNL 5-day	**28±12**	**67±13**	**5±9**	0.640
HYSPLIT EDAS/FNL 7-day	**29±13**	**68±15**	**3±11**	0.603
HYSPLIT EDAS/FNL 10-day	**27±13**	**73±16**	**0±11**	0.612
CAPITAMC EDAS/FNL 5-day	**30±9**	43±10	27±8	0.721
CAPITAMC EDAS/FNL 7-day	**33±10**	**50±10**	18±8	0.643
CAPITAMC EDAS/FNL 10-day	**30±9**	39±10	31±8	0.689

ATAD MM5 5-day	**34±12**	**60±13**	**6±9**	0.564
HYSPLIT MM5 5-day	82±18	18±18	**0±11**	0.484
HYSPLIT MM5 7-day	81±18	19±19	**0±11**	0.489
HYSPLIT MM5 10-day	81±18	19±18	**0±12**	0.502
CAPITAMC MM5 5-day	**23±16**	**77±19**	**0±12**	0.643
CAPITAMC MM5 7-day	**26±17**	**74±21**	**0±13**	0.616
CAPITAMC MM5 10-day	**24±17**	**76±21**	**0±14**	0.626

7.1.2 Forward Mass Balance Regression

The forward mass balance regression technique is a quantitative source apportionment technique that merges measured receptor data with forward airmass transport simulations. The technique is based upon the inversion of the source receptor technique to retrieve a source/sink term and is described in section 2.3.2.2. The basic equation is:

$$c_{ik} = \sum_j T_{i,k|j} \left(KE\right)_j + error_{ik} \qquad (2\text{-}26)$$

where c_{ik} are the concentration values at the receptor *i* and time k, $(KE)_j$ are the source/sink term for each source region j, and $T_{i,k|j}$ is the transit probability or the probability that mass emitted from source j will impact the receptor i at time k. Given c and T, equation 2-26 is inverted to retrieve (KE) which in turn can be multiplied by T to estimate the source contribution to the receptor concentrations, i.e. $c_{ikj} = T_{i,k|j}\left(KE\right)_j$.

As part of the BRAVO study four unique perfluorocarbon tracers were released to estimate dispersion from four industrial or urban sites (see section 2.1.1.2). The tracers were continually released at near constant rates from Eagle Pass and the Big Brown power plant in northeast Texas from about July 5–October 30 and from San Antonio and the Parish power plant in Houston from about September 17–October 30. The tracers are conservative species, so the source/sink term is equal to the tracer release rate and equation 2-26 describes the dispersion of the tracer plume. These data were used to test and validate the FMBR technique by inverting equation 2-26 to estimate individual tracer release points and locations. In addition, the tracer concentrations were added together, creating integrated concentrations, and the FMBR was used to reconstruct all four tracer release rates and source attributions to the combined tracer concentration. This last test is more synonymous with using FMBR to estimate the source attribution of Big Bend's sulfate concentrations.

7.1.2.1 Transit Probabilities

The transit probabilities were estimated using the CAPITA Monte Carlo (CMC) model. The model was used to generate forward 10-day plumes every two hours from ~670 sources evenly distributed over Mexico and most of North America about 100 km apart (Figure 7-2). A plume identifies the downwind three-dimensional location of particles that were previously released from the source and can be viewed as a direct simulation of the dispersion of a source's emissions. The plumes were calculated by releasing five tracer particles from each source every two hours and tracking their movement in space and time. Daily transit probabilities were calculated through simple particle accounting, where the particles, from each source at a 100 km grid cell at Big Bend within the first 1 km of the surface, were summed together over each day. These particle counts were then divided by the total number of particles comprising a source's

plume, e.g., 7 day plume * 12 releases/day * 5 particles/releases * 12 time increments /day= 5040 particles/day. The transit probabilities were calculated using both the 36 km MM5 meteorological data and the combined EDAS/FNL meteorological data. Both wind fields produced similar results so only the MM5 results are presented. In addition, as discussed in the previous section, the TrMB approach with MM5 data proved to be superior to the EDAS/FNL winds when tested against the tracer data.

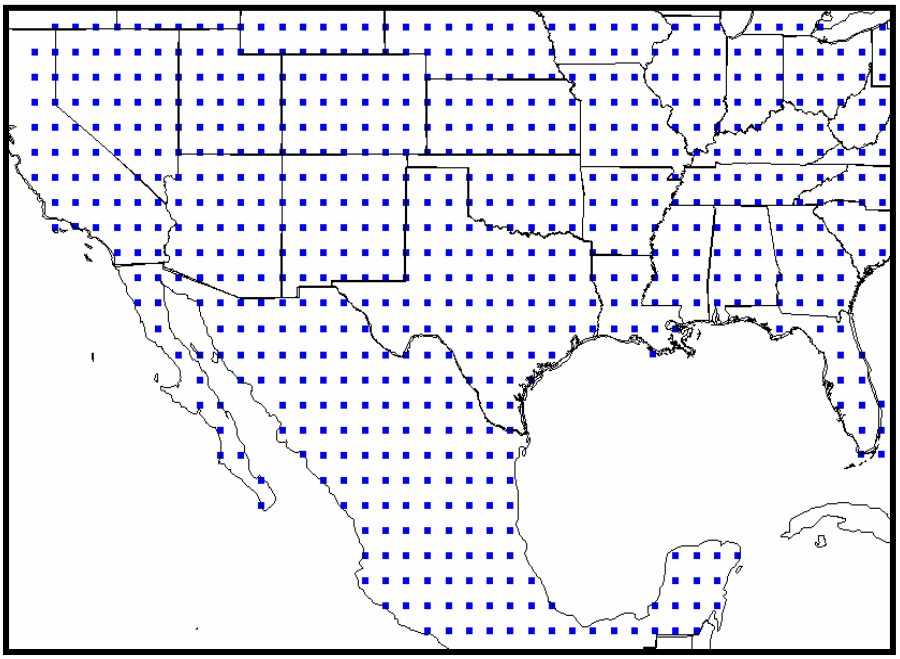

Figure 7-2. The source regions from which 7-day forward plumes were simulated using the CAPITA Monte Carlo model.

The Big Bend transit probabilities are presented in Figure 7-3 for the BRAVO time period and July and October. As shown, over the BRAVO time period transport to Big Bend primarily occurs from the Gulf of Mexico up along the Texas/Mexican border. Airmass transport also occurs from the north and northeast of Big Bend from Texas and the eastern U.S. There is a monthly pattern to the airmass transport with transport during July coming almost exclusively from the southwest of Big Bend along the Texas/Mexican border, and with more transport from Texas and the eastern U.S. during October. These transport patterns are similar to those derived from the residence time analysis in section 8.1.3.3. This is expected since these are similar transport assessments, but the transit probability identifies potential transport of airmasses from the surface to Big Bend, while the residence time analysis examines transport throughout the column.

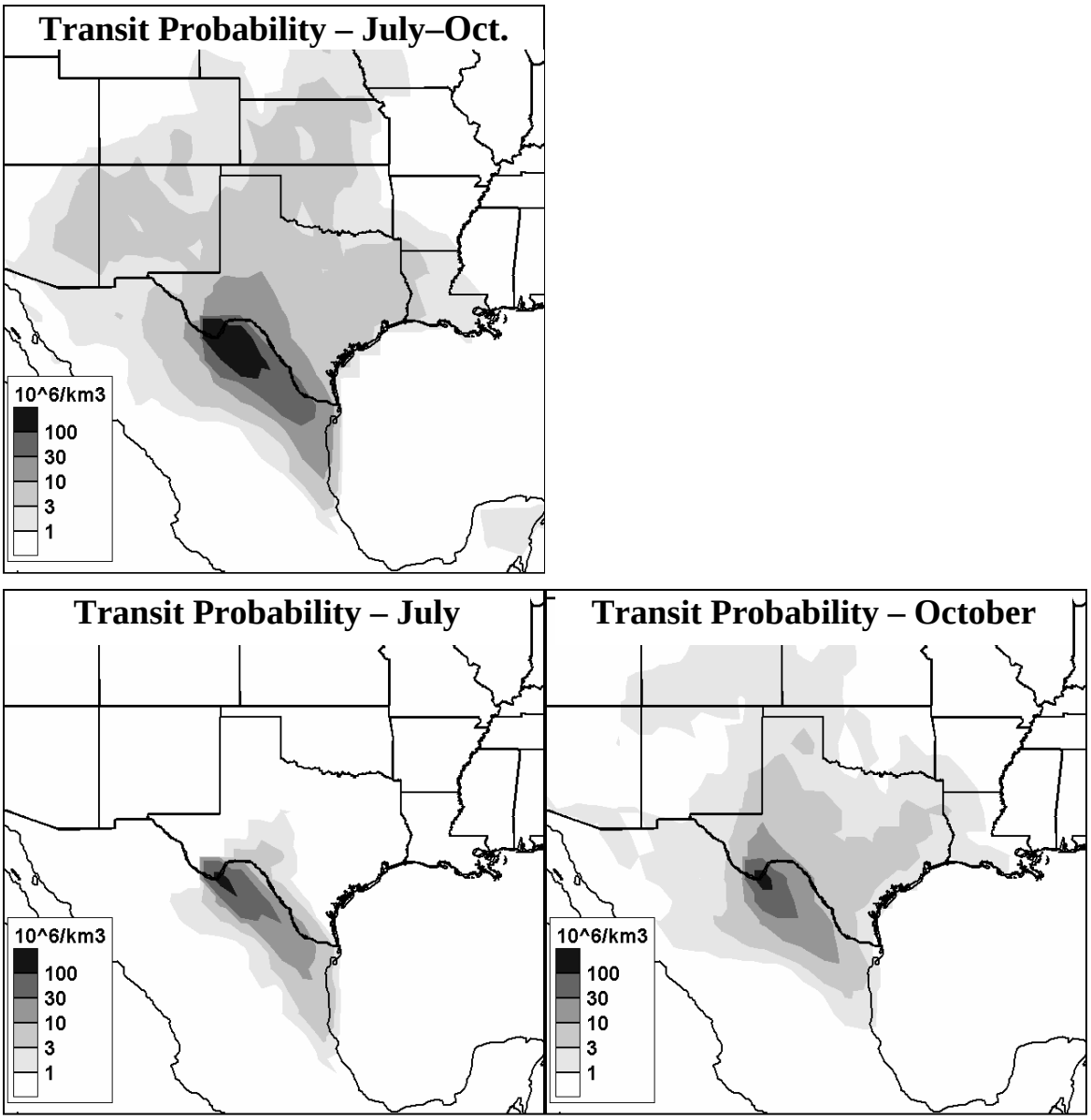

Figure 7-3. Big Bend transit probabilities for the July–October BRAVO time period and the months of July and October.

7.1.2.2 Retrieval of Tracer Emission Rates

The inversion technique was applied to the ocPDCH tracer continuously released from Eagle Pass from July 5–October 30 and to the iPPCH tracer continuously released from northeast Texas from July 9–October 30 in order to test the ability of the inversion technique to properly locate a source's location and emission rate. The tracer concentrations are the measured concentration minus an assumed background. A number of these delta concentrations are negative, reflecting the uncertainty in the measurement and background concentration. However, for the northeast Texas tracer there may have been a systematic bias in the concentrations; for example, the July average iPPCH tracer at Big Bend was negative. All negative values were included in the analysis. The transit probabilities from all ~670 source region plumes were also used in the analysis. The inversion was conducted using singular value decomposition (SVD)

which can invert an under-determined system and dampen instabilities that result in least square regressions of ill-conditioned systems, such as the source receptor relationship (see section 2.3.2.2).

The reconstruction of the Eagle Pass and northeast Texas tracer release sites and rates using all measured concentrations values are presented in Figure 7-4 and Table 7-2. This was an over-determined system with about 800 data points and 670 unknown potential source regions, and there were monitoring sites in the vicinity and partially surrounding the tracer release sites. As shown, in both cases the retrieval was able to properly identify the tracer release site. For Eagle Pass, the reconstructed total tracer release rate of 4.2 kg/day is close to the actual rate of 3.7 kg/day. However, the release rate for the northeast Texas tracer was underestimated by about a factor of 6. In both cases the average predicted tracer concentrations resulting from the inversion were within 10% of the measured concentrations and the correlation coefficient was about 0.6.

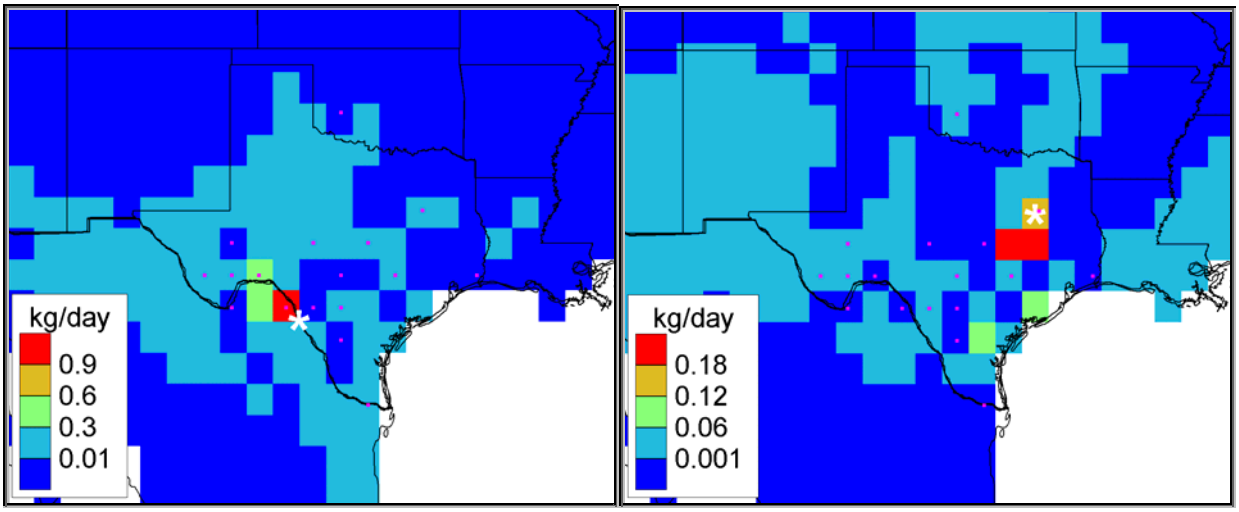

Figure 7-4. Reconstruction of the Eagle Pass and Big Brown tracer release sites and rates using tracer concentration measured all monitoring sites from July–October. The tracer release sites are identified by the stars and the monitoring site locations by the squares.

Table 7-2. The retrieved Eagle Pass and northeast Texas tracer release rates and inversion performance statistics.

			Average (ppq)			Tracer Release Rate (kg/day)	
Tracer	**Receptors**	**# Obs**	**Obs**	**Pred**	**r**	**Actual**	**Retrieved**
Eagle Pass (ocPDCH)	All	798	0.4	0.38	0.6	3.7	4.2
Eagle Pass (ocPDCH)	Big Bend	118	0.148	0.144	0.61	3.7	2
N.E. Texas (i PPCH)	All	798	0.03	0.027	0.59	2	0.34
N.E. Texas (i PPCH)	Big Bend	118	0.007	0.006	0.35	2	0.016

The perfluorocarbon tracers are an inert species not subjected to chemical and physical removal processes and receptor sites had the same source/sink term. However, this study is concerned with the attribution of sulfate, and sulfate is primarily a secondary species generated by the transformation of sulfur dioxide. Both sulfur dioxide and sulfate are removed from the

atmosphere by wet and dry deposition. These chemical and physical processes vary in space, and it is not appropriate to derive a single source sink term for distant receptor sites. Therefore application of the FMBR technique to Big Bend's sulfate source attribution can only use measured concentration data from the Big Bend region.

To test the inversion using this limited set of observations, FMBR was applied to only the Big Bend tracer concentrations. In this case, the inversion is a highly under-determined system with only 118 concentration values to resolve the impact from 670 potential sources. In order to get stable results, the SVD solution added more weight to the solution stability at the expense of the model fit and resolution. Therefore the retrieved release rates were spread out over a larger domain. This is seen in the spatial patterns of the retrieved tracer release rates in Figure 7-5 where the retrieved tracer emissions extend from the Big Bend receptor to the actual release sites and beyond.

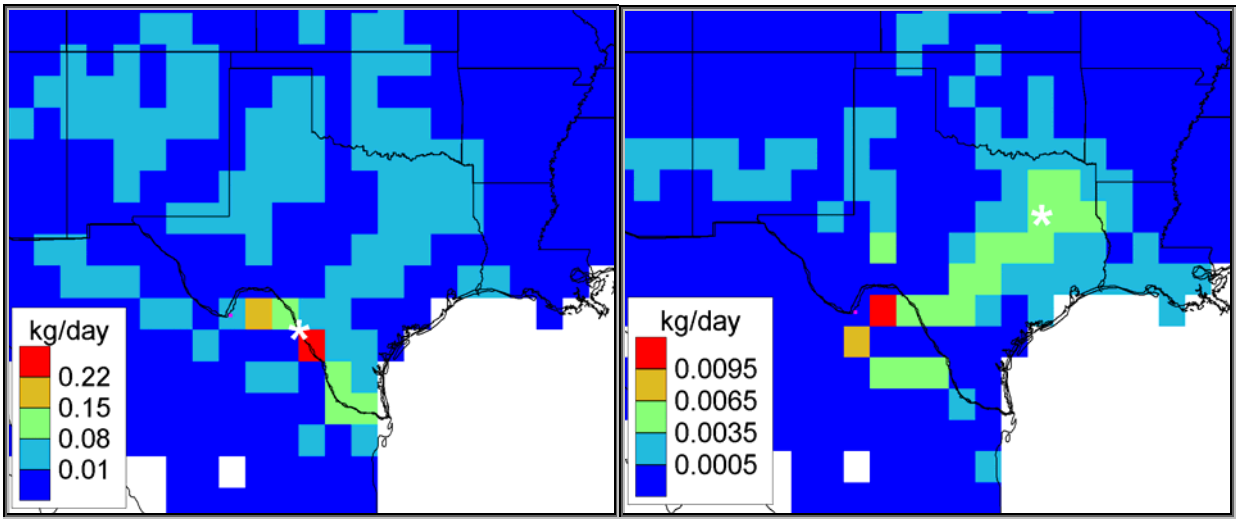

Figure 7-5. Reconstruction of the Eagle Pass and Big Brown tracer release sites and rates using tracer concentration from only the Big Bend monitoring site from July–October. The tracer release sites are identified by the stars and the monitoring site locations by the squares.

The retrieved Eagle Pass tracer still identifies the largest release rates around the true Eagle Pass release site, but now the release rates have been spread out from Big Bend to the Gulf of Mexico, along the Texas-Mexican border. In addition, the total retrieved release rate is about a factor of two lower than the actual rate, 2 kg/day compared to 3.7 kg/day. The retrieved release rates for the northeast Texas tracer cover a large domain with the highest release rates near Big Bend and a region of near constant release rates extending from Big Bend to the northeast Texas release sites. The total release rate severely underestimates the actual rate by over a factor of a hundred (Table 7-2). Also, the correlation of the observed values and predicted concentrations is only 0.35. The underestimation is likely due to a bias in the northeast tracer delta concentrations. The average northeast tracer at Big Bend was only 0.006 ppq and 70% of the delta concentrations were below zero. This demonstrates the fact that the FMBR technique will compensate for biases in both the model and observations.

The spatial patterns in the retrieved tracer release rates are similar to the transport patterns to the Big Bend receptor site for the highest 20% of the tracer concentrations explored in section 8.1.3. Therefore, without any addition information, FMBR when used with the Big Bend

receptor data is best suited for identifying the transport pathways. It is possible that if a longer time period were used, then the FMBR could better isolate the tracer release site.

7.1.2.3 Source Apportionment of Combined Tracer Concentrations

The previous section illustrated the difficulty of clearly identifying the tracer release sites and rates using only the Big Bend observed tracer concentrations. In this section, a different question is addressed: given the location of a small set of source regions, can FMBR properly retrieve the contribution of each source region to the ambient concentration at Big Bend? To investigate this question, the four tracer concentrations at Big Bend were added together, creating an integrated tracer concentration time series. Transit probabilities from four source regions encompassing the tracer release sites were estimated from the database of source plumes. The contribution of each individual tracer to the total was then estimated using FMBR. Least square regression was used to invert the relationship and obtain the source attributions. SVD was not used since the system was highly over determined with only four unknowns and 40 known concentration values.

Tracers were only released from the Houston and San Antonio sites from September 17 onward. This analysis included only data from September 19–October 30 and aggregated the values from San Vicente and K-Bar since they fell into the same 100 x 100 km cell around Big Bend. The combined tracer time series is presented in Figure 7-6, where it is evident that the San Antonio tracer dominated the total. The four source regions are presented in Figure 7-7. The sizes of the source regions were dictated by the modeled source regions as shown in Figure 7-2. In addition, the Eagle Pass source region was made smaller than the others to account for the fact that errors in transport increase with distance.

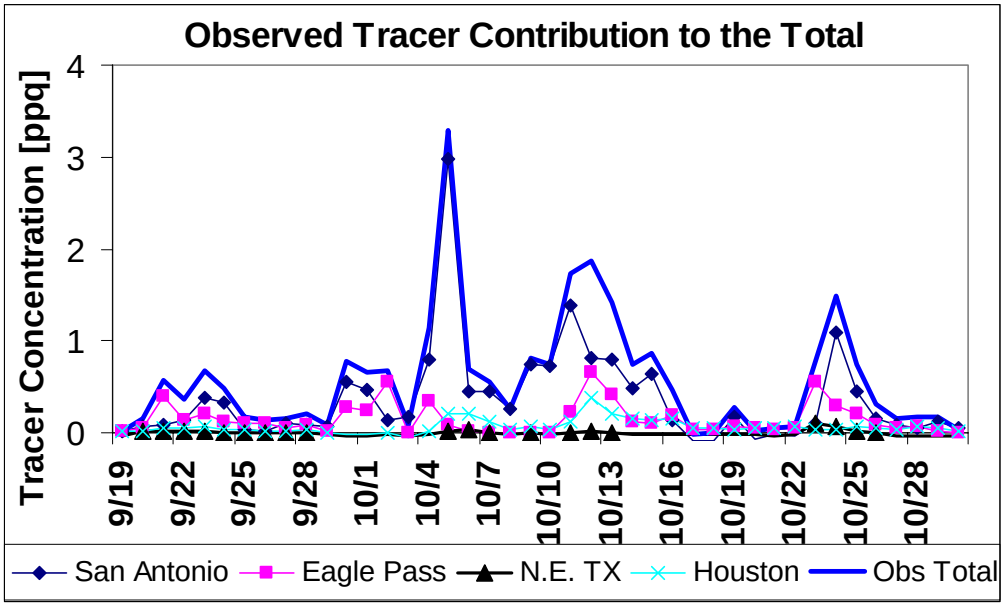

Figure 7-6. The combined tracer time series at Big Bend (K-Bar) monitoring site and the contribution of each tracer to the total.

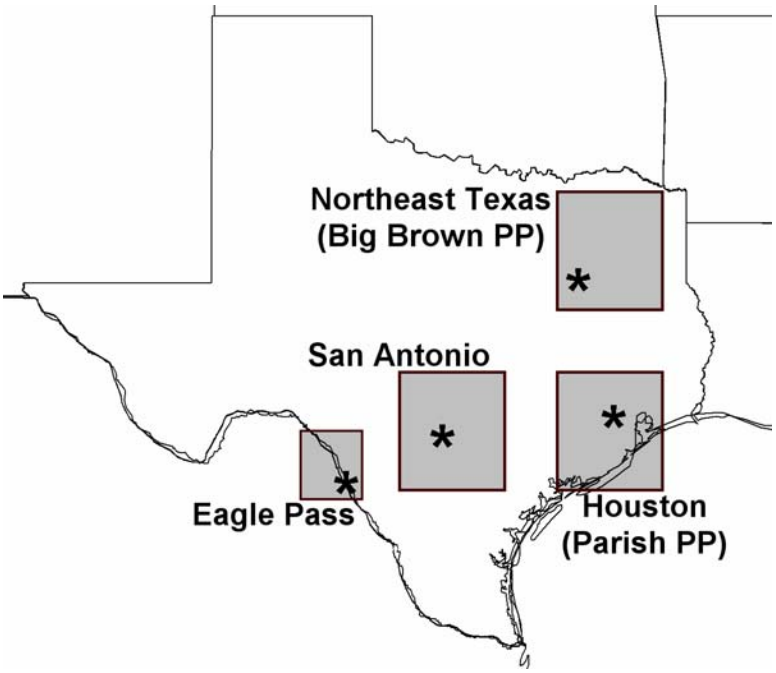

Figure 7-7. The four tracer source regions used in the FMBR analysis.

The results of the FMBR are presented in Table 7-3 and Figure 7-8. As shown, on average the retrieved source attributions properly identify the San Antonio tracer as the largest contributor and northeast Texas as the smallest. In addition, the average contributions are within the observed tracer contributions and the standard error for Eagle Pass, Houston, and northeast Texas. The retrieved San Antonio tracer plus the standard error is about equal to the observed contribution.

Table 7-3. Average observed and retrieved tracer emission rates and their contribution to the combined Big Bend trace concentrations.

Tracer Release Site	**Tracer Emission Rates [kg/day]**		**% source Attribution**	
	Actual	**Retrieved**	**Observed**	**Retrieved**
Eagle Pass	3.7	1.3 ± 2.2	26	28 ± 8
N.E. Texas	1.8	1.3 ± 3.5	-0.6	5 ± 9
San Antonio	9.3	9 ± 2.6	63	51 ± 11
Houston	2.3	4.9 ± 3	12	17 ± 7
Total	17	16.4 ± 5.7		

Performance Statistics

r^2	0.72
Mean Obs (ppq)	0.62
Mean Pred (ppq)	0.61
RMS Error (%)	54

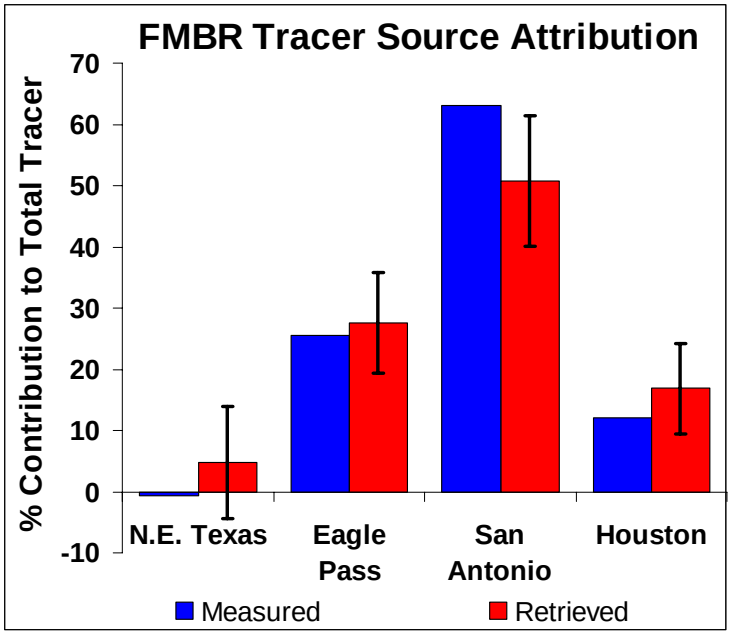

Figure 7-8. The tracer average source attribution and standard errors.

The kinetic probabilities for tracers are 1 and release rates were near constant. Therefore the predicted tracer concentrations and daily source attributions are valid. As shown in Figure 7-9 and Table 7-3, the predicted concentrations reproduce the observed total tracer concentrations well with an $r^2 = 0.72$ and no bias. Similar to the measured results, the retrieved San Antonio tracer is the largest contributor on a daily basis; however, from October 4–16 the San Antonio contribution is smaller than the average and is responsible for the retrieved San Antonio average contribution to be underestimated.

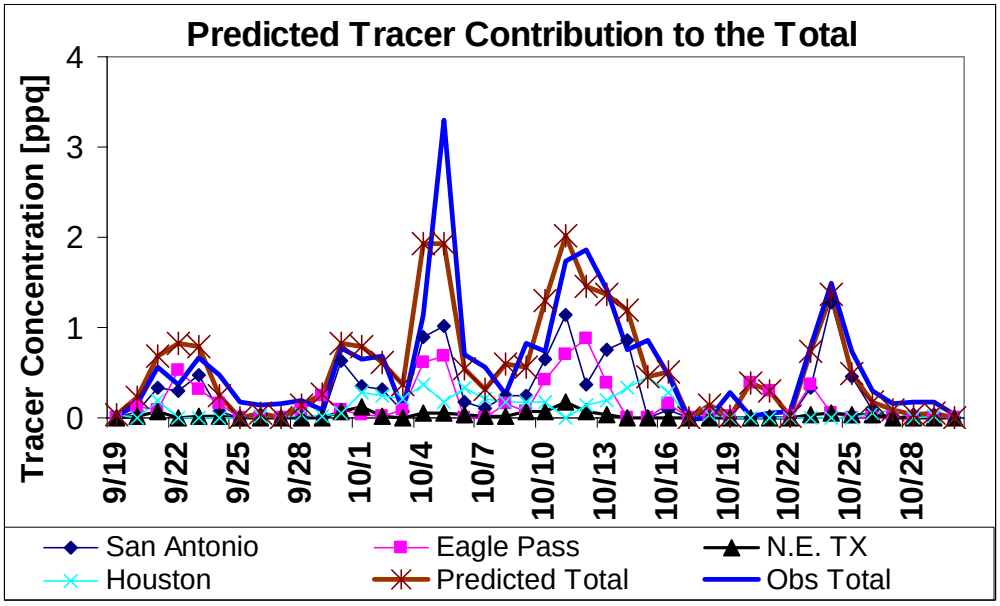

Figure 7-9. The observed and predicted total tracer and the predicted source attribution of each tracer to the total.

7.1.2.4 Discussion of FMBR Tests

These results illustrate that, provided enough data and sufficiently accurate transport model, FMBR can properly identify the tracer release sites and rates with no *a priori* information on the tracer release site locations. However, using only the Big Bend data, the resolution of the results diminish and it identifies the common transport pathways associated with the highest tracer concentrations at the Big Bend monitoring site. For the Eagle Pass tracer site, which frequently impacted the Big Bend monitor with concentrations several times the background concentrations, the FMBR was able to isolate the tracer release site from within the transport pathway. However, for the northeast Texas tracer, which was farther away, with Big Bend tracer concentration and usually near the background concentration FMBR could not isolate the tracer release site.

When the tracer release sites were added to the FMBR, the technique was able to decompose the integrated tracer time series into its contributions from the four individual tracers. The decomposition worked better for an on-average than on a day-by-day basis. Also, the average tracer release rate for each tracer was properly retrieved. Consequently, the FMBR is a valid technique for retrieving average source contributions of tracers. When using data from only Big Bend it is necessary to predefine a small set of source regions.

7.2 Source Apportionment of REMSAD Base Case Sulfate using Receptor Models

The previous section validated the TrMB and FMBR source attribution technique using inert tracer concentrations. However, sulfate source attribution has the complicating factor that the emitted sulfur undergoes transformation and removal processes during transport from the source to the receptor. To validate this technique for a reactive species, these analyses were applied to the REMSAD-predicted sulfate at Big Bend and compared to the REMSAD source attribution results. In addition to TrMB and FMBR techniques, synthesized REMSAD was applied to these artificial data.

7.2.1 Trajectory Mass Balance

7.2.1.1 Results

There are known concentrations of the 24-hour average sulfate predicted at K-Bar by the REMSAD model and known attributions of this simulated sulfate which are the REMSAD attributions of the predicted sulfate to the BRAVO source areas. For purposes of this test, there is no assertion that the REMSAD-simulated sulfate source attributions are accurate in the real world, only in the simulated REMSAD world. Only the MM5 meteorological data are used because this is what was used by REMSAD.

Table 7-4 summarizes the attributions of REMSAD sulfate to each of the four large BRAVO source regions. The attributions to the large areas were generated by aggregating the attributions of the 27 smaller source areas described in section 2.3.2.5. The top line of the table gives the REMSAD attributions both with and without the boundary conditions and non-linear fractions being redistributed proportionally. Values within 10 percentage points of the correct answer (defined as the REMSAD attributions with the redistributed boundary conditions and non-linearity) are shown in bold and in a larger font for easy identification.

Table 7-4. Columns 2–5 are the percent attributions of predicted REMSAD sulfate by TrMB, all using MM5 winds. For comparison, the top row shows the corresponding REMSAD attributions. REMSAD has boundary conditions = 7% and non-linear = 2%. Values in parentheses are the REMSAD attributions if these are proportionally redistributed. TrMB attributions within 10 percentage points of the REMSAD attributions are shown in larger font bold type. The last three columns are statistics comparing the TrMB predicted concentrations to "observed" (REMSAD predicted) sulfate concentrations. All values are for July 6–October 28, 1999 (115 days).

Model	Texas	Mexico	Eastern U.S.	Western U.S.	R^2	Mean Over-pred. SO_4 (ng/m^3)	Mean % Over-pred.
REMSAD ("Correct")	16 (18)	23 (25)	42 (46)	9 (10)	1.000	0	0
CAPITA 5-day	**19**	**31**	**39**	**11**	.778	-23	-1%
CAPITA 7-day	**20**	**24**	**36**	**20**	.798	-12	-1%
CAPITA 10-day	**21**	**21**	**37**	21	.775	-13	-1%
HYSPLIT 5-day	43	**25**	16	**17**	.768	11	+1%
HYSPLIT 7-day	43	**23**	16	**18**	.820	-26	-1%
HYSPLIT 10-day	46	**21**	19	**13**	.801	-14	-1%
ATAD 5-day	**25**	**33**	**36**	**8**	.735	-24	-1%

The best reproduction of the REMSAD sulfate attributions was with the CAPITA Monte Carlo model using 5-day back trajectories, although the 7-day and 10-day trajectories were nearly as good. The ATAD model with MM5 input also attributed the sulfate correctly to all four source regions within 10 percentage points of the correct values. The HYSPLIT model with MM5 input was able to reproduce the correct source attributions for Mexico and the western U.S., but was unable to correctly apportion sulfate from Texas and the eastern U.S., attributing much more to Texas and much less to the eastern U.S. than REMSAD.

Use of 5-, 7-, or 10-day trajectory lengths from the CAPITA Monte Carlo model made little difference in the predicted attributions except for the western U.S., which is predicted to be the source of twice as much sulfate with 7- or 10-day trajectories as with 5-day lengths. This is intuitively reasonable since airmasses rarely arrived at Big Bend directly from the western U.S. but more often traversed across the eastern U.S. and/or Texas prior to arrival. Thus, on average, the travel time from the western U.S. was longer than from the other large source areas and so longer trajectories attributed more to this region.

Why is HYSPLIT with MM5 input not accurately reproducing the REMSAD sulfate attributions when it uses essentially the same input meteorological data as CAPITA MC and ATAD? Figures 7-10 and 7-11 show time lines of the observed and predicted REMSAD sulfate and the number of back trajectory endpoints in each of the four large source areas. Figure 7-10 is for 5-day back trajectories using the CAPITA MC while Figure 7-11 is the same for the HYSPLIT model. A large difference between CAPITA MC and HYSPLIT occurs on September 1 (day 244). This is also the day of the highest measured sulfate concentration at Big Bend and so an influential point in the multiple linear regression. Notice that while the CAPITA MC model has most of the endpoints in the eastern U.S. on this day, HYSPLIT puts most of them in Texas. ATAD, which is not shown, also has most of the endpoints in the eastern U.S. on this day.

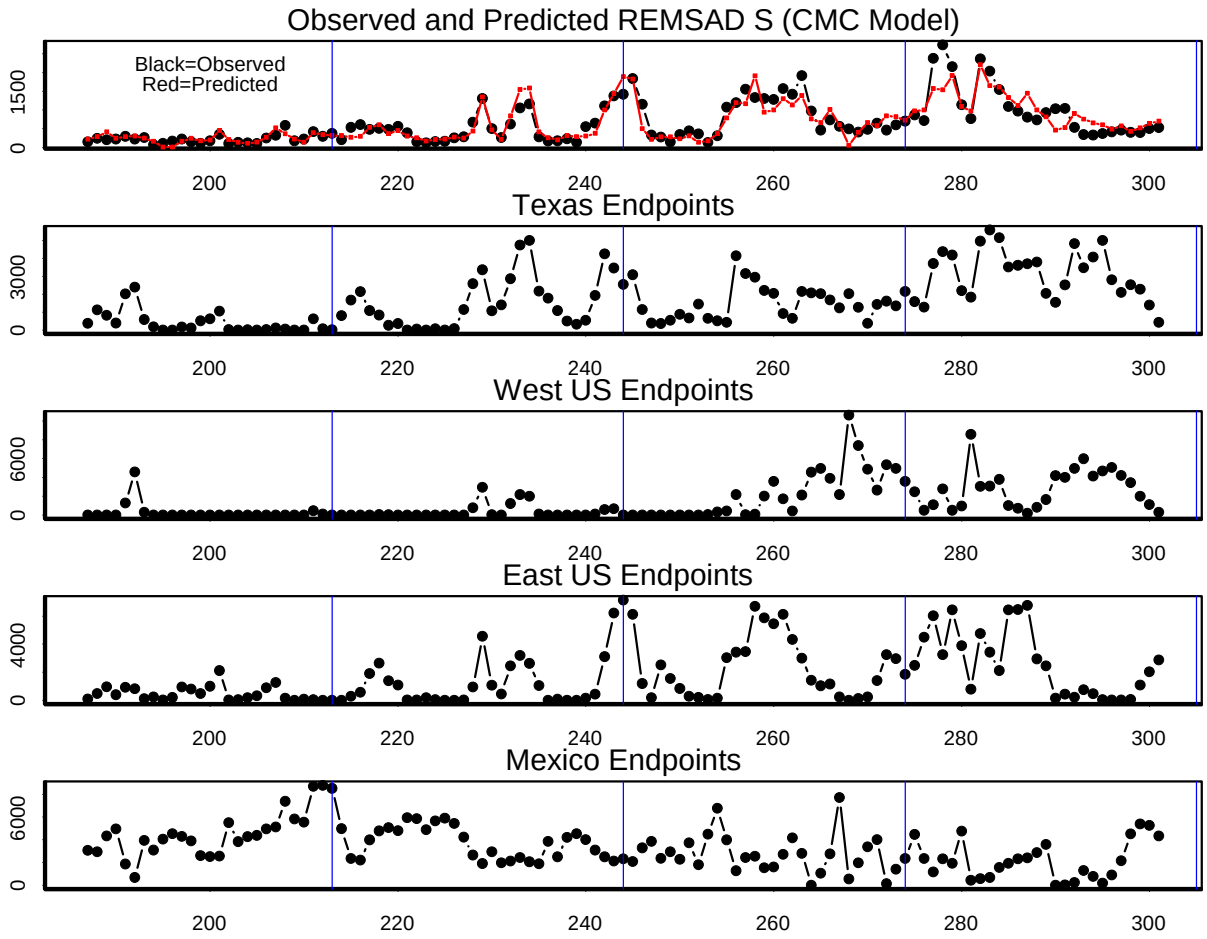

Figure 7-10. Time lines of the observed (black) and predicted (red) REMSAD sulfate in ng/m^3 (top) and number of back trajectory endpoints in each of the source areas using the CAPITA MC model and 5-day back trajectories. The blue vertical lines are the first days of August, September, October, and November.

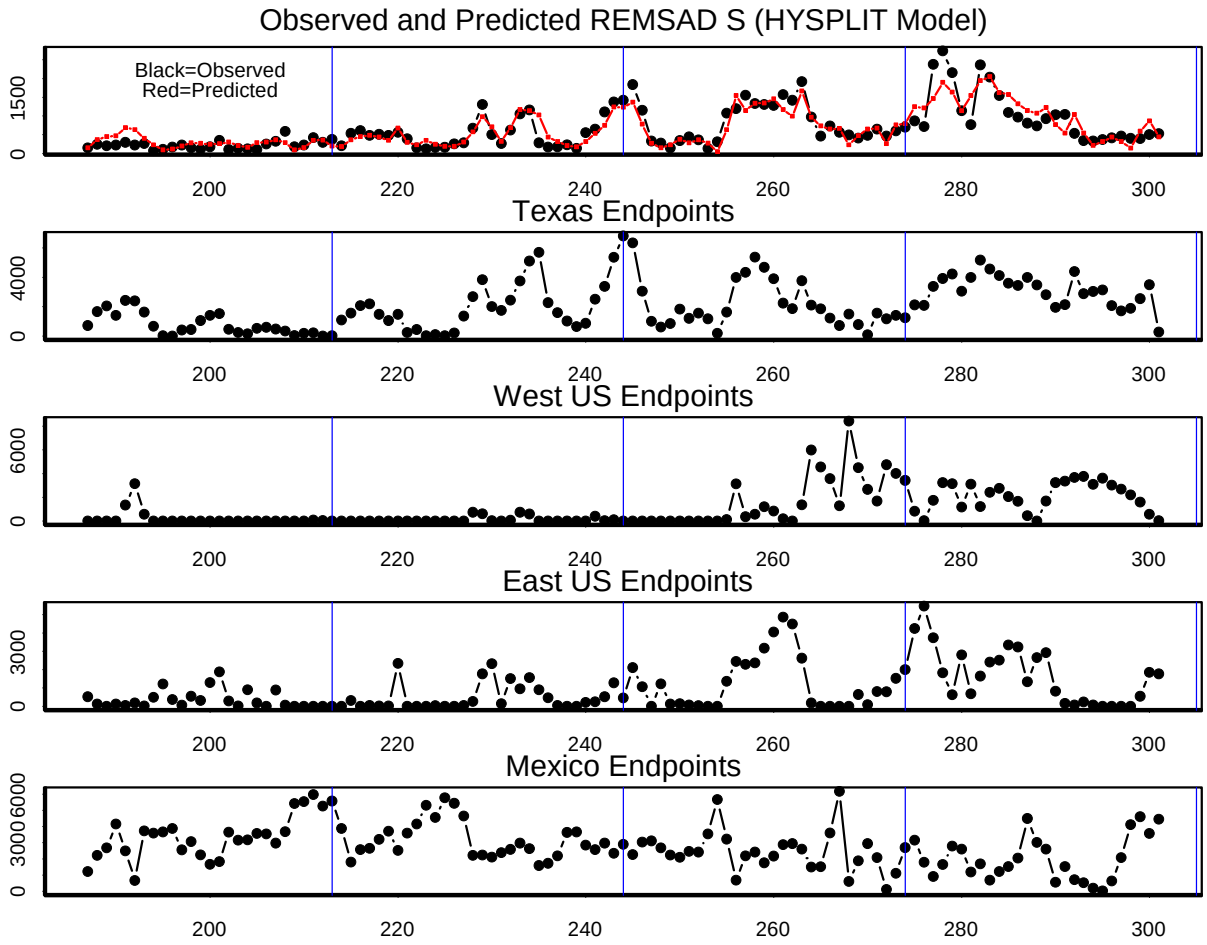

Figure 7-11. Time lines of the observed (black) and predicted (red) REMSAD sulfate (top) and number of back trajectory endpoints in each of the source areas using the HYSPLIT model and 5-day back trajectories. The blue vertical lines are the first days of August, September, October, and November.

Figure 7-12 shows the back trajectories generated by each of the three models for September 1. While they all have the same general direction, the HYSPLIT trajectories are much lower in height and in fact are essentially on the ground. This is true even for trajectories with a start height of 1000 m. Due to the lower height they also have much lower wind speeds and so remain in Texas while the CAPITA MC and ATAD trajectories extend into the eastern U.S. Because this was an influential day, the differences in trajectory heights on this day alone may explain why HYSPLIT was unable to reproduce the REMSAD source attributions.

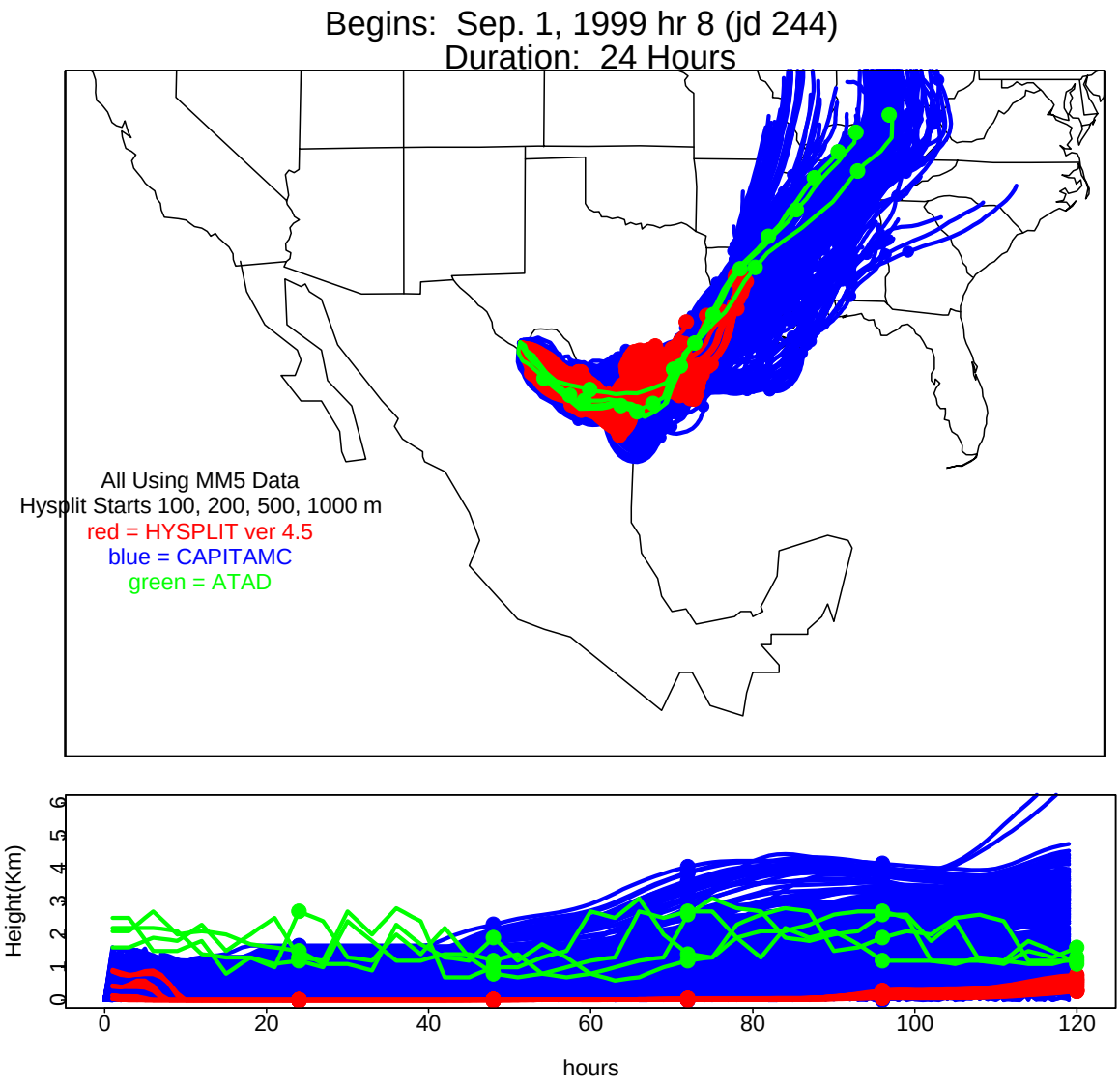

Figure 7-12. 5-day duration back trajectories arriving at Big Bend during the 24-hours beginning 9/1/99 at 8:00 a.m. Blue are CAPITA MC trajectories (20 every 2 hours), red are HYSPLIT trajectories (1 per hour for each of 4 start heights) and green are ATAD trajectories (4 per day).

In the case of the simulated REMSAD sulfate where we know the concentration of sulfate attributed to each source area, it's possible to examine the linearity of the relationship between endpoints and sulfate concentrations. Figures 7-13 and 7-14 show scatter plots of the daily number of endpoints in each of the four large areas vs. the sulfate attributed to the area for each day by REMSAD. The endpoints in Figures 7-13 and 7-14 were generated using the CAPITA MC model and the HYSPLIT model, respectively. The solid blue lines shown in each graph are the mean ratio of REMSAD sulfate from each region to the number of endpoints in the region. This is the "correct" relationship that the TrMB model would have to re-create in order to give the same attributions as REMSAD. Similarly, the dashed red line is a representation of the TrMB predicted relationship. If only these four source areas had been used in the regression, the slope of the dashed red line would be the regression coefficient. However, since each of the large

areas is a composite of several smaller areas, the dashed red line was estimated by dividing the mean TrMB predicted concentration for the composite large area by the mean number of endpoints in that area. The scatter about the solid blue lines gives some idea of the linearity of the true relationship between endpoints and concentrations and how far the attribution for an individual day could deviate from the mean attribution. The angle between the dashed red and solid blue lines shows how well the TrMB model was able to reproduce the mean REMSAD attribution of sulfate.

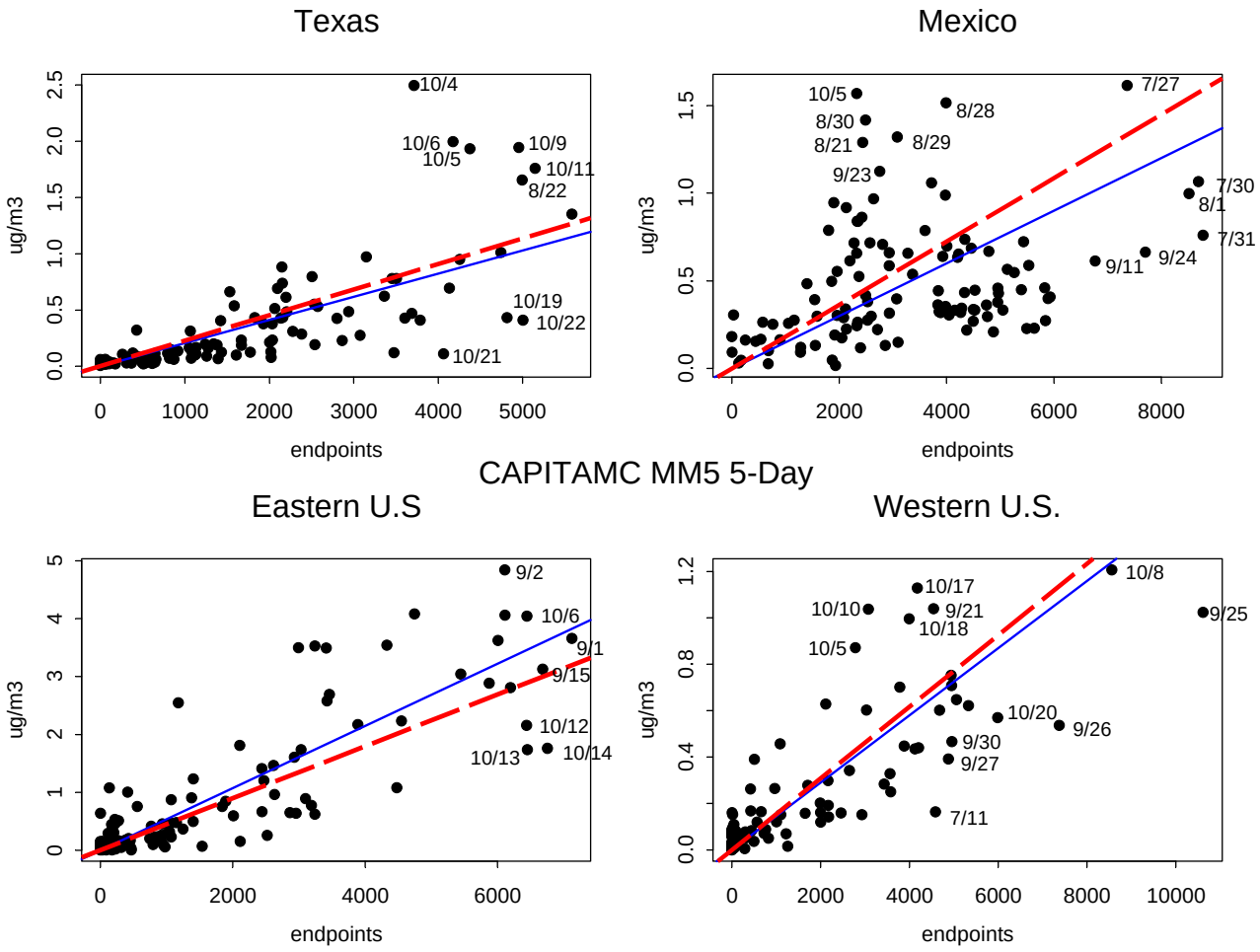

Figure 7-13. Scatter plots of REMSAD sulfate attributions vs. number of endpoints for each of four large source areas using 5-day back trajectories from the CAPITA MC model and MM5 winds. The solid blue lines are the "true" slopes; the dashed red lines are the TrMB modeled slopes.

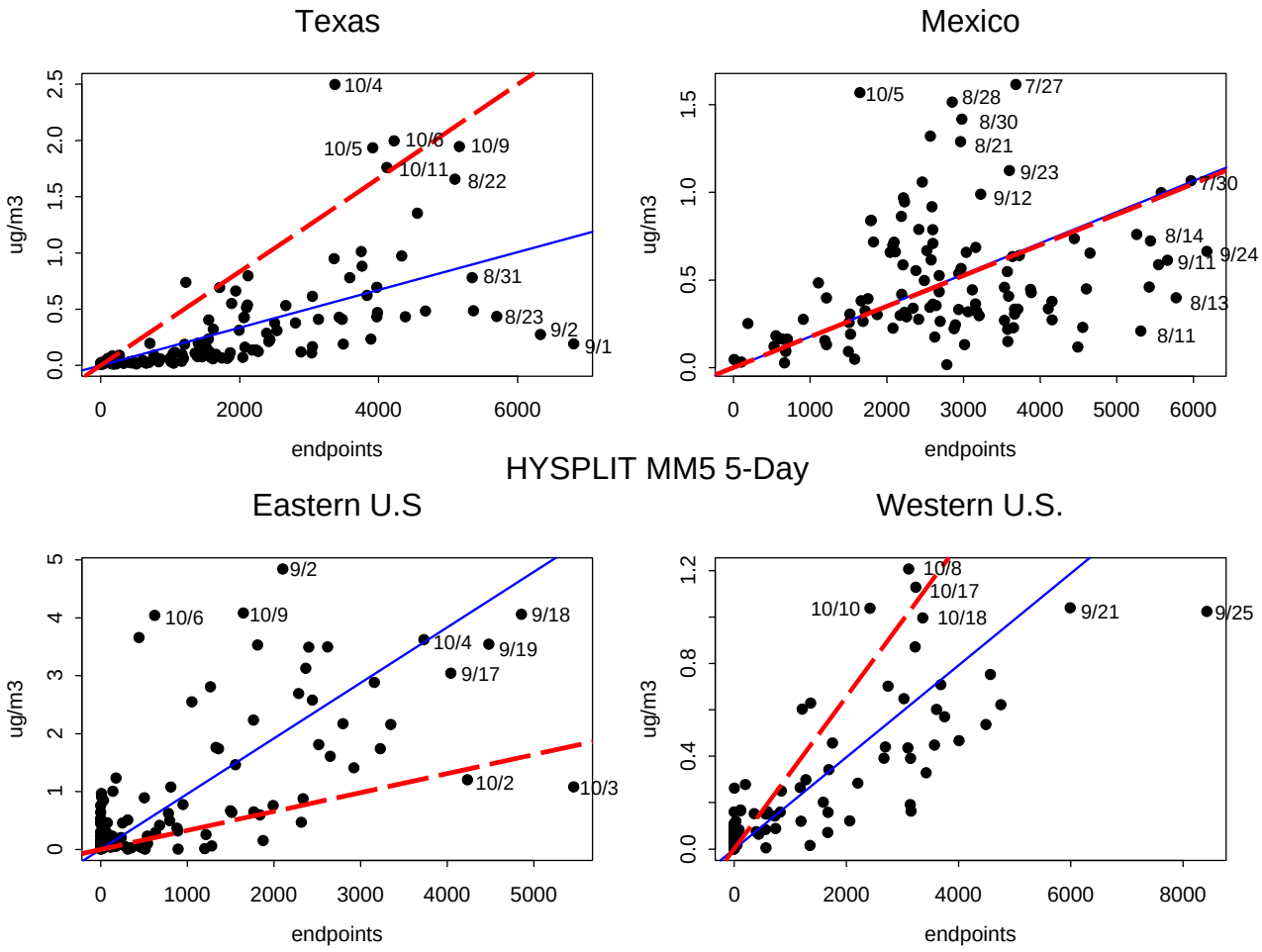

Figure 7-14. Scatter plots of REMSAD sulfate attributions vs. number of endpoints for each of four large source areas using 5-day back trajectories from the HYSPLIT model and MM5 winds. The solid blue lines are the "true" slopes; the dashed red lines are the TrMB modeled slopes.

When using endpoints generated by the CAPITA MC model, the assumption of linearity seems to be fairly good, though certainly some large deviations from the mean relationship exist. For example, for the Texas source area in Figure 7-13, all except a few days in October when REMSAD gives large attributions to Texas seem to fall close to the lines. These days probably had unusual meteorological or chemical characteristics that caused the relationship between sulfate at Big Bend and transport from areas within Texas to be different than average. In the case of October 4, it appears that the sulfate attribution to Texas on this individual day could be underestimated by TrMB by nearly a factor of 5, even though on average the mean attribution to Texas was within one percentage point of being correct. So, as expected, the errors in the attributions predicted by the TrMB model are larger for individual days than for the mean.

7.2.1.2 Discussion

Both the CAPITA MC and ATAD models, when run with the MM5 wind fields used by REMSAD, can reproduce the REMSAD sulfate attributions for four large source areas to within ten percentage points for all areas. HYSPLIT can similarly reproduce the attributions to Mexico and the western U.S., but is significantly overestimating the attribution to Texas and

underestimating the eastern U.S. This may be due to trajectory heights that are too low on a single highly influential day, thus giving too much influence to Texas and not enough to the eastern U.S. Similarly, HYSPLIT with MM5 input also failed the tracer attribution test. Use of EDAS and FNL wind fields could not be tested by this simulated sulfur attribution test since REMSAD was run only with the MM5 winds as input and these are the correct winds for this simulated world.

Examination of the relationship between sulfate attributions and endpoints indicates that caution should be exercised when using TrMB to examine source attributions on individual days. The model is, in general, much more accurate for the four-month average. Even if the mean source attributions were reproduced with total accuracy, the degree of accuracy of the model on any one individual day depends on how much the meteorological and chemical characteristics on that day deviated from the mean. In general, this will not be known.

7.2.2 Forward Mass Balance Regressions

The transit probabilities were generated for each source region using the plumes generated from the CAPITA Monte Carlo model driven by the MM5 wind fields (Figure 7-3). All plumes originating from virtual sources within a REMSAD source region were aggregated together. Transit probabilities from the two eastern U.S. source regions, LA/MISS & MO/IL/AR, were highly collinear so they were combined into one source region. Boundary conditions were not included in the FMBR since the simulation of the transport from the REMSAD boundary was not conducted, but they were incorporated in the percent source contributions so the FMBR source attributions could be compared to the REMSAD source attributions. The analysis was conducted using different plumes lengths of 5, 7, and 10 days to test the sensitivity of the FMBR on plume length. This is important since if the plumes are too short then contributions from distant source regions will not be represented, and if the plumes are too long then impacts from "old" particles will be too large due to the single average kinetic factors that are derived as part of the source/sink term.

Results are presented in Table 7-5 for the three different lengths of the simulated source plumes. As shown in the FMBR performance statistic, the predicted sulfate fits the REMSAD sulfate well, with $r^2 \sim 0.8$, an error of 40%, and bias of 4%. Consequently, the transport from 10 source regions, some 1000's of km^2 in size, multiplied by a constant explains 80% of the variance in the REMSAD sulfate daily time series.

The FMBR performance statistics are independent of the plume lengths. However, as the plume lengths increased, the number of source regions with contributions within one standard error of the REMSAD results increased from 4 of 9 for the 5-day plumes and to 8 of 9 using the 10-day plumes.

Using the 10-day plumes, all but the northeast Texas source region is within the standard error of the REMSAD results. Aggregating over the large source regions, the western U.S., the eastern U.S., Texas, and Mexico, the Texas source contribution is overestimated by about 9 percentage points and the western U.S. contribution is zero or underestimated by about 9 percentage points. Eastern U.S. and Mexican source regions properly reproduce the REMSAD result. Therefore it appears that the FMBR technique is unable to resolve the western U.S. source contributions and erroneously attributes them to the Texas source region.

Table 7-5. Source attribution results from the application of the FMBR technique to the REMSAD predicted sulfate concentrations. The REMSAD source attribution results are also provided. Bolded source attributions are within 1 standard error of the REMSAD results. Propagation of errors was used to estimate standard errors for aggregated regions.

	% Contribution ± Standard Error			
Source Regions	**5 day**	**7 day**	**10 day**	**REMSAD Model***
Carbón	**16.1 ± 4**	**16.5 ± 4**	**15.4 ± 4**	14.1
Rest of Mexico	**13.6 ± 10**	**12.2 ± 10**	**11.6 ± 11**	10.0
NE Texas	**7.8 ± 3**	9.5 ± 3	10.2 ± 3	5.4
SE Texas	14. ± 4	**11.9 ± 4**	**11.8 ± 5**	8.8
Rest of Texas	**5. ± 4**	**4. ± 5**	**3.7 ± 5**	2.3
LA/MISS & MO/IL/AR	33.8 ± 6	**28.7 ± 8**	**27.6 ± 8**	22.3
E Central	0.6 ± 2	7.4 ± 4	**8.8 ± 5**	13.6
Rest of E U.S.	2.1 ± 3	2.7 ± 4	**4. ± 5**	7.4
W U.S.	0. ± 8	0. ± 9	**0. ± 9**	9.3
GOCART BC	7	7	7	7.2
Mexico (all)	**29.6 ± 10**	**28.8 ± 11**	**27. ± 12**	24.0
Texas (all)	26.8 ± 6	25.4 ± 7	25.7 ± 7	16.5
Eastern U.S. (all)	36.5 ± 7	**38.8 ± 10**	**40.4 ± 11**	43.2
Western U.S. (all)	0. ± 8	0. ± 9	**0. ± 9**	9.3
GOCART BC	7	7	7	7.2

FMBR Performance Statistics				
Base Case Avg ($\mu g/m^3$)	1.81	1.81	1.81	
Predicted Avg ($\mu g/m^3$)	1.73	1.72	1.73	
Bias (%)	-4.4	-4.5	-4.1	
RMS Error (%)	42	41	41	
r^2:	0.79	0.80	0.80	
# Data Values	115	115	115	

***REMSAD source attributions were scaled by 2.7% to account for missing mass due to nonlinearities in the model simulations.**

To investigate the Texas and western U.S. bias, the FMBR technique was used with each source region in the western U.S. fixed at a constant *a priori* source/sink term so their total contribution to Big Bend's sulfate was about 9%. The results are presented in Table 7-6. Fixing the western U.S. contribution to 9% had little impact on the regression performance statistics, with r^2 dropping from 0.8 to 0.74 and the bias improving somewhat from -4% to -3%. The western U.S. was divided into two source regions, the central plains north of Texas and west of Texas. The central plains source contribution accounted for 3.8 % of the 9% western contribution. The increases in the contributions from western U.S. source regions were primarily compensated for by decreases in nearby source regions, with the largest changes occurring for Texas where the source contribution decreased from 25.7 to 21.2%. The airmasses from the western U.S. source regions traversed these nearby source regions en route to Big Bend. Therefore, for source regions with collinear transport, FMBR tended to increase the source attributions of the closer source regions at the expense of the more distant source regions.

Table 7-6. Source attribution results from the application of the FMBR technique to the REMSAD predicted sulfate concentrations. The REMSAD source attribution results are also provided. The FMBR used the 10-day plumes and was run under three different conditions defined below. Propagation of errors was used to estimate standard errors for aggregated regions.

	% Contribution ± Standard Error				% contribution Bias
Source Regions	**Run 1**	**Run 2**	**Run 3**	**REMSAD Model***	**Run3/REMSAD**
Carbón	15.4 ± 4	15.3 ± 4	16.7 ± 4	14.1	1.19
Rest of Mexico	11.6 ± 11	9.4 ± 11	13.8 ± 11	10.0	1.39
NE Texas	10.2 ± 3	9. ± 3	10.6 ± 3	5.4	1.96
SE Texas	11.8 ± 5	12.1 ± 5	12.9 ± 5	8.8	1.46
Rest of Texas	3.7 ± 5	0. ± 5	4.4 ± 5	2.3	1.93
LA/MISS & MO/IL/AR	27.6 ± 8	27.5 ± 8	27.9 ± 8	22.3	1.25
E Central	8.8 ± 5	8.4 ± 5	8.8 ± 5	13.6	0.65
Rest of E U.S.	3.9 ± 5	2. ± 5	4.9 ± 5	7.4	0.66
Western U.S.				9.3	
Central Plains	0. ± 3	3.8 ± 3	0. ± 3		
West of TX	0. ± 9	5.3 ± 9	0. ± 9		
GOCART BC	7	7		7.2	
Mexico (all)	27. ± 12	24.7 ± 12	30.5 ± 12	24.0	1.27
Texas (all)	25.7 ± 7	21.2 ± 7	27.9 ± 7	16.5	1.69
Eastern U.S. (all)	40.3 ± 11	38. ± 11	41.6 ± 11	43.2	0.96
Western U.S. (all)	0. ± 9	9.2 ± 9	0. ± 9	9.3	0.00
GOCART BC	7	7		7.2	

FMBR Performance Statistics			
	Run 1	**Run 2**	**Run 3**
Base Case Avg ($\mu g/m^3$)	1.81	1.81	1.94
Predicted Avg ($\mu g/m^3$)	1.73	1.75	1.85
Bias (%)	-4.1	-3	-4.7
RMS Error (%)	41	47	40
r^2:	0.8	0.74	0.79
# Data Values	115	115	115

***REMSAD source attributions were scaled by 2.7% to account for missing mass due to nonlinearities in the model simulations.**

Run 1: REMSAD sulfate minus the contribution from the boundary conditions, same run as in Table 7-5.
Run 2: REMSAD sulfate minus the contribution from the boundary conditions and the western U.S. and central plains source contributions fixed to a total contribution of 9%.
Run 3: Total REMSAD sulfate (includes the contribution from the boundary conditions).

This bias can also be seen by determining in which source regions the contributions from the REMSAD boundary conditions are placed. Ideally, this mass would be attributed to source

regions at the edge of the domain. The FMBR technique was applied to the total REMSAD sulfate concentration; that is, the contribution from the boundary conditions were included. These results are presented in Table 7-6 as Run 3. The boundary condition accounted for about 7% of the total REMSAD simulated sulfate at Big Bend. As shown, more than 80% of this mass was assigned to the closer-by Texas and Mexico (Carbón and Monterey) source regions, while the distant source regions in the western U.S., Mexico, and eastern U.S. had little change. This is consistent with the previous finding that the FMBR technique tended to overestimate the contribution from the closer source regions at the expense of more distant source regions with collinear transport.

The magnitude of these systematic biases was estimated by taking the ratio of the relative attribution of the FMBR in run 3 and the actual relative REMSAD source attribution results and are presented in Table 7-6. By taking the ratio of the relative contributions as opposed to absolute concentrations, the factors account for the differences in the distribution of the contributions from the various source regions as opposed to the absolute values of these contributions. As shown, Texas and Mexican sulfate contributions were biased high by 27% and 69%, respectively. The western U.S. was biased low by 100% and the eastern U.S. was biased low by only 4%.

In conclusion, the FMBR technique was successfully validated against the synthetic sulfate data generated by REMSAD and the 10-day plumes produced the best results. The contributions from the eastern U.S., Mexican, and Carbón source regions could be independently resolved. However, it appears that nearly all of the contributions from the western U.S. and boundary conditions were attributed to Texas and Mexican sources. Based upon these results, FMBR is applied to the measured fine particle sulfur at Big Bend National Park (see chapter 8) using the 10-day plumes. When interpreting those results, one needs to be mindful of the potential biases and relationship between the predicted western U.S. and boundary conditions and the Texas and Mexican source attributions.

7.2.3 Synthesized REMSAD

The apportionment of Big Bend's sulfate was also conducted using a synthesis inversion technique. In this method the REMSAD or CMAQ-MADRID source apportionment results are regressed against the observed sulfate concentrations throughout Texas. The same simulated attribution results are then scaled by the regression coefficients to derive alternative source attribution estimates that, when summed together, better fit the measured data. This approach compensates for some of the systematic errors present in the two simulations of the air quality models and thus should provide more accurate attributions of Big Bend aerosol.

The synthesis inversion method is based upon the inversion of the conservation of mass equation and is fully described in section 2.3.2.3.1. However, in brief, it can be shown that a discrete form of the conservation of mass equation can be derived from the Green function solution of a linear differential conservation of mass equation:

$$c_i = \sum_j G_{ij} s_j + \varepsilon_i = m_i + \varepsilon_i \qquad (2\text{-}33)$$

where c_i are the observed concentration values for each receptor site/time pair i, m_i are the modeled concentration values, ε_i are the errors in c_i,, s_j are the source attribution scaling coefficients for each source time pair $_j$, and G_{ij} are the absolute source contributions of

source/time pair j to observation i. In this application, c_i are the observed fine particle sulfur data scaled to sulfate and G_{ij} are calculated from the REMSAD model. Equation 2-33 is solved for s_j using constrained linear regression. If REMSAD is a perfect model, in the least square sense, then the source attribution scaling coefficients (s_j) will be equal to 1.

In order to test the synthesis inversion technique, it was applied to the synthetic REMSAD sulfate source apportionment results. To account for measurement error, a 10% normally distributed random error was added to all predicted observations:

$$\left(m_i + \varepsilon_i\right) = \sum_j G_{ij} s_j \qquad (7\text{-}1)$$

where $\left(m_i + \varepsilon_i\right)$ is the model prediction plus the 10% error. A valid model would result in regression coefficients of $s_j = 1$. Coefficients other than one would be due to highly collinear source attribution estimates between source regions and the regression could not resolve the source region contribution due to the error ε_i and non-linearities in the REMSAD model. Also, a source region's contribution may be smaller than the error in the system and the regression technique would be unable to properly resolve this source's contribution to the receptors.

The inversion process was conducted using a number of different configurations including using only the predicted Big Bend sulfate data for all four months, the predicted sulfate data from all BRAVO monitoring sites for all four months, and the predicted sulfate data from all BRAVO monitoring sites for different five-day periods. In most cases the source attribution scaling coefficients were within 15% of 1. For example, Table 7-7 presents the results from two analyses, one using the predicted daily sulfate concentrations from only the Big Bend monitoring site and the other using data from all BRAVO monitoring sites and times. As shown, when only the Big Bend data are used, the scaling coefficients are within 10% of 1, except for northeast Texas and then the r^2 is essentially one. When the predicted sulfate from all BRAVO monitoring sites are used, the regression coefficients are generally within 5% of 1 with most standard errors less than 1%.

Three conclusions can be drawn from this analysis. First, the technique is valid, provided sufficiently accurate data and model are used. Second, there is sufficient variability between the source regions with large contributions to Big Bend and Texas that the system can adequately resolve them. Last, the non-linearities in the REMSAD chemistry module are sufficiently small that the source regions' contributions from each other can be resolved with this linear technique. This testing does not account for errors in the REMSAD model itself. As shown in chapter 6, the REMSAD modeling error is on the order of a factor of 2. This is much larger than the 10% error added to the predicted sulfate and the error introduced by the non-linearities in REMSAD's chemistry module. Therefore this does not conclusively validate the system for application to observed data.

Table 7-7. The source attribution scaling coefficients and performance statistics resulting from regressing the REMSAD source attribution results for all modeled source regions against the REMSAD-predicted sulfate concentrations at Big Bend and at all BRAVO monitoring sites for the entire BRAVO time period. The predicted sulfate concentrations had a 10% normally distributed error added to them.

	Scaling Coefficients (s_i)	
Source Regions	**Big Bend Data**	**All Data**
Carbon	1 ± 0.01	1.01 ± 0.002
Rest of Mexico	1 ± 0.01	1 ± 0.003
NE Texas	1.13 ± 0.02	1.02 ± 0.001
SE Texas	0.95 ± 0.02	1 ± 0.001
Rest of Texas	1.08 ± 0.04	1.06 ± 0.005
LA/MISS	1.07 ± 0.02	1.01 ± 0.001
E Central	0.99 ± 0.01	1 ± 0.001
MO/IL/AR	0.97 ± 0.01	1 ± 0.001
Rest of E US	1.03 ± 0.02	1.01 ± 0.01
W US	1.03 ± 0.02	1.05 ± 0.02
GOCART BC	0.94 ± 0.03	0.95 ± 0.03

Regression Performance Statistics

	Big Bend Data	All Data
r^2	0.9999	0.9999
Basecase Avg ($\mu g/m^3$)	1.97	3.3
Predicted Avg ($\mu g/m^3$)	1.97	3.3
RMS error (%)	2.4	3
# Data Values	112	3628

7.3 Discussion and Conclusions of Test Results

Several tests of the abilities of trajectory-based receptor techniques to reproduce two known source attributions were conducted. The purposes of these tests were to 1) determine the accuracy of the techniques themselves, 2) to determine which wind field MM5 or EDAS/FNL is better for use in further source attribution of sulfate during BRAVO and 3) to determine the optimum trajectory length.

7.3.1 Model Accuracy

On the first point the tests were successful and demonstrated that both the TrMB and FRMB techniques could reproduce the known mean attributions of both the total tracer concentrations and the REMSAD-simulated sulfate concentrations within the standard errors of the method. There are caveats to this conclusion for both models. TrMB was successful only with back trajectories from some trajectory model and input wind field combinations. Since those sets of combinations that worked well were consistent for both tests, there is confidence in using this subset of back trajectories for attribution of measured sulfate. FMBR can identify the tracer release sites and rates. However, when using only one receptor site, the resolution of the results diminish and it identifies only the common transport pathways associated with the highest tracer concentrations. FMBR was also able to isolate the tracer release sites when the concentrations were sufficiently high. When the release sites were identified, FMBR was able to decompose the integrated tracer into its contributions from the four individual sites and the mean

release rate for each tracer was properly retrieved. As expected, both TrMB and FMBR give more accurate results for the four-month average source attribution than for individual days.

7.3.2 Wind Fields

On the second goal of determining which wind field is superior, these tests were not conclusive. Only the MM5 wind field could be tested with REMSAD-simulated sulfate concentrations so no insight regarding wind fields was gained by that test. For the attribution of the tracers, both wind fields did equally well in FMBR. For TrMB, MM5 input resulted in accurate tracer attributions when trajectories were generated by the CAPITA MC or ATAD model, but EDAS/FNL input was superior in the HYSPLIT model.

7.3.3 Trajectory Lengths

Trajectory lengths of 5, 7, and 10 days all performed similarly and within the uncertainties of the regressions in TrMB for the tracer. Insensitivity to trajectory length is not surprising for the tracers, since mean transport time to Big Bend for all of the tracer release sites is probably less than 5 days on average. Thus, longer trajectories do not change the relative fractions of endpoints in the source regions and so do not change the results of the regressions. For REMSAD sulfate, the western U.S. was better predicted by TrMB when using the CMC/MM5 5-day trajectories, while 7- and 10-day lengths over-predicted the contribution from this region. FMBR with REMSAD sulfate was able to reproduce the REMSAD sulfate attributions for all nine tested source regions within the standard error of the regression coefficients only with 10-day trajectories, while FMBR with 5-day and 7-day lengths could reproduce the results for 4 and 8 of the regions, respectively.

A significant difference between the forward and backward techniques is particle or endpoint height. In the forward technique (FMBR), particles were released from source areas at heights of 1 km or less. However, in the reverse technique (TrMB),all endpoints over a source region, regardless of height, were included in the regression. Many of the endpoints over the western U.S. between 7 and 10 days prior to arrival at Big Bend were at relatively high heights, > 3 km, and thus less likely to be in contact with emissions released in this region. It is possible that had the TrMB tests using trajectories from the CAPITA MC model limited the modeled endpoints to those below the mixing height, longer trajectories would have performed better since the information would not have been contaminated by the noise of endpoints above the mixed layer. Other analyses (see chapter 4) have shown that HYSPLIT trajectories are on average much lower than those generated using the CAPITA MC model, and HYSPLIT trajectories generated with EDAS/FNL input, which performed well in the tracer test, could not be tested with the REMSAD sulfate.

These tests therefore give us indications that: 1) for the tracers, which are less than 5 days away, trajectory length is not important, and 2) for sulfate, longer trajectories are probably better able to accurately reproduce the attributions as long as the endpoint or particle heights are limited to those below the mixed layer.

8) Receptor Oriented Apportionment for Big Bend National Park

8.1 Qualitative

8.1.1 Space/Time Pattern Analysis (EOF)

8.1.1.1 Introduction

Spatial and temporal relationships in the BRAVO fine particulate data are examined here using several techniques including Empirical Orthogonal Function (EOF) analysis [*Malm and Gebhart*, 1996, 1997; *Gebhart and Malm*, 1997; *Gebhart et al.*, 2000]. EOF analysis, described in detail in section 2.3.1.1, simplifies the dozens of daily spatial patterns into a few patterns that, when linearly re-combined, explain most of the variance in the data. Examination of spatial and temporal patterns is often useful to qualitatively examine dominant source-receptor relationships and to subjectively form hypotheses about significant source areas and physical factors likely to influence transport and transformation of aerosols in a region [*Malm and Gebhart*, 1996, 1997; *Gebhart and Malm*, 1997; *Gebhart et al.*, 2000; *Malm et al.,* 1990; *Henry et al.,* 1991].

One source of particular interest due in part to the proximity to Big Bend National Park has been the Carbón I (1200 MW) and Carbón II (1400 MW) coal-fired electric generating stations located near Piedras Negras, Coahuila, approximately 20 miles south of the U.S.-Mexico border. These power plants consist of 4 units each that are uncontrolled for SO_2 emissions. The BRAVO site nearest to these plants is Eagle Pass (See section 2.1.1.1 for a detailed description of BRAVO fine particulate monitoring, Figure 1-2 for a map of the study area, and Figure 2-1 for a map of the monitoring locations). Other source areas with high SO_2 emissions, close proximity, and frequent airmass transport to Big Bend include the Lignite Belt in northeast Texas which includes several coal-fired electric generating stations, the Gulf Coast region of southeast Texas and southern Louisiana where there are both large population centers and petrochemical and oil refining activities, the eastern U.S. including the Ohio River Valley with many high-sulfur, coal-burning power plants, industrial areas of Mexico including the Monterrey region, and southern Mexico which includes both Mexico City and an active volcano.

Prior to BRAVO, during September and October 1996, a field study consisting of 19 fine particle monitoring sites located in southern Texas and northern Mexico was conducted by the NPS and Procuraduria Federal de Proteccion al Ambiente (PROFEPA) [*Gebhart et al.*, 2000]. The particulate measurement and analysis techniques employed during this earlier study were essentially the same as during BRAVO. For several reasons it is of interest to compare the temporal, spatial, and interspecies patterns from BRAVO with those from the pilot study. The second half of BRAVO was during the same months of the year as the pilot study so it is possible to examine some inter-annual trends in fine particulate matter. Also, the spatial domains of the two studies overlapped with the 1996 study including sites in Mexico, but not extending as far north into Texas as did BRAVO. If the spatial patterns in the overlapping area are similar for both years, then we might be able to infer that the patterns in the non-overlapping areas were also similar, thus giving us a picture of the typical spatial patterns over a larger geographic area.

8.1.1.2 Imputation of Missing Data

During BRAVO there were 37 sites throughout Texas where speciated fine (< 2.5 μm diameter) particle concentrations were measured. These included four sites with 6-hour duration

samples and the remaining with 24-hour measurements. Summary statistics for most species at all sites are shown in Appendix 8a.

EOF analysis requires, and for other comparisons between sites we would like, a time-by-site matrix of concentrations with no missing values. Several schemes were used to fill missing or below detectable limit elements of the time-by-site matrix for each species. All 6-hour data were averaged to 24-hour concentrations and then missing values were either eliminated or estimated. Time periods and then sites with more than 25% of data missing were eliminated. This reduced the analysis period of June 29–October 31 to July 26–October 30, with August 5 and 6 also removed. Three sites, Padre Island, Guadalupe Mountains, and Wichita Mountains, were also removed, resulting in a matrix of 95 days by 34 sites. Next, all observations immediately preceded and followed by valid data at the same site were approximated by linear interpolation in time. Remaining missing data were filled by inverse distance weighted spatial interpolation. Concentrations below the minimum detectable limit (BDL) were set to 0. For the sulfur matrix, only 0.8% of the data were filled by time interpolation, 2.8% by spatial interpolation, and 0.3% were BDL. Similar fractions of the data matrices for other species were estimated in the same way. Due to the removal of most of July, results of EOF analyses are not expected to be directly comparable to other analyses of BRAVO data that include that time period. EOF analyses were completed for all measured species with adequate data.

8.1.1.3 Results for Sulfur

Because fine sulfate was the largest fraction of both the fine mass and the reconstructed light extinction (see chapter 3), insight into the source regions and transport pathways that lead to high sulfur concentrations at Big Bend are of high interest. Previous analyses of back trajectories arriving at Big Bend National Park over several years [*Gebhart et al.,* 2000, 2001] have also shown that there are dramatic seasonal differences in airmass transport patterns with airmasses more likely to arrive at Big Bend from Mexico during the summer than during other seasons and more likely to arrive from east Texas and other parts of the eastern United States during the fall than during other seasons. Thus it might be expected that sulfur source attributions and spatial patterns in the sulfur concentrations might be different during the early part of BRAVO than later in the study.

Time plots of 24-hour fine particulate elemental sulfur concentrations and some of the other major constituents of fine mass at Big Bend are shown in Figure 8-1. Daily spatial contour maps of sulfur are in Appendix 8b. Time lines and statistics for particulate sulfur for all BRAVO sites are in Appendices 6a and 6b. Maximum sulfur concentrations measured at Big Bend during BRAVO occurred during several 2–3 day episodes, with the highest concentrations occurring on September 1 and 2 (3080 & 2321 ng/m^3), September 15 (2545 ng/m^3), October 12 (2291 ng/m^3), and August 21 (2200 ng/m^3). The September 1–2 episode also had the highest organic carbon and second highest elemental carbon of the BRAVO study. The spatial patterns of measured sulfur on these days are shown chronologically in Figures 8-2 through 8-5. (See Appendix 8a and Figures 1-2 and 2-1 for detailed maps of site names, terrain, and points of interest). The first three of these days coincidentally happened to be days when IMPROVE network samplers were operating, so the spatial domain of sulfur measurements can be extended beyond Texas. The four patterns are all different with August 21 and October 12 being the most similar. These two days had higher sulfur concentrations in northeast Texas and around the Big Bend Area while central Texas had lower values. September 15 had the highest sulfur concentrations around Big Bend and on the southern Gulf Coast while concentrations in northeast Texas were the lowest in

the state. On September 1 the highest sulfur concentrations were in central Texas with the lowest being in three pockets in the east, far west, and southwest.

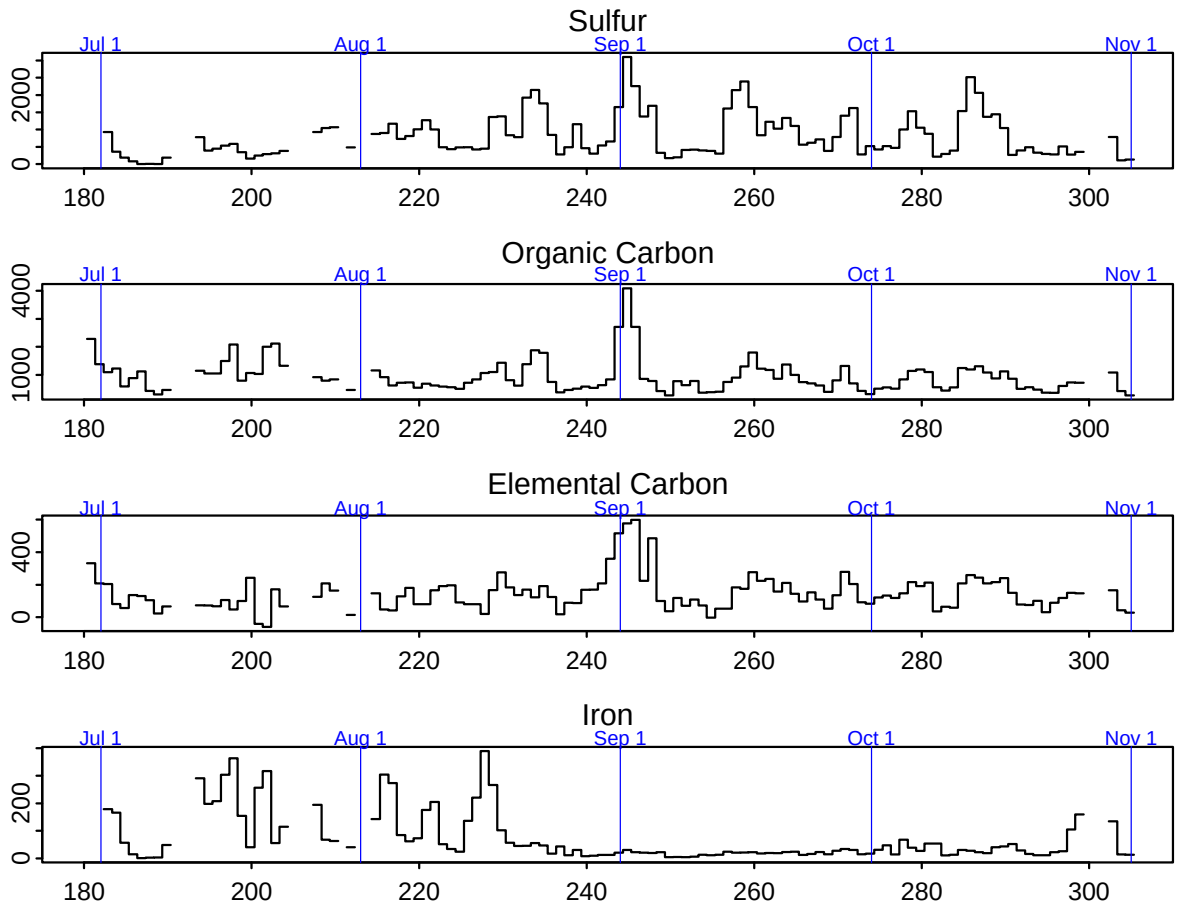

Figure 8-1. Time lines of the major constituents of fine mass (ng/m^3) at Big Bend. Labels on the x-axis are the day of the year. The vertical blue lines show the beginning of each month.

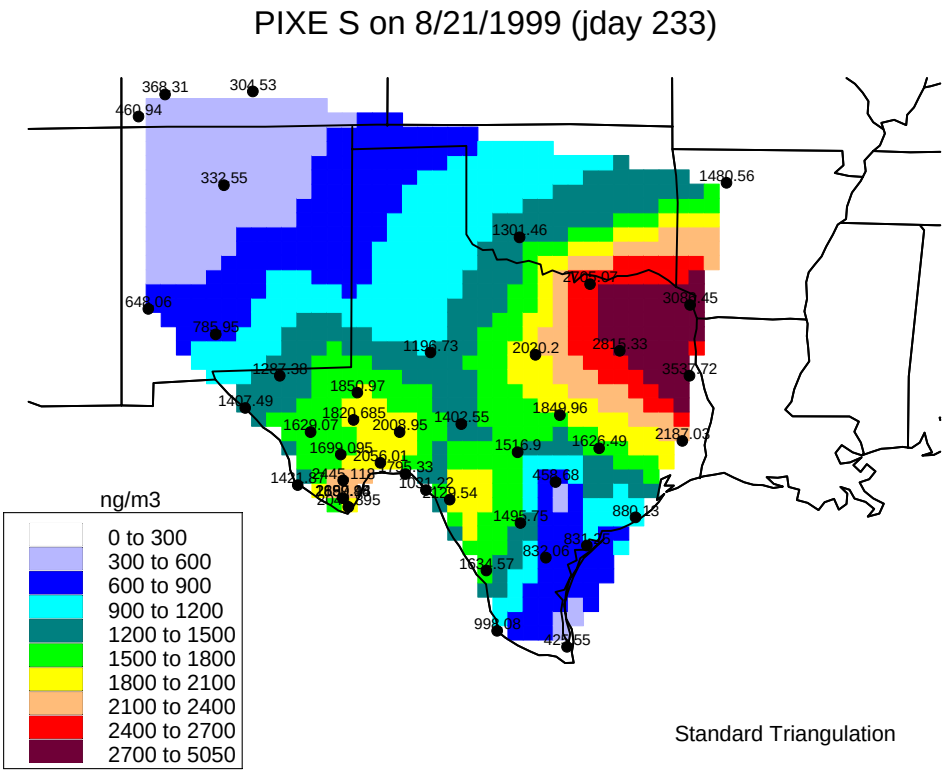

Figure 8-2. Spatial pattern of sulfur on August 21 when S at Big Bend was 2200 ng/m^3.

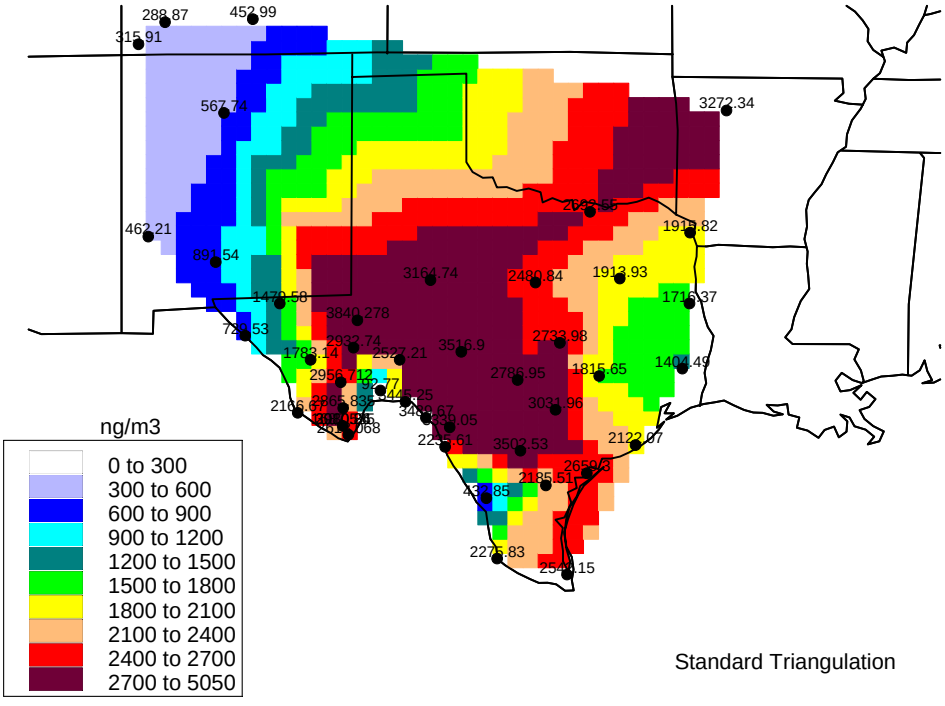

Figure 8-3. Spatial pattern of sulfur on September 1 when S at Big Bend was 3080 ng/m^3.

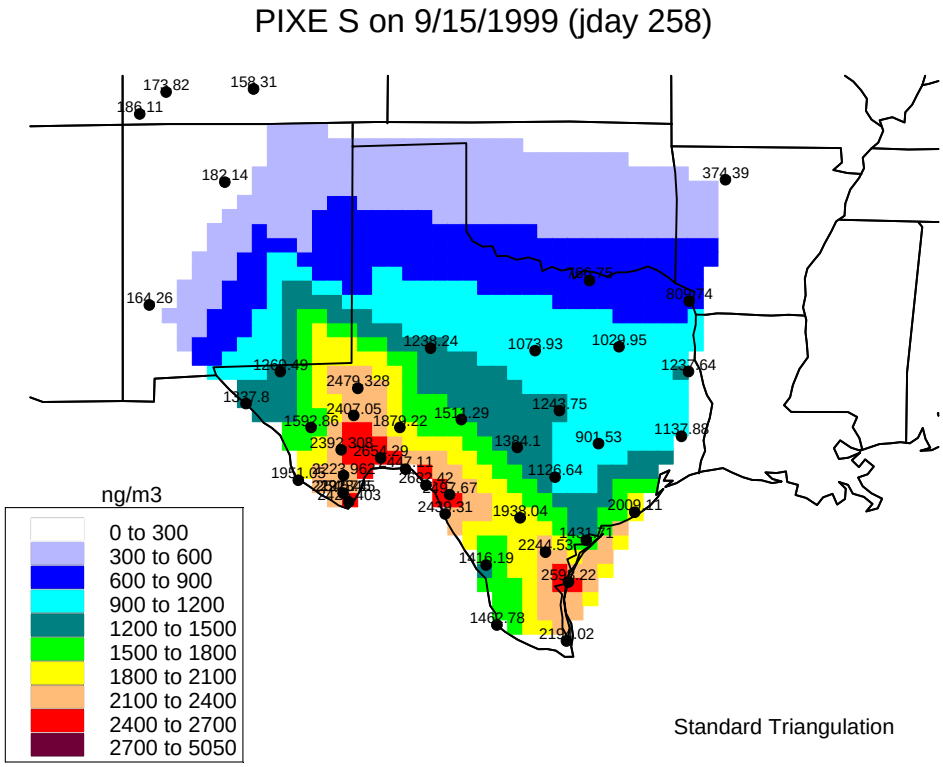

Figure 8-4. Spatial pattern of sulfur on September 15 when S at Big Bend was 2545 ng/m^3.

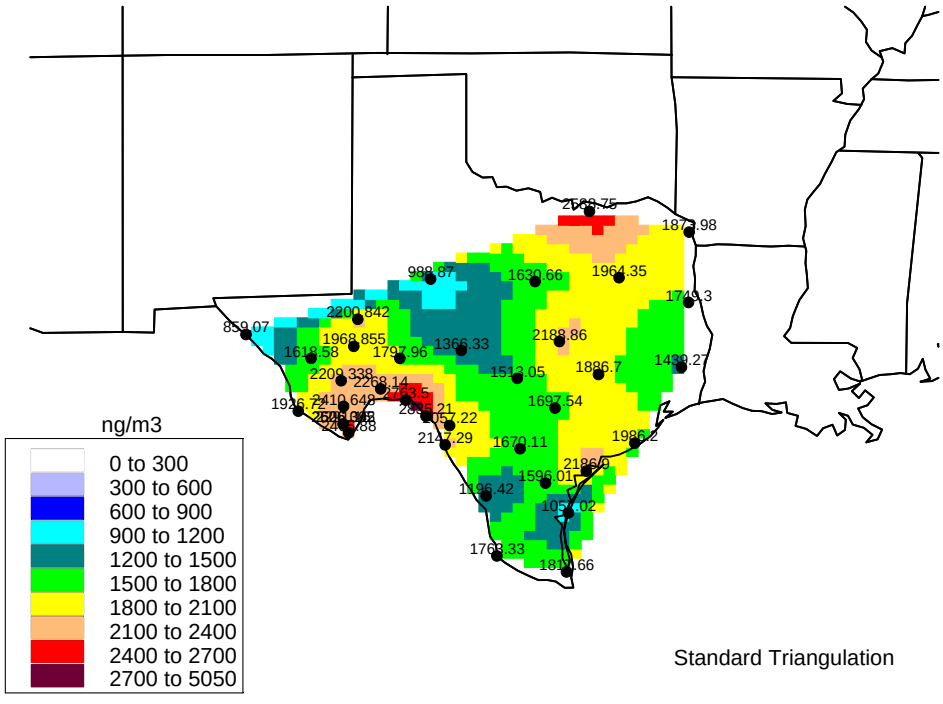

Figure 8-5. Spatial pattern of sulfur on October 12 when S at Big Bend was 2291 ng/m^3.

Mean sulfur concentrations during BRAVO are shown in Figure 8-6. Concentrations are highest on average in the northeast corner of the monitoring domain and lower towards the southwest, except an area east of Big Bend near the international border where there is a local maximum. That perturbation in the spatial pattern is indicative of at least some local influence from the nearby Carbón I/II plants.

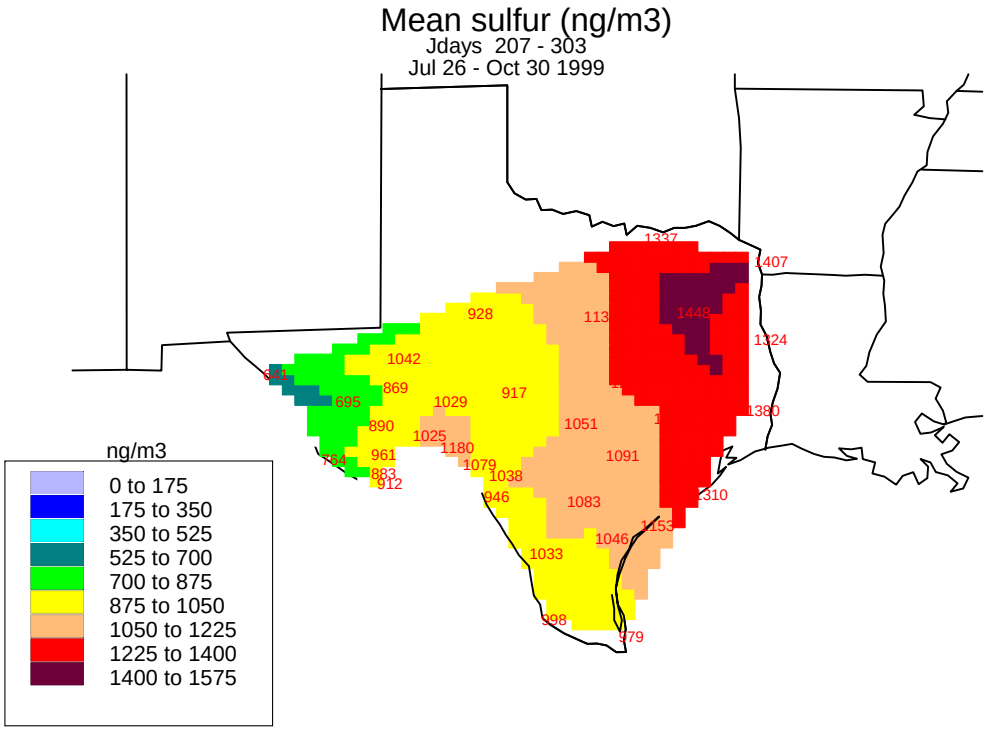

Figure 8-6. Mean sulfur concentrations for July 26–October 30, the portion of the study period when all sites had sufficient data.

Correlations of the sulfur concentrations at Big Bend to sulfur measured at other BRAVO sites are 0.6 or greater out to approximately 400 km from Big Bend and fall to below 0.3 at sites in eastern and northeastern Texas that are 700 km or more from the park as shown in Figure 8-7.

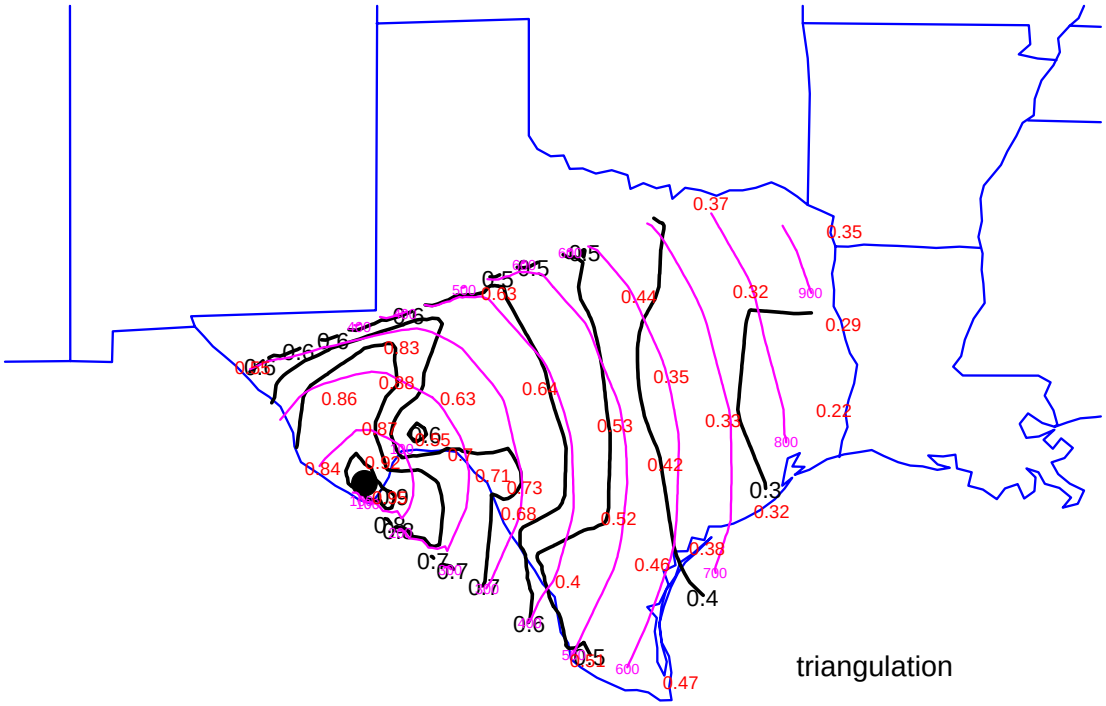

Figure 8-7. Correlations of sulfur measured at Big Bend to sulfur measured at other sites. Light magenta lines are distance in km from Big Bend.

Timeplots of the sulfur concentrations at sites other than Big Bend show that sulfur measured at locations within 200–300 km of each other are temporally very similar, though dissimilar to groups of more distant sites. A more compact illustration of this is shown in the monthly boxplots in Figure 8-8. The centerline of each box is the median concentration, tops and bottoms of the boxes are the 25th and 75th percentiles and the whiskers extend to 1.5 times the interquartile range. Values more extreme are shown as individual lines. The top left graph is for four sites located nearest to the Carbón I/II electric generating stations in northern Mexico, the top right graph is for five sites in the northeast corner of Texas in the lignite belt, the bottom left graph is for four sites in and near Big Bend National Park in southwest Texas, and the bottom right for four sites in southeast Texas near Houston. Sites in different areas of the state experienced their highest sulfur concentrations during different months of the study, with northeast Texas having maximum values during August, while sites closer to Big Bend had maximums during September. Sites nearest Carbón I/II experienced less monthly variation in sulfur concentrations than did sites in other corners of the monitoring domain. The relative lack of temporal variability at these sites, meaning the sulfur concentration is more or less constant no matter the predominant wind direction, is an indication of some relatively constant impact by nearby sources, possibly the Carbón I/II plants.

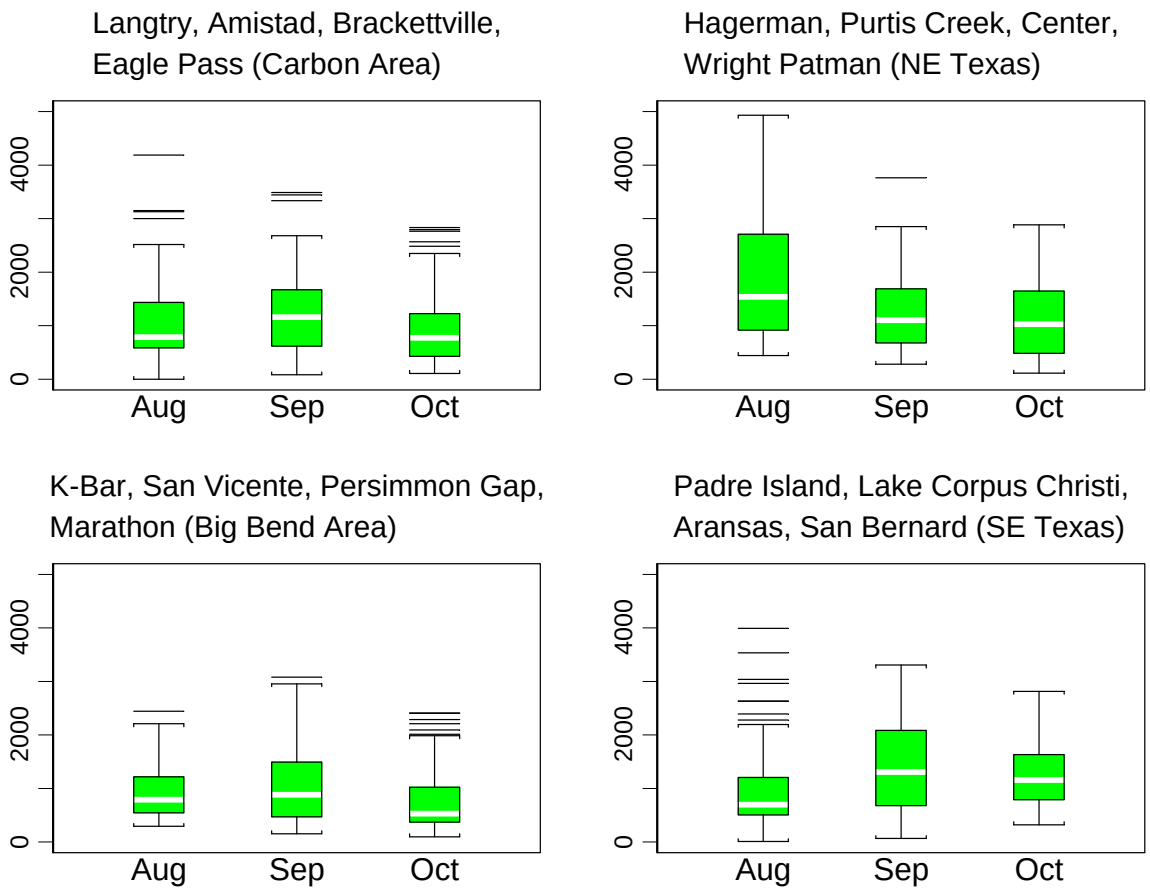

Figure 8-8. Boxplots of sulfur concentrations (ng/m^3) by month in four sections of the monitoring domain.

Seven fine particulate monitoring sites were common to both the 1996 and 1999 field studies. At five of these sites the differences between the mean September and October 1996 and mean September and October 1999 sulfur concentrations were 10% or less. The largest differences were 22% at Amistad and 12% at Fort Lancaster with 1996 being higher than 1999 for both. At Big Bend the difference between 1996 and 1999 was only 9 ng/m^3 or about 1% with 1999 being slightly higher. Since the sulfur concentrations appear to be quite similar between the two studies, the 1996 and 1999 means for these two months were plotted on a single map to visualize the "typical" mean sulfur concentrations for September and October over a larger area that includes both northeast Mexico sites of 1996 and the northeast Texas sites of 1999. This is shown in Figure 8-9.

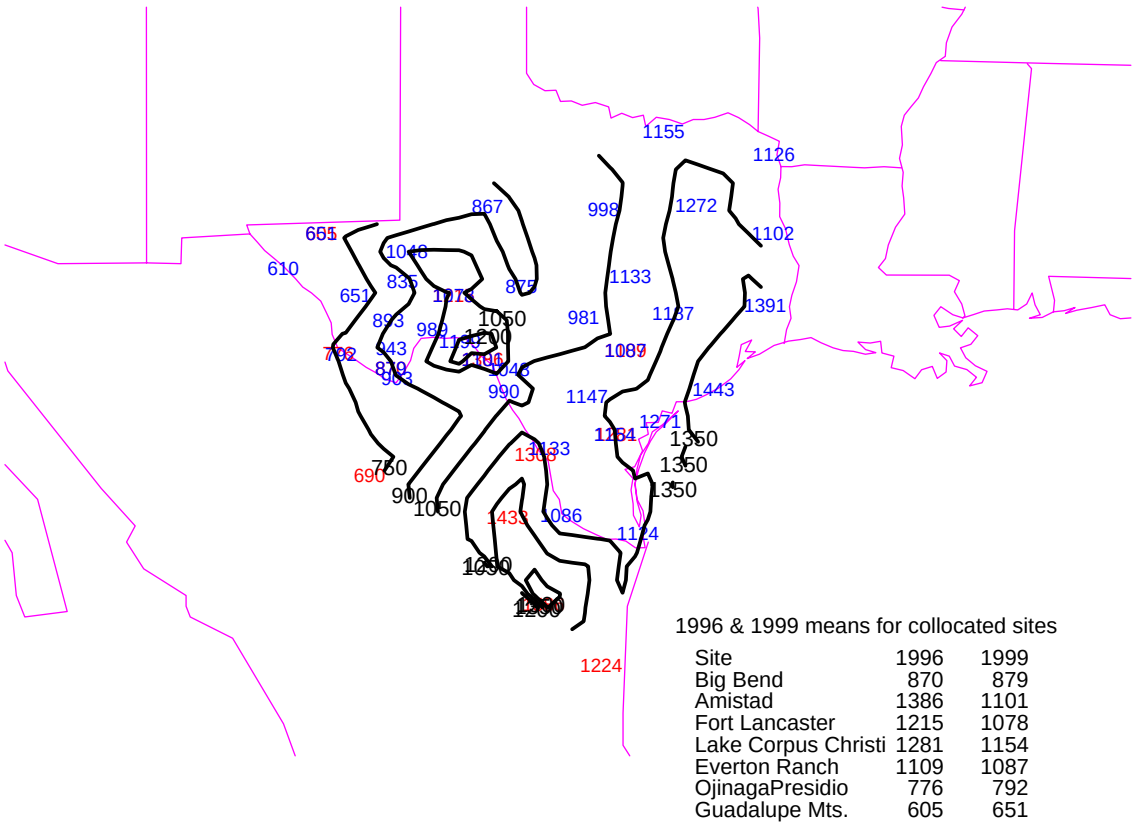

Figure 8-9. Overlaid mean sulfur concentrations during September and October 1996 and 1999. Sites listed in the bottom right corner are sites common to both years and the mean concentrations during each study period.

In general, mean fine sulfur across Texas decreases from east to west during September and October, but with a noticeable perturbation near and to the northwest of the Carbón I/II plants. Sulfur concentrations in northeast Mexico follow a similar east-west gradient, but with higher concentrations around the Monterrey area. The lower concentrations on the coast than inland in Mexico indicate that, although U.S. emissions may be transported across this area enroute to Big Bend, Mexican sources are certainly adding to the sulfur load in the airmass. Also, it is again evident by comparing the study-long (summer and fall) means in Figure 8-6 with the fall-only means in Figure 8-9 that the spatial patterns of sulfur within Texas vary seasonally. Northeast Texas has higher concentrations during July and August than during the fall, while sites closer to the Gulf Coast have similar concentrations during both seasons.

EOF analysis of the raw data cross product matrix for sulfur results in four factors (Figures 8-10 through 8-12 show EOFs 1–3) that cumulatively explain 82% of the variance. The factors were rotated using the Varimax criteria. The first rotated factor, explaining 33% of the variance, has highest values in the southwest and northeast corners of the state with lower values between. This indicates two likely source areas and transport pathways for sulfur for the days weighted highly for this pattern. First, sulfur is likely being transported into Texas from the

northeast or there are sulfur sources in the northeast corner of the state that influence the concentrations there. Also, sulfur is either being transported into Texas from the south or being generated in southwest Texas. The highest time weights for this pattern include the days of some of the highest concentrations at Big Bend including especially September 15, and to a lesser extent September 1, October 12, and the mid-August episode. This factor could represent local stagnation with light southerly flows yielding high concentrations in southwest Texas from nearby Mexican sources, while high concentrations in northeast Texas are due to local northeast Texas emissions or sources in nearby states. However, this pattern could also result from moderate wind speeds if wind directions in northeast Texas are arriving from the northeast while those in southwest Texas are from southerly directions. It's also possible that the lower concentrations in the center of Texas are due to conditions that caused enhanced deposition or reduced oxidation in this area.

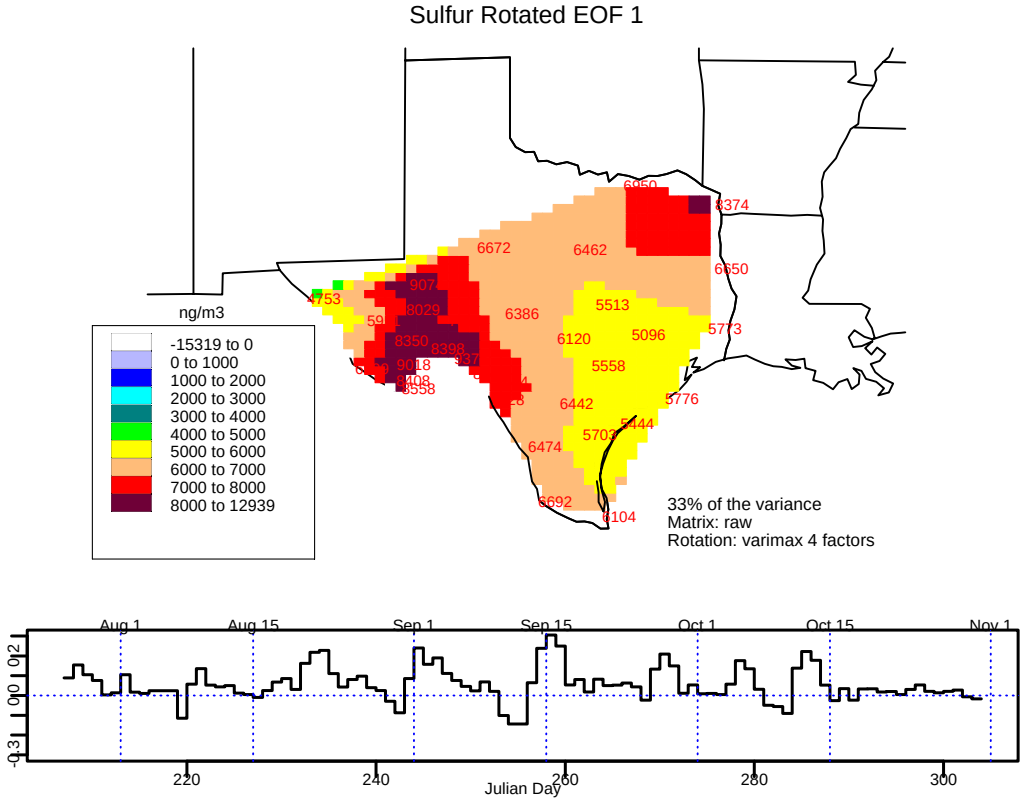

Figure 8-10. EOF 1 for sulfur.

The spatial pattern for rotated EOF 2, explaining 31% of the variance, is indicative of transport from northeast to southwest. This pattern has the strongest positive time weights on August 29–30, just before the high sulfur concentration at Big Bend on September 1. The highest value is in northeast Texas, with lower values all around. It is not possible to determine from EOF analysis alone whether this is because the source of the sulfate is in this location or whether the sources are primarily upwind, but the combined oxidation, transport, and deposition result in peak concentrations in this location. It seems most likely that the known sulfur sources

in northeast Texas are contributing to the sulfate load in the air being transported from east and northeast of the state.

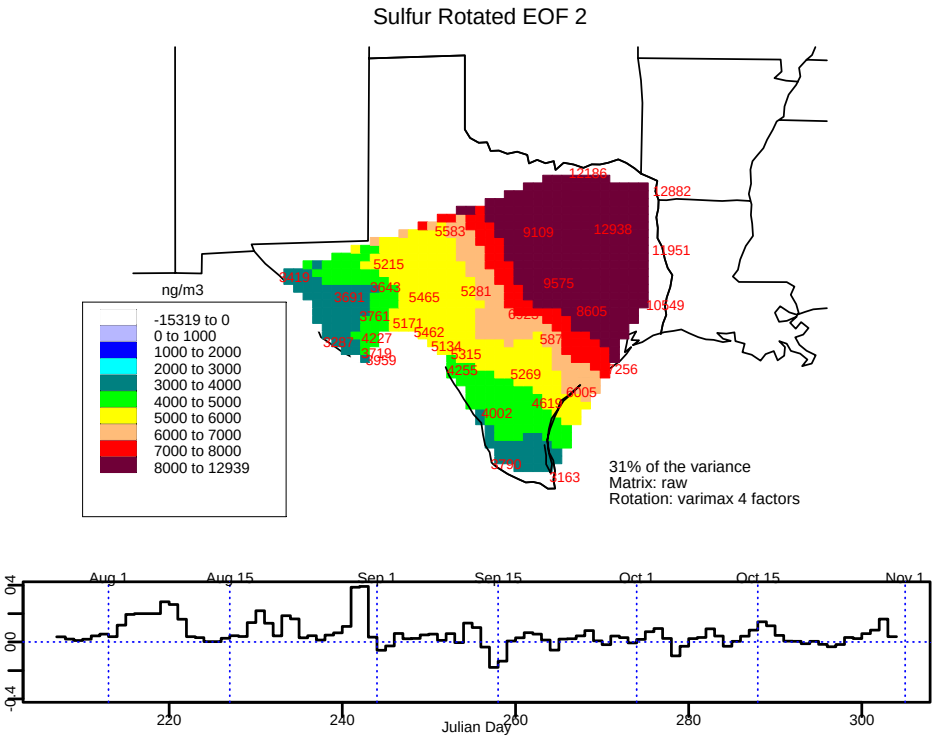

Figure 8-11. EOF 2 for sulfur.

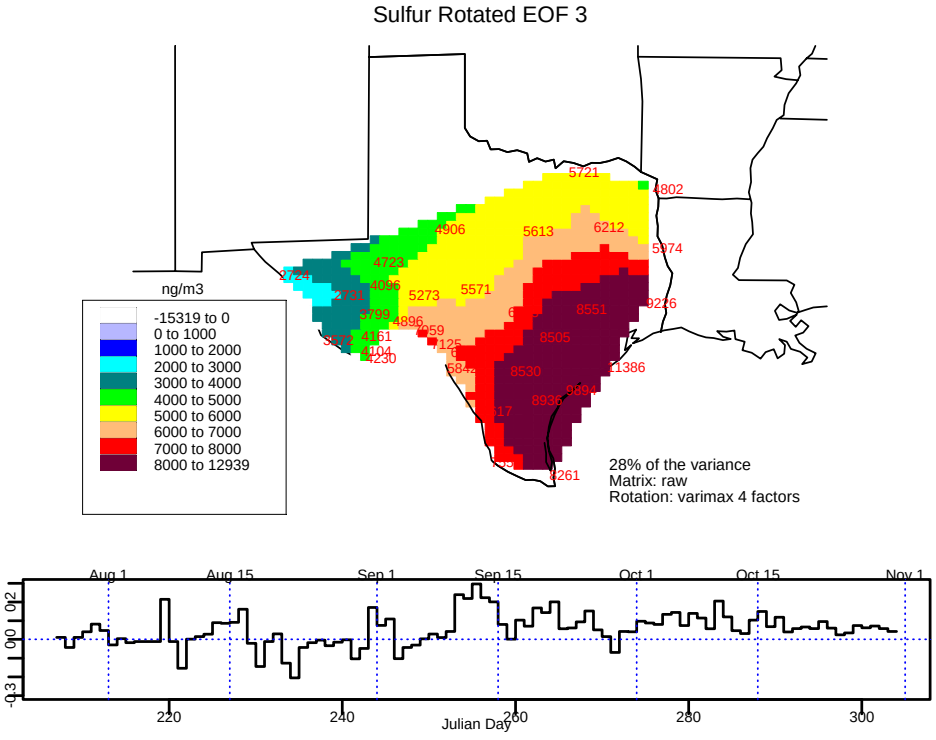

Figure 8-12. EOF 3 for sulfur.

EOF 3, explaining 28% of the variance, has highest values along the Texas Gulf Coast, suggestive of transport from the Gulf of Mexico or from the Houston area inland to central Texas. Highest time weights for this pattern are just prior to the September 15 episode at Big Bend.

The fourth factor explains only 3% of the variance and is not shown, but has highest concentrations in central Texas with lower values around the edges.

8.1.1.4 Iron

Spatial and temporal patterns of iron, representative of fine soil, are quite different from sulfur as illustrated in the time line of fine iron at Big Bend shown in Figure 8-1. By far the highest iron concentrations are during the summer and, in contrast to sulfur, mean iron concentrations are highest at the southernmost monitoring sites rather than at those in northeast Texas. While fine soil is, on average, less than 15% of the measured fine mass at Big Bend, it was greater than 50% during a few days early in the study. Figure 8-13 shows unrotated EOF 1 for iron, which explains 76% of the variance in the iron concentrations. Note that the only time factors significantly different from zero occur during July and early August. Rotating the iron factors resulted in four spatial patterns that all had high concentrations at southern sites. Previous analysis of historical particulate data at Big Bend [*Perry et al*., 1997; *Gebhart et al.*, 2001] has indicated frequent episodes of Saharan dust impacting the park during the summer. The spatial and temporal patterns in the BRAVO iron data suggest a similar phenomenon early in the BRAVO study, with the decreasing concentrations from south to north indicating the predominant transport pathway.

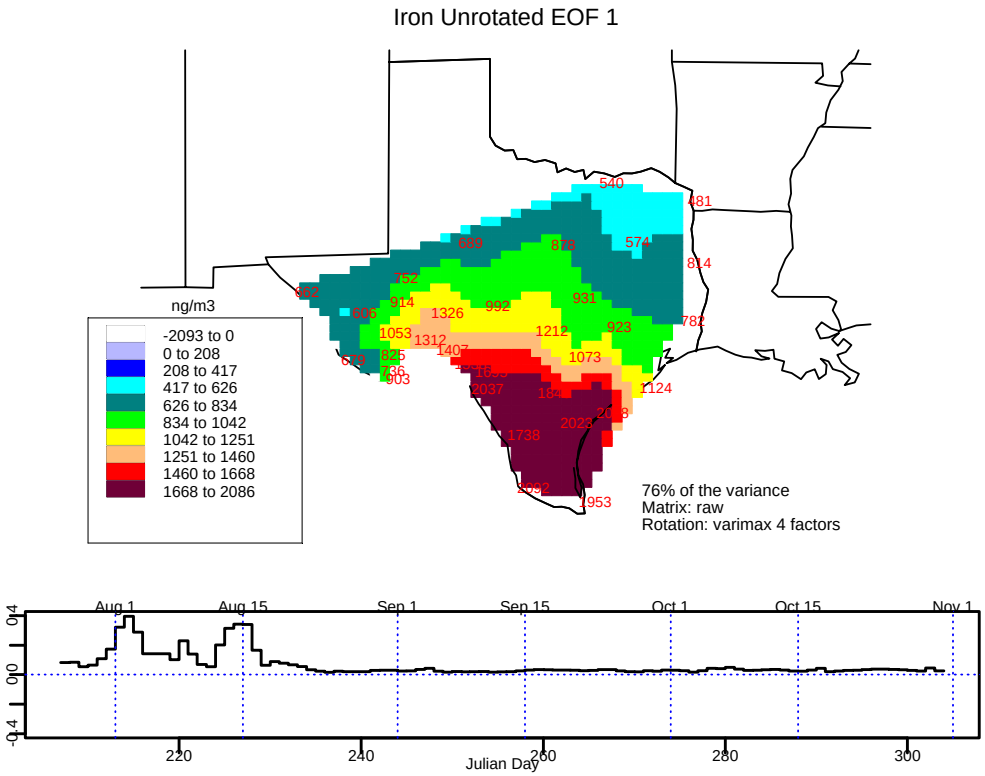

Figure 8-13. EOF 1 for iron.

Correlations of iron measured at Big Bend with iron measured at other BRAVO sites are 0.7 or higher out to approximately 200 km with some sites more than 300 km away having correlations this high. At several sites near and to the north of Big Bend, including San Vicente (0.961), Monahans Sandhills (0.930), McDonald Observatory (0.921), Fort Stockton (0.917), and Marathon (0.890), the correlations were 0.9 or greater. Even the most distant sites in northeast Texas have correlations of at least 0.25.

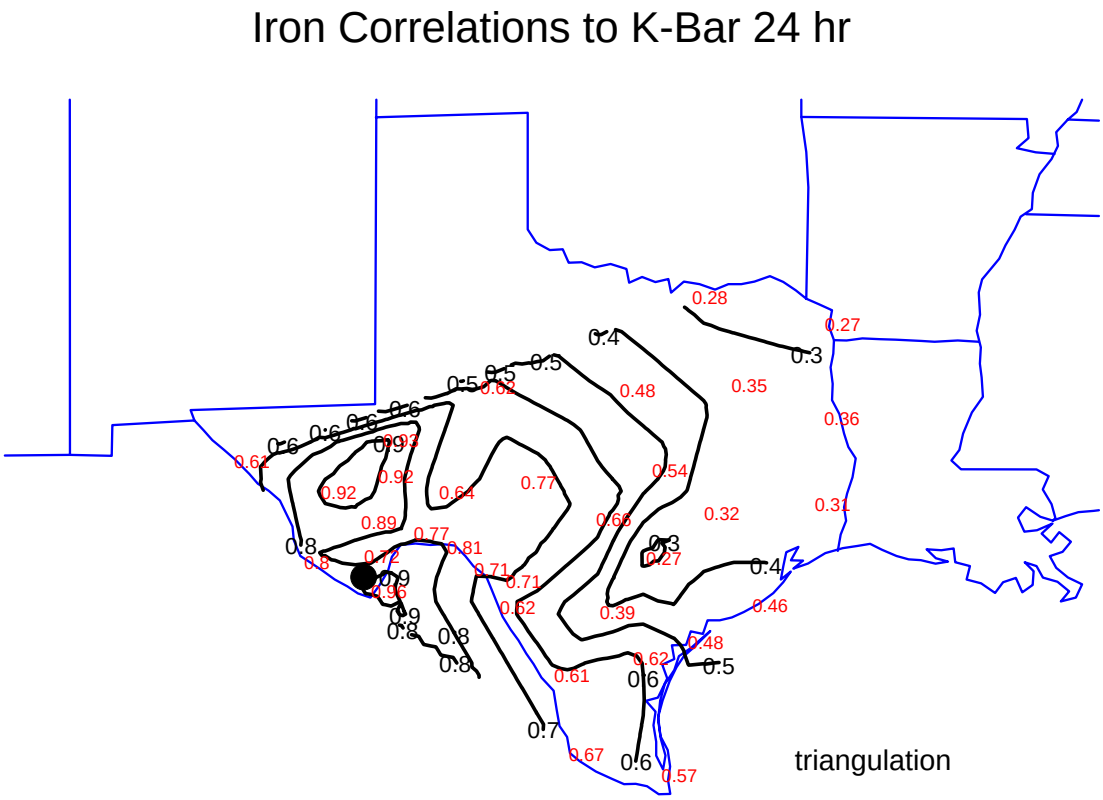

Figure 8-14. Correlations of iron measured at Big Bend to iron measured at other BRAVO sites.

High Al/Ca ratios have been associated with Saharan dust, which is known to be lower in Ca than North American soils [*Perry et al.*, 1997; *Gebhart et al.*, 2001]. During BRAVO, Al/Ca ratios were never greater than 1 at Big Bend after August 22, but were often between 2 and 3 during the early half of the study, with values greater than 3 on July 8, and August 3, 4, and 18. Figure 8-15, shows aluminum vs. calcium for all sites. Summer values are shown in red and fall values in black. This graph shows a clear separation between the seasons with calcium-poor fine soil concentrations being common throughout Texas during the summer, but not during the fall. Calcium concentrations at Big Bend are relatively constant throughout the study, indicating the local soil concentration of this element is relatively constant. During the Saharan dust episodes of the summer, Ca does not increase, but the other soil elements do. The correlations between iron and other elements associated with soil, Si, K, Al, Ti, and Sr, are all 0.9 or higher for Big Bend alone. For all BRAVO sites combined, the same is true except the correlation between Fe and Ti is slightly lower at 0.83. The Fe to Ca correlation is 0.68 at Big Bend and 0.57 for all BRAVO sites combined. Therefore scatter plots of almost any soil element against calcium would be similar in pattern to that shown in Figure 8-15. Aluminum is shown for consistency

with earlier literature, but Fe or Si would have fewer values below detectable limits.

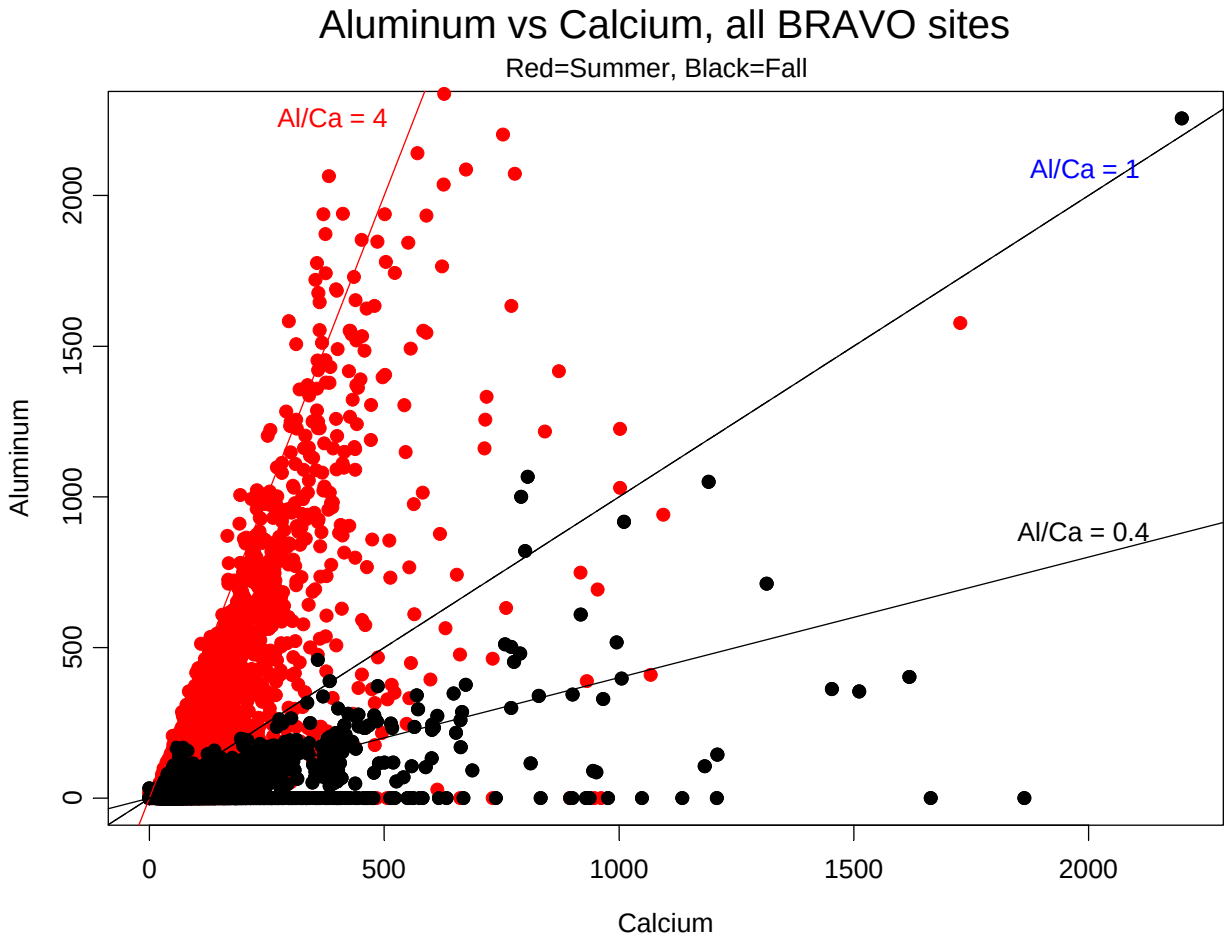

Figure 8-15. Aluminum vs. calcium (ng/m^3). Several lines have been added for reference.

Mean concentrations of iron during September and October 1996 were different enough from means during 1999 that it was not reasonable to plot them on the same map as was done for sulfur. All sites except Presidio/Ojinaga had 15–40% higher mean iron concentrations during fall 1999 than fall 1996.

8.1.1.5 Selenium

Selenium is of interest due to its association with coal-burning sources such as electric generating stations [*Olmez et al.*, 1988; *Malm and Gebhart*, 1997; *Gebhart and Malm*, 1997] and because it is more highly correlated with sulfur at Big Bend than are any other trace elements (0.79 during BRAVO, 0.73 during the 1996 Scoping Study—see section 1.2). During the 1996 Scoping Study, selenium was found to be indicative of airmasses originating in the United States as opposed to Mexico [*Gebhart et al.*, 2000]. Figure 8-16 shows the time lines of selenium and several other trace elements at Big Bend during BRAVO. The highest selenium concentration (0.83 ng/m^3) at Big Bend was measured on October 12 during one of the four highest sulfur episodes. Selenium was also moderately high (0.63 and 0.61 ng/m^3) on September 15 and August 21 during two other high sulfur concentrations, but much lower (0.38 ng/m^3) on

September 1 when the maximum sulfur was measured. This may indicate that the sulfur episodes of October 12, September 15, and August 21 were more heavily influenced by coal-burning sources than was September 1. Back trajectories support this hypothesis. Airmasses arriving at Big Bend on September 1 generally bypassed the lignite belt coal-fired plants in northeast Texas, while airmasses arriving during the remaining three episodes are more likely to have passed over that region. (See Appendices 4b, c, and d for daily trajectory plots.)

Figure 8-17 shows the mean selenium concentrations during BRAVO. The highest mean (1.03 ng/m^3) was at Purtis Creek in northeast Texas with lower concentrations at sites in all directions. This indicates sources of selenium within Texas. In general the mean selenium concentrations are higher in the eastern part of the state than in the western. There are also local maxima at Eagle Pass and Everton Ranch with the Eagle Pass value indicating that the Carbón I/II plants are also noticeable sources of selenium.

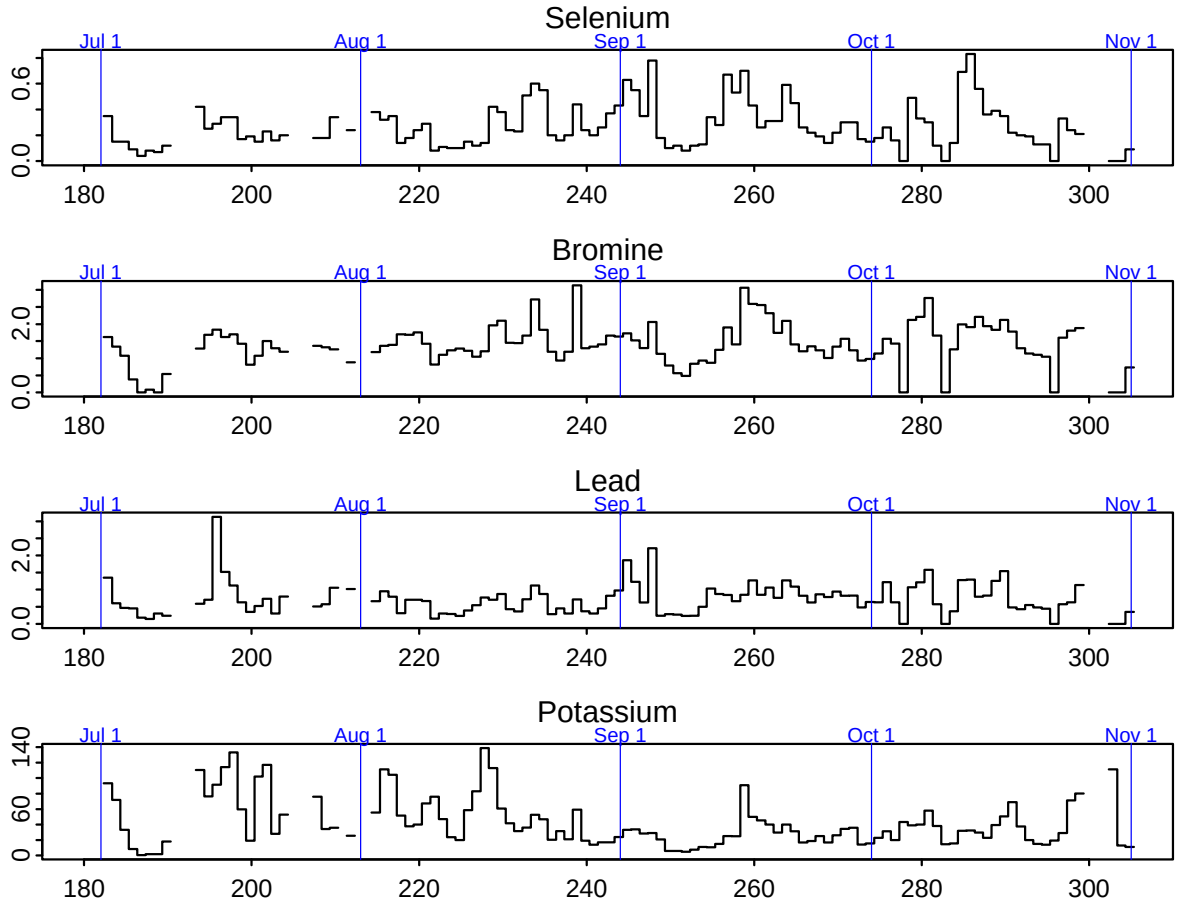

Figure 8-16. Time lines of several trace elements (ng/m^3) measured at Big Bend National Park during BRAVO. Labels on the x-axis are the day of the year. The vertical blue lines show the beginning of each month.

The spatial patterns for the four highest sulfur episodes at Big Bend are shown in Figures 8-18 through 8-21. On August 21 and September 1 there are selenium concentrations greater than 1.9 ng/m^3 in northeast Texas with generally lower concentrations all around. On October

12 the highest measured value is 1.54 ng/m^3 at Hagerman, west of and lower than the peak concentrations on August 21 and September 1. On September 15, Se concentrations are generally lower across the state, but still with the highest concentration, 1.22 ng/m^3, in northeast Texas.

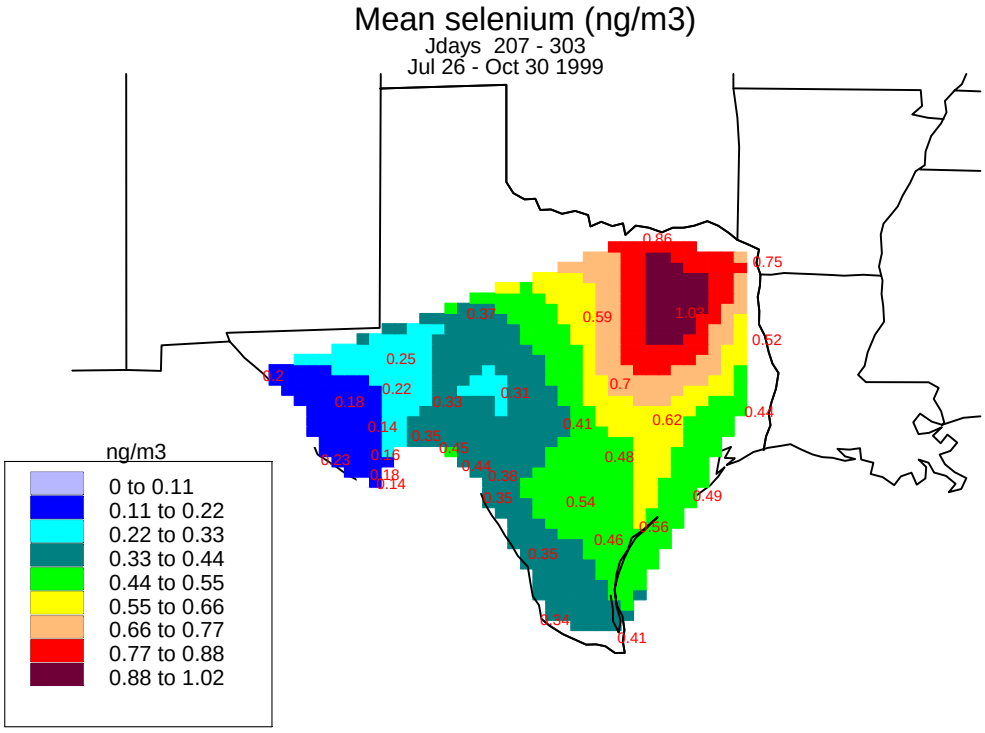

Figure 8-17. Mean selenium concentrations.

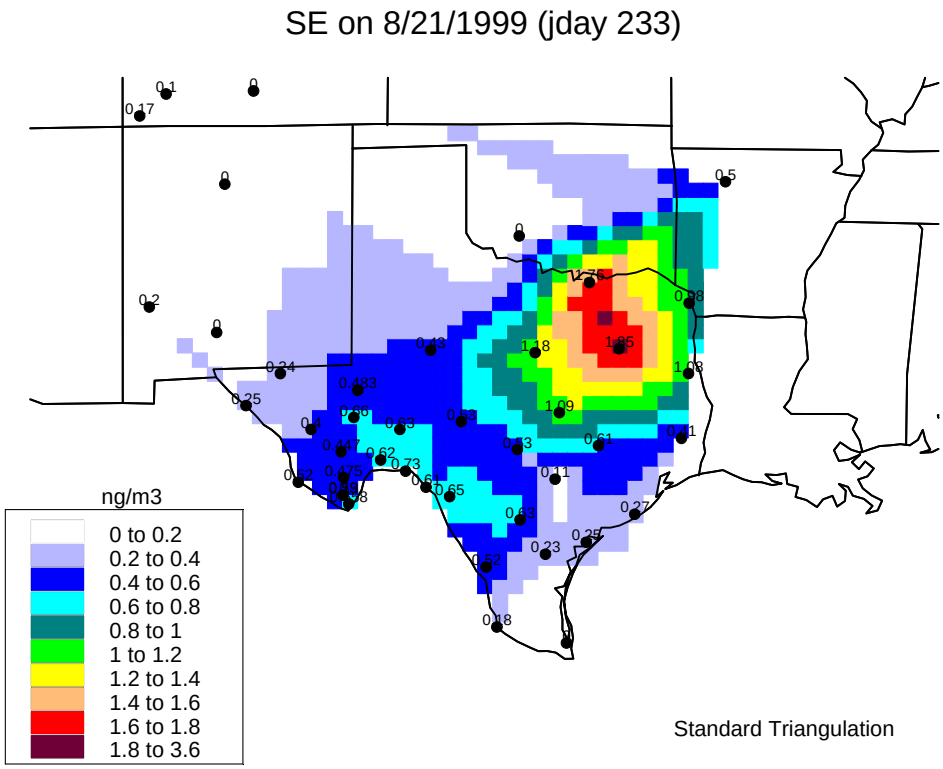

Figure 8-18. Selenium concentrations on August 21.

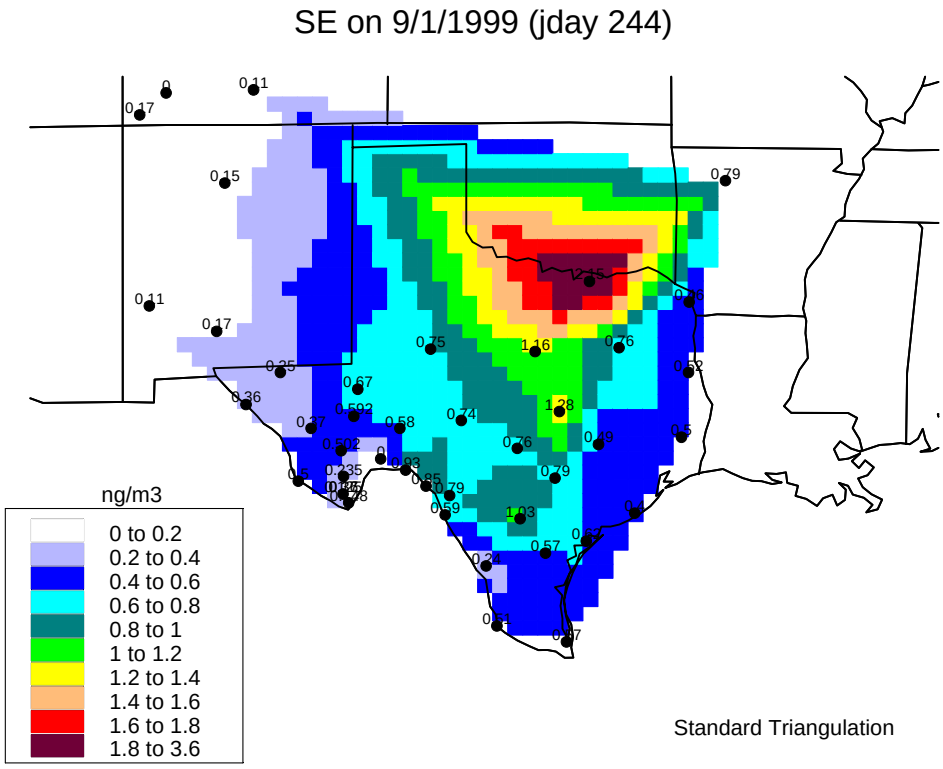

Figure 8-19. Selenium concentrations on September 1.

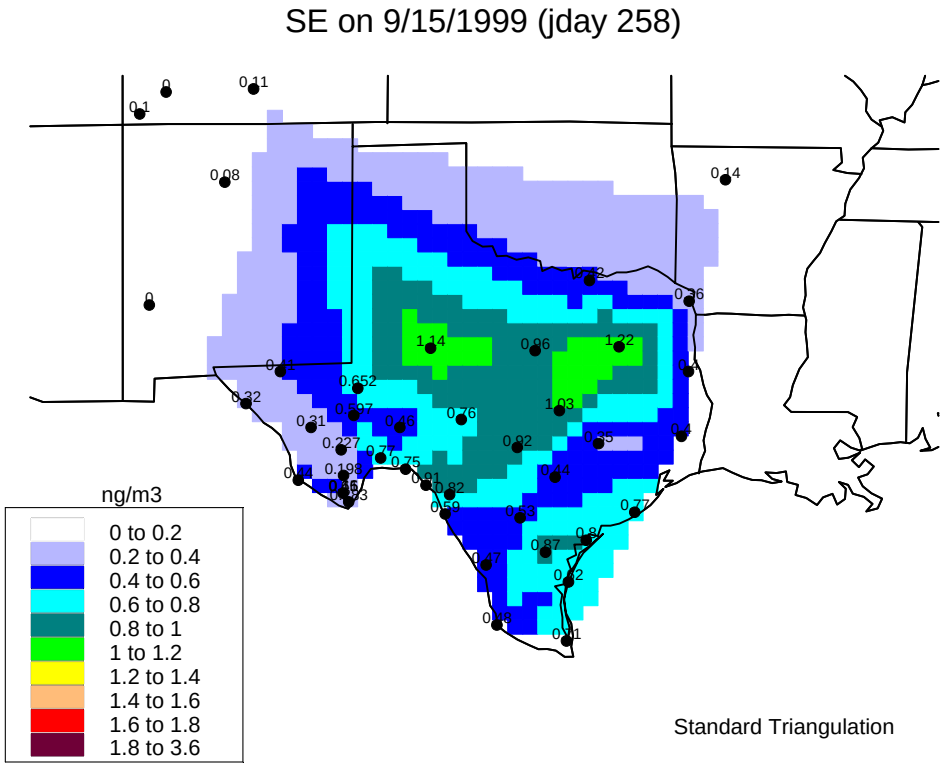

Figure 8-20. Selenium concentrations on September 15.

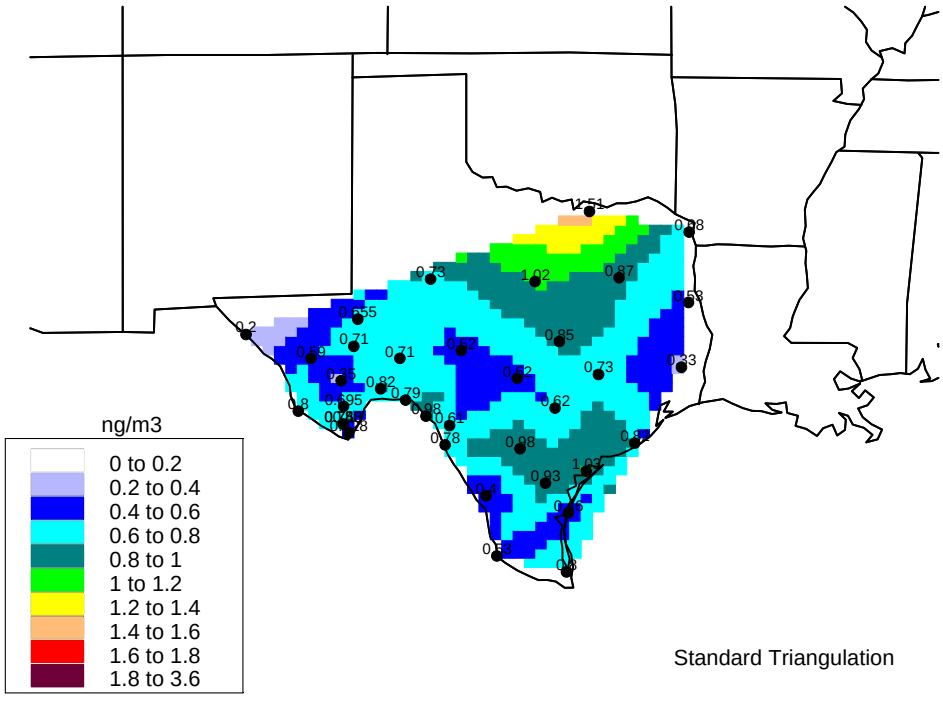

Figure 8-21. Selenium concentrations on October 12.

Correlations of selenium measured at Big Bend to selenium measured at other BRAVO sites, shown in Figure 8-22, are much lower than the corresponding correlations for sulfur, showing that selenium is less spatially homogeneous than sulfur. Correlations greater than 0.5 are generally seen only at sites within about 200 km and selenium measured at sites in northeast Texas are negatively correlated with selenium measured at Big Bend. Because selenium is a primary species, while sulfate is secondary, the spatial patterns in selenium are more indicative of sources of selenium than the spatial patterns in sulfate are of locations of SO_2 sources. Spatial patterns in sulfates are complicated by the locations of clouds, oxidants, and other factors that influence the locations of chemical processes.

EOFs (not shown) and correlation maps similar to Figure 8-22 for other sites also indicate the selenium measured across Texas is generally not highly correlated across the state. Monthly box plots of selenium for four different sections of Texas, shown in Figure 8-23, also illustrate the spatial differences in selenium. Northeast Texas (upper right), as seen in the spatial maps, has the highest concentrations and generally there are high values during all three months, with the greatest median in August and a maximum in October. In southeast Texas (lower right) selenium concentrations are much larger during October than during other months, indicating concentrations influenced by the differing transport patterns across the months. Selenium concentrations measured around Eagle Pass (upper left) and Big Bend (lower left) are much lower than in eastern Texas and without much monthly variation, though values in the Eagle Pass area, like values in southeast Texas, are highest during October.

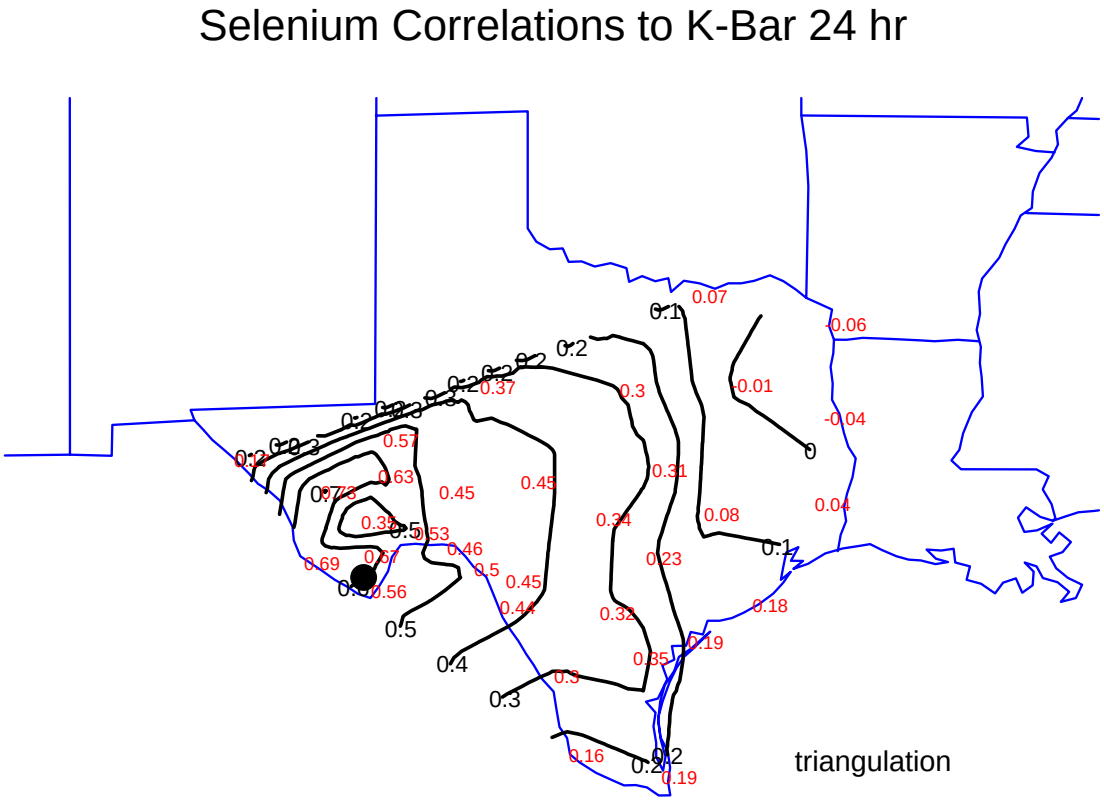

Figure 8-22. Correlations of selenium at Big Bend to selenium at other sites.

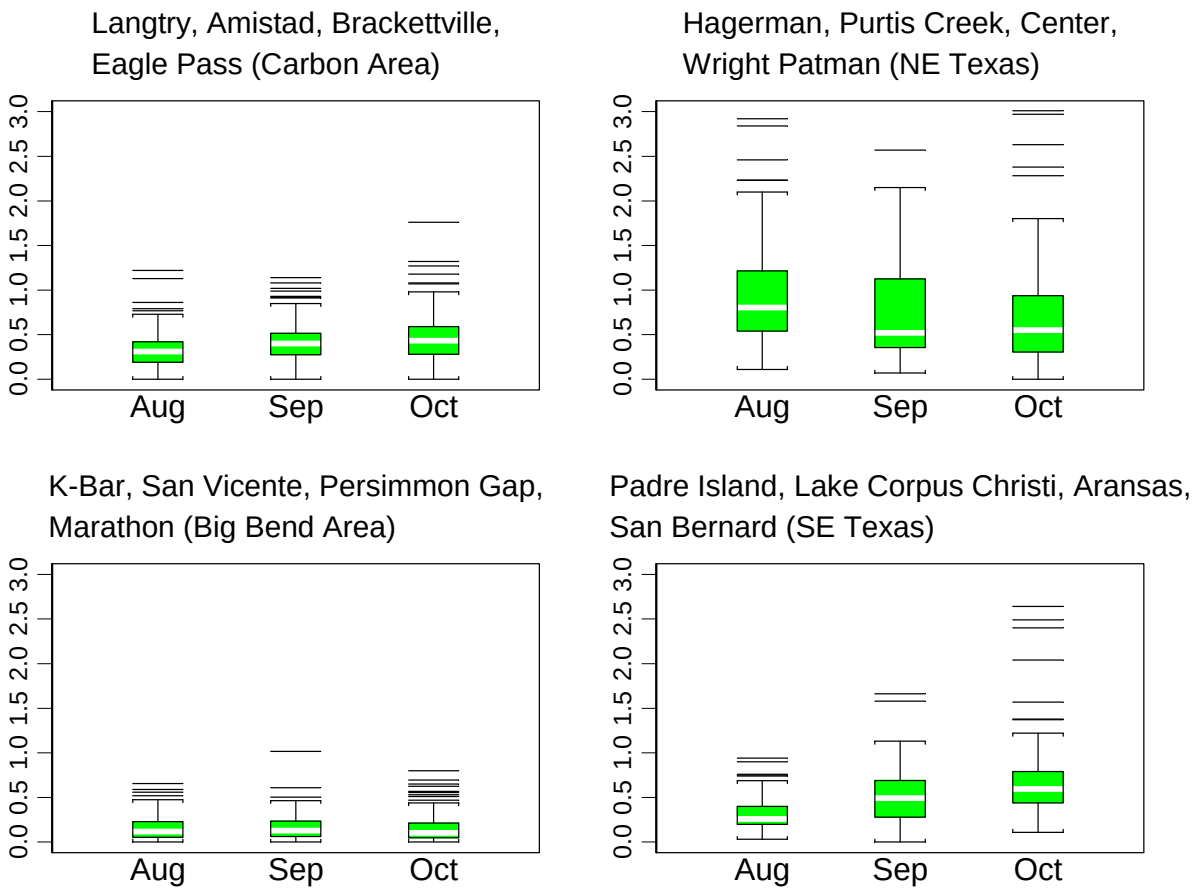

Figure 8-23. Monthly box plots of selenium (ng/m^3) for four different sections of the monitoring domain.

8.1.1.6 Vanadium & Other Tracers of Mexico

Vanadium concentrations, as well as lead, zinc, nickel, and manganese, were much higher at sites in Mexico than in Texas during the 1996 pilot study [*Gebhart et al.*, 2000]. Figure 8-24 shows the time lines of all of these species except lead at Big Bend during BRAVO. Lead was shown previously in Figure 8-16.

There is an unusual trace element day, October 29, near the end of the study when back trajectories indicate transport from northeast Mexico early in the day, with a wind shift due to a frontal passage and trajectories from the west, including both northern Mexico and southern Arizona and New Mexico, later in the day. October 29 had the highest coarse mass concentration measured at Big Bend during BRAVO, probably due to local blowing dust associated with high wind speeds. There were also high concentrations of fine K, V, Mn, and Br; only moderate concentrations of fine S, OC, EC, and Fe; and very low Se and Ni. The high V and Mn are consistent with transport from Mexico, though the high correlations of Mn with other soil elements indicate that Mn is usually mostly due to dust. Organic carbon, Br, and K can be indicators of smoke. But while non-soil K measured on October 29 at Big Bend was 30 ng/m^3, the 6th highest value at this site during BRAVO, the OC/EC ratio, another indicator of smoke, was only at about the 60th percentile for this site at 6.5. The carbon fractions O3 and O4 were higher than usual, but all other carbon fractions had moderate or lower concentrations on

this day. The mixed smoke indicators may be because there was smoke present, but perhaps only during either the early or the later half of the day and the mid-day wind shift makes the 24-hour concentrations difficult to interpret.

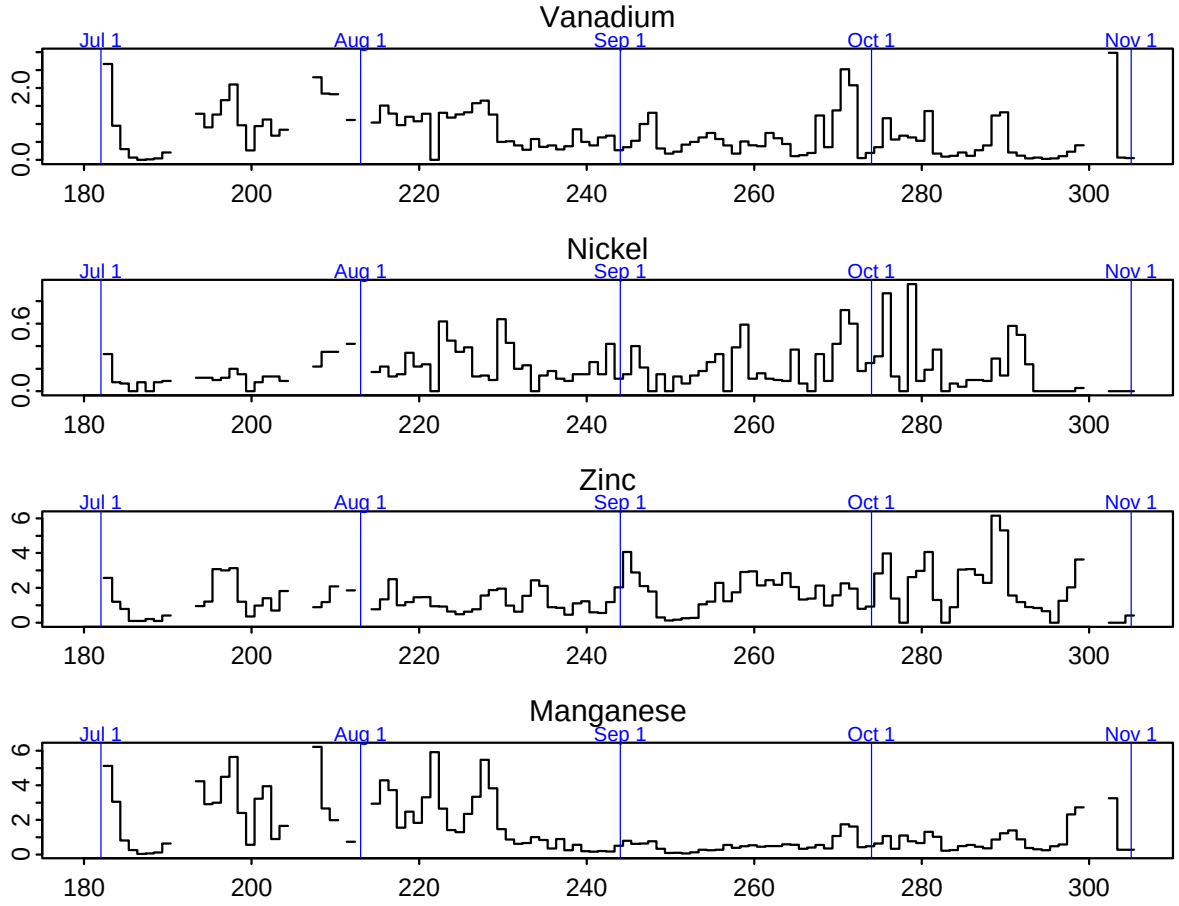

Figure 8-24. Time lines of several trace elements (ng/m^3) at Big Bend. Labels on the x-axis are the day of the year. The vertical blue lines show the beginning of each month.

Though there were no monitoring sites in Mexico during BRAVO, the concentrations of vanadium during BRAVO were mostly below minimum detectable limits except at sites near the Mexican border. Like iron, the highest concentrations of vanadium also occurred mostly during the summer rather than fall. Figure 8-25 illustrates mean vanadium during BRAVO showing the general south to north gradient and also generally higher values along the Texas Gulf Coast than inland in Texas. The combination of the spatial pattern of highest concentrations along the Mexican border, along with the temporal pattern of higher values during summer than fall, both indicate that vanadium is more likely to arrive at Big Bend from Mexico than from the United States. Because vanadium was so often below detectable limits, little further analysis is possible.

Nickel and vanadium, though both previously associated with transport from Mexico and both associated with residual oil combustion, are not highly correlated at Big Bend. Nickel was highest at Big Bend during August to early October in contrast to vanadium which was highest during July. The back trajectory patterns for high vanadium and high nickel concentrations are somewhat similar in that both are associated with transport from Mexico, but high nickel days

have more northerly transport across the Gulf and along the U.S. Gulf Coast, while high vanadium days do not. Airmasses associated with high vanadium arrive from farther south in Mexico. Non-correlation between nickel and vanadium has also been observed in the northeastern U.S. and may be explained by high variability of the ratios of these elements in different crude oil stocks. [*Poirot*, 2004]

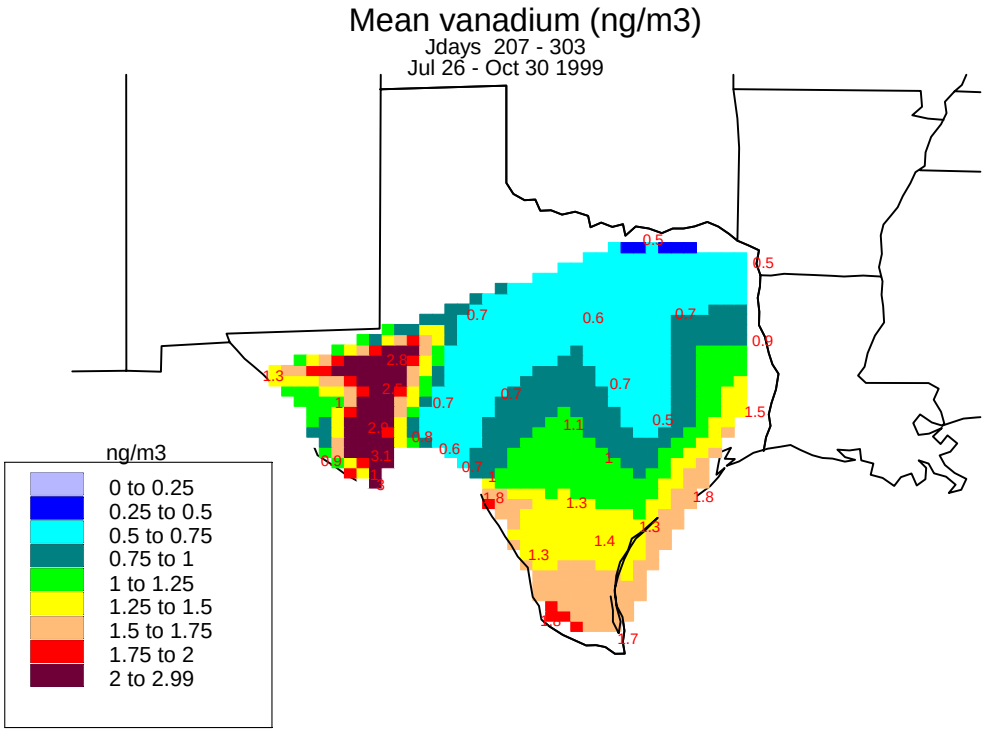

Figure 8-25. Mean vanadium.

8.1.1.7 Sodium

During the 1996 Scoping Study, sodium was of interest as a trace element due to its high correlation with sulfur at Big Bend (0.661). However, during BRAVO sodium (shown in Figure 8-26) had almost no correlation with sulfur (0.039), though relatively high sodium (244 ng/m^3) was measured at Big Bend on September 1 which was the day of the maximum sulfur concentration there. The highest sodium concentrations at Big Bend during BRAVO were very early in the study, June 29–July 2 and July 16, when the concentrations were 318–392 ng/m^3. Examination of the sodium concentrations at Big Bend measured in the IMPROVE network for 1988–2002 also shows that the highest concentrations generally occur during the summer, especially May through July, while the lowest concentrations are during the winter.

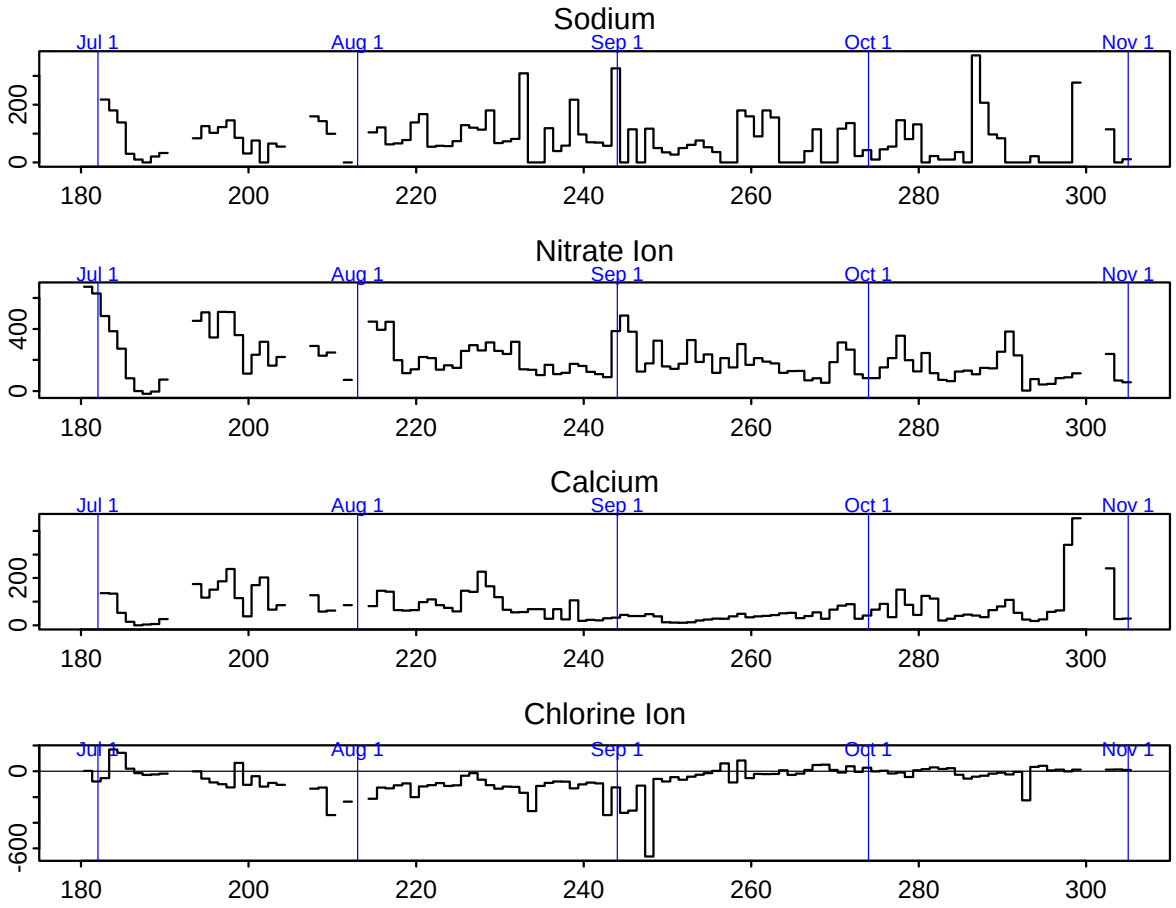

Figure 8-26. Time lines of Na, NO^-_3, Ca, and Cl^- (ng/m^3) at Big Bend. Labels on the x-axis are the day of the year. The vertical blue lines show the beginning of each month.

Spatially, the highest mean sodium concentrations during BRAVO were at sites long the Gulf Coast (Figure 8-27), suggesting transport across the Gulf of Mexico and indicating sea-salt as a source, though an additional sodium source south of the BRAVO area, as hypothesized during the pilot study, cannot be ruled out by the spatial patterns alone. *Collett et al.* [2001] found that during BRAVO the sum of sodium and calcium was highly correlated with coarse particle nitrate measured at Big Bend, suggesting that soil and sea salt particles provide a surface for condensation of nitric acid.

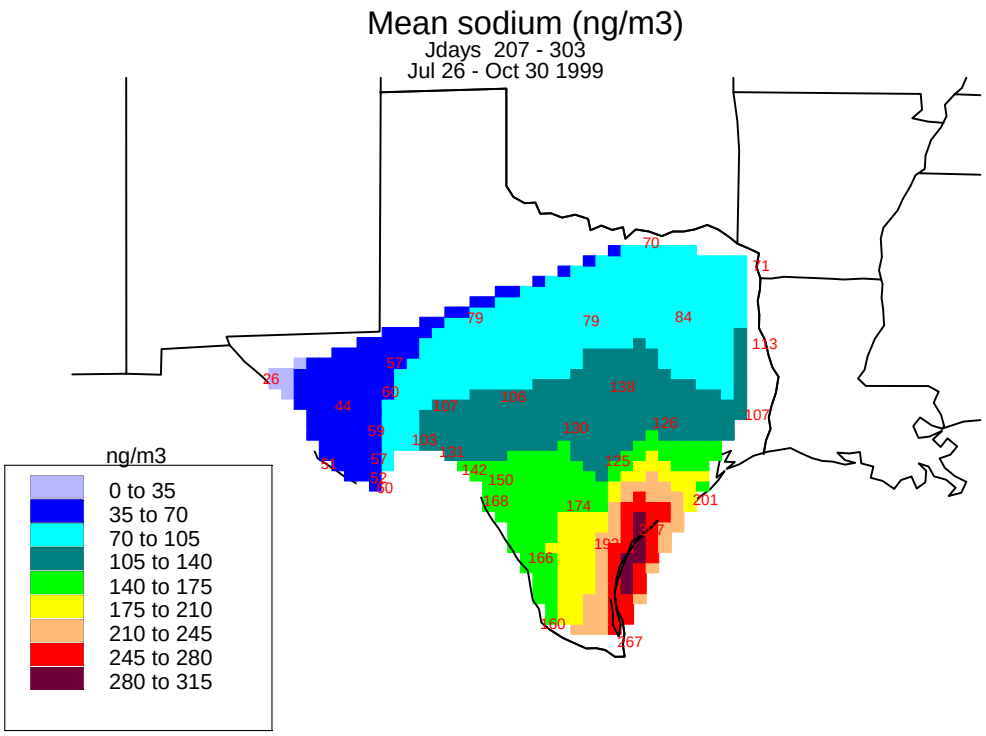

Figure 8-27. Mean sodium concentrations.

For the seven sites which had measurements during both the 1996 and 1999 studies, the 1999 concentrations during September and October were all 50–80% lower than in 1996 as shown in Table 8-1. Also, the number of concentrations below the minimum detection limit (MDL) was much higher during BRAVO than during the scoping study. In 1996 only 2% of the non-missing sodium was below MDL, while in BRAVO it was 46%.

The IMPROVE sodium data, collected at Big Bend since 1988 (Figure 8-28), does not show a long term decline, but does indicate that sodium concentrations measured during 1996 were unusually high.

The reasons for the highly different concentrations in 1996 and 1999 aren't known but there are at least three possibilities. 1) Transport patterns influencing sodium concentrations at Big Bend during the two studies may have been different, and in particular, transport of airmasses across the Gulf of Mexico to Texas may have been less frequent during 1999 than during 1996. Since sodium tends to be highest during the summer, it's possible that summer-like meteorology persisted longer than usual into the fall during 1996; 2) Sodium emissions or the sodium to sulfur ratios in emissions in one or more important source regions are variable and for some reason were higher than usual during 1996; or 3) Some important aspect of the measurement and/or analysis techniques for sodium may have been different during the two study periods. PIXE was used to analyze the filters for sodium in 1996. PIXE was also used at all sites while both PIXE and XRF were used at Big Bend during BRAVO. Either the first or third scenarios seem more likely than the second.

Table 8-1. Mean sodium concentrations (ng/m3) during the 1996 Scoping Study and during September and October of 1999 during BRAVO. Values in parentheses are the means with the zeros (below MDL) removed.

Site	Mean Na September & October 1996	Mean Na September & October 1999	Change (1999–1996)	% Change (Change/1996)
Big Bend	118	42 (77)	-76	-64%
Amistad	207	100 (153)	-107	-52%
Ft. Lancaster	163	95 (142)	-68	-58%
Lake Corpus Christi	318	164 (182)	-154	-48%
Everton Ranch	184	79 (119)	-105	-57%
Ojinaga/Presidio	212	44 (89)	-168	-79%
Guadalupe Mts.	100	25 (65)	-75	-75%

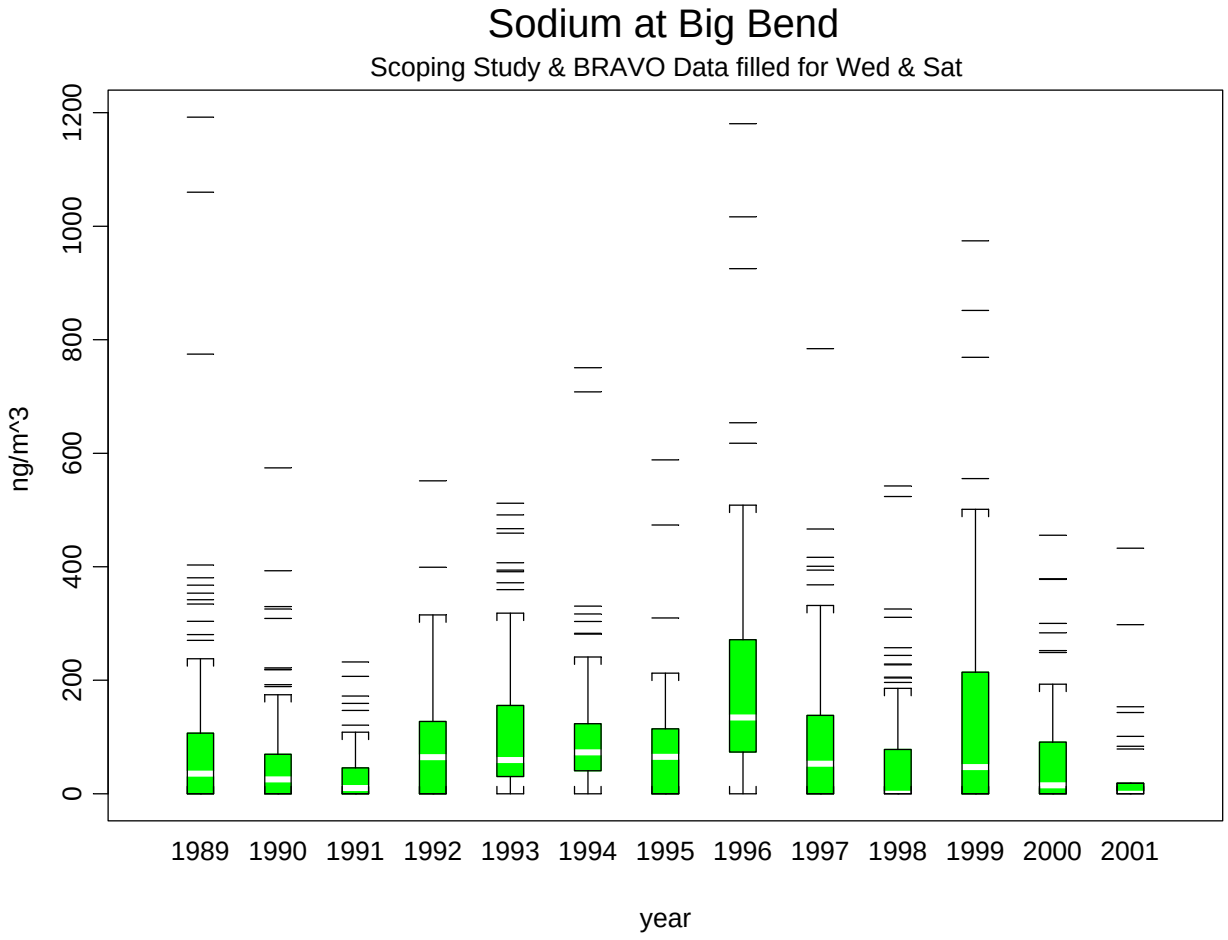

Figure 8-28. Box plots of sodium concentrations at Big Bend by year from the IMPROVE network.

8.1.1.8 Bromine

After selenium, the trace element next most highly correlated with sulfur at Big Bend during BRAVO was bromine. Correlations between sulfur and bromine were 0.57 during

BRAVO and 0.34 during the 1996 Scoping Study. The sulfur episodes on September 15 and August 21 were associated with high bromine, though the sulfur episodes of September 1 and October 12 were not. Spatial patterns of mean bromine (Figure 8-29) show highest bromine concentrations at sites along the Gulf Coast. The site with the highest mean concentration of bromine (3.13 ng/m^3) was at San Bernard, just south of Houston, the lowest (1.375 ng/m^3) at McDonald Observatory, and second lowest (1.41 ng/m^3) at Big Bend. Sites north and west, though farther from the Gulf, had higher bromine concentrations than Big Bend. A similar spatial pattern was seen in 1996. For most of the sites common to both studies, the mean fall bromine concentrations were similar. A combined 1996 and 1999 spatial pattern for September and October is shown in Figure 8-30.

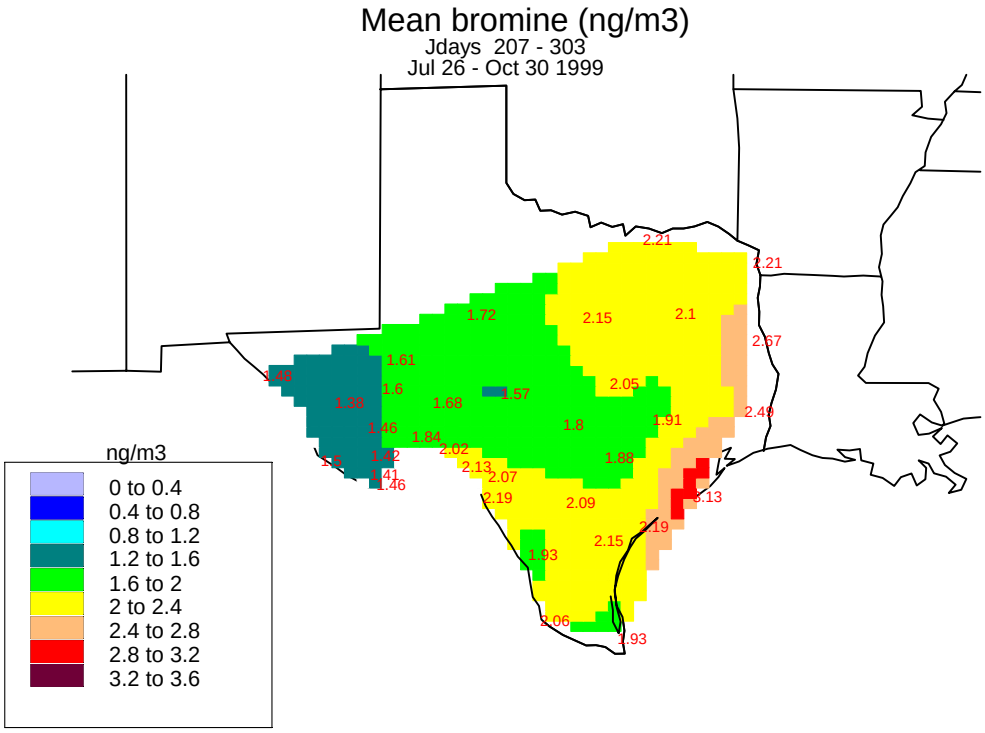

Figure 8-29. Mean bromine concentrations.

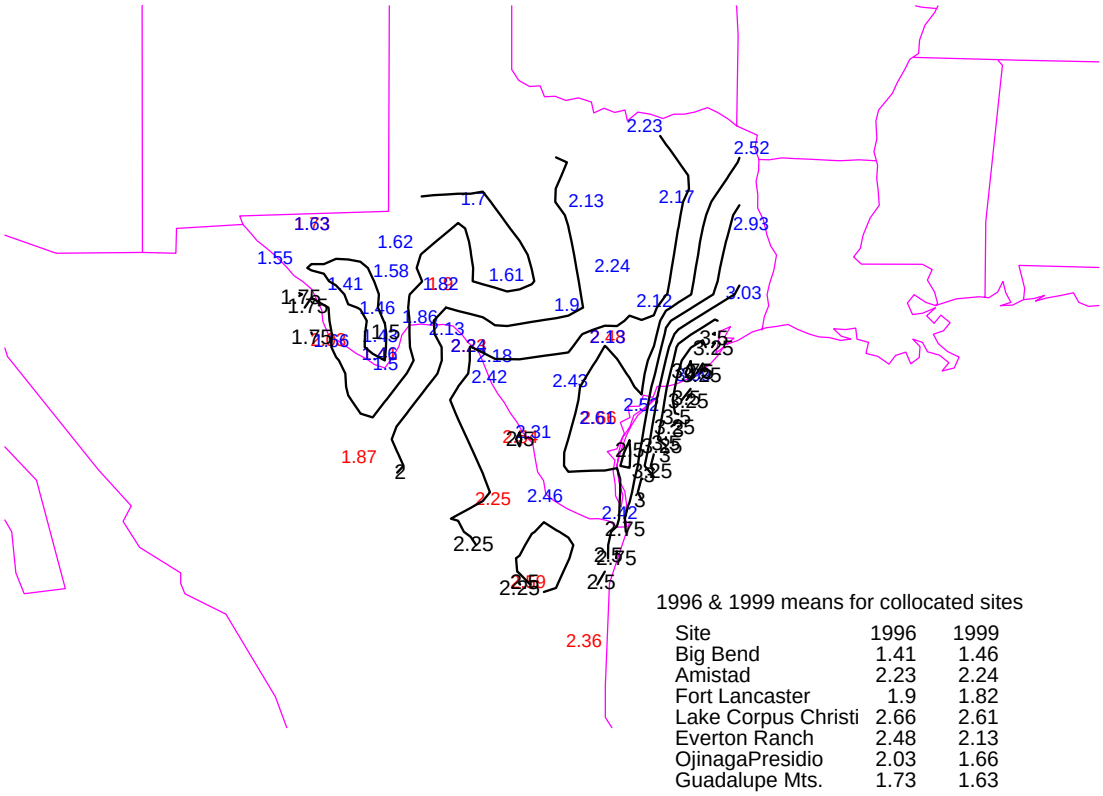

Figure 8-30. Combined 1996 and 1999 spatial pattern for Bromine.

8.1.1.9 Lead

Lead concentrations were much higher in Mexico than in Texas during the 1996 study [*Gebhart et al.*, 2000]. Previous analysis of lead concentrations collected at Big Bend since 1988 [*Gebhart et al.*, 2001] show that lead at Big Bend is highest during October–December and lowest during the summer. Also, back trajectory analysis of both the historical data and the 1996 Scoping Study data showed that lead concentrations were higher when airmasses were transported to the park from Mexico than when they were from the U.S. except during July and August when the reverse was true.

Mean lead concentrations during BRAVO, shown in Figure 8-31, show two local maximums, one in northeast Texas and another on the Texas-Mexico border at Eagle Pass.

Lead concentrations measured at Big Bend are negatively correlated with lead measured in the northeast half of the study area and no sites had correlations greater than 0.5 with the measurements at Big Bend indicating little spatial homogeneity across Texas and also indicating different sources of lead at Big Bend than in northeast Texas.

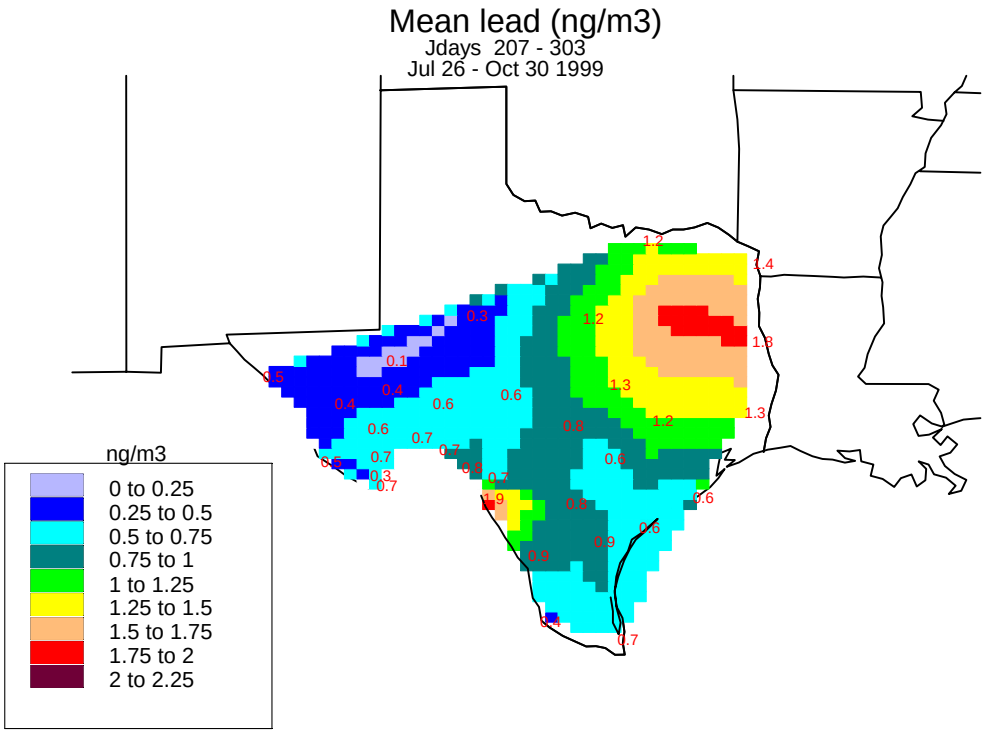

Figure 8-31. Mean lead concentrations.

Lead concentrations at Big Bend as measured in the IMPROVE network have dropped dramatically since measurements were begun in 1988 (see Figure 8-32). During 1988–1991 annual mean concentrations ranged from 2–3 ng/m^3, with maximums of 9–11 ng/m^3, while since 1997 mean concentrations have been 0.6–1.1 ng/m^3, with maximums of 3–7 ng/m^3. Comparing data from the BRAVO study to data from sites collocated in the 1996 study shows that the decline in lead occurred throughout the southern half of Texas. In 1999 the mean lead concentrations at the 7 collocated sites were 60–75% lower than at the same sites in 1996.

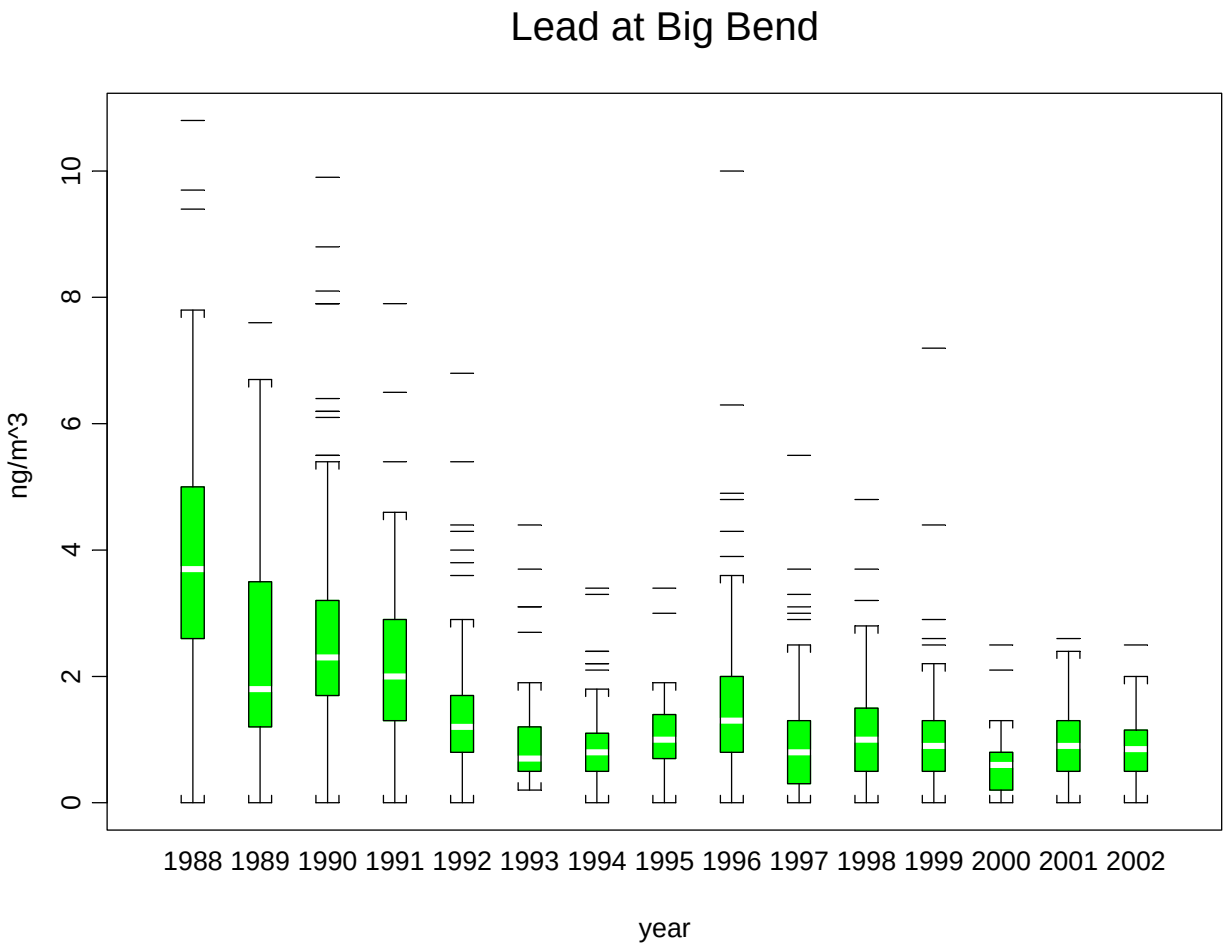

Figure 8-32. Box plots of lead at Big Bend by year.

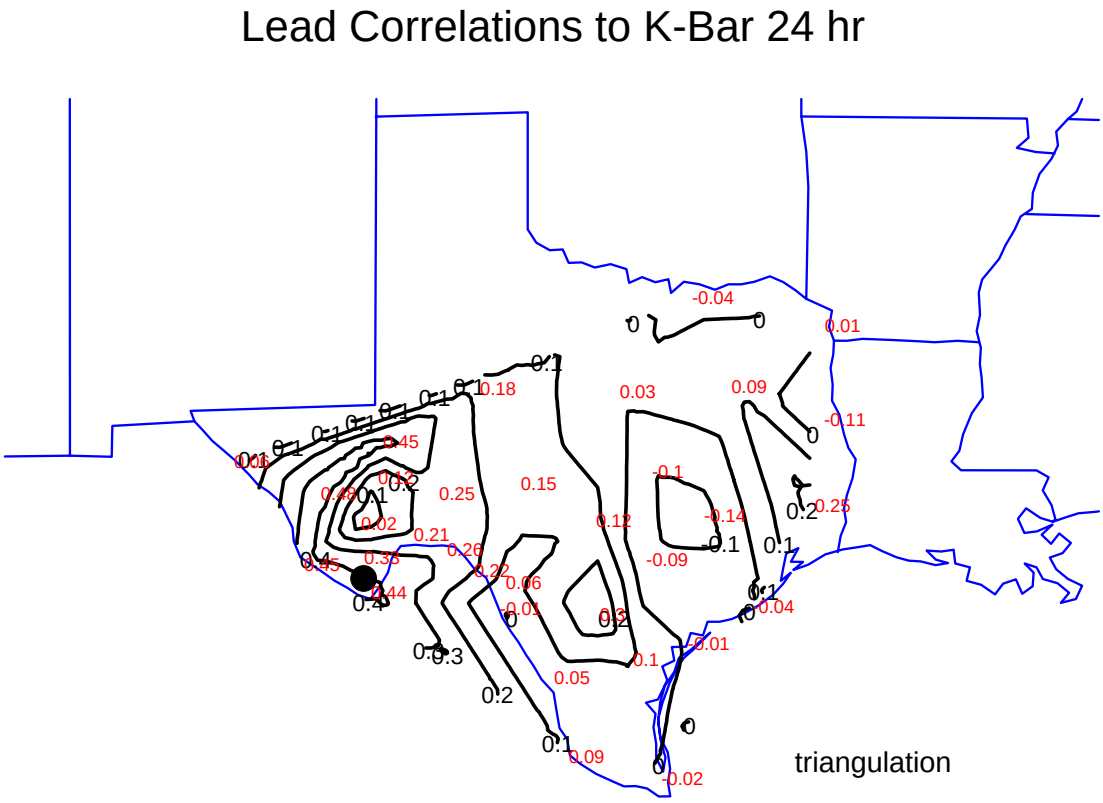

Figure 8-33. Correlations of lead at Big Bend to lead at other BRAVO sites.

8.1.1.10 Discussion of Spatial and Temporal Patterns

Examination of the spatial and temporal patterns in several fine particulate species measured during BRAVO suggests that there are unique sources for different aerosol types and that transport patterns are seasonal with more transport from Mexico to southern Texas during the summer than during the fall. Sulfur is of interest due to its large contribution to fine mass and light scattering at Big Bend National Park. Sulfur concentrations at Big Bend were highest during four episodes. September 1 and 2 had the highest sulfur and highest organic and elemental carbon concentrations, respectively, measured at Big Bend as well as moderately high zinc. The second highest sulfur on September 15 also had high sodium, the highest non-soil potassium, and moderately high selenium, bromine, arsenic, and zinc. October 12 was characterized by high sulfur, selenium, and arsenic. August 22 had moderately high sulfur and selenium. Sulfur concentrations measured within a few hundred km are generally highly correlated, but measurements in southwestern Texas were not highly correlated with measurements in northeast Texas and different regions of the state showing different seasonal patterns in sulfur concentrations. Highest sulfur concentrations measured during BRAVO were in northeast Texas during the summer while highest concentrations at Big Bend were during the fall. Spatial patterns in sulfur concentrations show influence from the Carbón I & II power plants on sulfur concentrations especially north and west of the plants, though the contribution is not quantifiable by these analyses.

Spatial and temporal patterns in the iron concentrations and the abrupt drop in Al/Ca ratios from summer to fall are evidence of Saharan dust episodes during the summer.

The trace element most associated with sulfur at Big Bend is selenium which is usually associated with coal combustion. Selenium concentrations were highest in northeast Texas with evidence of selenium sources within the state, at the Carbón I & II plants, and possibly entering Texas from the east. Sodium was highly correlated with sulfur in the 1996 Scoping Study, but was much less related to sulfur during BRAVO and seems to be primarily related to transport of airmasses across the Gulf of Mexico, though the difference may be attributable to measurement differences between the two studies. Vanadium was often below detectable limits, but is most frequently measurable at the southernmost sites. This seems to confirm earlier analyses that found vanadium to be associated with transport from Mexico into Texas. Bromine was second only to selenium in correlation to sulfur at Big Bend and was highest at Gulf Coast sites. Lead concentrations in southern Texas have dropped dramatically since the 1996 study.

8.1.2 Factor Analysis

Fine particulate concentrations measured with the IMPROVE sampler at K-Bar were examined to determine which species varied together during BRAVO. These analyses are of interest as a qualitative way of understanding which fine particulate species may be associated with common source areas or source types. It can also give an idea of which species are likely to fall together as source types in more quantitative multivariate receptor modeling which determines source types by common variations between species. Such models include Chemical Mass Balance (CMB), UNMIX, and Positive Matrix Factorization (PMF).

Input data for this analysis is from the May 19, 2003, "high sensitivity" data set that was generated for K-Bar only by re-analyzing the filters from the 24-hour IMPROVE sampler using higher sensitivity XRF analysis. This significantly improved the minimum detection limits of many of the trace elements. Several species, including SO_2, Cd, Ag, Ba, Co, Mg, Au, Y, Zr, Rb, Hg, and P were not included in the factor analysis because there were too many values below detectable limits. All remaining species had very few values below or near the detection limit. Figure 8-34 is a compact representation of the correlation matrix for data measured at K-Bar. The species are labeled on the diagonal of the matrix with the names given by scientists at University of California-Davis who measured and analyzed these data. In most cases the labels are the standard elemental abbreviations from the periodic table of elements. In some cases a "P" has been appended in front of the standard abbreviation to indicate that the element was originally measured using PIXE. When these data were later re-analyzed by XRF, the label remained the same. Labels in the top right corner of the figure (O1, O2, O3, OP, E1, E2, E3) refer to the organic and elemental carbon fractions. Details of the measurement techniques are given in section 2.1.1.

The row and column containing the label give the correlations of that species with all others. The colors are based on a topographic color scheme with the highest values being the brown through white-like mountains and the lowest values being blue like sea level. The highest correlations (near 1) are between sulfur, sulfate, and ammonium and also between the various soil elements, Fe, Si, Ti, Al, etc. The lowest correlations are between Cl ion and E3, one of the elemental carbon fractions. This same correlation matrix is also shown in tabular form in Table 8-2.

Although the correlation matrix is informative, factor analysis is as a more systematic method of identifying groups of species which are correlated or anti-correlated with each other.

Input to this factor analysis was the correlation matrix of the centered and scaled high sensitivity data collected at K-Bar. Varimax rotation was used.

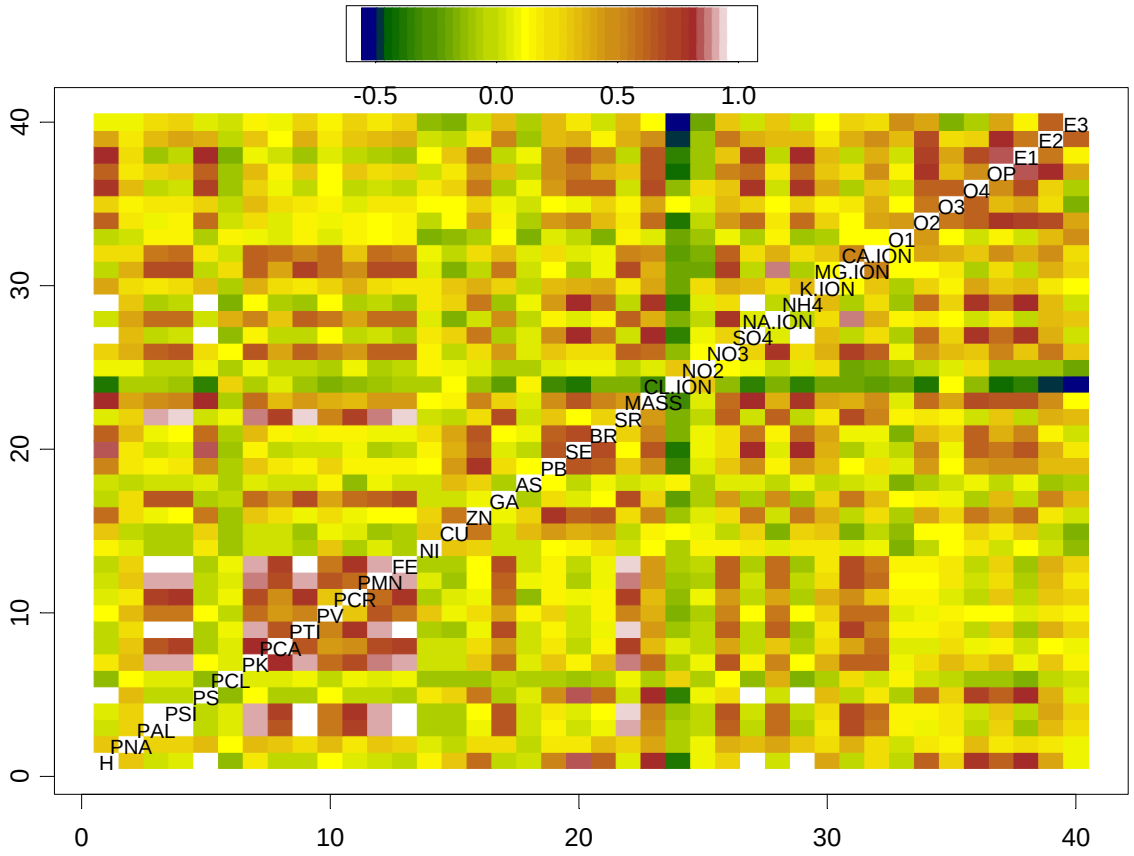

Figure 8-34. Correlations between fine particle species measured at K-Bar during BRAVO.

Figures 8-35 and 8-36 below show the variance and cumulative variance explained as increasing numbers of factors are added to the analysis. The number of factors to retain for rotation is somewhat subjective. There are several methods commonly used including the scree test [*Cattell,* 1966] which is to plot the variance explained by each factor, as in Figure 8-35 and then choose a number of factors where there is a large drop in the variance explained. Solutions with from 3 to 8 factors were all tried. The largest drop is with three factors; however, at least four factors seem to be required to get most of the physically meaningful divisions between the factors. There are four patterns that always emerge with four or more factors. These have arbitrarily been labeled "soil", "sulfur", "carbons with high EC", and "carbons with high O3 and O4." Another moderate drop in the scree plot is at eight factors. Also, as can be seen in Figure 8-36, eight factors explain between 80 and 90% of the total variance in the fine particle measurements. This was chosen as a reasonable number of factors to use.

Table 8-2. Correlations between fine particle species measured at K-Bar during BRAVO.

	H	Na	Al	Si	S	Cl	K	Ca	Ti	V	Cr	Mn	Fe	Ni	Cu	Zn	Ga	As	Pb	Se
H	1.00	0.30	0.00	0.04	0.98	-0.13	0.19	-0.01	-0.01	0.11	0.04	0.02	-0.02	0.17	0.29	0.58	-0.01	0.02	0.52	0.85
Na	0.30	1.00	0.26	0.28	0.32	0.13	0.33	0.29	0.25	0.35	0.21	0.29	0.25	0.04	-0.01	0.22	0.22	-0.03	0.17	0.20
Al	0.00	0.26	1.00	0.99	-0.04	0.06	0.89	0.67	0.98	0.54	0.75	0.89	0.98	-0.06	-0.07	0.10	0.66	0.02	0.15	0.00
Si	0.04	0.28	0.99	1.00	0.00	0.06	0.92	0.73	0.98	0.56	0.75	0.91	0.99	-0.05	-0.06	0.14	0.67	0.02	0.19	0.03
S	0.98	0.32	-0.04	0.00	1.00	-0.14	0.14	-0.06	-0.05	0.12	-0.01	-0.01	-0.07	0.20	0.27	0.56	-0.05	0.05	0.48	0.83
Cl	-0.13	0.13	0.06	0.06	-0.14	1.00	0.05	0.03	0.08	-0.04	0.08	0.04	0.07	-0.10	-0.08	-0.08	-0.01	-0.05	-0.06	-0.10
K	0.19	0.33	0.89	0.92	0.14	0.05	1.00	0.79	0.89	0.59	0.70	0.86	0.91	0.03	0.01	0.29	0.58	0.05	0.29	0.16
CA	-0.01	0.29	0.67	0.73	-0.06	0.03	0.79	1.00	0.66	0.46	0.48	0.71	0.73	0.00	0.02	0.24	0.44	0.02	0.19	-0.03
Ti	-0.01	0.25	0.98	0.98	-0.05	0.08	0.89	0.66	1.00	0.53	0.78	0.90	0.99	-0.07	-0.08	0.08	0.69	0.01	0.16	0.00
V	0.11	0.35	0.54	0.56	0.12	-0.04	0.59	0.46	0.53	1.00	0.30	0.67	0.54	0.31	0.08	0.23	0.42	0.16	0.27	0.03
Cr	0.04	0.21	0.75	0.75	-0.01	0.08	0.70	0.48	0.78	0.30	1.00	0.58	0.76	-0.06	0.06	0.08	0.60	-0.13	0.17	0.10
Mn	0.02	0.29	0.89	0.91	-0.01	0.04	0.86	0.71	0.90	0.67	0.58	1.00	0.91	0.03	-0.09	0.12	0.61	0.10	0.15	-0.05
Fe	-0.02	0.25	0.98	0.99	-0.07	0.07	0.91	0.73	0.99	0.54	0.76	0.91	1.00	-0.07	-0.07	0.11	0.68	0.02	0.17	-0.01
Ni	0.17	0.04	-0.06	-0.05	0.20	-0.10	0.03	0.00	-0.07	0.31	-0.06	0.03	-0.07	1.00	0.31	0.26	0.01	0.03	0.13	0.15
Cu	0.29	-0.01	-0.07	-0.06	0.27	-0.08	0.01	0.02	-0.08	0.08	0.06	-0.09	-0.07	0.31	1.00	0.57	0.03	0.34	0.44	0.36
Zn	0.58	0.22	0.10	0.14	0.56	-0.08	0.29	0.24	0.08	0.23	0.08	0.12	0.11	0.26	0.57	1.00	0.07	0.26	0.77	0.61
Ga	-0.01	0.22	0.66	0.67	-0.05	-0.01	0.58	0.44	0.69	0.42	0.60	0.61	0.68	0.01	0.03	0.07	1.00	-0.06	0.24	0.06
As	0.02	-0.03	0.02	0.02	0.05	-0.05	0.05	0.02	0.01	0.16	-0.13	0.10	0.02	0.03	0.34	0.26	-0.06	1.00	0.11	-0.04
Pb	0.52	0.17	0.15	0.19	0.48	-0.06	0.29	0.19	0.16	0.27	0.17	0.15	0.17	0.13	0.44	0.77	0.24	0.11	1.00	0.65
Se	0.85	0.20	0.00	0.03	0.83	-0.10	0.16	-0.03	0.00	0.03	0.10	-0.05	-0.01	0.15	0.36	0.61	0.06	-0.04	0.65	1.00
Br	0.61	0.34	0.08	0.10	0.59	-0.06	0.32	0.17	0.07	0.14	0.15	0.08	0.08	0.24	0.42	0.67	0.13	0.10	0.61	0.71
Sr	0.05	0.28	0.91	0.93	0.00	0.09	0.88	0.72	0.94	0.52	0.73	0.86	0.94	0.00	-0.01	0.22	0.69	0.03	0.31	0.13
PM2.5	0.82	0.40	0.47	0.50	0.79	-0.06	0.59	0.33	0.46	0.37	0.35	0.45	0.45	0.11	0.16	0.51	0.26	0.04	0.47	0.65
Cl-	-0.38	-0.07	-0.06	-0.08	-0.36	0.27	-0.05	0.04	-0.09	-0.18	-0.14	-0.10	-0.07	-0.06	0.13	-0.08	-0.25	0.16	-0.31	-0.38
NO2	0.09	0.07	-0.03	-0.04	0.07	-0.05	0.08	-0.03	-0.03	-0.06	0.09	-0.07	-0.02	0.14	0.09	0.03	-0.07	-0.04	0.04	0.10
NO3-	0.26	0.37	0.62	0.65	0.25	0.13	0.65	0.40	0.64	0.53	0.45	0.61	0.62	0.15	-0.03	0.23	0.46	0.03	0.30	0.22
SO4--	0.98	0.32	-0.01	0.02	0.99	-0.13	0.15	-0.03	-0.03	0.12	-0.02	0.02	-0.04	0.20	0.26	0.55	-0.05	0.06	0.46	0.82
NA+	0.03	0.41	0.59	0.59	0.03	0.38	0.53	0.31	0.62	0.54	0.40	0.58	0.59	0.06	-0.17	0.00	0.49	-0.02	0.15	0.05
NH4+	0.97	0.28	-0.07	-0.04	0.98	-0.17	0.11	-0.05	-0.09	0.12	-0.07	-0.01	-0.09	0.21	0.28	0.56	-0.09	0.10	0.46	0.79
K+	0.42	0.21	0.19	0.22	0.34	-0.07	0.36	0.25	0.19	0.27	0.37	0.23	0.19	0.19	0.32	0.36	0.27	-0.01	0.33	0.36
MG+	-0.04	0.36	0.70	0.70	-0.02	0.23	0.62	0.42	0.71	0.59	0.47	0.70	0.70	0.03	-0.18	-0.01	0.56	0.02	0.11	-0.05
CA++	0.24	0.24	0.54	0.59	0.21	0.01	0.61	0.57	0.52	0.58	0.31	0.59	0.55	0.08	-0.03	0.23	0.32	0.06	0.23	0.05
O1	-0.03	0.02	0.14	0.16	-0.06	0.16	0.07	0.05	0.17	0.05	0.14	0.10	0.16	-0.17	-0.14	-0.05	0.12	-0.15	0.06	-0.02
O2	0.62	0.20	0.09	0.15	0.59	0.00	0.21	0.05	0.15	0.08	0.14	0.11	0.15	-0.01	0.11	0.40	0.16	-0.07	0.43	0.53
O3	0.26	0.17	0.18	0.20	0.25	-0.02	0.32	0.21	0.19	0.14	0.06	0.20	0.21	0.10	0.11	0.28	0.09	0.02	0.14	0.08
O4	0.78	0.33	-0.02	0.01	0.75	-0.08	0.25	0.09	-0.04	0.12	-0.02	0.01	-0.02	0.18	0.26	0.54	-0.05	0.09	0.44	0.61
OP	0.64	0.19	0.26	0.31	0.61	-0.09	0.33	0.17	0.29	0.13	0.30	0.23	0.28	0.00	0.19	0.45	0.33	-0.01	0.48	0.56
E1	0.80	0.24	-0.08	-0.03	0.79	-0.15	0.09	0.02	-0.08	0.03	-0.03	-0.04	-0.08	0.13	0.30	0.58	-0.01	0.08	0.48	0.64
E2	0.40	0.18	0.35	0.39	0.38	-0.01	0.32	0.14	0.38	0.20	0.31	0.32	0.36	0.00	-0.01	0.20	0.50	-0.09	0.34	0.37
E3	0.09	0.08	0.22	0.26	0.04	0.03	0.17	0.09	0.28	0.16	0.28	0.20	0.26	-0.13	-0.15	0.02	0.35	-0.07	0.34	0.20

	Br	Sr	PM2.5	Cl-	NO2	NO3-	SO4--	NA+	NH4+	K+	MG+	Ca++	O1	O2	O3	O4	OP	E1	E2	E3
H	0.61	0.05	0.82	-0.38	0.09	0.26	0.98	0.03	0.97	0.42	-0.04	0.24	-0.03	0.62	0.26	0.78	0.64	0.80	0.40	0.09
Na	0.34	0.28	0.40	-0.07	0.07	0.37	0.32	0.41	0.28	0.21	0.36	0.24	0.02	0.20	0.17	0.33	0.19	0.24	0.18	0.08
Al	0.08	0.91	0.47	-0.06	-0.03	0.62	-0.01	0.59	-0.07	0.19	0.70	0.54	0.14	0.09	0.18	-0.02	0.26	-0.08	0.35	0.22
Si	0.10	0.93	0.50	-0.08	-0.04	0.65	0.02	0.59	-0.04	0.22	0.70	0.59	0.16	0.15	0.20	0.01	0.31	-0.03	0.39	0.26
S	0.59	0.00	0.79	-0.36	0.07	0.25	0.99	0.03	0.98	0.34	-0.02	0.21	-0.06	0.59	0.25	0.75	0.61	0.79	0.38	0.04
Cl	-0.06	0.09	-0.06	0.27	-0.05	0.13	-0.13	0.38	-0.17	-0.07	0.23	0.01	0.16	0.00	-0.02	-0.08	-0.09	-0.15	-0.01	0.03
K	0.32	0.88	0.59	-0.05	0.08	0.65	0.15	0.53	0.11	0.36	0.62	0.61	0.07	0.21	0.32	0.25	0.33	0.09	0.32	0.17
CA	0.17	0.72	0.33	0.04	-0.03	0.40	-0.03	0.31	-0.05	0.25	0.42	0.57	0.05	0.05	0.21	0.09	0.17	0.02	0.14	0.09
Ti	0.07	0.94	0.46	-0.09	-0.03	0.64	-0.03	0.62	-0.09	0.19	0.71	0.52	0.17	0.15	0.19	-0.04	0.29	-0.08	0.38	0.28
V	0.14	0.52	0.37	-0.18	-0.06	0.53	0.12	0.54	0.12	0.27	0.59	0.58	0.05	0.08	0.14	0.12	0.13	0.03	0.20	0.16
Cr	0.15	0.73	0.35	-0.14	0.09	0.45	-0.02	0.40	-0.07	0.37	0.47	0.31	0.14	0.14	0.06	-0.02	0.30	-0.03	0.31	0.28
Mn	0.08	0.86	0.45	-0.10	-0.07	0.61	0.02	0.58	-0.01	0.23	0.70	0.59	0.10	0.11	0.20	0.01	0.23	-0.04	0.32	0.20
Fe	0.08	0.94	0.45	-0.07	-0.02	0.62	-0.04	0.59	-0.09	0.19	0.70	0.55	0.16	0.15	0.21	-0.02	0.28	-0.08	0.36	0.26
Ni	0.24	0.00	0.11	-0.06	0.14	0.15	0.20	0.06	0.21	0.19	0.03	0.08	-0.17	-0.01	0.10	0.18	0.00	0.13	0.00	-0.13
Cu	0.42	-0.01	0.16	0.13	0.09	-0.03	0.26	-0.17	0.28	0.32	-0.18	-0.03	-0.14	0.11	0.11	0.26	0.19	0.30	-0.01	-0.15
Zn	0.67	0.22	0.51	-0.08	0.03	0.23	0.55	0.00	0.56	0.36	-0.01	0.23	-0.05	0.40	0.28	0.54	0.45	0.58	0.20	0.02
Ga	0.13	0.69	0.26	-0.25	-0.07	0.46	-0.05	0.49	-0.09	0.27	0.56	0.32	0.12	0.16	0.09	-0.05	0.33	-0.01	0.50	0.35
As	0.10	0.03	0.04	0.16	-0.04	0.03	0.06	-0.02	0.10	-0.01	0.02	0.06	-0.15	-0.07	0.02	0.09	-0.01	0.08	-0.09	-0.07
Pb	0.61	0.31	0.47	-0.31	0.04	0.30	0.46	0.15	0.46	0.33	0.11	0.23	0.06	0.43	0.14	0.44	0.48	0.48	0.34	0.34
Se	0.71	0.13	0.65	-0.38	0.10	0.22	0.82	0.05	0.79	0.36	-0.05	0.05	-0.02	0.53	0.08	0.61	0.56	0.64	0.37	0.20
Br	1.00	0.25	0.50	-0.18	0.10	0.25	0.57	0.14	0.57	0.42	0.10	0.08	-0.17	0.33	0.28	0.61	0.37	0.51	0.15	0.00
Sr	0.25	1.00	0.45	-0.16	-0.01	0.63	0.02	0.63	-0.04	0.21	0.71	0.50	0.17	0.20	0.16	0.02	0.32	-0.03	0.39	0.32
PM2.5	0.50	0.45	1.00	-0.31	0.05	0.57	0.81	0.38	0.77	0.40	0.37	0.47	0.05	0.58	0.42	0.68	0.68	0.66	0.49	0.14
Cl-	-0.18	-0.16	-0.31	1.00	0.29	-0.14	-0.34	-0.15	-0.36	-0.22	-0.19	-0.23	-0.19	-0.40	0.12	-0.12	-0.42	-0.35	-0.48	-0.54
NO2	0.10	-0.01	0.05	0.29	1.00	0.12	0.09	-0.03	0.05	0.22	-0.19	-0.17	-0.11	-0.03	0.05	0.22	-0.09	-0.11	-0.10	-0.19
NO3-	0.25	0.63	0.57	-0.14	0.12	1.00	0.26	0.78	0.21	0.37	0.73	0.61	0.10	0.45	0.34	0.30	0.50	0.28	0.55	0.30
SO4--	0.57	0.02	0.81	-0.34	0.09	0.26	1.00	0.04	0.98	0.35	-0.01	0.23	-0.06	0.58	0.26	0.76	0.60	0.78	0.37	0.03
NA+	0.14	0.63	0.38	-0.15	-0.03	0.78	0.04	1.00	-0.02	0.22	0.86	0.38	0.16	0.19	0.13	0.02	0.20	-0.04	0.35	0.30
NH4+	0.57	-0.04	0.77	-0.36	0.05	0.21	0.98	-0.02	1.00	0.35	-0.06	0.23	-0.10	0.57	0.27	0.78	0.58	0.80	0.34	0.00
K+	0.42	0.21	0.40	-0.22	0.22	0.37	0.35	0.22	0.35	1.00	0.13	0.31	-0.07	0.25	0.17	0.42	0.30	0.33	0.20	0.12
MG+	0.10	0.71	0.37	-0.19	-0.19	0.73	-0.01	0.86	-0.06	0.13	1.00	0.51	0.13	0.12	0.18	-0.06	0.23	-0.04	0.37	0.28
CA++	0.08	0.50	0.47	-0.23	-0.17	0.61	0.23	0.38	0.23	0.31	0.51	1.00	0.11	0.40	0.36	0.30	0.48	0.37	0.49	0.23
O1	-0.17	0.17	0.05	-0.19	-0.11	0.10	-0.06	0.16	-0.10	-0.07	0.13	0.11	1.00	0.45	0.12	0.01	0.16	0.00	0.35	0.48
O2	0.33	0.20	0.58	-0.40	-0.03	0.45	0.58	0.19	0.57	0.25	0.12	0.40	0.45	1.00	0.54	0.63	0.75	0.72	0.69	0.40
O3	0.28	0.16	0.42	0.12	0.05	0.34	0.26	0.13	0.27	0.17	0.18	0.36	0.12	0.54	1.00	0.63	0.32	0.40	0.23	-0.18
O4	0.61	0.02	0.68	-0.12	0.22	0.30	0.76	0.02	0.78	0.42	-0.06	0.30	0.01	0.63	0.63	1.00	0.49	0.70	0.28	-0.05
OP	0.37	0.32	0.68	-0.42	-0.09	0.50	0.60	0.20	0.58	0.30	0.23	0.48	0.16	0.75	0.32	0.49	1.00	0.85	0.82	0.40
E1	0.51	-0.03	0.66	-0.35	-0.11	0.28	0.78	-0.04	0.80	0.33	-0.04	0.37	0.00	0.72	0.40	0.70	0.85	1.00	0.54	0.15
E2	0.15	0.39	0.49	-0.48	-0.10	0.55	0.37	0.35	0.34	0.20	0.37	0.49	0.35	0.69	0.23	0.28	0.82	0.54	1.00	0.63
E3	0.00	0.32	0.14	-0.54	-0.19	0.30	0.03	0.30	0.00	0.12	0.28	0.23	0.48	0.40	-0.18	-0.05	0.40	0.15	0.63	1.00

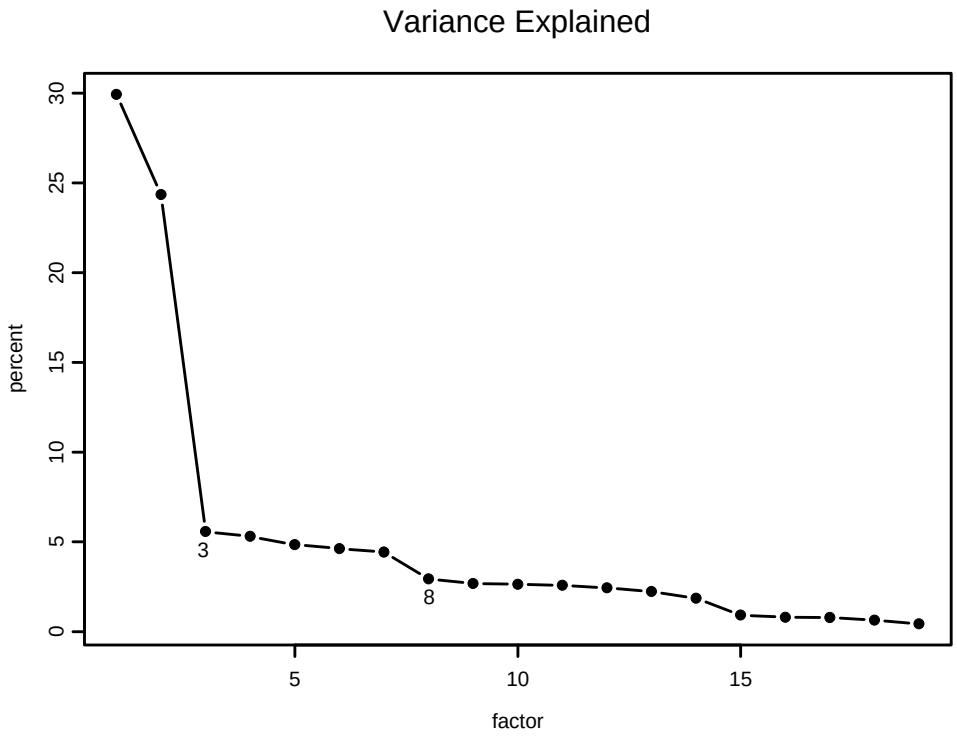

Figure 8-35. Variance explained by each factor in a factor analysis of measured fine particle concentrations at K-Bar.

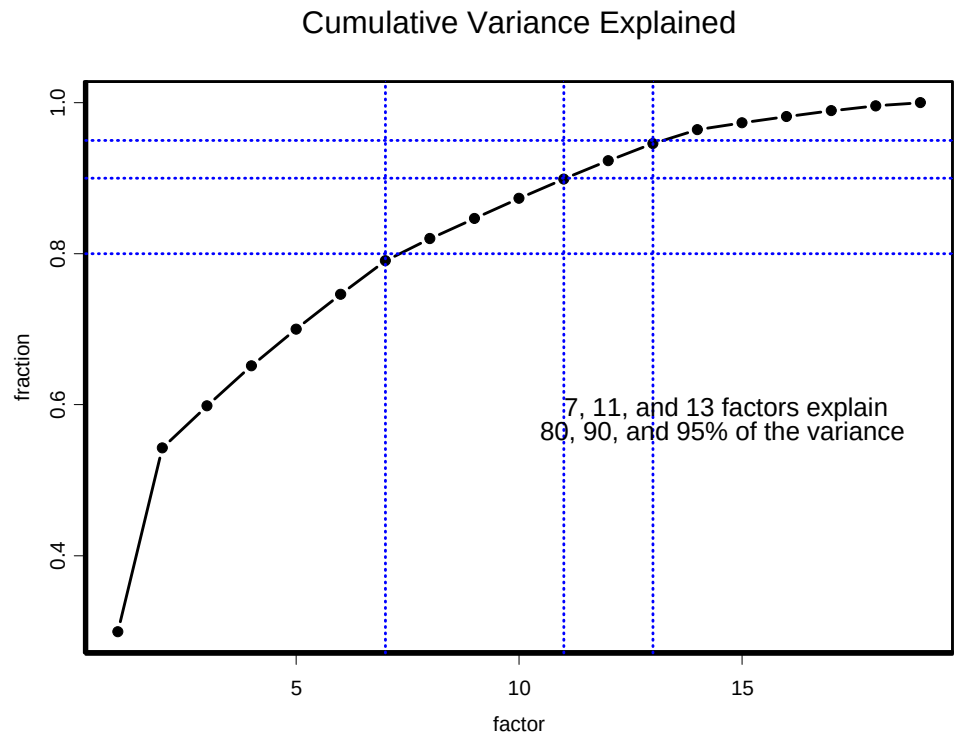

Figure 8-36. Cumulative variance explained by each factor in a factor analysis of measured fine particle concentrations at K-Bar.

Factor one (Figure 8-37) is clearly a soil factor. The typical soil elements of Al, K, Ca, Ti, Cr, Mn, Fe, Ga, Mg, and Sr all load strongly together on this factor which explains 35% of the variance. The daily factor scores also are high only early during the study, prior to about August 15, when other analyses (see section 8.1.1) have shown that there is likely impact from Saharan dust. The relatively high loading for V may either be indicative of V in soil or V may have been added to the airmass as it traversed across Mexico. Vanadium is usually thought to be indicative of the Mexican oil industry along the Gulf Coast. Also loading strongly on this factor are Na^+, NO^-_3, but not NH^+_4. This is further confirmation of the findings of *Collett et al.*, [2001] that the nitrate at Big Bend is mostly not in the form of ammonium nitrate, but more likely as sodium nitrate

The second factor (Figure 8-38), explaining 28% of the variance, is the sulfur factor on which the highest factor loadings are for S, SO_4, NH_4, H, all components of ammonium sulfate, as well as fine mass, of which ammonium sulfate is the largest fraction. Several trace elements also load strongly on this factor including especially Se, and to a lesser extent, Zn, Pb, and Br. The mid-temperature carbons, especially O4, OP, and E1, are also strong loaders on factor two. This factor has the highest factor score on September 1, which was the day of both highest sulfate and highest organic carbon concentrations during BRAVO. The factor scores tend to be near zero or negative during July and after mid-October. The temporal pattern of the factor scores combined with knowledge of the transport patterns indicate that this factor is more likely associated with sources in the U.S. than in Mexico. Transport from the eastern U.S. to Big Bend is most common during September. Additionally, Se emissions are thought to be higher from U.S. coal-fired generating stations than from Mexican sources, which also suggests that this factor indicates sources of U.S. origin. Back trajectories arriving at Big Bend on September 1 cross all three of the large major source regions, Mexico, Texas, and the eastern U.S. The relatively high mid-temperature carbon content on a sulfur factor has consistently been observed elsewhere. In a previous study in Toronto, Canada, where good quality NH_4 and organic acid data were collected, the high mid-temperature OC/S fraction was uniquely associated with acidic sulfates, and suggestive of an acid-catalyzed secondary organic aerosol (SOA) formation mechanism [*Poirot*, 2004].

Factor 3 (Figure 8-39) which explains 11% of the variance, also has the peak factor score on September 1, though the species with the largest loadings, all carbon fractions except O3 and O4, are different from factor 2. Also different from factor 2 are the higher factor scores during July and near-zero scores during mid-September through the end of October. Other analyses of the organic aerosol measured during BRAVO [*Brown et al.*, 2002] have shown that only about 6% of the organic matter measured during BRAVO was due to smoke while more than half was secondary organic aerosol.

Factor 4 (Figure 8-40) is noteworthy for the high factor loadings of several trace elements including especially Zn, Cu, Pb, and Br. This collection of trace elements may be indicative of smelting sources. Factor scores are generally low, but tend to be near zero or negative up until about September 11, after which there are higher magnitudes of both positive and negative scores, with the highest positive scores on October 14–15, October 7, and October 1–2. Back trajectories on these dates are somewhat unique in all having more transport from the western U.S. than did most days during BRAVO. As there are known smelters in that region of the country, the designation of this factor as a smelter factor may be accurate.

Factor 5 (Figure 8-41), explaining 6% of the variance, is weighted highest for the carbon fractions, O2, O3, and O4. O3 and O4 are the fractions that had near-zero loadings for factor 3, while the other carbon fractions loaded highly.

Factor 6 (Figure 8-42) is indicative of marine influence. The species that load highest are those associated with sea salt, Cl, Na, Mg, and also NO_3 which other BRAVO analyses have shown is likely reacting with sea salt to form ammonium nitrate. The factor scores are all generally low with the highest score on July 2. Back trajectories on this day show high speed trajectories arriving from across the Gulf of Mexico.

Factor 7 (Figure 8-43), with high loadings of Ni and V, is indicative of Mexican oil industry influence (see discussion in section 8.1.1.6.). Consistent with the source attribution modeling results discussed later in section 8.2, this factor has some influence on many days, but rarely a large influence. Highest factor scores occur on July 1, about July 28, and September 28–29. All of these days have trajectories arriving from Mexico and on some days also from the western U.S.

Factor 8 (Figure 8-44), explains about 3% of the variance. Species loading the strongest are Cr, NO_2, and K, with highest factor scores on September 14 and September 11, and with most other days having relatively low or negative scores. Back trajectories arriving on these days are not very similar, though both have trajectories that crossed the Gulf of Mexico and Gulf Coast areas.

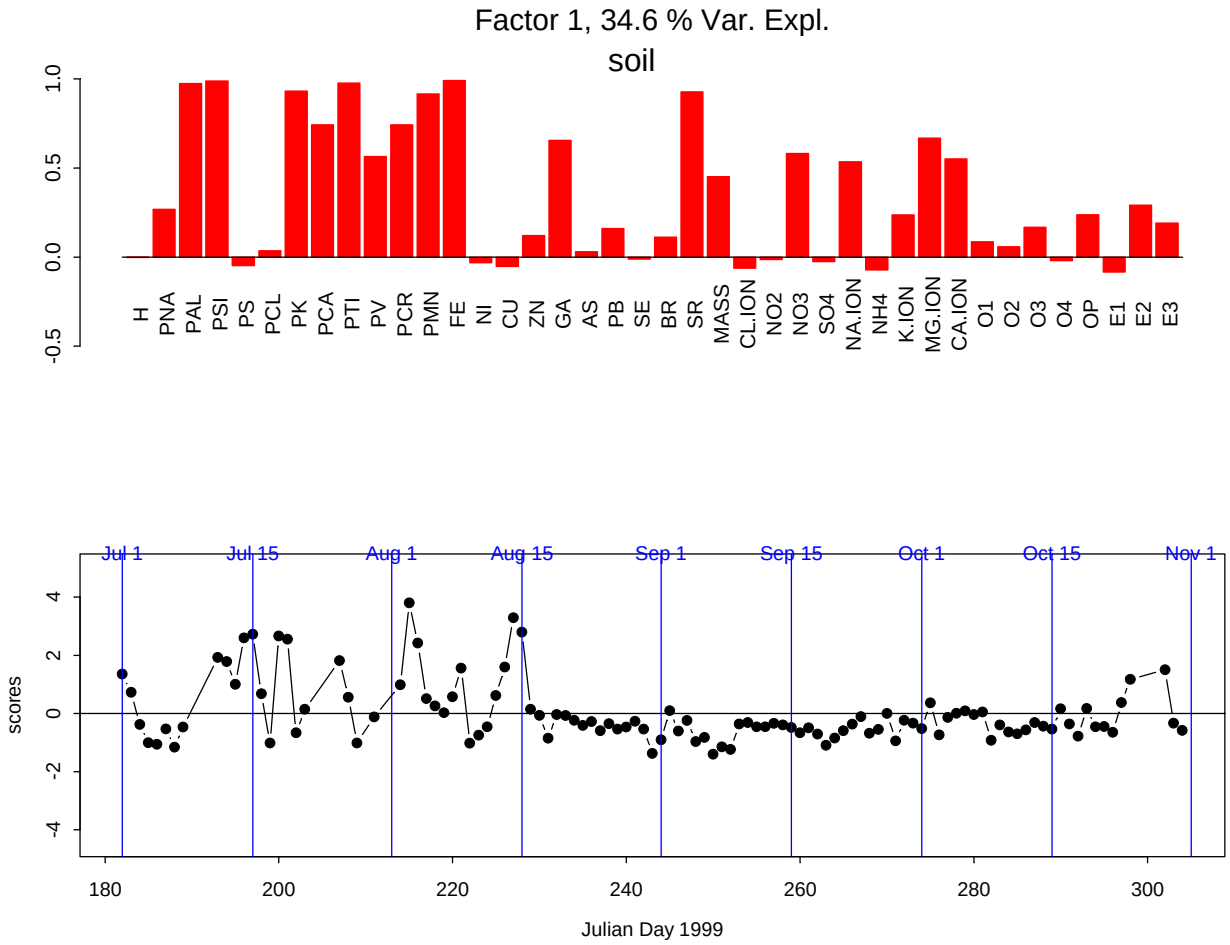

Figure 8-37. Factor loadings in the bar graph and daily factor scores in the line graph for factor one of eight factors.

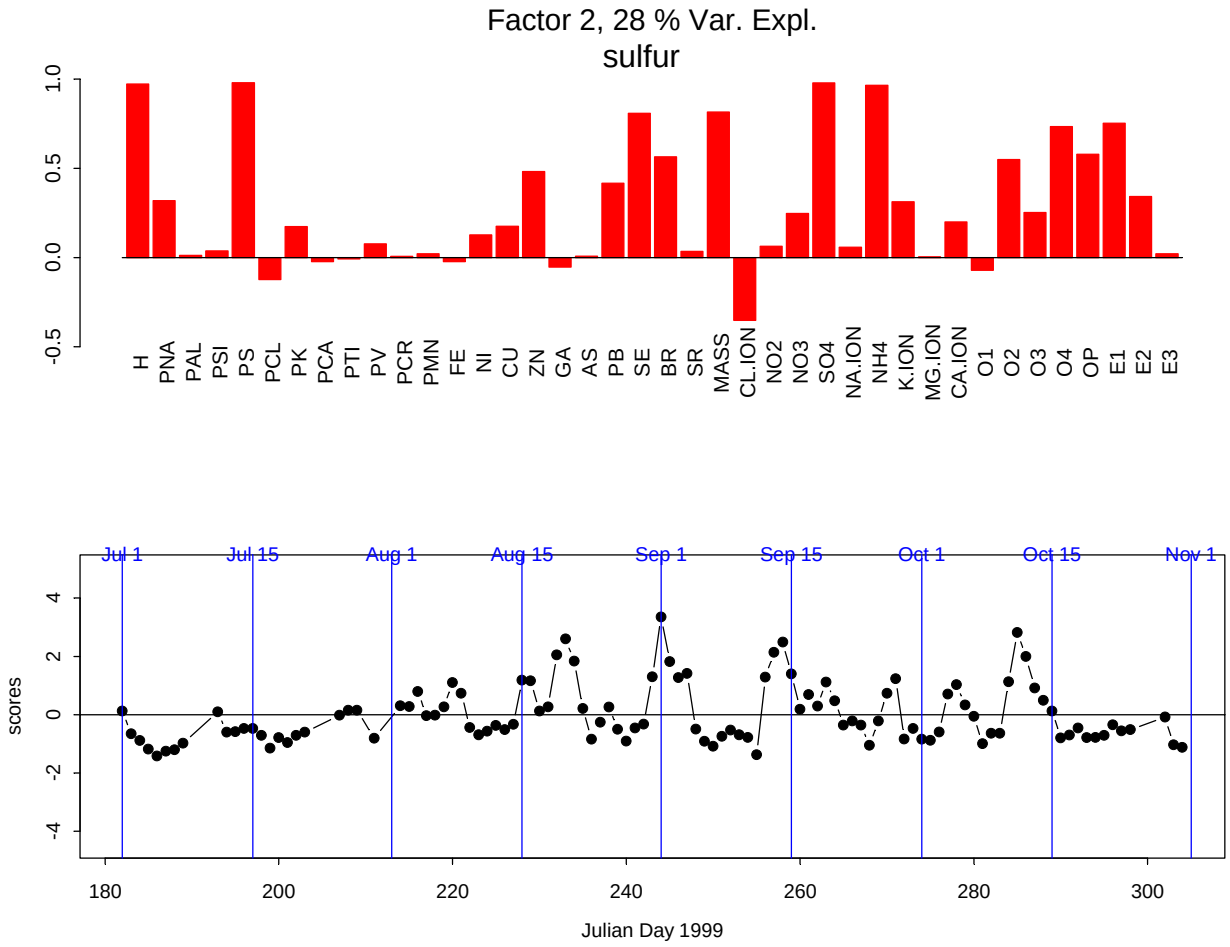

Figure 8-38. Factor loadings in the bar graph and daily factor scores in the line graph for factor two of eight factors.

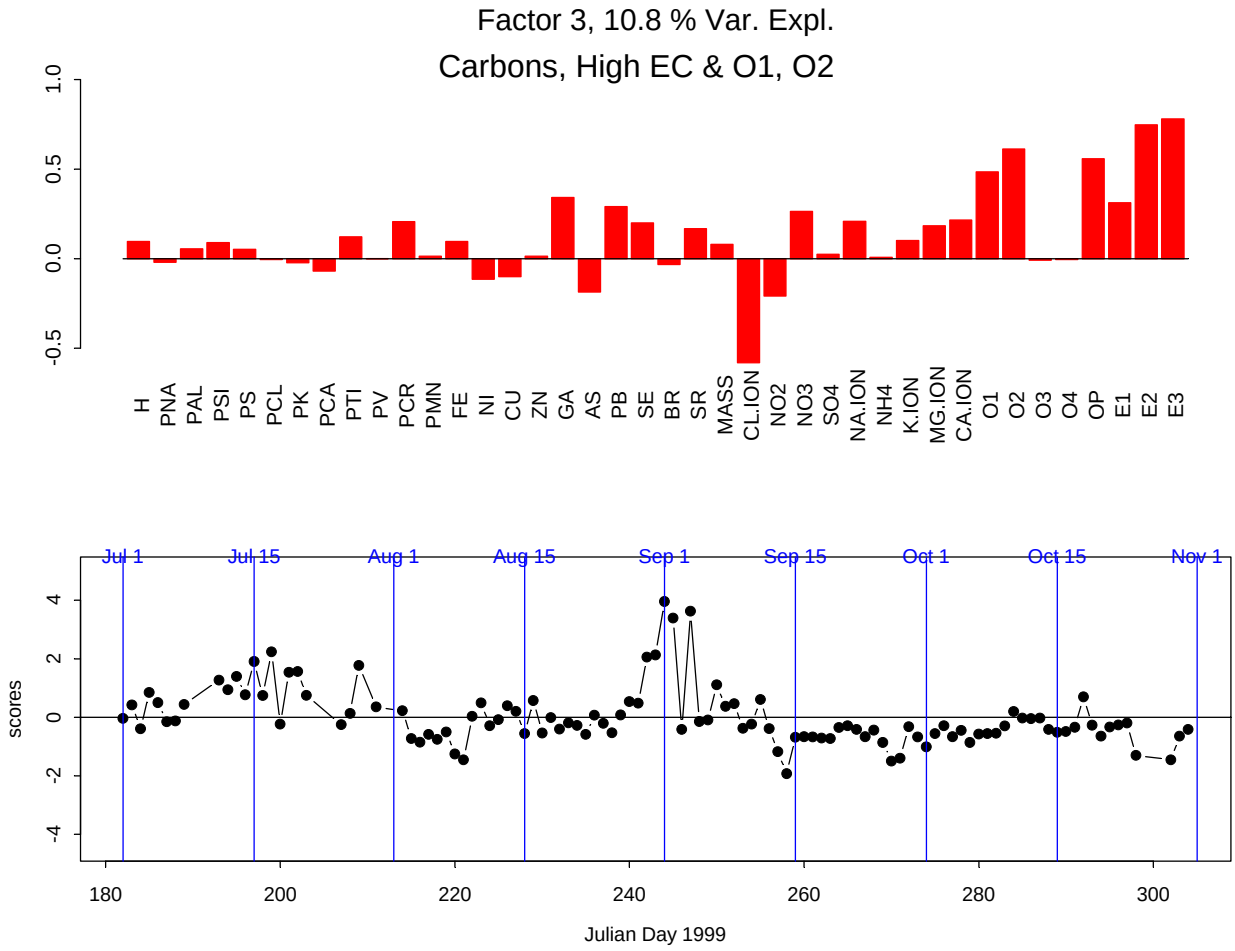

Figure 8-39. Factor loadings in the bar graph and daily factor scores in the line graph for factor three of eight factors.

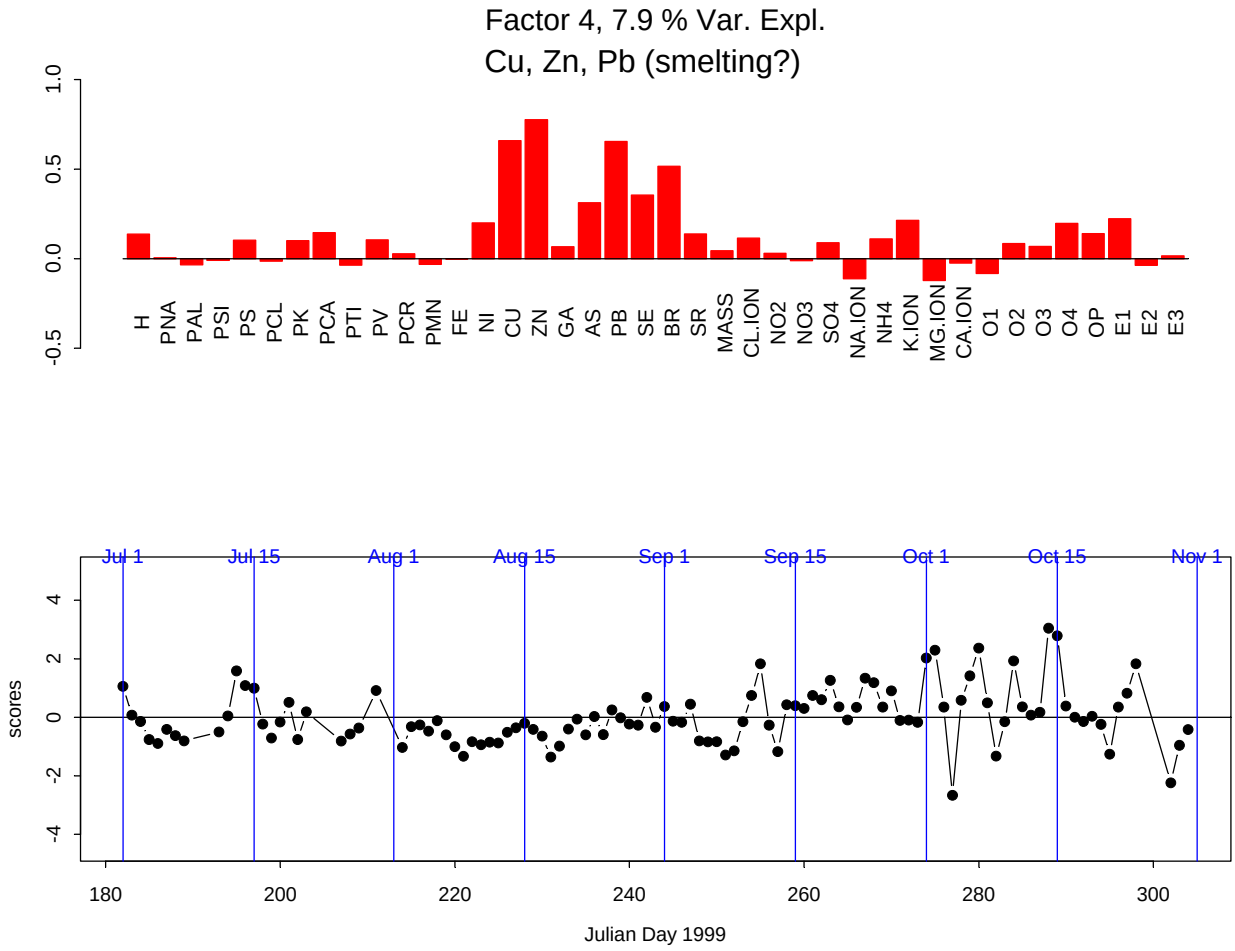

Figure 8-40. Factor loadings in the bar graph and daily factor scores in the line graph for factor four of eight factors.

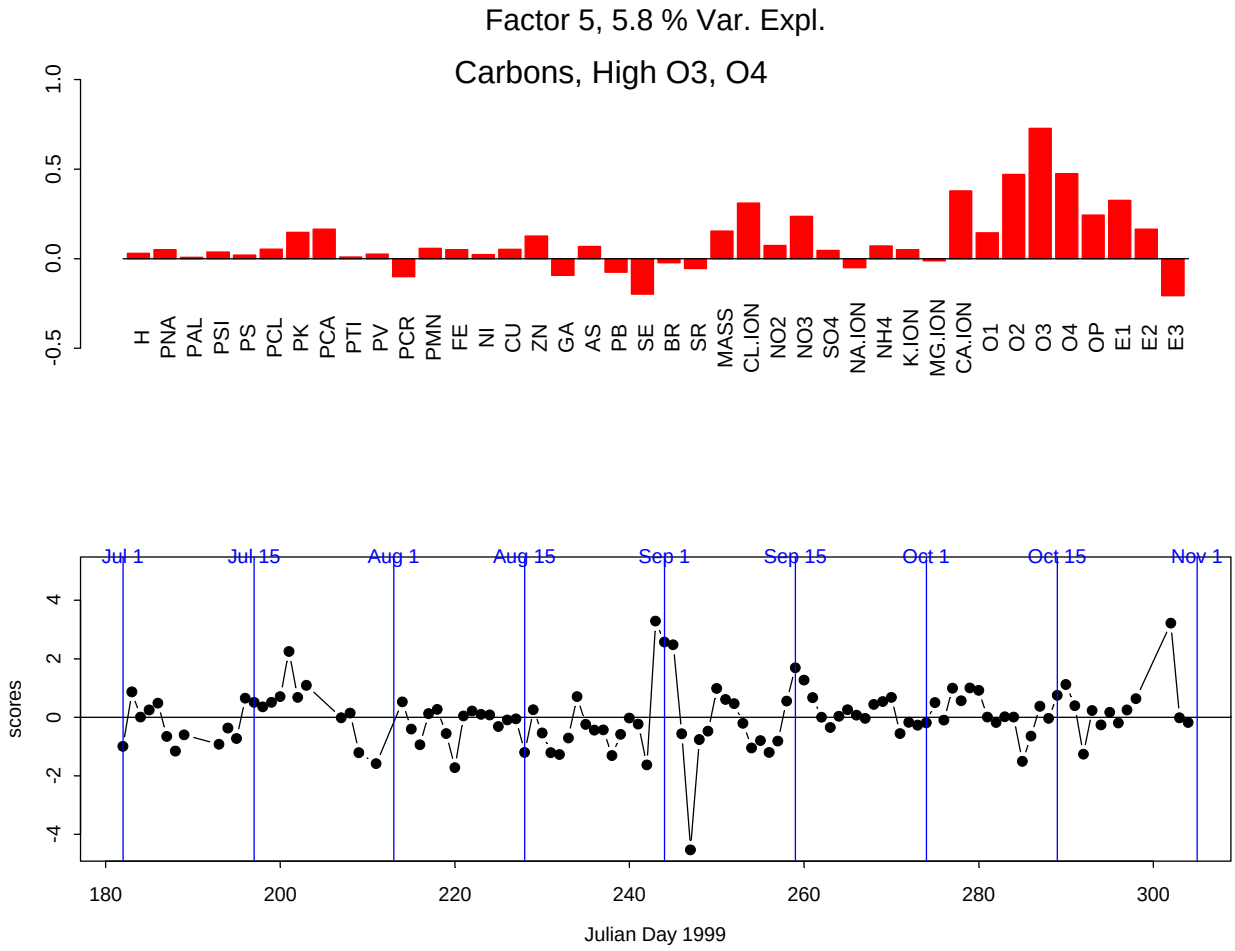

Figure 8-41. Factor loadings in the bar graph and daily factor scores in the line graph for factor five of eight factors.

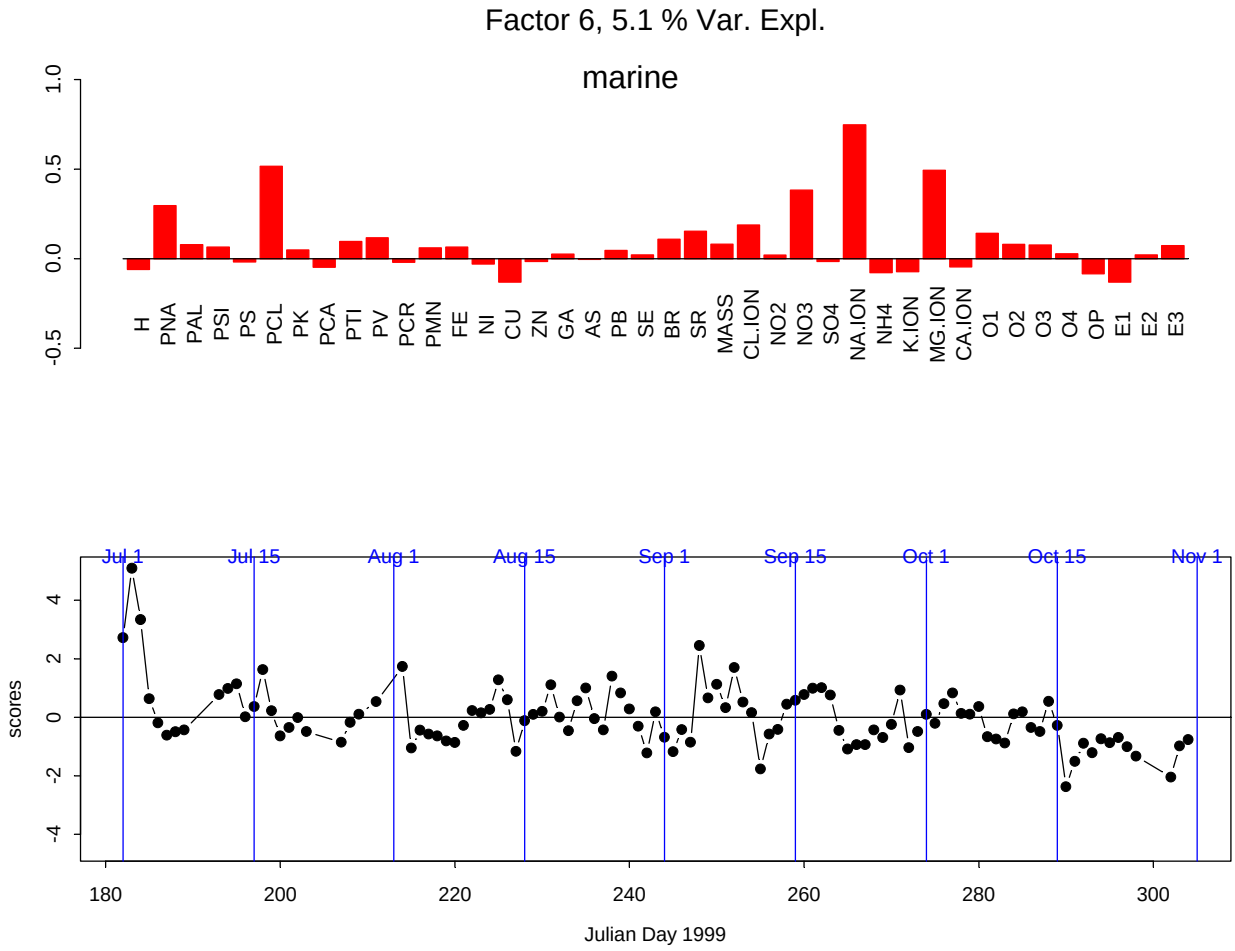

Figure 8-42. Factor loadings in the bar graph and daily factor scores in the line graph for factor six of eight factors.

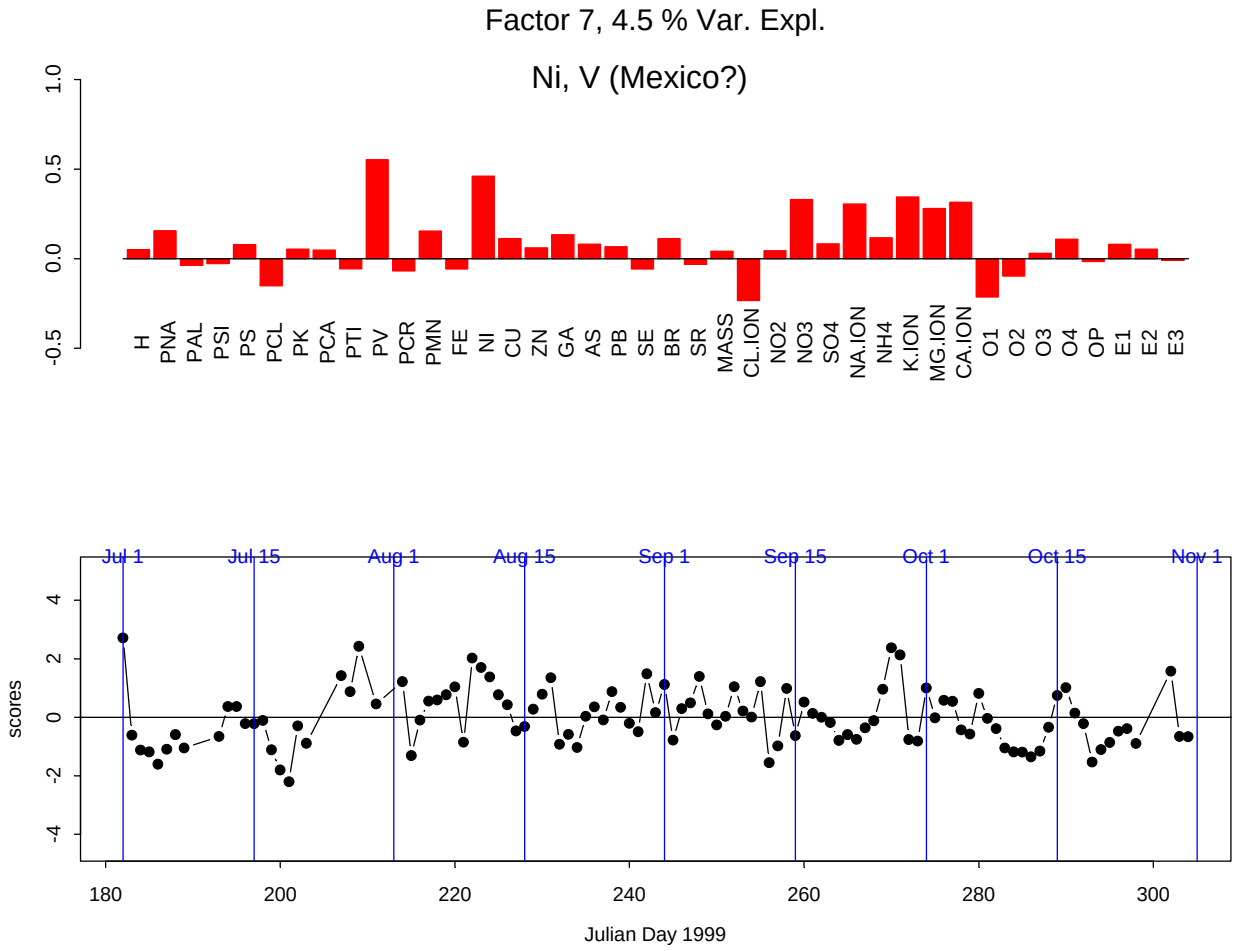

Figure 8-43. Factor loadings in the bar graph and daily factor scores in the line graph for factor seven of eight factors.

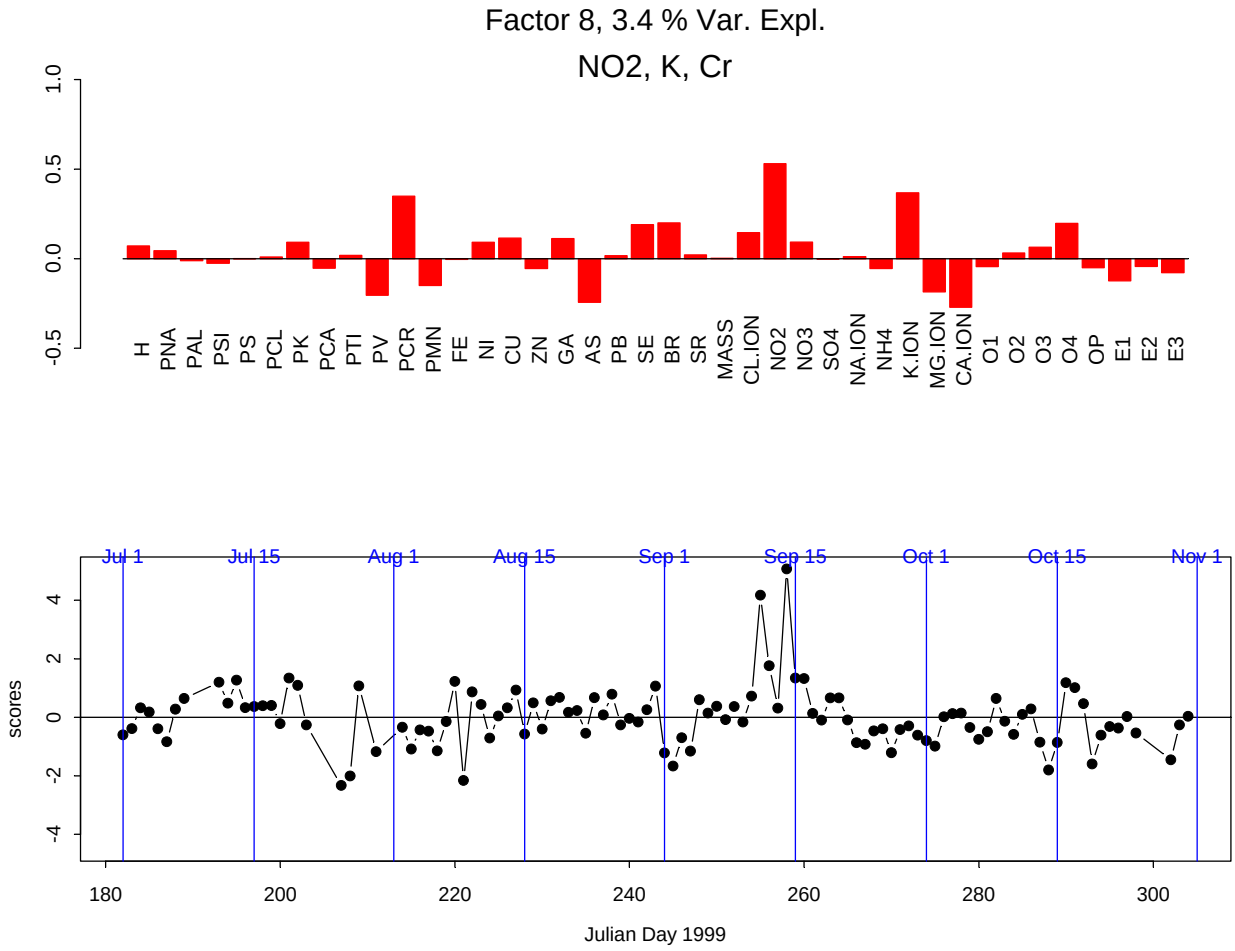

Figure 8-44. Factor loadings in the bar graph and daily factor scores in the line graph for factor eight of eight factors.

8.1.3 Evaluation of Airmass Transport to Big Bend National Park

The primary goal of BRAVO was to identify and quantify the contributions of specific U.S. and Mexican source regions and source types to the haze at Big Bend National Park. To address this goal, airmass histories were aggregated together using residence time analysis techniques (section 2.3.1.3) to develop relationships between long-range and trans-boundary transport and Big Bend's fine particle sulfur concentrations during BRAVO. The study focused on the sulfur concentrations because ammoniated sulfates comprised the majority of the fine mass and light scattering during the Big Bend study [*Malm et al.*, 2003] (see chapter 3).

In this section, the residence time analyses are first evaluated against the BRAVO tracer data. Then the airmass transport directions, speeds, and heights associated with average, high (above the 80th percentile), and low (below the 20th percentile) particulate sulfur concentrations at Big Bend are assessed. In addition, the transport pathways associated with individual Big Bend sulfur episodes are examined, and potential source regions for particle sulfur, sulfur dioxide, and selenium, a power plant tracer, are identified.

This work complements the other BRAVO source attribution analyses presented in this chapter in that the results help to delineate the boundaries of the source regions contributing to Big Bend on the highest sulfur days and identify regions that are not likely to contribute to the highest sulfur levels. These results also help to better understand, interpret, and support or call into question the attribution results.

8.1.3.1 Residence Time Analysis and Airmass History Calculation

The CAPITA Monte Carlo model (section 3.2.3) was used to generate five-day backward airmass histories from Big Bend every two hours from July through October. Each airmass history was composed of 75 particles or individual trajectories. In addition to the particles, three-dimensional location, temperature, humidity, and precipitation were saved along the airmass histories pathway. Two sets of airmass histories were generated with one using the combined EDAS/FNL meteorological data and the other using the 36 km MM5 meteorological data (sections 2.1.3.1–2.1.3.3). It was found in section 5.3 that both meteorological data sets simulated the measured tracer data with about equal skill, properly transporting tracer to Big Bend during the measured multi-day tracer events, and not transporting tracer to Big Bend when the tracer was near the background levels for multi-day periods. Therefore neither wind field could be considered superior, so both wind fields were used in the analysis. These airmass histories are able to characterize regional scale transport. However, they are poorly suited for and not intended for the identification of local flows or nearby source influences (<150 km).

The airmass history technique applied in this work is based upon the residence time analysis (section 3.3). The residence time analysis results in a probability density field identifying the most likely regions in which an airmass will reside en route to the receptor. The most likely transport directions to a receptor are then along the ridges of the probability fields. In this analysis, the airmass histories were sorted according to whether the sulfur was low (below the 20^{th} percentile) or high (above the 80^{th} percentile) and were aggregated together creating transport pathways during the high and low sulfur days. The implication from these sulfur sorted residence time PDFs is that sources, or lack of sources, along the most likely airmass transport pathways are responsible for Big Bend's air quality.

The residence time PDF is the result of the frequency that an airmass is transported over a region en route to the receptor and the length of time it spent over that region. In this analysis, the residence time PDF was decomposed into these two components by calculating a transport direction frequency and an accumulation potential where their product is equal to the residence time PDF (see Appendix 8c). The transport direction frequency is the fraction of time an airmass traverses a given region normalized by a characteristic length of the region to account for different sized regions. Therefore this addresses the question as to what fraction of the receptor concentrations are potentially influenced by emissions from a given region. The accumulation potential can be thought of as an inverse of a characteristic transport speed and is related to the inverse of the speed an airmass was transported over a grid cell and the number of times it traverses the grid cell due to recirculation or flow reversals. This is a better index for determining the exposure of an airmass to a source region's emission than the measured wind speed. For example, fast recirculating winds would spend more time over a source region than slower but directionally persistent winds. Therefore the recirculating airmass would be exposed to a region's emissions for a longer period of time, increasing the potential for pollutants to accumulate.

An important characteristic of airmass transport is the height of the airmasses when traversing a region. An elevated airmass is unlikely to accumulate emissions from surface sources. In this analysis, the airmass height is characterized by averaging the height of all particles that crossed the grid cell.

Relationships between the everyday and air quality sorted residence time analyses can be generated to further enhance the identification of potentially contributing source regions [*Ashbaugh et al*., 1985; *Vasconcelos et al*., 1996; *Stohl,* 1998]. These techniques rely on the triangulation of the source regions by the airmass histories crossing over a true contributing source region following different routes and arriving at the receptor carrying elevated levels of pollutants. Two metrics used in this analysis are the residence time conditional probability (CP) and incremental probability (IP) analyses (sections 3.3.1.3 and 3.3.1.4). The conditional probability is the likelihood that if an airmass passes through a given area it will arrive at the receptor with a high or low concentration. The incremental probability identifies regions that are more or less likely to be traversed during periods of high or low sulfur compared to an average day. These are complementary analyses in that the conditional probabilities tend to identify potential source regions further from the receptor than the incremental probabilities.

This analysis was originally conducted using the combined EDAS and FNL meteorological data. Most of the analysis was duplicated using the MM5 meteorological data when they became available. The following discussion is based upon the EDAS/FNL results, and differences in the transport patterns using the MM5 data are presented or discussed.

8.1.3.2 Evaluation of the Airmass History Techniques.

To evaluate the airmass history analyses' ability to properly identify the airmass transport pathways and known source locations, a residence time analysis was conducted for the upper 20th percentile of the Big Bend 24-hour averaged tracer concentrations. The analysis was conducted for the Eagle Pass tracer (ocPDCH) using data from July through October. Data for the San Antonio tracer, PDCB and the Parish power plant tracer, PTCH, were only released from these sites from September 17 through the end of October. Therefore, only data from September 19 through October 30 were used. iPPCH was continuously released from the Big Brown power plant throughout the study. However, only the tracer data from September 19 through October were used, since prior to this date the data had poor quality with a large fraction below zero. The tracer from Big Brown was intended to represent dispersion of all elevated sources from northeastern Texas and will be referred to as the northeastern tracer. Similarly, the Parish power plant tracer was intended to represent dispersion from Houston source and will be referred to as the Houston tracer.

The results are presented in Figure 8-45 as the residence time PDF weighted by the distance from the Big Bend receptor and the conditional and incremental probabilities. For all four tracers, the airmass transport pathways in the distance weighted residence time PDF correctly include the tracer release sites. However, the Houston release site is at the southern edge of the average airmass transport pathway. Examination of individual trajectories showed a northerly bias in the airmass histories during several of the Houston tracer hits at Big Bend. The conditional and incremental probabilities for the Eagle Pass and San Antonio tracers also properly identified the tracer release sites with the highest probabilities, CP > 0.5 and IP ≥ $1.6*10^{6}$ km^{-2}. The incremental probability had a strong decreasing gradient from these tracer release locations. However, for the conditional probabilities, other regions also had CP > 0.5

hundreds of kilometers from the tracer release sites, such as in southern Oklahoma for the Eagle Pass tracer. The conditional probability for the Houston tracer showed the region of the largest probability northeast of the release site, which was expected from the examination of the distance weighted residence time plots. The incremental probabilities for both the northeast Texas and San Antonio tracers did not clearly identify a potential source region, but did identify a transport pathway encompassing a region from most of eastern Texas to Eagle Pass.

The airmass transport pathways from the three eastern Texas tracer release sites, San Antonio, Houston, and northeast Texas, included the region around the Carbón power plants in Mexico. However, transport from the Eagle Pass tracer release site was not necessarily associated with transport from eastern Texas. Therefore these collinearities in airmass transport pathways over major sulfur dioxide source regions present difficulties in truly separating these source areas in these analyses.

The residence time analysis results using the MM5 trajectories are presented in Figure 8-46. The same general conclusions drawn from the EDAS trajectories can be made about the MM5 results. However, the MM5 results tend to show more distant transport results. This is most evident in the distance weighted residence time. For example, the MM5 results show the highest distance weighted probabilities in Arkansas, and for the EDAS/FNL results it is along the Texas-Louisiana border.

In chapter 4 it was shown that Big Bend airmass histories did not always traverse the tracer release site when there was measured tracer at the receptor. For example, the day with the largest northeast tracer concentration at Big Bend had airmass histories to the west of the tracer release site. However, the residence time results indicate that on average the airmass traversed the northeast Texas tracer release site, indicating that the errors in transport are random.

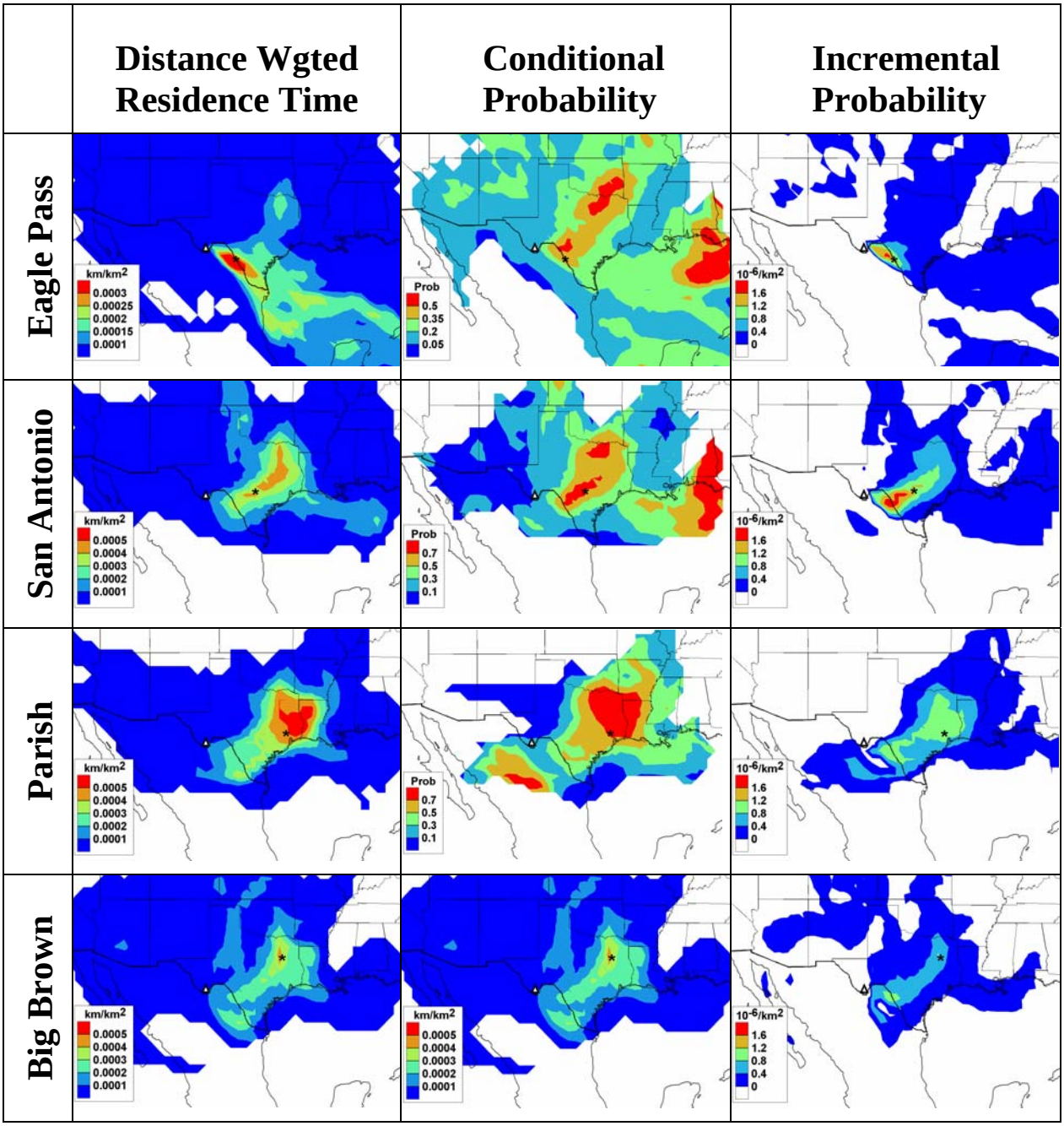

Figure 8-45. The distance weighted residence time analysis, conditional probability, and incremental probability functions for the upper 20th percentiles of the tracer data at Big Bend. These transport probabilities were created using airmass histories generated using the EDAS/FNL meteorological data. The * identifies the location of the tracer release site and the triangle is the location of Big Bend.

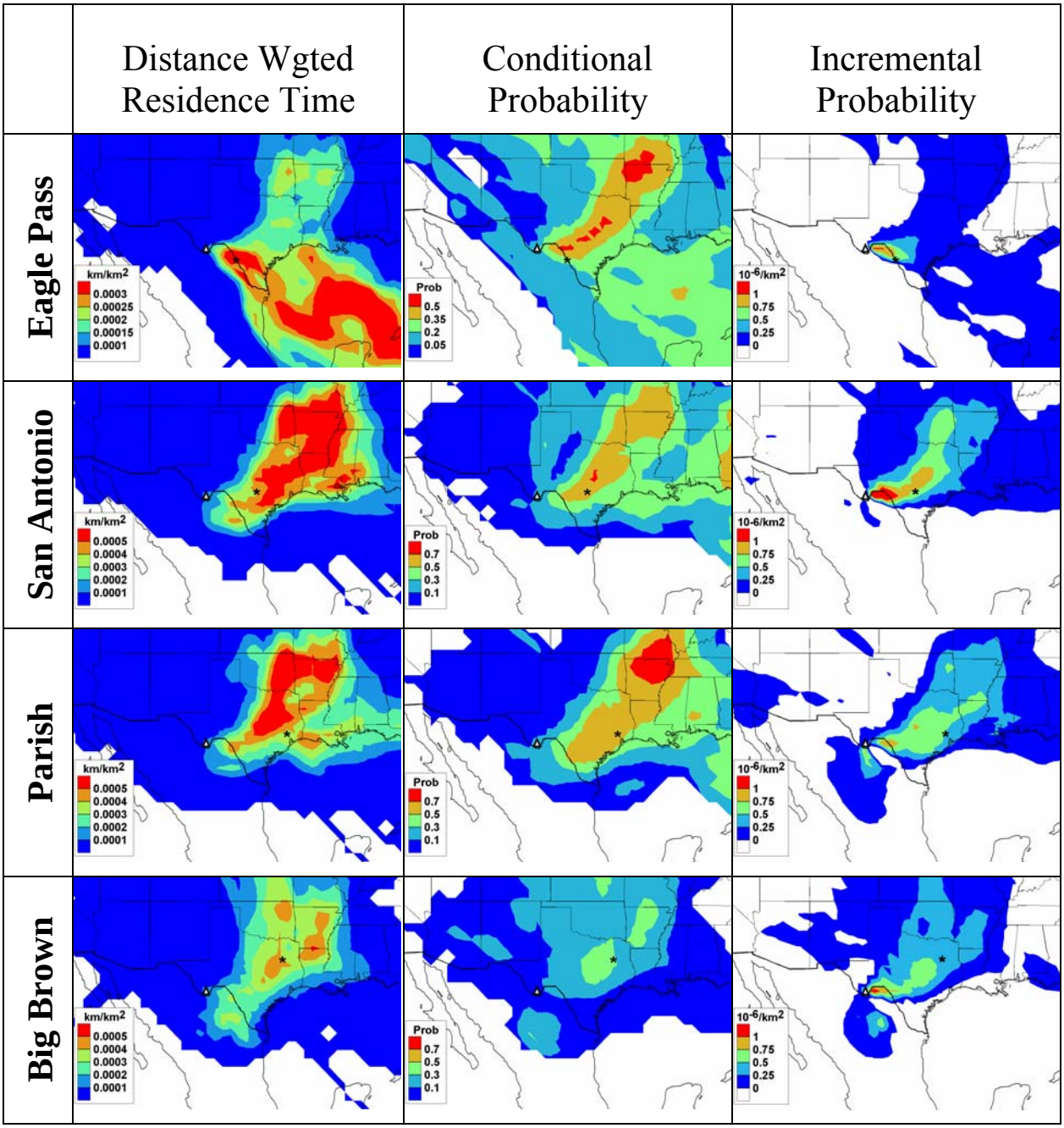

Figure 8-46. The distance weighted residence time analysis, conditional probability, and incremental probability functions for the upper 20th percentiles of the tracer data at Big Bend. These transport probabilities were created using airmass histories generated using the 36 km MM5 meteorological data. The * identifies the location of the tracer release site and the triangle is the location of Big Bend.

8.1.3.3 Airmass Transport to Big Bend, Texas, during the BRAVO Study.

The residence time probability density function and its decomposition for the entire four-month BRAVO study are presented in Figure 8-47. These airmass histories were generated using the Monte Carlo model driven by the EDAS/FNL wind fields. As shown, airmasses en route to Big Bend are most likely to have previously resided southeast of Big Bend, just south of the Mexican-Texas border. This is consistent with airmasses being transported from the Gulf of Mexico along northeastern Mexico to Big Bend. The next highest region of probable transport to Big Bend is over Texas northeast of Big Bend and from the eastern U.S. Airmass transport from west of Big Bend and from southern Mexico infrequently occurred during BRAVO. The airmass transport during BRAVO had two distinct periods. During July to the middle of August airmass histories almost exclusively came from the Gulf of Mexico and up along the Mexican-Texas border to Big Bend. This time period also had the lowest average sulfate concentration and haze during BRAVO (section 4). Airmass transport from Texas and the eastern U.S. was more prevalent after the middle of August, though transport along the Mexican-Texas border still dominated.

The spatial patterns in the residence time PDF are predominantly due to the frequency at which airmass trajectories traverse a given area prior to reaching the receptor. This is seen in Figure 8-47, where the residence time PDF and transport direction frequency plots have similar spatial patterns. The highest accumulation potentials (> 0.15 s/m) exist in a band from northwest Mexico to the Gulf of Mexico and throughout Texas. These are equivalent to effective airmass transport speeds of about 6 m/s. To the north and south of this band the accumulation potential decreases to between 0.1 and 0.15 s/m. The lowest average particle heights (< 1 km) are along the regions with the highest residence times, from the Gulf of Mexico up along the Texas-Mexican border (< 1 km), and throughout Texas (< 1.5 km). West of Big Bend and in the eastern U.S., the airmasses are higher, with average heights above 4 km in Ohio and northwest to Minnesota and in the intra-mountainous western U.S.

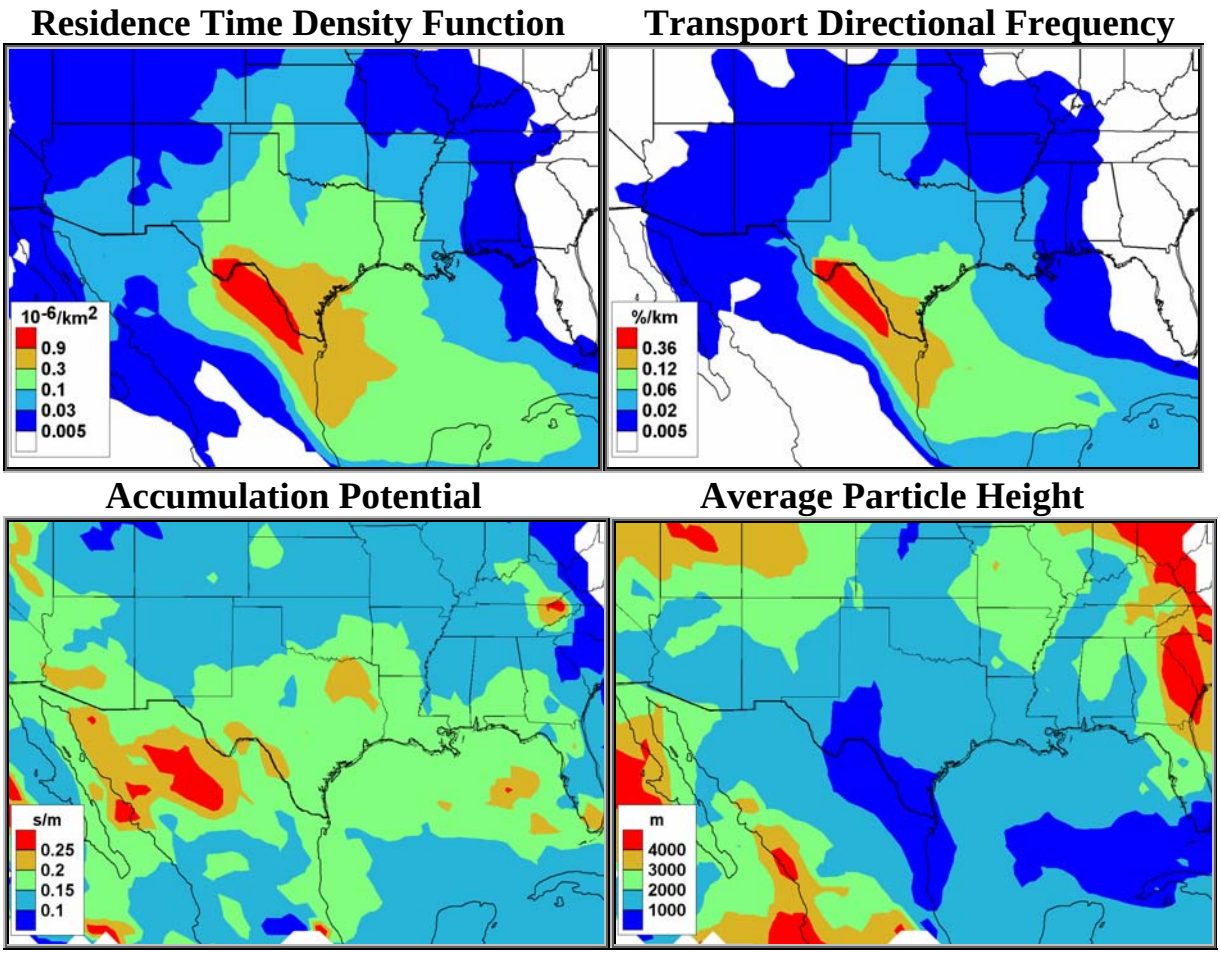

Figure 8-47. The residence time PDF and its decomposition for the entire BRAVO study. The airmass histories were generated using the EDAS/FNL wind fields.

8.1.3.3.1 Airmass Transport during High and Low Particulate Sulfur Days

In order to delineate preferential transport pathways for different particulate sulfur concentrations, the airmass histories were sorted and aggregated according to whether the particulate sulfur was low (below the 20th percentile) or high (above the 80th percentile). The residence time PDF and its decomposition for the high and low sulfur days are presented in Figures 8-48 and 8-49. As shown in Figure 8-48, Big Bend's highest particle sulfur concentrations were primarily associated with prior airmass transport from the southeast, along northeastern Mexico and along the Texas-Mexican border. Airmasses were also likely to have previously resided northeast of Big Bend over eastern Texas and the southeastern U.S. This transport pattern is consistent with airmasses coming from the southeastern U.S. through eastern Texas and up along the Mexican-Texas border to Big Bend. The transport over both northeastern Mexico and eastern Texas had high accumulation potentials (> 0.25 s/m) and low average particle heights (< 2 km). Transport from the industrial Midwestern states did occur, but it was infrequent and had lower accumulation potentials and average heights in excess of 3 km. In fact, over these states no particles were ever below 2 km.

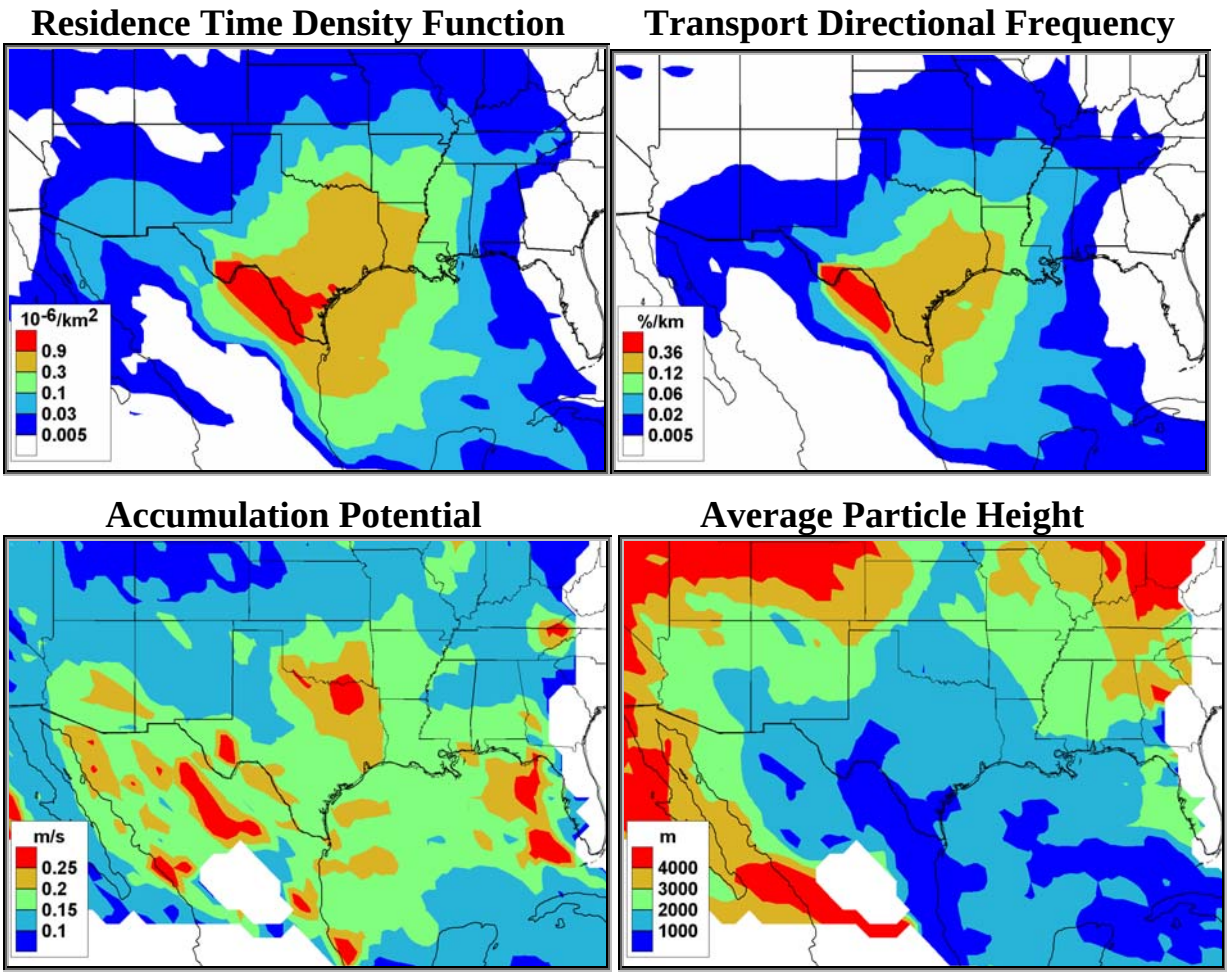

Figure 8-48. The Big Bend NP residence time PDF and its decomposition for the 20% of the days with the highest particulate sulfur. The airmass histories were generated using the EDAS/FNL wind fields.

Transport during the low sulfur days was persistently from the Gulf of Mexico along northeastern Mexico and from the north from the Great Plains states to Big Bend (Figure 8-49). Along these two transport pathways, the airmass histories had low average heights, ~ 1 km, and higher than average transport speeds. Unlike the high sulfur days, almost no transport from eastern Texas or the southeastern U.S. occurs prior to low Big Bend particulate sulfur concentrations. It is interesting that at Big Bend and to its southeast the accumulation potential was large (~ 0.3 s/m) compared to its surroundings, but on the high sulfur days the accumulation potential in this region was small (~0.15 s/m) compared to its surroundings. This is consistent with the fact that Big Bend and its immediate surroundings have few source of sulfur.

The airmass transport pathways to Big Bend NP for individual particulate sulfur episodes were also examined. As shown in Figure 8-50, the three common transport pathways associated with the particulate sulfur episodes were from eastern Texas, the southeastern U.S., and northeastern Mexico. The largest concentrations occurred when transport over several of these regions coincided. For example, the September 1 episode had transport over all three regions and had the highest particle sulfur concentration (3.2 $\mu g/m^3$) during the BRAVO study. Appendix 8c presents the decomposed residence time analysis for all seven Big Bend particulate sulfur episode during BRAVO.

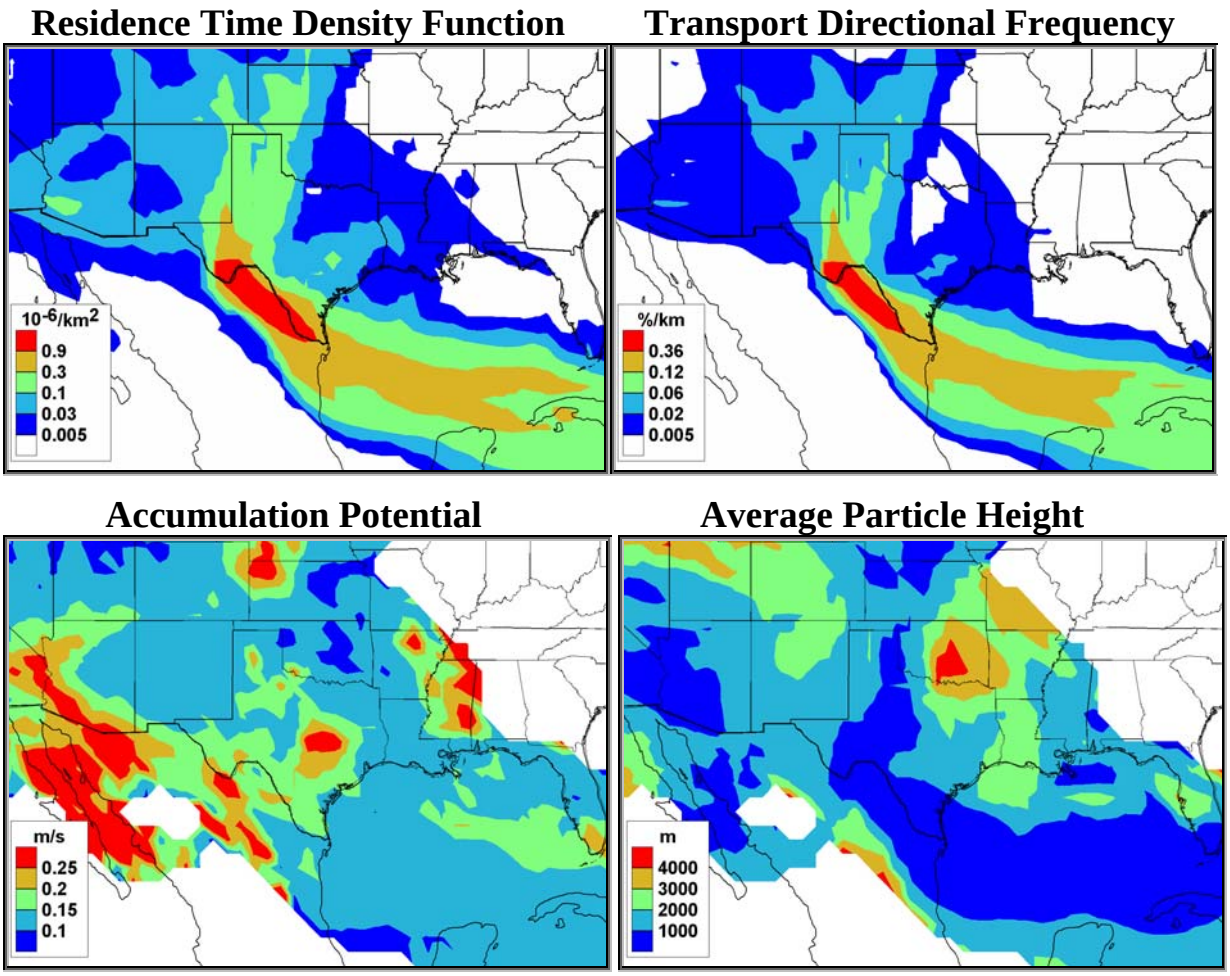

Figure 8-49. The Big Bend NP residence time PDF and its decomposition for the 20% of the days with the lowest particulate sulfur. The airmass histories were generated using the EDAS/FNL wind fields.

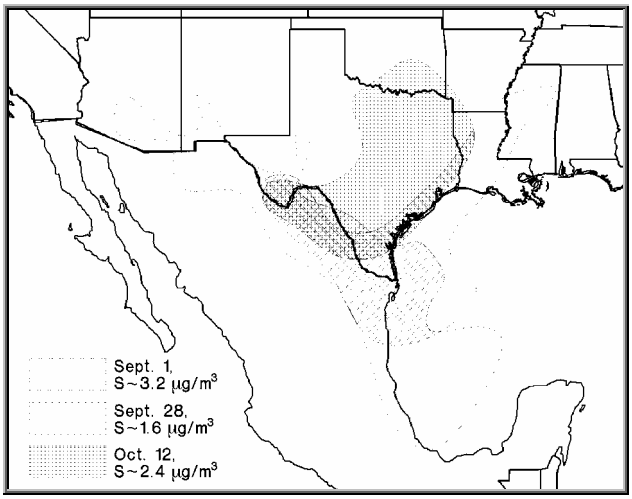

Figure 8-50. Airmass transport pathways to Big Bend NP during three particulate sulfur episodes. Each isopleth shows the most likely pathway the airmass traversed prior to impacting Big Bend. The transport pathways were created using residence time analysis and the contour lines encompass 75% of the residence time hours.

The airmass transport on the high sulfur days using the MM5 meteorological data had some important differences compared to the EDAS/FNL results. As shown in Figure 8-51, both the residence time PDF and transport directional frequency plots show that the likely airmass pathway was from the Mississippi-Louisiana region, down along the Texas coast, and across southern Texas to Big Bend. Therefore the MM5 results indicate a higher likelihood of airmasses traversing the southeastern U.S. and southern Texas en route to Big Bend, compared to the EDAS/FNL results which had a higher likelihood of airmasses traversing eastern Texas and northeastern Mexico. In addition, the MM5 airmass histories had higher transport speeds than those generated with the EDAS/FNL meteorological data. For example, the accumulation potential over Texas varied between 0.1 and 0.17 s/m compared to 0.13 and 0.27 s/m for the EDAS/FNL results. The MM5 and EDAS/FNL airmass histories had similar airmass transport patterns on the low sulfur days.

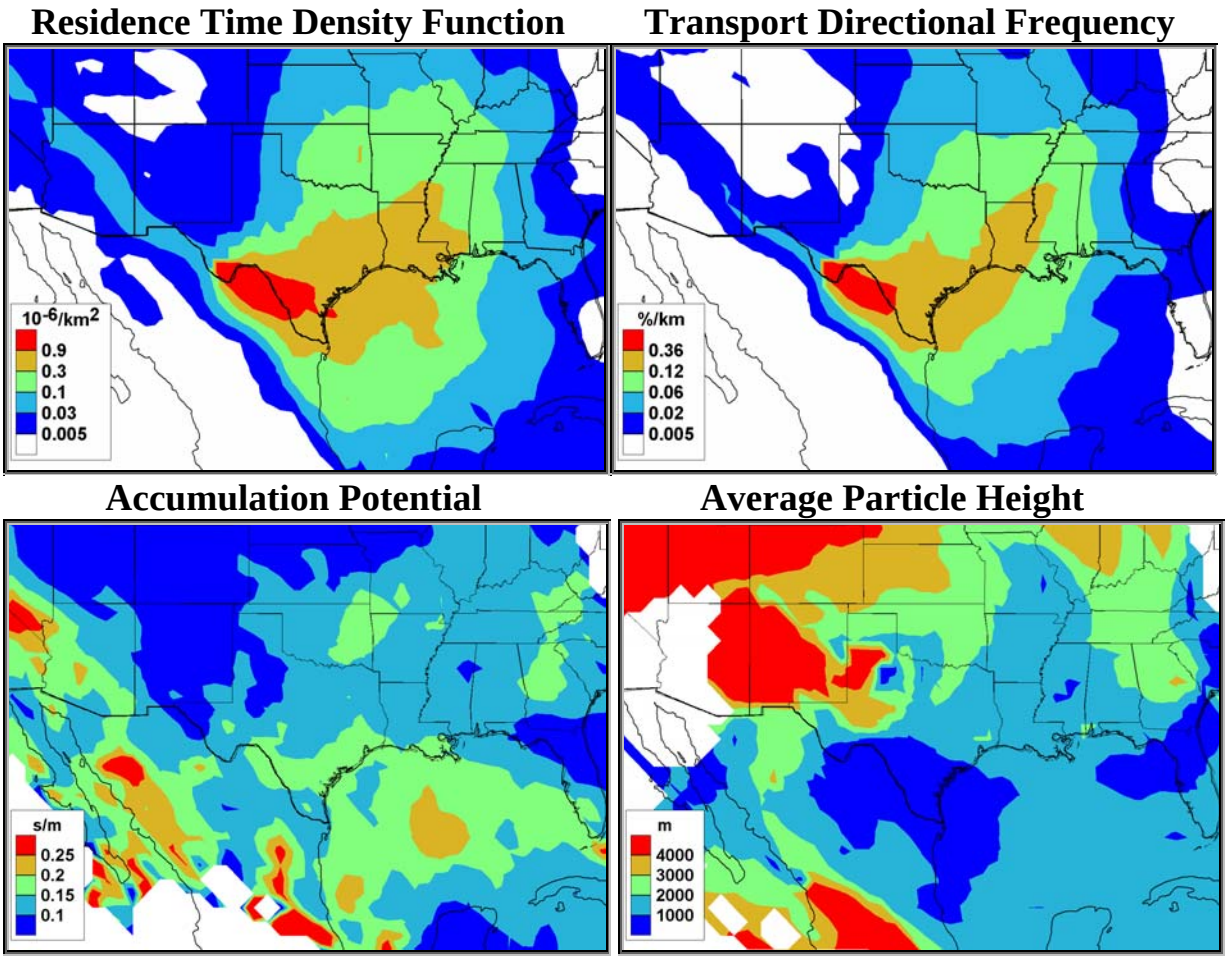

Figure 8-51. The residence time PDF and its decomposition for the 20% of the days with highest particulate sulfur at Big Bend. The airmass histories were generated using the MM5 wind fields.

8.1.3.3.2 Airmass Transport on High Particulate Sulfur Days Compared to Average Days

To better delineate the potential source regions contributing to Big Bend's particulate sulfur, incremental and conditional probability fields for the high sulfur days were examined. As shown in Figure 8-52A, the highest incremental probabilities exist over a broad region in eastern-southeastern Texas and over a region in the vicinity of the Carbón I & II power plants.

Conditional probabilities above 50% encompass a region from eastern Texas to the state of Mississippi. This indicates that, more than half of the time, when airmasses resided over the region they arrived at Big Bend with particulate sulfur concentrations above the 80th percentile. In addition, northeast Texas and eastern Tennessee had conditional probabilities above 70%. Northern Mexico had low conditional and incremental probabilities; however, this was expected since northern Mexico was the most common transport pathway to Big Bend during the entire BRAVO time period (Figure 8-46) and during the high particulate sulfur days (Figure 8-47).

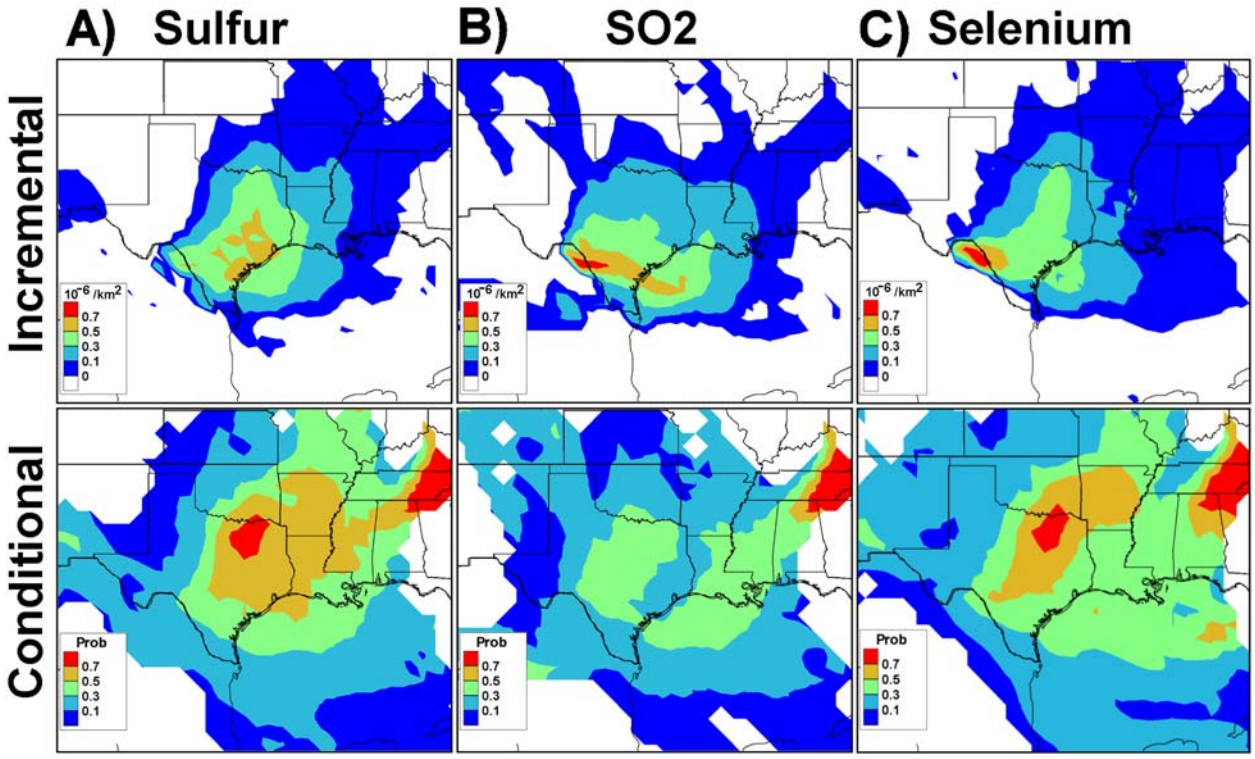

Figure 8-52. The incremental and conditional probabilities for the upper 20th percentiles of the A) fine particulate sulfur, B) sulfur dioxide, and C) fine particle selenium at Big Bend. These transport probabilities were created using airmass histories generated using the EDAS/FNL wind fields.

Incremental and conditional probability fields were also created for the 20% highest sulfur dioxide and selenium concentrations at Big Bend (Figures 8-52B and 8-52C). The highest incremental probabilities for both sulfur dioxide and selenium were in the vicinity of the Carbón I & II power plants. Beyond the Carbón region the airmass transport patterns diverged, with the sulfur dioxide incremental probability high over southern Texas, but for selenium, eastern and southern Texas have about equal incremental probabilities. This indicates a preferred airmass pathway though eastern Texas for the selenium and through southern Texas for sulfur dioxide. The conditional probabilities for sulfur dioxide and selenium do not identify the nearby Carbón region but rather more distant regions in Texas and eastern Tennessee. For eastern Tennessee, there is greater than 70% chance that if an airmass traversed this region it arrived at Big Bend with elevated sulfur dioxide and/or selenium. However, transport from eastern Tennessee was infrequent.

Similar results were found using the MM5 airmass histories, but for sulfur and selenium the incremental probabilities fields showed higher values further south in eastern Texas. In addition, the largest particulate sulfur incremental probability occurred along the Texas-Mexican

border in the vicinity of the Carbón power plants. This is consistent with the observation that during the high sulfur days the MM5 airmass histories had more southerly transport compared to the EDAS/FNL airmass histories.

8.1.3.4 Transport Patterns for 10-Day Airmass Histories

All of the transport analyses were conducted using five-day airmass histories. This was done based on the fact that on average sulfate has an atmospheric lifetime on the order of 3–5 days [*Husar and Husar*, 1978]. However, examination of REMSAD source attribution results indicated longer sulfate lifetimes, and it is known that in non-precipitation airmasses sulfate can have significantly longer lifetimes than 5 days. In addition, even if a 5-day lifetime is correct, after 5 days about one third of the pollutants still exist. In the eastern U.S. the SO_2 emissions are very large and one-third of initial ambient concentration can still be a significant contribution to Texas' and Big Bend's ambient sulfur concentrations. Therefore residence time analyses with longer than 5-day trajectories were conducted.

In order to determine the sensitivity of the airmass history analyses on trajectory length, the residence time analyses were duplicated using 10-day airmass histories. Figure 8-53 presents the decomposed residence time analysis for the ten EDAS/FNL airmass histories. Comparing the results of the 10-day airmass histories to the 5-day (Figure 8-48), it is seen that the largest differences are in the eastern U.S. As shown, the 10-day results show a higher frequency of transport from the eastern U.S., which tends to be at a lower level and slower speed. For example, the accumulation potentials around Georgia increased from ~0.15 s/m to over 0.25 s/m. Also, the average height of the particles along the Ohio River Valley decreased from 3–4 km to about 2 km.

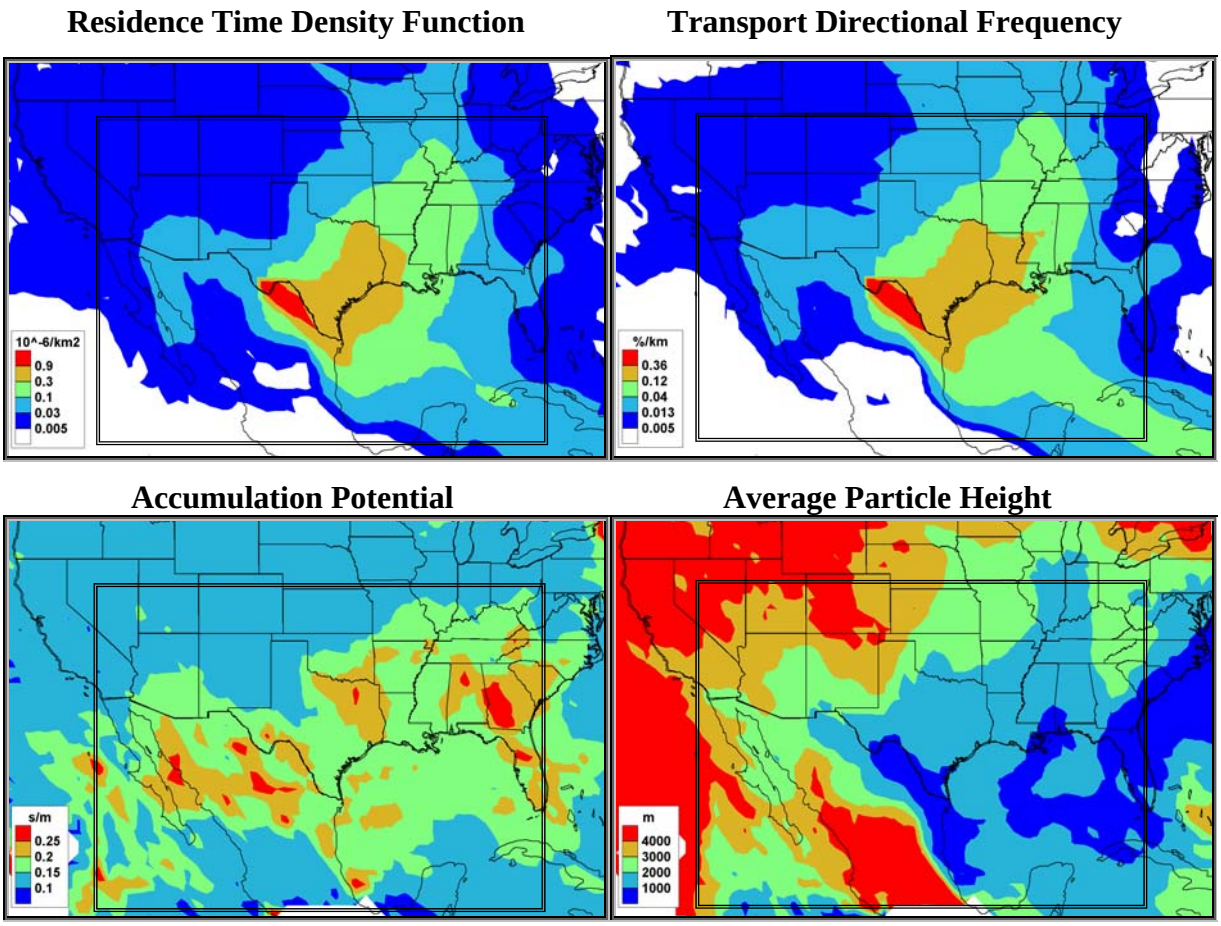

Figure 8-53. The Big Bend NP residence time PDF and its decomposition for the 20% of the days with the highest particulate sulfur. 10-day airmass histories were generated using the EDAS/FNL meteorological data. The box in each plot spans the geographic boundary of the residence time plots in Figure 8-48.

The causes for these changes in the transport conditions from the eastern U.S. due to the increased airmass history length can be seen be examining individual airmass histories. Figure 8-54 presents one of the 10-day airmass histories to Big Bend on September 1. As shown, this airmass was originally composed of elevated and surface level airmasses that converged about four days prior to reaching Big Bend. The elevated airmass traveled from Canada, and five days prior to reaching Big Bend was located 2 to 6 km above the Ohio River Valley. Ten days before reaching Big Bend, the surface level airmass was mostly located over the Midwestern states from Kentucky to Wisconsin. This airmass moved in a counter clockwise direction over this region and 4 to 5 days later was located over Tennessee and Arkansas, at which point it converged with the elevated airmass. Therefore the 5-day airmass histories had only a subset of the airmass trajectories traversing the Ohio River Valley, all of which were elevated and traveling at higher speeds.

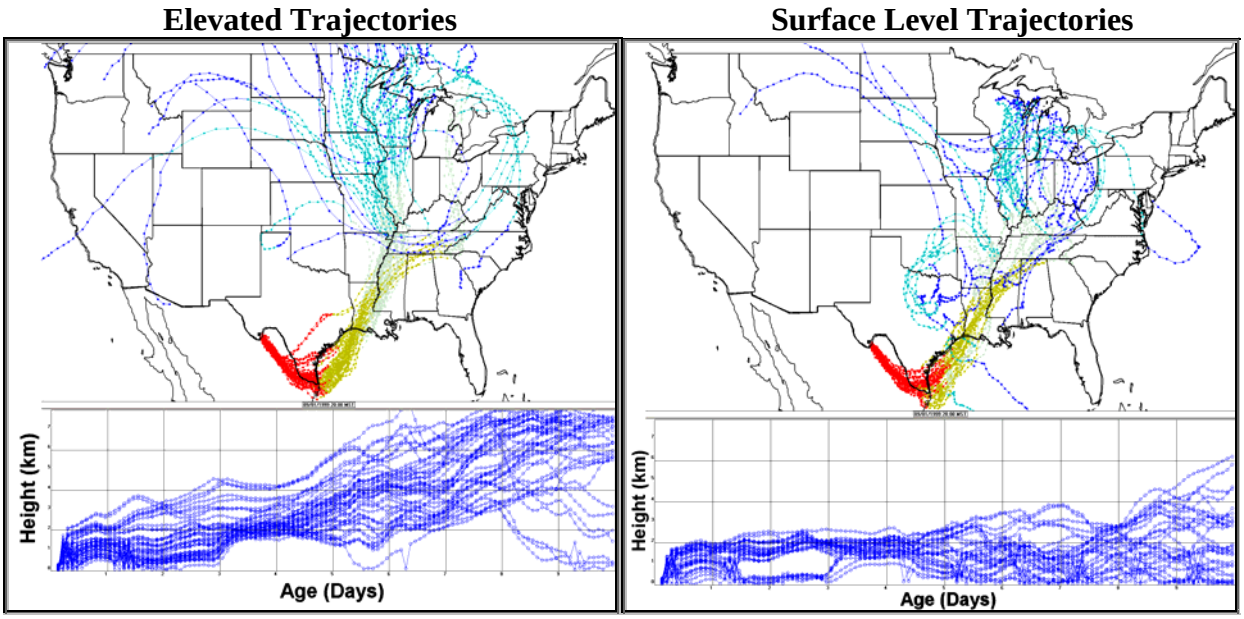

Figure 8-54. Big Bend ten-day airmass history for September 1, 20:00, 1999, generated using the EDAS/FNL data. The airmass history was divided into elevated and surface trajectories. Each color represents two days of transport with the red trajectories 0 to 2 days and blue 8–10 days prior to reaching Big Bend.

The incremental and conditional probabilities for the for the upper 20th percentiles of the particulate sulfur at Big Bend using 10-day airmass histories generated using the EDAS/FNL and MM5 meteorological data are presented in Figure 8-55. As shown, the incremental probabilities are similar to the results using the 5-day airmass histories, but the conditional probabilities show higher probabilities farther from Big Bend into the Great Lakes region. This is consistent with the fact that the incremental probabilities identify more nearby source regions and conditional probabilities tend to identify more distant source regions.

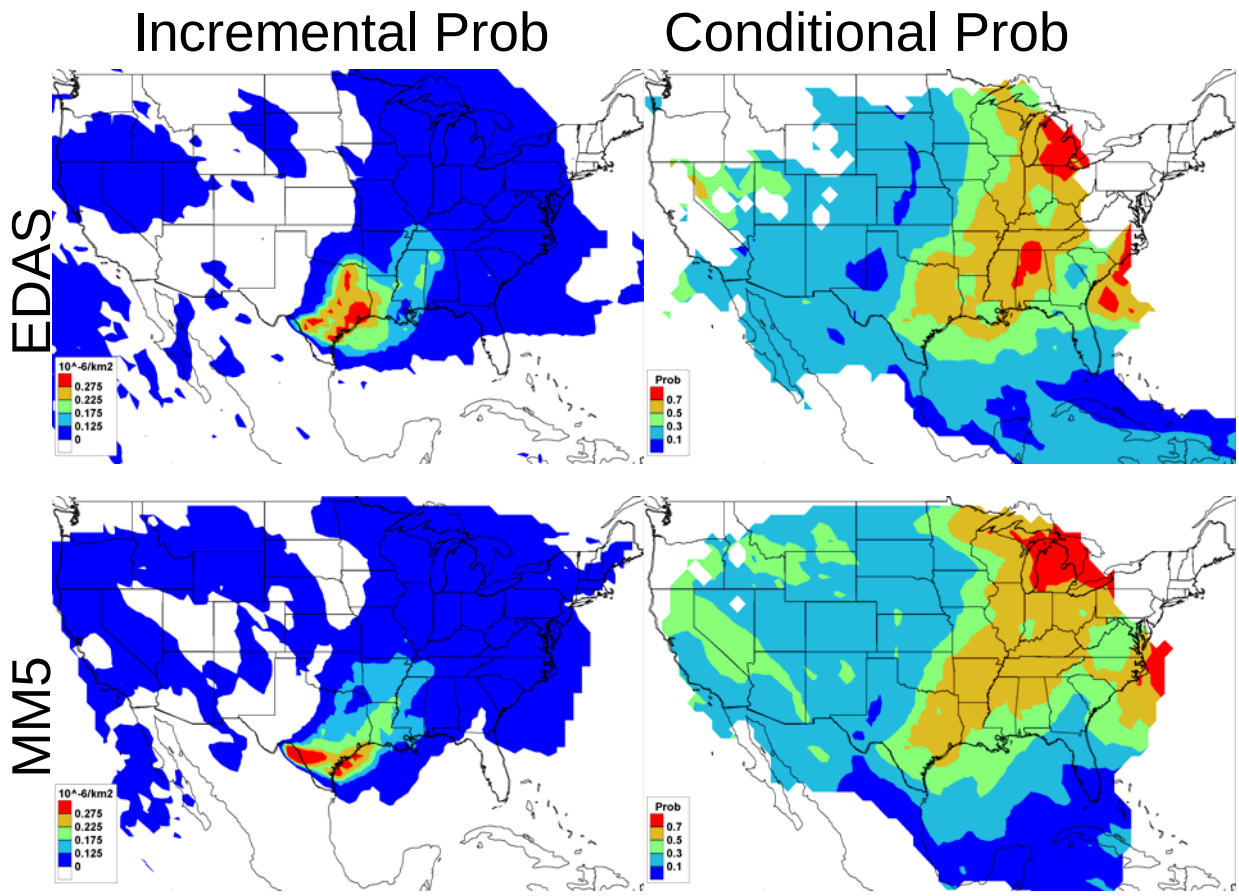

Figure 8-55. The incremental and conditional probabilities for the upper 20th percentiles of the particulate sulfur at Big Bend. These transport probabilities were created using 10-day airmass histories generated using the EDAS/FNL data.

8.1.3.5 Big Bend Climatological Airmass History Analysis

To evaluate the representativeness of the transport meteorology during the BRAVO period, both for other months of the year and for the same months in other years, hourly five-day-long trajectories arriving at Big Bend National Park were calculated with HYSPLIT using EDAS input data for a five-year period (1998 to 2002). Similar analyses for earlier years have been previously reported in *Gebhart et al*. [2000, 2001] and the results are similar.

Figure 8-56 shows the geographic distribution of trajectory residence times for a representative month during each season, aggregated over these years. Histograms of the monthly residence times for different discrete potential source regions in the U.S. and Mexico, showing the same data in a different way, are shown in Figure 8-57. The source areas in Figure 8-57 are the same as those used for TrMB modeling and discussed in chapter 2.

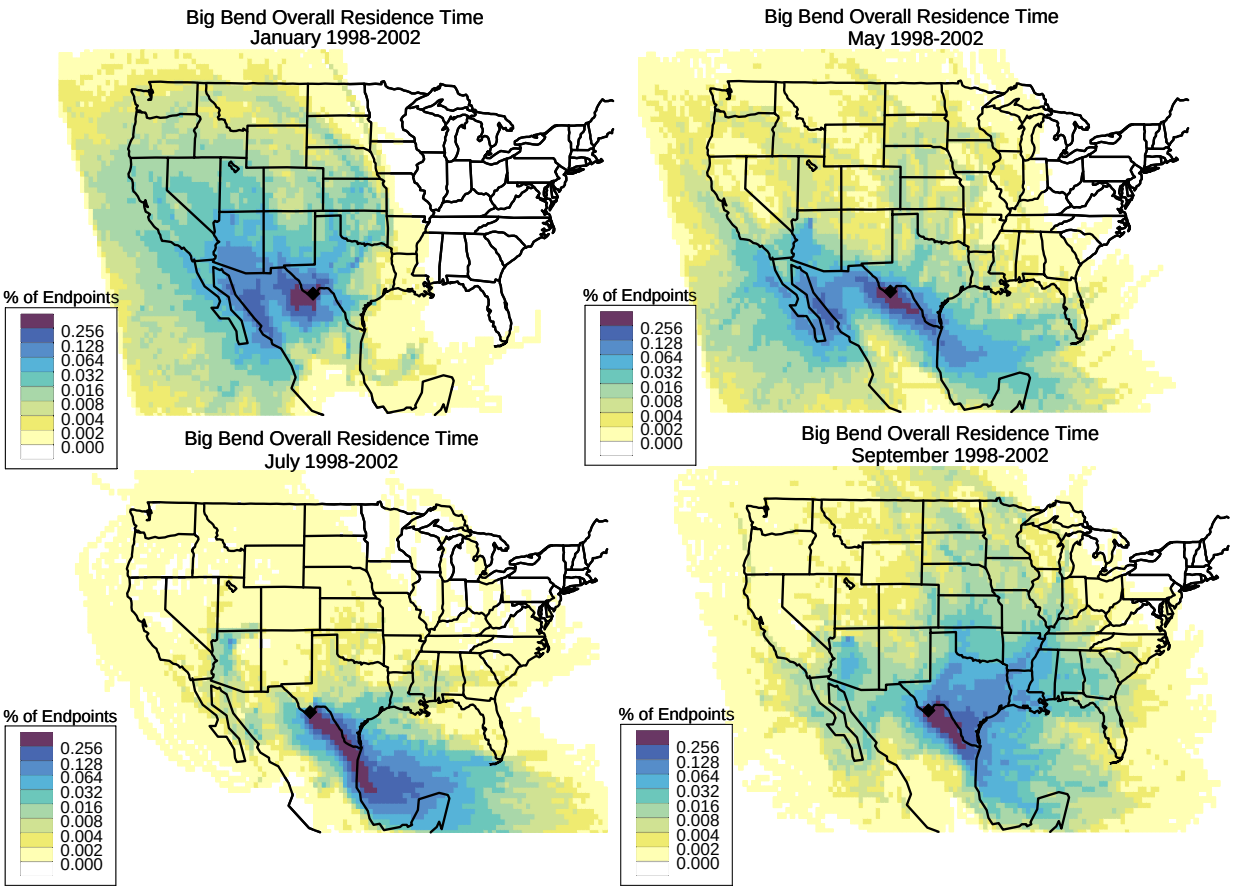

Figure 8-56. Examples of geographic distribution of the fraction of time that air parcels spend during the five days prior to arriving at Big Bend National Park for the months of January, May, July, and September based upon a five-year analysis period (1998 to 2002).

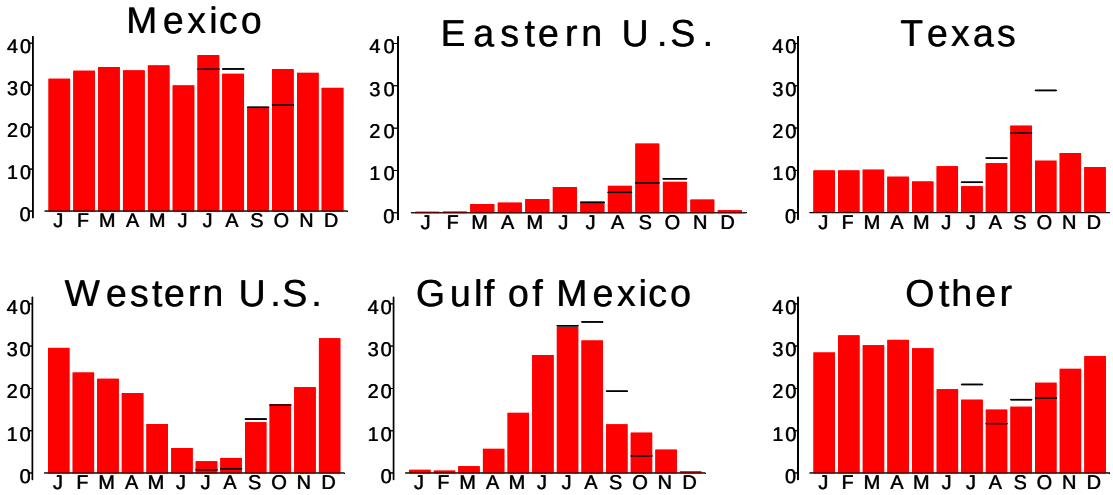

Figure 8-57. Monthly percentages of time that air parcels spend in a region prior to arrival at Big Bend based on 5-day back trajectory calculations for the five-year period from 1998 to 2002. The black lines shown over the months of July through October correspond to the values during the BRAVO study period in 1999. The black line for October was calculated using FNL data rather than EDAS. The plot labeled "Other" represents locations primarily over the Atlantic and Pacific Oceans.

8.1.3.6 Discussion

A fundamental assumption in any airmass history analysis is that the modeled airmass transport is an unbiased simulation of the actual airmass transport. To test this, the airmass histories were validated against measured tracer data using the residence time analysis. The results showed that the CMC model driven by the EDAS/FNL or 36 km MM5 meteorological data was able to properly identify the transport pathways of the tracer data to Big Bend. A similar conclusion was found from the forward simulation of the tracer data using the CMC model in section 5.3. However, there does appear to be a small northerly bias in the transport from the Parish power plant in Houston, Texas. This bias in transport could result in misallocating sulfur attribution to the north of Houston. The results from the conditional and incremental probability analyses highlighted the difficulty in uniquely identifying the tracer source regions using only 1.5 to 4 months of data. For example, transport from San Antonio and Houston to Big Bend often traversed the region where the Carbón power plants reside.

The purpose of this airmass history analysis was to help identify regions with a potential to contribute to the fine particulate sulfur and haze at Big Bend. These results clearly showed that prior to high Big Bend particulate sulfur concentrations, low level and speed transport often occurred over eastern-southeastern Texas and states east of Texas (LA, MS, AL, and AR). In addition, transport over these regions did not often occur prior to low Big Bend sulfur concentrations. These results combined with the fact that eastern Texas and the southeastern U.S. have high sulfur dioxide emissions support the notion that these areas contribute to the sulfate concentrations and haze at Big Bend.

Northeastern Mexico also has large sulfur point and area sources including the Carbón I & II power plants and the Monterrey urban center. However, the association of prior transport over this region with elevated Big Bend sulfur concentrations is inconclusive. The elevated particulate sulfur concentrations at Big Bend were more likely than average to have previously resided over the Carbón I & II plants, but it was found that this region was also a transport corridor for airmasses coming from eastern Texas to Big Bend. Therefore this association may be a coincidence. In addition, prior transport over the Carbón I & II plants and Monterrey regions was associated with low Big Bend particulate sulfur levels. On the other hand, these low particulate sulfur airmasses came directly off the Gulf of Mexico with higher speeds and/or precipitation occurred prior to impacting Big Bend. The higher speeds decrease the possibility of emissions accumulating in the airmass, and the precipitation efficiently removes SO_2 and sulfate particles.

The results using the 5-day airmass histories also showed that higher speeds (> 6 m/s) and elevated transport levels (above 3 km) occurred over the industrial Midwest and eastern Tennessee prior to high sulfur concentrations at Big Bend. The higher speeds and elevation of these airmasses are not conducive for the accumulation of emissions from this region. However, these two regions have some of the highest SO_2 emissions in the U.S. The analysis was redone using 10-day airmass histories. In this case, more frequent, lower level, and lower speed transport over the industrial Midwestern states occurred. These conditions are conducive to bringing emissions from this region to Big Bend, but this is dependent on a long lifetime for the particulate sulfur.

Confidence in the airmass histories and residence time analysis also comes from the examination of the transport patterns for elevated Big Bend concentrations of fine particle sulfur,

sulfur dioxide, and selenium compared to average days. Taken together, these results showed a consistency among the transport pathways that could be explained from known sources and atmospheric lifetimes of each species. Sulfur dioxide is a primary species with an atmospheric lifetime on the order of several days, about half of particulate sulfate's [*Husar et al.*, 1978]. Therefore Big Bend's sulfur dioxide concentration should be influenced by more nearby source regions compared to particulate sulfate. The sulfur dioxide incremental probabilities clearly identified the Carbón I & II power plant region, ~250 km from Big Bend, as a potential source region, while the sulfur incremental probabilities indicated more distant and distributed source regions from the Carbón region to eastern-southeastern Texas. Selenium is a primary fine particle species primarily emitted from coal-fired power plants without wet scrubbers [*Watson et al.*, 2001; *Chow et al.*, 2004]. These results identified the Carbón region as a likely source region as well as the more distant eastern Texas lignite belt which has a number of coal-fired power plants without wet scrubbers.

The robustness of the transport analysis associated with high particulate sulfur was also tested by using the two sets of meteorological data. This resulted in different airmass transport patterns with the EDAS/FNL airmass histories having greater transport from northeastern Texas than the MM5 airmass histories, while the MM5 airmass histories had a higher probability of transport from southeast Texas and states east of Texas. In addition, the MM5 results produced higher speed, thus longer-range airmass transport. These differences do not impact the conclusion from this analysis. However, these differences will result in different source apportionment estimates depending on the meteorological data used in the analysis.

8.1.4 Trajectory Max - Upper Bounds on Source Contribution to Big Bend's Particulate Sulfur

The trajectory max is a simple airmass history technique to place an extreme upper bound on a source region's contribution to Big Bend's particulate sulfur. Trajectory max assumes that if an airmass traversed a source region then the receptor concentration is solely due to emissions from that source region. Therefore the source region in which the receptor resides will have a maximum source contribution of 100%. This technique relies on an unbiased assessment of the average airmass transport from the source regions to the receptor. Section 2.3.1.4 describes the method in detail. This analysis used the same airmass histories generated from the EDAS/FNL and MM5 meteorological data that were used to evaluate the airmass transport to Big Bend National Park in chapter 5 and section 8.1.3.

The results of this analysis using the EDAS/FNL and MM5 airmass histories are presented on a uniform 80 x 80 km grid (Figures 8-58A and 8-59A) and in large source regions (Figures 8-58B and 8-59B) defined in Figure 2-16. As shown, the maximum source contribution patterns are similar to the residence time plots for the 20% highest particulate sulfur days (Figures 8-48 and 8-51). This is expected since the transport patterns on the highest particulate sulfur concentrations will have the largest weights in the source contribution averaging. Also, the maximum source contribution drops off sharply from the receptor to less than 25% past the Mississippi River, west of Texas, and in north Kansas (Figure 8-58A). However, maximum source contributions from the large source regions are above 35% in regions such as the Mid-Atlantic states.

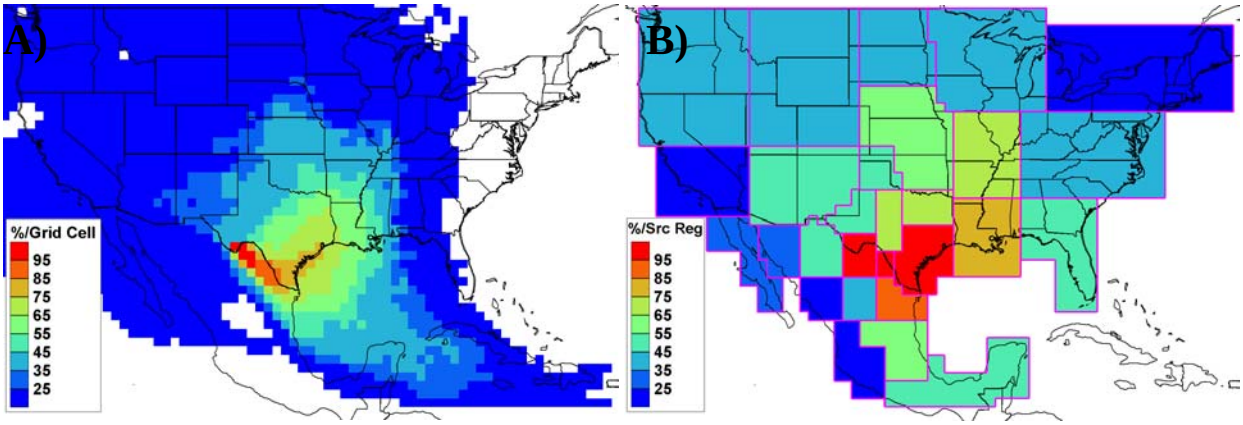

Figure 8-58. The maximum source contributions to Big Bend's particulate sulfur as estimated from EDAS/FNL airmass histories. A) The maximum source contribution for each 80 x 80 km_2 grid cell. B) The maximum source contribution for each source region defined in Figure 2-14.

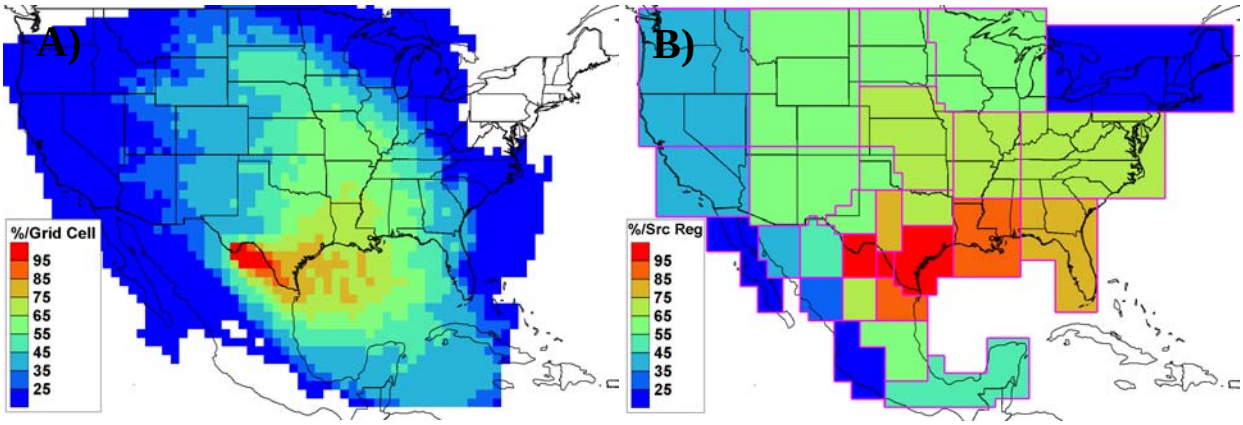

Figure 8-59. The maximum source contributions to Big Bend's particulate sulfur as estimated from MM5 airmass histories. A) The maximum source contribution for each 80 x 80 km_2 grid cell. B) The maximum source contribution for each source region defined in Figure 2-14.

There are two important differences between the EDAS/FNL- and MM5-derived maximum source contributions shown in Figures 8-12 and 8-13. First, the MM5 results have higher source contributions from distant source regions. For example, the MM5-derived maximum source contributions from the Dakotas and western Great Lakes states are 55 to 65% compared to 35 to 45% for the EDAS/FNL results. Second, the MM5 results estimate higher source maximum contributions from the eastern United States from the Ohio River Valley to the Gulf of Mexico with a maximum value of over 85% from the Louisiana region and 75% from Florida.

8.2 Quantitative

8.2.1 Synthesis Inversion – Merging Air Quality Model Source Apportionment Results and Receptor Data

The REMSAD model was employed to predict the sulfate concentrations in most of North America and to estimate the contribution of sulfate from ten major U.S. and Mexican source regions and the model boundary conditions to Big Bend and the other BRAVO monitoring sites. The CMAQ-MADRID model was similarly employed, but predicted sulfate over a smaller region centered on Texas and estimated the sulfate contributions from Texas,

Mexico, western U.S., and eastern U.S. source regions as well as the boundary conditions [*Electric Power Research Institute*, 2004]. The CMAQ-MADRID boundary conditions were generated from the REMSAD-simulated sulfate and SO_2 concentrations which were first nudged to observed data by comparing the REMSAD simulated sulfate and SO_2 concentrations to measured data from the IMPROVE and CASTNet monitoring networks. CMAQ-MADRID also used an upper estimate of the Carbón facilities' SO_2 emissions, 241,000 tons/yr compared to 152,000 tons/yr used by REMSAD. The other Mexican SO_2 emissions in the CMAQ-MADRID domain were doubled compared to what was used in REMSAD. This doubling of emissions was done due to an apparent underestimation in Mexico's contribution to sulfate throughout Texas in the REMSAD model runs.

Both REMSAD and CMAQ-MADRID were run using the 36 km MM5 wind field. CMAQ-MADRID was originally to be used to simulate concentrations on only the MM5 4 and 12 km grids which were nested in the larger 36 km grid. However, for performance reasons, CMAQ-MADRID was run with the 36 km MM5 meteorological data [*EPRI*, 2004]. The emission input fields were only available for the smaller 4 and 12 km domains. Therefore, the CMAQ-MADRID simulation was confined to the smaller 12 km domain.

Overall, REMSAD predicted sulfate across Texas with a 65% gross error, 76 % RMS error, and a bias (difference of averages) of 8%. At Big Bend the gross and RMS errors were 62% and 73%, respectively, and with a bias of -18%. The CMAQ-MADRID model had a gross error of 47%, RMS error of 86%, and bias of 29% for all BRAVO sites, and at Big Bend the gross and RMS errors were 46% and 60%, respectively, and had no bias. These are satisfactory modeling results, but there were spatial and temporal trends in the biases (see section 6.2). For example, REMSAD nearly uniformly underestimated the sulfate concentrations throughout Texas during July and overestimated them in October. The positive bias in eastern Texas was at least partly due to the contributions from the eastern U.S. sources being overestimated.

In order to account for these biases, the REMSAD and CMAQ-MADRID sulfate source attribution results were regressed against the observed sulfate concentrations throughout Texas. The same simulated attribution results are then scaled by the regression coefficients to derive alternative source attribution estimates that, when summed together, better fit the measured data. This approach compensates for some of the systematic errors present in the two simulations of the air quality models and thus should provide more accurate attributions of Big Bend aerosol. The technique is based on the synthesis inversion technique which is fully described in section 2.3.2.3.1 and validated in section 7.2.3. This technique is based upon the equation:

$$c_i = \sum_j G_{ij} s_j + \varepsilon_i = m_i + \varepsilon_i \qquad (2\text{-}33)$$

where c_i is a vector of sulfate observations (the measured fine particulate sulfur concentration multiplied by three.); G_{ij} is a matrix of the source attribution from each source region/time pair to each observation; s_j are the source attribution scaling coefficients; m_i are the modeled concentration values; and ε_i are the errors in c_i. s_j identify spatial or temporal biases in the original REMSAD source attributions due to errors in the emission, transport, chemistry and/or removal process of sulfur. s_j are found by using a constrained least squares regression to invert equation 2-33. In essence, the resulting scaling coefficients partition the underestimated mass back to the source regions and remove overestimated mass from the source regions. The revised predicted sulfate concentrations then best match the measured data in a least square sense. Once

the scaling coefficients are calculated, the synthesized REMSAD source attribution results are estimated by $c_{ij} = G_{ij} s_j$.

8.2.1.1 Spatial and Temporal Variability in the Source Attribution Scaling Coefficients

In general, as more data with varied source attributions are incorporated into the regression analysis, the source attribution scaling coefficients are more stable with smaller errors. Therefore, it is desirable to incorporate data for as long a time period and from as many sites as possible. However, the scaling coefficients compensate for errors in the modeled emissions and physical and chemical processes and will vary in time and space. If data with compensating biases are incorporated into the analysis, then the regression will not be able to account for either bias in the system. The scaling coefficients represent an average bias correction for the spatial and temporal periods used in the analysis. If the biases are large-scale, for example, errors in emissions or underestimation of diffusion, then the scaling coefficients will be applicable to a subset of the monitoring sites and time period used in the analysis. However, if the biases vary in a non-random way over spatial scales of interest, e.g., Texas, and over shorter time periods used in the analysis, then it will be inappropriate to apply these coefficients to a large subset of the monitoring sites or time period used in the analysis. This section examines the spatial and temporal variability to determine the best way to group the observed sulfate observation over the BRAVO monitoring sites and time period. The following uses the REMSAD model source attributions; however, similar results were found using the CMAQ-MADRID source attributions.

8.2.1.1.1 Spatial Variability

The spatial variability was examined by performing the regression analysis using data from each BRAVO monitoring site over the entire BRAVO time period. A constrained regression analysis was used where the coefficient could be within a factor of 4 of the REMSAD source attribution results, e.g., between 0.25 and 4. The regression was performed using all eleven source regions. The results for each monitoring site are presented in Table 8-3. Each regression used a maximum of 112 data points and a minimum of 84 valid data points or a 75% complete time series. Scaling coefficients are also only shown if the source region contributed 6% or more to the receptor site on average as estimated by REMSAD. The four eastern U.S. source regions were aggregated together and the west Texas source region is not shown since it contributed 6% or more too only two receptor sites.

Table 8-3. Source attribution scaling coefficients and standard errors resulting from the regression of the REMSAD source attributions against the particulate sulfur data measured at each BRAVO monitoring site over the entire time period. The monitoring sites needed 75% or 84 valid data points for the regression to be conducted. Regression coefficients are shown only if the source region contributed 6% or more to the receptor site on average as estimated by REMSAD. The West Texas source region is not shown because it rarely contributed 6% of the sulfate to any site. The four eastern U.S. source regions were aggregated together. Source regions with a regression coefficient more than a factor of two of the average standard error away from the average coefficients across all sites are bolded.

			Source Attribution Scaling Coefficients						
Monitoring Site	**Bias (%)**	**r**	**Carbón**	**Rest Mex.**	**NE TX**	**SE TX**	**E U.S.**	**W U.S.**	**Bndy Cnd**
K-Bar 24-hour	-10	0.57	1.9 ± 0.4	2.6 ± 0.6		1.4 ± 1.1	0.7 ± 0.5	0.3 ± 1.1	1.5 ± 1.7
San Vicente	-10	0.57	2.0 ± 0.5	2.7 ± 0.7		1.2 ± 1.1	0.7 ± 0.5	0.3 ± 1.1	
Persimmon Gap	-7	0.56	2.5 ± 0.5	1.8 ± 0.8		2.3 ± 0.8	0.5 ± 0.4	0.3 ± 1.0	1.8 ± 1.5
Marathon	-7	0.54	2.5 ± 0.5	1.7 ± 0.8		2.0 ± 0.7	0.4 ± 0.4	0.3 ± 0.9	1.7 ± 1.4
Fort Stockton	-7	0.56	2.1 ± 0.5	1.6 ± 0.8		2.2 ± 0.6	0.4 ± 0.4	0.3 ± 0.8	1.9 ± 1.2

Monahans Sandhills	-7	0.64	1.6 ± 0.6			**2.7 ± 0.6**	0.6 ± 0.3	0.3 ± 0.9	2.6 ± 1.1
Esperanza	-3	0.54	1.9 ± 0.3	1.3 ± 0.3		1.0 ± 0.5	0.4 ± 0.4	0.3 ± 0.4	3.7 ± 0.8
McDonald Obs.	-8	0.55	2.4 ± 0.4	0.8 ± 0.4		1.5 ± 0.5	0.5 ± 0.4	0.3 ± 0.5	2.3 ± 1.0
Presidio	-10	0.50	1.5 ± 0.4	1.4 ± 0.5	0.3 ± 1.0	0.6 ± 0.9	0.7 ± 0.5	0.3 ± 0.8	2.6 ± 1.5
LBJ NHS	-8	0.64			0.3 ± 0.6	1.5 ± 0.2	0.6 ± 0.2		0.5 ± 1.0
Fort McKavett	-5	0.71			0.3 ± 0.4	1.6 ± 0.3	0.6 ± 0.2	0.3 ± 0.8	1.2 ± 0.9
Lake Colorado City	-3	0.73			0.3 ± 0.3	1.7 ± 0.3	0.6 ± 0.2	0.3 ± 0.5	2.3 ± 0.7
Fort Lancaster	-7	0.54	1.1 ± 0.7		0.3 ± 0.6	2.3 ± 0.5	0.4 ± 0.3	0.3 ± 1.0	2.3 ± 1.1
Sanderson	-8	0.45	1.7 ± 0.7			2.3 ± 0.6	0.3 ± 0.4	0.3 ± 1.3	
Langtry	-9	0.59	1.5 ± 0.7			2.2 ± 0.5	0.6 ± 0.3	0.3 ± 1.2	
Amistad	-10	0.64	**0.3 ± 0.6**			2.3 ± 0.5	0.6 ± 0.3	0.3 ± 1.2	1.3 ± 1.3
Brackettville	-11	0.65			0.3 ± 0.7	2.0 ± 0.4	0.6 ± 0.2	0.3 ± 1.3	1.0 ± 1.2
Eagle Pass	-15	0.51			0.3 ± 0.8	1.7 ± 0.5	0.5 ± 0.2	0.3 ± 1.5	0.9 ± 1.4
Laredo	-14	0.61			0.3 ± 0.7	1.0 ± 0.7	0.7 ± 0.2		1.9 ± 1.4
Falcon Dam	-14	0.58		**4.0 ± 0.7**	0.3 ± 0.8	0.7 ± 1.0	0.5 ± 0.2		2.7 ± 1.2
Laguna Atascosa	-24	0.63			0.3 ± 1.2	**0.3 ± 0.8**	0.7 ± 0.2		3.5 ± 1.4
Lake Corpus Christi	-13	0.67			0.3 ± 0.7	0.6 ± 0.5	0.7 ± 0.2		2.1 ± 1.1
Pleasanton	-15	0.69			0.3 ± 0.8	0.9 ± 0.3	0.8 ± 0.2		0.8 ± 1.3
Everton Ranch	-16	0.71			0.3 ± 0.7	1.2 ± 0.4	0.6 ± 0.2		1.7 ± 1.3
Hagerman	-2	0.71			0.7 ± 0.4	2.1 ± 0.5	0.6 ± 0.1	0.3 ± 0.6	2.6 ± 0.7
Purtis Creek	-7	0.71			0.4 ± 0.3	1.7 ± 0.4	0.8 ± 0.1	0.0 ± 0.0	2.5 ± 0.7
Stephenville	-6	0.61			0.6 ± 0.6	1.3 ± 0.4	0.7 ± 0.2	0.3 ± 1.0	2.3 ± 0.9
Stillhouse Lake	-8	0.64			0.3 ± 0.5	1.1 ± 0.2	0.7 ± 0.1		2.2 ± 0.9
Somerville Lake	-8	0.66			0.3 ± 0.3	1.1 ± 0.2	0.7 ± 0.1		2.0 ± 0.9
Aransas	-14	0.71			0.3 ± 0.7	**0.3 ± 0.5**	0.8 ± 0.1		2.0 ± 1.1
San Bernard	-13	0.73				**0.3 ± 0.4**	0.7 ± 0.1		3.3 ± 1.0
Big Thicket	-6	0.74				1.6 ± 0.3	0.6 ± 0.1		2.1 ± 0.8
Center	-4	0.69				1.8 ± 0.4	0.6 ± 0.1		1.8 ± 0.7
Wright Patman	-0.5	0.67			0.8 ± 0.4		0.5 ± 0.1		2.4 ± 0.8
Guadalupe Mtn	Not Enough Data								
Wichita Mtn	Not Enough Data								
Padre Island	Not Enough Data								
Avg Coef ± Avg Err	-9	0.61	1.8 ± 0.5	2 ± 0.6	0.3 ± 0.7	1.45 ± 0.55	0.6 ± 0.3	0.3 ± 1	2.1 ± 1.1
Standard Deviation			0.6	1	0.17	0.7	0.13	0	0.75

As shown in Table 8-3, the scaling coefficients over most source regions are within the average standard error across all sites. The southeast Texas source region is an exception where half of the coefficients are more than one standard error from the average. Only six of the scaling coefficients are greater than the average by more than a factor of 2 of the average standard error. This occurs for the southeast Texas source region at the three Texas Gulf Coast sites, San Bernard, Aransas, and Laguna Atascosa, and Monahans Sandhills located in western Texas. The Carbón scaling coefficient for Amistad, Texas, is also significantly smaller than average. Amistad is about 70 km from the Carbón power plants. Last, the Rest of Mexico source region is significantly greater than average for Falcon Dam which is located along the Texas/Mexican

border. The correlation coefficient (r) for each inversion varied between 0.45 and 0.74 and was 0.57 at Big Bend.

8.2.1.1.2 Temporal Variability

The temporal variability in the source attribution scaling coefficients was examined by performing the regression analysis using data from all monitoring sites for five consecutive days which gave a maximum of 185 data values. The scaling coefficients were again constrained to be between 0.25 and 4. To give each monitoring site equal weight in the regression analysis, the observed data and REMSAD source attributions for each monitoring site were normalized by the monitoring site's average observed sulfate concentration. A moving five-day window was used over the entire time period and the scaling coefficients were attributed to the center day resulting in daily coefficients from July 9–October 28, 1999.

The daily variability of the regression coefficients are presented in Figure 8-60 and their averages over the BRAVO time period are presented in Table 8-4. As shown in Table 8-4, the average coefficients over Texas and the eastern U.S. are ~1, and 1.9 for Mexico. In general, the standard deviations of the coefficients over time are greater than they were over space, indicating greater temporal variability in time than in space. This is also evident in Figure 8-60, where the coefficients in most regions fluctuate between the lower bound of 0.25 and 3. The coefficients also show temporal trends with coefficients greater than 1 during July and early August and below 1 in October. This is expected due to the monthly biases in the REMSAD modeling results (see section 6.2).

Table 8-4. Synthesized REMSAD daily source attribution scaling coefficients and their standard error averaged over the entire BRAVO period for each source regions. The standard deviation of the scaling coefficients is also provided.

Source Region	Average Scaling Coef.	Average Std Error	Scaling Coef Std Dev
Carbón	1.44	0.41	0.90
Rest of Mexico	2.36	1.15	1.54
NE Texas	0.85	0.89	0.65
SE Texas	0.95	0.25	0.55
West Texas	1.36	2.06	1.52
Louisiana	1.16	1.20	1.16
East Central	1.08	3.92	1.25
MO/AR/IL	0.56	3.57	0.62
Rest of Eastern U.S.	1.01	1.02	1.11
Western U.S.	0.70	6.83	1.13
Boundary Cond.	3.26	2.33	1.09
Texas	1.05	1.07	1.03
Mexico	1.90	0.78	1.34
Eastern U.S.	0.95	2.43	1.09

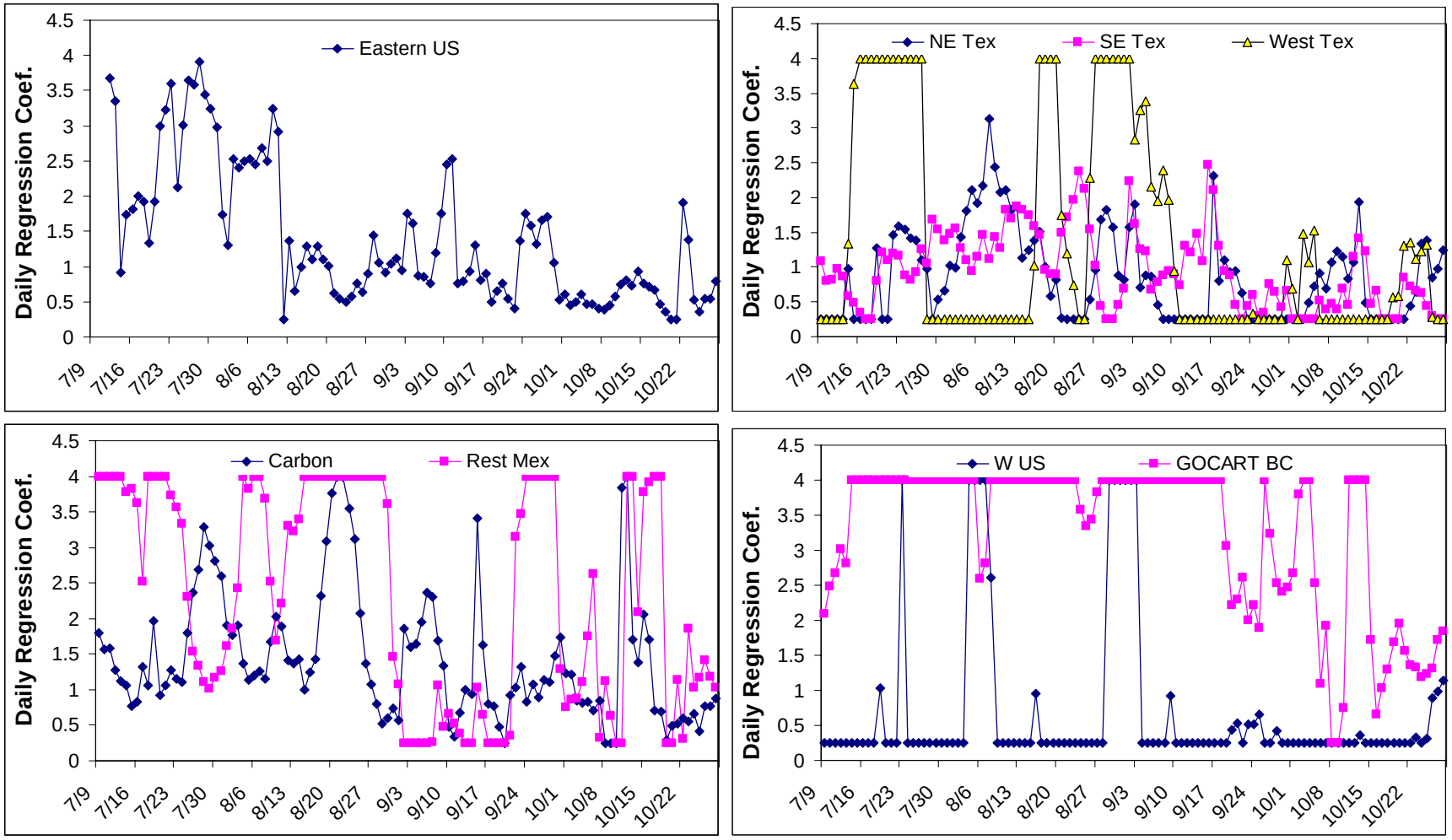

Figure 8-60. Synthesized REMSAD daily source attribution scaling coefficients using all sites and a 5-day moving window. The four eastern U.S. source regions were aggregated together because of high collinearities between these source regions.

Instabilities in the regression coefficients for several regions are also evident. The coefficients for the western Texas and western U.S. source regions fluctuate between the constraints 0.25 and 4. Both source regions had small contributions to the predicted sulfate in Texas and the regression analysis was most likely unable to resolve them due to the errors in the system. This is also reflected in the fact that most of these coefficients were not significantly different from 0 or 1 as defined by the standard error. Eastern U.S. sources also demonstrated instabilities during July and early August when they had little influence on the simulated sulfate. Last, the boundary conditions also illustrate instabilities particularly from July 14–September 20. During this period the boundary conditions were highly collinear with the other source regions.

The performance of the regression analysis is presented in Table 8-5 where the observed sulfur concentrations are compared to the predicted sulfate concentrations for each site, using the temporally varying regression coefficients. As shown, the correlation coefficients vary between 0.64 and 0.88 and have a relative RMS error between 33 and 65% and a bias between -25 and 13%. At the Big Bend monitoring site at K-Bar, r = 0.79 and the RMS error was 47%. For all monitoring sites the correlation coefficients are larger and the RMS errors are smaller compared to the results for the spatially varying regression coefficients (Table 8-3).

Table 8-5. The performance statistics for each BRAVO monitoring site using the temporally varying source attribution scaling coefficients derived from Synthesized REMSAD.

		Average				
Monitoring Site	**# Obs**	**Observation**	**Prediction**	**Bias (%)**	**RMS Error (%)**	**r**
K-Bar	109	2.47	2.11	-15	47	0.79
San Vicente	104	2.58	2.14	-17	44	0.81
Persimmon Gap	106	2.72	2.29	-16	42	0.81
Marathon	110	2.54	2.30	-9	40	0.80
Fort Stockton	112	2.51	2.41	-4	38	0.80
Monahans Sandhills	110	2.95	2.66	-10	38	0.83
Esperanza	91	1.95	2.06	6	38	0.68
McDonald Obs.	94	2.11	2.18	3	34	0.81
Presidio	94	2.30	2.18	-5	46	0.70
LBJ NHS	108	3.07	3.11	1	39	0.83
Fort McKavett	111	2.59	2.64	2	38	0.86
Lake Colorado City	97	2.80	2.95	5	35	0.85
Fort Lancaster	96	3.05	2.83	-7	46	0.68
Sanderson	110	3.01	2.58	-14	49	0.64
Langtry	102	3.46	2.88	-17	42	0.80
Amistad	110	3.05	2.80	-8	39	0.81
Brackettville	103	3.01	2.58	-14	40	0.84
Eagle Pass	101	2.75	2.58	-6	48	0.73
Laredo	108	2.88	2.58	-10	55	0.69
Falcon Dam	94	3.04	2.64	-13	43	0.75
Laguna Atascosa	108	2.87	2.14	-25	57	0.72
Lake Corpus Christi	81	3.13	3.00	-4	47	0.72
Pleasanton	101	3.18	3.05	-4	41	0.85
Everton Ranch	84	3.54	3.37	-5	45	0.78
Hagerman	93	4.07	3.78	-7	33	0.88
Purtis Creek	89	4.28	3.83	-11	35	0.83
Stephenville	91	3.55	3.35	-6	36	0.86

Stillhouse Lake	111	3.54	3.36	-5	36	0.86
Somerville Lake	101	3.58	3.59	0	39	0.81
Aransas	86	3.66	3.23	-12	43	0.81
San Bernard	97	3.94	3.62	-8	47	0.77
Big Thicket	88	4.18	3.98	-5	38	0.80
Center	96	4.00	4.19	5	36	0.84
Wright Patman	95	4.39	4.70	7	40	0.82
Guadalupe Mtns						
Wichita Mtns						
Padre Island						
Average	97	3.14	2.93	-7	42	0.79

8.2.1.2 The Optimum Synthesized REMSAD

It is evident from the above results that the regression coefficients vary more in time than in space over Texas, and the regression performance improved for the temporally varying coefficients over the spatially varying coefficients. Therefore the model is better able to account for the spatial variability in the observed sulfate, but does not capture the day-to-day variability.

Based on these results, the synthesis inversion was used to calculate spatially invariant but temporally variable source attribution scaling coefficients. This was done by incorporating data from most BRAVO monitoring sites and performing the inversion for each day. To better account for random spatial errors in the model biases and incorporate as much data as possible in each regression, multiple days were included in the analysis. Therefore errors such as the temporal displacements of a frontal passage by a day or so would be averaged out. The source contributions from the eastern U.S. were found to be collinear, so these four source regions were combined into a single eastern U.S. source region.

The constrained least square regression used in the previous analysis has several shortcomings. First, the constraints of 0.25 and 4 were subjective, and when the regression coefficients hit the constraint boundary, the standard errors are not the true standard error of the analysis. Second, the regression coefficients for source regions such as the western U.S. displayed large instabilities, indicating the analysis was unable to resolve their contribution, which could result in other biases in the system. To overcome these shortcomings, a Bayesian least square regression technique was used [*Enting,* 2002]. This technique incorporates into the regression analysis prior estimates of the source attribution scaling coefficients and an assumed normally distributed error for these coefficients. This *a-prior* information results in more stable regression coefficients for source regions that are poorly resolved in the constrained regression and has meaningful standard errors for all coefficients. The equation for the Bayesian least square regression is:

$$J(s) = \Sigma_{jk} (y_i - \Sigma_u G_{iu} s_u) X_{jk} (y_k - \Sigma_v G_{kv} s_v) + \Sigma_{uv} (s_u - z_u) W_{uv} (s_v - z_v) \quad (8\text{-}1)$$

where y is a vector of the observed values ($\mu g/m^3$), G is a matrix of the source attribution from each source region/time pair to each observation y_i ($\mu g/m^3$), X is a diagonal matrix of the observation variances $(\mu g/m^3)^2$, s is the source attribution scaling coefficient, z is a vector of the prior source attribution scaling coefficients, and W is a diagonal matrix of the prior source attribution scaling coefficients variances $(\mu g/m^3)^2$.

In this analysis the priors (z) were assumed to be 1, i.e. an unbiased model, and the variances were estimated from comparisons of the model results to IMPROVE and CASTNet measured sulfate data which were not used in this analysis. The comparison with the measured data showed that the REMSAD simulation of eastern U.S. sulfate could be a factor of three higher than the measured sulfate (see chapter 6). No observed data were available for Mexico, but it is known that the Mexican SO_2 emissions had large uncertainties compared to those in the U.S. Therefore the prior variances for the Mexican and eastern U.S. source regions were set to 4, or an error of 2. The variances for the two eastern Texas source regions were set to 2. A variance of 4 was not used since this resulted in some large negative coefficients. The variances for the West Texas, western U.S., and boundary condition source regions were set to 0.5. This smaller variance helped to constrain these coefficients to be around 1, minimizing the instabilities identified in the constrained regression analysis. The regression analyses occasionally resulted in small negative source attribution scaling coefficients and these coefficients were set to 0.

In section 8.2.1.1.1, it was shown that the source attribution scaling coefficients derived for each monitoring site using all data generally did not vary significantly in space. However, there were several monitoring sites that had significantly different coefficients. The inclusion of the data from these monitoring sites could result in scaling coefficients that were not directly applicable to the Big Bend data. To better identify the monitoring sites and time periods which had significantly different biases compared to Big Bend, the synthesis inversion was applied to each monitoring site over three different time periods: July 9–August 5, August 6–September 19, and September 20–October 28. Each of these time periods displayed distinct airmass transport patterns to Big Bend with transport primarily from east-southeast of Big Bend from July 9–August 5, transport primarily from northeast-southeast of Big Bend from August 6–September 19, and transport from any direction after September 20. The scaling coefficients and their errors for the Texas, Mexican, and eastern U.S. source regions are presented in Table 8-6. Note that some of the scaling coefficient had large negative number, < -1. These values mostly occurred for the NE Texas source region when this source region had a small (< 10%) average contribution to the receptor site.

A t-test was used to determine if the scaling coefficient for a given monitoring site was statistically different from Big Bend's. If a scaling coefficient for a monitoring site had a t value greater than 3 and the source region contributed 10% or more to the monitoring site on average, then it was excluded from the analysis. This is a conservative cut off, but was chosen to minimize any false positives and the exclusion of valid data. All bolded coefficients in Tables 8-6a, b, and c failed the hypothesis test and these data were excluded from the analysis. As shown, data from all monitoring sites were used from July 9–August 5 and September 20–October 28. However, data from 19 of the 37 sites were not used in the analysis from August 6–September 19.

Table 8-6a. Source attribution scaling coefficients and standard errors resulting from the regression of the REMSAD source attribution estimates against the particulate sulfate data measured at each BRAVO monitoring site from July 9–August 5. The source attribution scaling coefficients for each monitoring site were compared to the Big Bend values using Student t statistics. Source regions that contributed more than 10% of the sulfate as estimated by REMSAD are underlined and if they also had a t value greater than 3 they are bolded. The scaling coefficients for the West Texas, the western U.S., and boundary conditions are not shown.

Source Regions	Carbón	Rest of Mexico	NE Texas	SE Texas	Eastern U.S.
Big Bend (K-Bar)	1.7 ± 0.6	2.2 ± 0.5	1.1 ± 1.0	1.4 ± 1.0	2.0 ± 0.7
San Vicente	2.0 ± 0.6	2.0 ± 0.5	1.2 ± 1.0	1.6 ± 0.9	2.4 ± 0.7
Persimmon Gap	2.1 ± 0.5	1.5 ± 0.6	1.1 ± 1.0	1.3 ± 0.8	1.6 ± 0.6
Marathon	2.5 ± 0.5	1.5 ± 0.6	0.8 ± 1.0	1.2 ± 0.8	1.2 ± 0.6
Fort Stockton	2.3 ± 0.5	1.5 ± 0.6	0.8 ± 1.0	1.2 ± 0.7	1.5 ± 0.6
Monahans Sandhills	1.7 ± 0.6	1.3 ± 0.7	1.0 ± 1.0	1.6 ± 0.7	1.6 ± 0.5
Esperanza	2.0 ± 0.8	1.1 ± 0.5	1.0 ± 1.0	0.8 ± 0.9	0.9 ± 0.8
McDonald Obs	2.0 ± 0.7	0.8 ± 0.5	1.0 ± 1.0	1.6 ± 0.9	1.8 ± 0.7
Presidio	0.9 ± 0.7	1.1 ± 0.5	1.0 ± 1.0	0.9 ± 1.0	1.1 ± 0.8
LBJ	1.0 ± 1.0	1.0 ± 1.0	1.1 ± 1.0	1.4 ± 0.2	1.1 ± 0.4
Fort McKavett	1.4 ± 1.0	2.7 ± 0.8	1.0 ± 1.0	1.1 ± 0.4	1.0 ± 0.6
Lake Colorado City	1.2 ± 0.8	1.9 ± 0.8	0.7 ± 0.9	1.5 ± 0.6	0.8 ± 0.6
Fort Lancaster	2.0 ± 0.7	2.1 ± 0.8	1.1 ± 1.0	1.5 ± 0.7	0.2 ± 0.6
Sanderson	2.4 ± 0.5	3.0 ± 0.8	1.0 ± 1.0	1.3 ± 0.6	1.8 ± 0.5
Langtry	3.0 ± 0.5	1.6 ± 0.8	1.0 ± 1.0	1.5 ± 0.5	1.8 ± 0.5
Amistad	1.7 ± 0.5	2.2 ± 0.8	1.1 ± 1.0	1.1 ± 0.6	2.3 ± 0.5
Brackettville	0.2 ± 1.0	2.3 ± 0.8	1.1 ± 1.0	0.6 ± 0.5	2.5 ± 0.5
Eagle Pass	0.0 ± 1.0	3.1 ± 0.7	1.0 ± 1.0	1.1 ± 0.8	2.0 ± 0.5
Laredo	1.0 ± 1.0	3.5 ± 0.7	0.9 ± 1.0	0.8 ± 1.0	2.1 ± 0.4
Falcon Dam	1.0 ± 1.0	3.2 ± 0.9	1.0 ± 1.0	1.2 ± 1.0	1.8 ± 0.5
Laguna Atascosa	1.0 ± 1.0	1.0 ± 1.0	0.7 ± 1.0	1.0 ± 1.0	1.3 ± 0.3
North Padre Island	1.0 ± 1.0	1.4 ± 1.0	0.9 ± 1.0	1.3 ± 1.0	2.7 ± 0.3
Lake Corpus Christi	1.0 ± 1.0	1.0 ± 1.0	1.0 ± 1.0	2.1 ± 0.9	0.4 ± 0.3
Pleasanton	1.0 ± 1.0	1.6 ± 1.0	0.8 ± 1.0	1.0 ± 0.3	1.7 ± 0.3
Everton Ranch	1.0 ± 1.0	0.9 ± 1.0	1.2 ± 1.0	2.7 ± 0.8	2.0 ± 0.3
Hagerman	1.0 ± 1.0	1.0 ± 1.0	0.9 ± 0.8	1.3 ± 0.4	0.8 ± 0.1
Purtis Creek	1.0 ± 1.0	1.0 ± 1.0	1.2 ± 0.7	1.4 ± 0.6	1.1 ± 0.1
Stephenville	1.0 ± 1.0	1.0 ± 1.0	1.5 ± 0.8	1.5 ± 0.3	0.9 ± 0.2
Stillhouse Lake	1.0 ± 1.0	1.1 ± 1.0	1.9 ± 0.7	0.8 ± 0.2	1.1 ± 0.2
Somerville Lake	1.0 ± 1.0	1.0 ± 1.0	1.0 ± 1.0	1.0 ± 0.2	1.1 ± 0.2
Aransas	1.0 ± 1.0	0.9 ± 1.0	0.9 ± 1.0	0.9 ± 1.0	1.6 ± 0.3
San Bernard	1.0 ± 1.0	1.0 ± 1.0	1.0 ± 1.0	1.2 ± 0.5	1.4 ± 0.4
Big Thicket	1.0 ± 1.0	1.0 ± 1.0	2.0 ± 0.9	1.7 ± 0.3	0.6 ± 0.1
Center	1.0 ± 1.0	1.0 ± 1.0	1.3 ± 0.5	1.4 ± 0.3	0.7 ± 0.1
Wright Patman Lake	1.0 ± 1.0	1.1 ± 1.0	1.1 ± 0.3	2.1 ± 0.5	0.6 ± 0.1
Guadalupe Mtns					
Wichita Mtns					

Table 8-6b. Source attribution scaling coefficients and standard errors resulting from the regression of the REMSAD source attribution estimates against the particulate sulfate data measured at each BRAVO monitoring site from August 6–September 19. The source attribution scaling coefficients for each monitoring site were compared to the Big Bend values using Student t statistics. Source regions that contributed more than 10% of the sulfate as estimated by REMSAD are underlined and if they also had a t value greater than 3 they are bolded. The scaling coefficients for the West Texas, the western U.S., and boundary conditions are not shown.

Source Regions	Carbón	Rest of Mexico	NE Texas	SE Texas	Eastern U.S.
Big Bend (K-Bar)	1.4 ± 0.4	1.9 ± 0.9	1.9 ± 1.3	2.4 ± 0.8	1.3 ± 0.2
San Vicente	1.4 ± 0.4	2.4 ± 0.9	1.9 ± 1.3	2.1 ± 0.8	1.3 ± 0.2
Persimmon Gap	2.1 ± 0.4	2.1 ± 1.0	1.7 ± 1.3	2.9 ± 0.6	0.9 ± 0.1
Marathon	2.1 ± 0.5	1.5 ± 1.0	0.6 ± 1.2	2.8 ± 0.6	0.8 ± 0.1
Fort Stockton	1.7 ± 0.5	0.9 ± 0.9	1.4 ± 1.0	2.4 ± 0.5	0.8 ± 0.1
Monahans Sandhills	2.2 ± 0.6	0.6 ± 1.0	-0.2 ± 0.6	3.4 ± 0.5	1.1 ± 0.1
Esperanza	1.4 ± 0.5	1.5 ± 0.8	1.2 ± 1.4	2.3 ± 1.0	0.4 ± 0.3
McDonald Obs	2.3 ± 0.5	1.0 ± 0.8	1.5 ± 1.5	2.0 ± 0.7	0.8 ± 0.2
Presidio	1.3 ± 0.4	1.8 ± 0.7	2.5 ± 1.4	1.6 ± 0.9	1.1 ± 0.2
LBJ	1.1 ± 2.0	4.9 ± 1.8	-0.7 ± 0.6	1.1 ± 0.2	**0.8 ± 0.1**
Fort McKavett	-1.1 ± 1.8	0.8 ± 1.1	0.1 ± 0.3	2.3 ± 0.3	1.0 ± 0.1
Lake Colorado City	-0.6 ± 1.0	2.4 ± 1.5	0.2 ± 0.3	1.5 ± 0.3	1.2 ± 0.1
Fort Lancaster	1.5 ± 0.6	2.0 ± 0.9	0.3 ± 0.5	2.4 ± 0.4	**0.4 ± 0.1**
Sanderson	1.9 ± 0.6	1.9 ± 1.1	1.9 ± 0.8	2.3 ± 0.5	**0.2 ± 0.1**
Langtry	-0.3 ± 0.6	3.2 ± 1.1	-0.9 ± 0.7	2.6 ± 0.4	1.0 ± 0.1
Amistad	-0.2 ± 0.5	3.8 ± 1.0	-2.1 ± 0.7	2.7 ± 0.4	0.8 ± 0.1
Brackettville	3.4 ± 1.5	5.1 ± 1.2	-0.5 ± 0.6	2.1 ± 0.3	**0.7 ± 0.1**
Eagle Pass	1.1 ± 1.6	2.1 ± 1.0	-0.8 ± 0.8	1.2 ± 0.4	**0.5 ± 0.1**
Laredo	1.2 ± 2.0	2.7 ± 0.9	-1.3 ± 0.9	2.2 ± 0.6	**0.3 ± 0.1**
Falcon Dam	1.1 ± 2.0	3.5 ± 0.6	-3.7 ± 1.1	3.6 ± 1.0	**0.4 ± 0.1**
Laguna Atascosa	1.4 ± 2.0	5.8 ± 1.9	0.2 ± 1.3	0.8 ± 0.8	**0.4 ± 0.1**
North Padre Island	1.3 ± 2.0	0.6 ± 2.0	2.3 ± 1.9	1.6 ± 1.4	**0.5 ± 0.1**
Lake Corpus Christi	1.3 ± 2.0	3.2 ± 1.9	-0.4 ± 0.8	1.7 ± 0.5	**0.7 ± 0.1**
Pleasanton	1.5 ± 2.0	6.6 ± 1.7	-1.1 ± 0.7	1.2 ± 0.2	**0.8 ± 0.1**
Everton Ranch	1.8 ± 2.0	6.7 ± 1.8	-2.6 ± 0.7	1.5 ± 0.3	**0.7 ± 0.1**
Hagerman	1.6 ± 2.0	4.1 ± 1.9	-0.7 ± 0.3	3.2 ± 0.3	1.0 ± 0.1
Purtis Creek	1.5 ± 2.0	4.5 ± 1.9	0.1 ± 0.3	2.5 ± 0.4	**0.8 ± 0.1**
Stephenville	1.1 ± 2.0	4.8 ± 1.8	0.5 ± 0.4	1.0 ± 0.3	1.0 ± 0.1
Stillhouse Lake	1.6 ± 2.0	4.7 ± 1.9	-1.1 ± 0.5	1.6 ± 0.2	0.7 ± 0.1
Somerville Lake	1.5 ± 2.0	4.4 ± 1.9	-2.2 ± 0.8	1.1 ± 0.2	**0.7 ± 0.1**
Aransas	1.7 ± 2.0	5.1 ± 1.9	-1.0 ± 0.9	1.1 ± 0.6	**0.7 ± 0.1**
San Bernard	1.6 ± 2.0	4.0 ± 1.9	-0.6 ± 0.7	0.6 ± 0.3	**0.7 ± 0.1**
Big Thicket	1.9 ± 2.0	5.4 ± 1.9	1.3 ± 1.1	1.3 ± 0.2	**0.5 ± 0.1**
Center	1.5 ± 2.0	4.5 ± 1.9	1.2 ± 0.4	1.7 ± 0.3	**0.7 ± 0.0**
Wright Patman Lake	1.7 ± 2.0	3.8 ± 1.9	1.1 ± 0.3	3.1 ± 0.6	**0.4 ± 0.0**
Guadalupe Mtns	1.8 ± 0.7	0.9 ± 0.9	-0.4 ± 1.5	3.3 ± 0.9	**0.3 ± 0.2**
Wichita Mtns	0.6 ± 2.0	1.4 ± 2.0	2.8 ± 0.6	0.2 ± 0.4	0.7 ± 0.1

Table 8-6c. Source attribution scaling coefficients and standard errors resulting from the regression of the REMSAD source attribution estimates against the particulate sulfate data measured at each BRAVO monitoring site from September 20–October 28. The source attribution scaling coefficients for each monitoring site were compared to the Big Bend values using Student t statistics. Source regions that contributed more than 10% of the sulfate as estimated by REMSAD are underlined and if they also had a t value greater than 3 they are bolded. The scaling coefficients for the West Texas, the western U.S., and boundary conditions are not shown.

Source Regions	Carbón	Rest of Mexico	NE Texas	SE Texas	Eastern U.S.
Big Bend (K-Bar)	1.6 ± 0.5	2.4 ± 0.6	-0.1 ± 0.7	0.9 ± 0.7	0.6 ± 0.2
San Vicente	1.7 ± 0.5	2.5 ± 0.6	-0.2 ± 0.7	1.0 ± 0.7	0.6 ± 0.2
Persimmon Gap	1.8 ± 0.6	2.1 ± 0.7	-0.1 ± 0.7	0.4 ± 0.7	0.7 ± 0.2
Marathon	1.9 ± 0.6	2.2 ± 0.7	0.5 ± 0.8	0.1 ± 0.7	0.6 ± 0.2
Fort Stockton	2.0 ± 0.6	2.0 ± 0.7	0.8 ± 0.8	-0.1 ± 0.7	0.4 ± 0.2
Monahans Sandhills	2.0 ± 0.5	1.6 ± 0.8	1.3 ± 0.7	-0.1 ± 0.8	0.4 ± 0.2
Esperanza	1.4 ± 0.8	2.0 ± 0.8	1.0 ± 0.8	0.6 ± 0.7	0.3 ± 0.3
McDonald Obs	0.8 ± 0.7	1.4 ± 0.7	1.1 ± 0.7	0.0 ± 0.7	0.5 ± 0.3
Presidio	1.1 ± 0.5	1.7 ± 0.6	0.9 ± 0.7	0.4 ± 0.7	0.4 ± 0.2
LBJ	0.7 ± 1.0	1.2 ± 1.0	-0.1 ± 0.3	1.2 ± 0.3	0.4 ± 0.1
Fort McKavett	1.9 ± 0.9	3.0 ± 0.8	1.1 ± 0.5	0.7 ± 0.4	0.3 ± 0.1
Lake Colorado City	1.2 ± 0.5	2.0 ± 0.8	1.3 ± 0.6	0.5 ± 0.7	0.2 ± 0.2
Fort Lancaster	2.0 ± 0.4	2.2 ± 0.8	1.6 ± 0.6	0.3 ± 0.7	0.4 ± 0.2
Sanderson	2.4 ± 0.5	2.3 ± 0.7	0.5 ± 0.7	-0.4 ± 0.7	0.6 ± 0.2
Langtry	2.6 ± 0.4	2.0 ± 0.7	1.3 ± 0.6	-0.2 ± 0.6	0.6 ± 0.1
Amistad	1.1 ± 0.4	2.1 ± 0.7	1.0 ± 0.5	0.9 ± 0.6	0.5 ± 0.1
Brackettville	0.2 ± 0.5	4.0 ± 0.7	0.8 ± 0.5	1.1 ± 0.4	0.4 ± 0.1
Eagle Pass	0.4 ± 0.5	4.0 ± 0.7	1.4 ± 0.5	1.9 ± 0.5	0.3 ± 0.1
Laredo	0.5 ± 0.4	3.7 ± 0.7	1.1 ± 0.3	1.1 ± 0.5	0.4 ± 0.1
Falcon Dam	0.3 ± 0.8	3.1 ± 0.6	0.1 ± 0.5	1.6 ± 0.5	0.4 ± 0.1
Laguna Atascosa	0.9 ± 0.9	1.4 ± 0.9	-0.7 ± 0.4	1.5 ± 0.4	0.5 ± 0.1
North Padre Island	1.0 ± 1.0	1.5 ± 1.0	-1.0 ± 0.4	3.0 ± 0.5	0.4 ± 0.1
Lake Corpus Christi	0.7 ± 0.8	1.1 ± 1.0	0.2 ± 0.3	1.0 ± 0.4	0.5 ± 0.1
Pleasanton	0.9 ± 0.6	1.9 ± 1.0	0.7 ± 0.3	0.8 ± 0.3	0.4 ± 0.1
Everton Ranch	1.0 ± 0.9	1.3 ± 1.0	0.3 ± 0.3	0.9 ± 0.3	0.4 ± 0.1
Hagerman	1.0 ± 1.0	1.2 ± 1.0	1.6 ± 0.3	2.1 ± 0.4	0.4 ± 0.1
Purtis Creek	0.9 ± 1.0	1.2 ± 1.0	0.6 ± 0.3	1.6 ± 0.4	0.5 ± 0.1
Stephenville	1.4 ± 1.0	2.1 ± 0.9	0.8 ± 0.5	1.9 ± 0.3	0.2 ± 0.1
Stillhouse Lake	0.9 ± 1.0	1.4 ± 1.0	0.9 ± 0.3	1.0 ± 0.2	0.3 ± 0.1
Somerville Lake	0.9 ± 1.0	1.2 ± 1.0	0.6 ± 0.2	1.0 ± 0.2	0.5 ± 0.0
Aransas	0.7 ± 1.0	1.3 ± 1.0	-0.4 ± 0.3	0.7 ± 0.4	0.6 ± 0.0
San Bernard	1.1 ± 1.0	1.3 ± 1.0	0.1 ± 0.5	0.2 ± 0.3	0.6 ± 0.0
Big Thicket	0.9 ± 1.0	1.2 ± 1.0	0.9 ± 0.6	2.7 ± 0.8	0.6 ± 0.0
Center	0.9 ± 1.0	1.1 ± 1.0	0.8 ± 0.4	1.2 ± 0.8	0.5 ± 0.0
Wright Patman Lake	0.9 ± 1.0	1.1 ± 1.0	0.7 ± 0.4	1.4 ± 0.6	0.4 ± 0.0
Guadalupe Mtns	1.6 ± 0.9	1.5 ± 0.9	0.8 ± 0.9	0.6 ± 0.8	0.4 ± 0.3
Wichita Mtns	1.2 ± 1.0	1.4 ± 1.0	0.3 ± 0.9	0.5 ± 0.6	1.0 ± 0.4

The analysis was conducted using a number of different moving window widths. It was found that the average source attributions over the four-month BRAVO study period were not sensitive to the window width producing similar results for windows from 21 days to 1 day in width, but the regression performance did diminish as the window width increased. The source attribution results for some of the individual sulfate episodes at Big Bend were sensitive to the width of the window. This was most severe for the aggregation windows using 1 day and more than 15 days compared to the others. A 3-day window was chosen as the optimum aggregation window. This produced the best balance between stable scaling coefficients and model performance. Also, this captured the variability in the REMSAD model simulation due to synoptic forcing which is on the order of 3–5 days, and airmasses typically resided over Texas for less than three days. Last, the Big Bend sulfate episode duration was typically 5 days or longer so the 3-day window was able to capture variations in the biases across the episodes.

8.2.1.2.1 The Optimum Synthesized REMSAD Results

The overall Big Bend average source attributions and performance statistics are presented in Table 8-7 and Figure 8-61. Figure 8-62 presents the absolute and relative daily source attributions and compares the predicted and observed sulfate time series. As shown in Figure 8-62, the regressed REMSAD results properly reproduce the general temporal pattern in Big Bend's sulfate, particularly in July and August, and the overall correlation coefficient is 0.85 with an RMS error of 42%. In September and October the peak sulfate days are underestimated, leading to an overall average underestimation of 18%. Comparing these results to the original REMSAD simulation (chapter 6), the synthesized REMSAD has a higher correlation coefficient, and smaller bias and RMS error. In addition, REMSAD systematically underestimated the July and August sulfate at Big Bend by a factor of 2, while the synthesized REMSAD underestimated the observed by 13% in these months (Figure 8-62). Also, the synthesized REMSAD captured the September 28 episode which REMSAD missed and the October 12 episode, but the peak sulfate concentrations are still underestimated by nearly a factor of two.

Table 8-7. The optimum synthesized REMSAD average source attribution scaling coefficients and the average standard errors, and the source attribution and standard error for the entire BRAVO time period (7/9–10/28/1999). The regression performance statistics are also provided. The relative contributions are the ratios of average predicted absolute values and are reported as percents.

Source Region	Avg Scaling Coeff. and Avg Std Error	Absolute Source Contribution ($\mu g/m^3$)	Relative Source Contribution (%)	Original REMSAD Source Contribution (%)
Carbón	1.52 ± 1	0.46 ± 0.04	23 ± 1.8	14
Rest of Mexico	1.66 ± 1.6	0.32 ± 0.03	16 ± 1.4	10
NE Texas	0.85 ± 1	0.09 ± 0.02	5 ± 0.8	5
SE Texas	1.12 ± 0.8	0.19 ± 0.02	10 ± 1.0	9
West Texas	0.92 ± 0.7	0.03 ± 0.01	1 ± 0.3	2
Eastern U.S.	0.95 ± 0.3	0.65 ± 0.02	32 ± 1.2	42
Western U.S.	0.87 ± 0.6	0.12 ± 0.02	6 ± 0.7	9
Boundary Condition	1.07 ± 0.7	0.14 ± 0.01	7 ± 0.5	7
Texas	0.97 ± 0.05	0.31 ± 0.03	16 ± 1.2	16
Mexico	1.59 ± 1	0.78 ± 0.05	39 ± 2.3	23
Eastern U.S.	0.95 ± 0.3	0.65 ± 0.02	32 ± 1.2	42
Western U.S.	0.87 ± 0.6	0.12 ± 0.02	6 ± 0.7	9

Regression Performance statistics

r	0.85
Average Observation ($\mu g/m^3$)	2.58
Average Prediction ($\mu g/m^3$)	2.1
Bias (%)	-18
RMS Error (%)	42

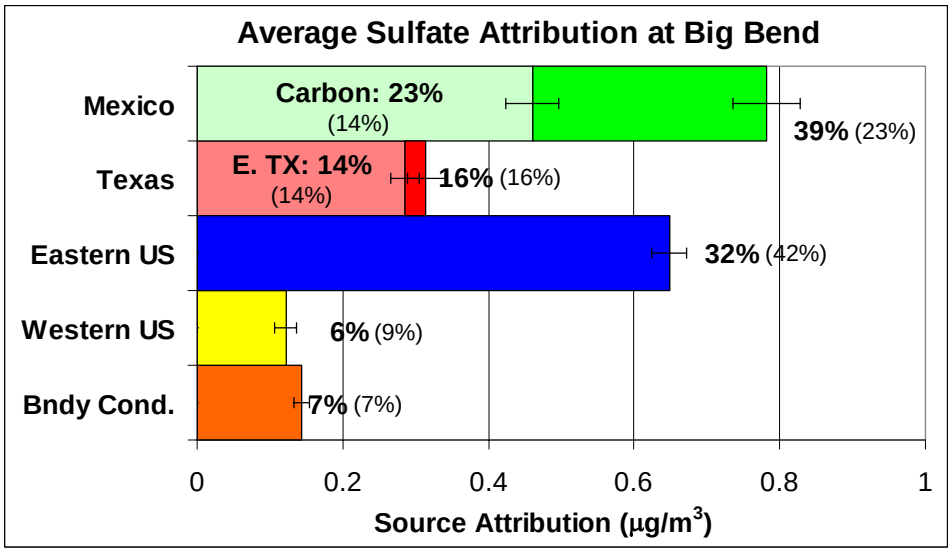

Figure 8-61. The optimum synthesized REMSAD average source attribution and standard errors to Big Bend's predicted sulfate for the entire BRAVO time period (7/9–10/28/1999). The bolded labels are the relative contributions, i.e., the ratios of average absolute values. The values in parentheses are the original REMSAD source attribution estimates.

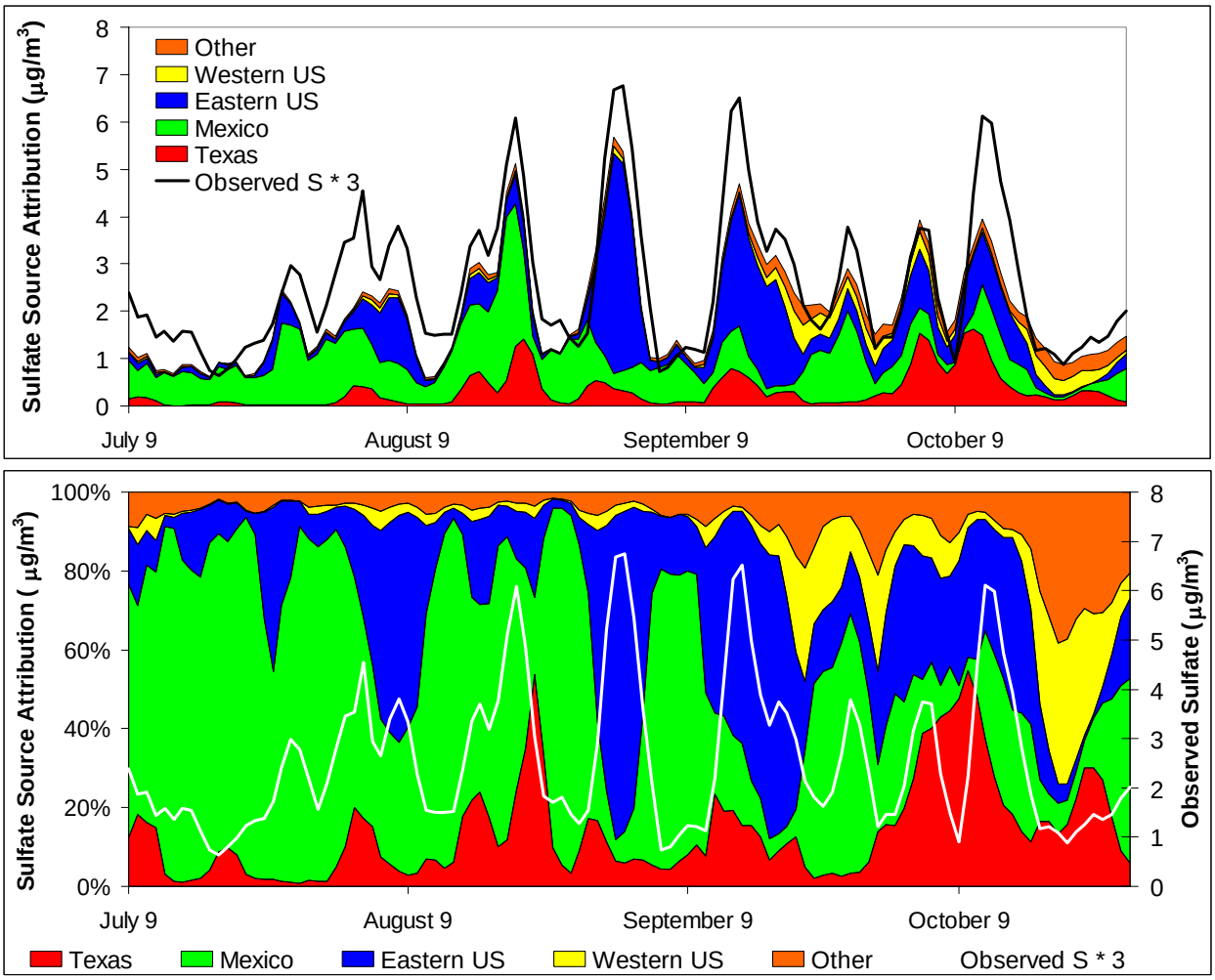

Figure 8-62. The optimum synthesized REMSAD absolute and relative source attribution to the predicted sulfate at Big Bend.

Although the synthesized REMSAD bias is smaller than the original results, it still underestimates the observed Big Bend concentrations by nearly 20%. This large underestimation has two potential causes. First, it is at least partially due to biases in the regression analysis. As equation 2-33 is written, the modeled source regions account for all sulfate at Big Bend. Therefore there is not a constant coefficient, i.e. intercept, in the regression analysis. The source attributions comprising the design matrix can have large errors, but these errors were not accounted for in the analysis. In such a case, it can be shown that the regression analysis will always underestimate the average concentrations. Future analyses will incorporate the errors in the source attributions to minimize this regression analysis bias. The second potential cause of the bias is due to spatial variability in the source attribution scaling coefficients. The original simulated concentrations generally had higher concentrations, relative to the measured data, in eastern Texas than western Texas and around Big Bend. The regression analysis will find a balance between all sites in Texas, so it is quite possible that Big Bend concentrations will be underestimated while the eastern Texas sites will be overestimated. This is supported by the results in Table 8-4, where the biases at the eastern Texas sites are generally smaller than those in western Texas and around Big Bend. However, note that the predicted average sulfate at most sites is underestimated due to the systematic bias in the regression analysis.

The average source attribution scaling factors are presented in Table 8-7. The overall average for the eastern U.S. and Texas is about 1 while for Mexico it is 2. Consequently, over the BRAVO time period, the original REMSAD eastern U.S. and Texan source contributions to the Texas monitoring sites are unbiased while the Mexican contributions are underestimated on average by a factor of two. This can be due to underestimation in Mexican emissions or a systematic bias in the modeled transport, chemistry, or removal processes. It is interesting that the scaling factor for Carbón is 1.52. The REMSAD model was run with the lower Carbón SO_2 emission rate of 152,000 tons/yr which is a factor 1.58 lower than the upper estimate of 241,000 tons/yr. The scaling factors for all three regions had a trend in time with the highest factors in July and the lowest in October. For example, the average scaling factor for the eastern U.S. was 1.2 in July and August, but 0.7 in September and October.

The average source attributions for each region are also reported in Table 8-7 and Figure 8-61 as well as the original REMSAD results. Mexico is the largest average contributor at 39% while the eastern U.S. contributes 32% and Texas 16%. In Mexico, the Carbón I & II power plants contributed 23% and in Texas, east Texas contributed 14%, or 90% of Texas' total contribution. Comparing these results to the original REMSAD source attribution it is seen that the Mexican contribution increased by 70% and the eastern U.S. contribution decreased by about 25% over the original REMSAD source attributions. Texas' contribution remained about the same.

As shown in Figure 8-62, each source region's contribution has unique trends over the four month period. Mexico's contributions dominate the predicted sulfate concentrations in July and August, contributing from 0.5 to 1.5 $\mu g/m^3$ of sulfate every day, and occasionally exceeding 2 $\mu g/m^3$. In September and October, the contribution from Mexico to Big Bend's sulfate decreased typically less than 1 $\mu g/m^3$ per day. The Texas source regions have little contribution in July and the largest contribution in October. The Texas sources also tend to have the largest absolute contribution (>1 $\mu g/m^3$) during the highest sulfate days. The eastern U.S. source regions' contributions are episodic, also occurring during Big Bend sulfate episodes where they exceeded 4 $\mu g/m^3$ during the September 1 episode. The western U.S. contributions are near zero until late September and October.

Table 8-8 and Figure 8-63 present the source attributions for each Big Bend sulfate episode. As shown, Mexico, the eastern U.S., and Texas all contribute 24% or more of the predicted sulfated in two or more of the episodes. Mexico is the dominant contributor for the July 22, August 18, and September 28 episodes at 79, 56, and 49%, respectively. The eastern U.S. is the dominant contributor for the August 30, September 12, and October 3 and 11 episodes at 62, 49, 37, and 38%, respectively. Texas contributes about 25% of the predicted sulfate to both the October 3 and 11 episodes.

Table 8-8. The optimum synthesized REMSAD relative source attribution and standard error to the predicted sulfate for each Big Bend sulfate episode. The relative contributions are the ratios of average predicted absolute values.

	Big Bend Fine Particulate Sulfur Episodes						
Source Region	**7/22-7/31**	**8/16-8/23**	**8/30-9/4**	**9/12-9/17**	**9/25-9/28**	**10/3-10/7**	**10/11-10/16**
Carbón	24 ± 5.3	51 ± 6.3	10 ± 4.5	13 ± 5.9	6 ± 3.9	14 ± 8.3	19 ± 4.1
Rest of Mexico	54 ± 10.5	4 ± 1.5	3 ± 2.2	4 ± 2.3	55 ± 7.3	6 ± 3.9	8 ± 3.0
NE Texas	0 ± 0.0	3 ± 3.0	2 ± 0.8	0 ± 0.8	0 ± 0.6	15 ± 6.9	13 ± 2.8
SE Texas	1 ± 0.2	21 ± 3.3	7 ± 2.9	16 ± 5.0	1 ± 1.0	16 ± 6.7	17 ± 3.4
West Texas	1 ± 0.1	0 ± 0.1	1 ± 0.2	1 ± 0.3	2 ± 1.2	3 ± 1.1	1 ± 0.4
Eastern U.S.	17 ± 3.2	15 ± 2.5	72 ± 4.3	58 ± 7.1	15 ± 2.1	31 ± 3.4	34 ± 2.3
Western U.S.	1 ± 0.4	2 ± 0.7	3 ± 0.8	3 ± 1.2	15 ± 5.4	9 ± 3.8	2 ± 1.5
Bndy Cond.	3 ± 0.7	3 ± 0.9	4 ± 1.0	5 ± 1.6	6 ± 1.9	6 ± 2.1	7 ± 1.4
Texas	17 ± 3.2	15 ± 2.5	72 ± 4.3	58 ± 7.1	15 ± 2.1	31 ± 3.4	34 ± 2.3
Mexico	1 ± 0.2	25 ± 4.4	9 ± 3.0	17 ± 5.1	4 ± 1.6	34 ± 9.7	31 ± 4.5
Eastern U.S.	78 ± 11.8	55 ± 6.5	13 ± 5.0	17 ± 6.4	60 ± 8.3	20 ± 9.1	27 ± 5.1
Western U.S.	1 ± 0.4	2 ± 0.7	3 ± 0.8	3 ± 1.2	15 ± 5.4	9 ± 3.8	2 ± 1.5

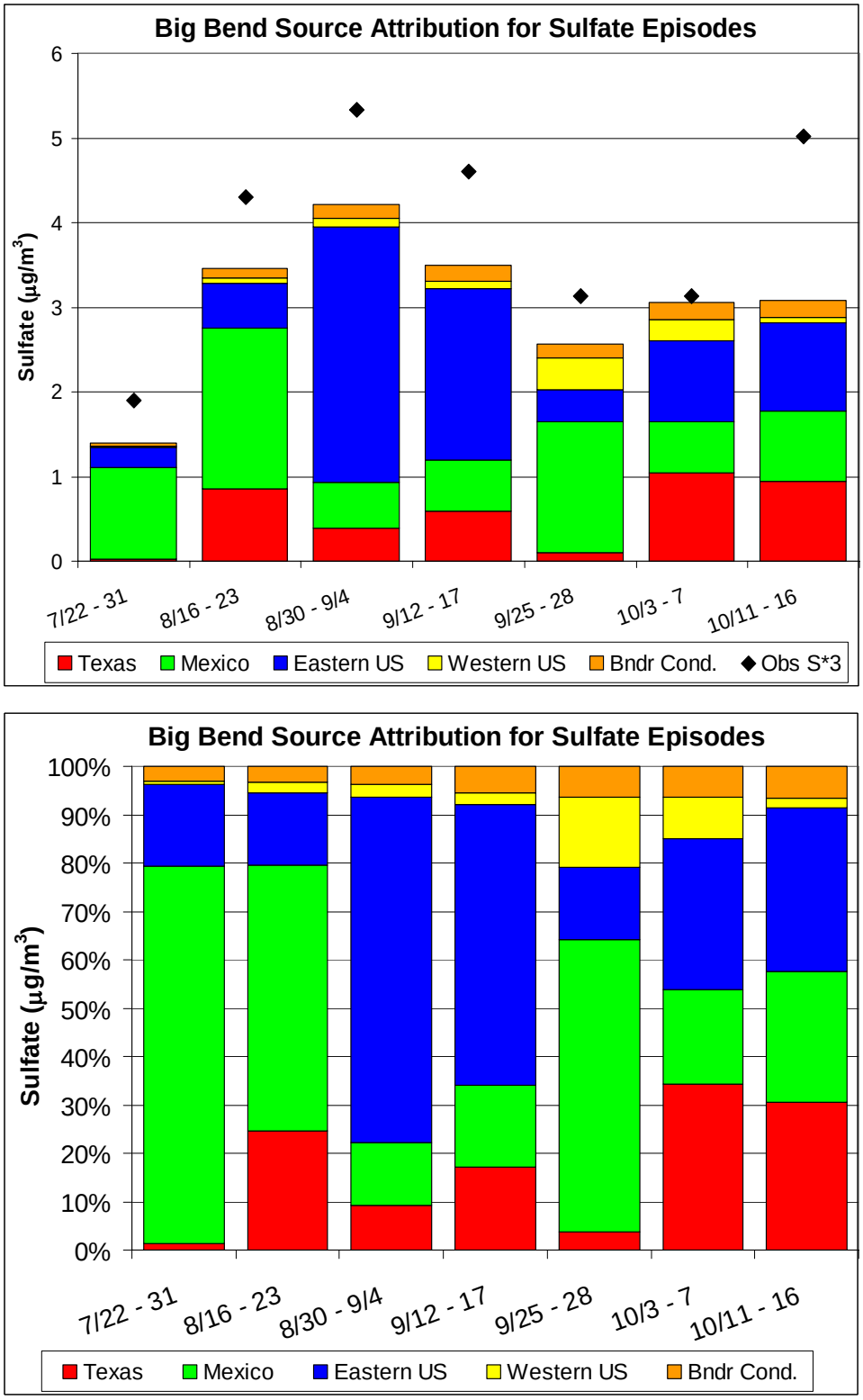

Figure 8-63. The optimum synthesized REMSAD average source attribution and standard error to Big Bend's predicted sulfate for each Big Bend sulfate episode.

As shown in Figure 8-62, Mexico is the largest contributor to Big Bend's sulfate during the days with the lowest sulfate concentrations. This is particularly so from July–September when the Mexican sulfate often accounted for more than 80% of Big Bend's sulfate concentrations when the overall concentrations were below 2 μg/m^3. In October, the western U.S. and boundary condition source regions also were major contributors to the lowest sulfur days, together accounting for 60–80% of the sulfur from October 19–24.

8.2.1.3 The Optimum Synthesized CMAQ Results

The same approached used in the synthesized REMSAD analysis was applied to the CMAQ-MADRID source attribution estimates. In the Bayesian regression analysis, the prior estimate of the five source attribution scaling coefficients was 1 and their variance was also set to 1. These variances are smaller than those used in the REMSAD synthesis approach. This was done because the original CMAQ-MADRID simulation had addressed eastern U.S. and Mexican biases by nudging the REMSAD boundary conditions to measured data and increasing the Mexican emissions. This resulted in CMAQ-MADRID having larger Mexican and smaller eastern U.S. contributions and the simulated sulfate concentrations compared better to the observed concentrations than REMSAD. The sensitivity of the results on the *a-prior* variances was explored. It was found that larger variances did not appreciably change the results, but did occasionally result in negative coefficients. Table 8-9 presents the result of the synthesis inversion applied to each monitoring site and identifies which site's data were not used and when in the regression analysis since their scaling coefficients were significantly different from Big Bend's.

Table 8-9. Source attribution scaling coefficients and standard errors resulting from the regression of the CMAQ-MADRID source attribution estimates against the particulate sulfate data measured at each BRAVO monitoring site for three time periods. The source attribution scaling coefficients for each monitoring site were compared to the Big Bend values using Student t statistics. Source regions with a t value greater than 3 and which contributed more than 10% to the receptor sites concentration as estimated by CMAQ-MADRID are bolded. The scaling coefficients for the western U.S. and boundary conditions are not shown.

Time Period	**7/9–8/5/1999**			**8/6–9/19/1999**			**9/20–10/28/1999**		
Source Region	**Mexico**	**Texas**	**E U.S.**	**Mexico**	**Texas**	**E U.S.**	**Mexico**	**Texas**	**E U.S.**
Big Bend (K-Bar)	1.6 ± 0.2	0.7 ± 0.6	0.8 ± 0.5	0.7 ± 0.2	1.1 ± 0.3	0.8 ± 0.1	0.6 ± 0.2	0.0 ± 0.3	1.2 ± 0.2
San Vicente	1.6 ± 0.3	0.9 ± 0.6	1.4 ± 0.5	0.9 ± 0.2	0.8 ± 0.3	0.7 ± 0.1	0.9 ± 0.2	0.0 ± 0.3	0.9 ± 0.2
Persimmon Gap	1.4 ± 0.3	0.5 ± 0.5	0.9 ± 0.5	0.9 ± 0.2	1.0 ± 0.3	0.7 ± 0.1	0.7 ± 0.2	0.0 ± 0.3	1.2 ± 0.3
Marathon	1.6 ± 0.2	0.3 ± 0.5	0.7 ± 0.4	1.1 ± 0.2	1.0 ± 0.2	0.6 ± 0.1	0.7 ± 0.2	0.1 ± 0.3	1.0 ± 0.3
Fort Stockton	1.2 ± 0.2	0.1 ± 0.5	0.8 ± 0.4	0.5 ± 0.1	1.5 ± 0.2	0.5 ± 0.1	0.7 ± 0.2	0.1 ± 0.3	0.9 ± 0.3
Monahans Sandhills	1.0 ± 0.2	0.5 ± 0.5	1.1 ± 0.4	0.8 ± 0.2	1.7 ± 0.2	0.7 ± 0.1	0.7 ± 0.2	0.6 ± 0.4	0.7 ± 0.3
Esperanza	1.7 ± 0.5	1.0 ± 0.7	1.1 ± 0.6	0.8 ± 0.2	1.1 ± 0.3	0.6 ± 0.2	1.1 ± 0.4	0.8 ± 0.4	0.1 ± 0.4
McDonald Obs	1.0 ± 0.3	1.2 ± 0.6	1.4 ± 0.5	1.0 ± 0.2	1.2 ± 0.3	0.5 ± 0.1	0.4 ± 0.3	0.4 ± 0.4	0.7 ± 0.3
Presidio	0.7 ± 0.3	0.9 ± 0.6	0.7 ± 0.5	0.8 ± 0.2	0.7 ± 0.3	0.9 ± 0.1	0.6 ± 0.2	0.4 ± 0.4	0.6 ± 0.3
LBJ	1.4 ± 0.7	1.4 ± 0.2	0.1 ± 0.3	1.6 ± 0.6	0.3 ± 0.1	0.8 ± 0.1	0.9 ± 0.5	0.7 ± 0.2	**0.3 ± 0.1**
Fort McKavett	1.7 ± 0.3	0.6 ± 0.4	0.7 ± 0.4	0.9 ± 0.5	0.9 ± 0.2	0.8 ± 0.1	1.6 ± 0.3	0.8 ± 0.2	**0.2 ± 0.1**
Lake Colorado City	1.2 ± 0.3	0.7 ± 0.5	0.9 ± 0.4	0.4 ± 0.3	1.0 ± 0.2	0.9 ± 0.1	0.5 ± 0.1	1.1 ± 0.3	**0.0 ± 0.2**
Fort Lancaster	1.3 ± 0.2	1.0 ± 0.4	0.1 ± 0.4	1.3 ± 0.2	1.8 ± 0.2	**0.2 ± 0.1**	0.8 ± 0.1	1.0 ± 0.3	**0.1 ± 0.2**
Sanderson	1.8 ± 0.2	0.4 ± 0.5	0.6 ± 0.4	1.1 ± 0.2	1.6 ± 0.2	**0.1 ± 0.1**	0.8 ± 0.2	0.3 ± 0.3	0.6 ± 0.2
Langtry	1.4 ± 0.1	0.5 ± 0.5	0.9 ± 0.3	0.5 ± 0.2	1.1 ± 0.2	0.8 ± 0.1	0.9 ± 0.1	1.1 ± 0.2	**0.2 ± 0.1**
Amistad	0.9 ± 0.1	0.6 ± 0.5	1.2 ± 0.3	0.5 ± 0.1	0.7 ± 0.2	0.8 ± 0.1	0.4 ± 0.1	**1.2 ± 0.2**	**0.2 ± 0.1**
Brackettville	2.0 ± 0.5	0.6 ± 0.5	1.2 ± 0.3	2.4 ± 0.4	0.7 ± 0.1	0.7 ± 0.1	0.4 ± 0.1	0.9 ± 0.2	**0.3 ± 0.1**
Eagle Pass	0.9 ± 0.1	1.0 ± 0.6	0.9 ± 0.3	0.7 ± 0.2	0.5 ± 0.2	**0.4 ± 0.1**	0.4 ± 0.1	**1.2 ± 0.2**	**0.1 ± 0.1**

Laredo	1.7 ± 0.3	0.8 ± 0.7	1.3 ± 0.3	1.1 ± 0.3	0.3 ± 0.2	**0.5 ± 0.1**	0.6 ± 0.1	0.6 ± 0.1	**0.3 ± 0.1**
Falcon Dam	2.5 ± 0.4	0.9 ± 0.7	0.4 ± 0.4	1.0 ± 0.2	0.0 ± 0.2	0.5 ± 0.1	0.9 ± 0.2	0.5 ± 0.1	**0.4 ± 0.1**
Laguna Atascosa	1.5 ± 0.7	0.8 ± 0.7	0.8 ± 0.2	3.2 ± 0.6	0.1 ± 0.2	**0.4 ± 0.0**	2.5 ± 0.5	0.5 ± 0.1	0.4 ± 0.0
North Padre Island	1.2 ± 0.7	1.0 ± 0.7	1.7 ± 0.2	1.4 ± 0.7	0.1 ± 0.3	**0.5 ± 0.0**	1.9 ± 0.7	0.7 ± 0.1	**0.4 ± 0.0**
Lake Corpus Christi	1.2 ± 0.7	0.6 ± 0.6	0.3 ± 0.2	1.4 ± 0.7	**0.2 ± 0.1**	**0.4 ± 0.0**	0.6 ± 0.5	0.5 ± 0.1	**0.3 ± 0.0**
Pleasanton	2.1 ± 0.6	1.1 ± 0.5	0.6 ± 0.2	1.9 ± 0.5	0.3 ± 0.1	0.7 ± 0.1	1.4 ± 0.4	0.7 ± 0.1	**0.3 ± 0.1**
Everton Ranch	1.3 ± 0.7	1.9 ± 0.4	0.2 ± 0.2	1.7 ± 0.7	**0.0 ± 0.1**	0.8 ± 0.1	1.6 ± 0.6	0.5 ± 0.1	0.5 ± 0.1
Hagerman	1.0 ± 0.7	0.7 ± 0.3	1.0 ± 0.2	1.1 ± 0.7	1.0 ± 0.1	1.0 ± 0.1	1.0 ± 0.6	0.7 ± 0.1	0.5 ± 0.1
Purtis Creek	1.0 ± 0.7	0.3 ± 0.1	0.9 ± 0.1	1.1 ± 0.7	0.9 ± 0.1	0.8 ± 0.0	1.4 ± 0.7	0.5 ± 0.1	0.4 ± 0.0
Stephenville	1.0 ± 0.7	1.1 ± 0.4	0.7 ± 0.2	1.2 ± 0.6	0.7 ± 0.2	0.9 ± 0.1	1.6 ± 0.4	0.9 ± 0.2	**0.2 ± 0.1**
Stillhouse Lake	1.3 ± 0.7	0.5 ± 0.2	0.9 ± 0.1	1.8 ± 0.7	0.3 ± 0.1	1.0 ± 0.1	1.9 ± 0.7	0.4 ± 0.1	0.5 ± 0.1
Somerville Lake	1.0 ± 0.7	0.5 ± 0.2	0.7 ± 0.2	1.3 ± 0.7	0.4 ± 0.1	0.7 ± 0.1	1.3 ± 0.7	0.5 ± 0.1	0.5 ± 0.0
Aransas	1.0 ± 0.7	0.7 ± 0.7	0.8 ± 0.2	1.7 ± 0.7	**0.0 ± 0.1**	0.7 ± 0.0	0.7 ± 0.6	0.3 ± 0.1	0.4 ± 0.0
San Bernard	1.0 ± 0.7	0.2 ± 0.2	0.8 ± 0.2	1.4 ± 0.7	**0.0 ± 0.1**	0.7 ± 0.0	1.6 ± 0.7	0.3 ± 0.1	0.4 ± 0.0
Big Thicket	1.0 ± 0.7	0.4 ± 0.1	0.6 ± 0.1	1.2 ± 0.7	0.9 ± 0.1	**0.5 ± 0.0**	1.2 ± 0.7	1.1 ± 0.3	0.5 ± 0.0
Center	1.0 ± 0.7	0.4 ± 0.1	0.7 ± 0.1	1.0 ± 0.7	0.9 ± 0.1	0.7 ± 0.0	1.1 ± 0.7	0.6 ± 0.2	**0.4 ± 0.0**
Wright Patman Lake	1.0 ± 0.7	0.6 ± 0.1	0.9 ± 0.1	1.1 ± 0.7	0.8 ± 0.1	0.6 ± 0.0	1.0 ± 0.7	0.4 ± 0.1	**0.4 ± 0.0**
Guadalupe Mtns				0.9 ± 0.3	1.5 ± 0.3	0.5 ± 0.2	0.9 ± 0.4	0.7 ± 0.4	0.4 ± 0.4
Wichita Mtns				0.8 ± 0.6	0.6 ± 0.2	1.0 ± 0.1	1.3 ± 0.6	1.1 ± 0.6	1.0 ± 0.6

The source attribution results are presented in Tables 8-10 and 8-11 and Figures 8-64 through 8-67. The synthesis inversion improved the comparison of Big Bend's predicted sulfate to the observed sulfate with a correlation coefficient of 0.89 compared to 0.72 and the RMS error of 36% compared to 61% (Table 8-10). However, the synthesis inversion had a bias of -16% compared to no bias for the original CMAQ-MADRID results. This bias is most notable during July and the sulfate episodes (Figure 8-66). These statistics are similar to those found for the synthesized REMSAD (Table 8-6), and the potential causes for the bias are the same as those discussed for the synthesized REMSAD results.

Table 8-10. The optimum synthesized CMAQ average source attribution scaling coefficients and the average standard errors, and the source attributions and standard errors for the entire BRAVO time period (7/9–10/28/1999). The regression performance statistics are also provided. The relative contributions are the ratios of average predicted absolute values.

Source Region	Avg Scaling Coeff and Avg Std Error	Absolute Source Contribution ($\mu g/m^3$)	Relative Source Contribution (%)	Original CMAQ Source Contribution (%)
Texas	0.75 ± 0.5	0.37 ± 0.03	16.9 ± 1.3	19.4
Mexico	1.1 ± 0.5	0.82 ± 0.04	38 ± 1.7	31.7
Eastern U.S.	0.73 ± 0.4	0.65 ± 0.03	30.1 ± 1.2	38.5
Western U.S.	1.1 ± 0.9	0.18 ± 0.02	8.5 ± 0.8	5.9
Boundary Condition	1.2 ± 1	0.14 ± 0.01	6.4 ± 0.6	4.7

Regression Performance statistics

	Synthesized CMAQ	Original CMAQ-MADRID
r	0.89	0.72
Average Observation ($\mu g/m^3$)	2.58	2.58
Average Prediction ($\mu g/m^3$)	2.17	2.58
Bias (%)	-16	0
RMS Error (%)	36	61

Table 8-11. The optimum synthesized CMAQ relative source attributions and standard errors to the predicted sulfate for each Big Bend sulfate episode. The relative contributions are the ratios of average predicted absolute values.

	Big Bend Fine Particulate Sulfur Episodes						
Source Region	**7/22–7/31**	**8/16–8/23**	**8/30–9/4**	**9/12–9/17**	**9/25–9/28**	**10/3–10/7**	**10/11–10/16**
Texas	1 ± 0.8	32 ± 3.7	13 ± 3.2	17 ± 4.4	2 ± 0.9	28 ± 9.2	46 ± 6.8
Mexico	85 ± 6.3	33 ± 5.4	6 ± 3.8	25 ± 4.7	49 ± 8.7	32 ± 9.	18 ± 4.3
Eastern U.S.	9 ± 2.	27 ± 2.6	73 ± 5.3	49 ± 6.4	9 ± 2.9	26 ± 4.2	30 ± 3.4
Western U.S.	1 ± 0.6	5 ± 1.4	1 ± 0.6	4 ± 1.2	35 ± 6.3	10 ± 3.9	5 ± 2.7
Bndy. Cond.	5 ± 1.2	4 ± 1.2	6 ± 1.5	5 ± 1.4	6 ± 2.4	4 ± 1.6	1 ± 0.4

The daily source attribution scaling coefficients are presented in Figure 8-64 and the average coefficients over the four month period in Table 8-10. Both Texas and the eastern U.S. are less than 1 at 0.77 and 0.7, respectively, indicating that these source regions were biased high on average over all of the BRAVO monitoring sites and time periods. The average scaling coefficients for the Mexican, western U.S., and boundary condition source regions were about 1, indicating unbiased average source contributions. The synthesized REMSAD average scaling coefficients for Carbón and Rest of Mexico were 1.5 and 1.7, respectively. These coefficients are similar to the amount that the Carbón and Rest of Mexico emissions were increased in the CMAQ-MADRID run compared to REMSAD.

Comparing the synthesized CMAQ source attribution of Big Bend's sulfate to the synthesized REMSAD results, it is seen that they produced similar average and daily source attributions, and so will not be discussed in detail. However, some differences occurred during the sulfate episodes. For example, during the August 20 episode, the synthesized REMSAD results predicted that the Mexican sources contributed more than 50% to Big Bend's sulfate (Figure 8-63), while synthesized CMAQ had Mexico, Texas, and the eastern U.S. each contributing about 30% of the sulfate (Figure 8-67). Also, during the October 13 sulfate episodes, the synthesized CMAQ estimated Texas' contribution to be almost 50% on average and up to 60% on an individual day during these two episodes (Figure 8-67) compared to a 30% average contribution using the synthesized REMSAD results (Figure 8-63).

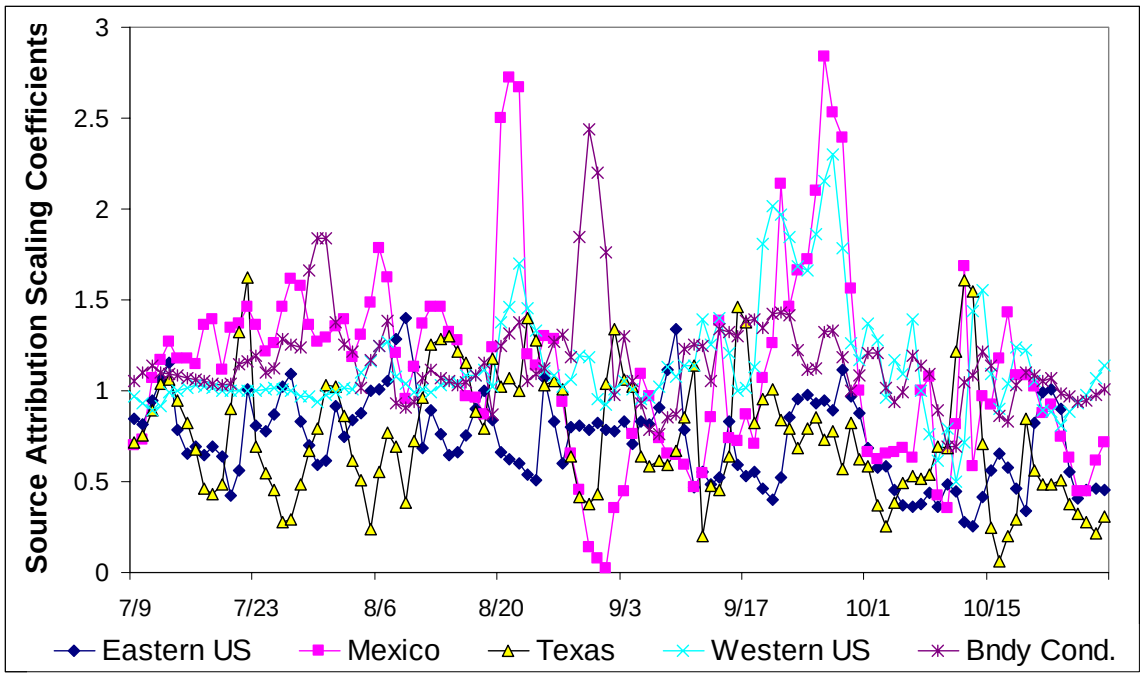

Figure 8-64. The optimum synthesized CMAQ daily source attribution scaling coefficients.

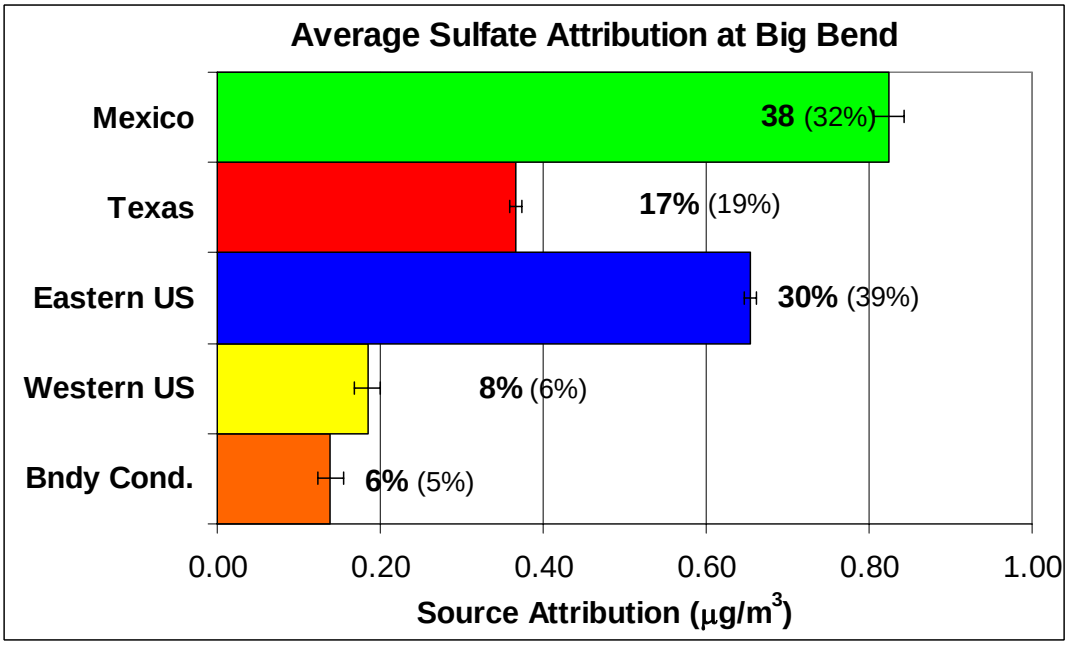

Figure 8-65. The optimum synthesized CMAQ average source attributions and standard errors to Big Bend's predicted sulfate for the entire BRAVO time period (7/9–10/28/1999). The bolded labels are the relative contributions, i.e. the ratios of average absolute values. The values in parentheses are the original CMAQ-MADRID source attribution estimates.

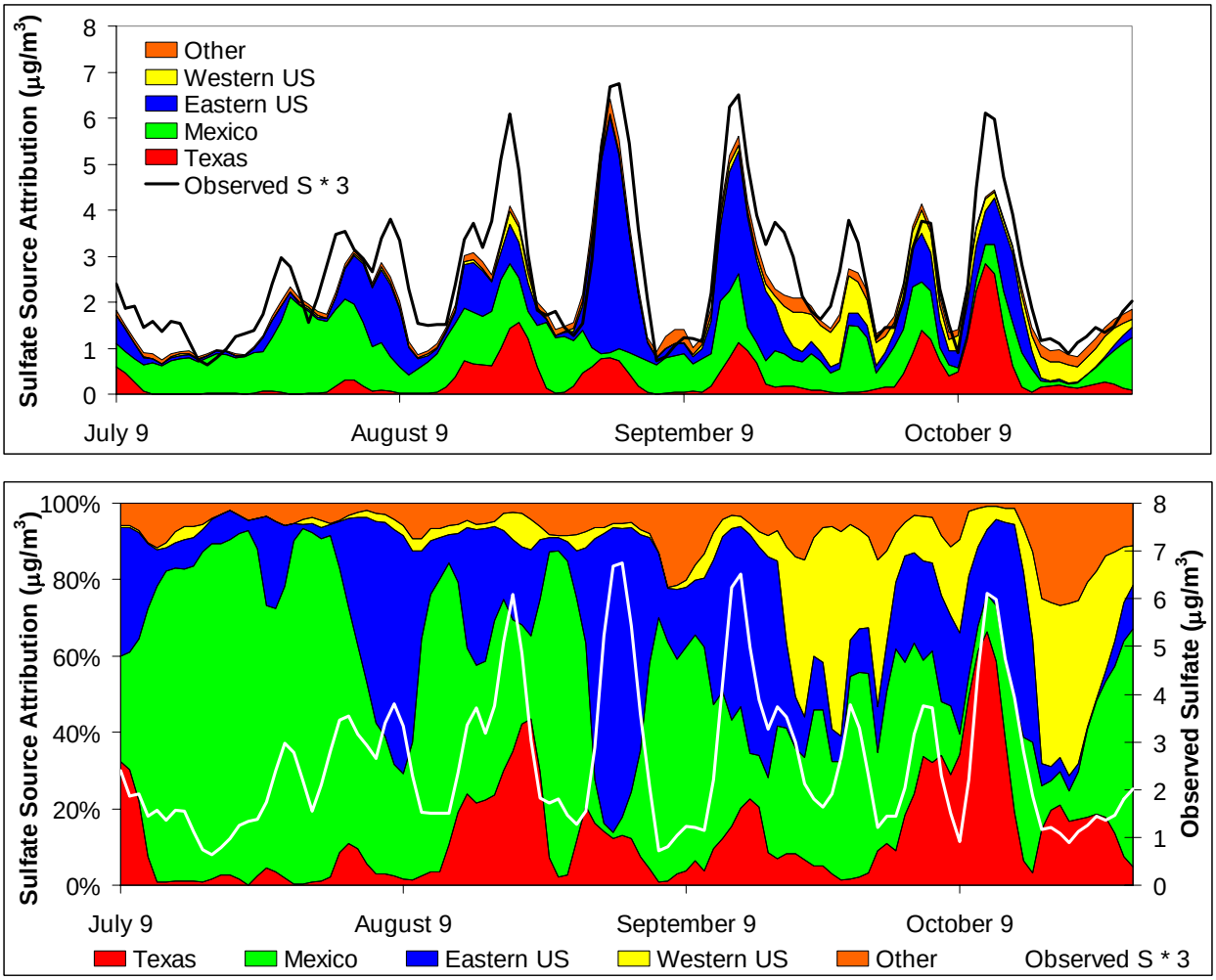

Figure 8-66. The optimum synthesized CMAQ daily absolute and relative source attributions to the predicted sulfate at Big Bend. The daily source attributions were smoothed using a three-day moving average.

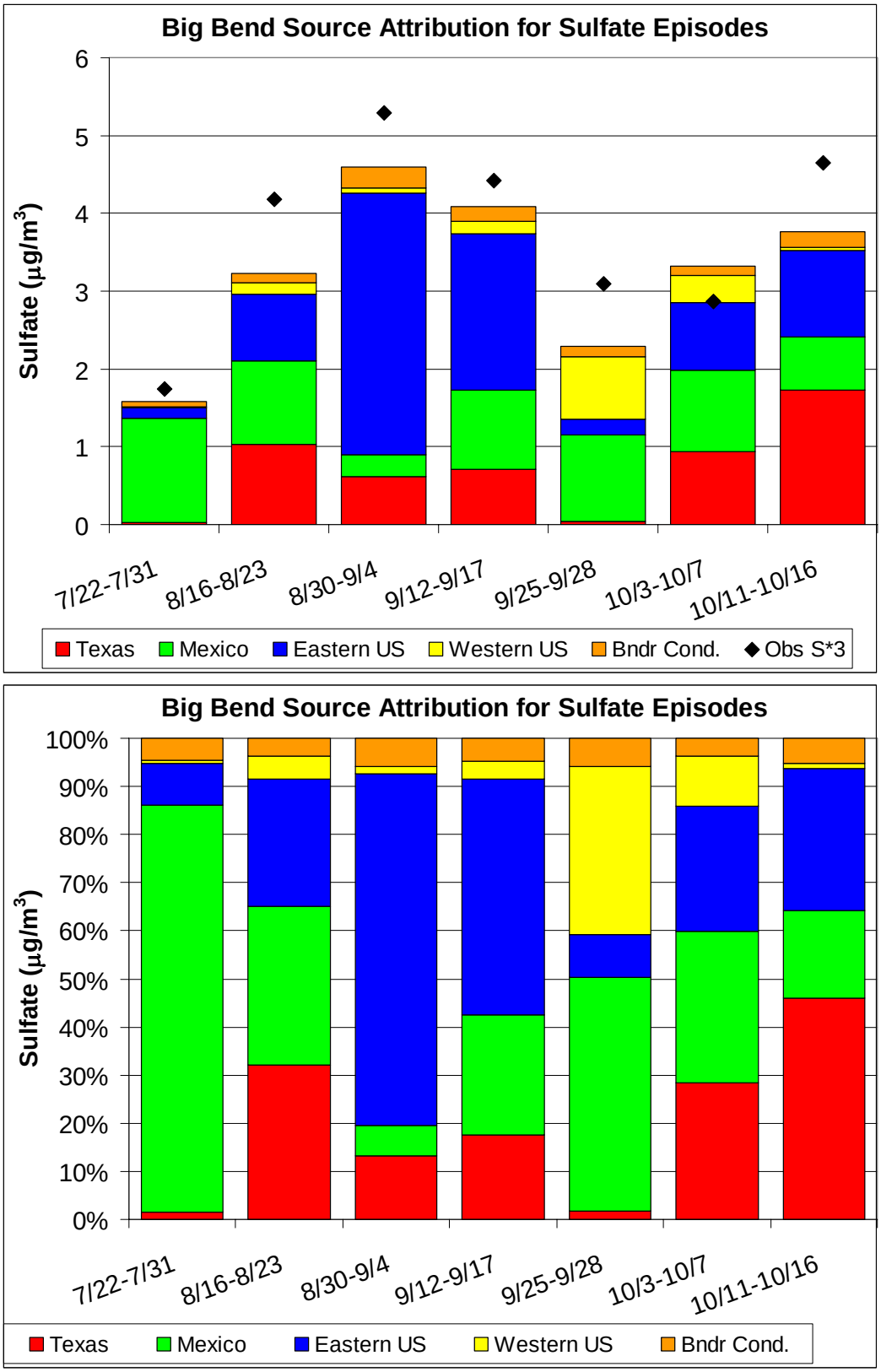

Figure 8-67. The optimum synthesized CMAQ average source attributions and standard errors to Big Bend's predicted sulfate for each Big Bend sulfate episode.

8.2.1.4 Summary and Discussion

In order to account for potential biases in the REMSAD and CMAQ-MADRID source attributions of Big Bend's sulfate, the model results were merged with the observed sulfate concentrations measured throughout Texas. The method is based on the synthesis inversion of the conservation of mass equation to derive source attribution scaling coefficients that varied in time but were fixed in space. In essence, these scaling coefficients partitioned the underestimated mass back to the source regions and removed overestimated mass from the source regions so that the predicted sulfate concentrations over Texas better matched the measured data.

The REMSAD and CMAQ synthesis inversions produced similar average contributions to Big Bend's sulfate, with Mexico having the largest contribution at 38%, while the eastern U.S. contributed about 30% and Texas 15%. The notable subregions from the REMSAD analysis were the Carbón I & II power plants, which contributed 23%, and east Texas, which contributed 14%, or 90% of the total Texas contribution. Comparing these results to the original model source attribution results, the Mexican contributions increased by 70% and 20% for the synthesized REMSAD and CMAQ results, respectively. The eastern U.S. contribution decreased by about 25% and the contributions from Texas remained about the same for both analyses.

Examining the seven largest sulfate episodes at Big Bend it was found that Mexico, eastern U.S., and Texas source regions were all large contributors during two or more episodes accounting for more than 30% of Big Bend's sulfate. The REMSAD and CMAQ-MADRID models completely missed the September 25–28 Big Bend sulfate episode and had temporal shifts in the October 11–16 episode. Therefore the synthesis inversion results for these two episodes need to be viewed with caution.

It is reassuring that the two synthesis inversions produced similar results. However, there were some differences on a higher time resolution, particularly during the Big Bend sulfur episodes. While neither result is truly correct, the synthesized CMAQ results are likely more trustworthy. The CMAQ-MADRID model was run using the REMSAD results for its boundary conditions, but these results were modified by the IMPROVE and CASTNet observed particulate sulfur and SO_2 concentrations. This reduced the eastern U.S. bias found in REMSAD. In the CMAQ-MADRID simulation, the Mexican emissions were increased by a factor of 2 within the CMAQ-MADRID domain and the upper bound on the Carbón emissions was used. This was done to address the underestimation from the Mexican sources. The resulting CMAQ-MADRID simulated sulfate concentrations at Big Bend compared better to the observed data than REMSAD results and had no bias. Therefore the synthesis inversion technique needed to correct for smaller biases.

8.2.2 Trajectory Mass Balance (TrMB)

The Trajectory Mass Balance (TrMB) Model (see section 2.3.2.1) is a receptor model in which measured concentrations at a receptor are assumed to be linearly related to the frequencies of airmass transport from several source regions to that receptor. TrMB is used to estimate the 4-month average contributions to fine particulate sulfur measured at Big Bend National Park from several source regions during July–October 1999.

8.2.2.1 Input and Modeling Details

Fine (< 2.5 μm diameter) 24-hour average particulate elemental sulfur concentrations (see chapter 3) measured at Big Bend by the IMPROVE sampler were originally used as the

dependent variable. However, there are two minor problems with this data set. First, data are missing for several days, including July 9–11, 23–25, 29, 31, August 1, and October 26–28. Since there are other measurements of fine sulfur and sulfate at Big Bend, it is possible to substitute other measurements for these missing concentrations. Other measurements at K-Bar include 24-hour averages of IMPROVE 12- and 24-hour sulfate and 6-, 12-, and 24-hour sulfur and the URG sampler's 24-hour sulfate concentrations. Once per week the URG sampler obtained replicate samples. Therefore there were from one to seven 24-hour averages of fine particulate sulfur or sulfate for each day. As shown in Figure 8-68, on some days the range of measured values was quite large. Days of particular interest are September 1, 14–15, and October 12, which, because they have high measured concentrations, are influential points in the TrMB regressions. On September 1 and 15 in particular, the IMPROVE 24-hour sulfur concentrations are at the maximum of a relatively large range of values.

Therefore, rather than use this single measurement for sulfur, the final source attribution for BRAVO was done using the daily median of all available 24-hour average sulfur concentrations for each day from July 5 through October 29. Although there are measured concentrations both before and after these dates, these are the time limits of what can be modeled using the BRAVO MM5 wind fields, so for consistency all model runs were for only these days. This gives a total of 117 days for the TrMB modeling. The final sulfur time series was within the measurement error of the sulfur measured by the URG sampler.

Source areas were chosen based on several criteria and are discussed in detail in section 2.3.2.5.

Back trajectories were started from Big Bend National Park (29.3 deg N Lat, 103.18 deg W Lon) and traced backwards in time for 5, 7, and 10 days. Original TrMB modeling for BRAVO utilized only 5-day back trajectories, but early results from REMSAD (section 2.2 and chapter 6) showed that, in general, REMSAD predicted more sulfate from distant source areas and less from closer source areas than did the back trajectory techniques. A possible reason for this result is that the lifetime of sulfur in the atmosphere was longer than 5 days on average or on a significant number of days during BRAVO. Trajectory lengths were therefore increased to determine if this alone would cause the TrMB results to more closely resemble the REMSAD results.

Three models, HYSPLIT version 4.5, the CAPITA Monte Carlo (CMC) model, and ATAD were used to generate back trajectories. All models were run with at least two input wind fields, the Mesoscale Meteorological Model (MM5) on a 36 km grid scale and EDAS when available with the lower resolution FNL when EDAS was missing. EDAS data were missing for the entire month of October and for several days in July. ATAD was also run with its traditional input of raw rawinsonde data. Sections 2.1.3 and 2.2 describe the details and differences between the wind fields and models. ATAD cannot generate trajectories longer than 5 days without significant code changes, so 7- and 10-day trajectories were not generated with this model.

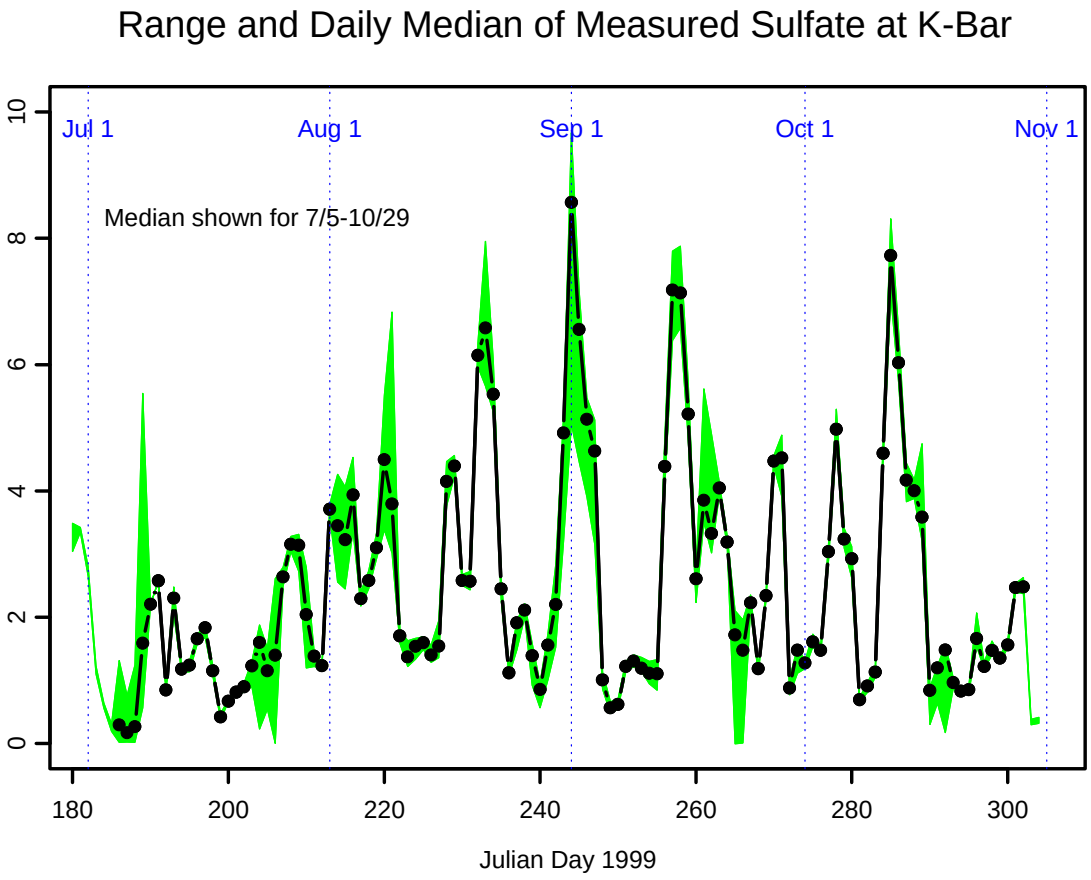

Figure 8-68. Range (in green) and daily median of IMPROVE and URG 24-hour averaged sulfur and sulfate measurements at K-Bar (in black).

HYSPLIT was started at heights of 100, 200, 500, and 1000 m above ground. An airmass location or "endpoint" was calculated hourly for each height. The number of endpoints in each source area was aggregated over these start heights. The CMC model released 20 particles every 2 hours with the position of each particle or endpoint calculated once every two hours for the EDAS/FNL data and once per hour for the MM5 data. Thus the total number of endpoints associated with a single 24-hour sulfur concentration for 5-day back trajectories is 11520 for HYSPLIT, 14400 for CMC with MM5, 28800 for CMC with EDAS/FNL and 160 for ATAD with any input.

All model/wind field combinations were tested with known attributions of the tracer data (section 7.1.1) and simulated sulfate from the REMSAD model (section 7.2.1). Based on the results of these tests HYSPLIT/MM5, CMC/EDAS/FNL, and ATAD/EDAS/FNL were dropped from consideration due to their poor performance. In addition, tests of biases in the wind fields (chapter 4) show that ATAD with raw rawinsonde data as input generates back trajectories that are too southerly, probably due to the sparse data in Mexico and the Gulf of Mexico. This leaves only the input combinations of HYSPLIT/EDAS/FNL and CMC/MM5 with 5-, 7-, and 10-day trajectories and ATAD/MM5 with 5-day trajectories for use in the measured sulfur attributions at Big Bend.

8.2.2.2 Results and Discussion

A summary of the TrMB results for measured fine particulate sulfur at K-BAR is shown in Table 8-12. The table includes the relative percent attributions and uncertainties. Also included are some statistics on goodness of fit between predicted and observed sulfur and number of observations.

Table 8-12. Relative attributions of median 24-hour sulfur at Big Bend to each source region by each model/wind field combination. Uncertainties are based on the standard errors of the regression coefficients. Model statistics are shown in the last 4 rows.

Percent Attribution of Sulfate to Each Source Area	**CAPITA MC with MM5**			**HYSPLIT with EDAS & FNL start heights 100–1000 m AGL**			**ATAD with MM5**
Trajectory Length (days)	5	7	10	5	7	10	5
North Central States (4)	0±3	0±4	0±5	0±2	0±3	0±4	0±2
Northeast (5)	0±2	1±2	1±4	2±1	3±1	0±3	0±1
MO/IL/AR (10)	5±3	9±4	10±5	0±3	0±6	0±9	5±2
East Central States (11)	1±3	5±6	9±7	1±2	4±3	6±4	0±2
LA/MS (20)	17±6	11±9	4±9	4±5	7±6	10±8	17±5
FL/GA (21)	0±3	0±4	0±4	0±2	0±3	0±4	0±2
Eastern U.S (4,5,10,11,20,21)	**23%**	**26%**	**24%**	**7%**	**14%**	**16%**	**17%**
Pacific Northwest (1)	3±3	3±3	5±4	0±3	0±3	0± 3	2±2
Northern Rockies (2)	0±4	0±4	0±5	0±6	1±6	0±7	0±3
Dakotas (3)	3±4	0±5	3±6	3±3	5±4	4±5	0±2
Southern California (6)	0±3	0±3	0±5	0±2	0±2	2±3	1±2
AZ/NM (7)	5±9	3±9	7±10	4±7	2±9	0±12	0±4
Central Plains (9)	3±10	15±11	10±12	1±7	0±6	0±8	0±5
Western U.S (1,2,3,6,7,9).	**14%**	**21%**	**25%**	**8%**	**8%**	**6%**	**3%**
Texas Panhandle (8)	0±4	0±5	0±5	0±6	0±7	5±8	0±2
West Texas (15)	0±5	3±5	0±5	1±7	0±8	0±10	1±3
North Central Texas (16)	2±5	0±5	0±5	4±5	1±6	1±7	9±5
Northeast Texas (17)	4±4	0±4	0±4	5±3	6±3	6±6	2±2
Southeast Texas (19)	13±10	9±11	12±11	35±8	29±10	18±12	8±8
Texas (8,15,16,17,19)	**19%**	**12%**	**12%**	**45%**	**36%**	**30%**	**20%**
Baja California (12)	0±3	1±4	0±6	1±3	0±5	0±6	No Ends
Northwest Mexico (13)	1±4	0±5	0±7	2±7	4±10	5±8	0±1
North Central Mexico (14)	0±4	0±4	1±5	0±3	0±3	0±4	2±4
Carbón I & II (18)	23±12	24±12	22±11	24±10	21±11	22±12	33±10
West Central Mexico (22)	1±5	1±5	1±5	0±3	4±4	6±4	0±2
Central Mexico (23)	0±3	0±3	0±3	0±3	0±3	0±4	0±2
Monterrey Region, MX (24)	5±10	0±9	0±9	4±7	5±8	7±8	6±6
SW Coast of Mexico (25)	0±2	0±1	0±1	1±1	0±2	1±3	0±1
Mexico City & Volcano (26)	9±6	8±6	10±6	7±4	8±4	6±5	10±5
S. Mexico/ Yucatan (27)	6±5	7±5	6±5	0±4	0±5	1±5	1±4
Mexico (12,13,14,18,22,23,24,25,26,27)	**45%**	**41%**	**40%**	**39%**	**42%**	**48%**	**50%**
Mean observed S (ng/m^3)	835.7	835.7	835.7	835.7	835.7	835.7	835.7
Mean predicted S (ng/m^3)	832.7	833.1	834.6	807.7	795.9	786.9	823.3
R^2	0.622	0.669	0.689	0.478	0.500	0.459	0.585
Number of observations	117	117	117	117	117	117	117

Detailed results and measures of model performance for each model and wind field combination are shown in Tables 8-13 through 8-19. Because of the different number of total endpoints for each combination, the regression coefficients with units of (ng/m^3 S/endpoint) are not directly comparable between cases. However, the predicted sulfur and percentages of sulfur attributed to the receptor from each source area are comparable.

Tables 8-13 through 8-19 also give indications of how well the model determined the regression coefficients. The coefficients and their standard errors are shown in column 2, the T statistic (coefficient/standard error) in column 3, the p value (probability that the coefficient could be zero) in column 4, and Variance Inflation Factor (VIF) in column 5. A T statistic of 2 corresponding to a p value of 0.05 is significant at the 95% confidence level with lower T statistics and higher p values being less significant.

The VIF is an indication of the collinearity of the source area with all other source areas. Source areas with VIFs of 10 and higher are considered to have significant collinearity with some linear combination of other regions. The more collinear a source region is with another region or a combination of other regions, the more difficulty in precisely determining the regression coefficient, resulting in higher standard errors for the coefficients, lower T statistics, higher p values, higher VIFs, and more uncertainty in the source attribution. With one exception (CMC MM5 10-day trajectories, E. Central States) VIFs greater than 10 occurred for source areas to the west and/or north from which airmasses usually arrived infrequently and from which the attributed sulfur is expected to be low.

Some source regions have negative coefficients indicating that the area is a net sink rather than a net source of sulfur. A negative coefficient would be likely to result if the daily endpoint counts in an area are inversely correlated with the sulfur concentrations or, in other words, the more air that arrives from that area the lower the sulfur concentrations at Big Bend. There were no negative coefficients that were statistically significant at the 95% level and all negative coefficients were small. Negative regression coefficients could be eliminated by restricting them to be zero or greater. This will probably be considered in future analyses.

Attribution results vary somewhat depending on the trajectory model/wind field combination used, though for most of the 27 smaller source regions the differences between combinations are within the uncertainties due to the standard errors of the regression coefficients.

In general, when comparing results between model runs, all combinations give approximately the same total attribution to Mexico. Values range from 39–50% with a median of 42%. With MM5 input in the CMC model, longer trajectories result in somewhat less attribution to Mexico, while the reverse is true for HYSPLIT with EDAS/FNL input for which longer trajectories result in slightly more sulfur being attributed to Mexico.

The biggest disagreement between model/wind field combinations is in the mean relative percent of sulfur attributed to Texas. HYSPLIT with EDAS/FNL input attributes approximately twice the percent of sulfur (30–45%) to Texas as is predicted from MM5 input modeled with ATAD (20%) or CMC (12–19%). Both HYSPLIT and CMC trajectory models attribute lower fractions of sulfur to Texas as the trajectory length increases.

MM5 input in both ATAD and CMC models results in a larger attribution (17–26%) to the eastern U.S. than HYSPLIT with EDAS/FNL (7–16%). The longer the HYSPLIT trajectories, the larger the fraction of sulfur attributed to the eastern U.S. The greatest percentage

attributed to the eastern U.S. by the CMC model was with the 7-day trajectories, with both 5- and 10-day lengths resulting in a lower percentage from this region.

For all model/wind field combinations the smallest relative attribution to any of the four large source regions was to the western U.S., though the percentages attributed by HYSPLIT/EDAS/FNL (6–8%) were only about half what was attributed by CMC/MM5 (14–25%). ATAD/MM5 had the lowest relative attribution to the western U.S. at just 3%. Longer HYSPLIT/EDAS/FNL trajectories caused slightly less relative attribution to the western U.S., while longer CMC/MM5 trajectories resulted in higher relative attributions to the western U.S.

Comparisons of these results with the results from the regional air quality model REMSAD show that TrMB predicts that larger fractions of sulfur arrive from Mexico and the western U.S. and a smaller fraction arrives from the eastern U.S. than is predicted by REMSAD. This is true for all input model/wind field combinations. Both CMC with MM5 and ATAD with MM5 give approximately the same average attribution to Texas as REMSAD, while HYSPLIT/EDAS/FNL attributes much more to Texas than REMSAD. Since REMSAD used the MM5 wind field as input, it is expected that TrMB modeling with the EDAS/FNL wind fields will be more different than with the MM5 input.

Reasons for the differences could include collinearities between TrMB source areas, inaccurate locations of the back trajectories, failure of the linearity assumptions, or any of many problems with the deterministic model including input data or parameterization of the physics and chemistry within the model. Model reconciliation is discussed in more detail in chapter 9.

The 7th column of Tables 8-13 through 8-19 gives the daily average fine elemental particulate sulfur (ng/m^3) attributed to each source area. These are calculated by multiplying the regression coefficient by the number of endpoints in the area for each day and then taking the mean, or equivalently by multiplying average number of endpoints per source area per day, shown in column 6, by the regression coefficient. Unlike the coefficients themselves, these values and the values in all columns to the right can be compared between tables. The uncertainty in the average predicted sulfur is calculated by multiplying the mean number of endpoints by the standard error of the coefficient. The raw percent attribution, shown in column 8, is 100% times the mean predicted sulfur attributed to the area divided by the total predicted sulfur. Column 9 is relative percent attribution and is the percent attribution that is usually reported and is shown in Table 8-12. It is calculated by setting the negative attributions to zero and then forcing the remaining positive values to sum to 100%. The uncertainties for these values are assumed to be the same as for the raw attributions, though this is likely an underestimate.

The final column in Tables 8-13 through 8-19 is the number of days when there were airmasses arriving at the receptor from each source area, and so is a measure of the frequency of impact of the source area on Big Bend. It is also of statistical interest since it is the number of days used to determine the regression coefficient. A single endpoint in a source region is enough to have the day count as a "hit" for that region, so trajectory models with fewer total endpoints will indicate that a source area impacted Big Bend on fewer days. As the trajectory lengths increase, the number of days with a potential impact also increases. Maximum possible number of days is 117.

Table 8-13. TrMB regression details for particulate sulfur at Big Bend and CAPITA MC MM5 5-day trajectory endpoints.

Source Area	Coef.±SE	T	P	VIF	Mean Ends/ day	Pred S (ng/m^3) ± unc	% Pred S	Relative % ± unc	No. days hit
North Central States (4)	-0.099±0.111	-0.89	0.38	2.0	204.8	-20±23	-2	0±3	50
Northeast (5)	1.117±3.559	0.31	0.75	2.1	3.9	4±14	1	0±2	13
MO/IL/AR (10)	0.110±0.061	1.82	0.07	2.0	434.0	48±26	6	5±3	58
East Central States (11)	0.125±0.243	0.52	0.61	2.6	93.5	12±23	1	1±3	40
LA/MS (20)	0.255±0.076	3.34	0.00	4.2	678.9	173±52	21	17±6	63
FL/GA (21)	-0.150±0.104	-1.44	0.16	1.7	240.5	-36±25	-4	0±3	72
Pacific Northwest (1)	0.273±0.229	1.19	0.24	5.3	96.8	26±22	3	3±3	33
Northern Rockies (2)	-0.169±0.124	-1.37	0.17	4.2	241.8	-41±30	-5	0±4	48
Dakotas (3)	0.140±0.151	0.92	0.36	4.5	227.1	32±34	4	3±4	43
Southern California (6)	-0.321±0.610	-0.53	0.60	5.9	37.3	-12±23	-1	0±3	26
AZ/NM (7)	0.283±0.407	0.70	0.49	30.7	188.1	53±77	6	5±9	41
Central Plains (9)	0.055±0.134	0.41	0.68	10.3	600.0	33±80	4	3±10	57
Texas Panhandle (8)	-0.022±0.456	-0.05	0.96	4.6	80.5	-2±37	-0	0±4	45
West Texas (15)	-0.030±0.231	-0.13	0.90	7.4	178.9	-5±41	-1	0±5	49
North Central Texas (16)	0.053±0.140	0.38	0.70	5.5	325.7	17±46	2	2±5	56
Northeast Texas (17)	0.201±0.169	1.19	0.24	3.3	194.3	39±33	5	4±4	60
Southeast Texas (19)	0.147±0.102	1.44	0.15	7.0	844.7	125±86	15	13±10	86
Baja California (12)	-0.183±1.520	-0.12	0.91	6.2	14.8	-3±22	-0	0±3	17
Northwest Mexico (13)	0.182±0.909	0.20	0.84	25.1	37.3	7±34	1	1±4	22
N Central Mexico (14)	-0.138±0.376	-0.37	0.72	6.7	91.1	-13±34	-2	0±4	32
Carbón I & II (18)	0.204±0.093	2.20	0.03	4.2	1112.2	227±103	27	23±12	98
W Central Mexico (22)	0.136±1.016	0.13	0.89	29.9	41.4	6±42	1	1±5	21
Central Mexico (23)	-0.203±0.229	-0.89	0.38	3.4	125.3	-25±29	-3	0±3	49
Monterrey Reg., MX (24)	0.052±0.091	0.57	0.57	5.9	890.9	46±81	6	5±10	90
SW Coast Mexico (25)	-0.220±1.051	-0.21	0.83	4.6	12.2	-3±13	-0	0±2	6
Mex City, Volcano (26)	0.195±0.119	1.63	0.11	3.8	443.3	86±53	10	9±6	66
S Mexico/ Yucatan (27)	0.116±0.077	1.52	0.13	2.4	500.5	58±39	7	6±5	60

Table 8-14. TrMB regression details for particulate sulfur at Big Bend and HYSPLIT EDAS/FNL 5-day trajectory endpoints.

Source Area	Coef.±SE	T	P	VIF	Mean Ends/ day	Pred S (ng/m^3) ± unc	% Pred S	Relative % ± unc	No. days hit
North Central States (4)	-0.159±0.273	-0.58	0.56	2.1	58.9	-9±16	-1	0±2	16
Northeast (5)	61.710±20.149	3.06	0.00	1.4	0.4	22±8	3	2±1	3
MO/IL/AR (10)	-0.250±0.188	-1.33	0.19	2.0	136.6	-34±26	-4	0±3	35
East Central States (11)	1.155±1.844	0.63	0.53	2.1	8.8	10±16	1	1±2	10
LA/MS (20)	0.114±0.123	0.93	0.36	2.9	347.3	40±43	5	4±5	53
FL/GA (21)	-0.282±0.190	-1.49	0.14	1.3	89.6	-25±17	-3	0±2	42
Pacific Northwest (1)	-0.568±0.972	-0.59	0.56	3.2	28.9	-16±28	-2	0±3	22
Northern Rockies (2)	-0.155±0.425	-0.36	0.72	4.7	108.4	-17±46	-2	0±6	31
Dakotas (3)	0.250±0.214	1.17	0.25	3.0	102.4	26±22	3	3±3	19
Southern California (6)	-0.080±0.397	-0.20	0.84	3.3	34.3	-3±14	-0	0±2	15
AZ/NM (7)	0.149±0.251	0.59	0.55	13.4	235.9	35±59	4	4±7	30
Central Plains (9)	0.042±0.184	0.23	0.82	5.5	306.5	13±56	2	1±7	44
Texas Panhandle (8)	-0.375±0.519	-0.72	0.47	8.5	101.1	-38±52	-5	0±6	32
West Texas (15)	0.038±0.239	0.16	0.87	9.2	237.4	9±57	1	1±7	32
North Central Texas (16)	0.153±0.142	1.08	0.29	3.4	283.3	43±40	5	4±5	42
Northeast Texas (17)	0.288±0.169	1.70	0.09	2.5	154.1	44±26	5	5±3	47
Southeast Texas (19)	0.295±0.060	4.91	0.00	2.8	1142.3	337±69	42	35±8	95
Baja California (12)	0.264±0.611	0.43	0.67	4.9	45.1	12±28	1	1±3	13
Northwest Mexico (13)	0.325±0.894	0.36	0.72	12.6	64.6	21±58	3	2±7	16
N Central Mexico (14)	0.031±0.234	0.13	0.90	2.6	87.0	3±20	0	0±3	24
Carbón I & II (18)	0.137±0.048	2.87	0.01	2.0	1711.0	235±82	29	24±10	99
W Central Mexico (22)	-0.149±2.275	-0.07	0.95	4.3	10.4	-2±24	-0	0±3	12
Central Mexico (23)	-0.487±0.604	-0.81	0.42	1.9	36.8	-18±22	-2	0±3	31
Monterrey Reg., MX (24)	0.045±0.065	0.69	0.50	2.5	898.2	40±58	5	4±7	85
SW Coast Mexico (25)	28.897±17.658	1.64	0.11	1.2	0.4	10±7	1	1±1	3
Mex City, Volcano (26)	0.384±0.163	2.36	0.02	1.8	187.1	72±30	9	7±4	47
S Mexico/ Yucatan (27)	-0.010±0.122	-0.08	0.94	1.7	246.4	-2±30	-0	0±4	51

Table 8-15. TrMB regression details for particulate sulfur at Big Bend and ATAD with MM5 input 5-day trajectory endpoints.

Source Area	Coef.±SE	T	P	VIF	Mean Ends/ day	Pred S (ng/m^3) ± unc	% Pred S	Relative % ± unc	No. days hit
North Central States (4)	-0.039±1.240	-0.03	0.98	1.5	12.1	0±15	-0	0±2	19
Northeast (5)	37.966±74.343	0.51	0.61	2.2	0.1	4±7	0	0±1	2
MO/IL/AR (10)	3.091±1.327	2.33	0.02	1.4	13.4	42±18	5	5±2	27
East Central States (11)	0.584±2.724	0.21	0.83	2.4	7.1	4±19	1	0±2	16
LA/MS (20)	6.839±1.876	3.65	0.00	3.6	22.7	155±43	19	17±5	35
FL/GA (21)	-0.119±2.425	-0.05	0.96	1.6	7.9	-1±19	-0	0±2	26
Pacific Northwest (1)	11.430±8.531	1.34	0.18	3.2	1.8	21±15	3	2±2	6
Northern Rockies (2)	-1.069±4.633	-0.23	0.82	4.9	4.8	-5±22	-1	0±3	13
Dakotas (3)	0.904±4.005	0.23	0.82	2.0	4.3	4±17	0	0±2	11
Southern California (6)	1.761±4.350	0.41	0.69	3.0	3.1	6±13	1	1±2	5
AZ/NM (7)	0.394±4.665	0.08	0.93	12.0	6.5	3±30	0	0±4	8
Central Plains (9)	-2.477±2.702	-0.92	0.36	5.7	15.1	-38±41	-5	0±5	24
Texas Panhandle (8)	-15.576±9.078	-1.72	0.09	3.8	1.9	-30±17	-4	0±2	10
West Texas (15)	1.795±4.870	0.37	0.71	4.4	5.2	9±25	1	1±3	17
North Central Texas (16)	8.975±4.741	1.89	0.06	7.3	9.2	83±44	10	9±5	26
Northeast Texas (17)	2.615±2.539	1.03	0.31	1.5	6.1	16±15	2	2±2	19
Southeast Texas (19)	2.596±2.249	1.15	0.25	5.3	29.6	77±67	9	8±8	67
Baja California (12)	NA	NA	NA	NA	0.0	0±0	0	0±0	0
Northwest Mexico (13)	-0.611±9.148	-0.07	0.95	4.1	1.2	-1±11	-0	0±1	3
N Central Mexico (14)	6.507±11.791	0.55	0.58	12.5	2.8	18±33	2	2±4	9
Carbón I & II (18)	8.268±2.205	3.75	0.00	3.7	36.6	303±81	37	33±10	95
W Central Mexico (22)	-8.373±23.453	-0.36	0.72	4.5	0.7	-6±16	-1	0±2	4
Central Mexico (23)	-0.846±3.177	-0.27	0.79	3.1	5.6	-5±18	-1	0±2	17
Monterrey Reg., MX (24)	1.716±1.491	1.15	0.25	2.8	34.4	59±51	7	6±6	71
SW Coast Mexico (25)	-4.108±17.338	-0.24	0.81	1.6	0.3	-1±5	-0	0±1	1
Mex City, Volcano (26)	5.367±2.270	2.37	0.02	2.7	17.5	94±40	11	10±5	44
S Mexico/ Yucatan (27)	0.738±1.717	0.43	0.67	1.9	17.4	13±30	2	1±4	43

Table 8-16. TrMB regression details for particulate sulfur at Big Bend and CAPITA MC MM5 input 7-day trajectory endpoints.

Source Area	Coef.±SE	T	P	VIF	Mean Ends/ day	Pred S (ng/m^3) ± unc	% Pred S	Relative % ± unc	No. days hit
North Central States (4)	-0.068±0.090	-0.76	0.45	2.4	333.8	-23±30	-3	0±4	62
Northeast (5)	0.373±0.566	0.66	0.51	3.7	35.6	13±20	2	1±2	36
MO/IL/AR (10)	0.164±0.056	2.98	0.00	2.6	623.9	102±34	12	9±4	64
East Central States (11)	0.207±0.172	1.21	0.23	7.0	271.4	56±47	7	5±6	56
LA/MS (20)	0.142±0.088	1.61	0.11	9.0	849.8	120±75	14	11±9	74
FL/GA (21)	-0.111±0.073	-1.53	0.13	1.8	449.0	-50±33	-6	0±4	82
Pacific Northwest (1)	0.226±0.157	1.44	0.15	5.0	159.9	36±25	4	3±2	53
Northern Rockies (2)	-0.175±0.094	-1.85	0.07	3.8	375.5	-66±35	-8	0±4	62
Dakotas (3)	-0.001±0.153	-0.01	1.00	5.5	295.3	0±45	-0	0±5	62
Southern California (6)	-0.139±0.422	-0.33	0.74	7.3	68.7	-10±29	-1	0±3	38
AZ/NM (7)	0.128±0.290	0.44	0.66	24.7	257.2	33±75	4	3±9	48
Central Plains (9)	0.224±0.126	1.78	0.08	11.5	726.5	163±92	20	15±11	64
Texas Panhandle (8)	-0.497±0.415	-1.20	0.23	4.7	95.0	-47±39	-6	0±5	53
West Texas (15)	0.188±0.218	0.86	0.39	7.5	197.4	37±43	4	3±5	52
North Central Texas (16)	-0.063±0.124	-0.51	0.61	4.8	347.7	-22±43	-3	0±5	59
Northeast Texas (17)	-0.102±0.153	-0.67	0.51	3.9	240.4	-25±37	-3	0±4	66
Southeast Texas (19)	0.112±0.103	1.08	0.28	8.8	901.9	101±93	12	9±11	89
Baja California (12)	0.326±1.006	0.32	0.75	8.0	31.8	10±32	1	1±4	27
Northwest Mexico (13)	0.016±0.780	0.02	0.98	29.5	58.0	1±45	0	0±5	29
N Central Mexico (14)	-0.180±0.309	-0.58	0.56	7.0	115.2	-21±36	-2	0±4	38
Carbón I & II (18)	0.236±0.086	2.73	0.01	4.1	1128.0	267±97	32	24±12	99
W Central Mexico (22)	0.156±0.750	0.21	0.84	30.4	56.2	9±42	1	1±5	26
Central Mexico (23)	-0.031±0.199	-0.16	0.88	3.1	136.3	-4±27	-1	0±3	50
Monterrey Reg., MX (24)	-0.007±0.084	-0.09	0.93	5.6	905.6	-7±76	-1	0±9	92
SW Coast Mexico (25)	-0.351±0.386	-0.91	0.37	3.3	26.4	-9±10	-1	0±1	13
Mex City, Volcano (26)	0.201±0.114	1.77	0.08	4.5	460.6	93±53	11	8±6	73
S Mexico/ Yucatan (27)	0.132±0.072	1.85	0.07	2.7	565.2	75±41	9	7±5	67

Table 8-17. TrMB regression details for particulate sulfur at Big Bend and HYSPLIT EDAS/FNL input 7-day trajectory endpoints.

Source Area	Coef.±SE	T	P	VIF	Mean Ends/ day	Pred S (ng/m^3) ± unc	% Pred S	Relative % ± unc	No. days hit
North Central States (4)	-0.147±0.114	-1.29	0.20	2.0	179.8	-26±20	-3	0±3	32
Northeast (5)	37.790±15.233	2.48	0.02	1.6	0.7	28±11	3	3±1	5
MO/IL/AR (10)	-0.163±0.140	-1.16	0.25	3.2	325.2	-53±46	-7	0±6	47
East Central States (11)	1.208±0.764	1.58	0.12	2.2	31.7	38±24	5	4±3	24
LA/MS (20)	0.134±0.079	1.69	0.09	3.4	588.9	79±47	10	7±6	57
FL/GA (21)	-0.132±0.112	-1.17	0.24	1.4	208.7	-28±23	-3	0±3	54
Pacific Northwest (1)	-0.216±0.334	-0.65	0.52	2.1	71.5	-15±24	-2	0±3	37
Northern Rockies (2)	0.043±0.240	0.18	0.86	3.4	192.6	8±46	1	1±6	44
Dakotas (3)	0.359±0.194	1.85	0.07	3.2	153.2	55±30	7	5±4	38
Southern California (6)	-0.020±0.331	-0.06	0.95	3.4	48.8	-1±16	-0	0±2	19
AZ/NM (7)	0.087±0.247	0.35	0.73	17.6	294.6	26±73	3	2±9	33
Central Plains (9)	-0.091±0.118	-0.77	0.44	4.0	436.9	-40±52	-5	0±6	55
Texas Panhandle (8)	0.040±0.507	0.08	0.94	9.3	113.9	5±58	1	0±7	36
West Texas (15)	-0.124±0.241	-0.51	0.61	10.5	264.9	-33±64	-4	0±8	34
North Central Texas (16)	0.023±0.141	0.16	0.87	3.9	318.3	7±45	1	1±6	49
Northeast Texas (17)	0.243±0.110	2.21	0.03	2.6	246.1	60±27	8	6±3	51
Southeast Texas (19)	0.252±0.066	3.83	0.00	3.7	1242.4	313±82	39	29±10	96
Baja California (12)	-0.218±0.544	-0.40	0.69	6.5	70.7	-15±38	-2	0±5	18
Northwest Mexico (13)	0.491±0.884	0.56	0.58	22.9	86.1	42±76	5	4±10	18
N Central Mexico (14)	0.016±0.220	0.07	0.94	2.6	99.2	2±22	0	0±3	25
Carbón I & II (18)	0.127±0.048	2.64	0.01	1.8	1753.1	223±84	28	21±11	99
W Central Mexico (22)	1.388±1.071	1.30	0.20	6.6	28.4	39±30	5	4±4	13
Central Mexico (23)	-1.291±0.567	-2.28	0.03	2.0	44.2	-57±25	-7	0±3	32
Monterrey Reg., MX (24)	0.057±0.066	0.85	0.40	2.4	912.4	52±60	7	5±8	88
SW Coast Mexico (25)	0.284±1.898	0.15	0.88	2.9	8.1	2±15	0	0±2	8
Mex City, Volcano (26)	0.437±0.174	2.50	0.01	2.1	197.7	86±34	11	8±4	50
S Mexico/ Yucatan (27)	-0.002±0.105	-0.02	0.99	2.0	342.4	-1±36	-0	0±5	55

Table 8-18. TrMB regression details for particulate sulfur at Big Bend and CAPITA MC MM5 input 10-day trajectory endpoints.

Source Area	Coef.±SE	T	P	VIF	Mean Ends/ day	Pred S (ng/m^3) ± unc	% Pred S	Relative % ± unc	No. days hit
North Central States (4)	-0.058±0.087	-0.66	0.51	3.7	461.5	-27±40	-3	0±5	69
Northeast (5)	0.085±0.362	0.24	0.82	7.0	85.9	7±31	1	1±4	53
MO/IL/AR (10)	0.155±0.057	2.73	0.01	3.4	741.2	115±42	14	10±5	70
East Central States (11)	0.252±0.150	1.68	0.10	10.8	400.8	101±60	12	9±7	65
LA/MS (20)	0.049±0.075	0.66	0.51	7.8	981.7	48±74	6	4±9	79
FL/GA (21)	-0.122±0.060	-2.03	0.05	1.8	603.4	-74±36	-9	0±4	85
Pacific Northwest (1)	0.232±0.153	1.52	0.13	6.4	232.5	54±36	6	5±4	64
Northern Rockies (2)	-0.118±0.089	-1.33	0.19	4.0	499.4	-59±44	-7	0±5	70
Dakotas (3)	0.110±0.152	0.72	0.47	6.0	349.0	38±53	5	3±6	69
Southern California (6)	-0.311±0.361	-0.86	0.39	9.8	120.4	-37±43	-4	0±5	56
AZ/NM (7)	0.236±0.250	0.94	0.35	24.6	337.6	80±84	10	7±10	59
Central Plains (9)	0.140±0.122	1.14	0.26	12.1	796.9	111±97	13	10±12	71
Texas Panhandle (8)	-0.155±0.405	-0.38	0.70	4.9	108.9	-17±44	-2	0±5	62
West Texas (15)	-0.004±0.208	-0.02	0.99	7.2	216.2	-1±45	-0	0±5	62
North Central Texas (16)	-0.067±0.120	-0.56	0.58	5.1	368.6	-25±44	-3	0±5	68
Northeast Texas (17)	-0.051±0.142	-0.36	0.72	3.9	262.7	-13±37	-2	0±4	69
Southeast Texas (19)	0.146±0.099	1.48	0.14	8.3	939.3	137±93	16	12±11	90
Baja California (12)	-0.207±0.838	-0.25	0.81	16.2	62.2	-13±52	-2	0±6	46
Northwest Mexico (13)	0.002±0.658	0.00	1.00	28.7	83.0	0±55	0	0±7	42
N Central Mexico (14)	0.069±0.265	0.26	0.80	6.8	147.6	10±39	1	1±5	50
Carbón I & II (18)	0.222±0.080	2.78	0.01	4.0	1139.0	253±91	30	22±11	99
W Central Mexico (22)	0.110±0.612	0.18	0.86	27.3	72.9	8±45	1	1±5	34
Central Mexico (23)	-0.115±0.190	-0.61	0.55	3.2	147.1	-17±28	-2	0±3	58
Monterrey Reg., MX (24)	-0.015±0.081	-0.19	0.85	4.8	920.6	-14±75	-2	0±9	93
SW Coast Mexico (25)	-0.538±0.327	-1.65	0.10	3.4	35.7	-19±12	-2	0±1	16
Mex City, Volcano (26)	0.237±0.110	2.15	0.03	4.9	486.4	115±54	14	10±6	80
S Mexico/ Yucatan (27)	0.120±0.067	1.79	0.08	2.6	599.2	72±40	9	6±5	76

Table 8-19. TrMB regression details for particulate sulfur at Big Bend and HYSPLIT EDAS/FNL input 10-day trajectory endpoints.

Source Area	Coef.±SE	T	P	VIF	Mean Ends/ day	Pred S (ng/m^3) ± unc	% Pred S	Relative % ± unc	No. days hit
North Central States (4)	-0.092±0.083	-1.11	0.27	1.8	350.2	-32±29	-4	0±4	43
Northeast (5)	-1.264±1.486	-0.85	0.40	3.8	15.2	-19±23	-2	0±3	17
MO/IL/AR (10)	-0.144±0.125	-1.15	0.25	6.5	566.9	-82±71	-10	0±9	51
East Central States (11)	0.881±0.341	2.58	0.01	2.4	96.5	85±33	11	6±4	38
LA/MS (20)	0.175±0.085	2.04	0.04	5.8	745.1	130±63	17	10±8	62
FL/GA (21)	-0.176±0.095	-1.84	0.07	1.5	353.6	-62±34	-8	0±4	67
Pacific Northwest (1)	-0.026±0.175	-0.15	0.88	2.0	154.1	-4±27	-1	0±3	51
Northern Rockies (2)	-0.133±0.175	-0.76	0.45	3.4	294.1	-39±51	-5	0±7	55
Dakotas (3)	0.244±0.200	1.22	0.23	3.4	199.8	49±40	6	4±5	46
Southern California (6)	0.344±0.321	1.07	0.29	4.5	83.8	29±27	4	2±3	32
AZ/NM (7)	-0.152±0.247	-0.62	0.54	22.5	376.4	-57±93	-7	0±12	42
Central Plains (9)	-0.143±0.109	-1.32	0.19	4.4	543.7	-78±59	-10	0±8	59
Texas Panhandle (8)	0.525±0.545	0.96	0.34	9.9	121.6	64±66	8	5±8	44
West Texas (15)	-0.087±0.277	-0.32	0.75	14.1	285.7	-25±79	-3	0±10	36
North Central Texas (16)	0.031±0.154	0.20	0.84	4.5	342.5	11±53	1	1±7	50
Northeast Texas (17)	0.270±0.147	1.84	0.07	5.2	299.6	81±44	10	6±6	52
Southeast Texas (19)	0.184±0.071	2.59	0.01	4.4	1310.6	242±93	31	18±12	97
Baja California (12)	-0.417±0.438	-0.95	0.34	7.6	106.0	-44±46	-6	0±6	23
Northwest Mexico (13)	0.528±0.565	0.94	0.35	15.7	113.4	60±64	8	5±8	24
N Central Mexico (14)	0.051±0.242	0.21	0.83	3.6	120.2	6±29	1	0±4	28
Carbón I & II (18)	0.166±0.053	3.14	0.00	2.1	1762.8	292±93	37	22±12	100
W Central Mexico (22)	1.961±0.852	2.30	0.02	6.4	38.8	76±33	10	6±4	16
Central Mexico (23)	-1.593±0.624	-2.55	0.01	2.6	50.1	-80±31	-10	0±4	34
Monterrey Reg., MX (24)	0.092±0.066	1.39	0.17	2.2	930.2	86±61	11	7±8	89
SW Coast Mexico (25)	0.734±1.904	0.39	0.70	4.4	13.8	10±26	1	1±3	10
Mex City, Volcano (26)	0.339±0.180	1.88	0.06	2.2	215.7	73±39	9	6±5	53
S Mexico/ Yucatan (27)	0.047±0.108	0.44	0.67	1.8	358.7	17±39	2	1±5	64

8.2.3 Forward Mass Balance Regression (FMBR)

The Forward Mass Balance Regression (FMBR) is a hybrid receptor model in which receptor concentrations are assumed to be linearly related to airmass transport from a number of source regions to the receptor. The transport is estimated using a forward particle dispersion model simulating transport from the source regions to the receptor. The FMBR methodology is explained in section 2.3.2.2 and validated using the measured tracer concentrations and the REMSAD source apportionment results in sections 7.1.2 and 7.2.2, respectively. FMBR is identical in concept to TrMB, but FMBR is based on forward transport using plumes from the sources, while TrMB is based upon backward transport using back trajectories from the receptor.

The evaluation of FMBR was conducted using both the BRAVO MM5 and EDAS/FNL wind fields. It was shown that FMBR was able to properly apportion the measured perfluorocarbon tracer at Big Bend to the four tracer release sites in Texas, within the uncertainties of the technique. Therefore the technique was able to account for source contributions of inert species from sources 250–750 km from Big Bend. FMBR was also tested against synthetic sulfate concentrations and their apportionment to nine source regions including the Carbón facilities. The synthetic data was derived from the REMSAD model runs. Again, FMBR was able to properly apportion the synthetic sulfate to the nine source regions within the uncertainties of the technique. The results were sensitive to the length of time that the transport from the sources to the Big Bend region was tracked, and 10-day transport times produced the best results. Distant (western U.S. and eastern U.S.) source regions tended to be underestimated while the closer source regions in Texas and Mexico were overestimated. Based upon these results, FMBR was applied to the measured Big Bend sulfate data and the analysis was conducted for both wind fields.

In this application, the 24-hour observed fine particulate sulfur concentrations at the K-Bar Ranch in Big Bend were used. Multiple sulfur measurements were made at K-Bar so the median daily concentration for each day was used. These are the same data used in the TrMB analysis in the previous section. The airmass transport was estimated using the CAPITA Monte Carlo model driven by both the BRAVO MM5 and EDAS/FNL wind fields to estimate plume transport from about 670 virtual sources about 100 km apart evenly distributed throughout the United States and Mexico. Each plume was tracked for 10 days. These plumes were aggregated together to represent transport from 17 large source regions. The location of the virtual plumes and the source regions are presented in Figure 2-17. Section 7.2.2 describes how the Monte Carlo Model was run and how the source-to-receptor transport was derived from the resulting plumes.

There were two differences between the application of FMBR and TrMB to Big Bend's sulfate data. The EDAS/FNL wind fields were used in FMBR, but the CMC back trajectories generated by the EDAS/FNL wind fields did not pass all of the TMBR evaluation tests and were not used in that analysis. Also, the FMBR technique used a modified version of the source regions used in TrMB. It was found that the transport from some of the source regions were highly collinear with $r^2 > 0.5$. These source areas were merged and adjusted until the r^2 between any two source regions was below 0.5. This process reduced the 27 source regions to only 17 which are presented in Figure 2-18.

8.2.3.1 Results

The detailed regression results are presented in Tables 8-20 and 8-21 using the MM5 and EDAS/FNL wind fields, respectively. Figures 8-69 and 8-70 present the source attributions for

the four major regions, Mexico, Texas, the eastern U.S., and the western U.S., and the major subregions, Carbón and east Texas. Using either wind field, the performance of the regression was about the same with an r^2 of 0.36 an RMS error of 60%; however, the bias using the MM5 winds was only -6% but was -18% using the EDAS/FNL winds. When FMBR was applied to the REMSAD-simulated sulfate, the r^2 was 0.8. The reduction in the r^2 is due to either errors in the transport or nonlinearities in the atmospheric transformation and removal processes in the atmosphere for which the REMSAD model does not account.

Table 8-20. The FMBR regression results using the MM5 10-day plumes. The bolded rows have p values less than or equal to 0.1 derived from a two sized t test. The FMBR used the MM5-derived 10-day plumes.

Source Region	SO_2 Emission [1000 Tons SO2/yr]	Src/Sink ± Error	P Value	VIF	Attribution ± Error %
Southeast Texas	**537,000**	**36.4 ± 9.3**	**0.0002**		**24.4 ± 6.2**
Northeast Texas	476,000	0. ± 13.5	1		0. ± 4.3
West Texas	114,000	0. ± 5.	1		0. ± 2.7
Carbón I & II	**152,000 - 241,000**	**56. ± 12.6**	**0.00002**		**26.2 ± 5.9**
Monterrey Region, MX	**114,000**	**6.8 ± 3.4**	**0.05**		**18.3 ± 9.1**
Baja California	64,000	26.1 ± 44.1	0.55		1.4 ± 2.4
Northwest Mexico	140,000	0. ± 4.7	1		0. ± 3.
Central MX	44,000	0. ± 5.2	1		0. ± 4.2
SW Coast of MX	6,000	0. ± 31.3	1		0. ± 1.5
Mexico City & Volcano	2,160,000	17.8 ± 11.5	0.12		8.2 ± 5.3
S. Mexico/ Yucatan	0	3.5 ± 17.2	0.84		0.9 ± 4.3
North Central East	256,000	0. ± 34.7	1.00		0. ± 4.2
MO/IL/AR - LA/MS	2,100,000	8.3 ± 5.1	0.11		10.9 ± 6.8
East Central	**3,326,000**	**27.4 ± 15.3**	**0.08**		**9.6 ± 5.3**
FL/GA	1,377,000	0. ± 12.3	1		0. ± 4.
Western U.S.	740,000	0.05 ± 1.28	0.97		0.1 ± 2.6
Central Plains	445,000	0. ± 2.9	1		0. ± 3.7
Aggregated Regions					
Texas	**1,127,000**	**36.4 ± 17.2**	**0.04**		**24.4 ± 8.**
Mexico	**2,680,000**	**110.3 ± 59.7**	**0.067**		**55. ± 14.1**
Eastern U.S	7,060,000	35.7 ± 40.2	0.38		20.5 ± 10.4
Western U.S./Central Plains	1,200,000	0.1 ± 3.2	0.99		0.1 ± 4.5

Performance Statistics

Observed Sulfate Avg (µg/m3)	2.49
Predicted Sulfate Avg (µg/m3)	2.34
Bias (%):	-6.2
RMS error (%):	59
r^2	0.36
# Data Values	118

Table 8-21. The FMBR regression results using the EDAS/FNL 10-day plumes. The bolded rows have p values less than or equal to 0.1 derived from a two sized t test. The FMBR used the EDAS/FNL-derived 10-day plumes.

Source Region	SO_2 Emission	Src/Sink ± Error	P Value	VIF	Attribution ± Error
	[1000 Tons SO2/yr]				%
Southeast Texas	**537,000**	**11.4 ± 6.9**	**0.1**		**17.5 ± 10.6**
Northeast Texas	476,000	11.7 ± 7.9	0.14		6.6 ± 4.4
West Texas	114,000	0. ± 3.2	1		0. ± 3.8
Carbón I & II	**152,000 - 241,000**	**26.2 ± 8.5**	**0.003**		**20.4 ± 6.6**
Monterrey Region, MX	**114,000**	**7.1 ± 2.8**	**0.01**		**18.9 ± 7.5**
Baja California	64,000	0. ± 31.7	1.00		0. ± 3.7
Northwest Mexico	140,000	0.5 ± 4.8	2		0.5 ± 5.1
Central MX	44,000	0. ± 7.	1		0. ± 4.
SW Coast of MX	6,000	0. ± 28.6	1		0. ± 1.1
Mexico City & Volcano	**2,160,000**	**29.2 ± 16.3**	**0.08**		**7.1 ± 3.9**
S. Mexico/ Yucatan	0	29.9 ± 26.7	0.26		4.7 ± 4.2
North Central East	256,000	0. ± 42.7	1.00		0. ± 5.6
MO/IL/AR - LA/MS	2,100,000	6.2 ± 4.1	0.14		10.7 ± 7.2
East Central	**3,326,000**	**36.7 ± 15.**	**0.02**		**9.4 ± 3.8**
FL/GA	1,377,000	17.6 ± 14.6	0.23		4.2 ± 3.5
Western U.S.	740,000	0. ± 1.4	1.00		0. ± 4.8
Central Plains	445,000	0. ± 3.9	1		0. ± 7.
Aggregated Regions					
Texas	**1,127,000**	**23.1 ± 10.9**	**0.04**		**24.1 ± 12.1**
Mexico	**2,680,000**	**93. ± 54.5**	**0.09**		**51.6 ± 14.**
Eastern U.S.	7,060,000	60.5 ± 47.7	0.21		24.3 ± 10.4
Western U.S./Central Plains	1,200,000	0. ± 4.1	1.00		0. ± 8.5

Performance Statistics

Observed Sulfate Avg (µg/m3)	2.49
Predicted Sulfate Avg (µg/m3)	2.04
Bias (%):	-18.1
RMS error (%):	64
r^2	0.37
# Data Values	118

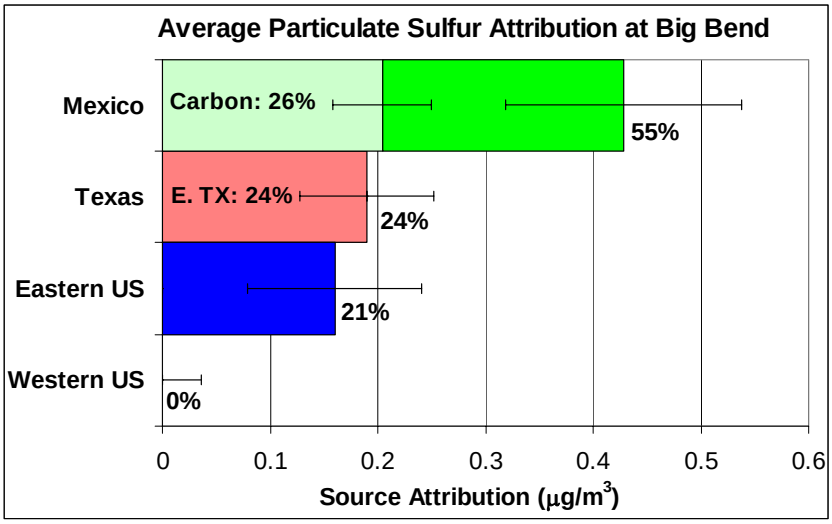

Figure 8-69. The average source attributions and standard errors to Big Bend's sulfate for the entire BRAVO time period (7/6–10/28/1999). The bolded labels are the relative contributions, i.e. the ratios of average absolute values. The FMBR used the MM5-derived 10-day plumes.

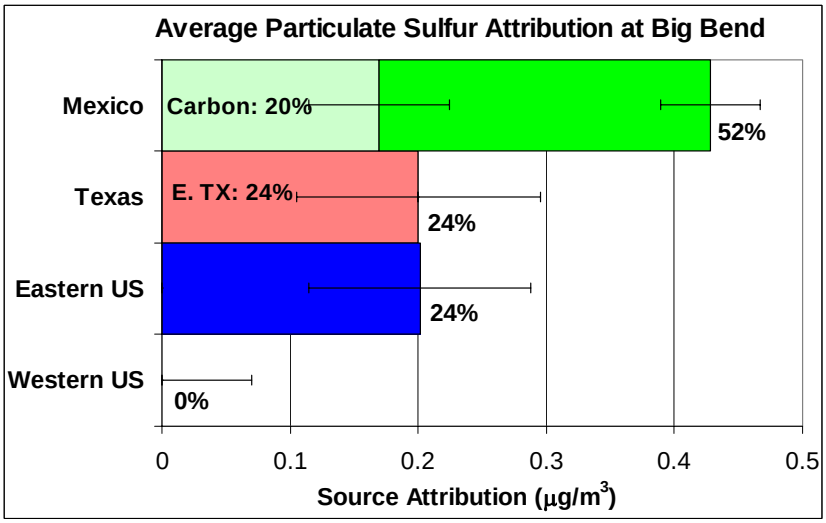

Figure 8-70. The average source attribution and standard errors to Big Bend's sulfate for the entire BRAVO time period (7/6–10/28/1999). The bolded labels are the relative contributions, i.e. the ratios of average absolute values. The FMBR used the EDAS/FNL-derived 10-day plumes.

As shown in Table 8-20, when using the MM5 wind fields, only four (southeast Texas, Carbón, Monterrey, Mexico, and the central eastern U.S.) of the 17 source regions were considered significant at p values of 0.1 or less. The two source regions encompassing MO/IL/AR - LA/MS and Mexico City and the Popocatepetl Volcano had p values less than 0.15. Note, each two letters in the MO/IL/AR - LA/MS source region represent a state in the eastern U.S. These 6 source areas accounted for nearly all of the sulfur contributions. As shown in Figure 8-69, Mexico was the largest average contributor to Big Bend's sulfur over the BRAVO period at about 55%. The Carbón and Monterrey Mexican subregions accounted for 26 and 18% of Big Bends sulfur, respectively. Texas accounted for about 24% of Big Bend's sulfur with all

of this coming from eastern Texas. The eastern U.S. accounted for the remaining 21%. The western U.S. had a predicted contribution of 0 with a standard error of 4.5%.

The source attribution using the EDAS/FNL wind fields produced similar results with Mexico accounting for 52% and Texas and the eastern U.S. each accounting for 24% of Big Bend's sulfur. The primary differences between the EDAS/FNL and MM5 results is that the EDAS winds had a smaller Carbón impact of 20.4 ± 6.6% compared to 26.2 ± 5.9% using the MM5 winds. In addition, the northeast Texas contribution was 6.6 ± 4.4% using the EDAS/FNL compared to 0. ± 4.3% when using the MM5 winds. These results are consistent with the fact that Big Bend back trajectories generated from the EDAS/FNL wind fields had greater transport from northeast Texas compared to those generated using the MM5 wind field (see chapter 4 and section 8.1.3).

8.2.3.2 Discussion

As discussed and demonstrated in chapter 7, the FMBR technique tends to overestimate the source contributions from nearby source regions and underestimate the contributions from more distant source regions. There are several explanations for this bias. First, common transport pathways between source regions result in collinearities in transport from neighboring source regions. For example, airmasses that traversed the eastern U.S. usually traversed Texas and northern Mexico en route to Big Bend (see section 8.1.3). Transport from more distant source regions usually occurs less frequently and the airmasses are more dispersed, decreasing their signal or impact on the receptor. If this signal is smaller than the error in the system, i.e. errors in the observations and transport, then the regression analysis cannot resolve the source's impact even though the source's actual contribution may be significant. This source attribution is then attributed to the collinear source region whose contribution is resolvable. A second potential cause is that the error in airmass transport tends to increase with transport time and distance. Therefore more distant source regions will have a larger transport error than nearby source regions. *White and Macias* [1987] showed that regression analyses are biased towards variables with less error.

In section 7.2.2, the FMBR technique was applied to a synthesis data set, generated by the REMSAD air quality model, where the sulfate concentrations and source contribution to Big Bend were known. This allowed the quantification of the FMBR biases on the synthesis data set. Presumably, similar biases exist in the application of the FMBR to the observed sulfate data, and the scaling of the FMBR results by these biases is a better estimate of the source attribution. These scaling factors were derived using the MM5 transport and are thus most appropriately applied to the FMBR-MM5 results.

The bias scaling factors and the scaled FMBR/MM5 source attribution of Big Bend's sulfate are presented in Table 8-22. As shown, both the Mexican and Texan source attributions decreased with Mexico decreasing from 55% to 43% and Texas from 24% to 17%. The contribution from the Carbón region also decreased to 22% for MM5. The eastern U.S. contribution increased, now accounting for 24% of Big Bend's predicted sulfate. The non-attributed contributions are the difference between the Mexican, eastern U.S., and Texan contributions from the total and can be thought of as the contributions from the western U.S. and the boundary conditions. This unaccounted contribution is 16% which is about equal to the contribution of the western U.S. and boundary conditions used to create the scaling coefficients. While the bias scaling factors were derived using the MM5 transport, similar biases should exist

in the FMBR using EDAS/FNL transport. Table 8-22 also presents the scaled FMBR-EDAS/FNL results which are similar to the scaled FMBR-MM5 results.

Table 8-22. The FMBR source attribution results for Big Bend scaled to account for biases that were estimated in section 7.2.2 (see Table 7-6).

		% Contribution ± Standard Error			
		Original Source Attribution		Scaled Source Attribution	
Source Regions	**Scaling Factors**	**MM5**	**EDAS/FNL**	**MM5**	**EDAS/FNL**
Carbón	0.84	26.2 ± 5.9	20.4 ± 6.6	22	17
Rest of Mexico	0.72	28.8 ± 13	31.2 ± 12	21	23
NE Texas	0.51	0. ± 4.3	6.6 ± 4.4	0	3.4
SE Texas	0.69	24.4 ± 6.2	17.5 ± 10.6	17	12
Rest of Texas	0.52	0. ± 2.7	0. ± 3.8	0	0
LA/MS & MO/IL/AR	0.8	10.9 ± 6.8	10.7 ± 7.2	8.7	8.5
E Central	1.54	9.6 ± 5.3	9.4 ± 3.8	15	15
Rest of E U.S.	1.5	0 ± 5.8	4.2 ± 6.6	0	6.3
[1]*Western U.S.*		0.1 ± 4.5	0. ± 8.5	0.1	**0**
[1]*GOCART BC*					
Mexico (all)		55. ± 14.1	51.6 ± 14.	43	40
Texas (all)		24.4 ± 8.	24.1 ± 12.1	17	15
Eastern U.S. (all)		20.5 ± 10.4	24.3 ± 10.4	24	29
[2]Non Attributed Contribution				17	16

1. The scaling factors were derived using a western U.S. contribution of 9% and boundary condition contribution of 7%.
2. The non attributed contribution is due to the scaling of the source contributions and is assumed to be due to a western U.S. contribution of 9% and boundary condition contribution of 7%.

Neither the MM5 nor the EDAS/FNL wind fields were shown to be superior at generating the forward transport for the FMBR technique in any objective analysis. Therefore it is not known which result, if either, is closer to the true source attribution. Since REMSAD was run with the MM5 wind fields, it could be expected that the FMBR-MM5 results would be more similar to REMSAD. This comparison is presented in chapter 9 which contrasts, compares, and reconciles all of the differences between the air quality and receptor modeling approaches. In this chapter it is shown that the FMBR-EDAS/FNL results are actually more similar to the REMSAD results. As shown in Table 8-22, the largest differences are that the FMBR-MM5 estimated larger source contributions from Carbón and southeast Texas, while the FMBR-EDAS/FNL estimated large contributions from northeast Texas and the rest of the eastern U.S. The transport from these source regions is collinear and the technique must properly divide the mass between these source regions. Collinearity inflates the standard errors and it is seen that the different source attributions using the two wind fields are within 1 to 1.5 standard errors. Thus, the techniques may have misappropriated mass between these source regions. The differences are not significant at even the 0.1 level. Also, the FMBR-MM5 source attributions

are larger for the closer source regions, e.g., Carbón and southeast Texas. As discussed, the FMBR most likely has positive biases for nearby sources. These biases appear larger for the FMBR-MM5 than the FMBR-EDAS/FNL results.

9) Reconciliation of Source Apportionment Results and Conclusions

The primary goal of BRAVO was to determine the contribution of major source regions in the United States and Mexico to Big Bend's haze. In support of this goal, the NPS/CIRA group conducted a number of sulfate source apportionment analyses. The analyses focused on sulfates because they were the largest contributor to haze, accounting for 55% of the haze on average. In addition, most sulfates are from anthropogenic industrial sources and have well-understood atmospheric processes that can be simulated in available air quality models.

The source apportionment techniques included source-oriented modeling using the Regional Modeling System for Aerosols and Deposition (REMSAD) air quality model, receptor-oriented modeling merging airmass transport and receptor data, and a hybrid technique which merged source attribution results from the source-oriented models with the receptor data. *EPRI* [2004] also used the source-oriented Community Multiscale Air Quality (CMAQ) model to estimate source attribution to Big Bend's sulfate. The receptor techniques used several wind fields and airmass transport models. All receptor techniques were validated by testing them against the BRAVO perfluorocarbon tracer data and synthetic (modeled) Big Bend sulfate concentrations and source attributions. The source attribution techniques that passed the various validation tests are summarized in Table 9-1.

This section examines and reconciles the differences between the source attribution approaches and derives a reconciled set of results. These results are then used to provide the best estimate for the sulfate source apportionment during the BRAVO period, the Big Bend high sulfate episodes, and for the days with the lowest sulfate concentrations. In addition, the contribution of the sulfur source regions to Big Bend's haze is estimated.

9.1 Average Source Attribution Results

The average source attribution for the source- and receptor-oriented techniques to Big Bend's sulfate during the BRAVO period are presented in Table 9-2. The source areas include Mexico, Texas, the eastern and western U.S., and the Carbón facilities in Mexico. This table also provides the average, range, and standard deviation across all techniques for each source region. Overall, the different techniques for Mexico, Carbón, and the western U.S. are in good agreement with a standard deviation of 5%. The eastern U.S. and Mexico standard deviations are larger at 11 and 12%, respectively. The REMSAD source attributions differed the most compared to the other techniques. The REMSAD Carbón and Mexico contributions were significantly lower, while the contribution from the eastern U.S. was significantly larger than with the other techniques. Significant is defined as more than one standard deviation from the mean. The TrMB-EDAS method also had significant differences with a larger Texas contribution and smaller eastern U.S. contribution than the mean. However, these two source regions also had large uncertainties and the confidence intervals encompass the mean estimates.

Differences are also evident between the source and receptor methods. The source-oriented models had smaller Mexican and Texas contributions and larger eastern U.S. contributions than the receptor techniques. For example, the source-oriented models attributed ~28% of Big Bend's sulfate to Mexican sources while the receptor models attributed ~50%. For the eastern U.S., the source-oriented models estimated their contribution at ~40% compared to ~20% for the receptor models.

Table 9-1. Summary of the source attribution techniques used in the BRAVO study. Only the receptor techniques that passed all validation studies are shown.

	Model	Model Orientation	Transport Model	Wind Field(s)	Airmass Max. Age	Domain	Boundary Conditions	Reference
1	[1]REMSAD	Source	REMSAD	MM5	Indefinite	U.S. and Mexico	GOCART Global Model	section 6
2	[2]CMAQ	Source	CMAQ	MM5	Indefinite	Texas and surrounding States and N. Mexico	REMSAD sulfate modified by IMPROVE and CASTNet measured SO_4 & SO_2	*EPRI*, 2004
3	[3]FMBR–MM5	Receptor	Monte Carlo Model	MM5	10 days	Most of U.S. and Mexico	None	section 8.2.4
4	[3]FMBR–EDAS	Receptor	Monte Carlo Model	EDAS/FNL	10 days	Most of U.S. and Mexico	None	section 8.2.4
5	[4]TrMB–MM5	Receptor	Monte Carlo Model	MM5	5 days	North America	None	Section 8.2.3
6	[4]TrMB-EDAS	Receptor	HYSPLIT	EDAS/FNL	5 days	North America	None	Section 8.2.3
7	Synthesized REMSAD	Hybrid	REMSAD	MM5	Indefinite	U.S. and Mexico	GOCART Global Model	Section 8.2.2
8	Synthesized CMAQ	Hybrid	CMAQ	MM5	Indefinite	Texas and surrounding states and N. Mexico	REMSAD sulfate modified by IMPROVE and CASTNet measured SO_4 & SO_2	Section 8.2.2

1. REMSAD - Regional Modeling System for Aerosols and Deposition model
2. CMAQ - Community Multiscale Air Quality model
3. FMBR - Forward Mass Balance Regression (FMBR)
4. TrMB - Trajectory Mass Balance

Model Orientation:

Source – Eulerian grid model that simulates source emissions
Receptor – technique that used receptor data with no information on the emission rates
Hybrid – technique that used both receptor data and source emission rates.

Table 9-2. Big Bend's relative sulfate source attribution results by the various air quality and receptor modeling techniques. The relative contributions are the ratio of the average source attributions to the average predicted concentration at Big Bend during the entire BRAVO period. The bolded values are all within one standard deviation of the mean attribution across all techniques.

Source Region	CMAQ[1] (%)	REMSAD (%)	FMBR - MM5 (%)	FMBR - EDAS/FNL (%)	TrMB - MM5 (%)	TrMB - EDAS(%)		Range (%)	Average (%)	Std Dev
Carbón	-	14	**26** ± 6	**20** ± 7	**23 ±** 12	**22** ± 12		14–26	21	5
Mexico	**32**	23	**55** ± 14	**52** ± 14	**45** ± 20	**48** ± 20		23–55	43	12
Texas	**19**	**16**	**24** ± 8	**24** ± 12	**19** ± 13	30 ± 20		16–30	22	5
Eastern U.S.	**39**	42	**20** ± 10	**24** ± 10	**23** ± 9	16 ± 14		16–43	28	11
Western U.S.	**6**	**9**	**0** ± 5	**0.** ± 9	14 ± 15	**6** ± 17		0–14	6	5
Outside of domain	**5**	**7**						5–7	6	1

1. The CMAQ model run to attribute sulfate to Carbón was not conducted due to time constraints .

Detailed analysis of the source and receptor modeling techniques identified potential systematic biases in both types of techniques. It was found that the REMSAD model likely overestimated the eastern U.S. contributions and underestimated the Mexican contributions (see chapter 6). The CMAQ modeling attempted to correct for these biases by adjusting the REMSAD predicted sulfate concentrations used at its boundaries with observed sulfate and sulfur dioxide concentrations. This generally lowered the concentration on the eastern boundary of the CMAQ modeling domain. In Mexico, CMAQ used an upper SO_2 emission rate from Carbón I & II which was about 160% larger than that used by REMSAD. Also, the other Mexican SO_2 emissions in the CMAQ domain were doubled to compensate for the apparent underestimation of Mexico's contribution to sulfate throughout Texas as estimated by REMSAD. The resulting CMAQ source attributions were larger from Mexico and smaller from the eastern U.S. compared to REMSAD. However, comparisons of the predicted to measured sulfate indicated that the eastern U.S. contributions were still overestimated and Mexico's underestimated.

The receptor techniques suffer from collinear transport, which increases the standard errors and biases due to generally more accurate transport from near source regions compared to far source regions. In chapter 7 it was shown that the FMBR analysis generally overestimated the contributions from nearby source regions in Mexico and Texas and underestimated the contributions from the more distant eastern and western U.S. source regions. In addition, the FMBR technique did not account for contributions from outside of the simulated source regions. Sensitivity testing using the REMSAD synthetic sulfate concentrations and source attributions found that the contribution from REMSAD boundary conditions were primarily placed in the Mexican and Texas source areas.

9.2 Reconciled Source Attribution Results – Fusion of Available Information

Several techniques were developed to account for and correct the identifiable biases. For the source-oriented modeling, the synthesis inversion technique was used. In this technique, the modeled source attribution results were regressed against the measured particulate sulfur data at Big Bend. The resulting regression coefficients then accounted for the biases in the original source attribution results. This is a technique similar to FMBR and TrMB, but in addition to the transport information which was incorporated into FMBR and TrMB, the source emission rates, atmospheric chemistry, and removal processes were incorporated into the analysis since these processes were directly incorporated into the REMSAD and CMAQ models.

The biases in the FMBR and TrMB analyses were quantified by applying these techniques to synthetic data derived from the REMSAD model. In this case, the predicted sulfate concentrations at Big Bend from REMSAD were used and the receptor techniques attempted to reproduce the REMSAD source contributions to Big Bend's predicted sulfate. As discussed in section 8.2.3.2, the ratio of the REMSAD attribution to the FMBR or TrMB attribution accounted for the bias. This technique is only applicable to the FMBR and TrMB attributions using the MM5 wind fields because these wind fields were used in the evaluation.

The biases in the Eulerian and receptor models are in opposite direction of each other for the same source regions. Therefore the ranges in the source attribution results in Table 9-2 appear to bound the correct source attribution results. Table 9-3 and Figure 9-1 present the reconciled source attribution results where the original model results are corrected for their respective biases. As shown, the differences between the techniques have narrowed with all

source attribution estimates within 5 percentage points of the mean. Mexico is the largest average contributor to Big Bend's sulfate at about 40%, of which ~22% is attributed to the Carbón facilities. The U.S. is responsible for about 55% of the sulfate, of which the eastern U.S. accounts for 28% and Texas accounts for 17%. The western U.S. and contributions from sources outside of the domain are each responsible for less than 10% of the sulfate.

Table 9-3. Reconciled relative source attributions of Big Bend's sulfate concentrations. The source attribution results by the various air quality and receptor modeling techniques have been adjusted to correct for identifiable biases. The relative contributions are the ratio of the average source attributions to the average predicted concentration at Big Bend during the entire BRAVO period.

Source Region	Synthesized CMAQ (%)	Synthesized REMSAD (%)	Scaled FMBR – MM5 (%)	Scaled TrMB – MM5 (%)		Range (%)	Average (%)
Carbón	-	23 ± 1.8	22	23		22–23	22
Mexico	38 ± 1.7	39 ± 2.3	43	34		34–43	39
Texas	17 ± 1.3	16 ± 1.2	17	16		16–17	17
Eastern U.S.	30 ± 1.2	32 ± 0.5	24	25		24–32	28
Western U.S.	8.5 ± 1	6 ± 1		11		6–11	9
Outside of domain	6.4 ± 1	7 ± 1				6–7	7
*Unaccounted Mass			17	14			

* The unaccounted mass is the difference between the scaled source attribution results and 100%. For the scaled FMBR this is primarily due to contributions from the boundary conditions and the western U.S., and for TrMB this is primarily due to contributions from the boundary conditions.

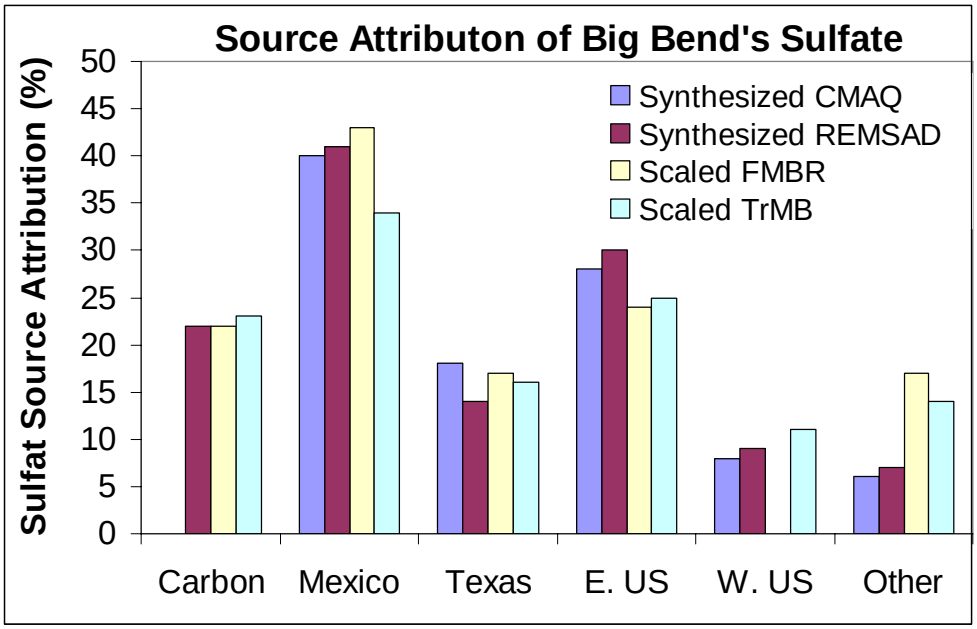

Figure 9-1. The average relative contribution of sulfate from major source regions to Big Bend's sulfate during the BRAVO study using various methods. The relative contributions are the ratio of the average source attribution to the average predicted Big Bend sulfate.

The close agreement between the reconciled values is encouraging. However, the four reconciled source attribution estimates are not independent attributions, and their close agreement does not insure that they are correct. All four techniques incorporated the measured particulate sulfate data at Big Bend into the analyses, and they all used the same MM5 wind fields in calculating airmass transport from the source to the receptor. The CMAQ and REMSAD simulations are closely linked since CMAQ used the REMSAD predicted sulfur concentrations at its boundary. Last, the scaling factors for the receptor modeling technique were derived using the REMSAD modeling results. Therefore these final values should be viewed as the result of the fusion of the best available information from all techniques applied in this study.

The only truly independent analysis was the TAGIT analysis conducted by *Green et al.* [2003]. In this analysis they used SO_2 concentrations measured in and around Big Bend as a tracer for the plume from the Carbón facilities. They estimated that Carbón was responsible for about 15% of Big Bend's sulfate during the BRAVO study. This is about 30% smaller than the reconciled values.

9.2.1 Daily Attribution of Big Bend's Sulfate Concentrations

The synthesized CMAQ and REMSAD results are applicable to shorter time periods, but the receptor techniques are not. On average, the two synthesis inversion results are nearly identical. However, there were some differences on a higher time resolution, particularly during the Big Bend sulfur episodes (see section 8.2.2). While neither result is truly correct, the synthesized CMAQ source attribution results are likely more trustworthy for the same source regions. The original CMAQ runs attempted to reduce known biases that occurred in REMSAD, and CMAQ compared better to the measured data. In addition, the synthesized CMAQ had smaller bias correction factors indicating the initial model results were less biased than REMSAD.

The following presents the source attributions results for everyday, and high and low sulfur days, using the synthesized CMAQ results. CMAQ did not apportion the contributions from Carbón. To estimate the Carbón contribution, the synthesized REMSAD results were used to calculate the ratio of Carbón's to Mexico's contribution and this ratio was applied to the synthesized CMAQ results.

The absolute and relative contributions on a daily basis are presented in Figure 9-2 smoothed by a three-day moving average. Each source region's contribution has unique trends over the four-month period. Mexico's contributions dominate the predicted sulfate concentrations in July and August, contributing from 0.5 to 1.5 $\mu g/m^3$ of sulfate every day and occasionally exceeding 2 $\mu g/m^3$. In September and October, the contribution from Mexico to Big Bend's sulfate decreased typically less than 1 $\mu g/m^3$ per day. The Texas sources contribute little in July and have their largest contribution in October. The Texas source contributions are episodic with their largest absolute contributions (> 1 $\mu g/m^3$) during the highest sulfate days. The eastern U.S. contributions also tend to occur during Big Bend sulfate episodes and exceeded 4 $\mu g/m^3$ during the September 1 episode. The coincidence of the Texas and Mexican contributions to Big Bend are corroborated by the airmass history analyses which showed that airmass transport from the eastern U.S. to Big Bend typically passed through Texas.

Mexico is the largest contributor to Big Bend's sulfate during the days with the lowest sulfate concentrations. This is particularly so from July–September where Mexico was often

responsible for more than 80% of Big Bend's sulfate concentrations when the overall concentrations were below 2 µg/m^3. In October, the western U.S. and boundary conditions were also large contributors to the lowest sulfur days, together accounting for 60–80% of the sulfur from October 19–24.

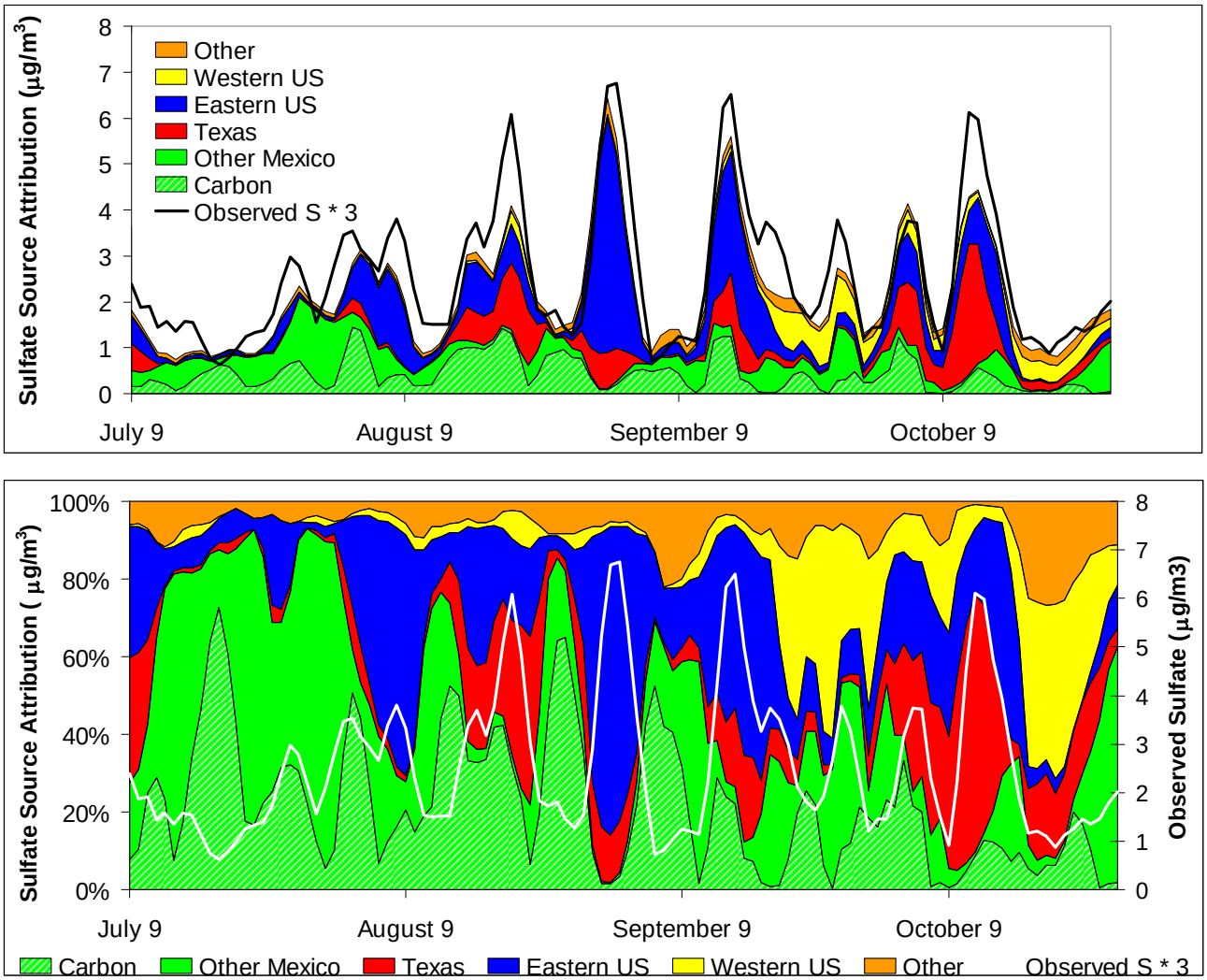

Figure 9-2. Synthesized CMAQ daily absolute and relative source attributions to the predicted sulfate at Big Bend. The daily source attributions were smoothed using a three-day moving average. The Carbón attributions are derived from synthesized REMSAD.

Figure 9-3 presents the Big Bend sulfate attribution for days with observed sulfate concentrations above the 80th percentile (high sulfate days) and below the 20th percentile (low sulfate days) during BRAVO. As shown, when Big Bend's sulfate concentrations were high, the United States was responsible for almost 70% of the sulfate, 43% from the eastern U.S. and 25% from Texas. Mexico was responsible for about 23% of the sulfate with the Carbón facilities accounting for 16%. However, on the low sulfur days, the United States' contribution decreased to about 40% with Texas and the western and eastern U.S. each contributing 11–15%. Mexico's contribution increased to about 48% with Carbón contributing 24%.

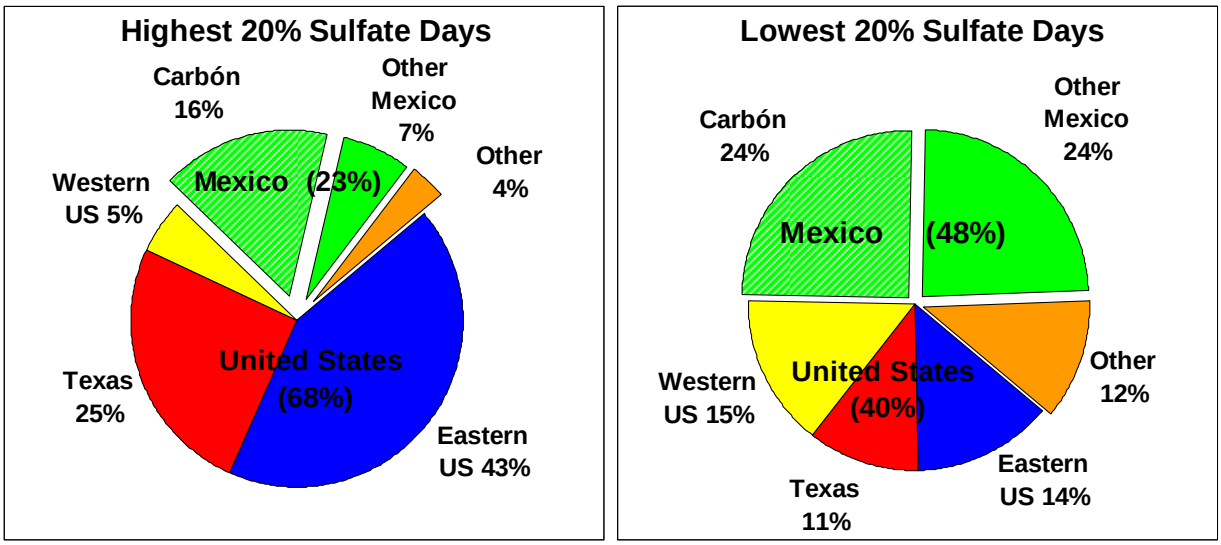

Figure 9-3. Big Bend's average sulfate attribution for days with the highest and lowest 20% measured sulfate concentration during BRAVO.

A detailed look at seven multi-day sulfate episodes (Figure 9-4) showed that Mexico, the eastern U.S., and Texas all contributed 30% or more of the predicted sulfate concentrations in two or more episodes. Also, usually more than one of the major source regions had significant contributions to the sulfate, the exception being for the September 1 episode, in which the eastern U.S. accounted for more than 70% of the sulfate.

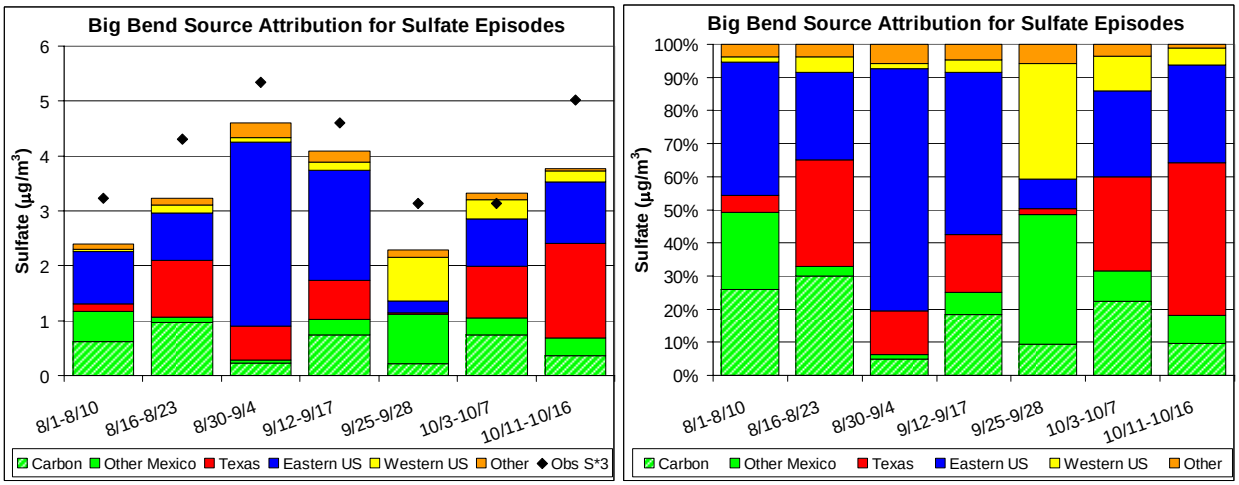

Figure 9-4. The synthesized CMAQ average source attribution to Big Bend's sulfate for each Big Bend sulfate episode. The Carbón contribution was derived from the synthesized REMSAD results.

The source attributions for six multi-day low sulfate periods are presented in Figure 9-5. In July and August the Mexican sources are responsible for more than 70% of the sulfate. This contribution decreases in September and October when contributions from the western U.S. and "other", i.e., the modeling boundary conditions, increase. During the October 17–24 period the western U.S. was responsible for about 40% of the sulfate and the boundary conditions about 25%. Sources in the eastern U.S. and Texas generally were responsible for less than 20% of the sulfate at Big Bend during these low sulfate periods.

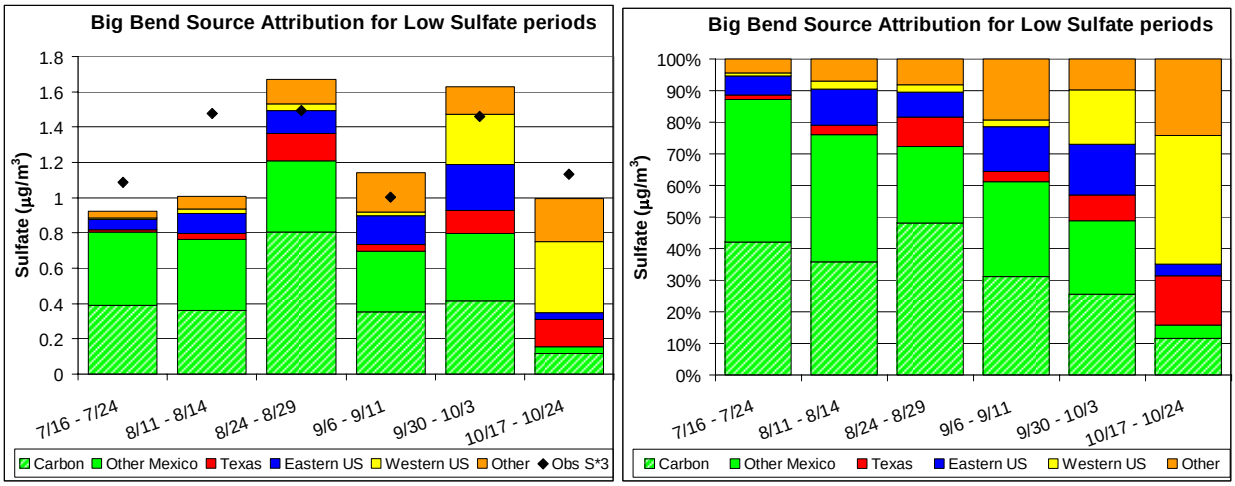

Figure 9-5. The synthesized CMAQ average source attribution to Big Bend's sulfate for each low sulfate periods at Big Bend. The Carbón contribution was derived from the synthesized REMSAD results.

9.2.2 The Relative Errors in the BRAVO Source Attribution Estimates

The synthesis inversion technique used to generate the final BRAVO source attribution results estimates a standard error for each three-day average source attribution. In order to perform the synthesis inversion, an estimated error, the prior error in the original CMAQ source attribution results of 100%, and an error of 200% for REMSAD were used. A higher prior error was chosen to prevent erroneously constraining the synthesis inversion technique. However, the resulting standard errors are sensitive to the chosen CMAQ and REMSAD prior errors and larger prior errors result in larger standard errors.

Each set of daily source attribution scaling coefficients resulting from the synthesis inversion was derived using data from multiple receptor sites for three consecutive days and then applied to the daily Big Bend source attribution results. If the assumption of linearity and independence in the regression analysis are met, then the scaling coefficients and standard errors are reasonable estimates for Big Bend. The source attribution biases were shown to be approximately constant over the monitoring sites used in the analysis, so the linear assumption should be valid for most days. There are known collinearities in the system, for example, transport from the eastern U.S. to Big Bend usually traverses Texas, but collinearities are reflected in the inversion procedure though increased standard errors. Therefore the standard errors resulting from the synthesis inversion are believed to be applicable to Big Bend's source attribution results.

The average daily relative standard error and the error in the average source attribution estimates during BRAVO are presented in Table 9.4. Note that these errors are relative to each source's average contribution to Big Bend's predicted sulfate. Previously, the errors were reported relative to the total predicted sulfate concentration, so these errors are larger. As shown, the standard errors in Big Bend's daily sulfate source attribution estimates are on average between 50 and 70% for the U.S. and Mexican source regions. The errors decrease with increased averaging. The sulfate episodes and low period lasted for 4 to 9 days and over these time periods the average errors would decrease about 2 to 3 times resulting in errors typically less than 25%. The averaging over the BRAVO period decreased the errors further resulting in errors from 4 to 10% (Table 9-4).

Table 9-4. The average of the three-day average relative standard errors and their standard deviation for the BRAVO estimated source contributions of Big Bend's sulfate and the error of the four-month average source contributions. In the aggregation of the errors, values were used only if the source contributed 5% or more to Big Bend's estimated sulfate concentration.

	Relative BRAVO Source Attribution Errors			
Source Region	**Average Daily Error ± Standard Deviation**	**Average BRAVO Day**	**Worst 20% haze days**	**Best 20% Haze Days**
Carbon	67% ± 29%	7%	12%	12%
Mexico	49% ± 33%	5%	9%	22%
Eastern US	53% ± 40%	4%	6%	21%
Texas	68% ± 39%	7%	7%	26%
Western US	69% ± 20%	9%	16%	27%
Outside of Domain	85% ± 15%	10%	14%	23%

9.3 The Sulfate Contribution to Haze from each Source Region.

The direct attribution of haze to its sources was not conducted in this study. However, the sulfate source attribution results can be related to haze by scaling the sulfate portion of the Big Bend haze budget (see chapter 3) by the relative sulfate source attribution results. Figure 9-6 presents the daily absolute and percent fractional contribution by sulfur source regions to Big Bend particulate haze. Particulate haze refers to the non-Rayleigh portion of the light extinction that is the result of both man-made and naturally occurring particles in the atmosphere. Rayleigh scattering, light scattered by particle-free air, was not included in these figures, since Rayleigh scattering is a natural and fixed consequence of the earth's atmosphere.

Sources in Mexico generally contribute a moderate amount of 5 Mm^{-1} to 15 Mm^{-1} of the light extinction on most days during the study period. However, during some of the smaller haze episodes in July and August their relative contributions are 30% to 40% of the average light extinction. Sources in Texas contributed less than 5 Mm^{-1} on most days of the study period, but during one of the periods of higher contribution Texas was responsible for nearly 30 Mm^{-1}, or about 40% of the light extinction on the haziest day in October. Sources in the eastern U.S. also contributed less than 5 Mm^{-1} on most days of the study period, but during the two haziest episodes its sources contributed about 50 Mm^{-1} and about 30 Mm^{-1}, respectively, corresponding to about 50% and 30% of the total light extinction.

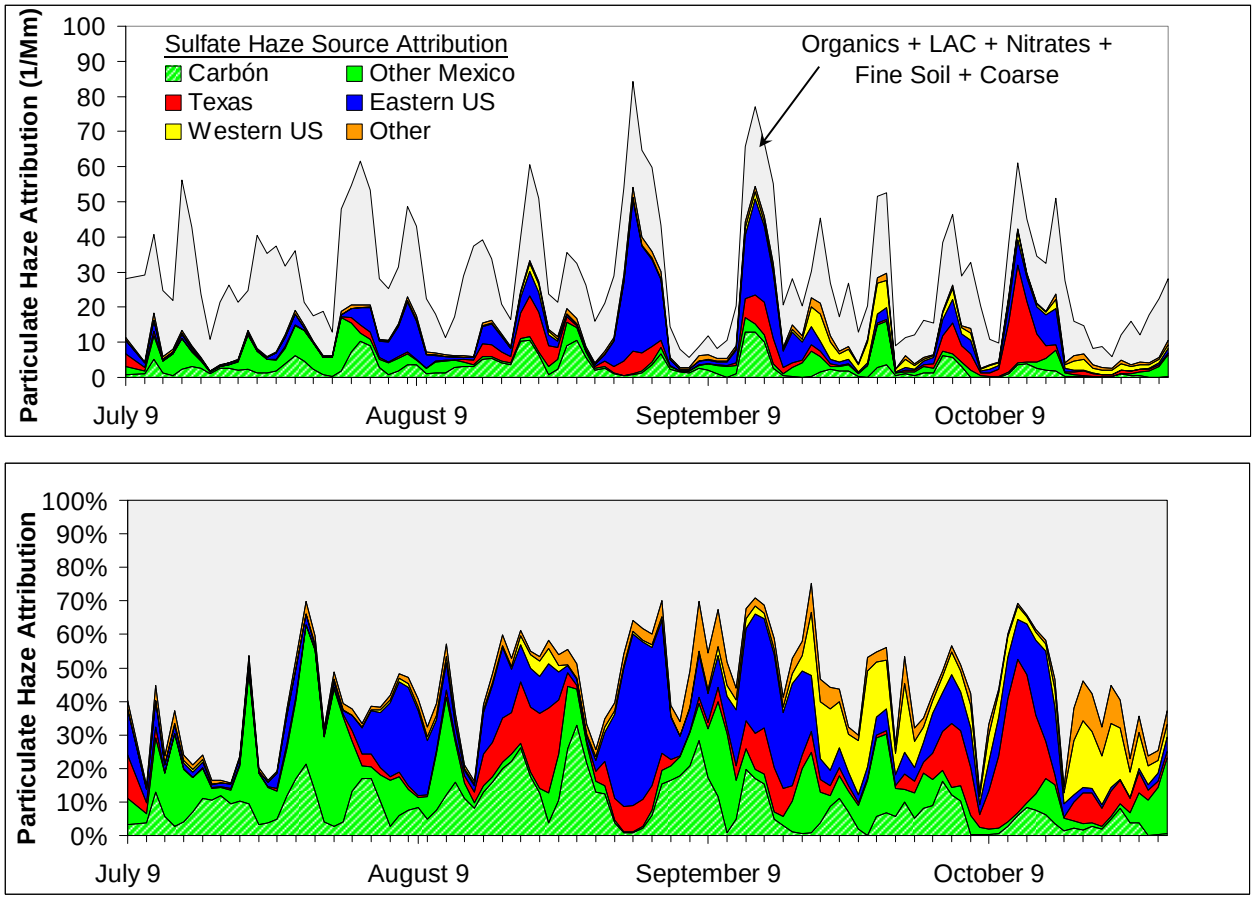

Figure 9-6. Estimated contributions to particulate haze by various particulate sulfate source regions. The top plot shows the absolute haze contributions by the various particulate sulfate sources as well as the total particulate haze level (black line). The bottom plot shows the fractional contribution to haze by the various sources.

Figure 9-7 presents pie diagrams illustrating the differences in particulate sulfate contributions by various source regions to particulate haze for the study period's 20% haziest days compared to the study period's 20% least hazy days. The numbers of 20% haziest days for each month of the BRAVO study from July 9th through October are 1, 8, 10, and 4, while the numbers per month for the 20% least hazy days are 3, 1, 10, and 9, respectively.

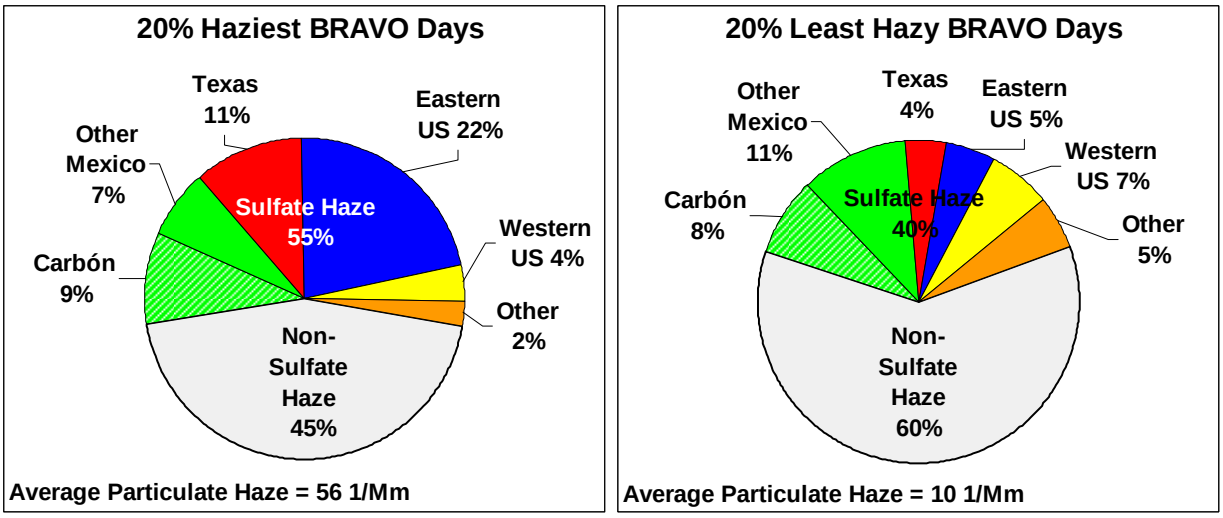

Figure 9-7. Estimated contributions by particulate sulfate source regions to Big Bend particulate haze levels for the 20% haziest days and the 20% least hazy days of the BRAVO study period.

As shown, particulate sulfate contributions to light extinction are higher on the haziest days compared to the least hazy days (55% compared to 40%). The non-sulfate haze is primarily due to dust (fine soil and coarse particles) and carbonaceous (organic and carbon) compounds. Compared to the least hazy days, the haziest days have a higher relative contribution to light extinction by dust (25% compared to 19%) and a lower relative contribution by carbonaceous particles (19% compared to 39%).

The increase in the sulfate contribution on the haziest days compared to the least hazy days is driven by increased relative contributions from the eastern U.S. and Texas. The relative contribution of sulfate on the haziest days from Texas increased by about a factor of 3 (4% to 11%), and from the eastern U.S. increased by about a factor of 4 (5% to 22%) compared to the least hazy days. In contrast, the relative contributions for the Carbón I & II power plants remained about the same at 8 to 9% and the contribution of other sources in Mexico decreased from 11% on the least hazy days to 7% on the haziest days. The relative contribution of sulfate sources in the western U.S. to Big Bend's sulfate haze also decreased from 7% on the least hazy days to 4% on the haziest days. These results are consistent with the observation that the Texas and eastern U.S. sources had their largest sulfate contributions during the highest sulfate episodes.

The errors for the haze attribution results in Figure 9-7 are presented in Table 9-4. As shown, for the 20% haziest BRAVO days, the errors are from 6–12% for the Mexican, Texas, and eastern U.S. source regions, but increase to about 15% for the western U.S. and other regions. The relative errors are larger on the 20% least hazy BRAVO days with errors between 22–26% for all source regions except Carbon which has an error of only 12%.

9.4 Application of the Source Attribution Results to other Months and Years

In order to assess the applicability of haze attribution results for the BRAVO study to other years or other times of year, it is necessary to compare the four-month study period with the same months in other years and with other months of the year. Emissions and meteorology are the two most important factors that influence haze levels. Between 1999 and the present the annual emissions responsible for particulate sulfate concentrations in North America have not

appreciably changed (U.S. emissions have decreased about 15%, but less is known about emission trends in Mexico). Seasonal variations in SO_2 emissions and in the SO_2 to particulate sulfate oxidation rate make extrapolations of the BRAVO study results to other months of the year prone to additional uncertainty. One of the most influential meteorological processes affecting the haze at Big Bend is the airflow patterns that determine which potential source regions are upwind of Big Bend. In spite of the uncertainties inherent in such a simple approach, comparisons of the meteorological flow patterns from the residence time analysis (section 8.1.3) were used alone in an attempt to assess the applicability of BRAVO study results to other years and times of year.

Residence time plots convey information about both the frequency of transport over potential source regions and its duration over the regions. In section 8.1.3 it was shown that the residence time transport patterns are driven by the variations in transport frequency over regions as opposed to duration variations. Consequently, a change that doubles the residence time over a source region for a specific month can be thought of as doubling the probability of influence of that source region during that month. In this example the monthly average contribution would likely double because the numbers of impacting periods would about double, but the amount of the peak impact is not expected to change much.

As shown in section 8.1.3.5, during the BRAVO study period airflow to Big Bend was mostly similar to the airflow conditions during the five-year period. However, in September 1999 there was typically less flow over the eastern U.S. than for the five-year average, implying that the BRAVO results may underestimate the average haze contributions by that region's sources. In addition, during October 1999 there was typically more flow over Texas and less flow over Mexico, implying that the average October BRAVO haze contributions may be overestimated for Texas and underestimated for Mexico compared to the five-year average. While the estimated average contributions by these source regions may change, the peak contributions are likely not affected by the atypical frequency of flow.

Comparing the airflow patterns for the BRAVO study period to that of the other months of the year (section 8.1.3.5), it is evident that SO_2 sources in Mexico are likely to contribute less in November through March. This is because airflow across Mexico is less in general and is over lower emission density regions of Mexico to the west of Big Bend. SO_2 sources in Mexico are likely to be contributing to the particulate sulfate portion of the Big Bend haze during the months of April through June comparable to their contributions during the BRAVO study for July and August months. Sources in Texas are likely to contribute little to the particulate sulfate portion of the Big Bend haze for the months from November through June since the airflow is not frequently over the high emissions regions of east Texas, similar to July 1999. Eastern U.S. sources are unlikely to contribute to Big Bend haze during the months from November through March since airflow to Big Bend is rarely over that region during those months. During the months from April to June, the eastern U.S. sources may contribute a modest amount to sulfate haze, comparable to that estimated for July and early August.

9.5 Implications.

There is no simple answer to the question of what sources are responsible for the haze at Big Bend National Park; sources in both the U.S. and Mexico are responsible. Mexican SO_2 emissions contribute to the sulfate haze more frequently, but to generate the haziest events that occur in the late summer and fall, contributions from Texas and the eastern U.S. must occur.

The greatest contributors to haze are the Carbón I & II power plants in northern Mexico. Substantial changes in those facilities' emissions would likely result in small but noticeable changes in haze levels on many days, but it would not make much difference to the worst haze episodes during late summer and early fall. To substantially affect all of the haze episodes during the late summer and fall where U.S. contributions are large at Big Bend will require SO_2 emission changes in both Texas and the eastern U.S. Because of the high frequency of air transported to Big Bend from the southeast along a corridor on both sides of the Rio Grande River, emission changes there have a potential to affect haze levels at Big Bend, especially during June through September when transport from this region is most frequent.

The clearest days at Big Bend also had low sulfate concentrations. The visual scene on a clear day is more sensitive to small changes in haze than a hazy or moderately hazy day, and small changes in sulfate concentrations can lead to perceptible changes in haze. On these clear days, the Carbón I & II power plants and other sources in northeast Mexico were the largest contributors to Big Bend's sulfate. Reduction in emissions from Carbón would likely result in creating more clear days. On the other hand, growth along this border region will likely further reduce the number of clear days.

References

Air Resource Specialists, Inc., Standard Operating Procedure and Technical Instructions for Nephelometer Systems, 4200-2000, 4100-3100, Fort Collins, CO, 1995**.**

Anfossi, D., D. Sacchetti, and S. Trini Castelli, Development and sensitivity analysis of a Lagrangian particle model for long range dispersion, *Environmental Software, 10,* 263-287, 1995.

Ansari, A.S. and S.N. Pandis, An analysis of four models predicting the partitioning of semivolatile inorganic aerosol components, *Aerosol Sci. Tech., 31*, 129-153, 1999.

Ashbaugh, L.L., A statistical trajectory technique for determining air pollution source regions, *J. of the Air Pollution Control Association, 33,* 1096-1098, 1983.

Ashbaugh, L.L., W.C. Malm, and W.Z. Sadeh, A residence time probability analysis of sulfur concentrations at Grand Canyon National Park, *Atmos. Environ., 19,* (8), 1263-1270, 1985.

Barna, M. and B. Lamb, Improving ozone modeling in regions of complex terrain using observational nudging in a prognostic meteorological model, *Atmos. Env*., *34*, 4889-4906, 2000.

Belsley, D.A., E. Kuh, and R.E. Welsch, *Regression Diagnostics – Identifying Influential Data and Sources of Collinearity*, John Wiley & Sons, New York, 92-93, 1980.

Big Bend Natural History Assoc., 1990.

Black, T.L., The new NMC mesoscale Eta model: Description and forecast examples. *Wea. Forecasting, 9***,** 265–278, 1994.

Brandt, J., A. Bastrup-Birk, J.H. Christensen, T. Mikkelsen, S. Thykier-Nielsen, and Z. Zlatev, Testing the importance of accurate meteorological input fields and parameterizations in atmospheric transport modelling using DREAM - Validation against ETEX-1, *Atmos. Environ. 32,* (24), 4167-4186, 1998.

Brown S.G., P. Herckes, L. Ashbaugh, M.P. Hannigan, S.M. Kreidenweis, and J.L. Collett, Characterization of organic aerosol in Big Bend National Park, Texas *Atmos. Environ 36,* (38), 5807-5818, 2002.

Carrico, C.M., M.J. Rood, and J.A. Ogren, Aerosol light scattering properties at Cape Grim, Tasmania, during the first Aerosol Characterization Experiment (ACE 1), *J. Geophys. Res., 103,* (D13), 16,565-16,574, 1998.

Carrico, C.M., M.J. Rood, J.A. Ogren, C. Neusüß, A. Wiedensohler, and J. Heintzenberg, Aerosol optical properties at Sagres, Portugal, during ACE 2, *Tellus, 52B,* 694-716, 2000.

Cattell, R. B., The scree test for the number of factors. *Multivariate Behavioral Research*, *1*, (2), 140-161, 1966.

Chin, M., R.B. Rood, S.J. Lin, J.F. Muller, and A.M. Thompson, Atmospheric sulfur cycle simulated in the global model GOCART: Model description and global properties, *J. Geophys. Res., 105,* (D20), 24671-24687, 2000.

Chow, J.C., J.G. Watson., L.C. Pritchett., W.R. Pierson, C.A. Frazier, and R.G. Purcell, *Atmos. Environ., 27A,* 1185-1201, 1993.

Chow, J.C., J.G. Watson, H. Kuhns, V. Etyemezian, D.H. Lowenthal, D.H. Crow, S.D. Kohl, J.P. Engelbrecht, and M.C. Green, Source profiles for industrial, mobile, and area sources in

the Big Bend Regional Visibility and Observational (BRAVO) study, *Chemosphere, 54*, (2), 185-208, 2004.

Clegg, S.L., K.S. Pitzer, and P. Brimblecombe, Thermodynamics of multicomponent, miscible, ionic solutions. II. Mixtures including unsymmetrical electrolytes, *J. Phys. Chem., 96*, 9470-9479, 1992.

Clegg, S.L., P. Brimblecombe, and A.S. Wexler, A thermodynamic model of the system H+-NH4+-SO42--NO3--H2O at tropospheric temperatures, *J. Phys. Chem., 102A*, 2137-2154, 1998a.

Clegg, S.L., P. Brimblecombe, and A.S. Wexler, A thermodynamic model of the system H+-NH4+-Na+-SO42—NO3—Cl—H2O at 298.15 K., *J. Phys. Chem., 102A*, 2155-2171, 1998b.

Cocker, D.R., N.E. Whitlock, R.C. Flagan, and J.H. Seinfeld, Hygroscopic properties of Pasadena, California, aerosol, *Aerosol Science And Technology, 35*, (2), 637-647, 2001.

Collett, J.L, T. Lee, D.E. Sherman, J.E. Reilly, S.G. Brown, and S.M. Kreidenweis, The composition of aerosol sampled at Big Bend National Park during the 1999 Big Bend Regional Aerosol and Visibility Observational Study (BRAVO), *Proceedings of the A&WMA/AGU International Specialty Conference – Regional Haze and Global Radiation Balance, Aerosol Measurements and Models: Closure, Reconciliation and Evaluation*, Oct. 2-5, Bend, OR, 2001.

Covert, D.S., A.P. Waggoner, R.E. Weiss, N.C. Ahlquist, and R.J. Charlson, Atmospheric aerosols, humidity and visibility, in *Character and Origins of Smog Aerosols*, Wiley, NY, 559-581, 1979.

Day, D.E., W.C. Malm, and S.M. Kreidenweis, Aerosol light scattering measurements as a function of relative humidity, *J. Air & Waste Manage. Assoc., 50*, 710-716, 2000.

Derber J.C., D.F. Parrish, and S.J. Lord, The new global operational analysis system at the National Meteorological Center, *Wea. Forecasting, 6*, 538-547, 1991.

Desiato, F., D. Anfossi, S. Trini Castelli, E. Ferrorero, and G. Tinarelli, The role of wind field, mixing height and horizontal diffusivity investigated through two Lagrangian particle models, *Atmos. Environ., 32***,** 4157-4165**,** 1998.

Dietrich, L. J.V. Molenar, and J.F. Faust, in *Visibility and Fine Particles*; C.V., Mathai, Ed., AWMA: Pittsburgh, PA, 374-383, 1989.

Draxler, R.R. and G.D. Hess, An overview of the HYSPLIT_4 modeling system for trajectories, dispersion, and deposition, *Australian Meteorological Magazine, 47*, 295-308, 1998.

Dudhia, J., Numerical study of convection observed during the winter monsoon experiment using a mesoscale two-dimensional model, *J. Atmos. Sci., 46*, 3077-3107, 1989.

Eldred, R.A., T.A Cahill, M. Pitchford, and W.C. Malm, IMPROVE- A new remote area particulate monitoring system for visibility studies, in *Proceedings of the APCA Annual Meeting, 81*, 1-16, 1988.

Electric Power Research Institute, *Modeling Analysis of the Big Bend Regional Aerosol Visibility Observational (BRAVO) Study*, EPRI:1009283, Palo Alto, CA, 2004.

Enting, I.G., Green's function methods of tracer inversion, in *Inverse Methods in Global Biogeochemical Cycles*, American Geophysical Union, Washington, DC, 19-31, 2000.

Enting, I.G., *Inverse Problems in Atmospheric Constituent Transport*. Cambridge University Press, Cambridge, 2002.

Gebhart, K.A. and W.C. Malm, Source apportionment of particulate sulfate concentrations at three national parks in the eastern United States, in *Transactions of the A&WMA/EPA Specialty Conference – Visibility and Fine Particles*, Estes Park, CO, Oct. 15-19, C.V. Mathai, Ed., 898-913, 1989.

Gebhart, K.A. and W.C. Malm, Source attribution and statistical summary of data measured at Grand Canyon National Park during 1989-1991, in *Proceedings of "Aerosols and Atmospheric Optics*", Snowbird, UT, 1098-1124, 1994.

Gebhart, K.A. and W.C. Malm, Spatial and temporal patterns in particle data measured during the MOHAVE study, *J. Air & Waste Management Association*, *47*, 119-135, 1997.

Gebhart, K.A., R.A. Alhbrandt, W. C. Malm, and H. K. Iyer, Estimating the fractional contribution of secondary aerosols from different source areas on a regional scale, *Preprints of the 81st Annual APCA Meeting, Dallas, TX, June 1988*, Paper No. 88-054.06, available from A&WMA, Pittsburgh, 1988.

Gebhart, K.A., W.C. Malm, and H.K. Iyer, Comparison of two back trajectory techniques for source apportionment, *Preprints of the 86th Annual A&WMA Meeting, Denver, CO*, 1993.

Gebhart, K.A., W.C. Malm, and M. Flores, A preliminary look at source-receptor relationships in the Texas-Mexico border area, *J. Air & Waste Management Association*, *50*, 858-868, 2000.

Gebhart, K.A., S. Kreidenweis, and W.C. Malm, Back-trajectory analyses of fine particulate matter measured at Big Bend National Park in the historical database and the 1996 scoping study, *Science of the Total Environment*, *276*, 185-204, 2001.

Geron, C., A. Guenther, and T. Pierce, An improved model for estimating emissions of volatile organic compounds from forests in the eastern United States, *Atmos. Environ.*, *99*, 12773-12791, 1994.

Gifford, F.A. Horizontal diffusion in the atmosphere: a Lagrangian-dynamical theory, *Atmos. Environ.*, *16*, 505-512, 1982.

Grasso, L., The differentiation between grid spacing resolution and their application to numerical modeling, *American Meteorological Society*, *81*, 579-580, 2000.

Green, P.E. *Mathematical Tools for Applied Multivariate Analysis*, Academic Press, New York, NY, 1976.

Green, M. H. Kuhns, V. Etyemezia, and M. Pitchford, *Big Bend Regional Aerosol and Visibility Observation (BRAVO) Study Plan*, Desert Research Institute, Las Vegas, NV, 1999.

Green, M., H. Kuhns, V. Etyemesian, and M.L. Pitchford, Final Program Plan for the Big Bend Regional Aerosol and Visibility Observational Study (BRAVO), http://vista.cira.colostate.edu/improve/Studies/BRAVO/reports/projectplan/BRAVOStudyPlan.htm, May 23, 2000.

Green, M., H. Kuhns, M. Pitchford, R. Dietz, L. Ashbaugh, and T. Watson, Application of the tracer-aerosol gradient interpretive technique to sulfur attribution for the Big Bend Regional Aerosol and Visibility Observational Study, *.J Air Waste Manage.*, *53*, (5), 586-595, 2003.

Grell, G.A., J. Dudhia, and D.R. Stauffer, *A description of the fifth generation Penn State/NCAR Mesoscale Model (MM5).* NCAR Technical Note (TN-398-STR), NCAR, Boulder, CO, 1994.

Hand, J.L., S.M. Kreidenweis, D. Eli Sherman, J.L. Collett, Jr., S.V. Hering, D.E. Day, and W.C. Malm, Aerosol size distributions and visibility estimates during the Big Bend Regional Aerosol Visibility and Observational Study (BRAVO), *Atmos. Environ., 36,* 5043-5055, 2002.

Hansen, A.D.A., H. Rosen, and T. Novakov, Real-time measurements of the absorption coefficient of aerosol particles, *Applied Optics, 21,* 3060, 1982.

Hansen, A.D.A., H. Rosen, and T. Novakov, The aethalometer - an instrument for the real-time measurement of optical-absorption by aerosol-particles. *Science of the Total Environment 36,* (JUN), 191-196, 1984.

Heffter, J.L., Air Resources Laboratory Atmospheric Transport and Diffusion Model (ARL-ATAD), *National Oceanic and Atmospheric Administration,* Technical Memo, ERL-ARL-81, 1980.

Henry, R.C., Y.J. Wang, and K.A. Gebhart, The relationship between empirical orthogonal functions and sources of air pollution, *Atmos. Env., 25A,* 503-509, 1991.

Holtslag, A.A.M., VanMeijgaard, E., and DeRooy,. W.C., A comparison of boundary layer diffusion schemes in unstable conditions over land, *Bound-Lay. Meteorol., 76,* (1-2), 69-95, 1995.

Husar J. and Husar, R., Sulfur in atmosphere, proceedings of International-Symposium held in Dubrouik, Yugoslavia, 7-14 September 1977 – Forward, *Atmos. Environ., 12,* (1-3), 3-5, 1978.

Husar, R.B., J.P. Lodge Jr., and D.J. Moore, Sulfur in the atmosphere, in *Proceedings of the International symposium held in Dubrovnik Yugoslavia, 7-14 September 1977,* Pergamon Press, Oxford, 1978.

Ishikawa, H., Evaluation of the effect of horizontal diffusion on the long-range atmospheric transport simulation with Chernobyl data, *Journal of Applied Meteorology, 34,* 1653-1665, 1995.

Iyer, H.K., W.C. Malm, and R.A. Ahlbrandt, A mass balance method for estimating the fractional contribution from various sources to a receptor site, *Transactions: Visibility Protection: Research and Policy Aspects,* Sep. 1986, Grand Teton National Park, WY, P.S. Bhardwaja, Ed., Air Pollution Control Association (now A&WMA), Pittsburgh, 861-869, 1987

Jackson, D.D., Interpretation of inaccurate, insufficient and inconsistent data, *Geophys. J. R. Astr. Soc., 28,* 97-109, 1972.

Kain, J.S. and J.M Fritsch, A one-dimensional entraining/detraining plume model and its application in convective parameterization, *J. Atmos. Sci., 47,* 2784-2802, 1990.

Kaiser, H.F, The Varimax criterion for analytic rotation in factor analysis, *Psychometrika, 23,* 187-199, 1958.

Kahl, J.D. and P.J. Samson, Uncertainty in trajectory calculations due to low resolution meteorological data, *J. Clim. Appl. Meteorol., 25,* 1816-1831, 1986.

Kanamitsu, M., Description of the NMC Global Data Assimilation and Forecast System, *Wea. Forecasting, 4***,** 335-342, 1989.

Kim, Y.P. J.H. Seinfeld, and P. Saxena, Atmospheric Gas-Aerosol Equilibrium I. Thermodynamic Model, *Aerosol Sci. and Tech., 19*, 157-181, 1993.

Kreyszig, E., *Advanced Engineering Mathematics*, 2nd Ed., J. Wiley & Sons, NY, 1968.

Kuhns, H., M. Green, V. Etyemezian, J. Watson, and M. Pitchford, Big Bend Regional Aerosol and Visibility Observational (BRAVO) Study emissions inventory, in *Proceedings of AWMA.: Regional Haze and Global Radiation Balance-Aerosol Measurements and Models*, October 2-5, Bend, Oregon, 2001.

Lamb, R.G. and M. Neiburger, An interim version of a generalized urban air pollution model, *Atmos. Environ*, *5*, 239-264, 1971.

Lawson, C.L. and R.J. Hanson, *Solving Least Squares Problems*, Princeton-Hall, Englewood Cliffs, NJ, 1974.

Lee, T. and J.L. Collett Jr., *The Ionic Composition of Aerosol in Big Bend National Park*. Report by Cooperative Institute for Research in the Atmosphere, Colorado State University, Fort Collins, CO, July, ISSN No. 0737-5352-59, 2002.

Lee, T., S.M. Kreidenweis, and J.L. Collett, Jr., Aerosol Ion Characteristics During the Big Bend Regional Aerosol and Visibility Observational Study, *J. Air & Waste Management Assoc., 54*, 585-592., 2004.

Malm, W.C. Characteristics and origins of haze in the continental United States, *Earth Science Reviews, 33*, 1-36, 1992.

Malm, W.C. and D.E. Day, Optical properties of aerosols at Grand Canyon National Park, *Atmos. Environ., 34*, 3373-3391, 2000.

Malm, W.C. and D.E. Day, Estimates of aerosol species scattering characteristics as a function of relative humidity, *Atmos. Environ., 35*, 2845-2860, 2001.

Malm, W.C. and K.A. Gebhart, Source apportionment of organic & light absorbing carbon using receptor modeling techinques, *Atmos. Environ., 30*, 843-855, 1996.

Malm, W.C. and K.A. Gebhart, Source apportionment of sulfur and light extinction using receptor modeling techniques, *J. Air & Waste Management Association, 47*, 250-268, 1997.

Malm, W.C. and S.M. Kreidenweis, The effects of models of aerosol hygroscopicity on the apportionment of extinction, *Atmos. Environ., 31*, 1965-1976, 1997.

Malm, W.C., H.K. Iyer, J. Watson, and D.A. Latimer, Survey of a variety of receptor modeling techniques, in *Transactions of the A&WMA/EPA Specialty Conference-Visibility & Fine Particles*, C.V. Mathai, Ed, Estes Park, CO, Oct. 15-19, 781-805, 1989.

Malm, W.C., K.A. Gebhart, and R.C. Henry, An investigation of the dominant source regions of fine sulfur in the western us and their areas of influence, *Atmos. Env., 24A*, 3047-3060, 1990.

Malm, W.C., J.F. Sisler, D. Huffman, R.A. Eldred, and T.A. Cahill, Spatial and seasonal trends in particle concentration and optical extinction in the United States, *J. Geophys. Res., 99*, 1347-1370, 1994.

Malm, W.C., D.E. Day, and S.M. Kreidenweis, Light scattering characteristics of aerosols as a function of relative humidity: Part I - A comparison of measured scattering and aerosol

concentrations using the theoretical models, *J. Air & Waste Manage., 50*, 686-700, 2000a.

Malm, W.C., M.L. Pitchford, M. Scruggs, J.F. Sisler, R. Ames, S. Copeland, K.A. Gebhart, and D.E. Day, *Spatial and Seasonal Patterns and Temporal Variability of Haze and its Constituents in the United States: Report III*, Cooperative Institute for Research in the Atmosphere, ISSN:0737-5352-47, 2000b.

Malm, W.C., R.B. Ames, L.L. Ashbaugh, R.A. Eldred, and M.L. Pitchford, A ten-year spatial and temporal trend of sulfate across the United States, *Proceedings of Air & Waste Management Conference:Regional Haze and Global Radiation Balance-Aerosol Measurements and Models: Closure, Reconciliation, and Evaluation*, Oct. 2-5, Bend, OR, 2001a.

Malm, W.C., D.E. Day, T. Lee, S.M. Kreidenweis, and J.L. Collett, Physical, chemical, and optical properties of fine and coarse particles in West Texas (Big Bend National Park), *Proceedings of the A&WMA/AGU International Specialty Conference – Regional Haze and Global Radiation Balance, Aerosol Measurements and Models: Closure, Reconciliation and Evaluation*, Oct. 2-5, Bend, OR, 2001b.

Malm, W.C., B.A. Schichtel, R.B. Ames, and K.A. Gebhart, A ten-year spatial and temporal trend of sulfate across the United States, *JGR-Atmospheres*, *107*, (22), 2002.

Malm, W.C., D.E. Day, S.M. Kreidenweis, J.L. Collett, and T. Lee, Humidity dependent optical properties of fine particles during the Big Bend Regional Aerosol and Visibility Observational Study (BRAVO), *JGR-Atmospheres*, *108*, (D9), art. 4279, 2003.

MCNC Environmental Modeling Center, Sparse Matrix Operator Kernel Emissions modeling system, http://www.emc.mcnc.org/products/smoke, 2002.

Molenar, J.V., Analysis of the real world performance of the Optec NGN-2 ambient nephelometers, in *Visual Air Quality: Aerosols and Global Radiation Balance*, Air & Waste Manage. Assoc., Pittsburgh, 243-265, 1997.

Molenar, J.V., D.L. Dietrich, and R.M. Tree, Application of a long range transmissometer to measure the ambient atmospheric extinction coefficient in remote pristine environments, in *Visibility and Fine Particles*, C.V., Mathai, Ed., AWMA, Pittsburgh, 374-383, 1989.

Munn, R.E., and B. Bolin, *Atmos. Environ., 5*, 363-402, 1971.

Nenes, A., S.N. Pandis, and C. Pilinis, ISORROPIA: A new thermodynamic equilibrium model for multiphase multicomponent inorganic aerosols, *Aquatic Geochemistry, 4*, 123-152, 1998.

Newsam, G.N and I.G. Enting, Inverse problems in atmospheric constituent studies: I. Determination of surface sources under a diffusive transport approximation. *Inverse Problems, 4*, 1037-1054, 1988.

Olmez, I., A.E Sheffield, G.E. Gordon, J.E. Houck, L.C. Pritchett, J.A. Cooper, T.G. Dzubay, and R.I. Bennett, Composition of particles from selected sources in Philadelphia for receptor modeling applications. *Journal of Air Pollution Control Association*, *38*, 1392-1402, 1988.

Ouimette, J.R., and R.C. Flagan, The extinction coefficient of multicomponent aerosols, *Atmos. Environ., 16*, 2405-2419, 1982.

Parrish, D.F. and J.C. Derber, The National Meteorological Center's spectral statistical interpolation analysis system, *Mon. Wea. Rev., 120***,** 1747-1766, 1992.

Parrish, D., J. Purser, E. Rogers, and Y. Lin, The regional 3D variational analysis for the Eta Model., *11th Conf. On Numerical Weather Prediction,* Norfolk, VA, Amer. Meteor. Soc., 454–455, 1996.

Patterson, D.E., R.B. Husar, W.E. Wilson, and L.F. Smith, *J. Appl. Meteor., 20,* 404-420, 1981.

Perrino, C., F.D. Santis, and A. Febo, Criteria for the choice of a denuder sampling technique devoted to the measurement of atmospheric nitrous and nitric acids, *Atmos. Environ., 24A,* 617-626, 1990.

Perry, K.D., T.A. Cahill, R.A. Eldred, and D.D. Dutcher, Long-range transport of North African dust to the eastern United States, *J. of Geophysical Research, 102,*11225-11238, 1997.

Petersen, R.A. and J.D. Stackpole, Overview of the NMC production suite, *Wea. Forecasting, 4,* 313-322, 1989.

Petterssen, S., *Weather Analysis and Forecasting,* McGraw-Hill Book Company, New York, 221-223, 1940.

Pielke, R.A., *Mesoscale Meteorological Modeling,* Academic Press, 612 pp., 1984.

Pitchford, M. and A. Pitchford, Analysis of regional visibility in the Southwest using principal component and back trajectory techniques, *Atmospheric Environment, 19,* 1301-1316, 1985.

Pitzer K.S. and J.M Simonson, Thermodynamics of multicomponent, miscible, ionic systems: Theory and equations, *J. Phys. Chem., 90,* 3005-3009, 1986.

Poirot, R.L. Personal communication, March 2004.

Poirot, R.L. and P.R. Wishinski, Visibility, sulfate and air mass history associated with the summertime aerosol in northern Vermont, *Atmospheric Environment, 20,* 1457-1469, 1986.

Poirot, R., P. Wishinski, B. Schichtel, P. Girton, Air trajectory pollution climatology for the Lake Champlain basin, *AGU Water Monograph on Lake Champlain Research and Implementation*, T. and P. Manley, Eds., American Geophysical Union, Washington, DC, 1999.

Poirot, R.L., P.R. Wishinski, P.K. Hopke, and A.V. Polissar, Comparative application of multiple receptor methods to identify aerosol sources in northern Vermont, *Environ Sci Tech., 35,* (23), 4622-4636, 2001.

Potukuchi, S. and A.S. Wexler, Identifying solid-aqueous phase transitions in atmospheric aerosol I. Neutral-acidity solutions, *Atmos. Environ., 29,* 1663-1676, 1995a.

Potukuchi, S. and A.S. Wexler, Identifying solid-aqueous phase transitions in atmospheric aerosol II. Acidic solutions, *Atmos. Environ., 29,* 3357-3364, 1995b.

Press, W.H., S.A. Teukolsky, W.T. Vetterling, and B.R. Flannery, *Numerical Recipes in C: the Art of Scientific Computing,* Cambridge University Press, Cambridge, 1988.

READY (Real-time Environmental Applications and Display System), Web address: http://www.arl.noaa.gov/ready/hysplit4.html, NOAA Air Resources Laboratory, Silver Spring, MD, 2003.

Richman, M.B., Rotation of principal components, *Journal of Climatology, 6,* 293-335, 1986.

Rolph, G.D. and R.R. Draxler, Sensitivity of three-dimensional trajectories to the spatial and temporal densities of the wind field, *J. of Appl. Met., 29,* 1043-1054, 1990.

Rood, M.J., M.A. Shaw, T.V. Larson, and D.S. Covert, Ubiquitous nature of ambient metastable aerosol, *Nature, 337,* (6207), 537-539, 1989.

Rotronic Instrument Corp. Humidity-Temperature Meteorological Pro, MP-100F, Fact Sheet, Rotronic Instrument Corp.: Huntington, NY, 1998**.**

SAI, *User's Guide to the Regional Modeling System for Aerosols and Deposition (REMSAD), Version 6,* Systems Applications International, Inc., San Francisco, CA, 2001.

Saltbones J., A. Foss, and J. Bartnicki, Norwegian meteorological institute's real-time dispersion model SNAP (Severe Nuclear Accident Program): runs for ETXE and ATMES II experiments with different meteorological input, *Atmos. Environ., 32,* 4277-4283, 1998.

Saxena P. and L.M. Hildemann, Water-soluble organics in atmospheric particles: A critical review of the literature and application of thermodynamics to identify candidate compounds, *J. Atmos. Chem., 24,* 57-109, 1996.

Schichtel B.A, Retrieval of Emission Fields, *Doctoral Dissertation presented at Washington University,* St. Louis, MO., 1996.

Schichtel B.A. and R.B. Husar, Regional simulation of atmospheric pollutants with the CAPITA Monte Carlo model, *Journal of the Air and Waste Management Association, 47,* 331-343, 1997.

Schwartz, B.E. and M. Govett, A hydrostatically consistent North American radiosonde data base at the Forecast Systems Laboratory, 1946-present, *NOAA Technical Memorandum ERL FSL-4*, NOAA/ERL/FSL 325 Broadway, Boulder, CO 80303, 1992.

Seaman, N.L. and D.R. Stauffer, Final Report to Electric Power Research Institute Contract EP-P3883/C1886 for MM5 Modeling in support of the Big Bend Regional Aerosol and visibility Observation Study (BRAVO), The Pennsylvania State University, Department of Meteorology, 503 Walker Building, University Park, PA 16802, Delivered to Naresh Kumar, Environment Division, Electric Power Research Institute, 3412 Hillview Avenue, Palo Alto, CA 94304-1395, 1 Aug 2003.

Seigneur, C., G. Hidy, I. Tombach, J. Vimont, and P. Amar, *Scientific Peer-Review of the Regulatory Modeling System for Aerosols and Deposition (REMSAD).* The KEVRIC Company, Inc, USEPA Contract No. 68-D-98-092, 1999.

Seinfeld, J. and S. Pandis, *Atmospheric Chemistry and Physics*, Wiley Interscience, New York, 1998.

Sela, J.G., Spectral modeling at the National Meteorological Center, *Mon. Wea. Rev., 108,* 1279-1292, 1980.

Shafran, P.C., N.L. Seaman, and G.A. Gayno, Evaluation of numerical predictions of boundary-layer structure during the Lake Michigan Ozone Study (LMOS), *J. Appl. Meteor., 39,* 412-426, 2000.

Sisler, J.F, D. Huffman, D.A. Latimer, W.C. Malm, and M.L. Pitchford, *Spatial and Temporal Patterns and the Chemical Composition of the Haze in the United States: An Analysis of Data from the IMPROVE Network, 1988-1991,* Cooperative Institute for Research in the Atmosphere (CIRA), Fort Collins, CO, ISSN No. 0737-5352-26, 1993.

Sloane, C.S., Effect of composition on aerosol light scattering efficiencies, *Atmos. Environ.*, *20*, (5), 1025-1037, 1986.

Sorensen, J.H., Sensitivity of the DERMA long-range Gaussian dispersion model to meteorological input and diffusion parameters, *Atmos. Environ.*, *32*, (24), 4195-4206, 1998.

Stauffer, D.R. and N.L. Seaman, On multi-scale four-dimensional data assimilation, *J. Appl. Meteor.*, *33*, 416-434, 1994.

Stohl, A., Computation, accuracy and applications of trajectories – a review and bibliography, *Atmos. Environ.*, *32*, 947-966, 1998.

Stunder, B.J.B., NCEP Model Output -- FNL Archive Data, National Climatic Data Center (NCDC) report TD-6141, 1997.

Trijonis, J.C., W.C. Malm, M. Pitchford, W.H. White, R. Charlson, and R. Husar, Visibility: Existing and historical conditions-causes and effects, *State of Sci. Technol., Rep. 24*, Natl. Acid Precip. Assess. Program, Washington DC, 1990.

Turpin, B. J. and H. J. Lim, Species contributions to PM2.5 mass concentrations: Revisiting common assumptions for estimating organic mass, *Aerosol Sci. Technol.*, *35*, 602-610, 2001.

Uliaz, M., Lagrangian particle dispersion modeling in mesoscale application, *Environmental Modeling*, P. Zannetti, ed, Computation Mechanics Publications, Southampton, U.K., *2*, 71-101, 1994.

U.S. Environmental Protection Agency, *National Air Quality and Emissions Trends Report*, 1999, EPA 454/R-01-004, 2001.

U.S. Environmental Protection Agency, *Guidance for Tracking Progress under the Regional Haze Rule*, EPA-454/B-03-004, Research Triangle Park, NC, September 2003a.

U.S. Environmental Protection Agency, National Emission Inventory, http://www.epa.gov/ttn/chief/trends/, 2003b.

Vasconcelos, L.A., J.D. Kahl, D. Liu, E.S. Macias, and W.H. White, A tracer calibration of back trajectory analysis at the Grand Canyon, *J. Geo. Res.*, *101*, 19329-19335, 1996.

Virkkula A., R. Van Dingenen, F. Raes, and J. Hjorth, Hygroscopic properties of aerosol formed by oxidation of limonene, alpha-pinene, and beta-pinene, *J. Geophys. Res.*, *104*, 3569-3579, 1999.

Vogelezang, D.H.P. and A.A.M. Holtslag, Evaluation and model impacts of alternative boundary-layer height formulations, *Bound-Lay. Meteoro.*,*l 81*, (3-4), 245-269, 1996.

Waggoner, A.P., R.E. Weiss, and T.V. Larson, In situ, rapid response measurement of H2SO4/(NH4)2SO4 aerosols in urban Houston - a comparison with rural Virginia, *Atmos. Environ.*, *17*, 1723-1731, 1983.

Watson, J.G., J.C. Chow, L.W. Richards, D.L. Dietrich, J. Molenar, J. Faust, S.R. Andersen, and C.S. Sloane, *The 1987-88 Metro Denver Brown Cloud Study*, Desert Research Institute: Reno, NV, Document No. 8810 1F2, 1988.

Watson, T.B., R. Johnson, M.L. Pitchford, M. Green, H. Kuhns, and V. Etyemezian, *The Perfluorocarbon Tracer Releases During the Big Bend Regional Aerosol and Visibility Observational (BRAVO) Study*, Desert Research Institute, 755 E. Flamingo Road, Las Vegas, NV 89119, 2000.

Watson, J.G., J.C. Chow, and J.E. Houck, PM2:5 chemical source profiles for vehicle exhaust, vegetative burning, geological material, and coal burning in northwestern Colorado during 1995, *Chemosphere, 43,* (8), 1141–1151, 2001.

White, W. H. and P. T. Roberts, On the nature and origins of visibility-reducing aerosols in the Los Angeles air basin, *Atmos. Environ., 11*, 803-812, 1977.

White, H.W. and E.S. Macias, On measurement error and the empirical relationship of atmospheric extinction to aerosol composition in the non-urban west, in *Transactions: Visibility Protection: Research and Policy Aspects*, P.S. Bhardwaja, Ed., Sep. 1986, Grand Teton National Park, WY, Air Pollution Control Association (now A&WMA), Pittsburgh, 783-794, 1987.

Zapotocny, T. H., S. J. Nieman, W. P. Menzel, J. P. Nelson III, J. A. Jung, E. Rogers, D. F. Parrish, G. J. DIMego, M. B. Timothy, and J. Schmit, A case study of the sensitivity of the Eta data assimilation system, *Wea. Forecasting, 15***,** 603–621, 2000.

Zapotocny, T. H., W. P Menzel, J.P. Nelson III, and J.A. Jung, An impact study of five remotely sensed and five in situ data types in the Eta data assimilation system, *Wea. Forecasting, 17*, 263–285, 2002.

Zhang, D.-L. and R.A. Anthes, A high-resolution model of the planetary boundary layer – sensitivity tests and comparisons with SESAME-79 data. *J. Appl. Meteor., 21*, 1594-1609, 1982.

Appendix 4a. Comparison of MM5, EDAS, and FNL Winds to Radar Wind Profiler Winds

Introduction

MM5, EDAS, and FNL wind fields were used for several source and receptor models applied for the study. REMSAD and CMAQ used MM5 fields. The receptor models used either MM5 or a combination of EDAS (July-September) and FNL (October). For some receptor models, both MM5 and the EDAS/FNL combination were used, with somewhat differing attribution results. It is of interest to evaluate the accuracy of the wind fields used to help reconcile the results.

Methodology

Wind data from the radar wind profilers were compared to wind data for the MM5, EDAS, and FNL output four times per day, at 6:00 am, noon, 6:00 pm, and midnight Central Standard Time. The radar wind profiler data is available for 60 meter thick layers up until about 2000-2500 m AGL, then every 100 m up to about 3500-4000 m AGL. The models have varying layer thicknesses, typically closer near the ground, and then telescoping upward. A simple approach was used to obtain "paired" data for the models and radar wind profilers. We selected the single radar wind profile level closest to the model layer height for comparison.

Several measures were used to compare model and radar wind profiler (RWP) winds, including:

- Average model wind and average RWP wind speed
- Magnitude of vector difference between modeled and RWP winds.
- Average difference in wind direction (degrees)
- Average absolute value of wind direction difference
- Percent of periods where model and RWP wind directions were within 20 degrees and 30 degrees
- Percent of wind directions from 8 general directions (N, NE, E, SE, S, SW, W, NW) of model and RWP by layers- 0-500 m, 500-1500 m, >1500

The typical number of model/observation comparisons by layer for each observation time is shown below:

Level/Model	MM5	EDAS	FNL
0-500 m	4	2-3	1
500-1500 m	5	4	1
1500-3800 m	5	4	1

The FNL fields have few vertical levels within the lower troposphere.

Because the EDAS fields were not available for October 1999, the summary of MM5 fields was done for the July- September and October periods separately. This facilitates the

comparison of the EDAS and MM5 performance measures for the same temporal periods. The performance of the MM5 fields can be compared to that of the FNL fields for the month of October.

Results

Some summary statistics for the MM5, EDAS, and FNL comparison to the radar wind profilers for the period July-September 1999 are shown in Table 1.

Table 1. Comparison of MM5, EDAS, and FNL winds to radar wind profiler winds for July-September. Data is averaged over all vertical levels and over all observation times. The column variables are described under the first 5 items in the bulleted list shown earlier.

MM5, EDAS, and FNL evaluation for July-September								
Location	**Model**	**ModelWS**	**rwp ws**	**Diff WS**	**M- rwp wd**	**abs value**	**20 deg?**	**30 deg?**
Big Bend	MM5	5.53	5.57	4.18	-3.19	38.54	0.37	0.52
Big Bend	EDAS	5.32	5.70	4.44	-6.97	43.20	0.33	0.47
Big Bend	FNL	6.05	5.69	5.66	-6.33	52.12	0.25	0.37
Llano	MM5	6.16	5.87	3.77	-6.17	31.19	0.52	0.67
Llano	EDAS	5.86	5.96	3.40	-3.19	31.04	0.53	0.67
Llano	FNL	5.55	6.22	6.53	-4.38	43.99	0.34	0.49
Brownsville	MM5	7.16	7.04	2.92	-3.62	20.24	0.67	0.81
Brownsville	EDAS	6.84	7.11	2.77	-2.80	20.58	0.67	0.79
Brownsville	FNL	6.73	7.19	4.53	-4.58	32.20	0.45	0.60
Eagle Pass	MM5	6.75	7.63	4.00	-3.37	26.29	0.56	0.71
Eagle Pass	EDAS	6.87	7.83	3.80	0.93	24.04	0.60	0.76
Eagle Pass	FNL	6.47	7.97	5.28	4.09	34.08	0.44	0.61

For both MM5 and EDAS, the model average wind speeds were quite close to the RWP average wind speed, although there was a slight under-prediction of wind speed by both models at Eagle Pass. The FNL showed somewhat larger differences compared to the RWP. The average vector differences in model and RWP wind speeds were the least at Brownsville for all 3 models. A slight counterclockwise bias of a few degrees in wind direction was noted at all sites for both models (except EDAS and FNL at Eagle Pass). The average absolute value of wind direction differences ranged from about 20 degrees for EDAS and MM5 at Brownsville to about 40 degrees for the models at Big Bend. For the FNL, differences were larger, averaging about 30 degrees at Brownville and 50 degrees at Big Bend. It will be shown that much of the difference at Big Bend is at the lower levels, likely due to channeling of flow by local terrain features. The fraction of model wind directions within ± 20 degrees ranged from one-quarter at Big Bend for

FNL to two-thirds at Brownsville for EDAS and MM5. The fraction of model winds within ± 30 degrees ranged from about three-eighths for FNL at Big Bend to about four-fifths at Brownsville for EDAS and MM5.

The FNL performed worse than EDAS and MM5 for all criteria except average wind direction difference (bias), where it was about the same. Some of this difference may be due to the use of a single radar wind profiler level to compare with the comparatively very coarse FNL vertical layers. Perhaps averaging the RWP data within each FNL layer would give better results.

Comparing Tables 1 and 2, it can be seen that MM5 performance for October was much worse than for the July to September period, while the FNL performance was slightly poorer for October than for July-September. The magnitude of the MM5 vector wind speed errors increased from 50-100% during October compared to July-September. Bias in wind directions increased substantially to (16-23 degrees counter-clockwise). The average absolute value of the wind direction difference increased substantially and the fraction of winds within ± 20 degrees and ± 30 degrees decreased substantially.

Even though the FNL performance degraded during October, the FNL performed about as well as MM5 for October. Wind speed differences were somewhat higher for FNL than MM5, but wind direction bias was less for FNL compared to MM5. Fraction of wind directions within 20 and 30 degrees was very similar for the models, with a slight edge to MM5.

Table 2. MM5 and FNL performance for July-September compared to October.

MM5 and FNL evaluation for October								
		ModelWS	**rwp WS**	**Diff WS**	**M- rwp wd**	**abs value**	**20 deg?**	**30 deg?**
Big Bend	MM5	5.20	6.15	6.18	-21.30	58.92	0.22	0.31
Big Bend	FNL	6.12	6.67	7.05	-12.00	64.31	0.22	0.32
Llano	MM5	6.07	7.00	6.14	-16.31	49.60	0.33	0.45
Llano	FNL	6.46	7.73	6.22	2.22	50.40	0.36	0.46
Brownsville	MM5	6.77	6.47	5.76	-16.51	44.58	0.35	0.47
Brownsville	FNL	6.59	6.68	6.16	6.99	50.53	0.31	0.43
Eagle Pass	MM5	6.12	7.60	6.45	-22.86	46.34	0.34	0.46
Eagle Pass	FNL	6.86	8.28	7.01	4.55	52.01	0.33	0.42

Comparison of model and RWP wind roses

In this section we compare the percent of wind directions from 8 general directions (N, NE, E, SE, S, SW, W, NW) of model and RWP by layers- 0-500 m, 500-1500 m, and >1500 m. The comparisons are done for the period July-September 1999 because we have MM5 and EDAS winds for these periods (no EDAS for October).

Llano

The comparison of frequency of MM5 and EDAS winds to radar wind profiler winds at Llano are compared in Figure 1. In the lowest 500 m, the wind direction frequency compared well to the radar wind profiler for both models. For the layer 500 m to 1500 m, the EDAS frequency was quite similar to the RWP frequency, while the MM5 showed more E and SE winds and fewer S and SW winds than did the RWP. For the 1500- 4000 m layer, both models showed substantial differences from the RWP, in particular with more easterly winds and fewer northerly winds.

Big Bend National Park

The comparison of frequency of MM5 and EDAS winds to radar wind profiler winds at Big Bend National Park are compared in Figure 2. The RWP winds at the lowest level are mainly from the south, while the models show winds predominantly from the SE and E. The low level winds at Big Bend are most likely due to channeling by local terrain; the model winds would not be expected to resolve this channeling. At the 500 m – 1500 m level, there is better agreement between the models and the RWP as the RWP winds shift more toward the southeast and east. The best agreement is for the layer above 1500 m, although both models are a bit low on northerly winds (especially MM5) and high for easterly and southeasterly winds.

Eagle Pass

Figure 3 compares Eagle Pass MM5 and EDAS winds to RWP winds for July-September. The models and RWP show that southeasterly winds dominate, particularly at the lowest level where 60% of observations show southeasterly winds. EDAS somewhat over-predicts the frequency of SE wind at 0-500 m, while MM5 has somewhat greater frequency of easterly winds at the expense of southerly winds observed. At 500-1500 m, the frequency distributions of both models match well with observations.

Brownsville

Brownsville model and observed wind are shown in Figure 4. The MM5 distribution very closely matches the observed distribution at the 0-500 and 500-1500 m levels. EDAS matches observations well over the 500-1500 m layer, but underestimates SE and NE winds and overestimates southerly winds in the 0-500 m layer. Both models show some discrepancy from observations above 1500 m.

Vertically Averaged MM5 and EDAS comparisons

Figure 5 shows the average MM5, EDAS, and RWP wind direction frequency distributions averaged over all vertical levels at Llano, Big Bend, Eagle Pass and Brownsville.

October comparisons for MM5

Because the October statistics showed poorer performance for MM5 compared to the July-September period, it is worth looking at October in some detail. Figure 6 compares MM5 wind direction frequency distribution to RWP distribution for October. Averaged over all levels, the MM5 frequency distribution is close to the observations. For each layer, particularly the 0-500 m layer, differences are more pronounced. Comparison of the 0-500 m level performance for July – September (Figure 4) to that for October illustrate why the performance statistics were so much worse for October at Brownsville.

Figure 7 compares MM5 to RWP wind direction frequencies for the 500 - 1500 m levels at Eagle Pass for July to September and October. Much better agreement can be noted for the July-September period than for the October period.

Summary

MM5 and EDAS performance was similar for the July to September period for which both models were available. MM5 performed similar to or slightly better than FNL for October, with the exception of a pronounced counter-clockwise bias for MM5 winds in October. The MM5 performance was much worse for October than for the July-September period.

A clear preference for the MM5 or EDAS/FNL combination of wind fields has not been established by this analysis.

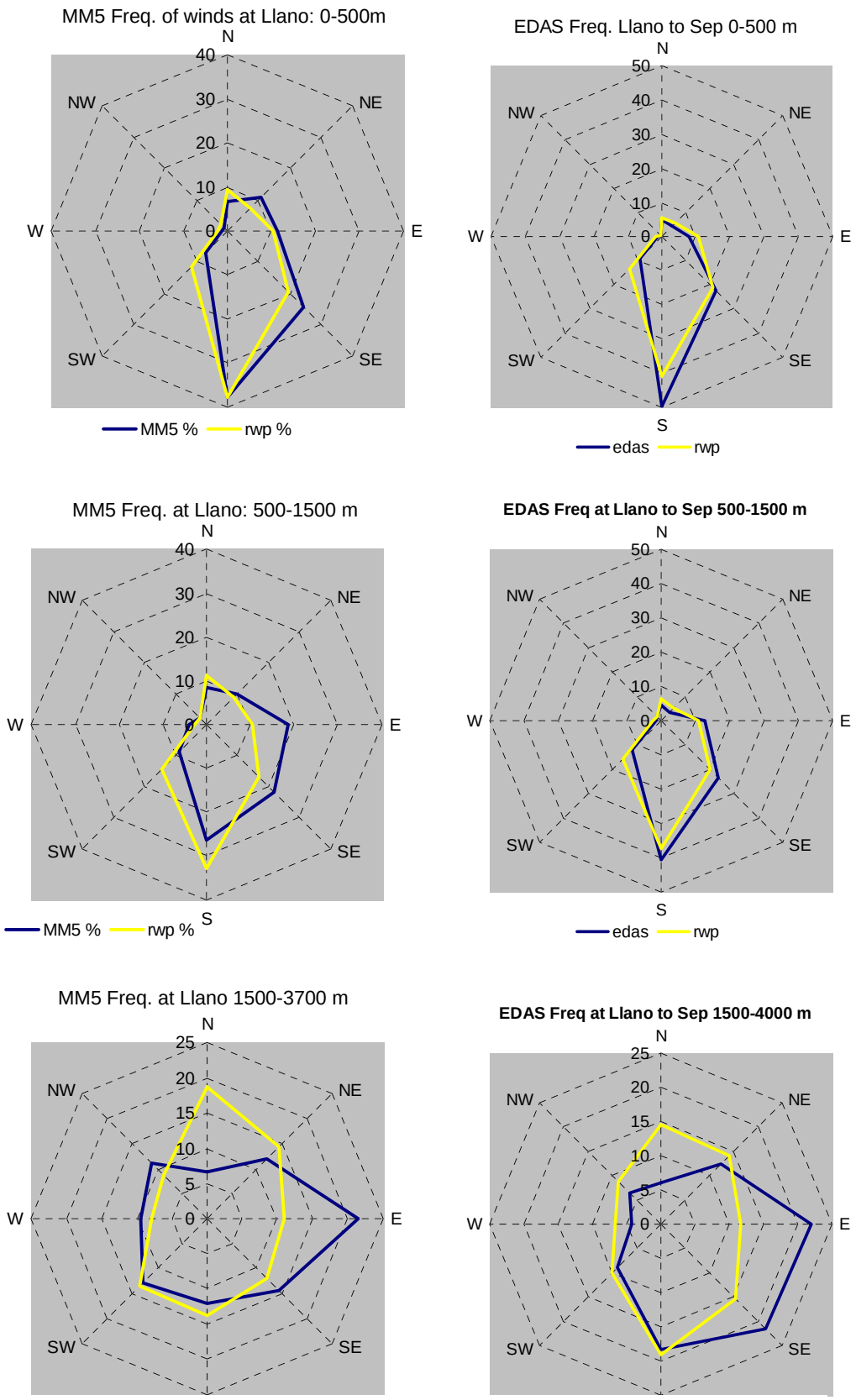

Figure 1. Comparison of MM5 and EDAS wind direction frequency to radar wind profiler winds by level at Llano.

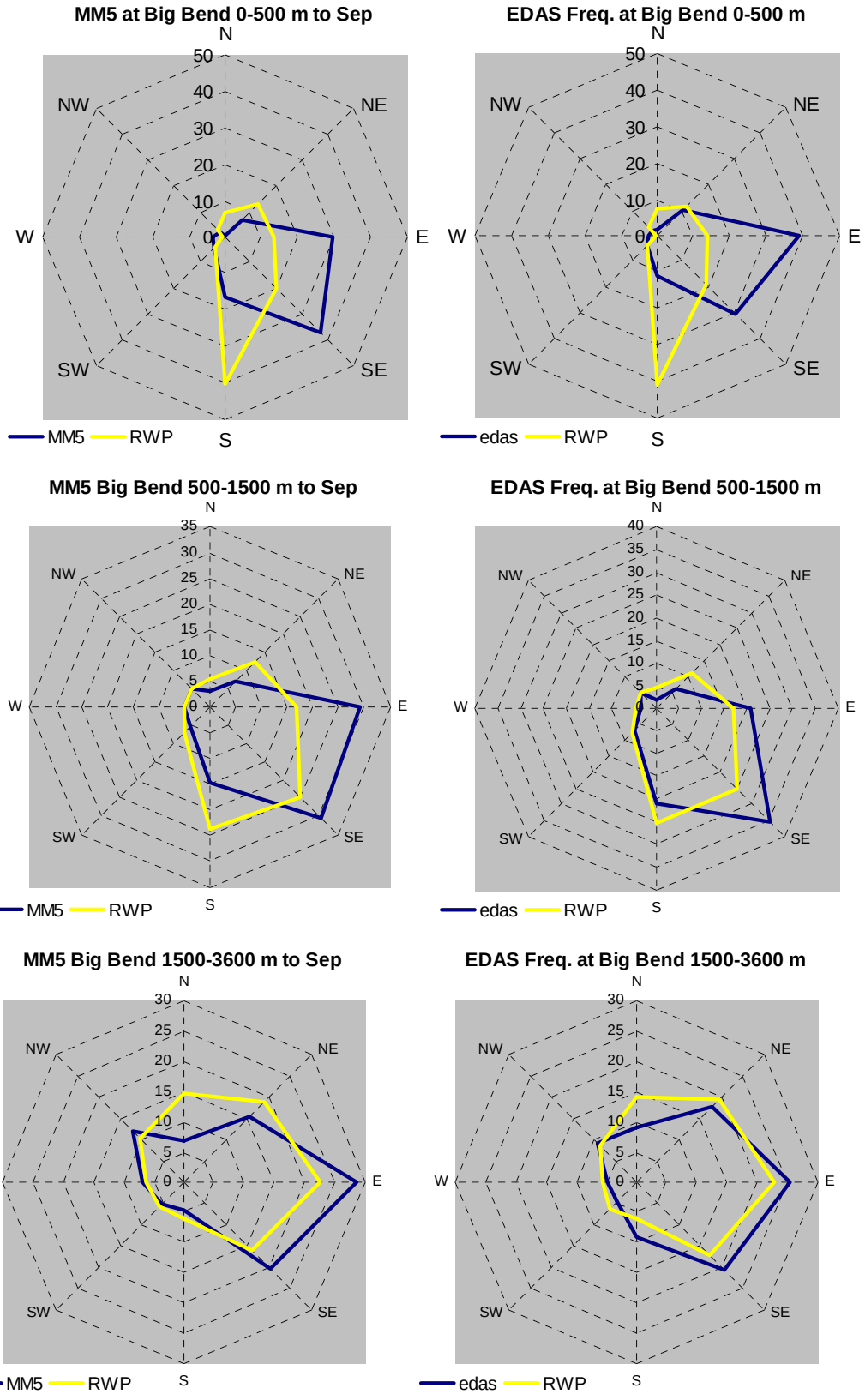

Figure 2. Comparison of MM5 and EDAS wind direction frequency to radar wind profiler winds by level at Big Bend.

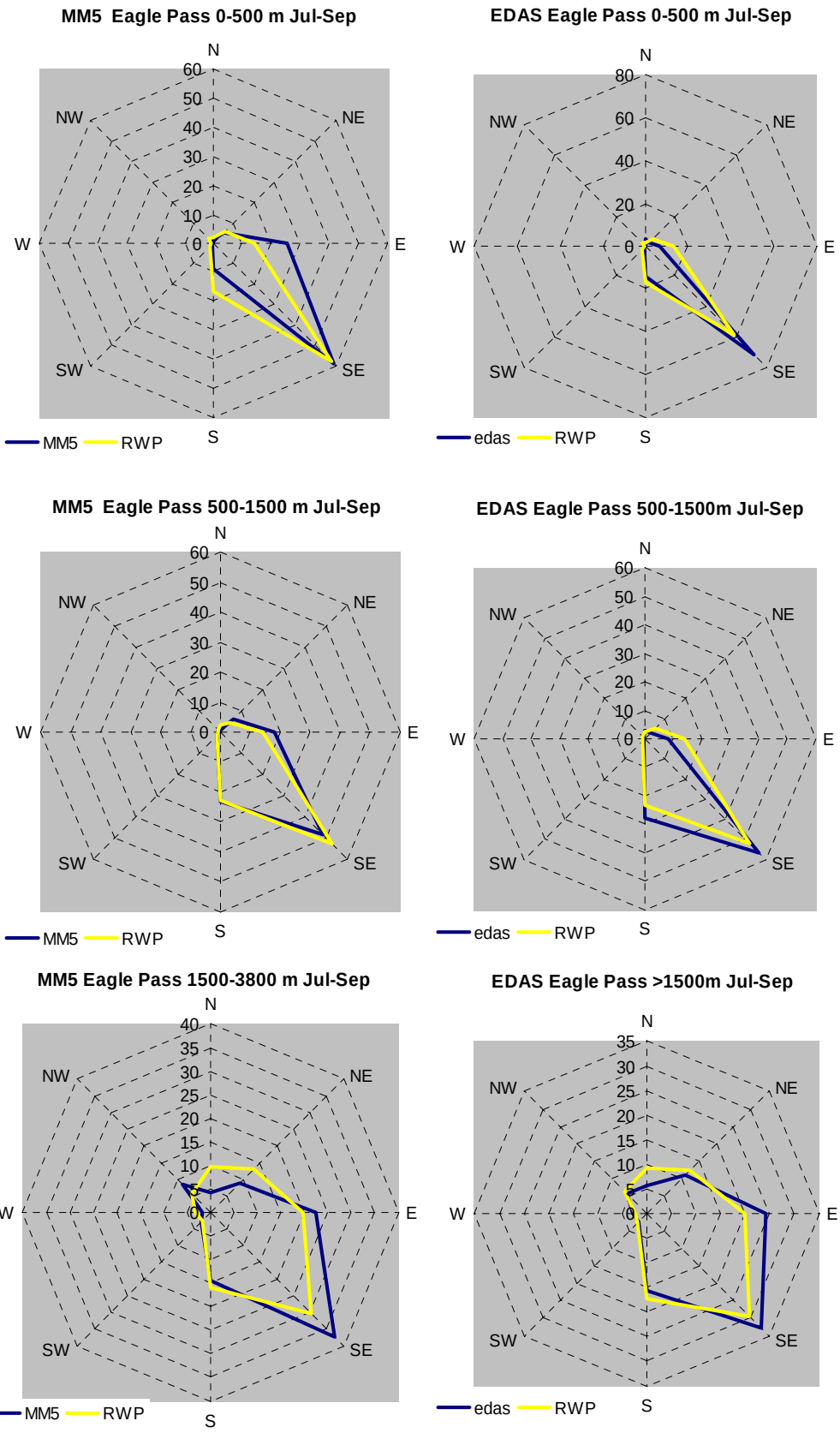

Figure 3. Comparison of MM5 and EDAS wind direction frequency to radar wind profiler winds by level at Eagle Pass.

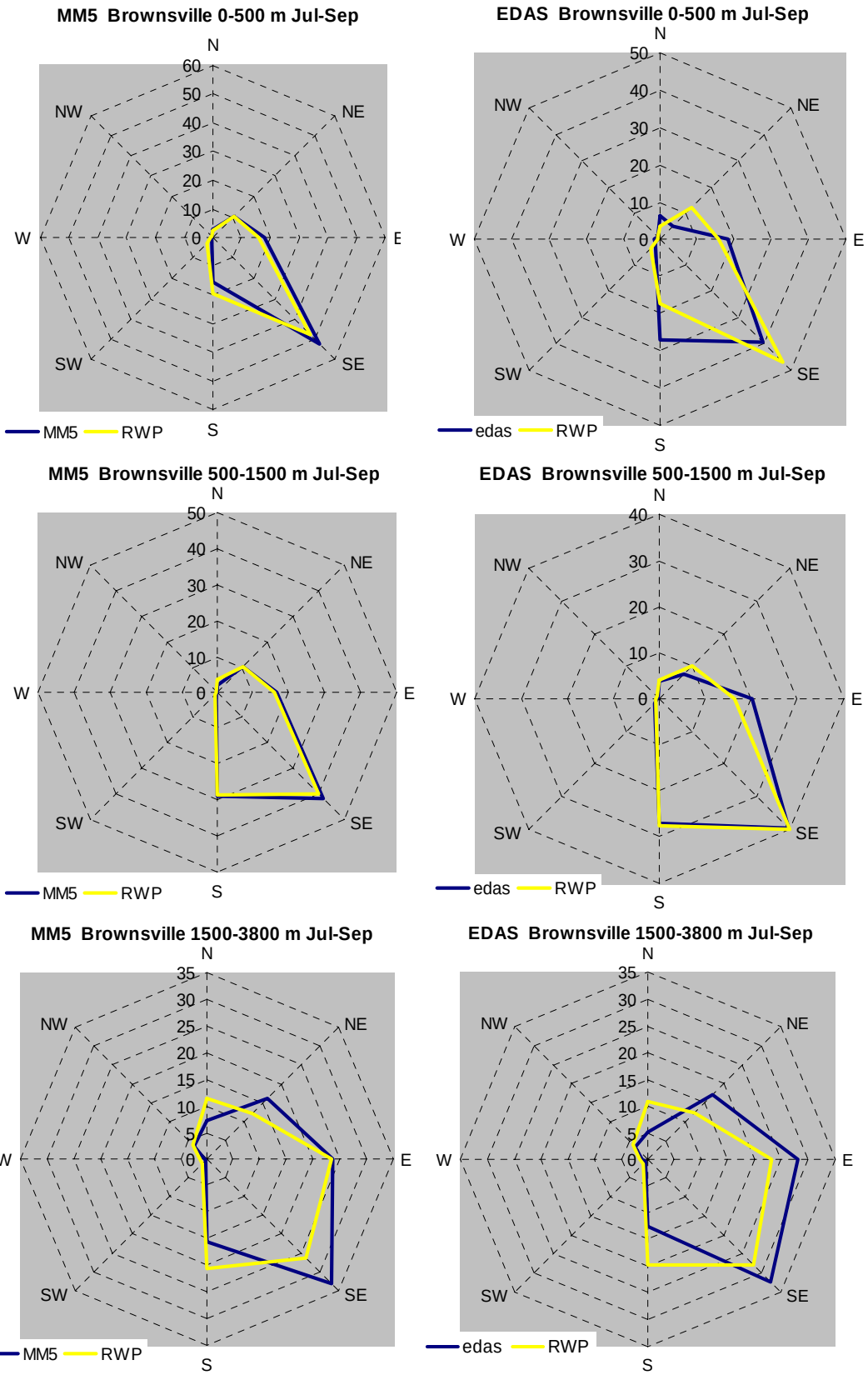

Figure 4. Comparison of MM5 and EDAS wind direction frequency to radar wind profiler winds by level at Brownsville.

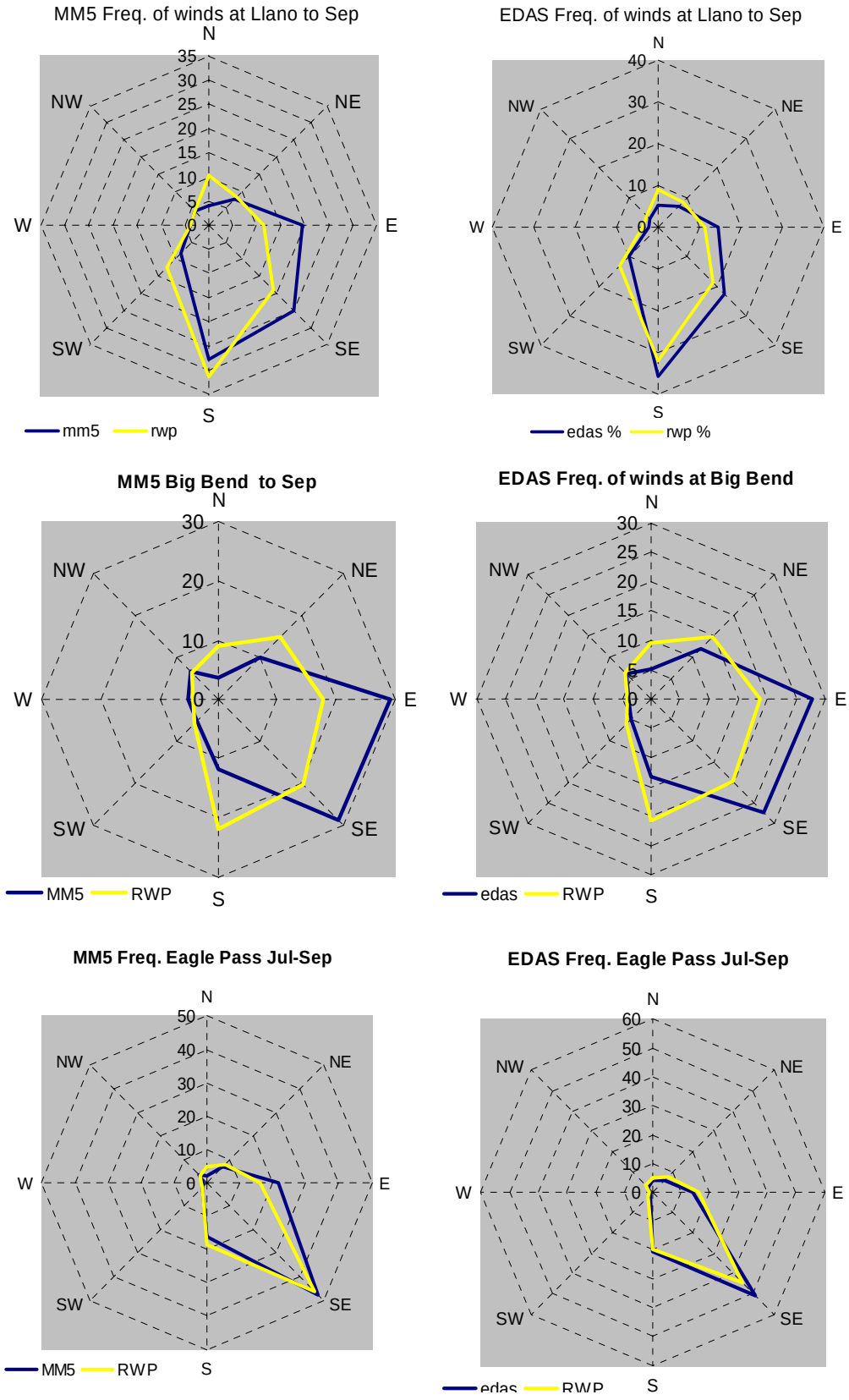

Figure 5. MM5 and EDAS comparisons to RWP, averaged over all vertical levels at Llano, Big Bend and Eagle Pass.

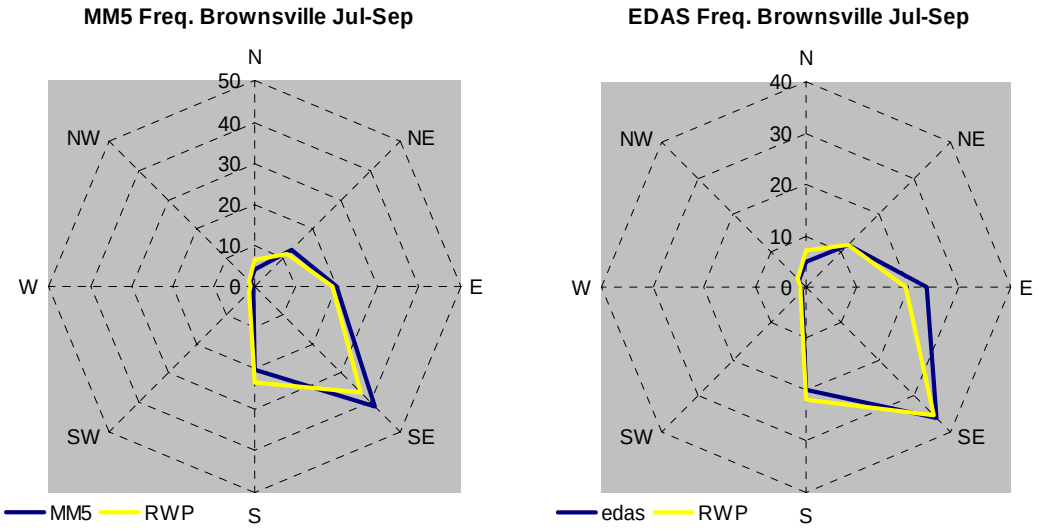

Figure 5 (continued). MM5 and EDAS comparisons to RWP, averaged over all vertical levels at Brownsville.

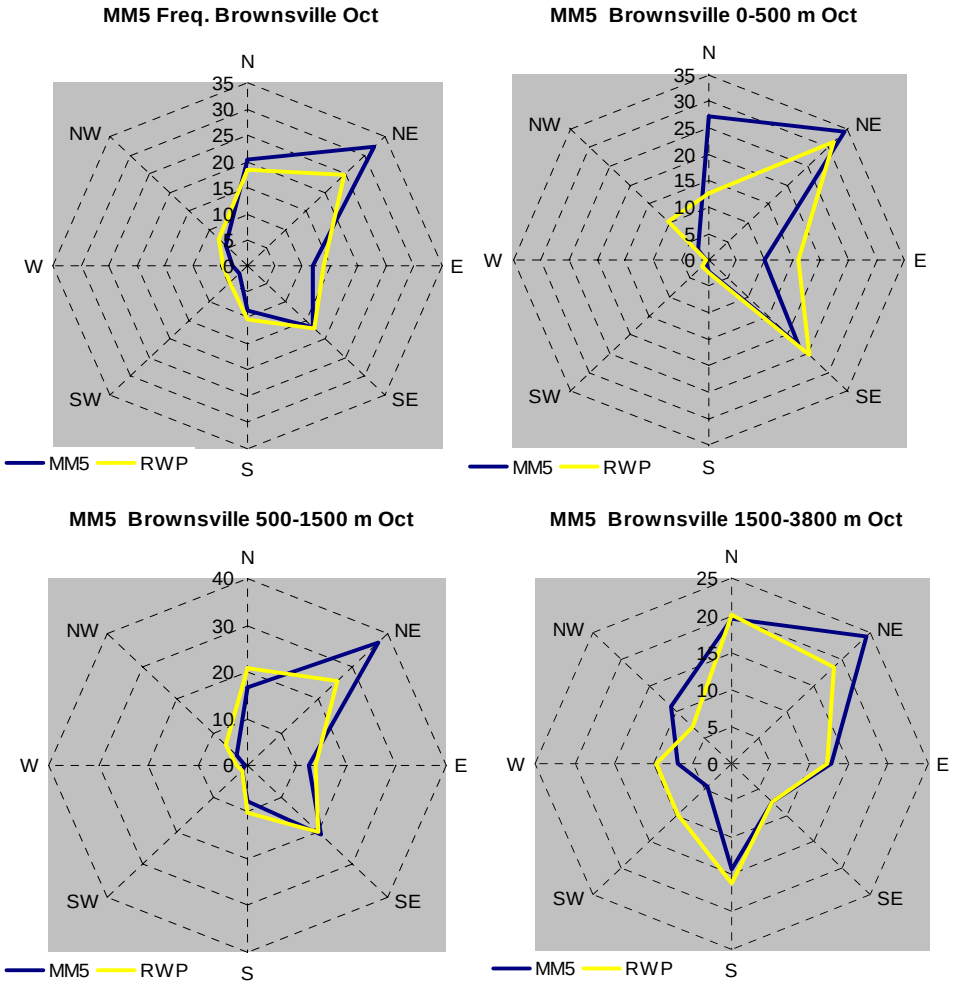

Figure 6. Comparison of MM5 to RWP at Brownsville, October 1999. First panel is average over all levels.

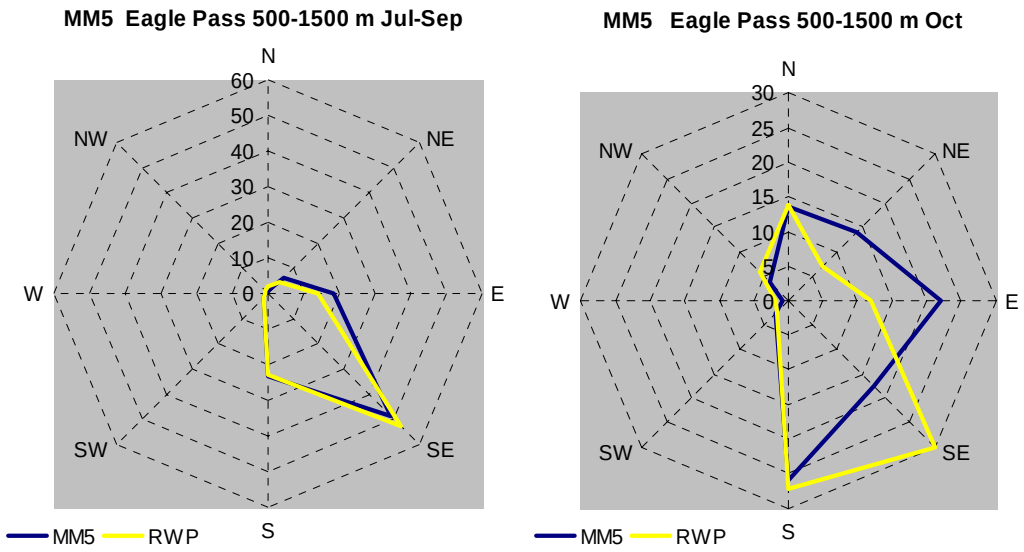

Figure 7. Comparison of MM5 and RWP frequency distributions for the 500–1500 m levels at Eagle Pass during July–September and October.

Appendix 8a – Summary statistics for BRAVO monitoring data

Table 1. Statistics for fine 24-hour high sensitivity particulate data collected at K-Bar (ng/m^3). Data are from the 19 May 2003 data set. The "P" in front of some elements signifies that the original analysis was done with PIXE. LRNC is absorption expressed as an equivalent concentration of black carbon.

Species	mean	se.mean	median	sd	max	min	nvalid	nmiss	nbdl
AG	0	0	0	0	0	0	111	14	111
AS	0.01	0	0	0.04	0.15	0	111	14	100
AU	0	0	0	0	0	0	111	14	111
BR	1.37	0.06	1.34	0.63	3.13	0	111	14	7
CA.ION	91	7.35	70.83	78.1	453.47	-15.22	113	12	0
CD	0	0	0	0	0	0	111	14	111
CL.ION	-63.16	10.01	-41.33	106.44	169.27	-663.96	113	12	0
CO	0	0	0	0	0	0	111	14	111
CU	0.22	0.02	0.19	0.18	1.07	0	111	14	11
E1	305.53	18.43	274.36	195.91	1481.21	-2.63	113	12	0
E2	104.67	8.86	66.17	94.18	622.79	9.64	113	12	0
E3	18.18	3.17	6.4	33.71	246.58	-11.94	113	12	8
FE	70.18	8.39	30.16	88.37	389.42	0.62	111	14	0
GA	0.04	0.01	0	0.06	0.3	0	111	14	60
H	304.8	19.34	248.44	203.78	1054.51	0	111	14	1
HG	0.03	0.01	0	0.06	0.41	0	111	14	85
K.ION	28.84	2.2	24.21	23.4	189.33	-4.23	113	12	0
LRNC	2.57	0.12	2.44	1.26	6.98	0.11	113	12	0
MASS	6472.85	371.08	6315.79	3944.63	17058.42	33.29	113	12	0
MG.ION	15.49	1.53	10.86	16.22	66.49	-14.12	113	12	0
NA.ION	92.14	7.67	79.32	81.49	438.88	-3.71	113	12	0
NH4	803.13	57.9	633.97	615.49	3036.12	-5.24	113	12	0
NI	0.2	0.02	0.14	0.19	0.95	0	111	14	19
NO2	9.36	4.64	-2.9	49.31	402.42	-86.84	113	12	0
NO3	206.14	12.79	168.63	136	671.99	-18.19	113	12	0
O1	85.84	13.02	46.92	138.36	786.19	-68.24	113	12	1
O2	242.81	16.73	205.45	177.88	1143.87	45.2	113	12	0
O3	132.11	11.12	109.82	118.2	517.33	-432.88	113	12	0
O4	183.98	12.04	151.49	128.02	694.76	11.33	113	12	0
OP	283.14	18.73	236.63	199.08	1629.65	0	113	12	2
PAL	110.83	13.85	49.86	145.89	722.5	0	111	14	3
PB	0.71	0.04	0.64	0.47	3.13	0	111	14	5
PBA	0	0	0	0	0	0	111	14	111
PCA	75.48	6.54	55.38	68.89	454.05	0.45	111	14	0
PCL	2.2	1.38	0	14.5	131.37	0	111	14	97
PCR	0.06	0.01	0.03	0.08	0.4	0	111	14	35
PK	41.71	2.98	32.12	31.44	138.71	0.39	111	14	0
PMG	6.69	1.09	2.31	11.53	71.22	0	111	14	55
PMN	1.35	0.14	0.67	1.46	6.22	0.03	111	14	0
PNA	77.68	7.15	63.2	75.28	370.73	0	111	14	24

PP	0	0	0	0.03	0.27	0	111	14	110
PS	802.37	58.59	539.27	617.34	3102.24	0.63	111	14	0
PSI	272.66	29.72	149.12	313.11	1486.89	1.74	111	14	0
PTI	8.63	1.09	3.22	11.53	50.23	0.04	111	14	0
Species	mean	se.mean	median	sd	max	min	nvalid	nmiss	nbdl
PV	0.72	0.06	0.52	0.64	2.98	0	111	14	2
RB	0.21	0.02	0.14	0.19	0.91	0	111	14	11
SE	0.27	0.02	0.23	0.17	0.83	0	111	14	5
SO2	737.38	91.44	491.52	807.61	3909.65	27.69	78	47	0
SO4	2536.84	182.95	1885.13	1944.8	9672.11	24.28	113	12	0
SR	0.57	0.05	0.4	0.54	2.45	0	111	14	8
Y	0.09	0.01	0.07	0.08	0.42	0	111	14	33
ZN	1.54	0.11	1.23	1.14	6.16	0	111	14	5
ZR	0.05	0.01	0	0.09	0.51	0	111	14	67

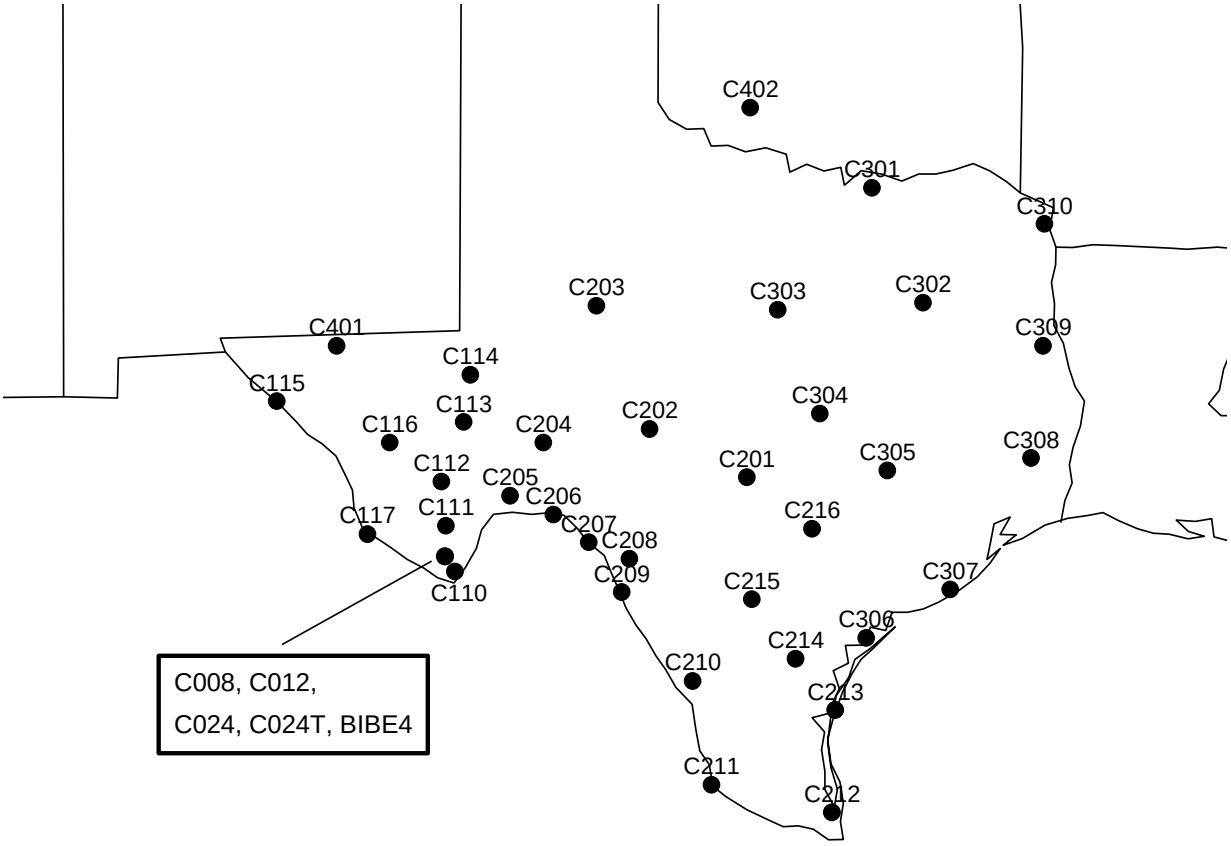

Figure 1. Map of BRAVO monitoring locations by site code.

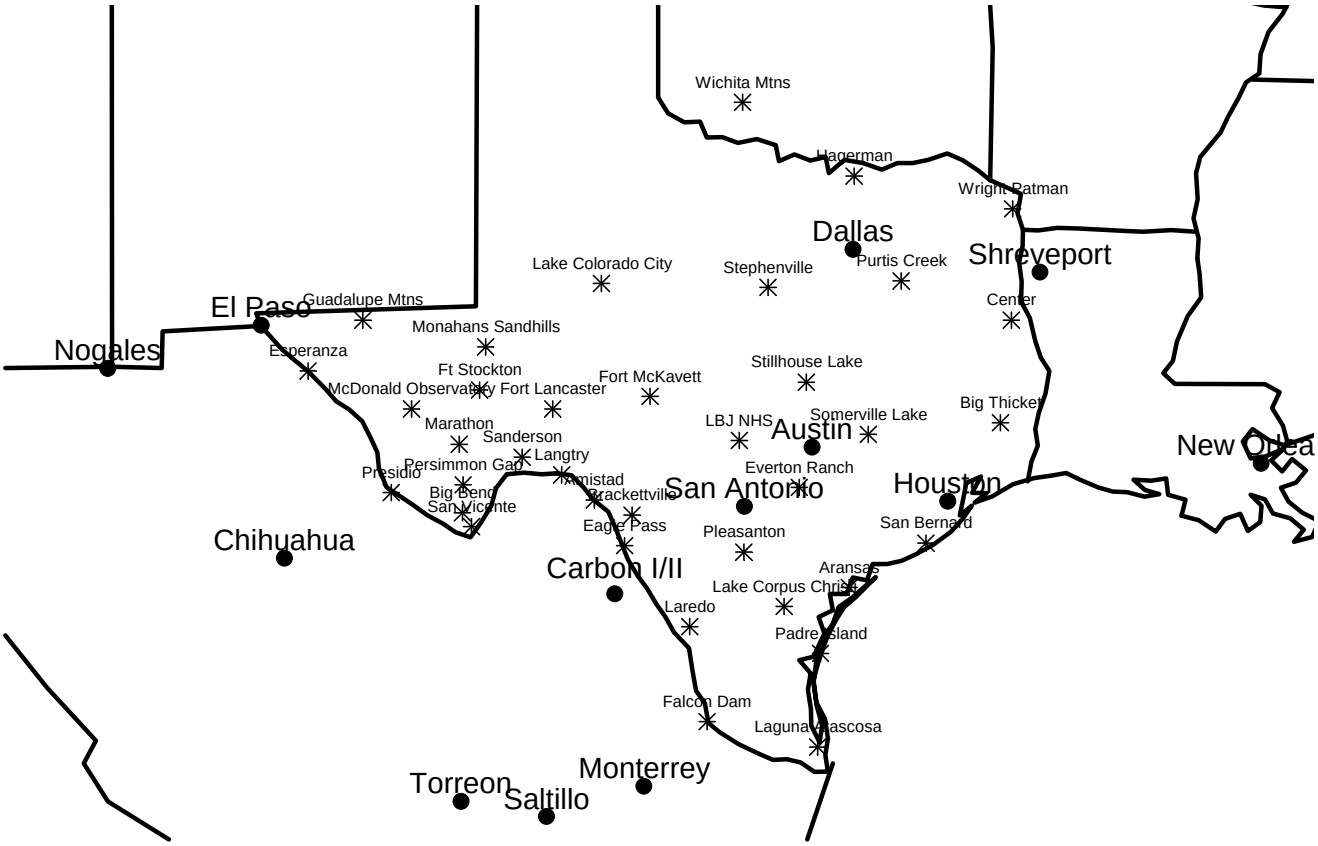

Figure 2. BRAVO monitoring site locations (small font) and some major cities and the Carbón I/II power plants (larger font).

The following tables are sorted alphabetically by species name. Species for which all or nearly all concentrations were below detectable limits are not shown. Unique sites are

BIBE4 – original IMPROVE location of IMPROVE monitor at Big Bend National Park. This monitor was later moved to K-Bar and rename C024.

C024T – K-Bar, speciated 24-hour PM10 data.

C008, C110, C111, C112, C113, C114 – 6-hour duration sites. C008 is at K-Bar.

C012 – K-Bar 12-hour duration site.

Note: - These statistics are for the entire monitoring period of BRAVO, not the truncated time period used for Empirical Orthogonal Function (EOF) analysis as discussed in Section 8.1.

Table 2. Statistics for aluminum by site (ng/m^3).

Site	mean	semean	median	sd	max	min	n	n.bdl
BIBE4	218.71	29.09	238.12	119.96	457.21	32.28	17	0
C008	85.14	11.87	0	232.38	2086	0	383	254
C012	102.53	15.27	30.9	197.35	1021.32	0	167	59
C024T	281.25	31.76	200.52	302.95	2255.28	0	91	4
C110	88.25	10.12	0	200.59	1160.6	0	393	258
C111	60.89	7.45	0	149.08	978.1	0	400	274
C112	71.91	8.5	0	173.68	1157.55	0	417	280
C113	89.29	9.61	0	197.19	1404.69	0	421	260
C114	97.91	10.34	0	209.64	1321.81	0	411	226
C115	78.21	12.27	16.4	119.56	514.02	0	95	45
C116	89.31	14.85	34.21	146.28	757.02	0	97	15
C117	124.03	13.68	72.12	132.62	747.98	0	94	3
C201	181	28.42	43.39	308.67	1624.88	0	118	16
C202	176.91	27.83	49.62	301.05	1742.16	0	117	19
C203	107.77	24.47	39.58	244.7	1389.26	0	100	41
C204	164.36	29.94	67.08	294.84	2036.11	0	97	2
C205	194.16	32.35	64.88	357.33	3214.22	0	122	9
C206	223.39	31.7	74.05	335.49	1842.84	0	112	7
C207	238.43	31.82	68.04	348.58	1633.41	0	120	7
C208	197.18	33.09	49.54	345.5	1551.38	0	109	22
C209	311.75	41.04	103.59	420.5	1683.71	0	105	6
C210	229.63	39.31	53.06	419.74	1846.91	0	114	28
C211	172.16	41.56	0	409.3	1938.91	0	97	49
C212	248.37	39.17	43.37	420.02	2064.24	0	115	24
C213	164.8	44.03	45.94	357.72	1775.4	0	66	22
C214	153.01	45.15	39.88	403.84	1937.15	0	80	23
C215	300.75	49.11	79.69	508	2336.93	0	107	10
C216	109.63	30.96	0	288.75	1932.97	0	87	46
C301	29.65	6.11	0	59.9	340.71	0	96	64
C302	42.72	11.19	0	107.37	720.87	0	92	63
C303	113.1	13.33	72.16	130.62	735.02	0	96	12
C304	178.69	35.17	46.28	368.87	2140.2	0	110	47
C305	136.24	30.38	35.14	318.67	1937.8	0	110	43
C306	170.77	45.93	0	433.32	2931.11	0	89	53
C307	86.24	22.58	0	225.77	1489.83	0	100	65
C308	53.04	13.37	0	127.53	885.46	0	91	55
C309	59.28	14.4	0	143.31	926.98	0	99	58
C310	37.89	11.81	0	117.49	772.66	0	99	73
C401	34.12	9.86	0	80.74	434.56	0	67	41
C402	6.23	2.92	0	17.79	97.2	0	37	30

Table 3. Statistics for arsenic by site (ng/m^3).

Site	mean	semean	median	sd	max	min	n	n.bdl
BIBE4	0.18	0.04	0.11	0.16	0.53	0	17	2
C008	0.1	0.01	0	0.22	1.27	0	383	287
C012	0.11	0.01	0	0.15	0.62	0	167	95
C024T	0.22	0.02	0.16	0.23	1.04	0	91	29
C110	0.12	0.01	0	0.21	1.15	0	393	269
C111	0.09	0.01	0	0.18	1.53	0	400	282
C112	0.13	0.01	0	0.23	1.5	0	417	267
C113	0.27	0.01	0.26	0.28	1.58	0	421	152
C114	0.28	0.01	0.27	0.25	1.91	0	411	114
C115	0.44	0.04	0.3	0.44	2.9	0	95	4
C116	0.17	0.02	0.15	0.23	1.89	0	97	32
C117	0.14	0.02	0.11	0.17	0.86	0	94	37
C201	0.18	0.02	0.16	0.17	0.88	0	118	38
C202	0.13	0.01	0.11	0.13	0.69	0	117	39
C203	0.29	0.01	0.27	0.15	0.93	0	100	2
C204	0.14	0.02	0.13	0.15	0.92	0	97	35
C205	0.11	0.01	0.1	0.12	0.49	0	122	49
C206	0.15	0.01	0.15	0.15	0.67	0	112	38
C207	0.15	0.01	0.14	0.15	0.67	0	120	47
C208	0.18	0.02	0.14	0.18	0.7	0	109	40
C209	0.14	0.02	0.08	0.17	0.6	0	105	52
C210	0.18	0.02	0.16	0.17	1.04	0	114	33
C211	0.34	0.02	0.31	0.19	0.81	0	97	5
C212	0.27	0.02	0.24	0.2	0.89	0	115	18
C213	0.43	0.06	0.32	0.49	2.48	0	66	13
C214	0.49	0.05	0.42	0.45	1.93	0	80	15
C215	0.26	0.02	0.24	0.2	0.96	0	107	18
C216	0.38	0.02	0.39	0.22	1.39	0	87	8
C301	0.48	0.03	0.49	0.26	1.31	0	96	8
C302	0.46	0.04	0.37	0.38	2.2	0	92	12
C303	0.19	0.02	0.17	0.19	1	0	96	36
C304	0.24	0.04	0.18	0.42	3.9	0	110	42
C305	0.27	0.02	0.24	0.24	1.21	0	110	31
C306	0.45	0.03	0.41	0.24	1.12	0	89	4
C307	0.6	0.03	0.56	0.33	1.96	0	100	1
C308	0.64	0.03	0.6	0.28	1.38	0	91	2
C309	0.73	0.04	0.68	0.39	2.61	0	99	5
C310	0.65	0.04	0.59	0.38	2.47	0	99	5
C401	0.18	0.03	0.11	0.26	1.31	0	67	23
C402	0.25	0.05	0.22	0.32	1.57	0	37	14

Table 4. Statistics for bromine by site (ng/m^3).

Species	mean	semean	median	sd	max	min	n	n.bdl
BIBE4	1.25	0.11	1.25	0.47	2.12	0.52	17	0
C008	1.4	0.03	1.36	0.61	3.74	0	383	8
C012	1.25	0.04	1.19	0.55	3.18	0	167	3
C024T	1.8	0.08	1.81	0.81	3.68	0	91	2
C110	1.46	0.03	1.37	0.66	4.65	0	393	7
C111	1.39	0.03	1.34	0.57	3.81	0	400	8
C112	1.44	0.03	1.36	0.59	3.4	0	417	7
C113	1.58	0.04	1.49	0.8	5.24	0	421	19
C114	1.59	0.04	1.51	0.79	8.67	0	411	17
C115	1.53	0.06	1.42	0.63	4.04	0.12	95	0
C116	1.4	0.06	1.32	0.61	5.36	0.47	97	0
C117	1.5	0.07	1.5	0.63	2.93	0.23	94	0
C201	1.68	0.08	1.4	0.9	4.6	0	118	2
C202	1.45	0.06	1.27	0.62	3.5	0.37	117	0
C203	1.7	0.06	1.62	0.58	3.03	0.59	100	0
C204	1.67	0.08	1.54	0.77	4.1	0	97	1
C205	1.78	0.08	1.68	0.93	7.59	0	122	2
C206	1.89	0.08	1.77	0.88	4.5	0	112	2
C207	1.98	0.09	1.72	0.98	4.97	0.58	120	0
C208	1.99	0.11	1.65	1.15	8.2	0	109	1
C209	2.15	0.1	1.96	1.05	5.1	0.36	105	0
C210	1.82	0.12	1.51	1.23	6.38	0	114	3
C211	2.06	0.13	1.6	1.3	6.84	0.57	97	0
C212	1.77	0.13	1.32	1.36	6.98	0.37	115	0
C213	4.6	0.52	3.08	4.2	19.28	0.78	66	0
C214	2.23	0.16	1.85	1.44	8.29	0	80	1
C215	2.03	0.12	1.57	1.22	6.97	0.22	107	0
C216	1.97	0.12	1.69	1.09	6.27	0.37	87	0
C301	2.21	0.09	2.12	0.87	4.51	0.62	96	0
C302	2.06	0.11	1.72	1.07	6.1	0	92	1
C303	2.2	0.08	2.18	0.79	4.59	0.66	96	0
C304	1.93	0.08	1.74	0.85	5.75	0.61	110	0
C305	1.85	0.09	1.64	0.96	5.86	0.56	110	0
C306	2.16	0.16	1.67	1.54	6.69	0.28	89	0
C307	2.98	0.31	2.12	3.13	24.11	0	100	1
C308	2.19	0.14	1.86	1.35	9.33	0.54	91	0
C309	2.65	0.14	2.33	1.36	7.94	0.82	99	0
C310	2.19	0.14	1.73	1.44	9.4	0.64	99	0
C401	1.63	0.07	1.63	0.54	3.13	0	67	1
C402	1.22	0.18	1.16	1.11	3.84	0	37	12

Table 5. Statistics for calcium by site (ng/m^3).

Site	mean	semean	median	sd	max	min	n	n.bdl
BIBE4	76.96	8.8	85.64	36.28	143.48	21.6	17	0
C008	84.78	3.94	63.49	77.11	674.34	0	383	8
C012	72.82	5.1	56.63	65.87	383.89	0	167	1
C024T	403.71	31.7	347.54	302.43	2198.76	0	91	2
C110	122.58	5.15	97.49	102.1	931.61	0	393	3
C111	70	2.8	52.5	55.97	486.27	0	400	2
C112	170.55	7.73	124.77	157.83	1314.91	2.32	417	0
C113	178.93	8.71	130.29	178.73	1618.66	14.09	421	0
C114	132.92	4.33	112.9	87.74	805.6	6.37	411	0
C115	174.38	17.68	110.5	172.35	966.56	16.04	95	0
C116	62.56	6.05	43.02	59.59	402.07	9.05	97	0
C117	147.28	13.9	100.06	134.76	776.46	12.06	94	0
C201	98.86	7	78.92	76.07	462.56	0	118	1
C202	106.78	7.97	79.53	86.26	522.64	17.91	117	0
C203	103.46	7.41	89.84	74.12	450	16.96	100	0
C204	132.86	9.6	105.43	94.52	626.9	20.84	97	0
C205	130.32	13.08	96.7	144.49	1092.67	0	122	1
C206	128.28	8.61	101.62	91.16	551.21	6.54	112	0
C207	152.64	9.32	114.21	102.08	479.54	20.81	120	0
C208	172.07	15.77	127.48	164.6	872.24	0	109	3
C209	250.83	24.43	179.87	250.34	1727	20.56	105	0
C210	102.91	9.44	74.03	100.77	503.51	0	114	1
C211	101.94	9.8	68.24	96.52	452.08	18.72	97	0
C212	92.58	9.92	43.7	106.34	522	15	115	0
C213	105.33	11.94	63.73	96.98	415.76	12.72	66	0
C214	73.46	9	51.51	80.53	375.66	0	80	1
C215	252.66	24.4	141.92	252.43	1209.89	15.81	107	0
C216	110.54	11.39	77.9	106.22	590.4	0	87	4
C301	146.87	9.27	134.72	90.84	506.73	6.22	96	0
C302	60.99	3.63	55.58	34.81	218.57	0	92	1
C303	181.92	11.09	168.25	108.63	564.41	14	96	0
C304	130.43	8.42	107.78	88.33	571.35	25.28	110	0
C305	75.24	7.94	51.8	83.26	556.7	14.12	110	0
C306	86.89	9.16	57.55	86.38	577.79	19.88	89	0
C307	261.69	34.97	112.7	349.72	1863.29	16.27	100	0
C308	43.3	3.39	34.3	32.38	234.73	12.67	91	0
C309	58.21	3.76	49.75	37.42	237.38	16.54	99	0
C310	52.56	3.68	42.72	36.58	216.13	13.53	99	0
C401	66.4	6.16	52.28	50.41	256.81	14.48	67	0
C402	84.41	13.79	59.62	83.85	484.24	0	37	1

Table 6. Statistics for chlorine by site (ng/m^3).

Site	mean	semean	median	sd	max	min	n	n.bdl
BIBE4	3.86	3.86	0	15.93	65.68	0	17	16
C008	0.7	0.34	0	6.68	117.42	0	383	374
C012	0.07	0.04	0	0.57	5.39	0	167	164
C024T	5.43	2.17	0	20.72	116.54	0	91	82
C110	1.26	0.55	0	10.91	158.18	0	393	380
C111	0.54	0.29	0	5.76	108.56	0	400	391
C112	0.16	0.09	0	1.8	28.06	0	417	413
C113	0.96	0.53	0	10.9	179.65	0	421	414
C114	1.04	0.53	0	10.67	186.26	0	411	398
C115	0	0	0	0	0	0	95	95
C116	0.04	0.04	0	0.44	4.33	0	97	96
C117	0.05	0.03	0	0.34	2.58	0	94	92
C201	3.09	2.13	0	23.15	210.29	0	118	114
C202	3.64	2.27	0	24.51	227.61	0	117	113
C203	0	0	0	0	0	0	100	100
C204	0.02	0.02	0	0.19	1.83	0	97	96
C205	0.1	0.06	0	0.62	4.41	0	122	119
C206	7.16	4.06	0	42.93	395.35	0	112	106
C207	14.07	6.33	0	69.35	534.03	0	120	111
C208	2.58	1.14	0	11.92	77.39	0	109	101
C209	4.67	3.64	0	37.26	360.4	0	105	103
C210	16.17	6.71	0	71.61	629.75	0	114	97
C211	5.69	3.39	0	33.36	282.03	0	97	93
C212	134.04	25.06	0	268.73	1796.15	0	115	73
C213	319.04	60.22	102.24	489.2	1963.42	0	66	31
C214	15.3	5.28	0	47.21	221.16	0	80	70
C215	83.99	25.66	0	265.42	1834.2	0	107	85
C216	3.69	3.69	0	34.45	321.35	0	87	86
C301	0	0	0	0	0	0	96	96
C302	0	0	0	0	0	0	92	92
C303	0	0	0	0	0	0	96	96
C304	0.98	0.98	0	10.33	108.33	0	110	109
C305	16.3	9.25	0	97.04	851.78	0	110	105
C306	109.72	32.99	0	311.21	2085.12	0	89	74
C307	38.69	12.62	0	126.2	714.59	0	100	88
C308	0	0	0	0	0	0	91	91
C309	0	0	0	0	0	0	99	99
C310	0	0	0	0	0	0	99	99
C401	0	0	0	0	0	0	67	67
C402	0	0	0	0	0	0	37	37

Table 7. Statistics for chromium by site (ng/m^3).

Site	mean	semean	median	sd	max	min	n	n.bdl
BIBE4	0.36	0.14	0	0.59	1.64	0	17	12
C008	1.54	0.2	0	3.92	40.75	0	383	291
C012	0.52	0.1	0	1.28	10.77	0	167	132
C024T	1	0.17	0	1.58	9.97	0	91	57
C110	1.54	0.24	0	4.81	79.76	0	393	281
C111	1.46	0.14	0	2.7	23.55	0	400	276
C112	1.37	0.13	0	2.55	24.18	0	417	293
C113	1.37	0.11	0	2.33	9.63	0	421	293
C114	1.52	0.12	0	2.44	13.63	0	411	269
C115	0.25	0.06	0	0.57	2.77	0	95	77
C116	0.59	0.09	0	0.89	6.03	0	97	53
C117	0.6	0.1	0	0.95	4.86	0	94	56
C201	0.57	0.07	0	0.81	4.09	0	118	69
C202	0.46	0.08	0	0.86	4.64	0	117	81
C203	0.22	0.05	0	0.45	1.99	0	100	79
C204	0.66	0.09	0	0.93	6.22	0	97	50
C205	0.53	0.08	0	0.85	5.33	0	122	78
C206	0.54	0.08	0	0.89	3.7	0	112	74
C207	0.55	0.09	0	0.93	3.75	0	120	82
C208	0.72	0.11	0	1.11	6.23	0	109	65
C209	1.11	0.22	0	2.28	18.92	0	105	60
C210	0.62	0.08	0	0.84	4.1	0	114	68
C211	0.23	0.05	0	0.51	2.3	0	97	78
C212	0.44	0.07	0	0.77	3.19	0	115	81
C213	0.5	0.13	0	1.06	4.61	0	66	49
C214	0.64	0.08	0	0.74	2.5	0	80	41
C215	0.74	0.12	0	1.2	5.36	0	107	67
C216	0.33	0.06	0	0.56	2.07	0	87	62
C301	0.44	0.08	0	0.74	3.34	0	96	67
C302	0.53	0.2	0	1.9	17.38	0	92	70
C303	0.35	0.07	0	0.68	2.61	0	96	74
C304	0.35	0.07	0	0.76	4.08	0	110	86
C305	0.33	0.07	0	0.71	3.76	0	110	84
C306	0.27	0.07	0	0.65	3.61	0	89	73
C307	0.49	0.11	0	1.1	7.48	0	100	77
C308	0.78	0.26	0	2.44	22.5	0	91	59
C309	0.62	0.12	0	1.23	8.3	0	99	68
C310	0.5	0.08	0	0.83	4.38	0	99	67
C401	0.47	0.1	0	0.84	3.58	0	67	48
C402	0.43	0.13	0	0.8	2.59	0	37	27

Table 8. Statistics for copper by site (ng/m^3).

Site	mean	semean	median	sd	max	min	n	n.bdl
BIBE4	0.2	0.15	0	0.61	2.41	0	17	15
C008	0.6	0.04	0	0.85	7.17	0	383	203
C012	0.39	0.04	0.28	0.52	3.84	0	167	78
C024T	0.2	0.06	0	0.61	5.03	0	91	67
C110	0.48	0.04	0	0.84	11.41	0	393	227
C111	0.49	0.04	0	0.71	5.82	0	400	213
C112	0.53	0.05	0.13	1.07	17.54	0	417	205
C113	0.31	0.04	0	0.89	14.04	0	421	287
C114	0.23	0.03	0	0.54	5.99	0	411	301
C115	0.97	0.25	0.23	2.46	22.37	0	95	30
C116	0.34	0.05	0.18	0.53	3.12	0	97	40
C117	0.18	0.03	0	0.29	1.5	0	94	48
C201	0.35	0.03	0.34	0.34	1.69	0	118	36
C202	0.27	0.03	0.2	0.33	2.08	0	117	42
C203	0.1	0.02	0	0.21	1.38	0	100	66
C204	0.47	0.14	0.27	1.36	13.26	0	97	27
C205	0.34	0.04	0.26	0.46	3.85	0	122	35
C206	0.41	0.05	0.27	0.48	2.41	0	112	34
C207	0.54	0.09	0.29	1.01	8.6	0	120	29
C208	0.48	0.13	0.32	1.34	13.61	0	109	30
C209	0.55	0.1	0.42	1.02	10.17	0	105	21
C210	0.25	0.03	0.16	0.32	1.8	0	114	46
C211	0.16	0.03	0	0.32	1.96	0	97	60
C212	0.27	0.05	0.07	0.56	4.51	0	115	57
C213	0.61	0.11	0.32	0.9	4.72	0	66	17
C214	0.38	0.05	0.27	0.49	2.21	0	80	34
C215	0.32	0.07	0.14	0.7	6.6	0	107	49
C216	0.33	0.05	0.17	0.44	2.38	0	87	36
C301	1.49	0.15	1.15	1.45	8.95	0	96	9
C302	1.07	0.43	0.24	4.09	34.99	0	92	32
C303	0.54	0.05	0.48	0.48	2.52	0	96	18
C304	0.63	0.06	0.45	0.65	3.5	0	110	23
C305	0.9	0.21	0.55	2.21	21.3	0	110	25
C306	0.22	0.04	0	0.4	2.1	0	89	51
C307	0.58	0.21	0.03	2.09	20.42	0	100	50
C308	0.61	0.06	0.55	0.56	3.44	0	91	17
C309	0.64	0.08	0.52	0.76	6.03	0	99	22
C310	1.18	0.27	0.77	2.73	26.83	0	99	18
C401	0.78	0.13	0.36	1.08	4.92	0	67	19
C402	0.44	0.11	0	0.65	2.89	0	37	19

Table 9. Statistics for iron by site (ng/m^3).

Site	mean	semean	median	sd	max	min	n	n.bdl
BIBE4	126.38	16.58	134.79	68.37	252.31	25.08	17	0
C008	69.89	6.36	30.11	124.46	1102.67	0	383	2
C012	65.9	8.2	26.06	105.91	575.81	0	167	1
C024T	153.03	15.18	107.57	144.82	1067.74	3.27	91	0
C110	82.05	5.47	42.55	108.5	707.46	0.56	393	0
C111	59.25	4.55	25.4	90.95	672.67	0	400	1
C112	104.25	5.29	67.16	108.08	649.79	1.38	417	0
C113	86.29	5.48	45.08	112.45	815.05	6.17	421	0
C114	84.29	5.35	50.05	108.42	736.14	0	411	1
C115	69.97	6.18	51.36	60.23	298.78	10.39	95	0
C116	53.6	7.87	23.25	77.52	402.96	5.59	97	0
C117	70.81	7	46.84	67.83	382.05	4.44	94	0
C201	111.59	15.2	37.8	165.14	852.87	2.11	118	0
C202	104.42	14.2	34.94	153.63	875.89	7.63	117	0
C203	80.71	12.41	41.6	124.08	713.19	14.04	100	0
C204	92.86	15.98	41.92	157.36	1060.36	13.77	97	0
C205	123.79	16.28	66.74	179.81	1593.67	0.75	122	0
C206	128.97	15.63	63.3	165.46	812.56	2.48	112	0
C207	139.82	16.7	52.3	182.9	773.68	14.71	120	0
C208	123.67	17.4	40.42	181.67	788.32	0.16	109	0
C209	178.05	20.95	71.95	214.64	790.77	10.84	105	0
C210	134.57	19.73	41.82	210.62	864.98	0	114	1
C211	105.07	20.25	28.59	199.4	906.17	8.29	97	0
C212	139.75	20.19	30.66	216.49	1099.55	5.98	115	0
C213	106.2	22.18	38.86	180.23	838.8	4.05	66	0
C214	95.34	23.13	31.94	206.88	1008.06	0.88	80	0
C215	181.2	30.36	51.65	314.05	1939.36	8.59	107	0
C216	82.46	16.25	41.06	151.53	1078.9	10.73	87	0
C301	69.74	3.51	66.57	34.4	201.09	9.28	96	0
C302	57.75	5.42	47.5	52.02	362.58	0.26	92	0
C303	76.75	6.93	57.62	67.91	368.61	12.25	96	0
C304	116.12	16.07	53.58	168.51	907.22	14.57	110	0
C305	104.46	17.61	46.93	184.75	1086.81	9.98	110	0
C306	119.06	22.47	44.86	212.01	1244.95	7.22	89	0
C307	76.7	11.83	40.96	118.31	743.57	7.46	100	0
C308	58.53	8.23	37.59	78.5	597.83	7.14	91	0
C309	97.01	8.39	73.9	83.5	538.69	15.11	99	0
C310	79.65	6.99	62.66	69.54	529.69	13.36	99	0
C401	35.49	5.15	23.76	42.16	240.74	3.93	67	0
C402	21.12	3.12	19.04	19	60.7	0	37	12

Table 10. Statistics for hydrogen by site (ng/m^3).

Sites	mean	semean	median	sd	max	min	n	n.bdl
BIBE4	221.17	45.44	159.73	187.36	870.06	76.44	17	0
C008	424.32	12.11	350.31	237.09	1286.43	0	383	6
C012	348.06	15.53	288.2	200.75	1049.63	0	167	4
C024T	377.43	23.22	295.4	221.54	996.1	0	91	2
C110	404.22	11.89	339.84	235.71	1394.46	0	393	3
C111	391.39	11.02	320.64	220.35	1169.45	0	400	1
C112	386.77	9.61	332.88	196.3	1269.63	0	417	1
C113	375.05	9.39	318.73	192.74	1224.93	118.88	421	0
C114	359.8	9.2	309	186.43	1355.01	0	411	2
C115	261.87	10.89	244.69	106.11	727.97	37.88	95	0
C116	262.64	13.38	227.63	131.78	656.25	76.95	97	0
C117	319.08	18.92	262.37	183.42	837.03	0	94	2
C201	449.97	25.89	369.3	281.2	1408.54	0	118	2
C202	344.85	21.13	260.34	228.56	1239.5	0	117	2
C203	377.62	21.83	301.66	218.27	1139.59	94.15	100	0
C204	388.52	20.38	345.33	200.73	817.99	30.72	97	0
C205	366.11	18.98	306.63	209.65	971.63	0	122	2
C206	436.79	24.14	375.55	255.52	1567.31	0	112	2
C207	401.23	22.46	318.47	246.05	1236.7	93.72	120	0
C208	363.41	22.98	289.79	239.96	1164.24	0	109	4
C209	364.25	19.14	317.91	196.15	987.77	0	105	1
C210	335.11	23.67	264.32	252.67	1401.34	0	114	6
C211	390.85	21.08	351.78	207.65	1008.33	97.59	97	0
C212	303.12	19.15	230.15	205.37	1102.1	0	115	1
C213	429.02	47.81	331.56	388.4	2602.79	76.28	66	0
C214	379.12	26.48	354.51	236.81	1023.46	0	80	3
C215	375.39	23.18	312.02	239.75	1229.86	0	107	2
C216	508.65	36.8	437.64	343.23	1721.71	0	87	3
C301	646.84	38.62	531.19	378.37	1932.02	163.79	96	0
C302	603.67	32.49	560.12	311.6	1595.8	0	92	1
C303	498.69	30.5	410.16	298.81	1571.44	109.65	96	0
C304	497.5	27.55	417.04	288.93	1450.54	145.33	110	0
C305	503.17	26.81	446.37	281.23	1452.58	138.71	110	0
C306	472.39	30.22	387.86	285.14	1338.15	77.12	89	0
C307	525.29	34.68	460.61	346.85	1581.41	82.81	100	0
C308	705.9	35.42	657.78	337.85	1686.69	203.8	91	0
C309	709.27	36.34	622.05	361.53	1909.23	166.37	99	0
C310	793.83	44.66	711.93	444.33	2525.73	174.34	99	0
C401	278.71	16.69	240.83	136.65	751.27	94.67	67	0
C402	494.52	52.11	417.03	316.96	1573.88	0	37	1

Table 11. Statistics for lead by site (ng/m^3).

Site	mean	semean	median	sd	max	min	n	n.bdl
BIBE4	0.26	0.08	0.13	0.32	0.9	0	17	7
C008	0.76	0.03	0.75	0.56	3.13	0	383	88
C012	0.61	0.04	0.57	0.5	3.31	0	167	28
C024	0.33	0.05	0.2	0.48	3.41	0	113	41
C024T	0.43	0.05	0.32	0.49	2.19	0	91	29
C110	0.72	0.04	0.71	0.76	9.76	0	393	104
C111	0.67	0.03	0.69	0.54	3.8	0	400	99
C112	0.58	0.03	0.62	0.51	2.56	0	417	143
C113	0.4	0.04	0	0.77	6.36	0	421	270
C114	0.13	0.01	0	0.29	1.68	0	411	328
C115	0.53	0.14	0.22	1.33	12.21	0	95	30
C116	0.37	0.04	0.32	0.4	1.97	0	97	35
C117	0.51	0.04	0.47	0.38	1.56	0	94	18
C201	0.88	0.05	0.79	0.58	3.75	0	118	7
C202	0.59	0.03	0.57	0.37	1.56	0	117	15
C203	0.24	0.03	0.18	0.27	1.22	0	100	39
C204	0.58	0.05	0.51	0.48	2.22	0	97	18
C205	0.68	0.07	0.56	0.74	6.01	0	122	14
C206	0.71	0.05	0.6	0.56	3.19	0	112	15
C207	0.86	0.06	0.73	0.7	5.28	0	120	9
C208	0.72	0.05	0.67	0.52	2.12	0	109	16
C209	2.04	0.22	1.44	2.23	17.81	0	105	6
C210	0.87	0.11	0.6	1.2	9.21	0	114	17
C211	0.44	0.05	0.36	0.46	2.23	0	97	26
C212	0.67	0.06	0.53	0.61	4.28	0	115	16
C213	1.08	0.14	0.88	1.12	6.06	0	66	10
C214	0.91	0.08	0.76	0.71	2.88	0	80	7
C215	0.75	0.06	0.62	0.64	3.83	0	107	16
C216	0.57	0.07	0.45	0.65	4.06	0	87	28
C301	1.15	0.09	0.94	0.85	4.33	0	96	6
C302	1.73	0.24	1.04	2.35	14.18	0	92	9
C303	1.16	0.08	1.12	0.79	3.95	0	96	9
C304	1.31	0.1	1.07	1.04	7.94	0	110	5
C305	1.3	0.11	1.06	1.15	7.53	0	110	4
C306	0.53	0.08	0.23	0.75	4.61	0	89	39
C307	0.54	0.06	0.4	0.59	3.42	0	100	28
C308	1.21	0.08	1.19	0.79	3.54	0	91	6
C309	1.78	0.16	1.49	1.59	8.59	0	99	6
C310	1.33	0.17	1	1.73	14.98	0	99	15
C401	0.52	0.06	0.46	0.52	2.53	0	67	14
C402	0.4	0.1	0	0.6	1.99	0	37	21

Table 12. Statistics for LRNC (absorption in equivalent concentration of EC) by site (ng/m^3).

Site	mean	semean	median	sd	max	min	n	n.bdl
BIBE4	1.98	0.23	1.63	0.94	4.08	0.82	17	0
C008	4.19	0.08	3.98	1.64	13.27	-0.1	383	0
C012	3.26	0.11	3.21	1.44	10.57	0.08	168	0
C024T	3.01	0.15	3	1.42	6.52	-0.23	91	0
C110	4.05	0.12	3.74	2.38	30.89	-0.53	393	0
C111	3.52	0.08	3.41	1.6	12.34	0.06	399	0
C112	5.2	0.13	4.91	2.68	33.65	-0.32	417	0
C113	3.79	0.1	3.51	2.01	13.57	-6.82	382	0
C114	5.55	0.11	5.42	2.25	14.46	-0.43	413	0
C115	3.41	0.18	3.01	1.74	9.88	0.15	95	0
C116	2.25	0.1	2.17	0.99	7.07	0.78	97	0
C117	2.78	0.11	2.8	1.09	5.76	0.42	94	0
C201	3.41	0.12	3.26	1.25	8.1	0.06	118	0
C202	2.97	0.1	2.8	1.03	5.53	1.03	117	0
C203	2.87	0.1	2.84	0.99	5.76	0.97	100	0
C204	3.09	0.11	3.02	1.11	6.52	-0.06	97	0
C205	3.28	0.14	3.17	1.57	13.79	0.38	122	0
C206	3.5	0.11	3.5	1.18	6.09	0.37	112	0
C207	3.74	0.11	3.61	1.23	7.24	1.21	120	0
C208	3.76	0.16	3.52	1.65	9.54	0.01	110	0
C209	3.83	0.16	3.76	1.64	10.4	0.87	105	0
C210	3.34	0.16	3.17	1.72	13.81	-0.02	114	0
C211	3.22	0.13	3.12	1.26	6.89	0.77	97	0
C212	2.63	0.1	2.46	1.06	5.8	0.84	114	0
C213	3.98	0.3	3.3	2.52	11.42	0.03	69	0
C214	3.47	0.16	3.52	1.42	6.67	-0.03	80	0
C215	3.21	0.13	3.18	1.32	7.25	1.03	107	0
C216	3.49	0.16	3.51	1.52	10.99	0.91	87	0
C301	5.34	0.17	5.14	1.67	12.11	2.29	96	0
C302	4.47	0.19	4.22	1.85	14.69	-0.23	92	0
C303	4.25	0.14	4.11	1.35	7.78	1.19	96	0
C304	4.83	0.15	4.53	1.57	8.66	2.03	114	0
C305	4.05	0.12	4.04	1.28	7.7	1.44	110	0
C306	3.37	0.19	3.02	1.81	13.76	0.23	89	0
C307	3.75	0.24	3.29	2.43	17.87	0.68	100	0
C308	3.7	0.12	3.66	1.19	7.56	1.56	91	0
C309	5.4	0.21	5.27	2.08	16.95	2.03	99	0
C310	6.39	0.25	6.1	2.45	21	2.2	99	0
C401	2.24	0.09	2.17	0.77	4.67	1.12	67	0
C402	3.79	0.23	3.81	1.72	7.68	-0.05	57	0

Table 13. Statistics for manganese by site (ng/m^3).

Site	mean	semean	median	sd	max	min	n	n.bdl
BIBE4	3.06	0.45	2.44	1.87	7.79	0	17	1
C008	2.19	0.24	0	4.72	57.71	0	383	264
C012	2.84	0.28	2.33	3.6	26.59	0	167	64
C024T	4.49	0.39	3.82	3.77	15.62	0	91	16
C110	1.87	0.16	0	3.1	14.37	0	393	264
C111	1.7	0.17	0	3.45	31.88	0	400	286
C112	2	0.16	0	3.23	13.42	0	417	285
C113	1.91	0.16	0	3.25	15.43	0	421	290
C114	2.57	0.17	0	3.51	20.16	0	411	231
C115	1.42	0.2	0	1.94	8.54	0	95	51
C116	1.88	0.21	1.51	2.05	14.07	0	97	23
C117	2.3	0.18	2.2	1.75	8.75	0	94	17
C201	2.4	0.25	1.72	2.71	13.35	0	118	37
C202	2.52	0.23	2.18	2.49	19.9	0	117	22
C203	2.13	0.75	0	7.5	71.67	0	100	60
C204	2.49	0.2	2.11	2.01	10.58	0	97	18
C205	2.96	0.3	2.38	3.27	30.06	0	122	18
C206	3.23	0.25	2.64	2.68	13.9	0	112	17
C207	3.28	0.23	2.6	2.47	10.38	0	120	13
C208	3.09	0.27	2.43	2.84	14.78	0	109	22
C209	3.88	0.32	3.08	3.23	17.2	0	105	17
C210	2.83	0.27	2.17	2.83	12.05	0	114	27
C211	1.91	0.33	0	3.22	13.84	0	97	54
C212	3.04	0.28	2.11	3.05	17.12	0	115	16
C213	2.81	0.37	2.41	2.98	13.5	0	66	16
C214	2.32	0.25	2.01	2.24	10.79	0	80	15
C215	4.04	0.39	2.89	4.06	20.08	0	107	20
C216	1.26	0.25	0	2.29	13	0	87	49
C301	1.62	0.21	0.55	2.05	9.17	0	96	48
C302	1.27	0.19	0	1.82	9.95	0	92	49
C303	3.59	0.22	3.36	2.19	10.47	0	96	11
C304	2.22	0.26	1.76	2.74	12.5	0	110	45
C305	2.36	0.23	2.06	2.45	14.67	0	110	28
C306	1.57	0.28	0	2.63	14.79	0	89	53
C307	1.29	0.26	0	2.57	13.29	0	100	67
C308	1.5	0.45	0	4.26	38.59	0	91	58
C309	1.86	0.31	1.43	3.05	24.82	0	99	47
C310	1.66	0.22	0	2.18	11.61	0	99	52
C401	0.85	0.2	0	1.62	7.82	0	67	45
C402	1.55	0.32	0.92	1.92	7.15	0	37	18

Table 14. Statistics for mass by site (ng/m^3). All are PM2.5 except CO24T is PM10.

Site	mean	semean	median	sd	max	min	n	n.bdl
BIBE4	6411.23	938.86	5194.18	3871	17807.75	1781.84	17	0
C024T	10143.66	616.3	9227.94	5879.12	35382.23	-37.01	91	1
C110	6355.3	707.17	6389.03	3316.93	12169.56	125.14	22	0
C111	8485.57	799.61	8175.89	3834.77	18683.48	3299.17	23	0
C112	7059.08	981.25	6445.98	4602.48	21262	110.97	22	0
C113	7984.52	582.65	7677.72	2670.03	12828.81	3945.92	21	0
C114	7247.19	476.78	7565.84	2286.56	11514.09	3505.61	23	0
C115	6535.15	282.94	6116.87	2757.74	21322.56	881.33	95	0
C116	5332.57	321.45	4427.35	3165.93	16524.7	-1342.52	97	0
C117	6858.29	323.4	6559.79	3118.74	14380.32	809.19	93	0
C201	9356.58	525.86	8163.76	5712.29	27152.36	-1745.81	118	0
C202	7657.41	398.47	6093.55	4291.63	20639.42	1432.32	116	0
C203	7817.1	408	6958.33	4059.55	21529.48	1900.97	99	0
C204	8709.68	464.05	7845.7	4546.79	25794.01	614.81	96	0
C205	8570.94	465.17	7751.62	5116.83	41772.84	-90.6	121	0
C206	10063.74	522.4	8661.61	5503.88	35192.7	1837.89	111	0
C207	9306.63	438.22	7896.76	4800.49	23039.43	239.05	120	0
C208	9649.11	517.47	8059.66	5427.3	22675.95	1582.28	110	0
C209	11095.06	532.19	9884.26	5479.19	24173.43	2013.42	106	0
C210	9716.56	624.5	8104.42	6609.05	43057.94	-94.11	112	0
C211	9243.22	517.04	7850.37	5092.26	24234.17	1437.05	97	0
C212	9000.29	470.41	7410.16	5022.56	25366.37	2471	114	0
C213	14119.6	1284.28	10576.05	10745.05	63396.51	1598.84	70	0
C214	10064.83	614.61	8675.27	5497.22	23047.66	666.16	80	0
C215	11384.34	675.6	9174.94	6955.72	34431.34	-30.66	106	0
C216	10665.15	804.8	8762.97	7463.42	52811.16	2482.65	86	0
C301	11874.84	652.44	10330.94	6392.58	34424.94	1494.44	96	0
C302	11443.8	584.22	10384.1	5603.66	29198.66	-536.43	92	0
C303	10524.32	589.35	9256.36	5774.43	30338.63	1344.09	96	0
C304	11017.82	513.44	9855.66	5457.99	28927.71	3500.84	113	0
C305	11012.46	621.93	9560.38	6493.15	33526.93	3032.87	109	0
C306	11646.52	717.11	9704.48	6765.25	39578.02	2486.56	89	0
C307	11621.6	700.52	9278.95	6970.13	34566.35	2196.84	99	0
C308	13107.96	631.65	11967.75	5992.41	30179.42	3742.38	90	0
C309	14363.53	716.44	12413.56	7092.39	34635.68	4643.74	98	0
C310	14797.78	768.45	13597.26	7607.29	36545.45	2969.39	98	0
C401	5668.96	314.98	5448.66	2578.22	13539.42	1420.78	67	0
C402	8872.63	749.76	7315.56	5610.69	29423.22	63.11	56	0

Table 15. Statistics for nickel by site (ng/m^3).

Site	mean	semean	median	sd	max	min	n	n.bdl
BIBE4	0.38	0.38	0	1.56	6.45	0	17	16
C008	0.12	0.1	0	2.01	39.33	0	383	374
C012	0	0	0	0.02	0.22	0	167	166
C024T	0	0	0	0.03	0.23	0	91	89
C110	0.09	0.03	0	0.63	8.04	0	393	378
C111	0.03	0.01	0	0.27	5.1	0	400	385
C112	0.14	0.08	0	1.63	22.43	0	417	409
C113	0.07	0.02	0	0.41	3.81	0	421	398
C114	0.03	0.01	0	0.2	2.46	0	411	394
C115	0	0	0	0	0	0	95	95
C116	0.02	0.01	0	0.09	0.74	0	97	88
C117	0.03	0.02	0	0.15	1.34	0	94	82
C201	0.05	0.01	0	0.15	0.87	0	118	99
C202	0.03	0.01	0	0.09	0.5	0	117	99
C203	0	0	0	0	0	0	100	100
C204	0.02	0.01	0	0.06	0.39	0	97	88
C205	0.04	0.01	0	0.15	0.81	0	122	112
C206	0.02	0.01	0	0.09	0.48	0	112	103
C207	0.05	0.02	0	0.18	1.29	0	120	102
C208	0.06	0.02	0	0.16	0.99	0	109	91
C209	0.01	0	0	0.04	0.34	0	105	101
C210	0.29	0.09	0	0.93	6.96	0	114	83
C211	0.05	0.02	0	0.16	0.85	0	97	84
C212	0.08	0.02	0	0.16	0.74	0	115	85
C213	0.17	0.04	0	0.36	1.87	0	66	48
C214	0.09	0.02	0	0.16	0.63	0	80	57
C215	0.05	0.02	0	0.16	0.94	0	107	92
C216	0.24	0.09	0	0.87	5.55	0	87	75
C301	0	0	0	0	0	0	96	96
C302	0.06	0.06	0	0.59	5.63	0	92	90
C303	0.17	0.07	0	0.71	5.01	0	96	81
C304	0.05	0.02	0	0.2	1.64	0	110	94
C305	0.07	0.02	0	0.17	1.17	0	110	84
C306	0.05	0.02	0	0.19	1.09	0	89	81
C307	0.13	0.04	0	0.36	2.63	0	100	79
C308	0.08	0.02	0	0.19	0.87	0	91	70
C309	0.03	0.03	0	0.27	2.67	0	99	98
C310	0.09	0.06	0	0.63	4.76	0	99	97
C401	0.1	0.03	0	0.25	1.05	0	67	51
C402	0.04	0.04	0	0.23	1.41	0	37	36

Table 16. Statistics for potassium by site (ng/m^3).

Site	mean	semean	median	sd	max	min	n	n.bdl
BIBE4	60.04	7.49	62.73	30.87	100.61	12.75	17	0
C008	54.14	2.41	42.42	47.1	429.67	0	383	12
C012	44.34	3.14	32.62	40.55	238.46	0	167	3
C024T	99.9	8.49	81.19	81.02	610.58	0	91	1
C110	57.33	2.25	46.51	44.65	346.62	0	393	18
C111	44.55	1.65	36.28	33.08	251.13	0	400	14
C112	53.86	1.89	42.9	38.63	294.13	0	417	17
C113	56.48	2.13	44.12	43.79	310.69	0	421	21
C114	55.77	2.1	43.98	42.62	356.77	0	411	8
C115	51.42	3.68	39.38	35.83	204.31	8.9	95	0
C116	36.85	3.26	26.42	32.11	160.91	6.53	97	0
C117	52.65	3.62	42.7	35.09	162.53	9.32	94	0
C201	67.12	5.59	42.56	60.72	317.72	3.87	118	0
C202	61.13	4.93	41.98	53.35	332.89	8.29	117	0
C203	58.72	4.51	48.3	45.06	265.48	14.56	100	0
C204	60.27	5.64	39.73	55.5	380.53	10.12	97	0
C205	61.65	6.43	44.4	70.97	663.36	0	122	1
C206	70.76	5.73	49.86	60.67	328.94	5.72	112	0
C207	79.19	5.82	59.75	63.75	289.01	10.52	120	0
C208	76.79	8.23	49.83	85.9	661.07	0	109	2
C209	100.01	7.41	74.76	75.9	319.79	12.84	105	0
C210	77.66	7.18	51.78	76.71	335.26	0	114	2
C211	73.24	7.04	51.03	69.37	356.14	12.05	97	0
C212	81.08	6.58	54.66	70.6	362.23	18.3	115	0
C213	106.26	10.87	68.7	88.29	381.05	10.14	66	0
C214	75.97	8.91	50.39	79.67	409.96	0	80	1
C215	100.23	10.01	56.1	103.52	556.19	17.29	107	0
C216	71.4	7	47.9	65.28	400.26	0	87	4
C301	60.61	3.23	56.17	31.61	184.36	13.05	96	0
C302	68.16	4.05	59.98	38.8	229.18	4.56	92	0
C303	67.99	3.83	58.33	37.5	176.55	18.74	96	0
C304	77.74	6.15	59.86	64.53	372.6	12.54	110	0
C305	71.51	6.65	46.96	69.79	440.57	18.17	110	0
C306	87.74	10.37	54.94	97.86	612.25	18.09	89	0
C307	94.45	12.79	57.56	127.92	1008.43	16.54	100	0
C308	89.7	5.25	79.36	50.04	375.66	31.06	91	0
C309	105.85	5.69	90.17	56.62	301.22	31.47	99	0
C310	83.81	5.44	73.57	54.1	384.33	31.3	99	0
C401	35.1	2.53	29.61	20.72	96.31	9.17	67	0
C402	49.41	7.44	41.52	45.23	273.87	0	37	1

Table 17. Statistics for rubidium by site (ng/m^3).

Site	mean	semean	median	sd	max	min	n	n.bdl
BIBE4	0.14	0.03	0.11	0.12	0.36	0	17	4
C008	0.18	0.02	0	0.3	2.42	0	383	246
C012	0.14	0.02	0	0.23	1.23	0	167	105
C024T	0.26	0.04	0.17	0.41	2.94	0	91	36
C110	0.19	0.02	0	0.4	6.21	0	393	242
C111	0.18	0.01	0	0.26	1.69	0	400	238
C112	0.17	0.01	0	0.25	1.27	0	417	253
C113	0.16	0.01	0	0.27	1.87	0	421	273
C114	0.09	0.01	0	0.19	1.42	0	411	319
C115	0.06	0.01	0	0.12	0.63	0	95	68
C116	0.04	0.01	0	0.12	0.85	0	97	85
C117	0.08	0.01	0	0.14	0.55	0	94	62
C201	0.12	0.02	0	0.24	1.14	0	118	83
C202	0.12	0.02	0	0.24	1.46	0	117	78
C203	0.07	0.02	0	0.19	1.05	0	100	80
C204	0.07	0.02	0	0.23	1.41	0	97	80
C205	0.09	0.02	0	0.25	2.1	0	122	91
C206	0.13	0.02	0	0.26	1.38	0	112	78
C207	0.15	0.03	0	0.28	1.12	0	120	82
C208	0.14	0.03	0	0.29	1.26	0	109	76
C209	0.2	0.03	0	0.32	1.11	0	105	65
C210	0.15	0.03	0	0.31	1.26	0	114	77
C211	0.12	0.03	0	0.32	1.55	0	97	76
C212	0.15	0.03	0	0.32	1.7	0	115	77
C213	0.08	0.03	0	0.24	1.12	0	66	57
C214	0.1	0.03	0	0.29	1.28	0	80	66
C215	0.22	0.05	0	0.51	3.15	0	107	77
C216	0.08	0.02	0	0.21	1.04	0	87	69
C301	0.01	0	0	0.05	0.22	0	96	87
C302	0.03	0.01	0	0.08	0.49	0	92	77
C303	0.06	0.01	0	0.13	0.65	0	96	77
C304	0.11	0.02	0	0.25	1.16	0	110	84
C305	0.1	0.03	0	0.28	1.83	0	110	88
C306	0.13	0.04	0	0.36	2.15	0	89	66
C307	0.07	0.02	0	0.19	1.13	0	100	79
C308	0.18	0.02	0.17	0.16	0.87	0	91	26
C309	0.1	0.02	0	0.18	0.77	0	99	68
C310	0.07	0.01	0	0.13	0.55	0	99	70
C401	0.01	0.01	0	0.05	0.29	0	67	63
C402	0	0	0	0	0	0	37	37

Table 18. Statistics for selenium by site (ng/m^3).

Site	mean	semean	median	sd	max	min	n	n.bdl
BIBE4	0.14	0.03	0.1	0.13	0.36	0	17	4
C008	0.12	0.01	0	0.19	1.57	0	383	246
C012	0.13	0.01	0	0.19	0.98	0	167	86
C024T	0.21	0.02	0.18	0.2	0.94	0	91	22
C110	0.15	0.01	0	0.26	1.87	0	393	242
C111	0.17	0.01	0	0.24	1.44	0	400	215
C112	0.15	0.01	0	0.21	1.13	0	417	232
C113	0.22	0.01	0.21	0.23	1.33	0	421	167
C114	0.25	0.01	0.24	0.23	1.47	0	411	127
C115	0.21	0.01	0.19	0.14	0.93	0	95	5
C116	0.18	0.01	0.16	0.1	0.59	0	97	3
C117	0.23	0.02	0.2	0.15	0.88	0	94	1
C201	0.41	0.03	0.31	0.27	1.34	0	118	2
C202	0.29	0.02	0.22	0.19	0.92	0	117	1
C203	0.36	0.02	0.27	0.25	1.23	0	100	1
C204	0.33	0.02	0.3	0.17	0.78	0	97	1
C205	0.33	0.02	0.3	0.18	0.97	0	122	1
C206	0.42	0.02	0.38	0.26	1.76	0	112	4
C207	0.41	0.02	0.36	0.23	1.32	0.12	120	0
C208	0.34	0.02	0.28	0.22	1.08	0	109	3
C209	0.33	0.02	0.29	0.22	1.27	0	105	2
C210	0.33	0.02	0.25	0.23	1.23	0	114	4
C211	0.33	0.02	0.28	0.22	1.28	0	97	2
C212	0.38	0.02	0.29	0.26	1.5	0	115	1
C213	0.75	0.1	0.45	0.83	4.6	0.08	66	0
C214	0.48	0.03	0.44	0.27	1.37	0.03	80	0
C215	0.51	0.04	0.4	0.42	3.55	0.11	107	0
C216	0.5	0.03	0.41	0.32	2.15	0.09	87	0
C301	0.87	0.05	0.78	0.52	2.23	0	96	1
C302	1.02	0.06	0.94	0.6	3.01	0	92	3
C303	0.61	0.04	0.48	0.41	1.84	0.1	96	0
C304	0.67	0.04	0.51	0.45	2.14	0.17	110	0
C305	0.61	0.05	0.42	0.54	2.92	0	110	1
C306	0.57	0.05	0.46	0.48	2.62	0	89	1
C307	0.48	0.03	0.38	0.33	2.04	0	100	1
C308	0.38	0.03	0.36	0.25	1.36	0.05	91	0
C309	0.52	0.04	0.4	0.42	2.97	0.05	99	0
C310	0.82	0.07	0.63	0.68	3.11	0	99	1
C401	0.21	0.02	0.17	0.15	0.97	0	67	4
C402	0.48	0.08	0.43	0.47	1.51	0	37	12

Table 19. Statistics for silicon by site (ng/m^3).

Site	mean	semean	median	sd	max	min	n	n.bdl
BIBE4	463.82	60.39	495.39	249	921.31	89.6	17	0
C008	273.36	23.54	122.76	460.71	4148.4	0	383	8
C012	250.53	30.99	102.02	400.51	2234.68	6.31	167	0
C024T	744.3	74.56	579.08	711.29	5429.56	24.63	91	0
C110	317.47	20.34	171.18	403.17	2619.57	0	393	3
C111	219.23	15.67	99.92	313.39	2226.18	0	400	2
C112	318.85	17.64	187.01	360.23	2351.03	6.57	417	0
C113	314.71	19.15	166.97	392.95	2836.06	17.97	421	0
C114	304.81	19.67	179.42	398.72	2785.27	0	411	2
C115	294.74	26.95	212.07	262.67	1371.61	36.45	95	0
C116	214.73	30.32	97.96	298.57	1547.52	23.51	97	0
C117	326.36	31.49	220.67	305.32	1480.22	20.68	94	0
C201	387.85	54.96	121.25	596.99	3137.9	16.43	118	0
C202	387.2	53.35	134.48	577.04	3341.01	26.19	117	0
C203	290.99	45.26	152.68	452.64	2725.05	44.87	100	0
C204	364.5	58.18	177.08	573.03	3916.58	63.23	97	0
C205	419.23	64	166.02	706.86	6295.5	7.64	122	0
C206	474.45	61.69	187.24	652.82	3428.59	0	112	1
C207	495.7	60.93	160.98	667.43	3052.43	45.03	120	0
C208	428.78	64.14	137.32	669.65	2929.27	0	109	3
C209	666.05	78.48	275.28	804.13	3199.91	50.29	105	0
C210	484.93	73.71	147.68	787	3466.91	0	114	1
C211	396.96	75.64	120.98	744.95	3566.67	33.5	97	0
C212	513.27	74.07	107	794.32	3825.81	15.6	115	0
C213	372.5	82.14	135	667.35	3257.19	15.49	66	0
C214	339.63	85.53	122.79	764.96	3702.16	0	80	1
C215	634.75	98.66	203.52	1020.51	4669.11	34.79	107	0
C216	280.46	58.04	141.51	541.33	3688.64	0	87	4
C301	175.35	10.73	151.04	105.08	693.82	20.86	96	0
C302	195.43	19.93	157.94	191.14	1389.44	0	92	1
C303	276.27	27.17	187.18	266.25	1452.74	45.27	96	0
C304	413.78	64.03	153.61	671.58	3782.02	23.23	110	0
C305	329.78	60.73	116.6	636.98	3770.77	37.77	110	0
C306	421.42	82.82	164.23	781.32	5288.75	20.7	89	0
C307	280.13	42.19	152.99	421.87	2917.87	32.25	100	0
C308	198.46	25.66	126.23	244.77	1832.07	31.8	91	0
C309	225.81	26.96	149.42	268.3	1810.28	34.78	99	0
C310	207.13	23.15	146.69	230.36	1642.31	31.87	99	0
C401	155.54	20.7	95.45	169.46	923.64	25.09	67	0
C402	123.94	13.55	98.97	82.4	448.88	0	37	1

Table 20. Statistics for sodium by site (ng/m^3).

Site	mean	semean	median	sd	max	min	n	n.bdl
BIBE4	139	26.61	132.55	109.7	358.35	0	17	3
C008	72.27	4.23	58.84	82.74	451.68	0	383	171
C012	61.11	5.81	28.16	75.12	346.97	0	167	78
C024T	123.77	15.83	73.78	150.99	708.14	0	91	38
C110	65.58	4.23	29.01	83.89	488.52	0	393	192
C111	62.06	3.79	0	75.75	325.3	0	400	204
C112	56.81	3.77	0	76.99	324.35	0	417	241
C113	60.23	4.48	0	92	825.6	0	421	234
C114	58.28	4.07	0	82.48	549.69	0	411	223
C115	23.65	4.46	0	43.49	175.57	0	95	68
C116	43.73	4.99	30.68	49.18	211.95	0	97	34
C117	51.39	6.23	29.78	60.45	255.73	0	94	43
C201	155.3	14.56	139.91	158.2	699.57	0	118	27
C202	127.2	12.49	94.04	135.14	611.72	0	117	33
C203	75.87	10.32	21.76	103.21	523.72	0	100	48
C204	108.65	10.28	117.09	101.29	463.05	0	97	30
C205	121.57	11.56	103.25	127.72	646.77	0	122	35
C206	182.62	21.4	147.16	226.51	1687.9	0	112	25
C207	188.07	17.17	156.63	188.07	921.02	0	120	27
C208	155.64	14.66	142.92	153.08	684.65	0	109	30
C209	189.73	21.21	136.01	217.36	1048.7	0	105	27
C210	207.44	21.21	165	226.44	1255.34	0	114	19
C211	157.65	13.75	162.27	135.46	679.7	0	97	24
C212	344.99	29.79	263.01	319.46	1989.14	0	115	8
C213	864.5	91.34	603.62	742.08	3379.16	0	66	2
C214	180.48	14.81	183.44	132.45	760.98	0	80	9
C215	253.06	30.61	191.5	316.68	2010.78	0	107	20
C216	115.47	14.09	107.88	131.47	700.84	0	87	28
C301	69.62	9.17	0	89.89	299.63	0	96	51
C302	84.64	11.5	29.76	110.33	581.01	0	92	44
C303	79.37	10.33	0	101.2	414.42	0	96	49
C304	151.7	15.61	131.88	163.71	827.44	0	110	39
C305	156.47	20.19	135.22	211.76	1412.47	0	110	31
C306	321.53	32.47	268.62	306.32	1923.3	0	89	16
C307	192.97	19.37	175.3	193.69	936.92	0	100	31
C308	90.5	10.5	81.22	100.13	555.58	0	91	36
C309	107.79	15.38	80.12	153.02	1158.92	0	99	34
C310	74.58	9.09	31.03	90.45	365.65	0	99	47
C401	36.01	6.25	0	51.13	209.35	0	67	38
C402	43.25	10.05	0	61.16	243.52	0	37	20

Table 21. Statistics for sulfur by site (ng/m^3).

Site	mean	semean	median	sd	max	min	n	n.bdl
BIBE4	457.93	71.43	357.13	294.51	1046.94	134.34	17	0
C008	936.16	35.82	690.97	700.92	3757.51	0	383	3
C012	883.68	48.58	641.12	627.76	2979.07	0	167	1
C024T	787.87	65.06	525.99	620.61	2524.67	0	91	3
C110	890.72	34.21	664.9	678.11	3934.25	0	393	1
C111	926.2	34.19	692.03	683.75	3506.92	89.18	400	0
C112	856.48	30.78	645.6	628.47	3536.06	3.74	417	0
C113	848.33	30.06	673.59	616.77	3829.3	95.02	421	0
C114	1011.93	35.65	793.38	722.75	4801.56	0	411	1
C115	648.76	33.87	576.09	330.09	1787.71	37.76	95	0
C116	706.67	42.21	593.17	415.7	1783.14	100.33	97	0
C117	768.36	51.18	594.03	496.16	2166.67	61.03	94	0
C201	997.77	61.66	829.3	669.83	3345.86	0	118	1
C202	840.24	55.86	635.6	604.24	3516.9	113.54	117	0
C203	917.36	62.08	722.84	620.78	3209.97	109.93	100	0
C204	1017	61.89	877.19	609.59	2527.21	8.35	97	0
C205	972.31	54.14	819.4	598.01	2654.29	5.07	122	0
C206	1119.81	68.01	930.44	719.72	4189.33	5.06	112	0
C207	976.49	60.47	750.06	662.46	3489.67	108.97	120	0
C208	956.27	68.02	730.53	710.1	3339.05	0	109	2
C209	904.58	58.35	733.02	597.92	2798.38	84.29	105	0
C210	937.39	62.53	670.94	667.65	3002	0	114	1
C211	1001.04	57.78	842.37	569.08	2571.31	172.45	97	0
C212	934.49	57.59	776.83	617.61	3455.29	193.8	115	0
C213	1426.74	134.62	1051.9	1093.62	5602.78	144.43	66	0
C214	1052.63	70.46	869.24	630.2	2632.73	8.68	80	0
C215	1031.56	72.44	784.58	749.33	3622.71	200.75	107	0
C216	1139.23	88.36	913.87	824.19	3881.2	0	87	4
C301	1337.35	96.17	1053.1	942.23	4917.44	113.63	96	0
C302	1392.99	90.23	1171.1	865.49	4565.75	0	92	1
C303	1154.25	83.86	980.55	821.62	4378.04	98.37	96	0
C304	1189.84	74.53	994.96	781.7	3765.54	179.7	110	0
C305	1149.4	68.92	942.14	722.84	3639.43	194.89	110	0
C306	1187.47	78.55	1034.5	741.07	3857.09	201.65	89	0
C307	1288.84	84.31	1035.9	843.1	3684.36	115.88	100	0
C308	1281.24	80.76	1137.88	770.41	3985.79	205.36	91	0
C309	1327.4	84.15	1105.98	837.27	4073.99	170.84	99	0
C310	1447.27	96.1	1301.6	956.2	4931.65	152.92	99	0
C401	653.71	45.51	543.77	372.5	1812.16	89.14	67	0
C402	1030.09	131.94	817.31	802.57	3878.85	0	37	1

Table 22. Statistics for strontium by site (ng/m^3).

Site	mean	semean	median	sd	max	min	n	n.bdl
BIBE4	0.84	0.12	0.9	0.51	1.94	0	17	1
C008	0.3	0.04	0	0.74	7.12	0	383	227
C012	0.31	0.04	0.11	0.56	2.78	0	167	78
C024T	1.52	0.15	1.22	1.39	10.7	0	91	3
C110	0.4	0.04	0	0.74	7.26	0	393	203
C111	0.27	0.03	0	0.51	3.77	0	400	233
C112	0.42	0.03	0.23	0.66	4.04	0	417	180
C113	0.59	0.04	0.39	0.75	4.72	0	421	118
C114	0.52	0.03	0.41	0.61	4.51	0	411	79
C115	0.71	0.07	0.46	0.69	3.26	0	95	1
C116	0.43	0.05	0.29	0.51	2.77	0	97	14
C117	0.79	0.06	0.57	0.59	2.81	0.09	94	0
C201	0.86	0.1	0.44	1.05	5.23	0	118	6
C202	0.83	0.09	0.43	0.95	5.61	0	117	2
C203	0.48	0.07	0.29	0.7	4.39	0	100	5
C204	0.82	0.09	0.58	0.9	5.46	0.11	97	0
C205	0.9	0.1	0.56	1.12	10.05	0	122	2
C206	1.03	0.1	0.66	1.01	5.4	0	112	2
C207	1.14	0.11	0.62	1.17	4.92	0	120	1
C208	1.03	0.1	0.58	1.07	4.51	0	109	1
C209	1.43	0.13	0.97	1.3	5.32	0.21	105	0
C210	1.1	0.12	0.58	1.32	6.17	0	114	3
C211	0.97	0.11	0.57	1.07	4.93	0.06	97	0
C212	1.13	0.12	0.52	1.3	6.01	0	115	2
C213	1.38	0.16	0.92	1.31	5.15	0.2	66	0
C214	0.71	0.13	0.39	1.12	5.26	0	80	4
C215	1.28	0.18	0.55	1.86	11.05	0	107	1
C216	0.49	0.08	0.27	0.79	5.13	0	87	5
C301	0.46	0.03	0.41	0.25	1.14	0	96	5
C302	0.36	0.03	0.3	0.32	2.41	0	92	5
C303	0.61	0.04	0.52	0.39	2.01	0	96	2
C304	0.92	0.09	0.56	0.99	5.37	0	110	2
C305	0.77	0.12	0.4	1.28	7.52	0	110	2
C306	0.82	0.12	0.44	1.16	7.14	0.11	89	0
C307	0.74	0.08	0.46	0.78	4.21	0	100	1
C308	0.4	0.05	0.29	0.49	3.77	0	91	7
C309	0.62	0.13	0.3	1.26	10.45	0	99	4
C310	0.47	0.05	0.29	0.53	2.57	0	99	2
C401	0.41	0.04	0.34	0.36	1.6	0	67	6
C402	0.17	0.03	0.13	0.18	0.54	0	37	15

Table 23. Statistics for titanium by site (ng/m^3).

Site	mean	semean	median	sd	max	min	n	n.bdl
BIBE4	15.91	2.05	16.42	8.46	30.72	3.43	17	0
C008	14.94	0.9	11.22	17.69	133.75	0	383	80
C012	11.55	1.1	6.95	14.16	91.96	0	167	22
C024T	17.38	1.5	14.13	14.31	90.98	0	91	1
C110	15.33	0.82	11.17	16.22	108.19	0	393	76
C111	12.2	0.66	9.34	13.21	93.68	0	400	92
C112	12.97	0.64	10.25	13.07	75.64	0	417	82
C113	13.61	0.7	10.61	14.31	85.67	0	421	87
C114	14.12	0.69	10.5	14.01	92.13	0	411	46
C115	7.88	0.7	5.96	6.84	40.51	0	95	3
C116	8.32	0.99	5.1	9.73	51.24	0	97	6
C117	9.74	0.79	7.54	7.67	45.24	1.25	94	0
C201	16.69	1.82	8.26	19.73	106.32	0	118	2
C202	14.54	1.69	7.09	18.3	113.67	0	117	1
C203	10.5	1.43	6.07	14.29	85.24	0	100	3
C204	14.16	1.79	8.23	17.64	121.09	2.12	97	0
C205	18.07	2.75	9.19	30.41	242.1	0	122	4
C206	18.44	1.87	10.81	19.84	105.69	0	112	2
C207	17.96	1.88	9.09	20.62	93.26	0	120	1
C208	15.45	1.93	7.91	20.18	91.6	0	109	6
C209	21.89	2.4	10.62	24.56	100.64	0	105	1
C210	18.63	2.34	8.07	24.94	109.89	0	114	5
C211	14.42	2.33	6.05	22.95	113.67	0	97	4
C212	20.13	2.33	9.4	24.93	120.08	0	115	3
C213	16.83	2.85	8.3	23.12	110.97	0	66	4
C214	14.87	2.64	7.46	23.64	119.31	0	80	2
C215	23.47	3.35	9.44	34.66	175.3	0	107	1
C216	11.45	1.91	6.21	17.85	117.16	0	87	7
C301	8.27	0.54	7.17	5.29	28.59	0	96	2
C302	9.32	0.77	7.82	7.39	48.01	0	92	3
C303	11.67	0.93	8.68	9.09	47.65	1.85	96	0
C304	15.83	2.04	7.74	21.44	115.24	0	110	3
C305	15.81	2.06	8.52	21.63	133.45	0	110	1
C306	17.03	2.66	9.13	25.07	164.59	0	89	4
C307	10.14	1.54	5.92	15.35	99.6	0	100	20
C308	10.05	0.99	7.97	9.44	65.15	0	91	4
C309	10.57	1.01	8.16	10.03	60.21	0	99	5
C310	11.4	1	8.36	9.93	60.64	0	99	1
C401	5.86	0.69	4.77	5.66	28.69	0	67	9
C402	8.1	1.25	6.07	7.6	41.62	0	37	4

Table 24. Statistics for vanadium by site (ng/m^3).

Site	mean	semean	median	sd	max	min	n	n.bdl
BIBE4	1.83	0.34	1.59	1.41	5.39	0	17	3
C008	3.33	0.21	0	4.11	24.95	0	383	198
C012	2.04	0.22	1.8	2.83	19	0	167	76
C024T	1.79	0.28	0	2.69	17.55	0	91	48
C110	2.99	0.22	0	4.41	37.02	0	393	209
C111	3.05	0.22	0	4.42	34.95	0	400	219
C112	2.8	0.19	0	3.79	22.36	0	417	235
C113	2.57	0.17	0	3.56	19.05	0	421	247
C114	2.82	0.18	0	3.56	17.88	0	411	214
C115	1.35	0.2	0.91	1.95	12.89	0	95	46
C116	1.1	0.15	0.92	1.44	6.77	0	97	45
C117	0.77	0.13	0	1.22	5.96	0	94	60
C201	1.31	0.29	0	3.14	28.35	0	118	73
C202	1.23	0.17	0	1.87	9.66	0	117	62
C203	0.67	0.12	0	1.15	5.78	0	100	64
C204	0.85	0.19	0	1.88	11.08	0	97	68
C205	1	0.18	0	1.94	12.93	0	122	79
C206	0.88	0.16	0	1.72	8.51	0	112	79
C207	1.29	0.19	0	2.09	11.99	0	120	67
C208	1.13	0.16	0	1.68	7.75	0	109	63
C209	2.06	0.29	1.17	2.94	12.55	0	105	52
C210	1.62	0.21	0.88	2.23	9.32	0	114	56
C211	1.88	0.21	1.56	2.11	10.23	0	97	35
C212	1.89	0.25	1.12	2.64	13.06	0	115	54
C213	1.4	0.23	0.64	1.87	10.15	0	66	33
C214	1.39	0.24	0	2.16	12.13	0	80	42
C215	1.64	0.26	0.88	2.7	18.87	0	107	53
C216	0.93	0.17	0	1.55	9.01	0	87	51
C301	0.45	0.1	0	1.02	7.2	0	96	74
C302	0.69	0.14	0	1.31	5.83	0	92	66
C303	0.66	0.14	0	1.33	6.64	0	96	70
C304	1.03	0.15	0	1.56	6.49	0	110	67
C305	0.79	0.13	0	1.35	8.15	0	110	70
C306	1.33	0.18	1.05	1.68	8.42	0	89	43
C307	1.8	0.21	1.58	2.08	9.31	0	100	45
C308	1.3	0.18	0	1.69	8.12	0	91	47
C309	0.94	0.14	0	1.38	7.31	0	99	57
C310	0.49	0.09	0	0.91	4.36	0	99	73
C401	1.62	0.25	1.15	2.06	8.09	0	67	29
C402	0.93	0.29	0	1.75	7.18	0	37	26

Table 25. Statistics for zinc by site (ng/m^3).

Site	mean	semean	median	sd	max	min	n	n.bdl
BIBE4	1.65	0.25	1.36	1.04	3.74	0.45	17	0
C008	2.94	0.14	2.32	2.71	20.39	0	383	47
C012	2.64	0.17	2.23	2.23	16.33	0	167	7
C024T	2.7	0.22	2.52	2.07	13.4	0	91	3
C110	2.92	0.14	2.37	2.86	32.81	0	393	42
C111	2.43	0.09	2.12	1.86	12.95	0	400	43
C112	2.69	0.11	2.33	2.25	27.85	0	417	39
C113	2.41	0.1	2.2	1.97	22.06	0	421	57
C114	2.63	0.09	2.33	1.81	9.52	0	411	45
C115	1.99	0.12	1.74	1.16	6.62	0.25	95	0
C116	1.65	0.12	1.36	1.18	8.91	0	97	3
C117	2.07	0.2	1.78	1.95	17.27	0	94	2
C201	3.23	0.18	2.8	1.94	7.97	0	118	1
C202	2.34	0.12	2.03	1.3	5.77	0.3	117	0
C203	5.1	2.82	1.92	28.22	283.98	0.19	100	0
C204	2.48	0.16	2.04	1.59	10.97	0.27	97	0
C205	2.82	0.41	1.96	4.51	47.99	0.13	122	0
C206	2.99	0.2	2.45	2.17	17.67	0	112	1
C207	3.01	0.19	2.51	2.12	16.21	0.53	120	0
C208	3.02	0.16	2.69	1.72	9.74	0.21	109	0
C209	3.69	0.22	3.11	2.27	13.24	0.52	105	0
C210	2.94	0.21	2.4	2.26	11.76	0	114	5
C211	2.95	0.22	2.38	2.12	10.62	0.26	97	0
C212	2.88	0.2	2.17	2.19	10.77	0	115	2
C213	5.84	0.79	3.98	6.44	32.77	0.43	66	0
C214	4.11	0.33	3.36	2.97	13.37	0	80	1
C215	3.3	0.21	2.89	2.21	10.7	0.3	107	0
C216	4.23	0.32	3.88	2.99	17.69	0.49	87	0
C301	7.76	0.36	7.18	3.51	17.99	1.47	96	0
C302	8.44	0.66	7.2	6.3	39.38	0	92	1
C303	5.09	0.35	4.18	3.39	16.9	0.97	96	0
C304	5.59	0.43	4.26	4.48	27.26	1.1	110	0
C305	5.43	0.4	4.73	4.24	26.61	0.79	110	0
C306	4.35	0.36	3.44	3.38	12.09	0	89	1
C307	5.61	0.51	3.76	5.13	19.69	0	100	1
C308	5.89	0.34	5.14	3.21	19.11	1.21	91	0
C309	8.49	0.53	8.01	5.24	45.99	1.5	99	0
C310	8.27	0.39	8	3.93	26.98	1.86	99	0
C401	1.85	0.2	1.32	1.68	11.61	0	67	3
C402	3.38	0.59	2.1	3.62	13.09	0	37	12

Appendix 8c. Airmass Transport to Big Bend, Texas, during Each Particulate Sulfur Episode

The following figures present the decomposed residence time analysis for the seven particulate episodes at Big Bend NP. All residence time analyses used 10-day airmass histories generated by the CAPITA Monte Carlo model driven by either the EDAS/FNL or 36 km MM5 meteorological data. See section 8.1.3.1 for a detailed description of the airmass histories used in this analysis.

July 22 – July 31

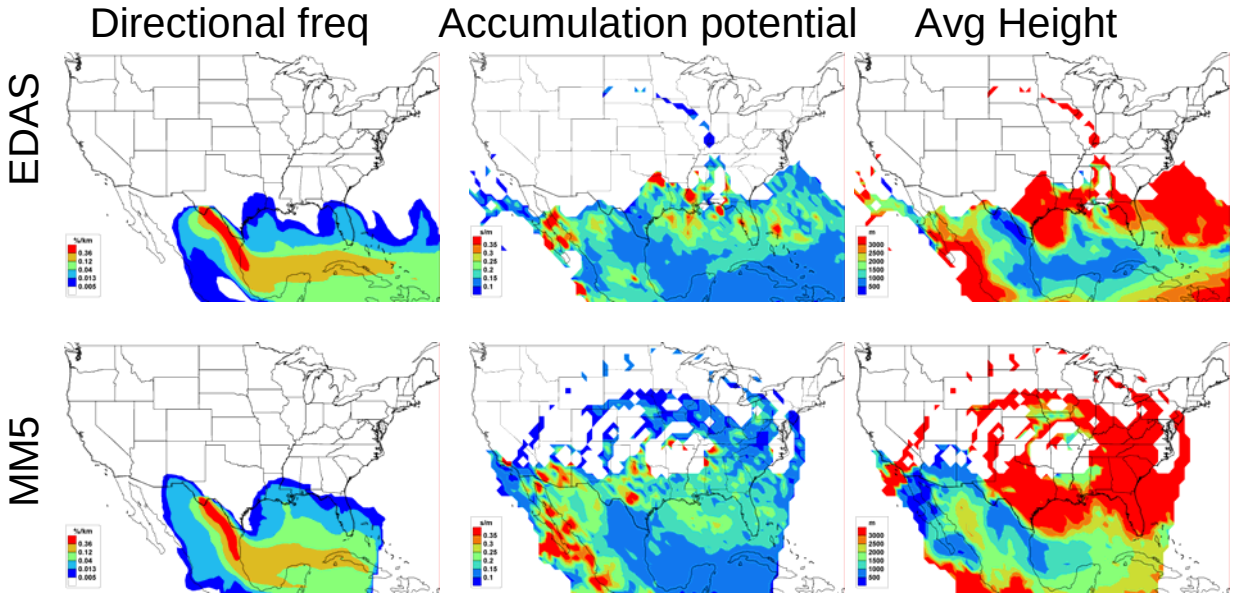

August 16 – August 23

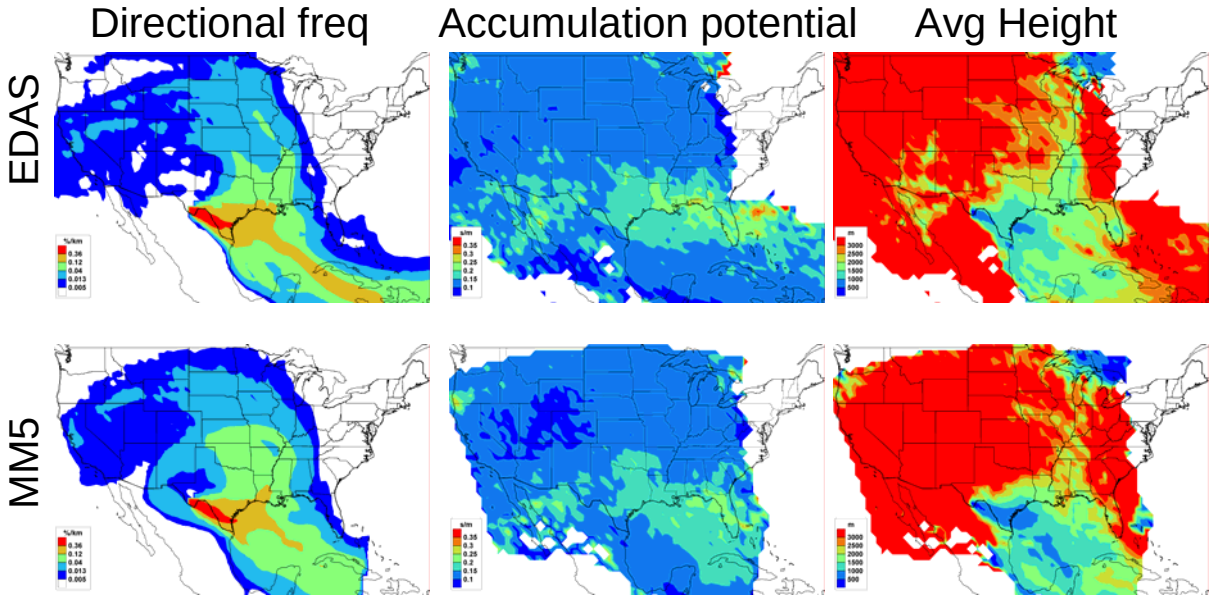

August 30 – September 4

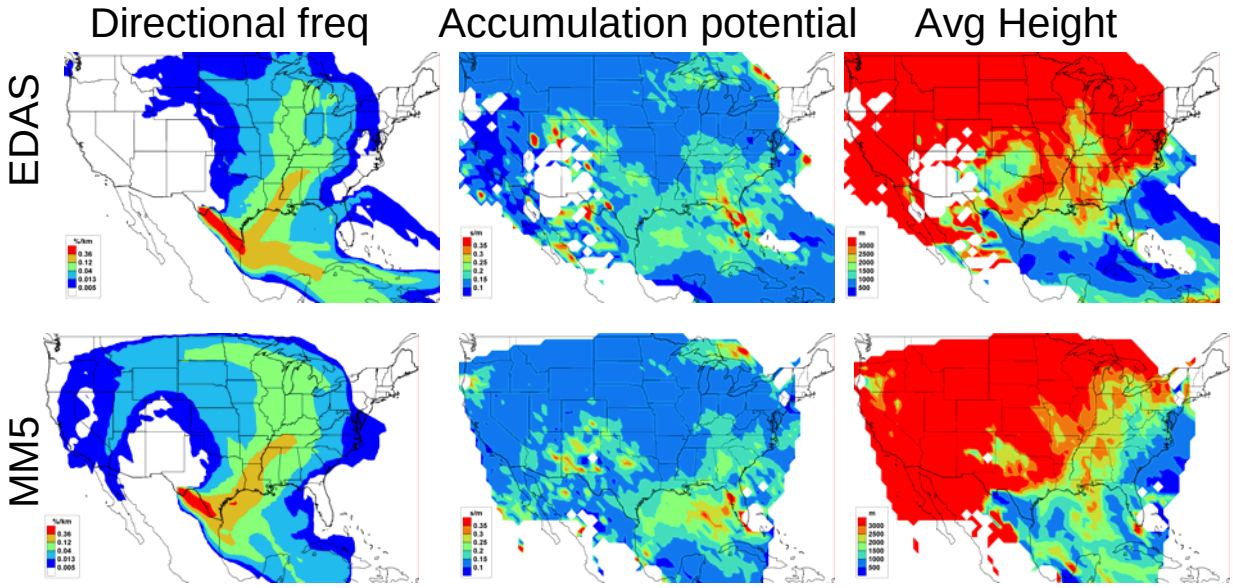

September 12 – September 17

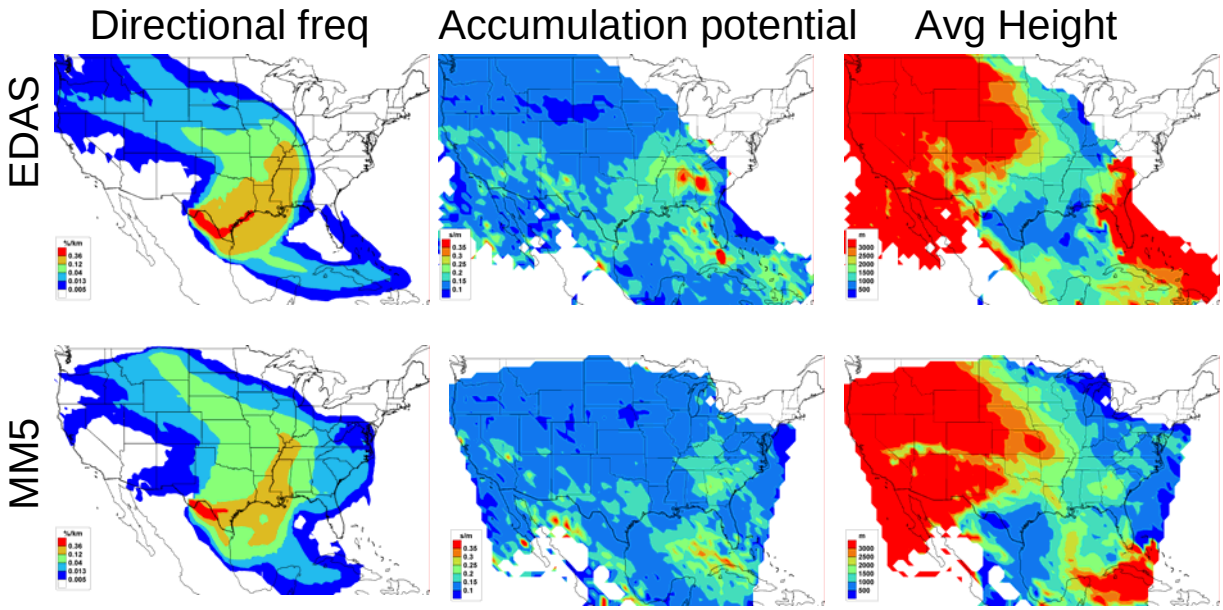

September 25 - September 28

Directional freq | Accumulation potential | Avg Height

EDAS

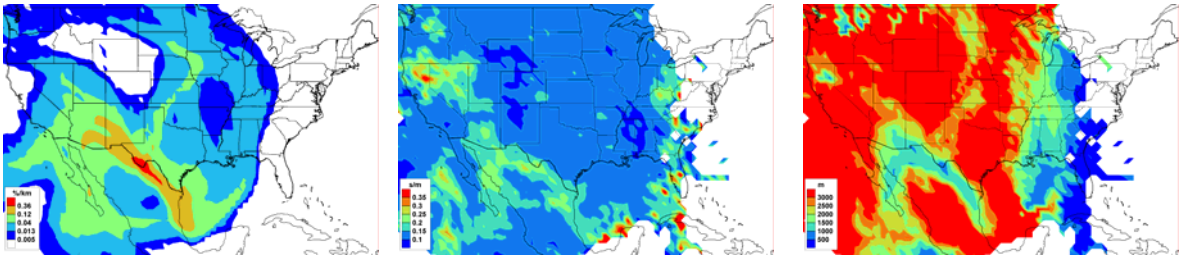

MM5

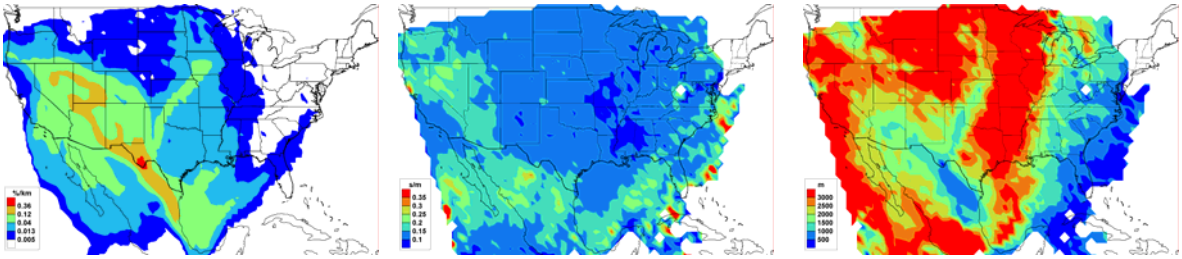

October 3 – October 7

Directional freq | Accumulation potential | Avg Height

EDAS

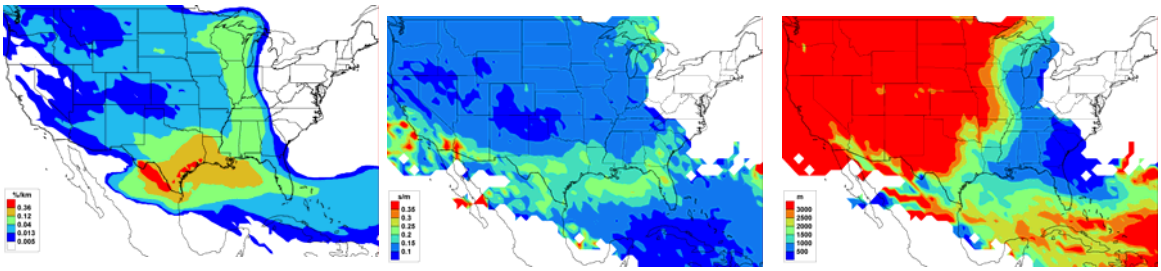

MM5

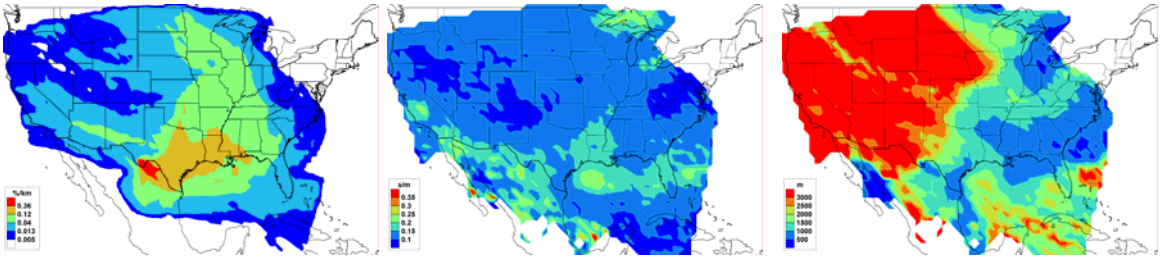

October 11 - October 16

Directional freq Accumulation potential Avg Height

EDAS

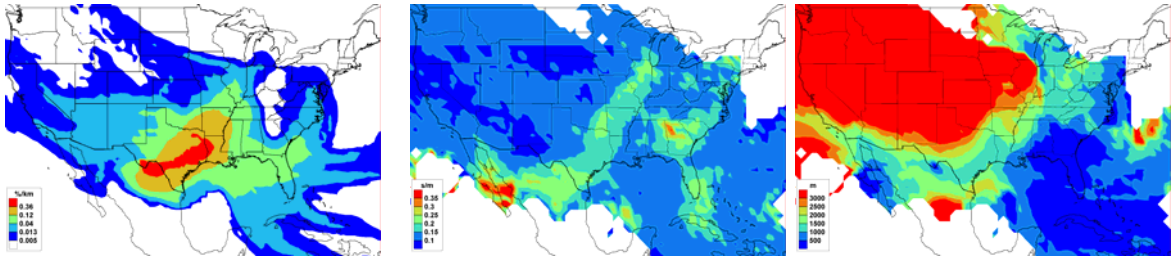

MM5

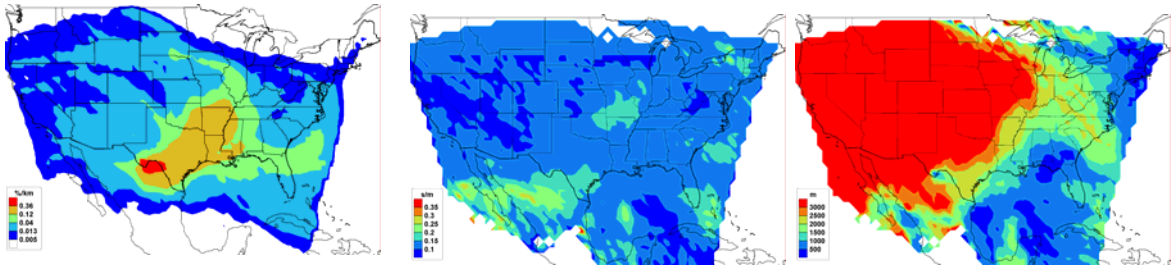

List of Acronyms and Abbreviations

#	number
$(NH_4)_2SO_4$	ammonium sulfate
µCB-IV	Micro Carbon Bond IV mechanism
$\mu g/m^3$	micrograms per cubic meter
µm	micrometer
σ_g	geometric standard deviation of particle diameters
σ_z	standard deviation of the vertical dispersion of a Gaussian plume
Δx	horizontal grid spacing
2-D	two-dimensional
3-D	three-dimensional
ACARS	Aircraft Communications Addressing and Reporting System
AER	Atmospheric and Environmental Research
AGL	above ground level
AIM	Aerosol Inorganics Model
Al	aluminum
AR	Arkansas
ARL	Air Resource Laboratory
As	Arsenic
ATAD	Atmospheric Transport and Dispersion Model
Avg.	Average
b_{abs}	light absorption coefficient
BBNP	Big Bend National Park
BC	Boundary Conditions
BEIS	Biogenic Emissions Inventory System
b_{ext}	light extinction coefficient
BIBE	Big Bend National Park
Bndy.Cond.	Boundary Conditions
Br	Bromine
BRAVO	Big Bend Regional Aerosol and Visibility Observational Study
b_{scat}	light scattering coefficient
C	Celsius
Ca^{++}	calcium ion
Ca^{2+}	calcium ion
CAPITA MC	CAPITA Monte Carlo Model
CAPITA	Center for Air Pollution Impact and Trend Analysis
CARB	carbonyls
CASTNET	Clean Air Status and Trends Network
CDT	Central Daylight Time
CEM	continuous emissions monitoring
CIRA	Cooperative Institute for Research in the Atmosphere
Cl^-	chlorine ion
CMAQ	Community Multi-Scale Air Quality Model
CMB	Chemical Mass Balance

CMC	CAPITA Monte Carlo Model
CO	carbon monoxide
Coef.	Coefficient
Cr	Chromium
CST	Central Standard Time
CSU	Colorado State University
Cu	Copper
D/D_o	ratio of wet diameter to dry diameter
D_{50}	50^{th} percentile of particle diameters
D_{aero}	aerodynamic diameter
d_g	mass median diameter
DRH	deliquescence relative humidity
E	East
E1	Elemental carbon fraction evolved by TOR at 550 C in He & O_2
E2	Elemental carbon fraction evolved by TOR at 550-700 C in He & O_2
E3	Elemental carbon fraction evolved by TOR at 700-800 C in He & O_2
EC	elemental carbon (used interchangeably with LAC)
EDAS	ETA Data Assimilation System
EOF	empirical orthogonal function
EPA	Environmental Protection Agency
EPRI	Electric Power Research Institute
EPS	equal probability surface
Err.	Error
ETA	a weather forecast model
ETL	NOAA's Environmental Technology Laboratory
f(RH)	function of relative humidity relating wet scattering to dry scattering
FDDA	four dimensional data assimilation
Fe	iron
FMBR	Forward Mass Balance Regression
FNL	final run data archive of GDAS model
FSL	Forecast Systems Laboratory
Ft.	Fort
GDAS	Global Data Assimilation System
GMT	Greenwich Mean Time (same as UTC)
GOCART	Global Ozone Chemistry Aerosol Radiation Transport
GTS	North American Global Telecommunications Service
H	Hydrogen
HCP	high conditional probability
He	Helium
HIP	high incremental probability
HNO_3	nitric acid
hr	hour
HRT	high concentration residence time
HSC	high concentration source contribution function
HYSPLIT	HYbrid Single-Particle Lagrangian Integrated Trajectory Model
IC	ion chromatography

IL	Illinois
IMPROVE	Interagency Monitoring of Protected Visual Environments
iPPCH	perfluoro-iso-propylcyclo-hexane
ISOP	biogenic organics
ISORROPIA	a thermodynamic equilibrium model
K	Kelvin
K	Potassium
K^+	Potassium Ion
K-Bar	monitoring location within Big Bend National Park
Km	Kilometer
LA	Louisiana
LAC	light absorbing carbon (used interchangeably with EC)
LBJ	Lyndon Baines Johnson
LRT	low concentration residence time
LSC	low concentration source contribution function
m	meter
m^2/g	square meters per gram
MARS-A	a thermodynamic model used in REMSAD
MDL	minimum detection limit
MDRH	mutual deliquescence relative humidity
Mg	magnesium
Mg/yr	megagrams per year
Mg^{2+}	magnesium ion
MISS	Mississippi
mL	milliliter
mm	millimeter
Mm^{-1}	inverse megameters
MM5	Fifth-Generation Penn State/NCAR Mesoscale Model
Mn	Manganese
MO	Missouri
MOUDI	Micro-Orifice Uniform-Deposit Impactor
MRF	Medium Range Forecast model
MS	Mississippi
Mtns.	Mountains
Mts.	Mountains
MW	Megawatt
N	North
Na	sodium
Na^+	sodium ion
NaCl	sodium chloride (salt)
$NaNO_3$	sodium nitrate
NCAR	National Center for Atmospheric Research
NCDC	National Climatic Data Center
NCEP	National Center for Environmental Prediction
NE	Northeast
NEI	National Emission Inventory

ng/m^3	nanograms per cubic meter
NH_3	ammonia
NH_4^+	ammonium ion
NHS	National Historic Site
Ni	Nickel
NO_2	nitrogen dioxide
NO_3^-	nitrate ion
NOAA	National Oceanic and Atmospheric Administration
NO_x	nitrogen oxides
NP	National Park
NPS	National Park Service
NWS	National Weather Service
O	Oxygen
O1	Organic carbon fraction evolved by TOR up to 120 C in He
O2	Organic carbon fraction evolved by TOR at 120-250 C in He
O_2	Oxygen
O3	Organic carbon fraction evolved by TOR at 250-450 C in He
O4	Organic carbon fraction evolved by TOR at 450-550 C in He
Obs	observed
OC	Organic Carbon
ocPDCH	Perfluoro-1,2-dimethylcyclohexane
OLS	ordinary least squares regression
OMC	organic mass calculated using carbon measurement
OMH	organic mass calculated using hydrogen measurement
OP	Pyrolized organic carbon
ORT	overall residence time
OSC	overall source contribution function
Pb	Lead
PDCB	1,1,2,2,3,4-hexafluoro-3,4-bis(trifluoro-methyl) cyclobutane
PESA	proton elastic scattering analysis
PIXE	Proton Induced X-ray Emission
PM_{10}	particulate matter with diameter less than 10 μm
$PM_{2.5}$	particulate matter with diameter less than 2.5 μm
PMF	Positive Matrix Factorization
ppq	parts per quintillion
pred	predicted
PROFEPA	Procuraduria Federal de Proteccion al Ambiente
PTCH	Perfluoro-1,3,5-trimethylcyclohexane
PVC	poly vinyl chloride
R	Spearman rank correlation coefficient
R^2	coefficient of determination
RASS	Radio Acoustic Sounding System
READY	Realtime Applications and DisplaY system
REMSAD	Regional Modeling System for Aerosols and Deposition
RH	relative humidity
Ri	Richardson Number

RMS	root mean square
RMSE	root mean square error
S	South
S	Sulfur
S*3	Sulfur multiplied by 3 to be equivalent to sulfate ion
SD	Standard Deviation
Se	Selenium
SE	Southeast
Si	Silicon
SMOKE	Sparse Matrix Operator Kernel Emissions
SO_2	sulfur dioxide
SO_4^{2-}	sulfate ion
SSI	Spectral Statistical Interpolation
SVD	singular value decomposition
TCEQ	Texas Commission on Environmental Quality
TDMA	tandem differential mobility analyzer
TES	total elemental sulfur
Tg/yr	terragrams per year
Ti	Titanium
TOR	thermal optical reflectance
TrMB	Trajectory Mass Balance
TX	Texas
U.S.	United States
UNMIX	a receptor model
URG	University Research Glassware
USEPA	United State Environmental Protection Agency (EPA)
UTC	Coordinated Universal Time (same as GMT)
V	Vanadium
VIF	Variance Inflation Factor
VOC	Volatile Organic Carbon
W	West
XRF	x-ray florescence
z	height
Zn	Zinc